V. 121, NO. 1
JANUARY 2024

ACI STRUCTURAL JOURNAL

A JOURNAL OF THE AMERICAN CONCRETE INSTITUTE

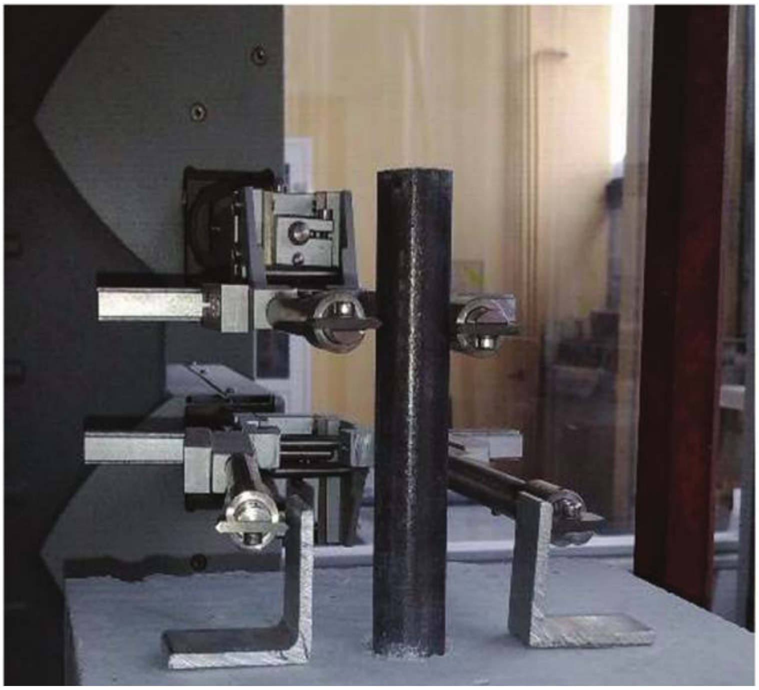

American Concrete Institute

CONTENTS

ACI STRUCTURAL JOURNAL

JANUARY 2024, V. 121, NO. 1

A JOURNAL OF THE AMERICAN CONCRETE INSTITUTE
AN INTERNATIONAL TECHNICAL SOCIETY

Contents continued on next page

Discussion is welcomed for all materials published in this issue and will appear ten months from this journal's date if the discussion is received within four months of the paper's print publication. Discussion of material received after specified dates will be considered individually for publication or private response. ACI Standards published in ACI Journals for public comment have discussion due dates printed with the Standard.

The *ACI Structural Journal* (ISSN 0889-3241) is published bimonthly by the American Concrete Institute. Publication office: 38800 Country Club Drive, Farmington Hills, MI 48331. Periodicals postage paid at Farmington, MI, and at additional mailing offices. Subscription rates: $199 per year, payable in advance. POSTMASTER: Send address changes to: *ACI Structural Journal*, 38800 Country Club Drive, Farmington Hills, MI 48331.

Canadian GST: R 1226213149.

Direct correspondence to 38800 Country Club Drive, Farmington Hills, MI 48331. Telephone: +1.248.848.3700. Facsimile (FAX): +1.248.848.3701. **Website: http://www.concrete.org.**

CONTENTS

MEETINGS

FEBRUARY

6-9—2024 PCI Convention at The Precast Show, Denver, CO, www.pci.org/PCI/News-Events/Event-Category?type=conv

8-10—The Precast Show, Denver, CO, https://precast.org/theprecastshow

11-13—Geo Week, Denver, CO, www.geo-week.com

24-25—Advanced Materials for Sustainable Infrastructure Development - Exploring Emerging Technologies for Reducing Carbon Emissions, Ventura, CA, www.grc.org/advanced-materials-for-sustainable-infrastructure-development-grs-conference/2024

MARCH

3-5—2024 ASA Shotcrete Convention and Technology Conference, Austin, TX, https://shotcrete.org/2024-asa-shotcrete-convention-and-technology-conference-online

3-7—AMPP Annual Conference + Expo, New Orleans, LA, https://ace.ampp.org/home

6-8—6th Symposium on Ultra-High Performance Concrete and High Performance Building Materials for Sustainable Construction (HiPerMat 2024), Kassel, Germany, www.uni-kassel.de/fb14bau/en/institute/institut-fuer-konstruktiven-ingenieurbau-iki/hipermat-2024

ACI CONCRETE CONVENTION: FUTURE DATES

2024—March 24-28, Hyatt Regency New Orleans, New Orleans, LA
2024—November 3-7, Philadelphia Marriott Downtown, Philadelphia, PA
2025—Mar. 30-Apr. 3, Sheraton Centre Toronto Hotel, Toronto, ON, Canada

For additional information, contact:
Event Services, ACI
38800 Country Club Drive
Farmington Hills, MI 48331
Telephone: +1.248.848.3795
email: conventions@concrete.org

ON COVER: 121-S12, p. 164, Fig. 4—Extensometer mounted at free end of plain steel bar during testing.

Contributions to *ACI Structural Journal*

The *ACI Structural Journal* is an open forum on concrete technology and papers related to this field are always welcome. All material submitted for possible publication must meet the requirements of the "American Concrete Institute Publication Policy" and "Author Guidelines and Submission Procedures." Prospective authors should request a copy of the Policy and Guidelines from ACI or visit ACI's website at **www.concrete.org** prior to submitting contributions.

Papers reporting research must include a statement indicating the significance of the research.

The Institute reserves the right to return, without review, contributions not meeting the requirements of the Publication Policy.

All materials conforming to the Policy requirements will be reviewed for editorial quality and technical content, and every effort will be made to put all acceptable papers into the information channel. However, potentially good papers may be returned to authors when it is not possible to publish them in a reasonable time.

Discussion

All technical material appearing in the *ACI Structural Journal* may be discussed. If the deadline indicated on the contents page is observed, discussion can appear in the designated issue. Discussion should be complete and ready for publication, including finished, reproducible illustrations. Discussion must be confined to the scope of the paper and meet the ACI Publication Policy.

Follow the style of the current issue. Be brief—1800 words of double spaced, typewritten copy, including illustrations and tables, is maximum. Count illustrations and tables as 300 words each and submit them on individual sheets. As an approximation, 1 page of text is about 300 words. Submit one original typescript on 8-1/2 x 11 plain white paper, use 1 in. margins, and include two good quality copies of the entire discussion. References should be complete. Do not repeat references cited in original paper; cite them by original number. Closures responding to a single discussion should not exceed 1800-word equivalents in length, and to multiple discussions, approximately one half of the combined lengths of all discussions. Closures are published together with the discussions.

Discuss the paper, not some new or outside work on the same subject. Use references wherever possible instead of repeating available information.

Discussion offered for publication should offer some benefit to the general reader. Discussion which does not meet this requirement will be returned or referred to the author for private reply.

Send manuscripts to:
http://mc.manuscriptcentral.com/aci

Send discussions to:
Journals.Manuscripts@concrete.org

LETTER FROM THE EDITOR-IN-CHIEF

As 2024 begins, we are fortunate to look back at a successful 2023 and look forward to an exciting new year. First and foremost, we thank all authors for their excellent contributions to the *ACI Structural Journal* and *ACI Materials Journal*. In 2017, ACI began a transition in journal management by appointing editorial boards. On behalf of the editorial boards, we thank the reviewers for their commitment to providing timely, high-quality reviews. We have been fortunate to have a great community of reviewers that have stepped up to provide these reviews while remaining dedicated to the high quality and success of the journals.

It is important to recognize that ACI has a phenomenal search engine that members can use to identify resources that have appeared in ACI publications (https://www.concrete.org/publications/internationalconcreteabstractsportal.aspx). The ACI journals are a great resource for ACI committees, ACI members, and students. Students are able to access these resources and more through their free membership (https://www.concrete.org/membership/becomeamember.aspx). This search engine also includes a large number of international partners. ACI has worked to inform readers of the contents of the journal when new issues of the journal are made available online and this service reaches over 27,000 members.

The editorial board has worked closely with ACI staff to institute new policies and practices for the journal. The dual-unit requirement has been eliminated to encourage the solicitation and publication of more international papers. The board has also permitted papers that are slightly longer, moving the word limit from 10,000 to 12,000 words per paper. Special issues were introduced in 2019 to provide focus on timely topics and emerging areas. Specifically, the *ACI Materials Journal* hosted special issues on pozzolans and chlorides in 2019, on computational modeling in 2020, on rheology and additive manufacturing in 2021, and on sustainability and resilience in 2023 (https://www.concrete.org/publications/acistructuraljournal/specialissues.aspx).

The board and staff have worked diligently to reduce the time to publication, reducing the average time from submission to publication from 11.2 to 8.0 months for the *ACI Structural Journal* and from 9.0 to 6.7 months for the *ACI Materials Journal*. It can also be noted that from 2014 to 2022, the impact score increased from 1.22 to 1.83 for the *ACI Materials Journal* and from 1.24 to 1.88 for the *ACI Structural Journal*.

While it is important to reflect on measures taken and their impact, it is also important to look toward the future. The editorial board is committed to continual improvement. During 2022-23, the editorial team has made several recommendations that will be implemented in 2024. First, the journals will institute associate editors for the first time. The associate editors will aid in recruiting high-quality manuscripts, providing strategic suggestions to the editorial board for journal development, and coordinating the manuscript review process. Second, ACI articles will be more prominently shared through SmartBrief.

Finally, the inaugural Editors-in-Chief, Robert Frosch for the *ACI Structural Journal* and Jason Weiss for the *ACI Materials Journal*, will complete their terms of appointment in 2023 and 2024, respectively. We want to personally thank all the authors, reviewers, editorial board members, and ACI staff for all their help throughout the last 6+ years. We are pleased to announce that Mike Kreger has been named Editor-in-Chief of the *ACI Structural Journal* and Shiho Kawashima has been named Editor-in-Chief for the *ACI Materials Journal*.

The ACI journals continue to strive to publish papers on high-quality research pertaining to civil engineering materials and structures. Specifically, ACI focuses on papers that impact practice using hypothesis-driven, high-level scientific research.

Sincerely,

Mike Kreger,
Editor-in-Chief

NOTES:

ACI STRUCTURAL JOURNAL TECHNICAL PAPER

Title No. 121-S01

Cellular Automata for Corrosion in Carbon Fiber-Reinforced Polymer-Strengthened Bridge Columns

by Jun Wang and Yail J. Kim

This paper presents the durability modeling of bridge piers subjected to corrosive environments including atmospheric, splash, and submerged conditions for a service period of 100 years. Two types of reinforced concrete columns are used—cast-in-place and accelerated bridge construction (ABC)—and their time-dependent performance is predicted by von Neumann's square lattice in conjunction with a novel evolutionary mathematics approach called cellular automata. The capacity of the corrosion-damaged columns is upgraded using carbon fiber-reinforced polymer (CFRP) sheets. Depending on the concrete strength and construction method, chloride migration mechanisms are evaluated to elucidate the variation of diffusion coefficients, chloride concentrations, and other corrosion-related issues for those columns with and without CFRP confinement. For the first 30 years, the chloride diffusion of the ABC column is slower than that of the cast-in-place column; otherwise, no difference is noticed. Under the splash condition incorporating periodic wetting-and-drying cycles, chloride concentrations remarkably increase relative to other exposure environments, particularly for the cast-in-place column. The development of corrosion current density is dominated by the pore structure of the concrete, and the corrosion initiation of the ABC column takes 4.3 times longer compared with its cast-in-place counterpart. At 100 years, the capacity of the cast-in-place and ABC columns decreases by 28.1% and 23.2%, respectively, primarily due to the impaired concrete near the degraded reinforcing bars in a corrosion influence zone. The columns' responses are enhanced by CFRP confinement in terms of toughness, energy dissipation, load-carrying capacity, and load-moment interactions.

Keywords: carbon fiber-reinforced polymer (CFRP); cellular automata; column; corrosion; model; rehabilitation; strengthening.

INTRODUCTION

Corrosion is prevalent in built environments, such as parking garages to highway bridges, and is often accompanied by a significant economic impact. It is estimated that more than 3% of the global gross domestic product (GDP), equivalent to \$2.5 trillion, is spent due to corrosion.[1] These dollar amounts could include all major aspects of design, construction, and maintenance concerning the corrosion problems of facilities. Corrosion-induced damage often leads to the failure of concrete members, especially when deicing agents are excessively used.[2] When iron-oxide residues surround steel bars, internal pressure causes cracking in the concrete cover[3] through which detrimental chemicals propagate, thereby accelerating the deterioration process, and eventually spalling the cracked concrete.[4] Partially submerged bridge columns are vulnerable to corrosion because wetting-and-drying cycles periodically supply moisture and oxygen.[5] The loss of a column section degrades both strength and ductility[6]; hence, preserving the integrity of structural configurations is an important requirement from a functional standpoint. As far as load-bearing members are concerned, accelerated bridge construction (ABC) is increasingly employed in the infrastructure community, which is a state-of-the-art concept integrating all major aspects of highway bridges. By erecting prefabricated members, transportation agencies benefit from project delivery time, on-site safety, and traffic interruption.[7] The majority of ABC-related research has been focused on seismic responses[8]; accordingly, little is known about other subjects. For example, supported by the fact that the durability of cast-in-place and ABC columns may not be the same on account of different quality control procedures, the need for investigations into corrosion-induced damage in ABC columns was raised recently.[9] Concrete patching and jacketing are traditional repair methods for impaired columns,[10] whereas the formation of incipient anodes elevates the likelihood of recurring corrosion problems.[11] In addition, those repairs are labor-intensive and demand considerable preparation for cage fabrication, form assembly, and casting.[6,12]

Wrapping with carbon fiber-reinforced polymer (CFRP) sheets is an effective approach to upgrading the capacity and ductility of a damaged column by reducing direct exposure to chlorides and minimizing potential corrosion activities in steel reinforcement.[13] When repairing columns possessing disintegrated concrete, surface preparation should be preceded with a cementitious patching material before applying CFRP to warrant even pressure distributions along the substrate.[14] It is necessary to maintain adequate contact between the concrete and CFRP; otherwise, moisture and chemicals can infiltrate into the locally debonded gap and promote corrosion in the repaired columns. Debaiky et al.[2] tested corrosion rates in reinforced concrete columns with and without CFRP wrapping. Electrochemical reactions were monitored by the half-cell potential and linear polarization resistance techniques. With one and two layers of CFRP, the corrosion current density of the columns decreased from 10 to 0.1 μA/cm^2 (65 to 0.65 μA/in.^{2}). Based on oxygen diffusion and cathodic reactions, Nossoni[3] developed an analytical model to predict the implications of CFRP wrapping in a corrosive environment. For representing actual

---

ACI Structural Journal, V. 121, No. 1, January 2024.

MS No. S-2021-149.R3, doi: 10.14359/51739181, received August 23, 2023, and reviewed under Institute publication policies. Pertinent discussion including author's closure, if any, will be published ten months from this journal's date if the discussion is received within four months of the paper's print publication.

site conditions that bring about corrosion, the core of a concrete column was assumed to contain a sufficient amount of chloride before repair. After wrapping with CFRP, a low corrosion rate was noticed in comparison to unconfined specimens, and the longevity of the column was extended. Amran et al.[15] reported moisture permeability in CFRP-wrapped concrete, which controlled the degree of corrosion. Pursuant to ASTM C1585-04,[16] permeability coefficients were measured and an empirical expression was proposed. Compared with plain concrete, the presence of CFRP layers significantly lowered the permeability, contingent upon the number of bonded layers. Although CFRP wrapping was not yet used for repairing deteriorated ABC columns, possibly due to their relatively short application history, this rehabilitation method can be applicable to such bridge elements, and a precedent assessment would be of interest.

This paper discusses the ramifications of corrosion in the simulated performance of cast-in-place and ABC columns under various exposure conditions. Cellular automata, an evolutionary mathematics approach, are adopted to simulate the intricate progression of diffusive chlorides through mutual interactions among multiple discrete entities controlling regional responses, which are instrumental in determining the global behavior of the deteriorated columns. Additionally, the efficacy of CFRP wrapping is examined with a focus on strength recovery and reductions in chloride ingress rate.

RESEARCH SIGNIFICANCE

The corrosion of pier columns has repercussions for the entire bridge system; thus, proper repair solutions are required before a catastrophic event occurs. Conventional jacketing enlarges the cross section of a damaged column to raise the capacity, relying on adhesion and friction between the original and added components[17]; by contrast, CFRP wrapping confines the column concrete and increases the strength of the core itself. As to CFRP strengthening for reinforced concrete structures, the influence of deterioration by residual chlorides (permeated before applying CFRP) and continued diffusion through the CFRP layers is not accounted for, despite the usefulness of ACI 440.2R-17.[14] Published literature concerning CFRP-confined concrete subjected to chloride-induced corrosion emphasizes experimental investigations into the material characteristics and axial load-bearing capacities of laboratory-scale specimens[2,18]; as a result, scarce information is available on the full-range behavior of load-moment interactions. Given that corrosion is critical for existing members, regardless of construction method, the durability of cast-in-place and ABC columns needs to be appraised as well.

BENCHMARK COLUMN

Pursuant to the American Association of State Highway and Transportation Officials (AASHTO) Load and Resistance Factor Design (LRFD) Bridge Design Specifications (BDS),[19] a simulated two-column bridge pier is designed to support a two-span concrete box-girder bridge. Described in the following subsections are the materials and structural details of the column exposed to aggressive service environments, and a CFRP-strengthening technique for restoring a capacity loss caused by corrosion damage.

Outline and parameters

The benchmark column was a circular shape with a diameter of $\phi = 1070$ mm (3.5 ft) at a length of 5.3 m (17.5 ft). Each of No. 14 Grade 60 reinforcements ($d_b = 43$ mm [1.69 in.], where d_b is the nominal diameter, with a yield strength of $f_y = 414$ MPa [60 ksi]) had a cross-sectional area of $A_s = 1452$ mm^2 (2.25 in.^{2}), and 12 reinforcing bars were distributed around the column section (Fig. 1(a)). It was assumed that transverse ties were adequately placed to prevent the local buckling of the longitudinal reinforcing bars. In view of practical significance, a variable range of concrete strength was used from $f_c' = 30$ to 45 MPa (4350 to 6530 psi). Table 1 enumerates the ingredients of the concrete mixtures based on ACI 211.1-91,[21] which were necessary for modeling chloride migration. The cover depth of the column (Table 2) was assigned as specified in AASHTO LRFD BDS[19] along with modification factors in relation to the water-cement ratio (w/c) of the concrete (Table 1). Regarding the construction of the column, the cast-in-place and ABC methods were taken into consideration.

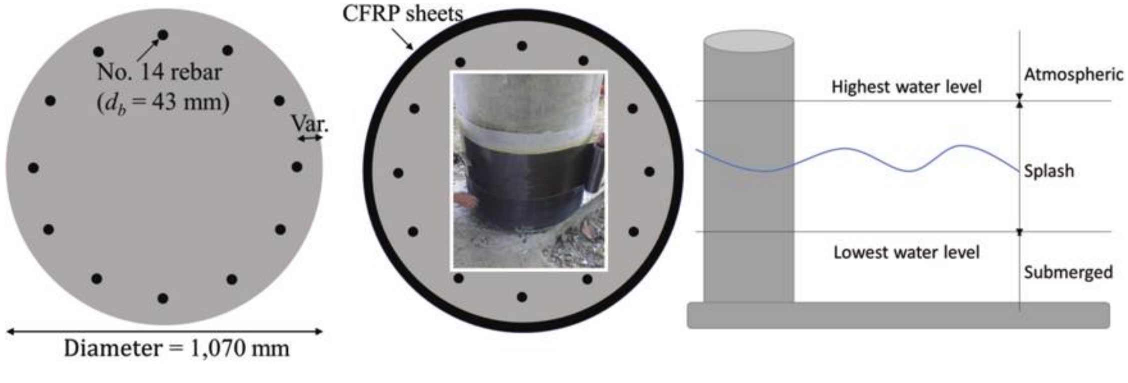

(a) (b)

[1 mm = 0.0394 in.]

Fig. 1—Benchmark column: (a) dimensions and strengthening scheme (picture[20] used with permission, American Concrete Institute); and (b) service environments.

Service condition

In compliance with NACE SP0176-2007,[22] the column was exposed to three service environments: atmospheric, splash, and submerged zones (Fig. 1(b)). The atmospheric zone is not wet, but airborne chlorides permeate the column concrete. The splash zone suffers from the continual fluctuation of water level, accelerating the adverse consequences of wetting-and-drying cycles in tandem with capillary suction and diffusion.[23] The submerged zone is permanently saturated, and electrochemical reactions among chlorides, electrolytes, and dissolved oxygen facilitate a corrosion process.[24] The performance of the column under those simulated corrosive environments was examined for 100 years, which can fully cover the design life of 75 years in AASHTO LRFD BDS.[19] It is worth noting that the 75-year design life was conservatively taken because the actual service life of bridge structures is generally longer than 100 years.[25]

Table 1—Details of concrete mixture

Component	Compressive strength, MPa			
	30	35	40	45
w/*c*	0.54	0.47	0.42	0.37
Water, kg/m^3	193	193	193	193
Cement, kg/m^3	358	406	455	524
Coarse aggregate, kg/m^3	1144	1144	1144	1144
Fine aggregate, kg/m^3	679	639	597	539

Note: 1 MPa = 145 psi; 1 kg/m^3 = 0.062 lb/ft^3.

CFRP strengthening

The provisions of ACI 440.2R-17[14] were referenced to strengthen the corrosion-damaged column

$$f_{cc}' = f_c' + \psi_f 3.3\kappa_a f_l \tag{1}$$

$$f_l = \frac{2E_f n t_f \varepsilon_{fe}}{\phi} \tag{2}$$

where f_{cc}' is the compressive strength of the confined concrete; ψ_f is the reduction factor ($\psi_f = 1$ for a nominal capacity prediction); κ_a is the efficiency factor ($\kappa_a = 1$ for a circular section); f_l is the confining pressure; E_f, n, and t_f are the elastic modulus, number of plies, and thickness of CFRP,

Table 2—Modeling parameters

Concrete strength f_c', MPa	Construction method	Service environments	Concrete cover c, mm	Diffusion coefficient $D(0)$, $\times 10^{-12}$ m^2/s	Age parameter, η	Surface chloride C_0, % wt. of cement	Corrosion initiation year t_i, years
30	CIP	Atmospheric	125	4.29	0.19	1.33	54.1
		Splash	125	6.43	0.019	$1.65t^{0.484}$	8.9
		Submerged	125	10.72	0.114	3.31	9.6
	ABC	Atmospheric	125	1.00	0.19	1.33	232.8
		Splash	125	2.30	0.019	$1.65t^{0.484}$	25.8
		Submerged	125	3.97	0.114	3.31	25.9
35	CIP	Atmospheric	100	3.15	0.295	1.17	55.6
		Splash	100	4.72	0.03	$1.37t^{0.484}$	8.8
		Submerged	100	7.87	0.177	2.93	9.1
	ABC	Atmospheric	100	0.73	0.295	1.17	238.9
		Splash	100	1.69	0.03	$1.37t^{0.484}$	25.5
		Submerged	100	2.91	0.177	2.93	24.5
40	CIP	Atmospheric	100	2.41	0.37	1.05	85.7
		Splash	100	3.62	0.037	$1.17t^{0.484}$	11.9
		Submerged	100	6.03	0.222	2.63	12.8
	ABC	Atmospheric	100	0.56	0.37	1.05	368.4
		Splash	100	1.29	0.037	$1.17t^{0.484}$	34.3
		Submerged	100	2.23	0.222	2.63	34.7
45	CIP	Atmospheric	85	1.75	0.445	0.92	108.3
		Splash	85	2.63	0.045	$0.97t^{0.484}$	12.7
		Submerged	85	4.38	0.267	2.29	14.2
	ABC	Atmospheric	85	0.41	0.445	0.92	465.7
		Splash	85	0.94	0.045	$0.97t^{0.484}$	36.7
		Submerged	85	1.62	0.267	2.29	38.3

Note: CIP is cast-in-place; 1 MPa = 145 psi; 1 mm = 0.0394 in.; 1 m = 3.28 ft.

respectively; and ε_{fe} is the effective CFRP strain ($\varepsilon_{fe} = 0.55\varepsilon_{fu}$, in which ε_{fu} is the rupture strain). Commercially available CFRP sheets, consisting of unidirectional carbon fibers and an epoxy resin, were used with the following properties: ultimate strength (f_{fu}) = 3800 MPa (550 ksi), E_f = 227 GPa (32,900 ksi), ε_{fu} = 0.0167, and t_f = 0.165 mm (0.0065 in.). The damaged column was confined at a capacity loss of 10%, and the strengthening effect was maintained up to 100 years (illustrative explanations will be given).

THEORETICAL MODELING

A modeling approach is elaborated on the initiation and progression of corrosion in the benchmark column and corresponding structural responses. The interdependency of axial load and bending moment is delineated for the prediction of the column capacity when linked with unfavorable operational environments.

Cellular automata

Cellular automata are a branch of computational mathematics which are intended to understand the complexity of discrete dynamical systems.[26] The architecture of cellular automata comprises an array of multiple grids in a finite dimension, responding to a preset rule that defines a relationship between adjacent cells. With an increase in time, the assembled cohort evolves with the absence of a governing entity at the global level (that is, the engagement of the constituting cells is completely autonomous), and a generalized pattern is manifested. For the present numerical study, the von Neumann neighborhood with orthogonal cells[27] was chosen to simulate the migration of chlorides in the column concrete. Further information on the development, principle, and application of cellular automata is available elsewhere.[28,29]

Chloride diffusion

Kinetics—Diffusive interactions among discrete cells may be represented by Fick's second law

$$\frac{\partial C}{\partial t} = D\frac{\partial^2 C}{\partial^2 x^2} \tag{3}$$

where C is the chloride concentration at position x and time t; and D is the diffusion coefficient. Conforming to the von Neumann's square lattice (Fig. 2(a)), the concentration of the center cell at time $t + 1$ ($C_{x,y}(t + 1)$) can be estimated by[30]

$$C_{x,y}(t+1) = \Phi_1 C_{x,y}(t) + \Phi_2 C_{x,y-1}(t) + \Phi_3 C_{x+1,y}(t) + \Phi_4 C_{x,y+1}(t) + \Phi_5 C_{x-1,y}(t) \tag{4}$$

$$\sum_{i=1}^{5}\Phi_i = 1 \tag{5}$$

where x and y are the abscissa and ordinate of the two-dimensional space, respectively; and Φ_i is the evolutionary coefficient satisfying the principle of mass conservation (Eq. (5)). Assuming that the progression of chlorides is isotropic,[31] $\Phi_1 = 0.5$ for $C_{x,y}$ and $\Phi_{2,3,4,5} = 0.125$ are suggested with Eq. (6)[30]

$$\Delta t = \Phi_i\frac{\Delta s}{D} \tag{6}$$

where Δt is the time step; and Δs is the size of the cell. The outbound coefficient Φ_6 from the center cell ($C_{x,y}$) is obtained by $\Phi_6 = (1 - \Phi_1)/4$. The initial and time-dependent diffusion coefficients ($D(0)$ and $D(t)$, respectively) of ordinary concrete may be determined by[32,33]

$$D(0) = ke^{(-\sqrt{10/wc})} \tag{7}$$

$$D(t) = D_e(0)t^{-\eta} \tag{8}$$

$$\eta = k_a(1 - 1.5wc) \tag{9}$$

where k and k_a are the service environment and adjustment factors, respectively (k = 10,000 mm^2/year [15.5 in.^{2}/year] and k_a = 1.0 for atmosphere, k = 15,000 mm^2/year [23.3 in.^{2}/year] and k_a = 0.1 for splash, and k = 25,000 mm^2/year [38.8 in.^{2}/year] and k_a = 0.6 for submerged conditions); $D_e(t)$ is the diffusion coefficient under a specific exposure environment; and η is the age coefficient. Considering the different curing conditions of concrete between the cast-in-place and ABC columns, Eq. (10) is adopted

$$D_e(0) = k_c D(0) \tag{10}$$

where k_c is the curing factor (k_c = 1 for the concrete that is moisture-cured for 28 days, representing ABC members, and k_c = 4.3, 2.8, and 2.7 for the cast-in-place concrete [cured under a typical site condition at a relative humidity of 40 to 50% and 19 to 23°C (66 to 73°F)]) that is subsequently exposed to atmospheric, splash, and submerged conditions, respectively.[34]

Simulation space—The functional mapping of the cellular automata is depicted in Fig. 2(a). A total of 164,000 agents were employed for the circular column (160,000 agents) and the surrounding environment (4000 agents). The size of the individual agents (4 x 4 mm [0.16 x 0.16 in.]) was figured out by sensitivity analysis, as shown in Fig. 2(b), where converged chloride gradients are visible across the column section (details on the corrosion properties will follow). One of the notable advantages of the proposed approach is that it can overcome the limitation of conventional finite difference modeling; specifically, such a simplified simulation handles one-dimensional chloride migration without taking into account mutual interactions among multiple agents in the radial direction.[35] Figure 2(c) compares the chloride contents of these methods in the column section. Unlike the one-dimensional case showing a monotonic decrease, the two-dimensional model revealed more chloride contents owing to the synergistic reciprocity. The simulation results given in Fig. 2(d) display the multidirectional ingress of chlorides up to 100 years.

Validation—The aforementioned approach was validated against other research programs.[36-39] According to the properties listed in Table 3, chloride contents were computed at the respective chloride exposure times and locations denoted in the cited literature (Fig. 3). It should be noted that, for the purpose of consistency, the units of the contents were intentionally kept as presented in the literature. In spite of the marginal differences possibly due to randomly dispersed aggregates in the concrete specimens, the prediction was sufficiently close to the collated data.

Corrosion

Initiation—The corrosion initiation of the column may be attained by[40,41]

$$t_i = \frac{(c/10)^2}{4D}\left(\mathrm{erf}^{-1}\left(\frac{C_{cr}-C_0}{C_i-C_0}\right)\right)^{-2}$$

for atmospheric and submerged conditions (11a)

$$t_i = \left(\frac{\ln(1.08 i_{corr}) - 8.37 - 0.618\ln 1.69 C_f(t) + 3034/T + 0.000105 R_c}{2.32}\right)^{0.215}$$

for splash (11b)

where t_i is the initiation time; c is the concrete cover in mm; erf is the Gauss error function; C_{cr} and C_i are the critical and initial chloride concentrations, respectively (C_{cr} = 0.4% and C_i = 0% of the cement weight[42]); C_0 is the surface chloride concentration; i_{corr} is the corrosion current density (i_{corr} = 0.3 μA/cm^2 [1.94 μA/in.^{2}] was adopted[43]); C_f is the free chloride concentration at the reinforcing bar level in kg/m^3; T is the absolute temperature at the surface of the reinforcing bar in Kelvin (T = 293.15 K); and R_c is the resistance of the cover concrete in ohms (R_c = 1500 ohms). For the atmospheric and submerged conditions, the surface chlorides were assumed to be constant (C_0 = 0.2% and 0.5% of the concrete weight, respectively[44]); however, for the splash exposure, variable chlorides were considered to reflect

Table 3—Properties used for model validation

Reference	Surface chloride	Diffusion coefficient, m^2/s
Cao et al.[36]	0.5% wt. of concrete	3.22×10^{-12}
Titi and Biondini[37]	3% wt. of concrete	1×10^{-11}
Wang et al.[38]	$1.95(t/360)^{1.28715}$ mg/g*	$2.588(360/t)^{-0.9574} \times 10^{-13}$
Yin and Pan[39]	2% wt. of binder	$1.38(28/t)^{-0.53} \times 10^{-13}$

*Mass of chloride ions per mass of cementitious binder.

Note: t is time in days. 1 g = 0.0022 lb; 1 m = 3.28 ft.

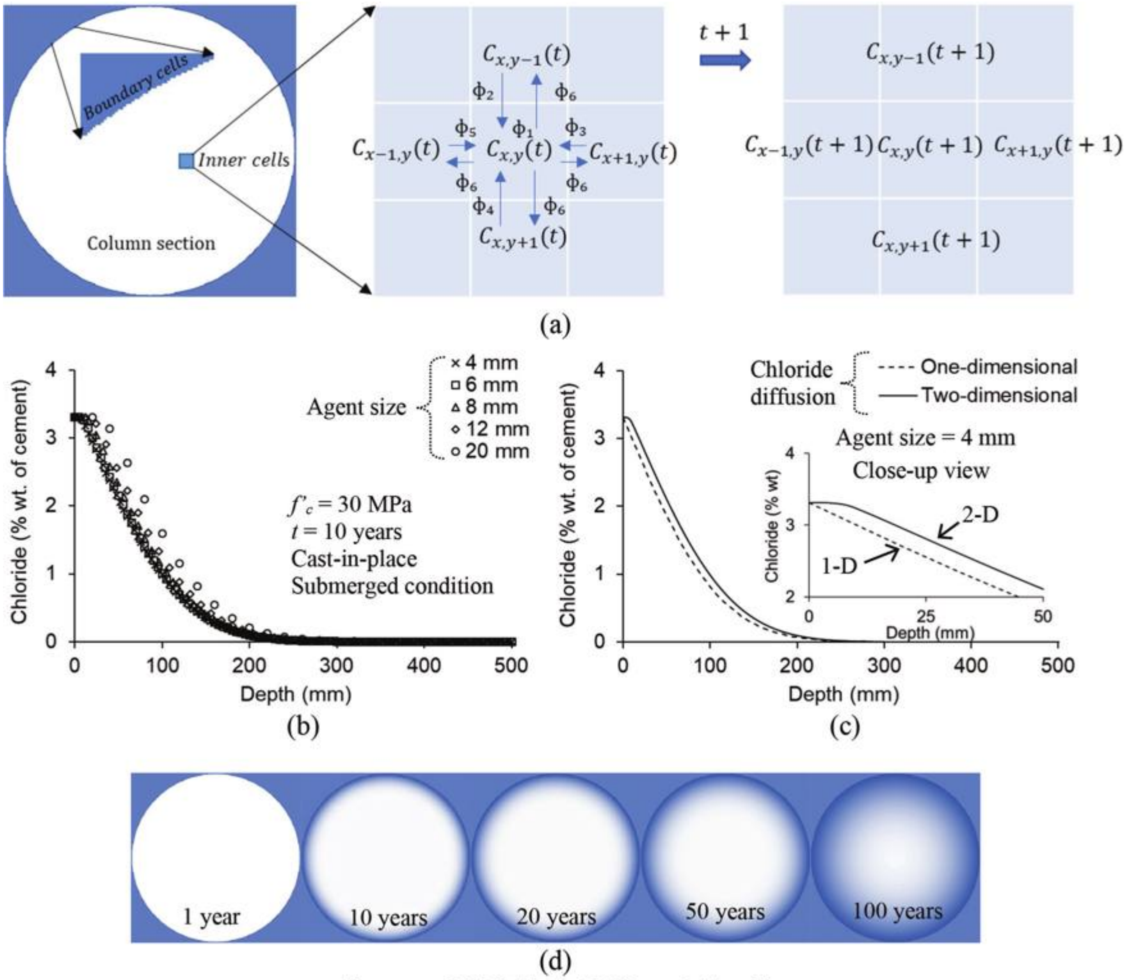

[1 mm = 0.0394 in.; 1 MPa = 145 psi]

Fig. 2—Two-dimensional cellular automata for benchmark column: (a) configuration of von Neumann's square lattice; (b) sensitivity analysis; (c) proposed versus conventional approaches; and (d) simulated chloride migration in cast-in-place column with concrete strength = 30 MPa under submerged condition.

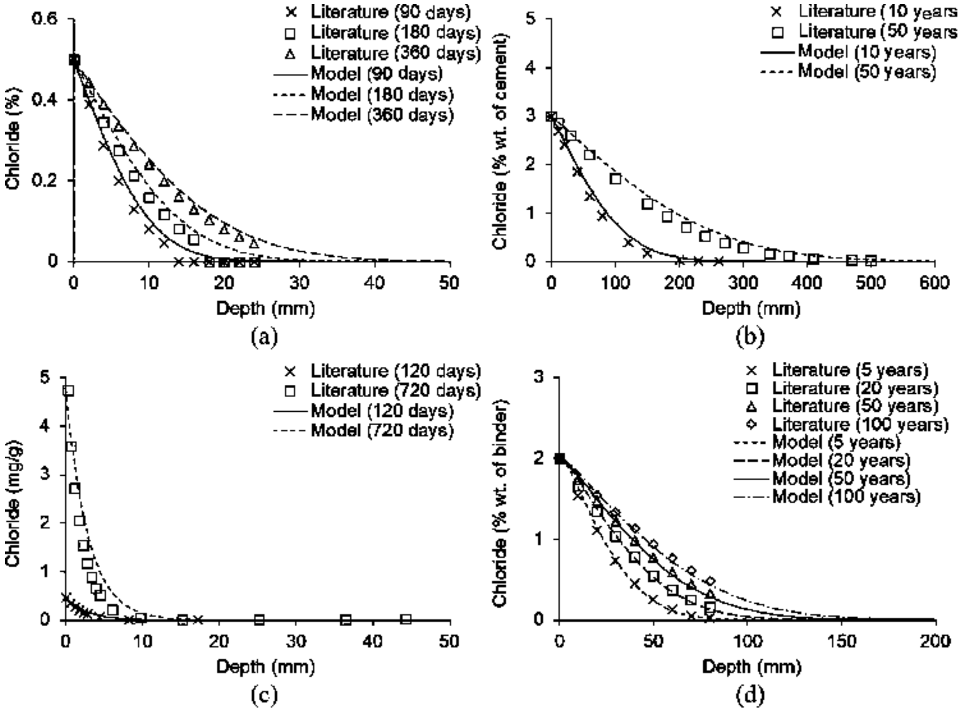

[1 mm = 0.0394 in.; 1 g = 0.0022 lb]

Fig. 3—Validation of modeling approach: (a) Cao et al.[36]; Titi and Biondini[37]; (c) Wang et al.[38]; and (d) Yin and Pan.[39]

periodic wetting-and-drying cycles with time t in years alongside the percent weight of the concrete[45,46]

$$C_0(t) = (0.213wc + 0.134)t^{0.484} \tag{12}$$

Progression—Upon initiation of corrosion damage, the cross-sectional area of the reinforcement is reduced[47]

$$d_b(t) = d_{b0} - 0.0232(t - t_i)i_{corr} \tag{13}$$

where $d_b(t)$ and d_{b0} are the diameters of the reinforcing bar at time t and its initial counterpart, respectively. The corrosion current density (i_{corr}) with increasing corrosion time t in years may be calculated using Eq. (14), which originated from 2927 measured data at the surface of steel reinforcing bars for up to 5 years of outdoor exposure[41]

$$\ln(1.08i_{corr}) = 8.37 + 0.618\ln 1.69C_f(t) - (3034/T) - 0.000105R_c + 2.32t^{-0.215} \tag{14}$$

Although Eq. (14) is comprehensive, several limitations are acknowledged because it did not account for geometry, oxygen availability, the dynamic nature of corrosion, and other factors that influence corrosion rate. Because the free chlorides (C_f) affect the progression of corrosion, the total chlorides imparted from the cellular automata model (C_t) in kg/m^3 need to be converted[48]

$$C_f = 0.8541C_t \tag{15}$$

When the column is wrapped with CFRP, the ingress of chlorides is impeded, and previous research demonstrates that the magnitude of the current density decreases by one-third.[49]

Impaired concrete—The volumetric expansion of the corroded reinforcing bars weakens the cover concrete of the column. For modeling convenience, the occurrence of cracking and spalling is frequently replaced by the equivalent compressive strength ($f_c^*(t)$) of the cover concrete[50,51]

$$f_c^*(t) = \frac{f_c'}{1 + k^*\varepsilon_1(t)/\varepsilon_{co}} \tag{16}$$

where k^* is the characteristic coefficient ($k^* = 0.1$); ε_{co} is the strain at the peak stress of the concrete ($\varepsilon_{co} = 0.002$); and $\varepsilon_1(t)$ is the average tensile strain of the cracked concrete[51]

$$\varepsilon_1(t) = (n_b W_{cr}(t))/\phi \tag{17}$$

where n_b is the number of reinforcing bars in compression; and $W_{cr}(t)$ is the average crack width in mm[52]

$$W_{cr}(t) = K(\Delta A_s(t) - \Delta A_{so}) \tag{18}$$

where K is an empirical factor ($K = 0.00575$/mm); $\Delta A_s(t)$ is the cross-sectional loss of the reinforcing bars in mm^2; and ΔA_{so} is the loss of the reinforcing bar section in mm^2 when the column concrete cracks

$$\Delta A_{so} = A_{so}\left(1 - \left(1 - \frac{\alpha_p}{d_{bo}}x_0 10^{-3}\right)^2\right) \tag{19}$$

where A_{so} is the cross-sectional area of the intact steel reinforcing bars; α_p is the pitting factor ($\alpha_p = 2$ for uniform corrosion); and x_0 is the corrosion penetration in μm associated with cover depth c in mm[53]

$$x_0 = 7.53 + 9.32(c/d_{b0}) \tag{20}$$

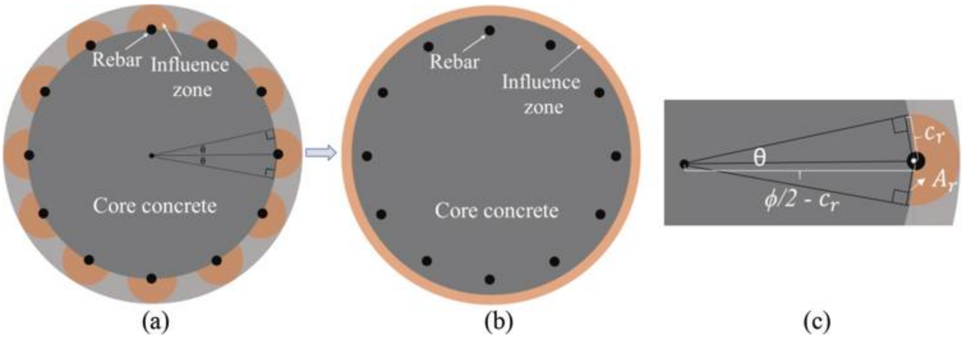

Fig. 4—Cover-strength reduction: (a) spalling and cracking zones; (b) equivalent area; and (c) geometric details.

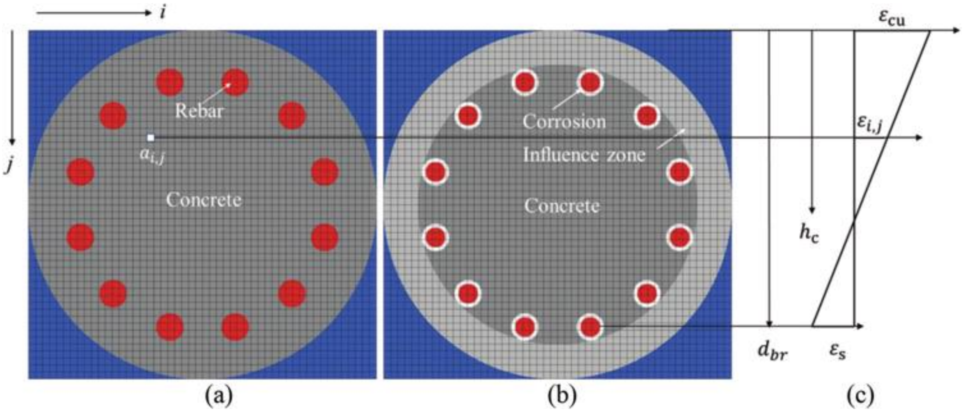

Fig. 5—Sectional model: (a) intact column; (b) corrosion-damaged column; and (c) strain profile.

The pitting type of corrosion in Eq. (19) is attributed to the interaction between the chloride ions (Cl^-) and iron hydroxide ($Fe(OH)_2$), which generates autocatalytic reactions.[54]

Structural model

Load-bearing—The nominal capacity of the column ($P_n(t)$) under axial compression is calculated

$$P_n(t) = 0.85[A_s(t)f_y + 0.85(f_c'(A_g - A_s(t) - A_{iz}) + f_c^*(t)A_{iz})] \tag{21}$$

$$A_{iz} = n_b\left(\frac{(360° - 2(90° - \theta°))}{360°}\pi c_r^2 - 2A_r\right) \tag{22}$$

$$A_r = \frac{\pi(\phi/2 - c_r)^2\theta°}{360°} - \frac{c_r^2/\tan\theta°}{2} \tag{23}$$

$$\sin\theta° = \frac{c_r}{\phi/2 - c_r} \tag{24}$$

where A_g is the gross cross-sectional area of the column; A_{iz} is the area of the influence zone for $f_c^*(t)$ in Eq. (16) (Fig. 4(a) and (b)); n_b is the number of reinforcing bars; c_r is the distance from the concrete surface to the reinforcing bar center; A_r is the difference between the arc and triangular areas (Fig. 4(c)); and θ is the angle of the component triangle in degrees. As noted earlier, the equivalent strength of $f_c^*(t)$ in the influence zone (A_{iz}) is activated when the concrete cracks, and the reduced strength reflects the accelerated chloride ingress in the cracked column.

The axial capacity of the column is independently computed by the cellular automata model (Eq. (25)) and verified against Eq. (21)

$$P_n(t) = \begin{pmatrix} \sum_{j=1}^{j=n_c}\sum_{i=1}^{i=n_c}\sigma_{c,i,j}(t) + \\ \sum_{j=1}^{j=n_s}\sum_{i=1}^{i=n_s}\sigma_{s,i,j}(t) \end{pmatrix} A_a \tag{25}$$

where i and j are the abscissa and ordinate, respectively, in Fig. 5(a); n_c and n_s are the number of agents for the concrete and steel reinforcement, respectively; A_a is the area of a single agent; and $\sigma_{c,i,j}(t)$ and $\sigma_{s,i,j}(t)$ are the stress in the concrete and steel, respectively

$$\sigma_{c,i,j}(t) = f_{c,i,j}'\left[\frac{2\varepsilon_{c,i,j}(t)}{\varepsilon_{co}} - \left(\frac{\varepsilon_{c,i,j}(t)}{\varepsilon_{co}}\right)^2\right] \tag{26}$$

$$\sigma_{s,i,j}(t) = \varepsilon_{s,i,j}(t)E_s \leq \sigma_y \tag{27}$$

where $f_{c,i,j}'$ is the compressive strength of the concrete agent $a_{c,i,j}$ at time t (f_c' and $f_c^*(t)$ are used for the core and the impaired area, respectively, in Fig. 4); E_s and σ_y are the elastic modulus and yield strength of the steel (E_s = 200 GPa [29,000 ksi] and σ_y = 414 MPa [60 ksi]); $\varepsilon_{c,i,j}(t)$ is the strain of $a_{c,i,j}$; and $\varepsilon_{s,i,j}(t)$ is the strain of the steel agent $a_{s,i,j}$ (Fig. 5(a) to (c)). The moment capacity of the column ($M_n(t)$) is expressed in a similar manner

$$M_n(t) = \begin{pmatrix} \sum_{j=1}^{j=n_c}\sum_{i=1}^{i=n_c}\sigma_{c,i,j}(t) + \\ \sum_{j=1}^{j=n_s}\sum_{i=1}^{i=n_s}\sigma_{s,i,j}(t) \end{pmatrix} A_a\left(\frac{\phi}{2} - j_a\right) \tag{28}$$

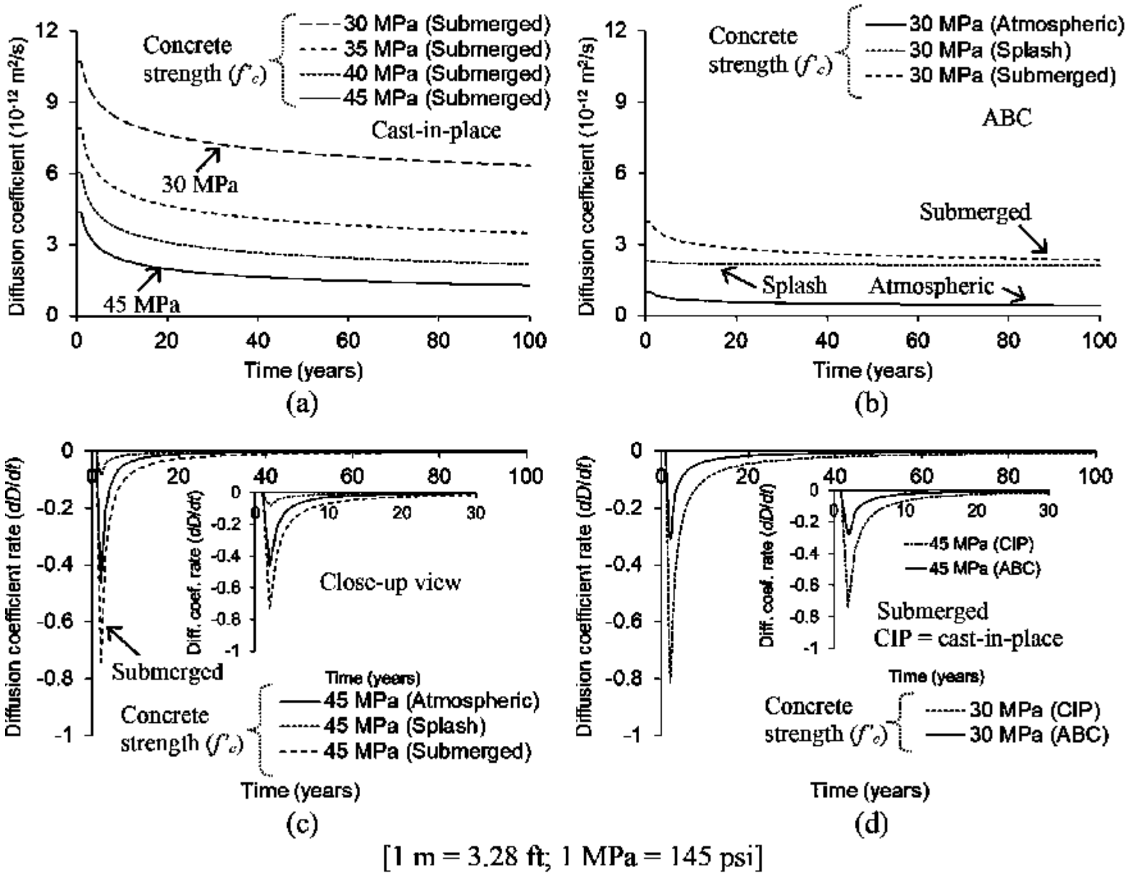

Fig. 6—Diffusion coefficient: (a) cast-in-place column with concrete strength; (b) ABC column with service environment; (c) rate in cast-in-place column with service environment; and (d) comparison of rates between cast-in-place and ABC columns under submerged condition.

where j_a is the ordinate of the agent.

Interaction diagram—The capacity of the column can be obtained under compression (P_n) and flexural (M_n) loadings. The pure compression of the section is associated with the uniform strain of $\varepsilon_{cu} = 0.003$, in which ε_{cu} is the maximum usable strain of concrete.[55] For other general cases, the steel strain at the bottom of the section (ε_s in Fig. 5(c)) is incremented and, then, the aforementioned $\varepsilon_{i,j}$ strain is determined

$$\varepsilon_{i,j} = \frac{(\varepsilon_s + \varepsilon_{cu})\left(\frac{\varepsilon_{cu}}{\varepsilon_{cu} + \varepsilon_s} d_{br} j_a\right)}{d_{br}} \tag{29}$$

where d_{br} is the distance from the top of the section to the bottom reinforcing bar (Fig. 5(c)). For the CFRP-confined column, the interaction diagram may be constructed in accordance with the procedure explained in ACI 440.2R-17.[14] To accommodate the equivalent compressive strength (Eq. (16)) within the influence zone (A_{iz}), the unconfined concrete strength (f_c') in Eq. (1) is replaced by

$$f_i'(t) = (f_c'(A_g - A_s(t) - A_{iz}) + f_c^*(t)A_{iz})/A_g \tag{30}$$

where f_i' is the adjusted concrete strength for CFRP confinement with corrosion damage.

IMPLEMENTATION

The durability of cast-in-place and ABC columns, predicted by discrete computational cellular automata models, is expounded from material and structural points of view. Emphasis is placed on the diffusivity of chlorides, consequences of corrosion, and the efficaciousness of CFRP strengthening.

Chloride migration

Diffusion—The coefficients of chloride diffusion are provided in Fig. 6(a) and (b) for the cast-in-place and ABC columns, respectively. The exponentially diminishing coefficients illustrate that the concrete pores became partially clogged by surplus chlorides over time; in other words, the permeated chlorides reduced the effective porosity of the cement binder.[56] As the compressive strength of the concrete was increased from 30 to 45 MPa (4350 to 6530 psi), the flux of the chlorides noticeably dropped (Fig. 6(a)). This observation aligns with the fact that greater hydration in concrete leads to a strength gain and decreases the size of micropores; consequently, the transport of chloride ions in the electrolytes is retarded.[57,58] Compared with the cast-in-place column, the diffusion coefficient of the ABC column was lower (Fig. 6(b)) and the submerged condition showed a consistently higher coefficient than other environments, owing to the increased conductivity of the pore solution.[59] Likewise, the rate of the diffusion coefficient rapidly developed under the submerged

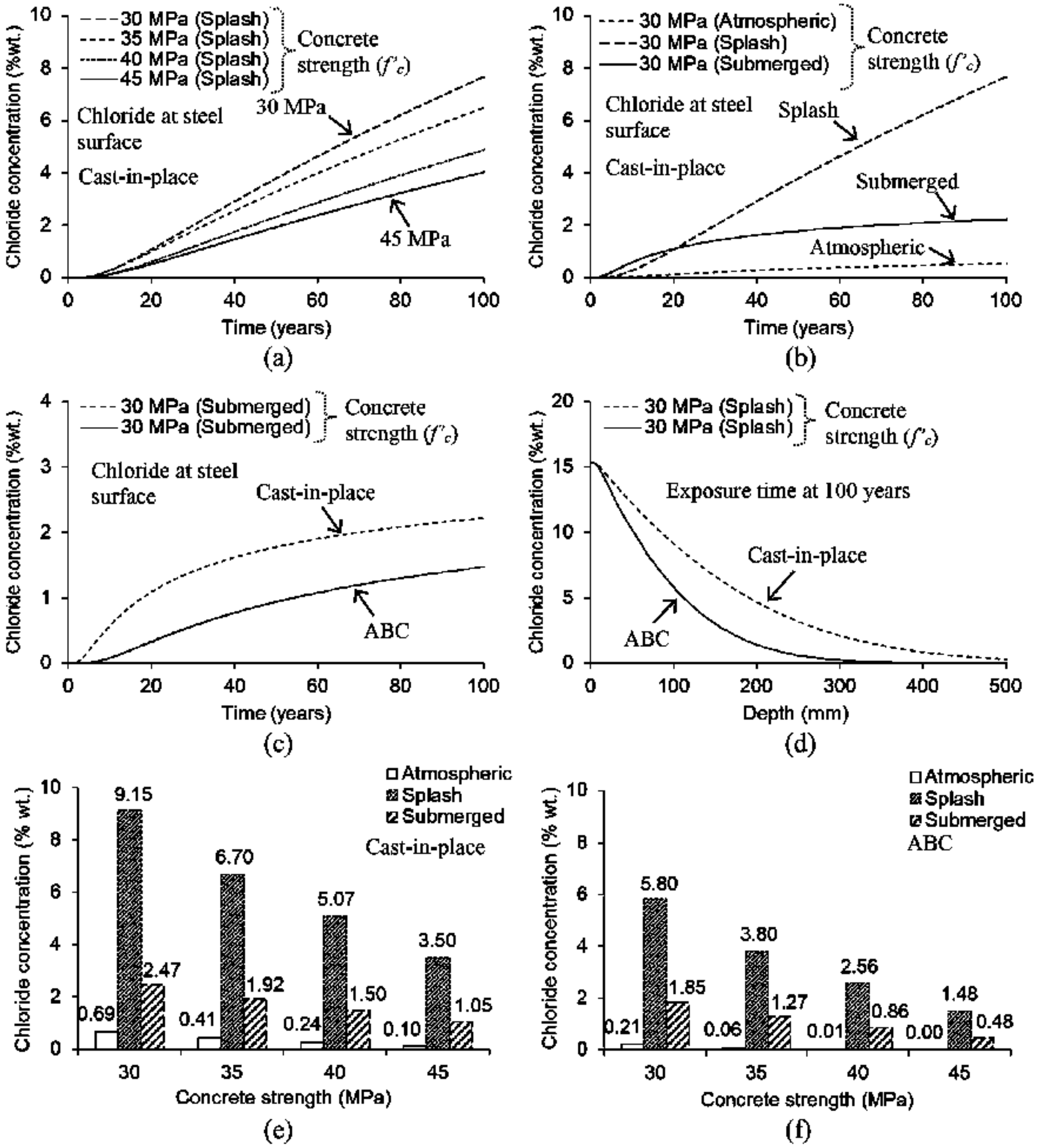

[1 mm = 0.0394 in.; 1 MPa = 145 psi]

Fig. 7—Chloride concentration: (a) cast-in-place column with concrete strength; (b) cast-in-place column under variable environments; (c) cast-in-place versus ABC columns with time; (d) cast-in-place versus ABC columns across concrete; (e) cast-in-place column at 100 mm from surface; and (f) ABC column at 100 mm from surface.

condition for the cast-in-place column (Fig. 6(c)), whereas marginal differences were noted among the three environments after 30 years (Fig. 6(c), inset). Shown in Fig. 6(d) is a comparison between the diffusion coefficient rates of the cast-in-place and ABC columns. Irrespective of concrete strength (f_c' = 30 and 45 MPa [4350 and 6530 psi]), the ABC column outperformed, and its peak rates were 37% of those of the cast-in-place column, on average.

Concentration—The chloride concentrations of the cast-in-place column at the level of the steel surface are plotted in Fig. 7(a) and (b), dependent upon concrete strength and exposure condition, respectively. The ingress of chlorides in the column with f_c' = 30 MPa (4350 psi) was 1.9 times relative to the case with f_c' = 45 MPa (6530 psi) at 100 years (Fig. 7(a)). The high *w/c* of the low-strength concrete (Table 1) allowed more chlorides on account of the increased permeability.[60] In regard to the environmental exposure (Fig. 7(b)), the concentration was prominent under the splash condition because the wetting-and-drying cycles expedited the sorptivity of the concrete.[61] As concrete resistance to chlorides declines when saturated,[62] the asymptotic concentration curve under the submerged condition was graphed above the curve under the atmospheric condition. It is worth noting that, even if both were subjected to water, the mechanisms of chloride progression under the splash and submerged conditions differed: the former was based on absorption and capillary suction, while the latter was related to pure diffusion caused by a concentration gradient in the electrolyte across the column.[63]

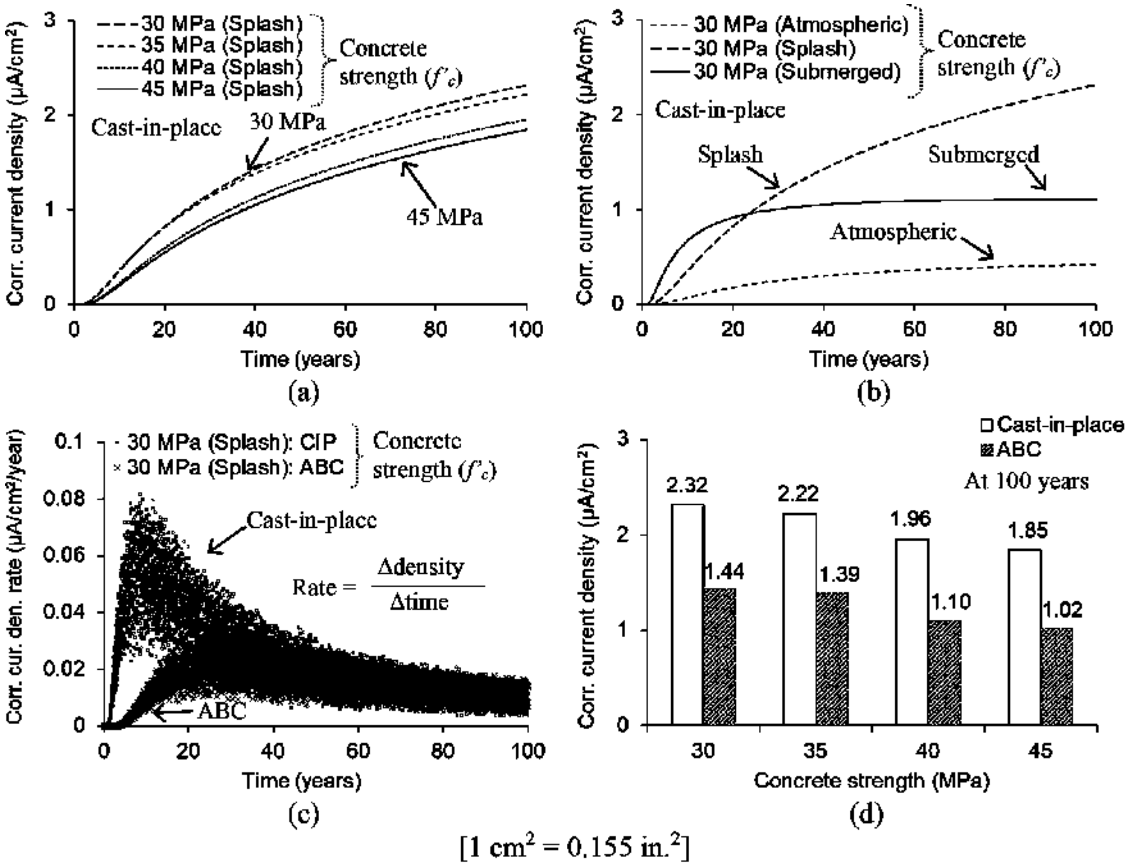

Fig. 8—Corrosion current density at surface level of reinforcement: (a) cast-in-place column with concrete strength; (b) cast-in-place column under variable environments; (c) cast-in-place versus ABC columns with time; and (d) comparison at 100 years.

Figure 7(c) exhibits the elevation of chloride concentrations in the cast-in-place and ABC columns under the submerged condition. The response slope of the cast-in-place column was steep up to 12 years, followed by a transition to the gradually rising concentrations. Except for the distinguishable development trend between 0 and 30 years, the slopes of these column categories were virtually identical, meaning that the superior durability of the ABC column was due to the betterment of its performance during the relatively early ages. For this reason, the ABC column allowed less chlorides inside the concrete (Fig. 7(d)). A comprehensive summary of the chloride concentrations at a depth of 100 mm (4 in.), the average cover of the columns, is charted in Fig. 7(e) and (f). The use of ABC was beneficial for all occasions, especially under the splash condition.

Effects of corrosion

Corrosion current density—The ascending pattern of the corrosion current density was a function of the concrete strength (Fig. 8(a)), which is concerned with the connectivity of the micropores that dominates the transport of chloride ions.[56] The difference in the initial diffusion coefficient ($D(0)$ in Table 2) was responsible for the grouping of the densities above and below the concrete strength of $f_c' =$ 40 MPa (5800 psi). Figure 8(b) reaffirms that the alternate cycles of saturation and desiccation raised the conductivity of the micropores with the dissolved chloride ions,[64] thereby lessening the resistivity of the column concrete under the splash condition (that is, the increased corrosion rate). Such a prediction, however, does not necessarily signify invariant local conductivity because the activation energy of the concrete oscillated as per the degree of saturation.[31] The evolution tendency of the current density under the submerged condition in Fig. 8(b) clarifies the importance of continued oxidation for the electrochemical process of corrosion: the plateau-like response was attributable to the limited supply of oxygen in the pores that partially filled with chlorides, which slowed down cathodic reactions.[65] Shown in Fig. 8(c) are the corrosion current densities normalized by time. The growth rate of the density for the cast-in-place column was more rapid than the rate for the ABC column, whereas their dissimilarity disappeared after 40 years. It is thus stated that the high current density of the cast-in-place column (Fig. 8(d)) was the result of the accelerated rate before the 40-year alteration time.

Detrimental consequences—Figure 9(a) demonstrates the corrosion initiation year of the cast-in-place column. Under the splash and submerged conditions that were linked with direct contact with water, the initiation time was 11 years, on average. Contrarily, the initiation time under the atmospheric condition was longer than 54 years and the case with a concrete strength higher than 40 MPa (5800 psi) would not corrode within the 75-year design life of AASHTO LRFD BDS.[19] The corrosion initiation of the ABC column took substantially longer, up to 4.3 times that of the cast-in-place column (Fig. 9(b)). Once the columns corroded, the

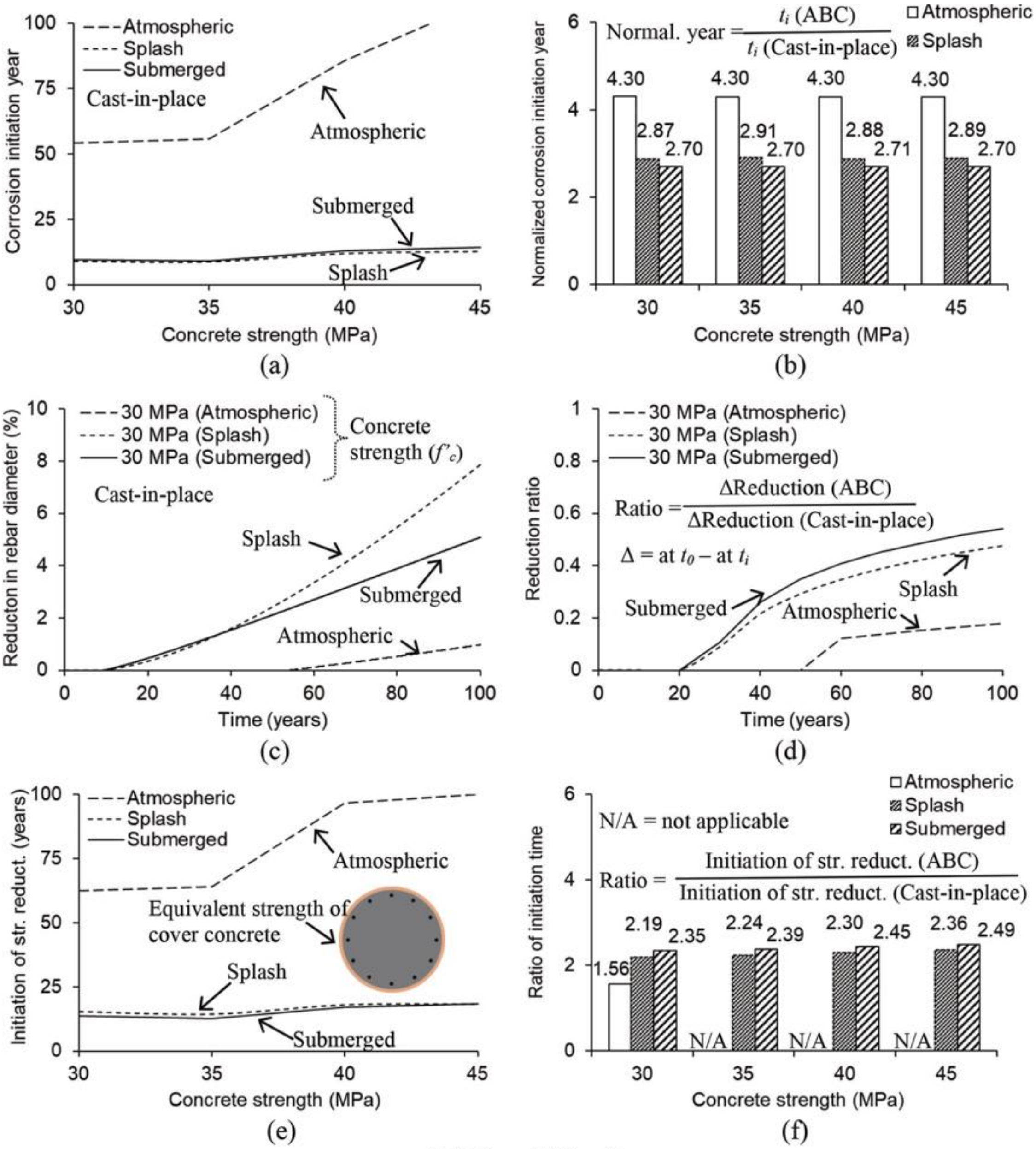

[1 MPa = 145 psi]

Fig. 9—Consequences of corrosion: (a) corrosion initiation year for cast-in-place column; (b) normalized corrosion initiation year; (c) reduced reinforcing bar diameter in cast-in-place column; (d) ratio of reduced reinforcing bar diameter between ABC and cast-in-place columns; (e) initiation of strength reduction in cover concrete of cast-in-place column; and (f) ratio of initiation time for strength reduction between ABC and cast-in-place columns.

diameter of the reinforcing bars began to dwindle (Fig. 9(c)), and the use of the ABC technique remarkably inhibited a reduction magnitude (Fig. 9(d)). The strength decrease of the equivalent cover concrete for the cast-in-place column was noticed at 16.5 years and 15.4 years under the splash and submerged conditions, respectively (Fig. 9(e)), which were incomparable with the case under the atmospheric exposure (>62 years). As shown in Fig. 9(f), the ratio of the cover-strength reduction time between the ABC and cast-in-place columns was over 1.56 (no reduction occurred for the ABC column with a concrete strength greater than 35 MPa [5080 psi]).

Structural aspect

Axial capacity—The reduced capacity of the cast-in-place column under the splash condition inducing corrosion is provided in Fig. 10(a). The ratio of the capacities between the damaged and undamaged states diminished with time. It should be noted that the proximity of the responses with f_c' = 35 and 40 MPa (5080 and 5800 psi) resulted from the same cover depth of 100 mm (4 in.), as shown in Table 2. The contribution of each constituent to the capacity drop is visible in Fig. 10(b) and (c). The capacity variation caused by the equivalent compressive strength (Eq. (16)) was the primary factor (Fig. 10(b)), while the influence of the steel corrosion was marginal (Fig. 10(c)). In particular, the dependency of the concrete strength pertaining to the chloride

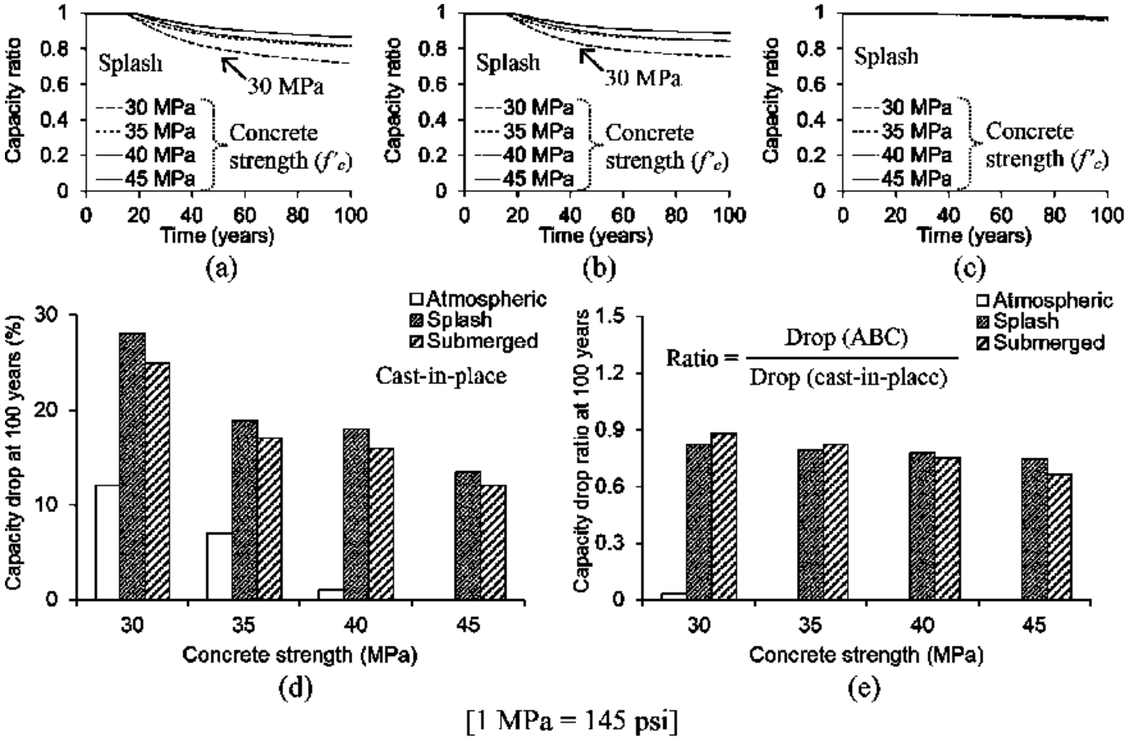

Fig. 10—Reduction in axial capacity of column: (a) normalized capacity of cast-in-place column; (b) concrete portion of normalized capacity; (c) reinforcing bar portion of normalized capacity; (d) capacity drop of cast-in-place column at 100 years; and (e) ratio of capacity drop between ABC and cast-in-place columns at 100 years.

flux was significant on the capacity decrease of the column exposed to water (the splash and submerged conditions in Fig. 10(d)). The benefit of the ABC column was pronounced for a low-strength concrete; for instance, the capacity-drop ratios between the ABC and cast-in-place columns under the submerged condition were 0.88 and 0.67 for f_c' = 30 and 45 MPa (4350 and 6530 psi), respectively (Fig. 10(e)).

Effectiveness of CFRP confinement—Complying with the provisions of ACI 440.2R-17[14] (Eq. (1) and (2)), the number of CFRP layers was calculated and then rounded for practical application (Fig. 11(a)). The more durable ABC column necessitated fewer layers than the cast-in-place column, and the propensity was preserved without regard to the strength of the unconfined concrete (f_c'). The constitutive relationship of the confined concrete (Fig. 11(b)) was bilinear until the maximum usable strains of CFRP were reached (all values did not exceed the strain limit of 0.01 specified in ACI 440.2R-17[14]). Although the increased f_c' from 30 to 45 MPa (4350 to 6530 psi) raised the confined strength (f_{cc}'), the usable strain was shortened from ε_{ccu} = 0.0065 to 0.0044. An average toughness ratio of 1.97 was noted between the confined and unconfined cases (toughness is defined as the area under a stress-strain curve up to failure); scilicet, CFRP confinement improved the energy dissipation of the column concrete. Figures 11(c) and (d) show the time-dependent capacity ratio of the cast-in-place and ABC columns, respectively. In line with the strengthening philosophy established earlier, the columns were strengthened when a 10% reduction was noticed in the capacity, and the enhanced ratios were maintained above unity for the rest of service life to 100 years (confined capacity ≥ intact capacity). The temporal span of the adjusted capacity ratio for the cast-in-place column (27.4 to 100 years) was 46.4% longer than the span for the ABC column (50.4 to 100 years); on the contrary, the efficacy of strengthening was indistinguishable, which corroborates the fact that CFRP-based rehabilitation is a recommendable technique for both column types.

Load-moment interaction—The interaction diagram of the axial load (P_n) and bending moment (M_n) for the cast-in-place column at 100 years is given in Fig. 12(a). The size of the interaction envelope conspicuously decreased under the splash condition. With CFRP confinement, the envelope was enlarged over the control curve, indicating the fully recovered performance of the abated column. The abruptly dropping moment at the balance point of the confined column (P_b and M_b) was ascribed to the restriction of ACI 440.2R-17[14]: strength enhancement is only allowed in the compression-controlled region. As the core strength (f_c') was increased (Fig. 12(b)), the resistance level of the upgraded column became elevated against the combined axial compression and bending. The ABC column exhibited structural efficiency with fewer CFRP layers (Fig. 12(c)). The transition moment from compression- to tension-controlled failure modes went up in proportion to the core strength (Fig. 12(d)) and, albeit inappreciable, the ABC column outperformed the cast-in-place column.

SUMMARY AND CONCLUSIONS

This paper investigated the detrimental effects of chloride migration in cast-in-place and accelerated bridge construction (ABC) column models exposed to atmospheric, splash, and submerged environments. Employing a novel simulation

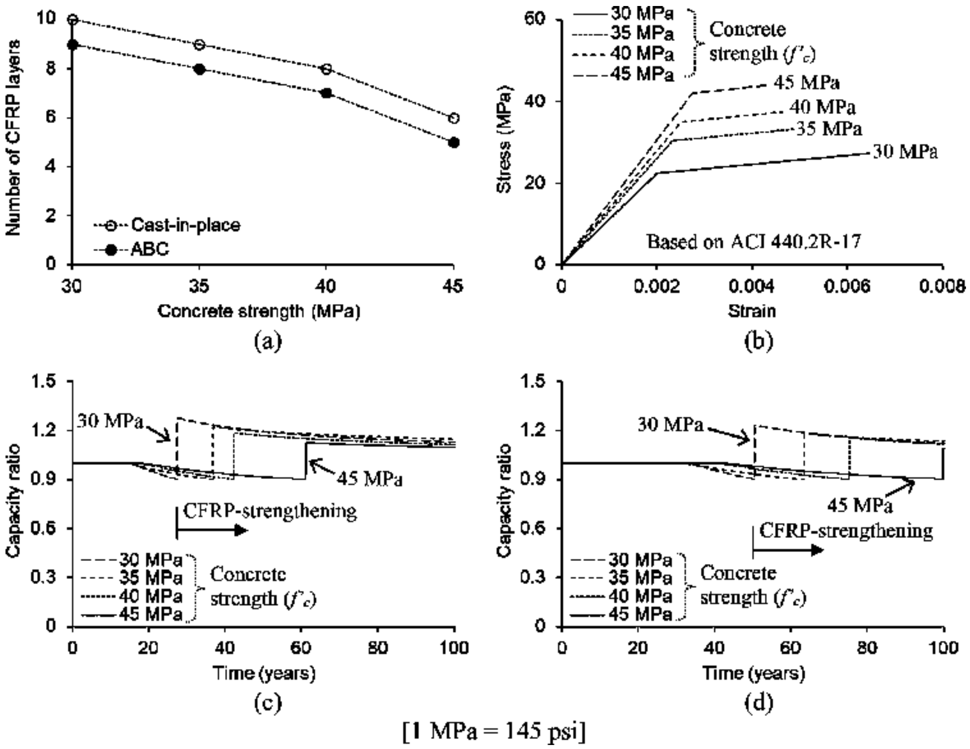

Fig. 11—Strength recovery with CFRP confinement: (a) CFRP layers; (b) stress-strain relationship of cast-in-place concrete (f_{cc}'*); (c) cast-in-place column; and (d) ABC column.*

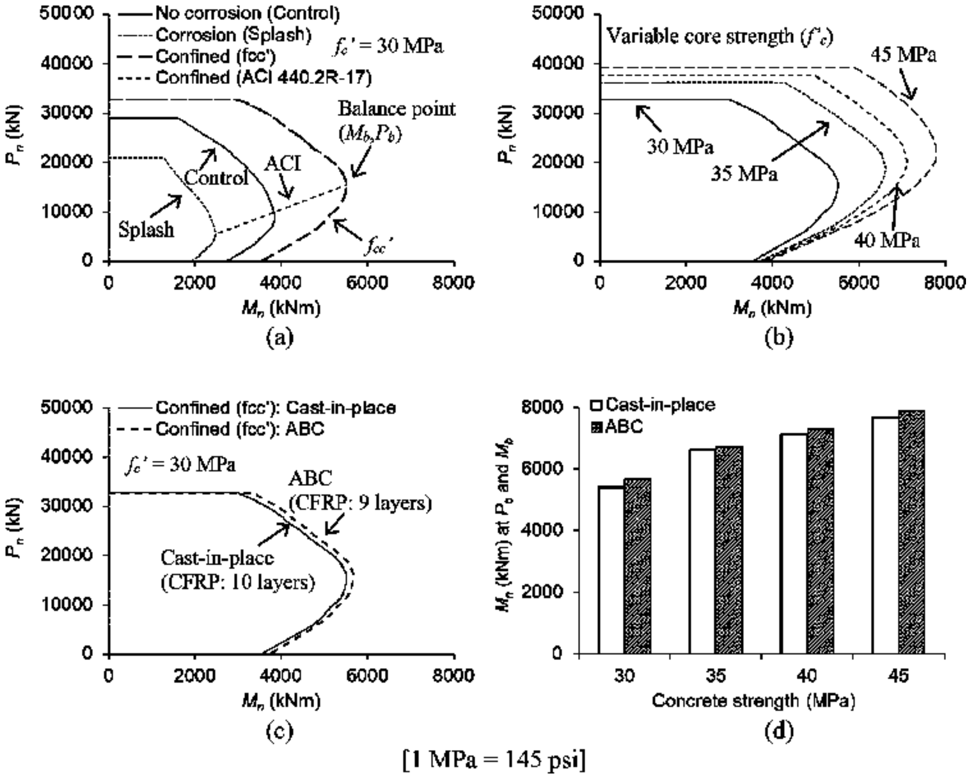

*Fig. 12—Load-moment interaction at 100 years: (a) cast-in-place column; (b) cast-in-place column confined with *f_{cc}'*; (c) cast-in-place versus ABC columns; and (d) comparison at balance load (*P_b*) and moment (*M_b*).*

approach called cellular automata, chloride diffusivity and various levels of corrosion were computed during a service period of 100 years. The degraded columns were strengthened with carbon fiber-reinforced polymer (CFRP) sheets in conformity with ACI 440.2R-17,[14] and their load-carrying capacity was examined. Attention was directed toward full-range interactions between axial and flexural loadings. The study substantiated that CFRP confinement was a favorable technique for both column types. The following are concluded:

- Because of the concrete pores partially filled by surplus chlorides, as documented in the literature, the diffusion coefficient of the columns exponentially decreased with time. The microstructural characteristics of the concrete relating to the compressive strength also dominated the ingress of chlorides. The chloride diffusion of the ABC column was slower than that of the cast-in-place column; however, their distinction in the diffusion rate disappeared after 30 years.
- The chloride concentration of the columns under the splash condition was noticeable owing to the expedited sorptivity of the concrete subjected to wetting-and-drying cycles, which was properly documented by others. The development of chloride concentrations in the cast-in-place column was faster than the case of the ABC column, which led to the superior durability of the latter, particularly under the splash exposure.
- The corrosion current density of the columns steadily rose up to 100 years, while the growth pattern was a function of the concrete strength related to the connectivity of micropores. Compared with the ABC column, the cast-in-place column revealed a rapid increase rate in the current density until 40 years, beyond which both cases showed similar responses.
- When the cast-in-place column was exposed to water (splash and submerged), the average corrosion initiation time was 11 years. By contrast, the ABC column required up to a 4.3-times longer period and effectively impeded a loss in the cross-sectional area of the reinforcement. The reduction in the equivalent strength due to corrosion-induced cracking and spalling was not noticed for the ABC column with a concrete strength of 35 MPa (5080 psi) and greater.
- With the presence of corrosion damage, the axial capacity of the cast-in-place and ABC columns decreased by 28% and 23% under the splash condition at 100 years, respectively. The primary factor for such an observation was the impaired concrete in the corrosion influence zone, whereas the direct contribution of the deteriorated reinforcement was less than 5%.
- The CFRP strengthening raised the toughness of the existing concrete by almost two times; accordingly, the confined columns were able to carry more moments without flexural failure. Notwithstanding the reduced number of CFRP layers, the ABC column's performance was comparable to that of the cast-in-place column under synergistic distress from axial compression and bending.

AUTHOR BIOS

ACI member **Jun Wang** *is a Postdoctoral Fellow in the Department of Civil Engineering at the University of Colorado Denver, Denver, CO. She received her BS from Northeast Forestry University, Harbin, Heilongjiang, China, and her MS from the University of Colorado Denver. She is a member of ACI Committee 345, Bridge Construction and Preservation. Her research interests include multi-object interaction and concrete structures.*

Yail J. Kim, *FACI, is President of the Bridge Engineering Institute, An International Technical Society, and a Professor in the Department of Civil Engineering at the University of Colorado Denver. He is Chair of ACI Subcommittee 440-I, FRP-Prestressed Concrete; past Chair of ACI Committee 345, Bridge Construction and Preservation; and a member of ACI Committees 342, Evaluation of Concrete Bridges and Bridge Elements; 377, Performance-Based Structural Integrity & Resilience of Concrete Structures; and 440, Fiber-Reinforced Polymer Reinforcement; and Joint ACI-ASCE Committee 343, Concrete Bridge Design. He received the ACI Chester Paul Siess Award for Excellence in Structural Research in 2019. His research interests include advanced composite materials for rehabilitation; structural informatics; complex systems; and science-based structural engineering, including statistical, interfacial, and quantum physics.*

ACKNOWLEDGMENTS

The authors would like to acknowledge support from the U.S. Department of Transportation through the National Center for Transportation Infrastructure Durability & Life-Extension (TriDurLE). Technical contents presented in this paper are based on the opinion of the authors and do not necessarily represent that of others.

REFERENCES

1. Koch, G.; Varney, J.; Thompson, N.; Moghissi, O.; Gould, M.; and Payer, J., "International Measures of Prevention, Application, and Economics of Corrosion Technologies Study," NACE International, Houston, TX, 2016, 216 pp.

2. Debaiky, A. S.; Green, M. F.; and Hope, B. B., "Carbon Fiber-Reinforced Polymer Wraps for Corrosion Control and Rehabilitation of Reinforced Concrete Columns," *ACI Materials Journal*, V. 99, No. 2, Mar.-Apr. 2002, pp. 129-137.

3. Nossoni, G., "Modeling the Corrosion Rate of Steel Reinforcement in FRP-Wrapped Concrete," *Journal of Composites for Construction*, ASCE, V. 20, No. 3, June 2016, p. 04015068. doi: 10.1061/(ASCE)CC.1943-5614.0000625

4. Chen, E.; Tang, S.; and Leung, C. K. Y., "Corrosion-Induced Cracking in Reinforced Concrete due to Chloride Contamination and Ingress," *ACI Materials Journal*, V. 116, No. 5, Sept. 2019, pp. 99-111. doi: 10.14359/51716831

5. Hussain, R. R.; Al-Negheimish, A.; Alhozaimy, A.; and Singh, D. D. N., "Corrosion Characteristics of Vanadium Micro-Alloyed Steel Reinforcement Bars Exposed in Concrete Environments and Industrially Polluted Atmosphere," *Cement and Concrete Composites*, V. 113, Oct. 2020, Article No. 103728. doi: 10.1016/j.cemconcomp.2020.103728

6. Hamilton, C. H.; Pardoen, G. C.; Navalpakkam, S.; and Kanzanjy, R. P., "Reinforced Concrete Bridge Column Performance Enhancement through Shotcrete Jacketing," *ACI Structural Journal*, V. 101, No. 3, May-June 2004, pp. 332-340.

7. Khan, M. A., *Accelerated Bridge Construction: Best Practices and Techniques*, Butterworth-Heinemann, Oxford, UK, 2014.

8. Zhang, Q., and Alam, M. S., "State-of-the-Art Review of Seismic-Resistant Precast Bridge Columns," *Journal of Bridge Engineering*, ASCE, V. 25, No. 10, Oct. 2020, p. 03120001. doi: 10.1061/(ASCE)BE.1943-5592.0001620

9. Liu, R., and Palermo, A., "Ten Years of Experiments on Bridges Using Resilient Damage-Resistant Systems and Accelerated Construction Techniques," *Structural Engineering International*, V. 30, No. 2, 2020, pp. 224-231. doi: 10.1080/10168664.2020.1717406

10. Grantham, M.; Mechtcherine, V.; and Schneck, U., eds., *Concrete Solutions*, CRC Press, London, UK, 2012.

11. Christodoulou, C.; Goodier, C.; Austin, S.; Webb, J.; and Glass, G. K., "Diagnosing the Cause of Incipient Anodes in Repaired Reinforced Concrete Structures," *Corrosion Science*, V. 69, Apr. 2013, pp. 123-129. doi: 10.1016/j.corsci.2012.11.032

12. Bousias, S. N.; Biskinis, D.; Fardis, M. N.; and Spathis, A.-L., "Strength, Stiffness, and Cyclic Deformation Capacity of Concrete Jacketed Members," *ACI Structural Journal*, V. 104, No. 5, Sept.-Oct. 2007, pp. 521-531.

13. El Maaddawy, T.; Chahrour, A.; and Soudki, K., "Effect of Fiber-Reinforced Polymer Wraps on Corrosion Activity and Concrete Cracking in Chloride-Contaminated Concrete Cylinders," *Journal of Composites for Construction*, ASCE, V. 10, No. 2, Apr. 2006, pp. 139-147. doi: 10.1061/(ASCE)1090-0268(2006)10:2(139)

14. ACI Committee 440, "Guide for the Design and Construction of Externally Bonded FRP Systems for Strengthening Concrete Structures (ACI 440.2R-17)," American Concrete Institute, Farmington Hills, MI, 2017, 112 pp.

15. Amran, Y. H. M.; Alyousef, R.; Alabduljabbar, H.; Alaskar, A.; and Alrshoudi, F., "Properties and Water Penetration of Structural Concrete Wrapped with CFRP," *Results in Engineering*, V. 5, Mar. 2020, Article No. 100094. doi: 10.1016/j.rineng.2019.100094

16. ASTM C1585-04, "Standard Test Method for Measurement of Rate of Absorption of Water by Hydraulic-Cement Concretes," ASTM International, West Conshohocken, PA, 2004, 6 pp.

17. Ramírez, J. L., "Ten Concrete Column Repair Methods," *Construction and Building Materials*, V. 10, No. 3, Apr. 1996, pp. 195-202. doi: 10.1016/0950-0618(95)00087-9

18. Karimipour, A., and Edalati, M., "Retrofitting of the Corroded Reinforced Concrete Columns with CFRP and GFRP Fabrics under Different Corrosion Levels," *Engineering Structures*, V. 228, 2021, Article No. 111523. doi: 10.1016/j.engstruct.2020.111523

19. AASHTO, "AASHTO LRFD Bridge Design Specifications," ninth edition, American Association of State Highway and Transportation Officials, Washington, DC, 2020.

20. Cuzzilla, R.; Di Ludovico, M.; Prota, A.; and Manfredi, G., "Seismic Rehabilitation of RC Bridges by Using FRP and SRP: Case Study of a Bridge in the South of Italy," SP-277, *Recent Advances in Maintenance and Repair of Concrete Bridges*, Y. J. Kim, ed., American Concrete Institute, Farmington Hills, MI, 2011, 20 pp.

21. ACI Committee 211, "Standard Practice for Selecting Proportions for Normal, Heavyweight, and Mass Concrete (ACI 211.1-91) (Reapproved 2009)," American Concrete Institute, Farmington Hills, MI, 1991, 38 pp.

22. NACE International, "Corrosion Control of Submerged Areas of Permanently Installed Steel Offshore Structures Associated with Petroleum Production (NACE SP0176-2007)," Association for Materials Protection and Performance, Houston, TX, 2007,.

23. Gao, J.; Yu, Z.; Song, L.; Wang, T.; and Wei, S., "Durability of Concrete Exposed to Sulfate Attack under Flexural Loading and Drying–Wetting Cycles," *Construction and Building Materials*, V. 39, Feb. 2013, pp. 33-38. doi: 10.1016/j.conbuildmat.2012.05.033

24. Eyu, G. D.; Will, G.; Dekkers, W.; and MacLeod, J., "Effect of Dissolved Oxygen and Immersion Time on the Corrosion Behaviour of Mild Steel in Bicarbonate/Chloride Solution," *Materials (Basel)*, V. 9, No. 9, Sept. 2016, Article No. 748. doi: 10.3390/ma9090748

25. Freyermuth, C., "Service Life and Sustainability of Concrete Bridges," *ASPIRE*, V. 3, No. 4, 2009, pp. 12-15.

26. Wolfram, S., "Cellular Automata as Models of Complexity," *Nature*, V. 311, No. 5985, Oct. 1984, pp. 419-424. doi: 10.1038/311419a0

27. Wolnik, B., and De Baets, B., "Ternary Reversible Number-Conserving Cellular Automata Are Trivial," *Information Sciences*, V. 513, Mar. 2020, pp. 180-189. doi: 10.1016/j.ins.2019.10.068

28. Hoekstra, A. G.; Kroc, J.; and Sloot, P. M. A., eds., *Simulating Complex Systems by Cellular Automata*, Springer, Heidelberg, Germany, 2010, 384 pp.

29. Baetens, J. M., and Kutrib, M., *Cellular Automata and Discrete Complex Systems: 24th IFIP WG 1.5 International Workshop, AUTOMATA 2018: Ghent, Belgium, June 20-22, 2018 – Proceedings*, Springer, Cham, Switzerland, 2018, 143 pp.

30. Podroužek, J., and Teplý, B., "Modelling of Chloride Transport in Concrete by Cellular Automata," *Engineering Mechanics*, V. 15, No. 3, 2008, pp. 213-222.

31. Wang, Y.; Gong, F.; Zhang, D.; and Ueda, T., "Estimation of Ice Content in Mortar Based on Electrical Measurements under Freeze-Thaw Cycle," *Journal of Advanced Concrete Technology*, V. 14, No. 2, 2016, pp. 35-46. doi: 10.3151/jact.14.35

32. Frederiksen, J. M.; Mejlbro, L.; and Poulsen, E., "The HETEK Model of Chloride Ingress into Concrete Made Simpler by Approximations," *Testing and Modelling the Chloride Ingress into Concrete: Proceedings of the 2nd International RILEM Workshop*, C. Andrade and J. Kropp, eds., Paris, France, 2000, pp. 317-336.

33. Poulsen, E., and Mejlbro, L., *Diffusion of Chloride in Concrete: Theory and Application*, Taylor & Francis, New York, 2006.

34. Alizadeh, R.; Ghods, P.; Chini, M.; Hoseini, M.; Ghalibafian, M.; and Shekarchi, M., "Effect of Curing Conditions on the Service Life Design of RC Structures in the Persian Gulf Region," *Journal of Materials in Civil Engineering*, ASCE, V. 20, No. 1, Jan. 2008, pp. 2-8. doi: 10.1061/(ASCE)0899-1561(2008)20:1(2)

35. Wu, L.; Wang, Y.; Wang, Y.; Ju, X.; and Li, Q., "Modelling of Two-Dimensional Chloride Diffusion Concentrations Considering the Heterogeneity of Concrete Materials," *Construction and Building Materials*, V. 243, May 2020, Article No. 118213. doi: 10.1016/j.conbuildmat.2020.118213

36. Cao, J.; Wang, Y.; Li, K.; and Ma, Y., "Modeling the Diffusion of Chloride Ion in Concrete Using Cellular Automaton," *Journal of Materials in Civil Engineering*, ASCE, V. 24, No. 6, June 2012, pp. 783-788. doi: 10.1061/(ASCE)MT.1943-5533.0000440

37. Titi, A., and Biondini, F., "On the Accuracy of Diffusion Models for Life-Cycle Assessment of Concrete Structures," *Structure and Infrastructure Engineering*, V. 12, No. 9, 2016, pp. 1202-1215. doi: 10.1080/15732479.2015.1099110

38. Wang, Y.; An, M.; Yu, Z.; Han, B.; and Ji, W., "Experimental and Cellular-Automata-Based Analysis of Chloride Ion Diffusion in Reactive Powder Concrete Subjected to Freeze–Thaw Cycling," *Construction and Building Materials*, V. 172, May 2018, pp. 760-769. doi: 10.1016/j.conbuildmat.2018.03.271

39. Yin, G., and Pan, L., "The Effect of Shape on Chloride Penetration of Circular Reinforcement Concrete Columns and Its Durability Design," *Applied Sciences*, V. 10, No. 2, Jan. 2020, Article No. 459. doi: 10.3390/app10020459

40. Thoft-Christensen, P.; Jensen, F. M.; Middleton, C. R.; and Blackmore, A., "Assessment of the Reliability of Concrete Slab Bridges," *Reliability and Optimization of Structural Systems: 7th IFIP WG 7.5 Working Conference*, D. M. Frangopol, R. B. Corotis, and R. Rackwitz, eds., Boulder, CO, 1996, pp. 1-8.

41. Liu, T., and Weyers, R. W., "Modeling the Dynamic Corrosion Process in Chloride Contaminated Concrete Structures," *Cement and Concrete Research*, V. 28, No. 3, Mar. 1998, pp. 365-379. doi: 10.1016/S0008-8846(98)00259-2

42. Elsener, B., and Angst, U., "Corrosion Inhibitors for Reinforced Concrete," *Science and Technology of Concrete Admixtures*, P.-C. Aïtcin and R. J. Flatt, eds., Woodhead Publishing, Sawston, UK, 2016, pp. 321-339.

43. Yoon, S.; Wang, K.; Weiss, W. J.; and Shah, S. P., "Interaction between Loading, Corrosion, and Serviceability of Reinforced Concrete," *ACI Materials Journal*, V. 97, No. 6, Nov.-Dec. 2000, pp. 637-644.

44. Roy, S. K.; Chye, L. K.; and Northwood, D. O., "Chloride Ingress in Concrete as Measured by Field Exposure Tests in the Atmospheric, Tidal and Submerged Zones of a Tropical Marine Environment," *Cement and Concrete Research*, V. 23, No. 6, Nov. 1993, pp. 1289-1306. doi: 10.1016/0008-8846(93)90067-J

45. Song, H.-W.; Lee, C.-H.; and Ann, K. Y., "Factors Influencing Chloride Transport in Concrete Structures Exposed to Marine Environments," *Cement and Concrete Composites*, V. 30, No. 2, Feb. 2008, pp. 113-121. doi: 10.1016/j.cemconcomp.2007.09.005

46. Liu, Q.-F.; Hu, Z.; Lu, X.-Y.; Yang, J.; Azim, I.; and Sun, W., "Prediction of Chloride Distribution for Offshore Concrete Based on Statistical Analysis," *Materials*, V. 13, No. 1, Jan. 2020, Article No. 174.

47. Val, D. V., and Melchers, R. E., "Reliability of Deteriorating RC Slab Bridges," *Journal of Structural Engineering*, ASCE, V. 123, No. 12, Dec. 1997, pp. 1638-1644. doi: 10.1061/(ASCE)0733-9445(1997)123:12(1638)

48. Cheewaket, T.; Jaturapitakkul, C.; and Chalee, W., "Long Term Performance of Chloride Binding Capacity in Fly Ash Concrete in a Marine Environment," *Construction and Building Materials*, V. 24, No. 8, Aug. 2010, pp. 1352-1357. doi: 10.1016/j.conbuildmat.2009.12.039

49. Suh, K.; Mullins, G.; Sen, R.; and Winters, D., "Effectiveness of Fiber-Reinforced Polymer in Reducing Corrosion in Marine Environment," *ACI Structural Journal*, V. 104, No. 1, Jan.-Feb. 2007, pp. 76-83.

50. Vecchio, F. J., and Collins, M. P., "The Modified Compression-Field Theory for Reinforced Concrete Elements Subjected to Shear," *ACI Journal Proceedings*, V. 83, No. 2, Mar.-Apr. 1986, pp. 219-231.

51. Coronelli, D., and Gambarova, P., "Structural Assessment of Corroded Reinforced Concrete Beams: Modeling Guidelines," *Journal of Structural Engineering*, ASCE, V. 130, No. 8, Aug. 2004, pp. 1214-1224. doi: 10.1061/(ASCE)0733-9445(2004)130:8(1214)

52. Vidal, T.; Castel, A.; and François, R., "Analyzing Crack Width to Predict Corrosion in Reinforced Concrete," *Cement and Concrete Research*, V. 34, No. 1, Jan. 2004, pp. 165-174. doi: 10.1016/S0008-8846(03)00246-1

53. Alonso, C.; Andrade, C.; Rodriguez, J.; and Diez, J. M., "Factors Controlling Cracking of Concrete Affected by Reinforcement Corrosion," *Materials and Structures*, V. 31, No. 7, Aug. 1998, pp. 435-441. doi: 10.1007/BF02480466

54. Ahmad, A., and Kumar, A., "Chloride Ion Migration/Diffusion through Concrete and Test Methods," *International Journal of Advanced Scientific and Technical Research*, V. 6, No. 3, Nov.-Dec. 2013, pp. 151-180.

55. ACI Committee 318, "Building Code Requirements for Structural Concrete (ACI 318-19) and Commentary (ACI 318R-19) (Reapproved 2022)," American Concrete Institute, Farmington Hills, MI, 2019, 624 pp.

56. Koleva, D. A.; Copuroglu, O.; van Breugel, K.; Ye, G.; and de Wit, J. H. W., "Electrical Resistivity and Microstructural Properties of Concrete Materials in Conditions of Current Flow," *Cement and Concrete Composites*, V. 30, No. 8, Sept. 2008, pp. 731-744. doi: 10.1016/j.cemconcomp.2008.04.001

57. Purnell, P., "Degradation of Fibre-Reinforced Cement Composites," *Durability of Concrete and Cement Composites*, C. L. Page and M. M. Page, eds., Woodhead Publishing Limited, Cambridge, UK, 2007, pp. 316-363.

58. Shi, Y.; Chen, X.; Li, J.; Li, X.; and Peng, Z., "Micro–Macro Properties of Plastic Concrete Anti-Seepage Wall Materials Mixed with Low-Liquid Limit Clay," *Advances in Mechanical Engineering*, V. 11, No. 5, May 2019, pp. 1-9. doi: 10.1177/1687814019849736

59. Zhang, Y.; Zhang, M.; and Ye, G., "Influence of Moisture Condition on Chloride Diffusion in Partially Saturated Ordinary Portland Cement Mortar," *Materials and Structures*, V. 51, No. 2, Apr. 2018, Article No. 36. doi: 10.1617/s11527-018-1162-7

60. Espinoza-Hijazin, G., and Lopez, M., "Extending Internal Curing to Concrete Mixtures with W/C Higher than 0.42," *Construction and Building Materials*, V. 25, No. 3, Mar. 2011, pp. 1236-1242. doi: 10.1016/j.conbuildmat.2010.09.031

61. Stanish, K. D.; Hooton, R. D.; and Thomas, M. D. A., "Testing the Chloride Penetration Resistance of Concrete: A Literature Review," Report No. DTFH61-97-R-00022, Federal Highway Administration, Washington, DC, 1997, 33 pp.

62. Basheer, P. A. M.; Gilleece, P. R. V.; Long, A. E.; and McCarter, W. J., "Monitoring Electrical Resistance of Concretes Containing Alternative Cementitious Materials to Assess Their Resistance to Chloride Penetration," *Cement and Concrete Composites*, V. 24, No. 5, Oct. 2002, pp. 437-449. doi: 10.1016/S0958-9465(01)00075-0

63. Andrade, C., "Calculation of Chloride Diffusion Coefficients in Concrete from Ionic Migration Measurements," *Cement and Concrete Research*, V. 23, No. 3, May 1993, pp. 724-742. doi: 10.1016/0008-8846(93)90023-3

64. Cosoli, G.; Mobili, A.; Tittarelli, F.; Revel, G. M.; and Chiariotti, P., "Electrical Resistivity and Electrical Impedance Measurement in Mortar and Concrete Elements: A Systematic Review," *Applied Sciences*, V. 10, No. 24, Dec. 2020, Article No. 9152. doi: 10.3390/app10249152

65. Hornbostel, K.; Larsen, C. K.; and Geiker, M. R., "Relationship between Concrete Resistivity and Corrosion Rate – A Literature Review," *Cement and Concrete Composites*, V. 39, May 2013, pp. 60-72. doi: 10.1016/j.cemconcomp.2013.03.019

ACI STRUCTURAL JOURNAL TECHNICAL PAPER

Title No. 121-S02

Effect of Prestressing on Shear Strengths of Cylindrical and Planar Walls with Low Aspect Ratio

by Hyeon-Keun Yang and Hong-Gun Park

To investigate the effect of prestressing on the shear strength of nuclear power plant containment structures, five reinforced or post-tensioned semi-cylindrical concrete walls and two planar walls were tested under cyclic lateral loading. The major test parameters were the presence of unbonded post-tensioning, the magnitude of horizontal prestressing force, and the use of crossties. The test results showed that because of the high reinforcement and prestressing ratio, web-crushing failure occurred in all specimens. The shear strengths of reinforced concrete (RC) and prestressed concrete (PSC) walls were greater than the nominal shear strength specified in the current design/evaluation methods. In the case of walls subjected to horizontal prestressing force, early delamination cracking occurred due to radial tensile stress. The delamination cracking was restrained by the use of crossties. Further, the effect of prestressing on the web-crushing strength was not significant. When the diameter of the cylindrical wall was the same as the length of the planar wall, the peak shear strength of the cylindrical wall was equivalent to that of the planar wall despite the different wall shape.

Keywords: cyclic loading; cylindrical wall; delamination zone; post-tensioning; shear strength.

INTRODUCTION

Nuclear power plants (NPPs) require a high level of safety as buildings that handle radioactive materials. In particular, the containment buildings of NPPs are the final safeguard against radioactive leakage in case of an emergency accident such as earthquakes or airplane crashes. In the event of an emergency, the containment building withstands the increased internal pressure due to the vapor pressure or explosion. Thus, prestressed concrete (PSC) is commonly used to resist membrane tensile stresses caused by internal pressure.

In general, due to the high strength demand, NPP containment walls are designed with a high reinforcement ratio. In this case, the walls are susceptible to diagonal concrete crushing of the web (web crushing). Eom et al. (2013), Oesterle et al. (1984), and Burgueño et al. (2014) reported the web-crushing behavior of reinforced concrete (RC) walls based on numerical and experimental results.

However, while most existing experimental studies were performed for planar RC walls, the studies of cylindrical walls with prestressing are rare. Aoyagi et al. (1981) and Ogaki et al. (1981) studied cylindrical walls under horizontal loading and torsional loading. The tangential shear strength of the reinforced cylindrical concrete vessel (RCCV) and the prestressed cylindrical concrete vessel (PCCV) was evaluated by the truss analogy. Uchida et al. (1979) tested RCCVs with internal pressure using a water tank and verified the shear strength and ductility. Wu et al. (2019) studied the seismic performance of RC cylindrical walls. The failure modes of the specimens were shear sliding and web crushing. Katoh et al. (1987) studied the behavior of the PCCV using static loading and the shake-table test. The behavior of the two specimens were similar, showing shear sliding failure mode, and the ultimate strengths were two times greater than the allowable strength.

Although prestressing is effective in restraining concrete cracking, due to the cylindrical shape of containment buildings, horizontal prestressing force causes tensile stress in the radial direction along the horizontal prestressing tendon. Due to the tensile stress, internal cracking can occur in the radial direction. Acharya and Menon (2003), Choi (2018), and Choi et al. (2017) confirmed concrete cracking based on the test results of cylindrical concrete walls with horizontal prestressing. Such concrete delamination occurred in actual containment walls: Unit-3 containment of Turkey Point NPP (Florida Power and Light Company 1970), Unit-3 containment of Crystal River in Florida (Nuclear Regulatory Commission 2010; Florida Power and Light Company 1976), and the Kaiga Atomic Power Project (Basu et al. 2001). For this reason, ACI 359 (Joint ACI-ASME Committee 359 2015), requires radial crossties for dome and cylindrical walls. The effect of crossties on the shear strength of cylindrical wall should be experimentally verified.

In the present study, the in-plane shear strengths of cylindrical and planar walls were investigated focusing on the following considerations: 1) the effect of horizontal prestressing on concrete delamination in cylindrical walls; 2) the effect of delamination on the shear strength of cylindrical walls; 3) the effect of crossties on concrete delamination; and 4) the effect of horizontal and vertical prestressing on the shear strength and failure mode. For this purpose, semi-cylindrical and planar RC and PSC wall specimens were tested under cyclic lateral loading. The test parameters were the presence of unbonded post-tensioning (RC versus PSC), the magnitude of vertical and horizontal prestressing forces (vertical prestressing only; 100% of vertical prestressing + 50% of horizontal prestressing; and 100% of vertical prestressing + 100% of horizontal prestressing), the shape

---

ACI Structural Journal, V. 121, No. 1, January 2024.
MS No. S-2022-034.R1, doi: 10.14359/51739182, received May 10, 2023, and reviewed under Institute publication policies. Pertinent discussion including author's closure, if any, will be published ten months from this journal's date if the discussion is received within four months of the paper's print publication.

of the wall (cylindrical versus planar shape), and the use of crossties.

RESEARCH SIGNIFICANCE

The results of the present study confirmed that horizontal prestressing can cause concrete delamination in cylindrical walls. Nevertheless, the tested shear strength was greater than the prediction of the current design codes. Further, crossties satisfactorily restrained concrete delamination. In particular, the strengths of cylindrical or planar walls with and without prestressing were directly compared with those of the planar and RC walls to investigate the effects of wall shape and prestressing on the shear strength. This result can be used as evidence for the seismic design and evaluation of NPP walls with a high reinforcement ratio.

TEST PLAN

Major test parameters

In NPP containment walls, because of the high seismic demand, the shear reinforcement ratio is over 1.0%. Thus, the test specimens were designed with high horizontal and vertical reinforcement ratios. Due to the limitation of actuators, cylindrical test specimens were designed as semi-cylindrical walls (Fig. 1). Because of the asymmetric shape of the specimen, two actuators were used to apply a balanced lateral load, restraining torsional deformation. Figure 1(b) shows the out-of-plane displacement measured at the end of the slab during the test. This result shows that torsional displacement was restrained.

In the present study, five semi-cylindrical walls and two planar walls were tested (Table 1). The names of the specimens indicate the test parameters. The first letters, C and I, refer to cylindrical and planar shapes. The next letters—R, V, VH, and Vh—indicate the RC without prestressing (R) and the magnitude of prestressing: 100% vertical prestressing without horizontal prestressing (V), 100% vertical + 100% horizontal prestressing (VH), and 100% vertical prestressing + 50% horizontal prestressing (Vh). The last letter, C, indicates a specimen with crossties. For example, C-VH-C indicates the semi-cylindrical-shaped specimen with 100% vertical + 100% horizontal prestressing and crossties. The design of the test specimens follows current design/evaluation methods. The design methods are presented in Appendix A.

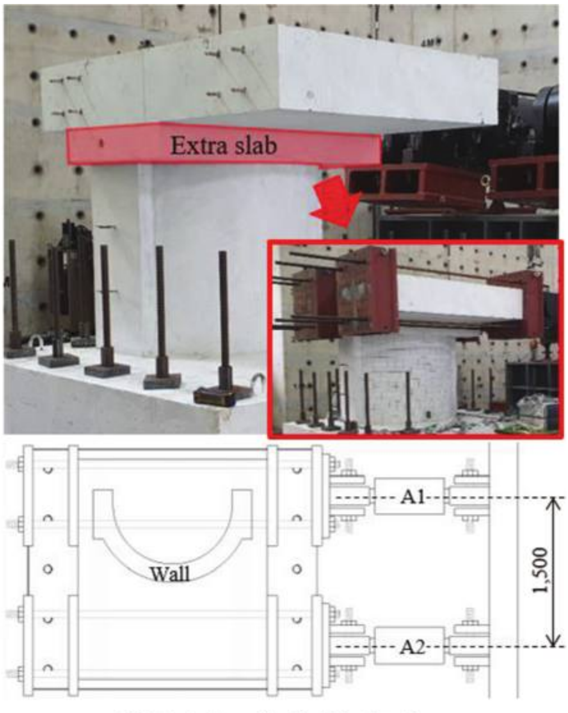

(a) Test plan of cylindrical wall

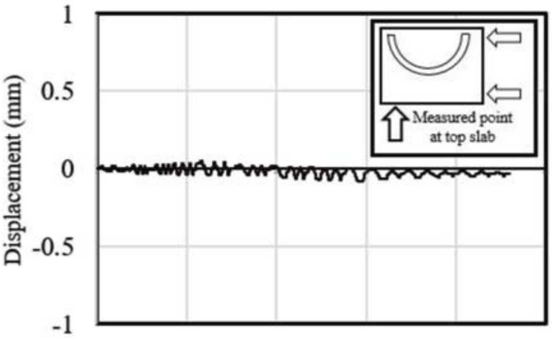

(b) Out-of-plane displacement of C-VH

Fig. 1—Test plan and measured out-of-plane displacement of C-VH.

Table 1—Design parameters of test specimens

				Prestressing bar				Reinforcing bar			Design strength prediction				
				Vertical		Horizontal		Vertical		Horizontal					
Specimens	Shape	Crossties	f_c', MPa	ρ_{pv}, %	F_{pv}, MPa	ρ_{ph}, %	F_{ph}, MPa	ρ_w, %	ρ_f, %	ρ_h, %	V_f, kN	$V_{n,\text{ACI}}$, kN	V_{sf}, kN	$V_{n,\text{EPRI}}$, kN	$V_{n,\text{CSA}}$, kN
C-R	Cylindrical	—	36	—	—	—	—	1.86	5.71	0.93	3775	542	3121	1163	1485
C-V	Cylindrical	—		0.64	1300	—	—				4794	542	3121	1758	1365
C-Vh	Cylindrical	—		0.64	1300	1.00	650				4869	972	3121	1758	1600
C-VH	Cylindrical	—		0.64	1300	1.00	1300				4972	972	3121	1758	1885
C-VH-C	Cylindrical	O		0.64	1300	1.00	1300				4972	972	3121	1758	1885
I-R	Planar	—		—	—	—	—				2575	1434	2305	1380	1485
I-VH	Planar	—		0.64	1300	1.00	650				3263	1434	2305	1981	1885

Note: f_c' is compressive strength; V_f is flexural strength prediction (sectional analysis); $V_{n,\text{ACI}}$ is shear strength prediction based on Joint ACI-ASME Committee 359 (or ACI 349 for planar walls); V_{sf} is shear-friction strength prediction based on Joint ACI-ASME Committee 359 (or ACI 349 for planar walls); $V_{n,\text{EPRI}}$ is shear strength prediction based on EPRI; $V_{n,\text{CSA}}$ is shear strength prediction based on CSA A23.3; 1 kN = 0.225 kip; 1 MPa = 0.145 ksi.

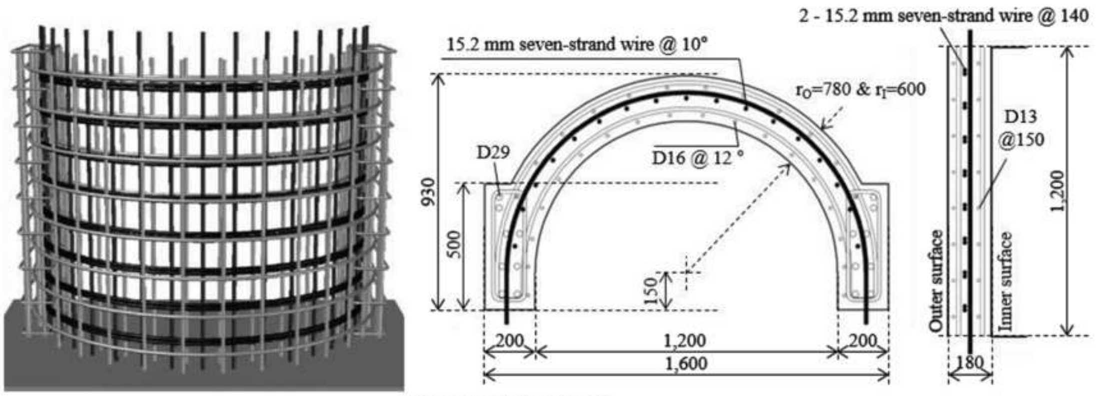

(a) Cylindrical wall

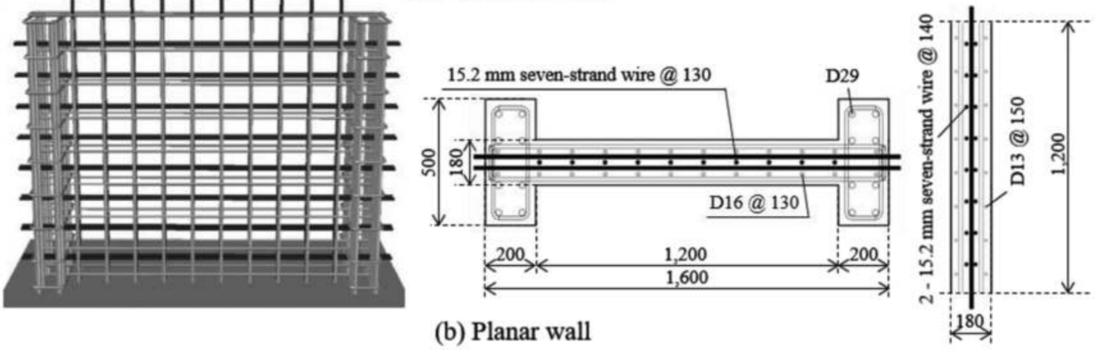

(b) Planar wall

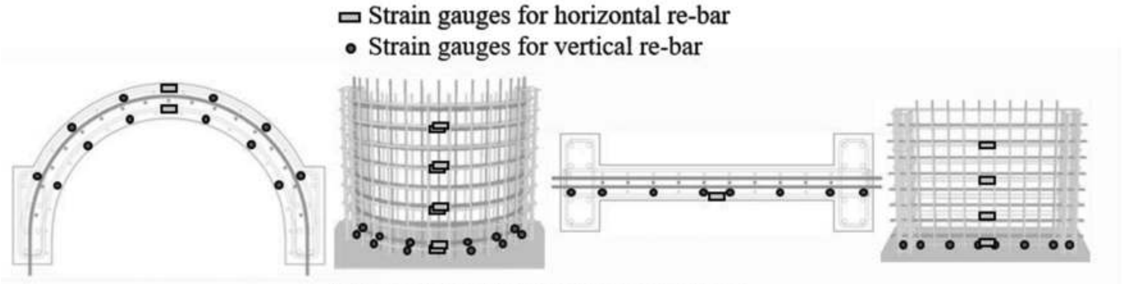

(c) Location of internal instrumentation

Fig. 2—Dimensions and reinforcement details of test specimens. (Note: All dimensions are in mm and vertical reinforcing bars or tendons are in degrees; 1 MPa = 0.145 ksi; 1 mm = 0.0394 in.)

Test specimens

Figure 2 shows the dimensions and details of the specimens. Table 1 presents the design parameters. The aspect ratio of all the specimens was determined as 1.0, considering the lateral moment-shear ratio (*M*/*V*) of the prototype containment building.

The dimensions of the semi-cylindrical wall specimens were 930 mm (external half diameter) x 1200 mm (height) x 180 mm (thickness) (30.42 x 46.80 x 7.02 in.). The flanges were added for anchorage of the horizontal prestressing. Thus, the length of the walls was 1600 mm (62.40 in.), and the flanges' lengths were 500 mm (19.5 in.). The wall thickness (180 mm [7.02 in.]) was determined to accommodate double layers of reinforcing bars and tendons. Thus, the wall diameter-to-thickness ratio of the test specimens was smaller than that of the actual cylindrical wall in the prototype NPP containment building.

The reinforcing bar ratios of all specimens except the flange reinforcement were 1.86% and 0.93% for vertical and horizontal reinforcements, respectively (Table 1). The reinforcing bar ratios were the same as those of the prototype containment structure. In the case of planar wall specimens, the dimensions were 1600 mm (length) x 1200 mm (height) x 180 mm (thickness) (62.40 x 46.80 x 7.02 in.). The length of the planar walls was the same as that of the cylindrical wall, and the flange area was the same (500 x 200 mm [19.50 x 7.80 in.]).

In the cylindrical RC specimen, C-R, the vertical and horizontal reinforcement ratios were 1.86% and 0.93%, respectively, using Grade 420 MPa (60 ksi) reinforcing bar (Table 1). In the flanges, the vertical reinforcement ratio was intentionally increased to induce shear failure before flexural yielding, using eight D29 (No. 9) reinforcing bars (Fig. 2). The nominal flexural strength and shear-friction strength were V_f = 3775 kN (849 kip) and V_{sf} = 3121 kN (702 kip), respectively. The nominal flexural strength V_f was calculated by sectional analysis assuming linear strain distribution. The shear-friction strength was predicted based on ACI 359. The shear strengths predicted by ACI 359, EPRI (2018), and CSA A23.3-14 (2014) were $V_{n,\mathrm{ACI}}$ = 542 kN (122 kip), $V_{n,\mathrm{EPRI}}$ = 1163 kN (262 kip), and $V_{n,\mathrm{CSA}}$ = 1485 kN (334 kip), respectively (refer to Appendix A for the calculation methods). The

Table 2—Mixture design of concrete

w/c, %	Unit weight, kgf/m^3				Slump, mm	Maximum aggregate size, mm
	W	C	CA	HRWRA		
34.8	168	707	10,026	4.83	150	25

Note: w/c is water-cement ratio; W is water; C is cement; CA is coarse aggregate; and HRWRA is high-range water-reducing admixture.

shear strengths were smaller than the flexural and shear-friction strengths. The CSA A23.3 method, which is based on a simplified Modified Compression Field Theory (MCFT) (Vecchio and Collins 1986) formulation developed by Bentz et al. (2006), did not provide a shear strength equation for circular walls. The shear strengths $V_{n,\mathrm{CSA}}$ were calculated using the squat planar wall shear strength equations, with the wall length (l_w) assumed to be the diameter of the wall ($2r$).

The post-tensioned specimen C-V was planned to investigate the effect of vertical prestressing on the shear strength of cylindrical walls. In the flanges, the vertical reinforcing bar ratio was intentionally increased to induce shear failure before flexural yielding, using eight D29 (No. 9) reinforcing bars (Fig. 2) (ρ_{fv} = 5.71%, Table 1). The nominal flexural strength (V_f = 4794 kN [1079 kip]) and the nominal shear-friction strength (V_{sf} = 3121 kN [702 kip]) were greater than the nominal shear strength $V_{n,\mathrm{ACI}}$ (= 542 kN [122 kip]), $V_{n,\mathrm{EPRI}}$ = 1758 kN (396 kip), and $V_{n,\mathrm{CSA}}$ = 1365 kN (307 kip), which are both significantly greater than $V_{n,\mathrm{ACI}}$. The low shear strength of $V_{n,\mathrm{ACI}}$ is because ACI 359 does not consider the contributions of concrete and vertical components of reinforcing bars and prestress.

In post-tensioned wall C-Vh (100% vertical + 50% horizontal prestressing force), the effect of the magnitude of horizontal prestressing on shear strength and concrete delamination was investigated. In the cases of other post-tensioned specimens C-VH and C-VH-C with 100% vertical and horizontal prestressing forces, the effects of crossties and horizontal prestressing were investigated. The vertical and horizontal tendon ratios were 0.64% and 1.00%, respectively (ASTM A416/A416M Grade 270, 15.2 mm [0.6 in.] seven-strand wires). Because of the small wall thickness, high-density polyethylene (HDPE) greased strands without sheath were used. The post-tensioning stress for 100% prestressing force was 1300 MPa (217 ksi), which was 70% of the yield stress of the tendon (= 1860 MPa [310 ksi]). The 100% vertical prestressing force developed a compressive stress of 8.32 MPa (1.21 ksi) in the vertical concrete section. The 100% and 50% horizontal prestressing forces developed compressive stresses of 13 and 6.5 MPa (3.10 and 1.55 ksi) in the horizontal concrete section. The stress level and tendon ratios were similar to those of the prototype containment structure. The nominal flexural strengths were V_f = 4849 kN (1096 kip) for C-Vh and V_f = 4972 kN (1119 kip) for C-VH and C-VH-C. The shear-friction strengths were V_{sf} = 3121 kN (702 kip) for the three specimens (ACI 359). Because of the high reinforcement ratios and prestressing, the nominal shear strengths were limited by the web-crushing strength. Thus, the nominal shear strengths of C-VH and C-VH-C predicted by ACI 359, EPRI, and CSA A23.3 were $V_{n,\mathrm{ACI}}$ = 972 kN (219 kip), $V_{n,\mathrm{EPRI}}$ = 1758 kN (396 kip), and $V_{n,\mathrm{CSA}}$ = 1885 kN (424 kip), respectively. The nominal shear strengths of C-Vh were $V_{n,\mathrm{ACI}}$ = 972 kN (219 kip), $V_{n,\mathrm{EPRI}}$ = 1758 kN (396 kip), and $V_{n,\mathrm{CSA}}$ = 1600 kN (360 kip), respectively.

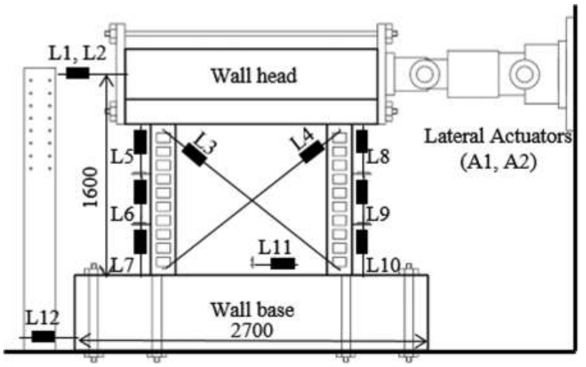

Fig. 3—Test setup.

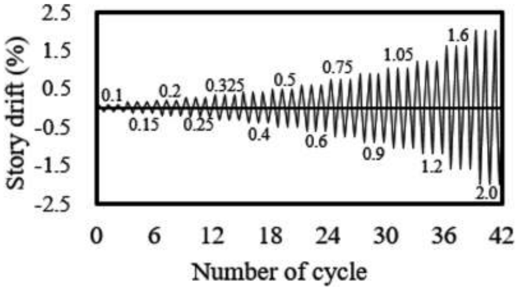

Fig. 4—Lateral loading protocol.

Planar walls I-R and I-VH were designed as RC and post-tensioned specimens, respectively (Fig. 2 and Table 1). The ratios of the reinforcing bars and tendons were the same as those of C-R and C-VH. The nominal shear strengths of I-R without prestressing were $V_{n,\mathrm{ACI}}$ = 1434 kN (323 kip), $V_{n,\mathrm{EPRI}}$ = 1380 kN (310 kip), and $V_{n,\mathrm{CSA}}$ = 1485 kN (334 kip), and those of I-VH with prestressing were $V_{n,\mathrm{ACI}}$ = 1434 kN (323 kip), $V_{n,\mathrm{EPRI}}$ = 1981 kN (446 kip), and $V_{n,\mathrm{CSA}}$ = 1885 kN (424 kip). For planar walls, the nominal shear strength $V_{n,\mathrm{ACI}}$ was predicted by ACI 349 (ACI Committee 349 2013) rather than ACI 359. $V_{n,\mathrm{ACI}}$ for planar walls (ACI 349) was close to $V_{n,\mathrm{EPRI}}$. In the strength prediction, the effect of the vertical prestressing force was considered using an equivalent axial force N_u. The nominal flexural strengths of I-R and I-VH were 2575 and 3263 kN (579 and 734 kip), respectively.

Table 2 shows the concrete mixture design. The maximum aggregate size was 25 mm (1 in.). The 28-day compressive strength was 36 MPa (5.22 ksi). The yield strengths of the reinforcing bars were 473, 473, and 458 MPa (68.6, 68.6, and 66.5 ksi) for D13, D16, and D29 (No. 4, 5, and 9), respectively. These material properties were similar to those being used for the actual construction of NPP walls.

Test procedure and instrumentation

Figure 3 shows the test setup. Cyclic lateral loading was applied by two dynamic actuators (Fig. 1). The lateral displacements of the two actuators were controlled to be the same to restrain torsion. The lateral loading protocol followed ACI 374.2R-13 (Fig. 4): three repeated cyclic loads were applied at each load step, as the drift ratio was increased to 1.25 or 1.5 times the previous drift ratio. Figure 3 shows the linear variable displacement transducers (LVDTs) for the measurement of lateral displacements L1 and L2, shear deformations L3 and L4, flexural deformations L5 to L10, and sliding at the wall base L11. Strain gauges were used to measure the strain of reinforcing bars (Fig. 2). The test was conducted at the Hybrid Structural Testing Center (Hystec) in Yongin, South Korea.

Application of post-tensioning

A major concern in the use of prestressing is the loss of the prestressing force due to the seating of wedges. Figures 5(a) and (b) show the anchorage details. To measure the prestressing force, load cells were installed at both ends. To apply the planned force (180 kN [40.5 kip]) at each tendon for the vertical and horizontal directions, a higher jacking force was applied considering the loss of force. The measurements were continued during jacking and until the wedge was settled. Because the loss of prestressing was not uniform, the jacking force was increased step-by-step (Fig. 5(c)). Figure 5(c) shows the measurements at live and dead ends of the horizontal direction. Due to friction and the elastic shortening of concrete, instantaneous loss occurred (that is, 190 kN [42.8 kip] at the live end and 165 kN [37.1 kip] at the dead end of the horizontal anchorage). However, in the vertical direction, because the dead-end anchorages were embedded in the base slab of the specimen, only prestressing forces at the live ends were measured (that is, 185 kN [41.6 kip]).

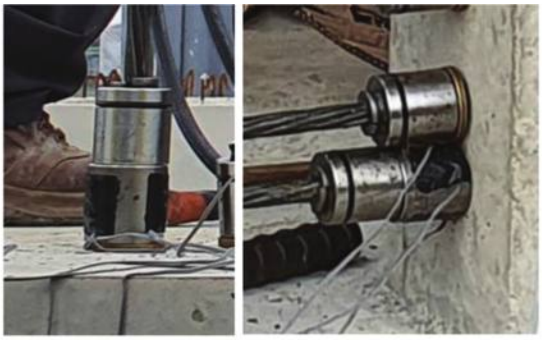

(a) Anchorage of vertical and horizontal tendons

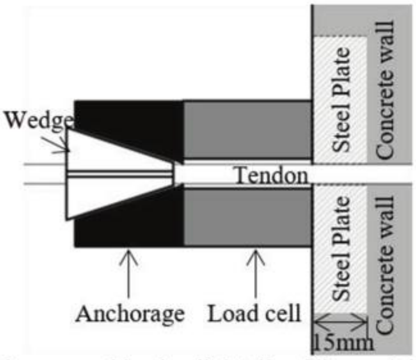

(b) Anchorage and load-cell details of live and dead ends

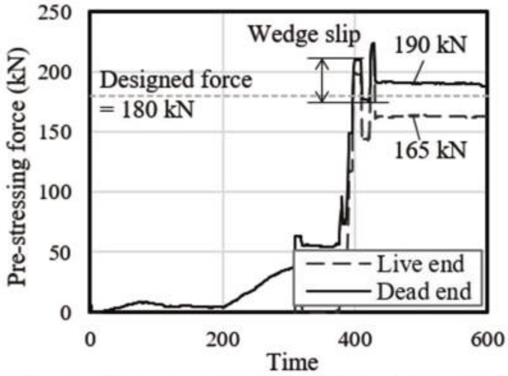

(c) Measured pre-stressing force at live and dead ends

Fig. 5—Anchorage of tendon. (Note: 1 mm = 0.0394 in.; 1 kN = 0.225 kip.)

TEST RESULTS

Lateral load-displacement relationships

Figure 6 shows the lateral load-displacement relationships of the test specimens. The lateral displacement indicates the average of the displacements measured in two LVDTs (L1 and L2) excluding slip displacement measured at the base slab (L12). The lateral load indicates the sum of the two actuator forces A1 and A2. Because of the asymmetric shape of the specimens, the magnitude of A1 and A2 were different. Figure 6 also shows the nominal shear strength $V_{n,\mathrm{ACI}}$, $V_{n,\mathrm{EPRI}}$, and $V_{n,\mathrm{CSA}}$ predicted by ACI 359 (or ACI 349 for planar walls), EPRI, and CSA. In all specimens except I-R, the maximum strength in the positive direction (push) was greater than that of the negative direction (pull). The primary reason for the asymmetric behavior of the test specimens is that the failure mode of the test specimens was concrete crushing in the web. Unlike flexural or diagonal tension failure, web concrete crushing causes damage that affects the web strength in both loading directions, as the location of the web-crushing damage is the same in both directions. Therefore, the web-crushing strength under pull loading is degraded by the preceding crushing damage under push loading.

In the case of RC specimen C-R (Fig. 6(a)), at drift ratios of +1.02% and –1.00%, the peak strengths reached +2014 kN (453 kip) and –1931 kN (424 kip), respectively. Immediately after the peak load, the load-carrying capacity decreased.

In the post-tensioned specimen C-V (Fig. 6(b)) with only vertical prestressing force, the maximum test strength was +1853 kN (417 kip) at a drift ratio of 0.75%, and –1636 kN (368 kip) at 0.68%. Unlike the expectation, the maximum strengths were 8% and 15% lower than those of C-R without prestressing force. This is because the unidirectional compressive stress reduces the allowable shear stress in the concrete and changes the crack angle. In the case of post-tensioned specimen C-Vh (Fig. 6(c)) with 100% vertical + 50% horizontal prestressing force, the peak strengths were +2044 kN (460 kip) and –2021 kN (455 kip) at 0.75% and 0.73%, respectively, which were higher than those of C-V and C-R.

In specimen C-VH (Fig. 6(d)) with 100% vertical and horizontal prestressing, the peak strengths were +2067 kN (465 kip) and –2059 kN (463 kip). These values were 2% and 6% higher than those of RC specimen C-R, respectively. On the other hand, in the case of C-VH-C with crossties, the maximum strength was +2347 kN (528 kip) and –2193 kN (493 kip) in the positive and negative directions, respectively (Fig. 6(e)). The peak strengths were 13% and 6.5% greater than those of C-VH without crossties.

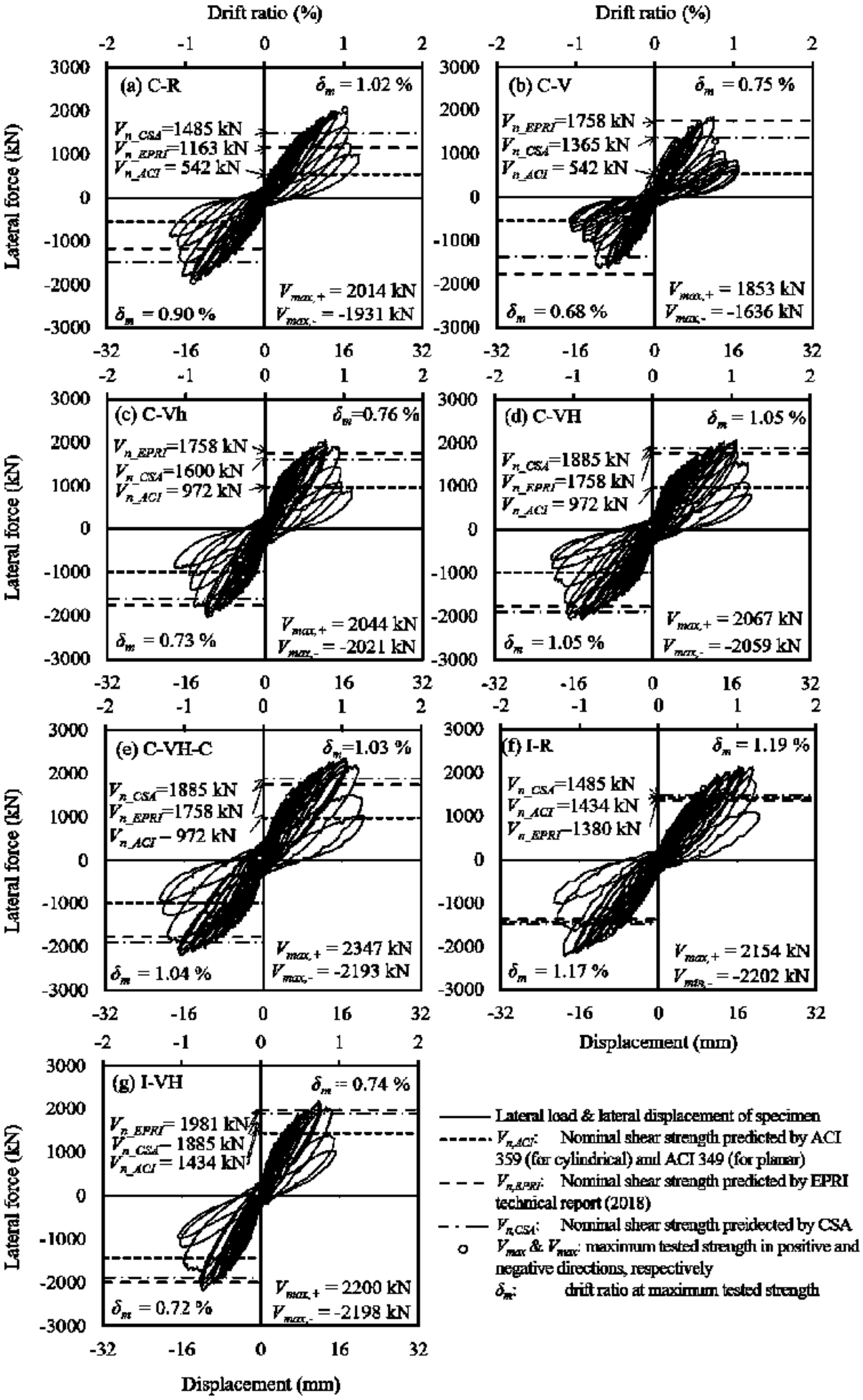

Fig. 6—Lateral load-displacement relationships of specimens. (Note: 1 mm = 0.0394 in.; 1 kN = 0.225 kip.)

In planar RC specimen I-R, the maximum strengths were +2154 kN (485 kip) and –2202 kN (495 kip) in the positive and negative directions, respectively (Fig. 6(f)). The average maximum strength of I-R was 10% greater than that of cylindrical specimen C-R. In planar specimen I-VH with prestressing, the maximum strengths were +2200 kN (495 kip) and –2198 kN (495 kip) in the positive and negative directions, respectively, which were close to those of the RC specimen (I-R) (Fig. 6(g)). The maximum strengths of I-VH were 7% greater and 3% less than those of cylindrical specimens C-VH and C-VH-C, respectively.

Damage modes

Figure 7 shows the damage modes of the cylindrical specimens at the end of the test. In the outer surface of specimens C-R and C-V without horizontal prestressing (Fig. 7(1-a) and

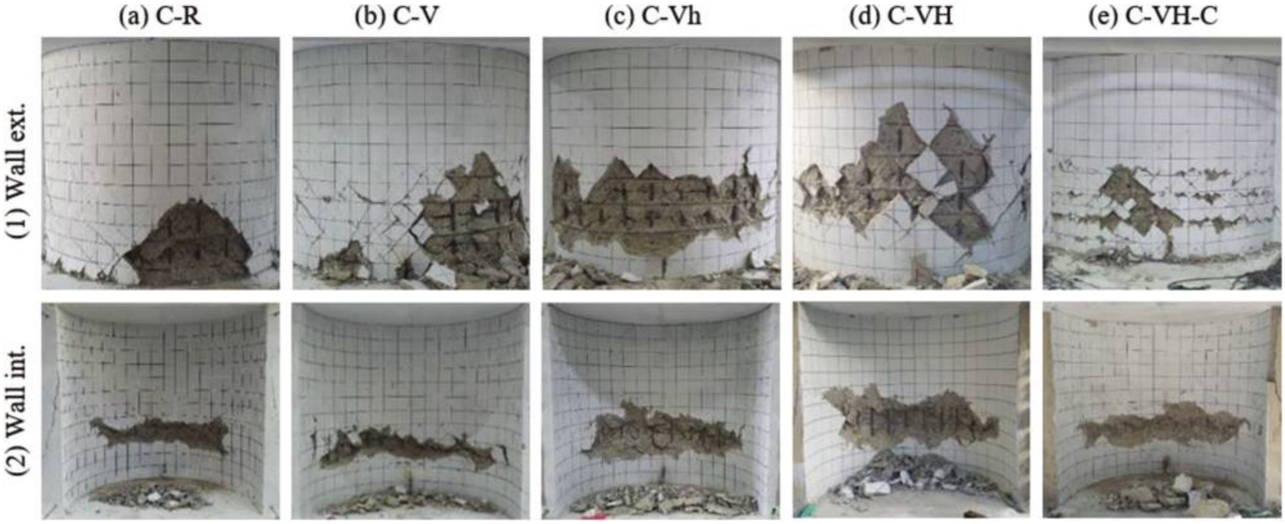

Fig. 7—Damage to semi-cylindrical specimens at end of test.

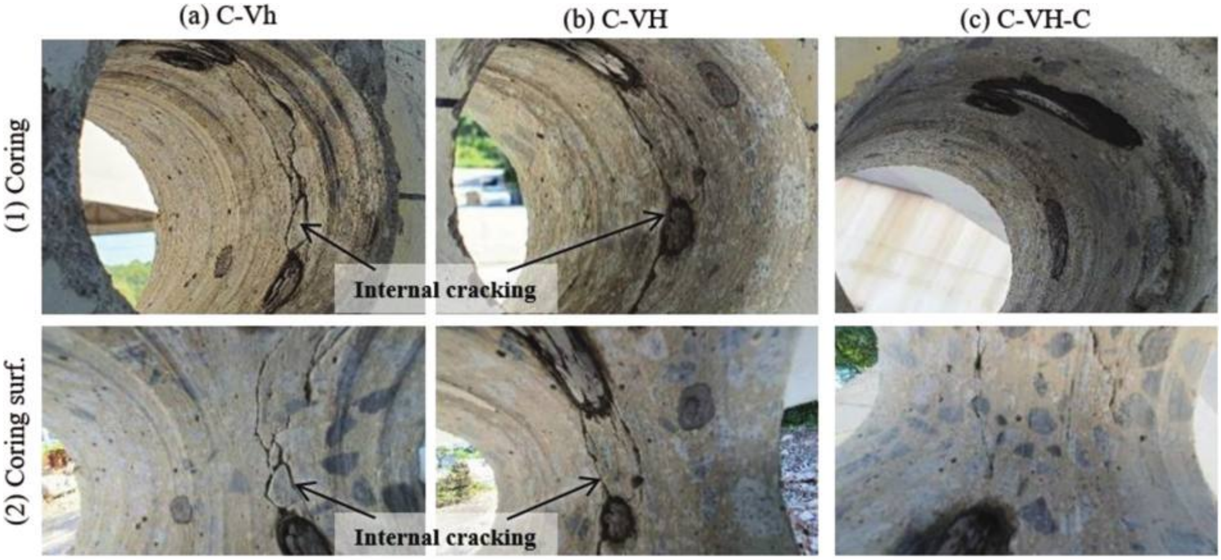

Fig. 8—Internal cracking due to horizontal prestressing in semi-cylindrical specimens.

(1-b)), diagonal tension cracking occurred, and the spacing of diagonal cracks was similar to that of ordinary planar RC walls. In the case of C-Vh and C-VH with horizontal prestressing (Fig. 7(1-c) and (1-d)), macro diagonal cracks with a large spacing developed, and cover concrete spalling occurred. In the case of C-VH-C with crossties, macro horizontal cracks occurred after micro diagonal cracking, and concrete spalling was not severe.

On the other hand, on the inner surface (Fig. 7(2)) of all specimens, large horizontal cracks occurred in the lower part after diagonal cracking. Ultimately, concrete crushing occurred at the lower part of the wall.

After testing, concrete core boring was performed in the test specimens to check delamination cracking during horizontal post-tensioning (Fig. 8). The concrete boring was performed at the top of the wall where damage from lateral loading was minimized. Figure 8 shows the internal surface of the bored hole of the test specimens. In the case of specimens with horizontal prestressing (C-Vh and C-VH), internal cracking occurred along the horizontal tendon layer. On the other hand, internal cracking did not occur in the other specimens, including C-VH-C with crossties.

Figure 9 shows the damage to the planar walls at the end of the test. The concrete cracks and failure modes were similar to those of the inner surface of the cylindrical specimens. The spacing of cracks was greater in I-VH with prestressing force (Fig. 9(b)).

Reinforcing bar strains

Figure 10 shows the strain distributions of the horizontal reinforcing bars along the wall height at $0.5V_{max}$, $0.75V_{max}$, and $1.0V_{max}$, where V_{max} indicates the peak strength. In the case of C-R without prestressing (Fig. 10(a) and (b)), the strains of all horizontal reinforcing bars at the midheight of the wall exceeded the yield strain at V_{max}. In C-V with only vertical prestressing (Fig. 10(c) and (d)), the yield strain developed only in the inner layer at the midheight. In the case of specimens with horizontal prestressing (Fig. 10(e) to (h)), the strains of the outer horizontal reinforcing bar layer were greater than those of the inner one, and the strains of all horizontal reinforcing bars, except the outer bar layer of C-Vh, were smaller than the yield strain. In the case of planar wall I-R (Fig. 10(k)), the strains of horizontal reinforcing bars exceeded the yield strain even in the upper part of the wall. In planar wall I-VH with prestressing (Fig. 10(l)), the strains of all horizontal reinforcing bars did not exceed the yield strain until the end of the test. This result indicates that: 1) in the case of specimens with horizontal prestressing force, the strains of horizontal reinforcing bars were smaller than those of specimens without prestressing; and 2) the failure of specimens with horizontal prestressing occurred before the yielding of horizontal reinforcing bars.

Figure 11 shows the strain distributions of vertical reinforcing bars along the circumference length of the wall at $0.5V_{max}$, $0.75V_{max}$, and $1.0V_{max}$. Some strain gauges failed during or before the test. The gray area in Fig. 11 indicates the flanges. In C-R without prestressing (Fig. 11(a) and (b)), only in the flange area, the strain of the outer reinforcing bar layer exceeded the yield strain. In the case of cylindrical walls with prestressing (Fig. 11(c) to (h)), the strains of vertical reinforcing bars did not exceed the yield strain, except for the flange area of C-VH. Also, in the case of planar walls (Fig. 11(k) and (l)), the strains of vertical reinforcing bars were lower than the yield strain. This result indicates that shear failure occurred before flexural yielding.

Displacement contributions

The overall lateral displacement of the specimen is defined as the sum of the contributions of shear, flexural, and sliding displacements. The overall displacement and components were measured from LVDTs in Fig. 3 (lateral displacements L1 and L2, shear deformations L3 and L4, flexural deformations L5 to L10, and sliding at the wall base L11). Figure 12 presents the test results. The contribution of shear deformation was calculated from the diagonal LVDTs, as shown in Fig. 12. The figure shows that the sum of the displacement components generally agrees with the overall displacement of the specimens. As the specimens failed in shear (diagonal tension cracking and web crushing), the contribution of shear deformation was the greatest (approximately 50 to 70%), while the contribution of sliding was the lowest.

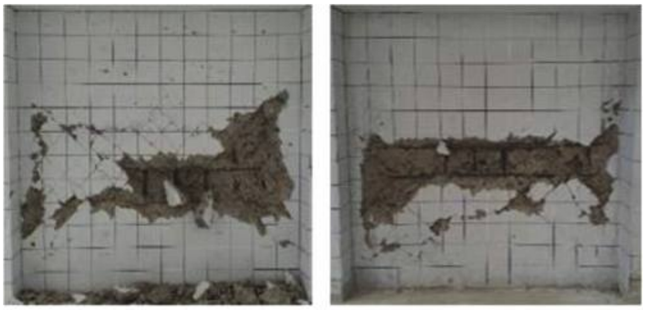

(a) I_RC (b) I_VH

Fig. 9—Damage to planar specimens at end of test.

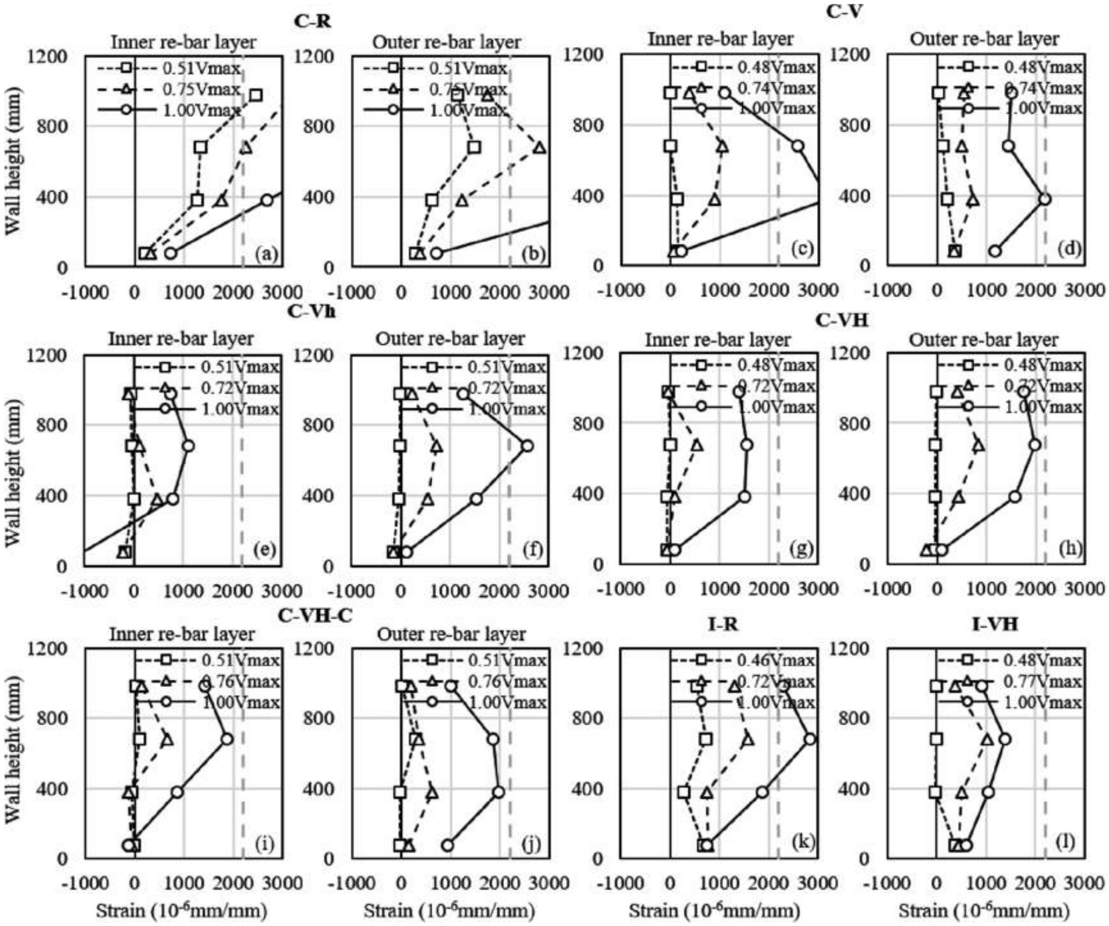

Fig. 10—Measured strains of horizontal reinforcing bars. (Note: 1 mm = 0.0394 in.)

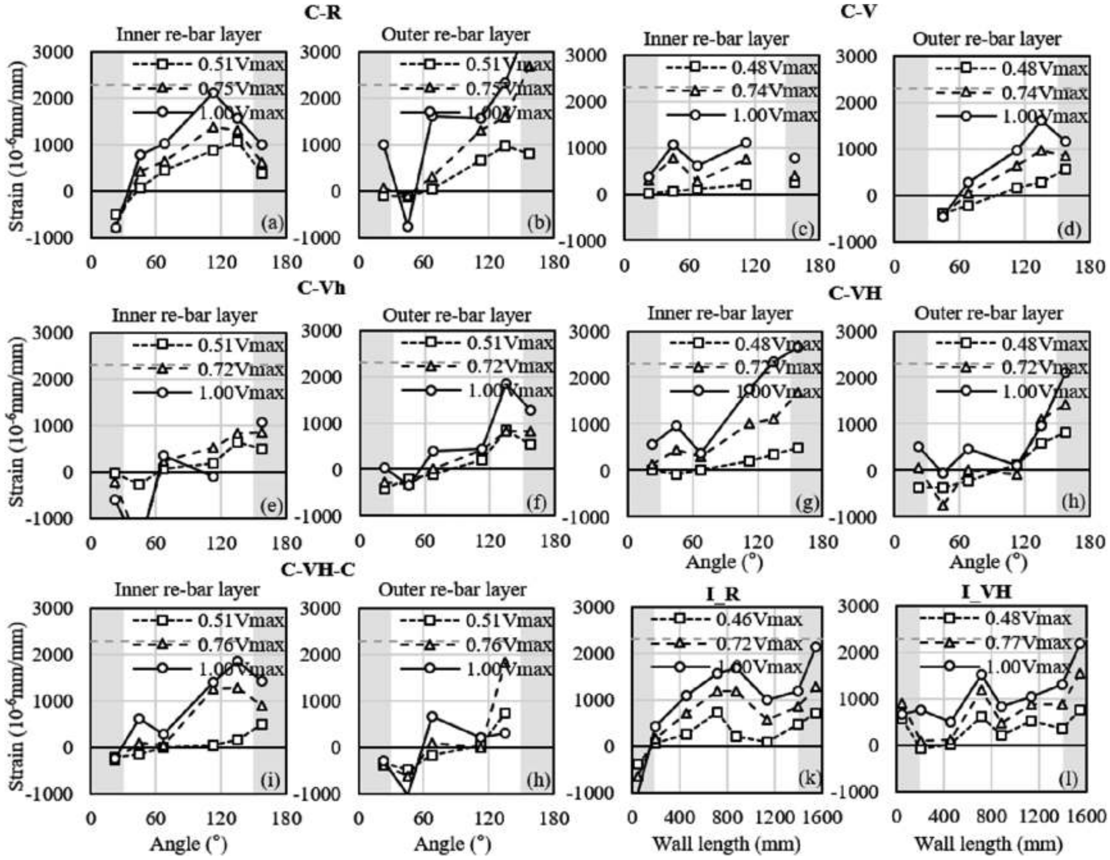

Fig. 11—Measured strains of vertical reinforcing bars. (Note: 1 mm = 0.0394 in.)

STRENGTH PREDICTIONS OF EXISTING DESIGN METHODS

Table 3 shows the test strengths V_{test}, the drift ratio at peak strength, and the failure mode, while Table 1 shows the shear strength predictions of ACI 359 (or ACI 349 for planar walls), EPRI, and CSA. The test strength V_{test} indicates the average of the peak strengths in the negative and positive loading directions. For cylindrical walls, ACI 359 was used, while for planar walls, ACI 349 was applied. In the case of ACI and EPRI, because of the high reinforcement ratio and prestressing, the shear strength was determined as the web-crushing strength. For C-R and I-R without prestressing, the ratios of the test shear strength V_{test} to the predictions of ACI 359 (or ACI 349 for I-R), EPRI, and CSA were $V_{test}/V_{n,\mathrm{ACI}} = 3.64$ (C-R) and 1.52 (I-R), $V_{test}/V_{n,\mathrm{EPRI}} = 1.83$ (C-R) and 1.58 (I-R), and $V_{test}/V_{n,\mathrm{CSA}} = 1.33$ (C-R) and 1.47 (I-R). ACI 359 excessively underestimated the test strength of C-R. CSA showed better predictions for both specimens.

In the case of C-V with vertical prestressing, the strength ratios were $V_{test}/V_{n,\mathrm{ACI}} = 3.22$, $V_{test}/V_{n,\mathrm{EPRI}} = 0.99$, and $V_{test}/V_{n,\mathrm{CSA}} = 1.28$. In ACI 359, as the effect of vertical prestressing is not considered, the shear strength was excessively underestimated. In the case of CSA considering varying crack angles, the predicted strength of C-V was lower than that of C-R. This trend is similar to that of the test results.

For the specimens with horizontal prestressing (C-Vh, C-VH, C-VH-C, and I-VH), the strength ratios were 2.09, 2.12, 2.34, and 1.53 for ACI 359 (ACI 349 for I-VH), respectively; 1.16, 1.17, 1.29, and 1.11 for EPRI; and 1.27, 1.09, 1.20, and 1.17 for CSA. For cylindrical walls, EPRI and CSA showed better predictions. As mentioned, in both the ACI and EPRI predictions, the predicted strengths were limited by web-crushing strength. However, the web-crushing strengths were significantly different: for cylindrical walls, the web-crushing stress strength was $\overline{v}_{\mathrm{ACI},W} = 10\sqrt{f_c'}bt$ for ACI 359, which is half of $v_{\mathrm{EPRI},W} = 21.1\sqrt{f_c}$ for EPRI (psi units, both). This result indicates that the web-crushing strength of ACI 359 needs to be increased for better predictions of shear strength.

EFFECT OF DESIGN PARAMETERS ON WEB-CRUSHING SHEAR STRENGTH

Vertical prestressing for cylindrical wall

The test results of C-R and C-V show the effect of vertical prestressing on shear strength. Figure 13(a) compares the lateral load-displacement relationships according to vertical prestressing. In the case of C-V with vertical prestressing, the maximum strengths were 8.0% and 15.3% lower than that of C-R without prestressing in the positive and negative directions, respectively. Further, the deformation at the peak strength was decreased in the case of C-V. Because horizontal prestressing was not applied, diagonal cracking and delamination of cover concrete occurred early in the loading ($0.38V_{max}$ and $0.39V_{max}$ for C-V and C-R, respectively). This result indicates that vertical prestressing (without horizontal prestressing) has an adverse effect on the web-crushing strength of cylindrical walls, causing the early delamination of cover concrete.

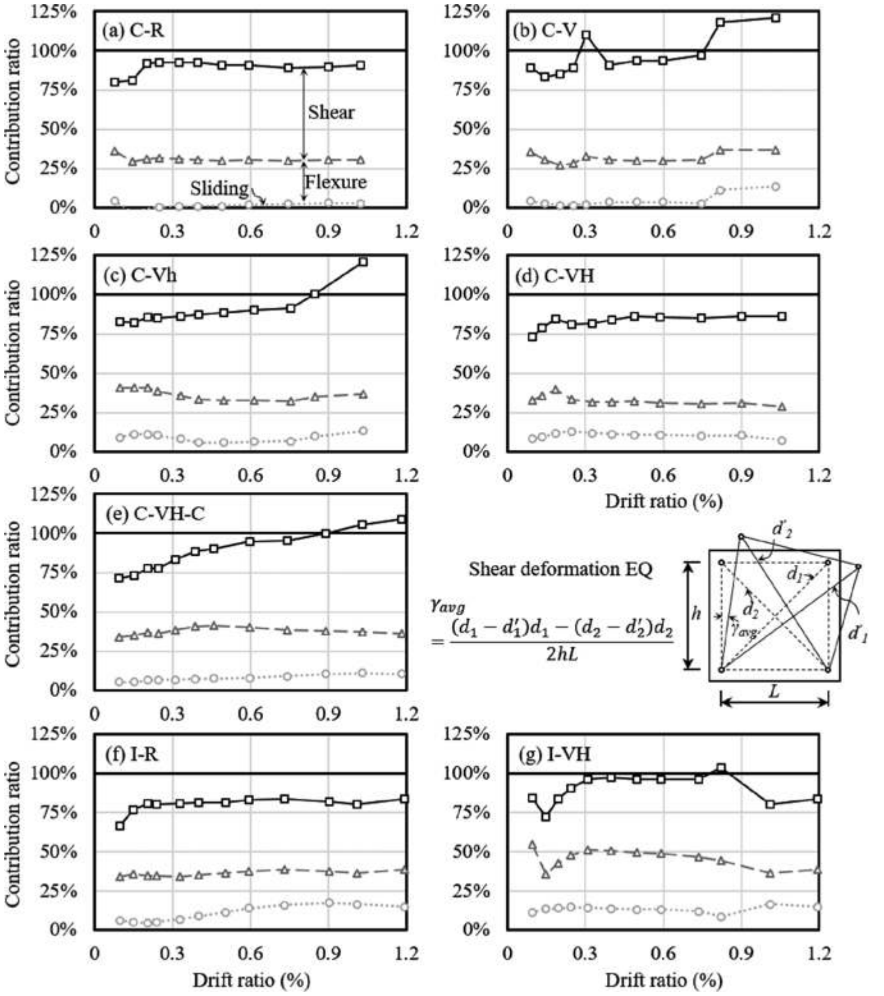

Fig. 12—Contributions of components to overall lateral displacement.

Table 3—Summary of test results

Specimens	Test results				Failure mode		Ratio of test strengths to predictions		
	$V_{test,+}$, kN	$V_{test,-}$, kN	V_{test}, kN	Drift ratio at V_{test}, %	Inner surface	Outer surface	$V_{test}/V_{n,\mathrm{ACI}}$	$V_{test}/V_{n,\mathrm{EPRI}}$	$V_{test}/V_{n,\mathrm{CSA}}$
C-R	2014	1931	1973	+1.02/–0.90	W.C.	D.T.	3.64	1.70	1.33
C-V	1853	1636	1745	+0.75/–0.68	W.C.	D.T.	3.22	0.99	1.28
C-Vh	2044	2021	2033	+0.76/–0.73	W.C.	C.S	2.09	1.16	1.27
C-VH	2067	2059	2063	+1.06/–1.05	W.C.	C.S	2.12	1.17	1.09
C-VH-C	2347	2193	2270	+1.03/–1.04	W.C.	W.C.	2.34	1.29	1.20
I-R	2154	2202	2178	+1.19/–1.17	W.C.		1.52	1.58	1.47
I-VH	2200	2198	2199	+0.74/–0.72	W.C.		1.53	1.11	1.17

Note: $V_{test,+}$, $V_{test,-}$, and V_{test} are the positive, negative, and average values of the measured maximum loads, respectively; $V_{n,\mathrm{ACI}}$ is shear strength prediction based on Joint ACI-ASME Committee 359 (or ACI 349 for planar walls); $V_{n,\mathrm{EPRI}}$ is shear strength prediction based on EPRI; $V_{n,\mathrm{CSA}}$ is shear strength prediction based on CSA A23.3; W.C., D.T., and C.S indicate failure of web crushing, diagonal tension, and cover concrete spalling, respectively; 1 kN = 0.225 kip; 1 MPa = 0.145 ksi.

Vertical and horizontal prestressing for cylindrical wall

In the case of C-VH and C-Vh with both vertical and horizontal prestressing, the initial cracking load was greater than that of C-R. However, the strength increase is only 4.6% and 3.0% (Fig. 13(b)), respectively: the effect of horizontal prestressing on web-crushing strength is marginal. In the comparison of C-V, C-Vh, and C-VH having 100% vertical, 100% vertical + 50% horizontal, and 100% vertical + 100% horizontal prestressing, respectively (Fig. 12(c)), the strengths of C-VH and C-Vh, respectively, were 18.2% and 16.5% greater than that of C-V.

Vertical and horizontal prestressing for planar wall

In the case of planar specimens I-R and I-VH, the maximum shear strength was similar regardless of prestressing ($V_{I\text{-}VH}/V_{I\text{-}R}$ = 1.01) (Fig. 13(d)). Prestressing increased the stiffness

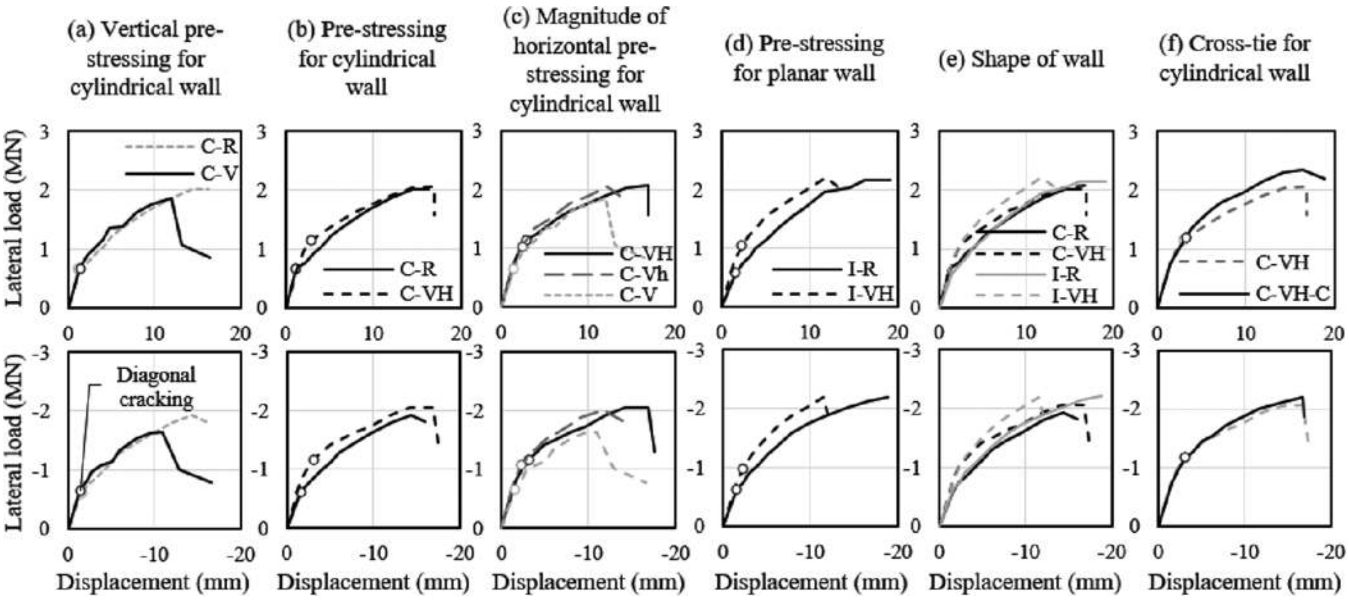

Fig. 13—Comparison of envelope curves according to design parameters. (Note: 1 mm = 0.0394 in.; 1 kN = 0.225 kip.)

and restrained concrete cracking. However, the effect of prestressing on web-crushing strength was not significant.

Wall shape

Figure 13(e) shows the effect of wall shape on shear strength and stiffness. The maximum strength ratios of planar to cylindrical walls were $V_{I\text{-}R}/V_{C\text{-}R} = 1.10$, $V_{I\text{-}VH}/V_{C\text{-}VH} = 1.07$, and $V_{I\text{-}VH}/V_{C\text{-}VH\text{-}C} = 0.97$; the maximum strengths of cylindrical specimens were similar to those of planar specimens. This result indicates that the web-crushing shear strength of a cylindrical wall with a complete circular cross section can be estimated by using a planar wall that has a wall length equivalent to the cylindrical wall diameter and wall thickness equivalent to two times the cylindrical wall thickness.

Crossties for cylindrical wall with horizontal prestressing

Figure 13(f) shows the effect of crossties on delamination cracks. The peak strengths of C-VH-C with crossties were 14% and 7% (10.5% on average) greater than those of C-VH without crossties in the positive and negative directions, respectively. The strength decrease (10.5% on average) is close to the area ratio of the cover concrete (11.1%). Further, in the case of C-VH-C, the stiffness after diagonal cracking was greater than that of C-VH. This result indicates that crossties restrained delamination cracking (Fig. 8(b) and (c)). In fact, internal cracking occurred along the horizontal tendon (Fig. 8(a) and (b)). However, the strength decrease was limited to 10.5%, which is close to the area ratio of cover concrete. This result indicates that the outer reinforcing bar layer restrained internal cracking and only cover concrete was severely damaged by internal cracking.

FINITE ELEMENT ANALYSIS OF TEST SPECIMENS

To verify the effect of post-tensioning force on the overall shear strength of cylindrical walls, nonlinear finite element analysis (FEA) was performed for the test specimens using Advanced Tool for Engineering Nonlinear Analysis (ATENA) (Cervenka et al. 2002). Figure 14 shows the analysis model. For reinforcing bars or tendons, line elements were used. The multi-linear stress-strain relationship was used to describe the post-yield strain-hardening behavior of reinforcing bars and tendons. Perfect bond was assumed between the reinforcing bars and concrete. On the other hand, in the case of tendons, slip between the tendon and concrete was allowed to address the effect of the smooth surface of the tendon. Therefore, shear force in the circumference direction was not transferred between the tendons and the concrete. Post-tensioning force was applied to the tendon using initial strain. Tetrahedral elements with 24-DOF (degrees of freedom) were used for concrete. The mesh of the model was generated by an auto-generated mesh function. At the interface between the wall and top and bottom slabs, fixed contact elements were used. The maximum size of the finite element models was limited to one-third of the wall thickness. The measured material strengths (yield strength of reinforcing bars and compressive strength of concrete) were used for the constitutive stress-strain relationships of the materials. The tensile strength of the concrete was defined as $f_t = 0.47\sqrt{f_c'}$ (SI units) (Zheng et al. 2001), where f_t and f_c' are the direct tensile strength and cylinder compressive strength of concrete, respectively.

To describe the behavior of RC walls subjected to in-plane shear, the biaxial compression-tension behavior of concrete is important. For this purpose, a simplified constitutive relationship of concrete was used: the nonlinear behavior of concrete in the biaxial stress state is described by the equivalent uniaxial stress-strain relationship in the principal stress axes (Chen and Saleeb 2013). To describe the tensile cracking of RC, a smeared crack model was used, assuming a fixed tensile crack angle. After tensile cracking, post-cracking shear stiffness with variable shear retention was used. Further, the tension-stiffening effect was considered to address the interaction between cracked concrete and reinforcing bars. In compression-tension, the compressive strength of concrete is decreased by the transverse tensile

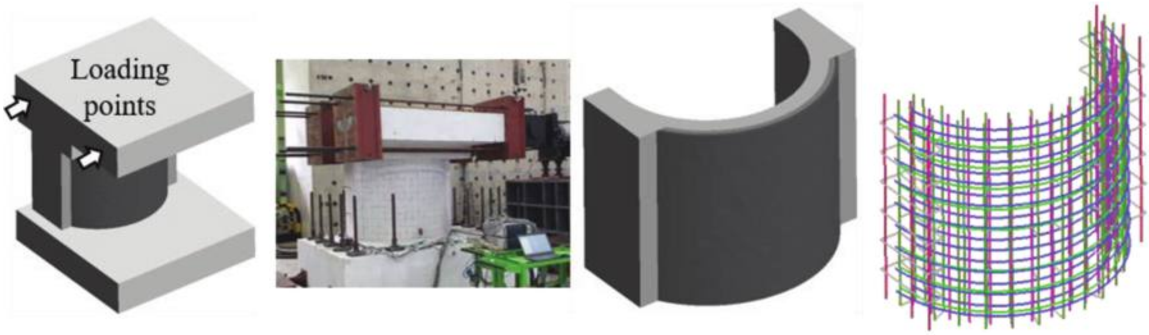

(a) FEA model (b) Actual specimen (c) Tetrahedral element for concrete (d) Line element for tendons and re-bar

Fig. 14—Finite element analysis model.

cracking. The compressive strength degradation due to tensile cracking was addressed based on the test results of Kollegger (1988) and Vecchio and Collins (1993) (Fig. 14). For FEA, monotonic loading was applied, though cyclic loading was applied in the tests.

Figure 15 shows the failure mode of specimens and principal stresses corresponding to the maximum strength. The dark color indicates an area of high compressive and tensile stresses. The stresses of the inner surface in the web were higher than those of other areas. This result indicates that diagonal tension cracking and web crushing occurred at the inner surface of the web, which agree with the test results. However, in the numerical analysis, crushing damage appeared only in the compression part because monotonic loading was applied. On the other hand, in the cyclic loading test, crushing damage occurred in the symmetric mode.

Figure 16 compares the load-displacement relationships of the specimens between the test results and nonlinear FEA. In the case of C-R without post-tensioning, the predicted maximum strength was 10% lower than the actual test results (Fig. 16(a)). Also, in the case of C-VH-C with crossties, the predicted strength was 2% lower than the tested strength (Fig. 16(e)). On the other hand, in the cases of C-V, C-Vh, and C-VH, which have post-tensioning without crossties, the nonlinear FEA overestimated the shear strength of the test specimens by 4 to 8%, and the stiffness after cracking. This is because the FEA did not describe the early delamination of cover concrete due to post-tensioning.

DESIGN RECOMMENDATIONS

Based on the present test results, the following design considerations are recommended. The web-crushing strength of walls is similar, regardless of the presence of horizontal and vertical prestressing. In particular, in NPP walls with high-demand seismic load, because of the high reinforcement ratio, the shear strength of the walls is determined as web-crushing shear strength rather than diagonal cracking strength. In this case, prestressing does not affect the shear strength. When only vertical prestressing is applied, the web-crushing strength can be lower than that of the RC specimen without prestressing. Horizontal prestressing causes internal cracking in the radial direction, which decreases the shear strength of the cylindrical wall under earthquake load. However, the outer reinforcement layer restrains the radial cracking. Thus, the strength loss was limited to 7 to 14%. Nevertheless, to use shear contribution of cover concrete, crossties are necessary. The shear strength of the cylindrical wall can be approximately estimated using that of a planar wall with a wall length equivalent to the cylindrical wall diameter. Thus, when other loading conditions, such as internal vapor pressure, are not considered, the equivalent planar wall design method can be conveniently used.

CONCLUSIONS

To investigate the horizontal shear strength of cylindrical and planar walls without and with post-tensioning, seven specimens were tested under cyclic lateral loading. The test parameters were the shape of the wall, the magnitude of prestressing, and the use of crossties. The major findings of the present study are summarized as follows:

1. In cylindrical walls, due to a high reinforcement ratio, web-crushing failure occurred in the inner surface of the walls. On the other hand, in the outer surface of walls, diagonal cracking occurred. In planar walls, diagonal cracking and web crushing occurred.
2. After testing, concrete core boring was performed. The result confirmed that concrete internal cracking occurred due to horizontal prestressing.
3. The maximum shear strength of specimen C-V with only vertical prestressing was 12% lower than that of reinforced concrete (RC) wall C-R: the vertical prestressing without horizontal prestressing had an adverse effect on the web-crushing strength of the wall.
4. The shear strength of C-Vh and C-VH with both vertical and horizontal prestressing were close to that of C-R: the effect of horizontal prestressing on the web-crushing shear strength of cylindrical walls was marginal.
5. The maximum shear strength of C-VH-C with crossties was 10% greater than that of C-VH without crossties, as the crossties restrained concrete delamination. However, as the outer reinforcement layer restrained internal cracking, the strength loss of C-VH was limited to 10.5%, which is the area ratio of cover concrete.
6. In the planar walls I-R and I-VH, the shear strengths were similar, regardless of the presence of prestressing: the effect of vertical and horizontal prestressing on web-crushing shear strength of planar walls was negligible. Further, the shear strengths of I-R and I-VH were close to those of C-R

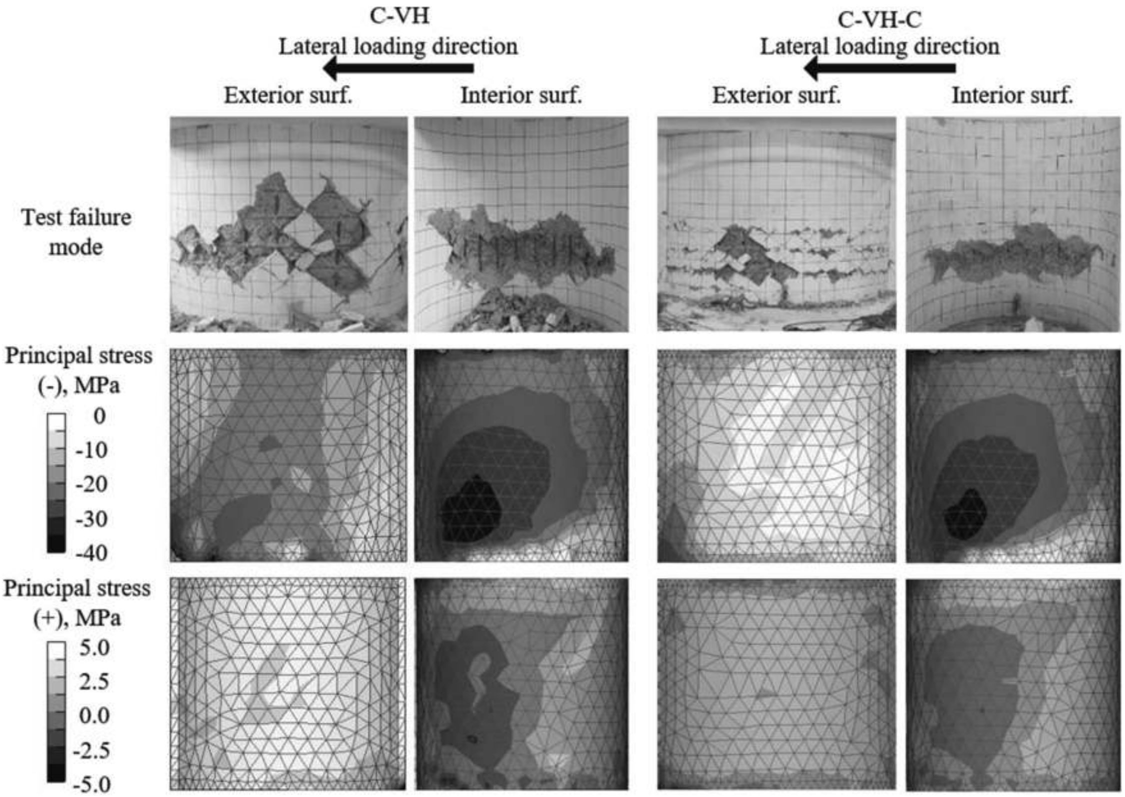

Fig. 15—Failure modes of specimens and principal stress from test results at maximum strength.

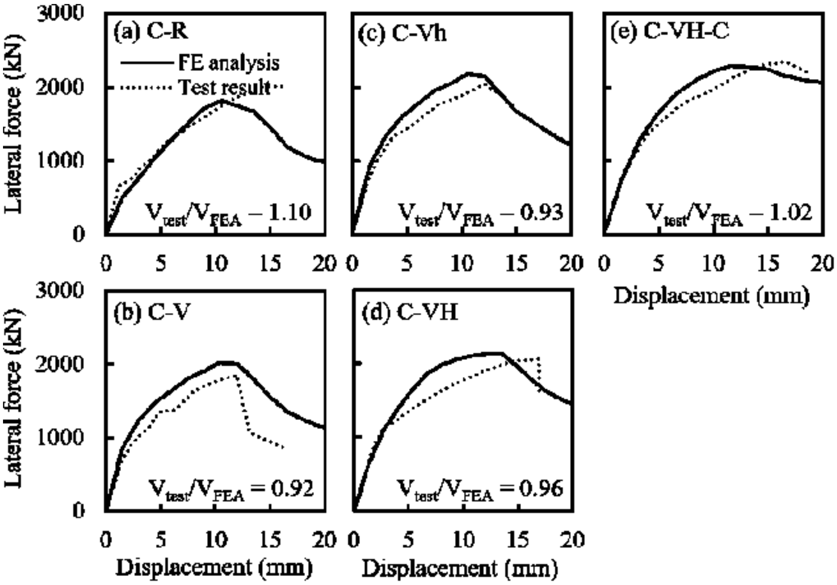

Fig. 16—Comparison between test results and nonlinear FEA results. (Note: 1 mm = 0.039 in.; 1 kN = 0.225 kip.)

and C-VH. These results indicate that the web-crushing shear strength of a cylindrical wall with a complete circular cross section can be estimated by using a planar wall that has a wall length equivalent to the cylindrical wall diameter and wall thickness equivalent to two times the cylindrical wall thickness.

7. In all specimens, the maximum test strengths were greater than the nominal strengths predicted by ACI and EPRI. In particular, the ACI 359 strengths excessively underestimated the web-crushing shear strength of cylindrical walls with and without prestressing. The web-crushing strength of ACI 359 needs to be increased for better prediction.

AUTHOR BIOS

Hyeon-Keun Yang *is a Researcher in the Korea Atomic Energy Research Institute (KAERI), Daejeon, South Korea. He received his BE and PhD in architectural engineering from Seoul National University, Seoul, South Korea. His research interests include the shear strength of reinforced concrete (RC) structures and seismic evaluation of nuclear power plant buildings.*

Hong-Gun Park, *FACI, is a Professor in the Department of Architecture and Architectural Engineering at Seoul National University. He received his BE and MS in architectural engineering from Seoul National University and his PhD in civil engineering from The University of Texas at Austin,*

Austin, TX. His research interests include inelastic analysis and the seismic design of RC structures.

ACKNOWLEDGMENTS

This work was supported by the Korea Institute of Energy Technology Evaluation and Planning (KETEP) and the Ministry of Trade, Industry and Energy (MOTIE) of the Republic of Korea (No. 20201510100010).

REFERENCES

Acharya, S., and Menon, D., 2003, "Prediction of Radial Stresses Due to Prestressing in PSC Shells," *Nuclear Engineering and Design*, V. 225, No. 1, pp. 109-125. doi: 10.1016/S0029-5493(03)00135-3

ACI Committee 349, 2013, "Code Requirements for Nuclear Safety-Related Concrete Structures (ACI 349-13) and Commentary," American Concrete Institute, Farmington Hills, MI, 196 pp.

ACI Committee 374, 2013, "Guide for Testing Reinforced Concrete Structural Elements under Slowly Applied Simulated Seismic Loads (ACI 374.2R-13)," American Concrete Institute, Farmington Hills, MI, 18 pp.

Aoyagi, Y.; Ohmori, S.; and Yamada, K., 1981, "Strength and Deformational Characteristics of Orthogonally Reinforced Concrete Containment Models Subjected to Lateral Forces," *Proceedings*, 6th International Conference on Structural Mechanics in Reactor Technology (SMiRT 6), V. J(a), Paris, France.

Basu, P. C.; Gupchup, V. N.; and Bishnoi, L. R., 2001, "Containment Dome Delamination," *Proceedings*, 16th International Conference on Structural Mechanics in Reactor Technology (SMiRT 16), Washington, DC, 8 pp.

Bentz, E. C.; Vecchio, F. J.; and Collins, M. P., 2006, "Simplified Modified Compression Field Theory for Calculating Shear Strength of Reinforced Concrete Elements," *ACI Structural Journal*, V. 103, No. 4, July-Aug., pp. 614-624.

Burgueño, R.; Liu, X.; and Hines, E. M., 2014, "Web Crushing Capacity of High-Strength Concrete Structural Walls: Experimental Study," *ACI Structural Journal*, V. 111, No. 2, Mar.-Apr., pp. 235-246.

Cervenka, V.; Cervenka, J.; and Pukl, R., 2002, "ATENA—A Tool for Engineering Analysis of Fracture in Concrete," *Sādhanā*, V. 27, No. 4, pp. 485-492. doi: 10.1007/BF02706996

Chen, W.-F., and Saleeb, A. F., 2013, *Constitutive Equations for Engineering Materials, Volume 1: Elasticity and Modeling*, Elsevier, Amsterdam, the Netherlands.

Choi, J., 2018, "Investigating Delamination Behavior of Curved Post-Tensioned Concrete Structures," doctoral dissertation, The University of Texas at Austin, Austin, TX.

Choi, J.; Woods, C. R.; Hrynyk, T. D.; and Bayrak, O., 2017, "Behavior of Curved Post-Tensioned Concrete Structures without Through-Thickness Reinforcement," *ACI Structural Journal*, V. 114, No. 4, July-Aug., pp. 983-994. doi: 10.14359/51689783

CSA A23.3-14, 2014, "Design of Concrete Structures," CSA Group, Toronto, ON, Canada.

Eom, T.-S.; Park, H.-G.; Kim, J.-Y.; and Lee, H.-S., 2013, "Web Crushing and Deformation Capacity of Low-Rise Walls Subjected to Cyclic Loading," *ACI Structural Journal*, V. 110, No. 4, July-Aug., pp. 575-584.

EPRI, 2018, "Seismic Fragility and Seismic Margin Guidance for Seismic Probabilistic Risk Assessments," Electric Power Research Institute, Palo Alto, CA.

Florida Power & Light Company, 1970, "Containment Dome Report: Turkey Point Unit 3," Docket No. 50-250, Juno Beach, FL.

Florida Power & Light Company, 1976, "Reactor Building Dome Delamination Report: Crystal River Unit 3," Docket No. 50-302, Juno Beach, FL.

Gulec, C. K., and Whittaker, A. S., 2011, "Empirical Equations for Peak Shear Strength of Low Aspect Ratio Reinforced Concrete Walls," *ACI Structural Journal*, V. 108, No. 1, Jan.-Feb., pp. 80-89.

Joint ACI-ASME Committee 359, 2015, "Code for Concrete Containments (ACI 359-15)," Part of ASME Boiler and Pressure Vessel Code, Section III, American Concrete Institute, Farmington Hills, MI.

Katoh, M.; Tamura, S.; Watanabe, Y.; Takeda, T.; and Yamaguchi, T., 1987, "Dynamic and Static Loading Tests Using 1/30 Scale Model of PCCV," *Puresutoresuto Konkurito*, V. 28, pp. 74-92.

Kollegger, J., 1988, "Experimentelle und analytische untersuchungen zur aufstellung eines materialmodels für gerissene stahlbetonscheiben," Forschungsbericht, No. 6.

Nuclear Regulatory Commission, 2010, "Public Meeting Summary – Special Inspection Results Crystal River Nuclear Power Plant," Rockville, MD.

Oesterle, R. G.; Aristizabal-Ochoa, J. D.; Shiu, K. N.; and Corley, W. G., 1984, "Web Crushing of Reinforced Concrete Structural Walls," *ACI Journal Proceedings*, V. 81, No. 3, May-June, pp. 231-241.

Ogaki, Y.; Kobayaski, M.; Takeda, T.; Yamaguchi, T.; Yoshizaki, S.; and Sugano, S., 1981, "Shear Strength Tests of Prestressed Concrete Containment Vessels," *Proceedings*, 6th International Conference on Structural Mechanics in Reactor Technology (SMiRT 6), V. J(a), Paris, France.

Uchida, T.; Ohmori, N.; Takahashi, T.; Watanabe, S.; Abe, H.; and Aoyagi, Y., 1979, "Behavior of Reinforced Concrete Containment Models under the Combined Action of Internal Pressure and Lateral Force," *Proceedings*, 5th International Conference on Structural Mechanics in Reactor Technology (SMiRT 5), V. J, Berlin, Germany, 9 pp.

Vecchio, F. J., and Collins, M. P., 1986, "The Modified Compression-Field Theory for Reinforced Concrete Elements Subjected to Shear," *ACI Journal Proceedings*, V. 83, No. 2, Mar.-Apr., pp. 219-231.

Vecchio, F. J., and Collins, M. P., 1993, "Compression Response of Cracked Reinforced Concrete," *Journal of Structural Engineering*, ASCE, V. 119, No. 12, pp. 3590-3610.

Wu, C.-L.; Hsu, T. T. C.; Chang, C.-Y.; Lu, H.-J.; Yang, H.-C.; Chang, C.-C.; and Yang, Y.-S., 2019, "Reversed Cyclic Tests of 1/13 Scale Cylindrical Concrete Containment Structures," *Concrete Structures in Earthquake*, T. T. C. Hsu, ed., Springer, Singapore, pp. 131-149.

Zheng, W.; Kwan, A. K. H.; and Lee, P. K. K., 2001, "Direct Tension Test of Concrete," *ACI Materials Journal*, V. 98, No. 1, Jan.-Feb., pp. 63-71.

APPENDIX A—CURRENT DESIGN/ EVALUATION STANDARDS

ACI 359 (for cylindrical wall)

In ACI 359-15, for shear design of containment buildings under lateral load, the maximum tangential shear flow calculated from elastic theory for a cylindrical wall is used without considering shear force redistribution along the wall length.

The shear flow demand ($\overline{V_u}$, force per unit length, N/m [kip/in.]) can be calculated as follows

$$\overline{V_u} = \tau t = \frac{VQ}{I} = \frac{V}{I}\int y dA \qquad \text{(A1)}$$

From Eq. (A1), the maximum shear stress of a cylindrical wall with a thin circular section is calculated as follows

$$\tau_{max} = \frac{V}{\pi r t}\text{(thin cylindrical wall)} \qquad \text{(A2)}$$

where A is the gross area of the section; t is the thickness of the section; and r, r_1, and r_2 are the average, outer, and inner radius, respectively.

In ACI 359, the shear flow strength $\overline{V_n}$ of containment walls is basically defined as the sum of the contributions of concrete $\overline{V_c}$ and shear reinforcement $\overline{V_s}$. In the case of an RC wall, the contribution of concrete is neglected ($\overline{V_c} = 0$). In the case of a PSC wall, when $\overline{V_u}$ exceeds $0.85\overline{V_c}$, the entire tangential shear should be resisted by shear reinforcement $\overline{V_s}$.

The area of hoop reinforcement required to resist $\overline{V_u}$ is calculated as follows

$$\overline{A_{sh}} = \frac{\overline{N_h} + \left(\overline{N_{hl}}^2 + \overline{V_u}^2\right)^{1/2}}{0.9 f_y}$$
$$\text{(SI and psi units, mm}^2\text{/m [in.}^2\text{/ft])} \qquad \text{(A3)}$$

where $\overline{V_u}$ is the maximum tangential shear flow resulting from lateral load (N/m); $\overline{A_{sh}}$ is the area per unit length of bonded reinforcement in the hoop direction (mm^2/m); $\overline{N_h}$ is the membrane shear flow in the hoop direction due to pressure, prestress, and dead load (N/m); $\overline{N_{hl}}$ is the membrane shear flow in the hoop direction from lateral load (N/m); and f_y is the yield strength of reinforcement (MPa).

For the present test specimen subjected to a concentrated lateral load, $\overline{V}_u$ is equal to $\overline{N}_{hl}$. Thus, from Eq. (A2) and $\overline{V}_{c,\mathrm{ACI}} = \overline{V}_u = \overline{V}_s$, the shear flow strength of hoop reinforcement $\overline{V}_s$ can be calculated as follows

$$\overline{V}_{c,\mathrm{ACI}} = \overline{V}_s = \frac{0.9 f_y \overline{A}_{sh} - \overline{N}_h}{\sqrt{2}}$$
$$\text{(SI and psi units, N/m [k/ft])} \qquad \text{(A4)}$$

To prevent diagonal crushing failure, the shear flow strength $\overline{V}_n$ in Eq. (A4) should satisfy the following condition.

$$\overline{V}_{c,\mathrm{ACI}} \leq 0.83\sqrt{f_c'}bt \text{ (SI units, N/m) or}$$
$$10\sqrt{f_c'}bt \text{ (psi units, kip/ft)} \qquad \text{(A5)}$$

where f_c' is the compressive strength of concrete (MPa [psi]); b is the unit length of the section (m/m); and t is the net wall thickness considering any reduction due to tendon ducts (mm). From Eq. (A4) and (A2), the overall strength of a wall can be calculated as $V_{c,\mathrm{ACI}} = \pi r \overline{V}_{c,\mathrm{ACI}}$.

ACI 349 (for planar wall of nuclear power plants)

In ACI 349, the overall shear strength of a wall is defined as the sum of the contributions of concrete V_c and shear reinforcement V_s

$$V_{p,\mathrm{ACI}} = V_c + V_s \qquad \text{(A6)}$$

The shear strengths of concrete and shear reinforcement are expressed as follows

$$V_c = (\sqrt{f_c'}/6)hd \text{ (SI units)} \qquad \text{(A7a)}$$

$$V_c = 0.28\sqrt{f_c'}hd + N_u d/4l_w \text{ (SI units)} \qquad \text{(A7b)}$$

$$V_c = \left[0.05\sqrt{f_c'} + \frac{l_w\left(0.1\sqrt{f_c'} + 0.2N_u/l_w h\right)}{M_u/V_u - l_w/2}\right]hd \text{ (SI units)}$$
$$\text{(A7c)}$$

$$V_s = A_v f_{yh} d/s \qquad \text{(A8)}$$

$$\overline{V}_{p,\mathrm{ACI}} \leq 0.83\sqrt{f_c'}hd \text{ (SI units, N/m) or}$$
$$10\sqrt{f_c'}bd \text{ (psi units, kip/ft)} \qquad \text{(A9)}$$

where f_c' is the concrete compressive strength (MPa); h, d, and l_w are the thickness of the wall, distance from the extreme compression fiber to the centroid of longitudinal tension reinforcement ($d = 0.8l_w$), and overall length of the wall, respectively (mm); A_s is the area of shear reinforcement within spacing s (mm^2); f_{yh} is the yield strength of shear reinforcement (MPa); M_u and V_u are the applied flexural moment and shear force, respectively (N·mm and N); and N_u is the axial force in the wall (kip). The shear contribution of concrete V_c is determined as the smaller values of Eq. (A7b) and (A7c), unless Eq. (A7a) is used.

CSA A23.3

In CSA A23.3, the shear strength of a wall is defined as the sum of the contributions of concrete V_c, shear reinforcement V_s, and prestressing V_p based on the simplified MCFT

$$V_{n,\mathrm{CSA}} = V_c + V_s + V_p \leq 0.25 f_c bd + V_p \qquad \text{(A10)}$$

The contributions of concrete V_c and reinforcement V_s are calculated as follows

$$V_c = \beta\sqrt{f_c'}bd \qquad \text{(A11)}$$

$$V_s = \frac{A_s f_y d_v}{s}\cot\theta = f_y \rho_h bd\cot\theta \qquad \text{(A12)}$$

where V_p is a component of the effective prestressing force in the direction of the applied shear. In the present test specimens, V_p is zero.

The β and θ in Eq. (A11) and (A12) are determined as follows

$$\beta = \frac{0.40}{1 + 1500\varepsilon_x} \qquad \text{(A13)}$$

$$\theta = 29° + 7000\varepsilon_x \qquad \text{(A14)}$$

$$\varepsilon_x = \frac{M_f/d_v + V_f - V_p + 0.5N_f - A_p f_{po}}{2(E_s A_s + E_p A_p)} \qquad \text{(A15)}$$

where N_f is the axial load; and M_f and V_f are the moment due to loads and shear force.

EPRI (evaluation guideline)

Cylindrical wall—In EPRI (2018), the overall shear strength is considered, unlike ACI 359 using the maximum shear flow. The overall horizontal shear strength $V_{c,\mathrm{EPRI}}$ of a cylindrical concrete wall is calculated using an effective shear area A_{eff}

$$A_{eff} = A_g/\alpha \qquad \text{(A16)}$$

where A_g is the gross section area of the cylindrical wall (in.^{2}); α is a factor from 2.0 to 2.5 according to M/Vd_0; and d_0 is the outside diameter of the cylindrical wall. The shear strength is determined based on Ogaki et al. (1981) and Aoyagi et al. (1981)

$$V_{c,\mathrm{EPRI}}/A_{eff} = 0.8\sqrt{f_c'} + (\rho f_y)_{AVER} \text{ (psi units)} \qquad \text{(A17a)}$$

$$V_{c,\mathrm{EPRI}}/A_{eff} \leq 21.1\sqrt{f_c'} \text{ (psi units)} \qquad \text{(A17b)}$$

$$(\rho f_y)_{AVER} = \frac{(\rho_{hp} + \rho_m)}{2}f_y - \frac{(\sigma_h + \sigma_m)}{2} \qquad \text{(A18)}$$

where ρ_{hp} and ρ_m are the hoop and meridional reinforcement ratios, respectively; f_c' is the concrete compressive strength (psi); f_y is the yield stress capacity of the reinforcing steel (psi); and σ_h and σ_m are the hoop and meridional stresses resulting from dead load, internal pressures, and lateral load (psi, tension positive).

Planar wall with boundary element—In the case of low-rise shear walls with boundary elements and an aspect ratio less than 1, the shear strength proposed by Gulec and Whittaker (2011) is used

$$V_{p,\text{EPRI}} = \frac{2.9\sqrt{f_c'}A_{eff} + 0.43F_{vw} + 0.11F_{be} + 0.35N_a}{\sqrt{h_w/l_w}} \tag{A19}$$

$$V_{c,\text{EPRI}}/A_{eff} \leq 15\sqrt{f_c} \text{ (psi units)} \tag{A20}$$

where f_c' is the concrete compressive strength (psi); h_w and l_w are the wall height and length, respectively (in.); b_{eff} and A_{eff} are the effective flange width and wall effective area (in. and in.^{2}), respectively; F_{vw} and F_{be} are the force carried by vertical reinforcement in the web and boundary, respectively (kip); and N_a is the axial force in the wall (kip).

APPENDIX B—CALCULATION EXAMPLE OF SHEAR STRENGTH

A calculation example of shear strength of specimen C-Vh is provided. The design properties of the specimen are: R_o = 780 mm, R_i = 600 mm, t = 180 mm, f_c' = 36 MPa, f_y = 470 MPa, ρ_v = 1.86%, ρ_h = 0.93%, ρ_{pv} = 0.64%, ρ_{ph} = 1.00%, σ_{pv} = 1300 MPa, and σ_{ph} = 650 MPa.

ACI 359 (for cylindrical wall)

Based on the design properties, the shear flow contribution of reinforcing bars is determined using Eq. (A4) in Appendix A

$$\overline{V_s} = \frac{0.9f_y\rho_{sh} - \rho_{ph}\sigma_{ph}}{\sqrt{2}}bt = 1328.0 \text{ (N/mm)} \tag{B1}$$

The maximum shear flow strength of the cylindrical wall due to concrete crushing is calculated from Eq. (A5)

$$\overline{V_{n,\text{ACI}}} \leq 0.83\sqrt{f_c'}bt = 896.4 \text{ (N/mm)} \tag{B2}$$

Therefore, the shear strength of the gross area is calculated from Eq. (A2)

$$V = \tau_{max}\pi rt = \overline{V_{n,\text{ACI}}}\pi r = 1973.1 \text{ (kN)} \tag{B3}$$

However, in the present test, a semi-cylindrical wall was used for the specimen. Thus, the shear strength of specimen C-Vh is calculated as (1973.1)/2 = 971.6 kN.

CSA A23.3

In CSA A23.3, the equation of shear contribution of concrete is determined by ε_x, which is related to the shear demand force (V_f). Therefore, the shear strength is obtained by iterative calculations. Figure B1 shows the iterative calculation flow to obtain the ultimate strength.

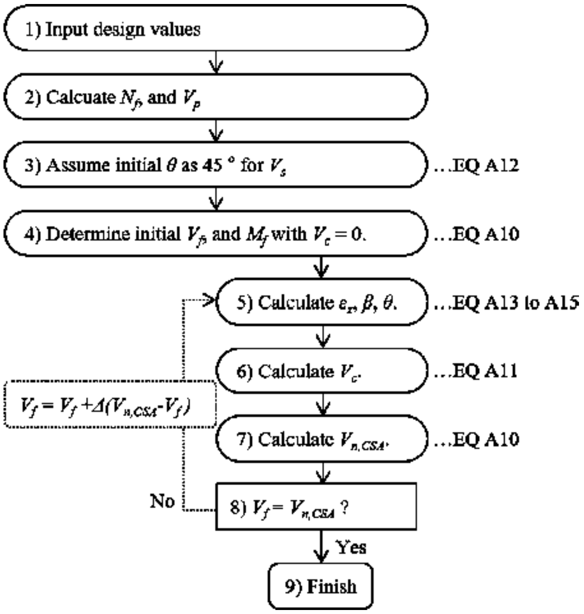

Fig. B1—Flowchart for calculating shear strength based on CSA A23.3.

The CSA standard does not provide a specific shear strength equation for cylindrical walls. Thus, the shear strength equation for squat planar walls was used. The wall length was assumed to be the same as the diameter of the semi-cylindrical wall (2r). The shear strength of specimen C-Vh was calculated as 1600 kN.

EPRI (evaluation guideline)

The effective shear A_{eff} is calculated from Eq. (A16)

$$A_{eff} = A_g/\alpha = 334{,}445 \text{ mm}^2 \tag{B4}$$

For the aspect ratio of the test specimen = 1.0 (= 1600/1560), the factor α is 2.33.

The shear strength of cylindrical walls is determined from Eq. (A17) and (A18).

$$v_{c,\text{EPRI}} = 0.8\sqrt{f_c'} + (\rho f_y)_{AVER} = 12.29 \text{ (MPa)} \tag{B5a}$$

$$v_{c,\text{EPRI}} \leq 1.75\sqrt{f_c'} = 10.51 \text{ (MPa)} \tag{B5b}$$

$$(\rho f_y)_{AVER} = \frac{(\rho_{hp} + \rho_m)}{2}f_y - \frac{(\sigma_h + \sigma_m)}{2} = 11.89 \text{ (MPa)} \tag{B6}$$

The concrete crushing strength (Eq. (B5b)) was lower than the diagonal tensile strength (Eq. (B5a)). Thus, the shear strength of C-Vh is determined as 10.51 MPa. The overall strength of cylindrical walls is calculated as $A_{eff} \times v_{c,\text{EPRI}}$. In the present test, a semi-cylindrical wall was used for the specimen. Thus, the shear strength of specimen C-Vh is calculated as 3516/2 = 1758 kN.

ACI STRUCTURAL JOURNAL TECHNICAL PAPER

Title No. 121-S03

Alternative Methods for Failure Prediction in Twin-Cell Box-Girder Bridges

by J. Chithra, Praveen Nagarajan, and A. S. Sajith

Intense research works on twin-cell box-girder bridges are limited when compared to single-cell box-girder bridges and hence, not many sources are available to study the simultaneous effect of bending and torsion in them. The estimation of ultimate load in a twin-cell box-girder bridge under different modes of failure using the two existing simplified methods—namely, the space truss analogy and collapse mechanism—demands more research attention. The primary objective of this paper is to develop simplified equations for twin-cell box-girder bridges using the principles of collapse mechanism. The second main objective is to check the suitability of using space truss analogy and collapse mechanism in different modes of failure. Experimental work for studying the effects of various structural actions due to an eccentric loading on a simply supported twin-cell concrete box-girder bridge is conducted and numerical analyses are presented to understand the effect of load positions and reinforcement ratios in the failure modes.

Keywords: collapse mechanism; failure modes; space truss analogy; twin-cell box-girder bridges.

INTRODUCTION

Box-girder bridges are considered to be one among the finest choices when designing long-span bridges. Due to their structural efficiency in handling torsion, as well as economic and aesthetic reasons, they have become very popular in the highway bridge design industry. These structures are thin-walled and hence have very peculiar stress and deformation patterns under the effects of torsion and distortion. To know more about the structural actions and reactions in box-girder bridges, various research is being conducted all over the world. As traffic congestion increases day by day, there comes high demand on larger carriageway width, which can be accomplished by using multi-cell box cross sections. As the number of cells increases, however, the risks involved in its construction also shoot up. Considering all these aspects, twin-cell box-girder bridges are considered an ingenious solution in the design of long-span bridges with larger carriage way width. Hence, studies on such structures are very essential. The complete behavior of a structure can be analyzed only by conducting nonlinear analysis. This can be achieved either by conducting experimental analysis or using three-dimensional (3-D) finite element analysis (FEA). Even though the results of these analyses are realistic and accurate to a certain extent, they are time consuming and expensive. As a bridge designer is always interested in the ultimate load of the structure, there is always a need to understand simplified methods used in estimating the ultimate load of a structure. A thorough knowledge on the existing simplified methods like the space truss analogy and the collapse mechanism may avoid the risks involved in conducting experimental and 3-D finite element studies. A brief review on the various investigations conducted in the area of simplified methods used in estimating the ultimate load of a structure is also included in this paper.

RESEARCH SIGNIFANCE

Simplified methods are largely used in estimating the failure load to avoid the rigorous 3-D FEA. It is found that simplified equations based on collapse mechanism are not available in the case of twin-cell box-girder bridges. Hence, the availability of equations to find the capacity of twin-cell box-girder bridges will be a major breakthrough in this area. Moreover, studies are conducted on finding suitability of space truss analogy and collapse mechanism in different modes of failure. This helps with identifying the best method that can provide safe results while estimating the collapse load in different failure mechanisms.

Brief literature review

The space truss analogy constitutes a landmark in the research on torsion in reinforced concrete structures. The truss theory was first postulated by Ritter (1899) with parallel tension and compression chords inclined at 45 degrees to depict the behavior of a simply supported prismatic reinforced concrete beam. Similar to that of shear, the truss theory for torsion was developed by Rausch (1929), where the reinforced concrete member is assumed to act like a tube and torsion is resisted by a circulatory shear flow in the walls of the tube. This thin-walled tube comprises the longitudinal and transverse reinforcement along with the surrounding layer of concrete, which becomes fully effective in the post-cracking phase. Evans and Sarkar (1965) assumed in their work that all the reinforcements passing through the failure surface reach their yield value. Lampert and Thürlimann (1968) and Hsu (1968) established the difference in the pre- and post-cracking stages in reinforced concrete members subjected to torsion. The test results proved that the cracking torque is less in hollow sections when compared to equivalent solid sections, thus establishing the contribution of concrete core in handling cracking torque. But this difference was not observed in ultimate torque. The reason behind this scenario

---

ACI Structural Journal, V. 121, No. 1, January 2024.
MS No. S-2022-279.R2, doi: 10.14359/51739183, received June 18, 2023, and reviewed under Institute publication policies. Pertinent discussion including author's closure, if any, will be published ten months from this journal's date if the discussion is received within four months of the paper's print publication.

was explained as owing to the elongation of stirrups in the reinforced concrete member. After cracking, the concrete core no longer contributes to the torsional forces; instead, a thin layer of concrete surrounding the reinforcement may remain active in resisting the torsional moment. The present form of the space truss model used to estimate the capacity of a box girder was proposed by Lampert and Thürlimann (1971). They proposed a failure model based on the plastic theory of concrete. By using the variable angle truss model, the combined effects of bending and torsion can be brought out more effectively in the truss model. This angle is based on the ratio of effective proportions of longitudinal and transverse reinforcements. The researchers Kuyt (1971) and Karlsson and Elfgren (1972) compared the results of space truss analogy with the existing theoretical and experimental results. This was done in case a reinforced concrete beam was subjected to torsion, thereby confirming the reliability of this method. This method is now the basis for many codes all over the world, including several European codes and the CEB-FIP model code. Strut-and-tie models used in the design of regions where there exist no standard design recommendations are more generalized versions of the truss analogy. It was Park and Paulay (1975) who extended many of the analytical and design concepts used in truss analogy to develop strut-and-tie models for the design of both B and D regions in a structure.

By the mid-twentieth century, extensive research works commenced in the field of box-girder bridges to understand the non-linear behavior of deformable reinforced concrete box section. Until then, the design of box-girder bridges was done using linear elastic analysis of simplified models. The post-cracking behavior of box-girder bridges was first studied by Spence and Morley (1975) to introduce certain theoretical formulations to obtain the ultimate load in the case of a simply supported box-girder bridge subjected to eccentric load. In this theory, collapse mechanism principles were used to estimate the collapse load in a structure. Two such mechanisms were established by Spence and Morley (1975) in the case of box girders. Collapse mechanism principles use the upper-bound theorem based on the plastic theory of structures. Here, the principle of virtual work is used to estimate the collapse load of a structure. As the work equations suggested by Spence and Morley (1975) did not accommodate the distortional deformability, the collapse load obtained from the work equations was erroneous. Danesi and Edwards (1983) conducted experimental studies and concluded that both thickness and reinforcement ratio influence the collapse load in box sections. Contrary to the assumption made by Spence and Morley (1975), Rasmussen and Baker (1999) found that the length of plastic hinge does not extend throughout the length of the box girder in case of distortion-bending collapse mechanism. They also suggested that the length of plastic hinge in a structure such as a box girder is greatly influenced by the ratio of longitudinal and transverse reinforcement. Kurian and Menon (2007) suggested a remedy to this situation by using modified plastic hinge length in the work equations based on the then-available experimental results of box-girder bridges. They suggested that the ratio of the area of reinforcement provided to that required in a unit length possess an empirical relationship with the ratio of modified plastic hinge length to the total length of girder. This modified plastic hinge length was used to revise the work equation for distortion bending collapse mechanism. With the modified plastic hinge length, the work equation for distortion bending collapse mechanism was revised and applied to get more accurate results. With the beginning of twentieth century, revolutionary developments had happened in the field of computer science, thus making 3-D FEA much simpler and less time consuming. However, even with this fast development in the computer industry, researchers like El-Sheikh (1996) suggested the need for development in approximate analysis methods, especially for preliminary designs and redesign. Hence, the development of simplified models for the analysis and design of various structures are inevitable in the field of structural engineering. Sennah and Kennedy (2002) suggested that, except for 3-D FEA, all the other simplified methods have limitations in their scope and applicability. Hence, more research work is required in this field to understand the suitability of these methods for various failure modes in case of twin-cell box-girder bridges.

Present study

Knittel and Worsh (1965) resolved a concentrated load acting at the midspan of a box girder into its symmetric and asymmetric components. Kupfer (1969) proved that the asymmetric component can be again resolved into its torsion and distortion components. These components act in the horizontal and vertical directions of the plane of plate elements in a box-girder bridge. The effect of these force components differ in various situations based on the predominance of certain forces. Both individual action and the combination of these actions lead to different failure modes of the specimen. The two major failure patterns identified in this study in the case of a twin-cell box-girder bridge are:

1. Pure bending collapse mechanism
2. Distortion-bending collapse mechanism

In pure bending collapse mechanism, the symmetric component of loading (bending component) acts through the plane of web element. In case of distortion-bending collapse mechanism, the anti-symmetrical component of loading causes the cross section of the box to distort along with bending. The details of these two mechanisms are provided along with simplified equations to estimate the collapse load in the later sections of this manuscript.

From the available literatures, it was observed that works concentrating on this area of simplified methods are mainly on single-cell box-girder bridges. Hence, such works on twin-cell box-girder bridges are necessary. In this paper, a detailed study on the behavior of twin-cell box-girder bridges subjected to the combined action of bending and torsion is provided. This experimental study is conducted on a scaled down model, the results of which are used in the validation of numerical analysis. Simplified methods are used to predict the capacity of the structure in different failure modes and the results are compared with the experimental studies and numerical studies.

EXPERIMENTAL INVESTIGATION

The experimental data aimed at understanding the realistic behavior of twin-cell box-girder bridges, available in literature, are found to be inadequate. Hence, in this paper, a detailed report on the experimental study conducted on a scaled-down model of a twin-cell box girder is presented. Due to the rising demand in decreasing the self-weight of bridges, thin-walled cross sections are essential while fixing the box dimensions. To make the cross section thin-walled, the dimensions are selected as per Vlasov's thin-walled criterion (Maisel and Roll 1974).

Here, a twin-cell box-girder bridge with end diaphragms and constant cross section simply supported at two ends was tested to collapse under eccentric loading. The dimensions of the twin-cell box section were fixed approximately to a scale of 1:10 in relation to a box-girder bridge prototype. The cross-sectional and longitudinal dimensions are provided in Fig. 1(a) and (b). The span-depth ratio adopted for the bridge model is 12, with a depth of 0.25 m (9.84 in.) and span of 3 m (118.11 in.), as the usual span-depth ratio adopted in box-girder bridges lies in the range of 12 to 30. A thickness of 60 mm (2.36 in.), which is the smallest possible thickness that can be adopted to accommodate two layers of 6 mm (0.236 in.) stirrup reinforcement, with 10 mm (0.394 in.) cover is used throughout the structure. A flange overhang length of 0.2 m (7.87 in.) is provided, as the usual practice is to provide a maximum of 0.45 times the distance between webs as the overhang length. The ratio of wall thickness to flange width and the ratio of depth to length of the specimen are 0.0984 and 0.083, confirming to Vlasov's criterion. End diaphragms of thickness 60 mm (2.36 in.) are provided at the two supports.

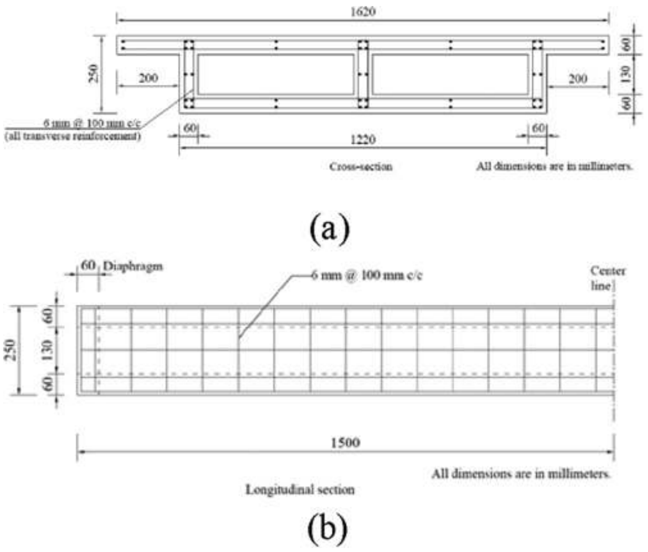

Fig. 1—Reinforcement details of twin-cell box girder (half span).

To prepare the reinforcement cage, steel rods of 6 mm (0.236 in.) diameter conforming to IS 1786 with yield stress 562 MPa (81.51 ksi) and ultimate stress 678 MPa (98.34 ksi) are used. The reinforcement details are clearly shown in Fig. 1(a) and (b). The mold used in casting, reinforcement cage, and the casting of the twin-cell are shown in Fig. 2(a), (b), and (c).

The fabrication of specimen, cement, fine aggregate, coarse aggregate, and water are mixed in the ratio 1:1.87:2.17:0.36 to prepare Grade M40 concrete. The mixture was achieved after doing mixture design as per IS 10262-2019. The results of the companion cube specimens cast to find the characteristic compressive strength is provided in Table 1. Portland pozzolana cement conforming to IS 1489 is used in the construction.

A loading frame with 40 ton capacity was used to apply the load, which was placed at an eccentricity of 290 mm (11.42 in.) to achieve a combined effect of bending and torsion in the bridge model. To avoid punching failure, the load was applied on an area of 660 x 260 mm (25.98 x 10.236 in.). The experimental test setup adopted in this work is shown in Fig. 2(d). The specimen was mounted on stiff pedestal supports at its two ends. The pedestal was placed on the floor, ensuring that it was rigidly fixed at its bottom. A steel rod was embedded on the top face of the pedestal on which the diaphragm rested, ensuring a simply supported support condition for the box-girder bridge specimen. The schematic diagram of the test setup adopted in the study is shown in Fig. 3(a). The first crack was observed at 47.5 kN (10.68 kip) on the midspan of exterior web where the load is applied. The crack was found at a distance of 50 mm

Table 1—Compressive strength of companion cubes

Specimen No.	Mixture	Compressive strength, MPa (ksi)
1	1:1.87:2.17:0.36	47.33 (6.86)
2	1:1.87:2.17:0.36	51.22 (7.43)
3	1:1.87:2.17:0.36	49.71 (7.21)

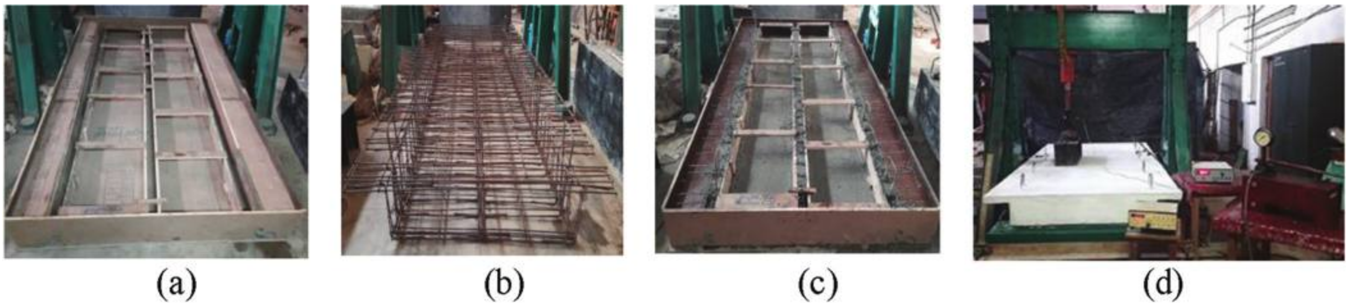
(a) (b) (c) (d)

Fig. 2—(a) Wooden mold; (b) reinforcement cage; (c) casting of box girder; and (d) experimental setup for twin-cell box-girder bridge.

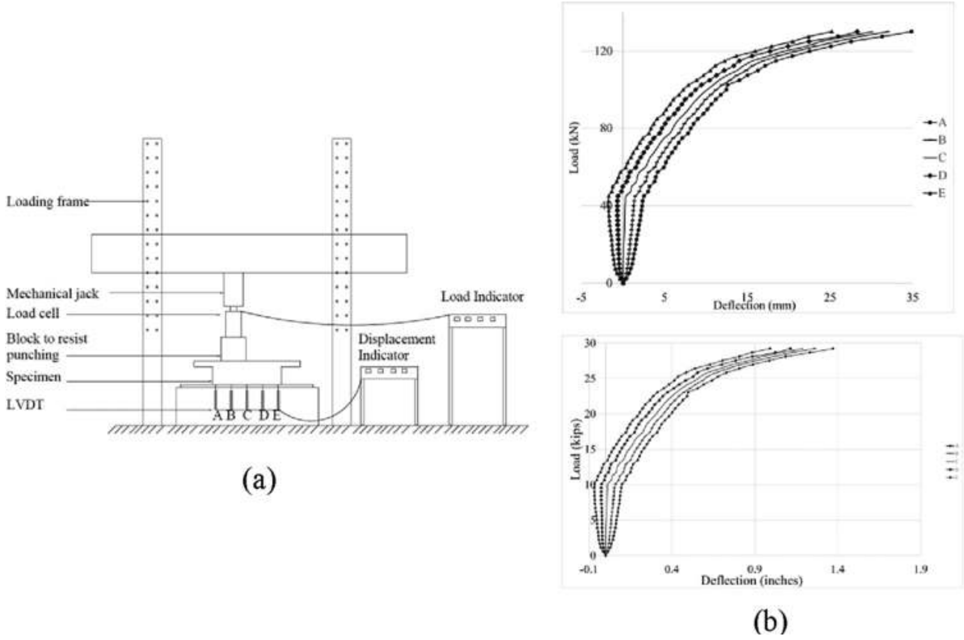

(a)

(b)

Fig. 3—(a) Schematic diagram of experimental test setup; and (b) load-deflection curve from experimental study.

(1.97 in.) from the center span. With the increase in load applied, more cracks appeared on both webs along with the widening of existing cracks. The second crack was seen at a load of 55 kN (12.36 kip), followed by the third crack at 57.5 kN (12.93 kip). The cracks were initially vertical and later inclined with the application of load. It was observed that the cracks formed at the web near the loading showcased more inclination when compared to the cracks in the web away from loading. The specimen finally collapsed at a load of 130 kN (29.23 kip). It was observed that the final deflected shape of the specimen showcased effects of distortion. Linear variable displacement transducers (LVDTs) were kept at five different locations at the bottom flange at points marked A, B, C, D, and E, as in Fig. 3(a), to find the deflection of the specimen. The load-deflection curves obtained from the experimental study are plotted in Fig. 3(b).

NUMERICAL INVESTIGATION

To capture the actual behavior of the bridge model up to failure and to compare the results with those of the experiment, a 3-D FEA was carried out using the ANSYS software package. The concrete and steel in the reinforced concrete bridge was modeled using the SOLID 65 and LINK 180 elements using perfect elasto-plastic constitutive relations. The SOLID 65 element is an isoperimetric element with eight nodes and three degrees of freedom at each node—that is, the translation degree of freedom in the nodal *x*, *y*, and *z* directions. The SOLID 65 element is capable of crushing under compressive stress and cracking under tensile forces. It is also capable of depicting plastic deformations and creep. LINK 180, a 3-D spar element, is a uniaxial tension compression element with three degrees of freedom at each node. The twin-cell box-girder was modeled using 678,062 nodes and 618,884 elements. During meshing, the aspect ratio was kept constant and mesh convergence studies were conducted to find the most suitable mesh size. With an aspect ratio of 1, it was observed that 10 mm (0.39 in.) mesh size is the optimum. When the mesh size is made coarser, the results turned out to be less satisfactory, and with finer mesh size, the computational time taken for an analysis happens to be very high. The constitutive relation used to model the stress-strain relationship in concrete is shown in Fig. 4(a). A bilinear plot was used to model the stress-strain relationship of steel and is shown in Fig. 4(b). The properties of the materials used for the numerical study are the same as those used for the experimental study. Properties—namely, modulus of elasticity, stress-strain relations, Poisson's ratio, and compressive strength—are provided as input data for the concrete. The cross-sectional area, Young's modulus, Poisson's ratio, and a bilinear stress-strain relation are assigned to model reinforcement. The Young's modulus and Poisson's ratio of the structural steel are 200 GPa and 0.3, respectively, and that for concrete are 31.6 GPa and 0.2, respectively. The model created for the numerical analysis is shown in Fig. 5(a). Due to the eccentric load, the effects of torsion and distortion were clearly visible. These effects are prominent in the midspan under the load. The final distorted shape at the midspan and vertical deflection at various positions obtained from numerical study are shown in Fig. 5(b). The load-deflection curve obtained from the numerical study is compared with that of the experimental study, and the same is shown in Fig. 6. The crack pattern obtained from both the experimental and numerical study are provided in Fig. 7 and 8, respectively.

Numerical analysis to study distortion bending in twin-cell box-girder bridges

To learn the distortion bending mechanism in twin-cell box-girder bridges, numerical analysis was conducted. In this study, the reinforcement ratio in the twin cell is varied by providing different stirrup dimensions. The various stirrup diameters used are 8, 7, 6, 5, and 4 mm (0.315, 0.276, 0.236, 0.197, and 0.157 in.) contributing to various reinforcement ratios (ϕ_0) of 0.12, 0.09, 0.07, 0.05, and 0.03,

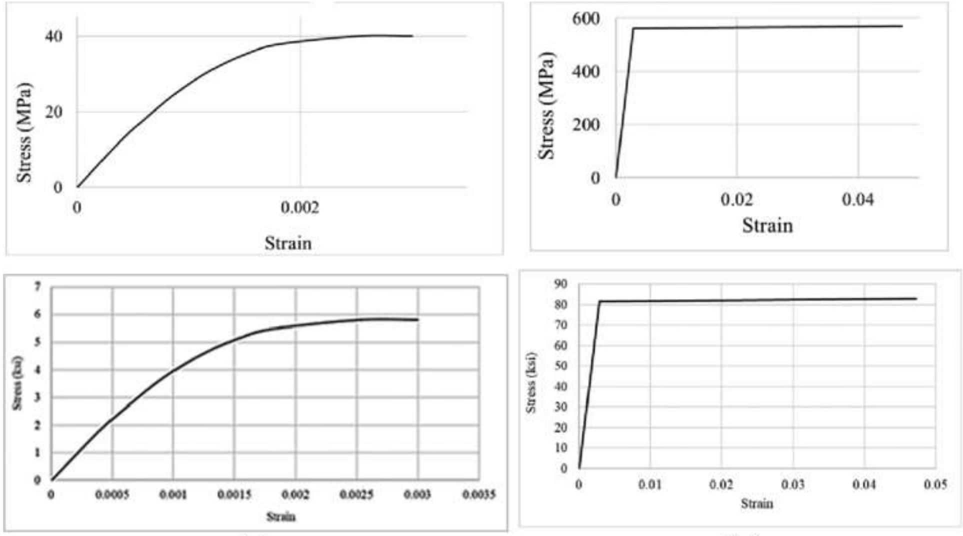

(a) (b)

Fig. 4—Stress-strain relationship: (a) concrete; and (b) steel.

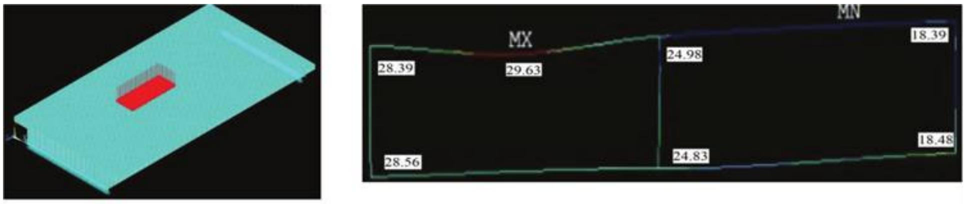

(a) (b)

Fig. 5—(a) Numerical model; and (b) distorted shape of cross section (vertical deflection, mm).

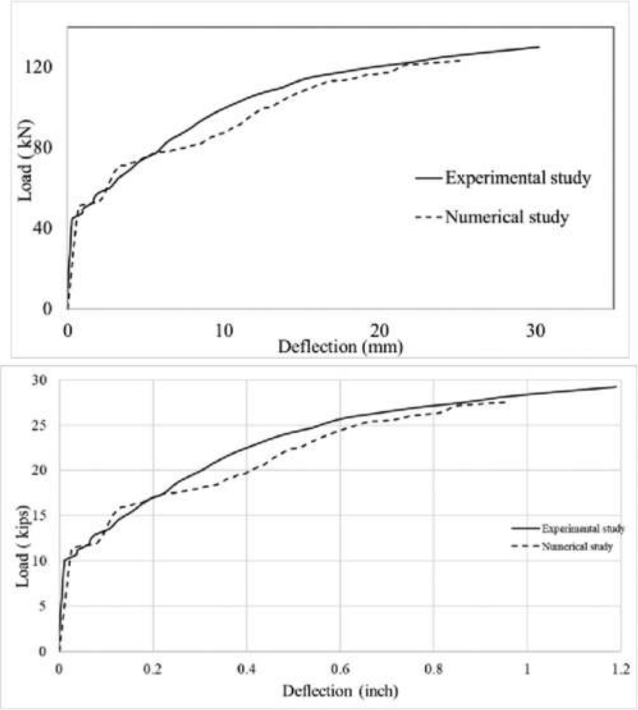

Fig. 6—Load-deflection curve obtained from experimental and numerical study.

respectively. Each of these cases may be mentioned as case 1, 2, 3, 4, and 5, respectively, where the load is applied on the web at midspan. The load is applied vertically on an area of 60 x 200 mm (2.36 x 7.87 in.) depicting a concentrated load on the specimen. Displacements at all three webs were noted at each increment of load. The displacements at each web are denoted as S_1, S_2, and S_3, as shown in Fig. 9(a), and the displacement increments are denoted as dS_1, dS_2, and dS_3. The displacement increment ratio of web 2 and 3 with respect to web 1 is denoted as dS_2/dS_1 and dS_3/dS_1, respectively. To understand the relative displacement of unloaded webs (webs 2 and 3) with respect to the loaded web (web 1), graphs are plotted showing the variation of displacement ratios with respect to the displacement of the loaded web as shown in Fig. 9(b), (c), (d), (e), and (f) for cases 1, 2, 3, 4, and 5, respectively.

From the study, it is observed that, at the final stage of loading, hinges are formed at four corners: two hinges at the loaded web and two in the middle web. The transverse reinforcement has yielded at four corners in addition to the longitudinal reinforcement. Hence, with the formation of hinges at corners directly below the load and at the adjacent web-flange junctions along with the yielding of longitudinal reinforcement, the structure has reached its collapse state by distortion bending mechanism. It is also observed from Fig. 9 that at the collapse stage, the relative displacement of web 3 with respect to web1 (loaded web) is negligible in cases 3, 4, and 5. To substantiate this finding, the longitudinal strain readings in webs (case 3) at midspan is provided in Fig. 10. It is observed that there is zero strain in the unloaded web. Hence, among the two cells in a twin-cell box-girder bridge,

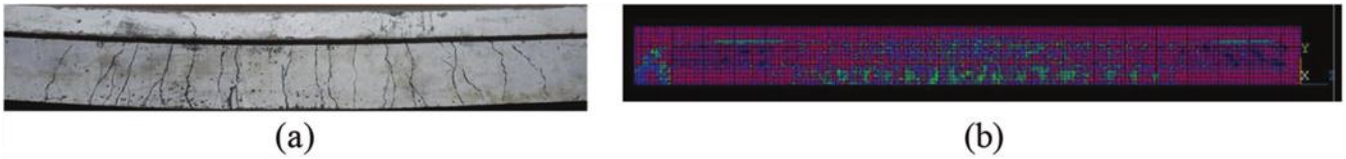

Fig. 7—Cracks in exterior web near load: (a) experimental study; and (b) numerical study.

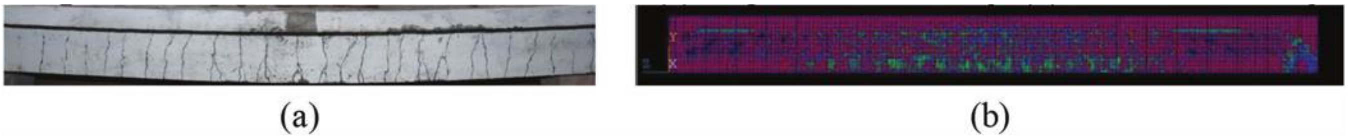

Fig. 8—Cracks in exterior web away from load: (a) experimental study; and (b) numerical study.

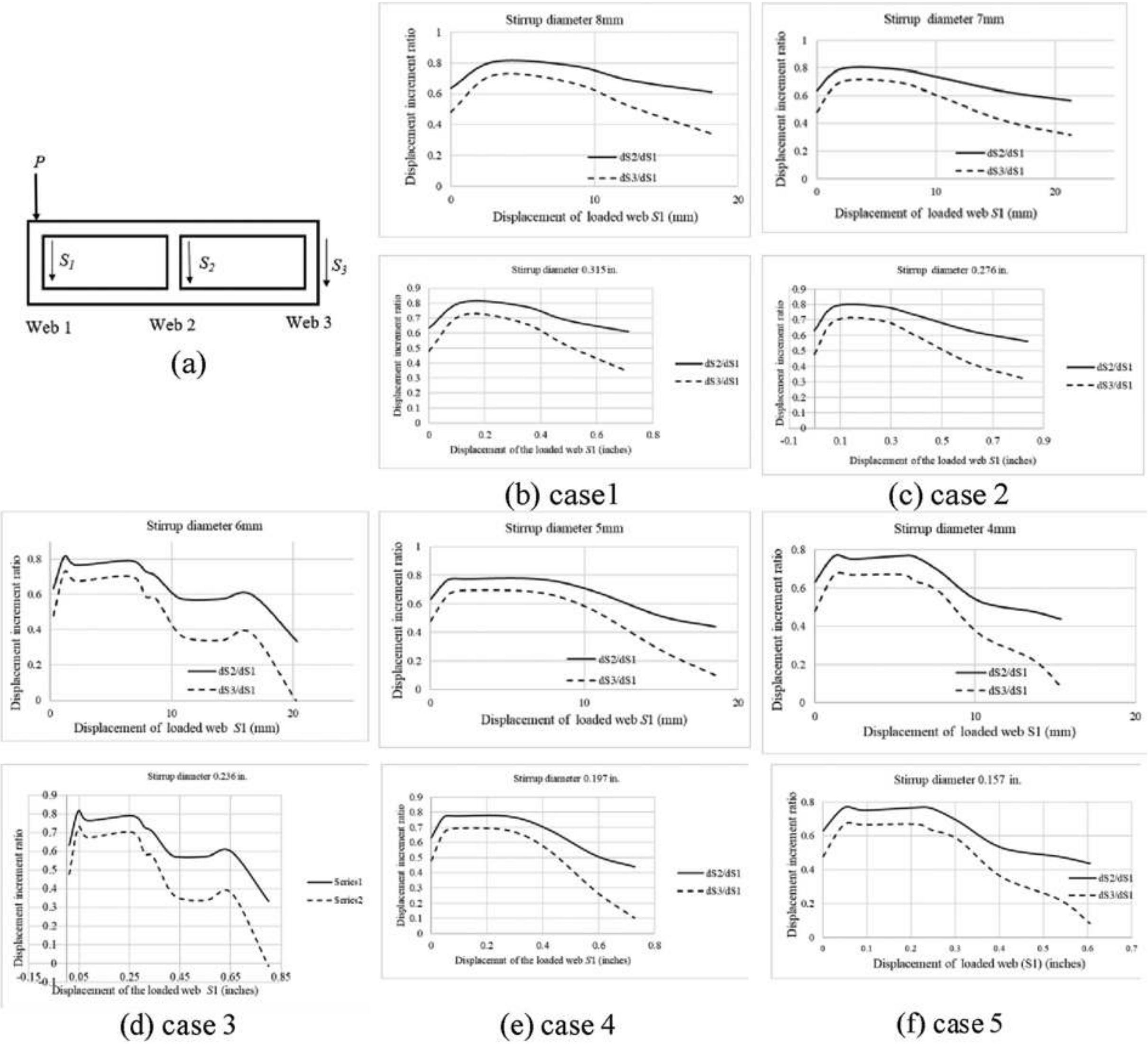

Fig. 9—Displacement increment ratios versus displacement of loaded web.

only the cell on which the load acts are actively contributing to the distortion bending mechanism. Hence, as the loaded cell reaches its ultimate capacity, the twin cell fails in distortion bending mechanism. Due to these reasons, to find the capacity of a twin-cell box girder in distortion-bending mechanism, the work equation used in the case of single-cell box girder can be used with slight modifications.

COLLAPSE LOAD ESTIMATION USING SPACE TRUSS ANALOGY

The space truss analogy is based on the lower-bound theorem of plasticity. Space frame comprises of longitudinal bars at each corner known as stringers, accompanied by transverse ties depicting stirrup reinforcements which are interconnected by diagonal compression members representing concrete inclined at an angle θ, with six degrees of

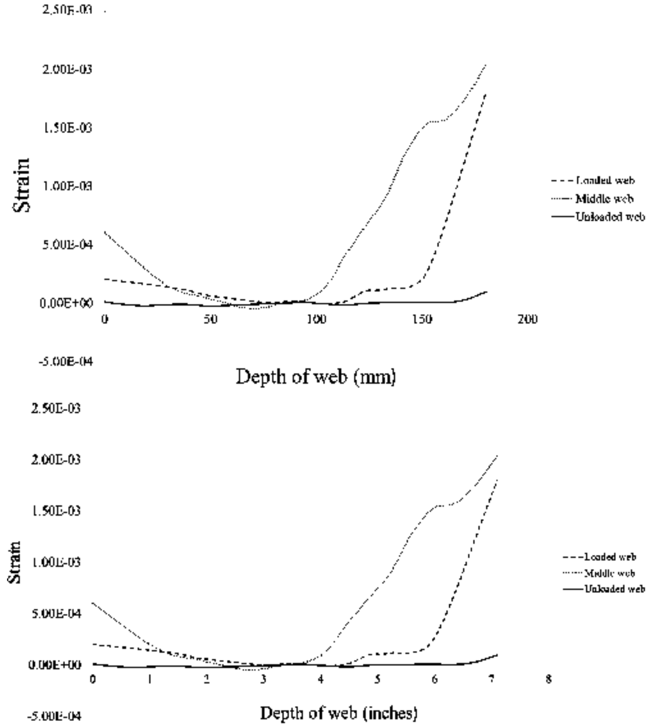

Fig. 10—Longitudinal strain readings of webs at midspan.

freedom at each joint. In the case of combined bending and torsion, Lampert and Thürlimann (1971) suggested a parabolic interaction formula depicting the relationship between the applied torsion (T_u) and bending moment (M_u) with that of the torsional capacity (T_{ur}) under pure torsion and bending capacity (M_{ur}) under pure bending cases of the specimen considered. These equations were originally formulated using the studies conducted on rectangular reinforced beams, but these can be used for hollow sections also as the failure mode is the same in both scenarios

$$\frac{{T_u}^2}{{T_{ur}}^2} = \frac{A_s\left(1 - \frac{M_u}{M_{ur}}\right)}{A_s'} \tag{1}$$

where A_s and A_s' are the area of steel in the tension and compression zones, respectively.

Modeling of space truss for twin-cell box-girder bridge

There are always infinite options in creating a truss model for a particular case. Using the minimum strain energy approach, it is observed that when the struts are inclined at 45 degrees, the optimum model is obtained. These struts are provided in all four different planes in the space truss. The inclined struts throughout the structure represent concrete cracks when the box girder is subjected to pure torsion. The truss model created for the present study is provided in Fig. 11.

The space truss is created based on the geometry and amount of reinforcement present in the box girder. The dimensions of the diagonal members are kept based on ACI 318-08. As shown in Fig. 11(a), loads are applied as point loads, where the bending component is provided vertically downwards and the anti-symmetric component is provided as couple in horizontal and vertical directions. At a load of 126 kN (28.33 kip), the bottom stringer reaches its yield and the truss reached its ultimate capacity.

To further study the effects of distortion in estimating the ultimate capacity of box girder using space truss analogy, an eccentric load acting at one of the external webs is considered. For case 3, when the ϕ_0 is 0.07, the ultimate load obtained from space truss analogy is 95 kN (21.36 kip) and the result obtained from the numerical study is 88.45 kN (19.88 kip). It is observed that in case of distortion, more overestimation of collapse load occurs leading to unsafe results. This shows the inability of space truss to accommodate distortion effects. Rasmussen and Baker (1999) suggested reducing the torsion capacity obtained from space truss analogy by 25% while designing a single-cell box-girder bridge subjected to extreme distortion, but similar studies had not happened in twin-cell box-girder bridges.

COLLAPSE LOAD ESTIMATION USING PLANE TRUSS ANALOGY

The critical web in a twin-cell box-girder is selected for the plane truss analogy. The optimum model is obtained using the minimum strain energy principle when the strut angle is kept at 45 degrees. The dimensions of the diagonal members are kept based on ACI 318-08. The load is applied as a point load on the truss along with the self-weight of the truss. As the load is increased gradually, the bottom truss member is found to reach its yield value. The shear force in the vertical truss member is then compared with the force obtained from Knittel and Worsh's (1965) resolution of forces. Considering the shear force distribution in a simply supported beam with load at midspan, and applying the Bredt-Batho theory (Megson 2019), the total shear stress acting at the critical web due to the symmetric and antisymmetric components of loading is obtained. The ultimate load obtained from plane truss analogy is 102.17 kN (22.97 kip). Hence, it is found that in case of box-girder bridges subjected to eccentric loading, the space truss analogy results are more accurate than those of the plane truss.

COLLAPSE LOAD ESTIMATION USING COLLAPSE MECHANISM

The major assumptions followed by Spence and Morley (1975) in developing the work equations for collapse mechanism are that the webs and flanges are sufficiently thin to develop thin-walled action, and large areas of webs and flange have rigid body motion in their planes with no shear strain. The tensile strength of concrete is neglected, and plastic energy dissipation occurs in steel. Even though these assumptions overestimate the strength in the structure, they are likely to give the true shape of collapse locus. Later, Kurian and Menon (2007) modified the collapse mechanism equations by introducing the concept of plastic hinge length (L') to get more accurate results.

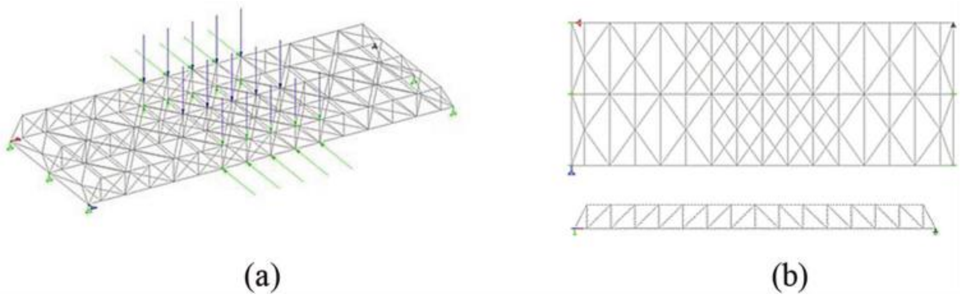

Fig. 11—Space truss model: (a) isometric view; and (b) top view and elevation.

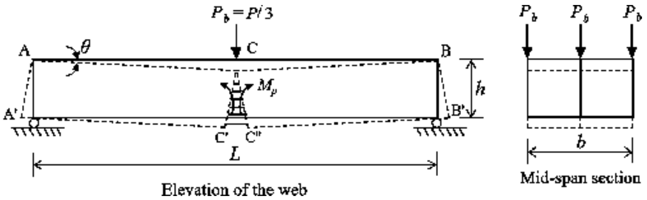

Fig. 12—Pure bending collapse mechanism in twin-cell box girder.

Pure bending collapse mechanism in twin-cell box-girder bridges

In pure bending collapse mechanism, the box girder is assumed to divide into two and rotate about a transverse axis at the midspan. At this stage, all the longitudinal reinforcement bars yield in tension. Here, the failure is caused by the symmetrical loading component and the work done associated with the antisymmetric component is not considered. The symmetric component P_b (= $P/3$) acting along each web is shown in Fig. 12. The equation for pure bending collapse mechanism can be formulated as in Eq. (2) with reference to Fig. 12. When a uniformly distributed load w acts over a distance of $2a$ at the midspan, the equation for collapse load can be modified as in Eq. (3)

$$P = 4\frac{h}{L}\left(F_b + \frac{3}{2}F_w\right) \tag{2}$$

$$w = 2h\frac{\left(F_b + \frac{3}{2}F_w\right)}{a\,(L-a)} \tag{3}$$

where M_p is the midspan plastic yield moment; θ is the hinge rotation angle in Fig. 11; and F_b and F_w are the total yield force contributed by the reinforcing bars present in the bottom flange and one web, respectively.

It was observed that the twin-cell box-girder bridge subjected to experimental investigations collapsed due to pure bending collapse mechanism. This mode of failure is expected due to the symmetrical component of loading. Substituting the values in Eq. (3), the collapse load is obtained as 108.55 kN (24.40 kip). Hence, it is found that the theoretical prediction of the failure mechanism and the collapse load are found to be comparable with respect to experimental results.

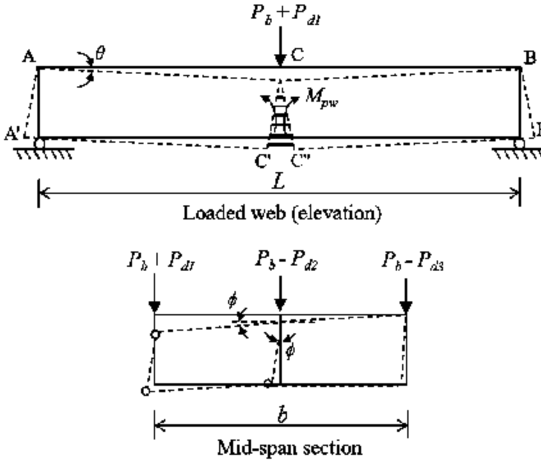

Fig. 13—Distortion bending collapse mechanism in twin-cell box-girder bridge.

Distortion bending collapse mechanism in twin-cell box-girder bridge

To demonstrate distortion bending failure in twin-cell box-girder bridges, numerical studies are conducted and the results of the studies are provided in earlier sections of this manuscript. From the numerical study, it was observed that, in distortion bending failure mode, the transverse bending happens along with the bending and yielding of longitudinal reinforcing bars and four corner hinges are formed at the web-flange junctions of the loaded web and the junctions of adjacent web. It is assumed that the vertical bending of the lightly loaded webs is neglected and the heavily loaded web undergoes rigid body rotation about the horizontal plane, causing the longitudinal steel in the web to yield. The bottom flange is assumed to rotate about a vertical axis passing through the midspan causing the longitudinal steel to yield. The cross section distorts by the formation of four hinges at the web flange junctions directly under the heavily loaded web and at the adjacent web. The out-of-plane angles of web and flanges are equal at midspan denoted as ϕ, as shown in Fig. 13. Here, ϕ is as provided in Eq. (4)

$$\phi = \theta L/b \tag{4}$$

As the diaphragms prevent cross-sectional distortion, the angle of distortion is considered as zero at diaphragms. The angle of distortion is assumed to vary from zero at the supports to 2ϕ at the midspan and hence, the average angle of rotation at each corner is taken as ϕ at the midweb. The angle of distortion at the extreme unloaded web (web 3) is observed to be very small and hence neglected. From the numerical studies, it was also observed that with the distortion of the loaded cell, the entire twin cell reaches its collapse in case of distortion bending collapse mechanism. The amount of external work done by the load in a twin-cell box girder can be calculated using Eq. (5).

The external virtual work done by the load ($P_b + P_{d1}$) act on the heavily loaded web.

$$= (P_b + P_{d1})b\phi/2 \tag{5}$$

The internal virtual work is contributed by the yielding of longitudinal reinforcing bar in the bottom flange and at the heavily loaded web. In addition to yielding of reinforcement, the transverse bending at the four web-flange junctions also contribute to the internal virtual work.

Hence, the work equation for distortion bending collapse mechanism can be formulated as in Eq. (6)

$$\left(\frac{P}{3} + P_{d1}\right)b = \frac{2bh(F_b + F_w)}{L} + 4\,m_c\,L \tag{6}$$

From all these findings and considering the modified plastic hinge length concept suggested by Kurian and Menon (2007), the work equation for distortion bending collapse mechanism in case of twin-cell box-girder bridge can be formulated as provided in Eq. (7).

$$\left(\frac{P}{3} + P_d\right)b = \frac{2bh(F_b + F_w)}{L} + 8\,m_c\,L' \tag{7}$$

Using Eq. (7), the collapse load found for case 3 (mentioned earlier in the section "Numerical analysis to study distortion bending in twin-cell box girder bridges") is 81.43 kN (18.31 kip).

RESULTS AND DISCUSSIONS

In this work, the ultimate load of a twin-cell concrete box-girder bridge exposed to the collective effects of bending and torsion are found experimentally and numerically. The results are compared with the results of truss analogy and the collapse mechanism. The results obtained from the various methods are tabulated in Table 2.

It is observed from Table 2 that all the different methods of analysis can satisfactorily predict the collapse load, but subjected to certain restrictions. In the case of eccentric loading ($e = b/4$), the numerical study was found to match well with the results of the experiment with a deviation of just 5% from the experimental result, which is negligible. The results of the space truss analogy found great agreement with both the experimental and numerical results with a small deviation of 4% and 2%, respectively, depicting the reliability of this method in analyzing a box girder subjected to the combined effects of bending and distortion. The plane truss analogy results are found to deviate from that of the experimental results by 21% due to its two-dimensional nature. The collapse mechanism also provided conservative results, leading to safe design of the structure.

Table 2—Collapse load obtained for twin-cell box girder bridge

Sl. No.	Method of analysis	Collapse load, kN (kip)	
		$e = b/4$	$e = b/2$ (case 3)
1	Experimental study	130.00 (29.23)	—
2	3-D FEA	123.13 (27.68)	88.45 (19.88)
3	Space truss analogy	126.00 (28.33)	95.00 (21.36)
4	Plane truss analogy	102.17 (22.97)	75.18 (16.90)
5	Collapse mechanism	108.55 (24.40)	81.43 (18.31)

When the twin-cell box girder is subjected to distortion ($e = b/2$), the space truss has provided an overestimated capacity leading to unsafe design of the structure. In this case, the collapse mechanism is found to give conservative results and can be safely used for design purposes. It is hence advisable to reduce the capacity of space truss analogy results in case the twin-cell box girder is subjected to extreme eccentric loads.

CONCLUSIONS

This paper throws light on the different aspects concerning the design and analysis of a twin-cell concrete box-girder bridge. A numerical study is conducted to validate the experimental results using load-deflection curves and more parametric studies were conducted to comprehend the distortion effects in twin-cell box-girder bridges. An attempt is made to develop work equations based on the collapse mechanism principle for twin-cell box-girder bridges. Using truss analogy principles, two- and three-dimensional (3-D) truss models are created, and collapse load is found for different load cases. From the different analyses conducted, the following conclusions are drawn.

- The method of plane truss can be adopted when trial and error procedures are required in the early stages of design and construction, as the results are obtained in very short time. Due to the 3-D nature, a space truss can distribute any kind of difficult loading pattern in a more efficient and realistic way when compared to a plane truss. The space truss analogy is found to be reliable in estimating the capacity of a structure except in case of extreme torsion cases. In such cases of extreme eccentric loading, the results obtained from the truss analogy must be reduced by 25% for creating safe designs. As these kind of extreme distortion cases are unrealistic, space truss analogy can be used in the design of box-girder bridges. This drawback of space truss analogy creates serious issues in forensic studies associated with box-girder bridges.
- Collapse mechanism leads to safe design as it provides conservative results. Especially in cases of extreme distortion, collapse mechanism proves to be more reliable than any other existing simplified method used in establishing collapse load in box-girder bridges. A detailed understanding of the deflection profiles is required while using this method to estimate the collapse of a structure.

AUTHOR BIOS

J. Chithra *is a Research Scholar at the Structural Engineering Division, National Institute of Technology Calicut, Kerala, India. She received her BTech from Thangal Kunju Musaliar College of Engineering, Kollam, Kerala, and her MTech from National Institute of Technology Calicut. Her research interests include bridge engineering and reinforced concrete structures.*

Praveen Nagarajan *is a Professor at the Structural Engineering Division, National Institute of Technology Calicut, where he also received his BTech and PhD. He received his MTech from the Indian Institute of Technology Madras, Chennai, India. His research interests include reinforced and prestressed concrete, bridge engineering, and structural reliability.*

Sajith A. S. *is a Professor at the Structural Engineering Division, National Institute of Technology Calicut, where he also received his PhD. He received his BTech from College of Engineering, Trivandrum, Thiruvananthapuram, India, and his MTech from PSG College of Technology, Coimbatore, India. His research interests include structural dynamics, earthquake engineering, and structures.*

REFERENCES

Danesi, R. F., and Edwards, A. D., 1983, "The Behaviour up to Failure of Prestressed Concrete Box Beams of Deformable Cross-Section Subjected to Eccentric Load," *Proceedings - Institution of Civil Engineers*, V. 75, No. 1, pp. 49-75. doi: 10.1680/iicep.1983.1552

El-Sheikh, A., 1996, "Approximate Analysis of Space Trusses," *International Journal of Space Structures*, V. 11, No. 3, pp. 321-330. doi: 10.1177/026635119601100304

Evans, R. H., and Sarkar, S., 1965, "A Method of Ultimate Strength Design of Reinforced Concrete Beams in Combined Bending and Torsion," *The Structural Engineer*, V. 43, No. 10, pp. 337-344.

Hsu, T. T., 1968, "Torsion of Structural Concrete-Behavior of Reinforced Concrete Rectangular Members," *Torsion of Structural Concrete*, SP-18, American Concrete Institute, Farmington Hills, MI, pp. 261-306.

Karlsson, I., and Elfgren, L., 1972, "Torsional Stiffness of Reinforced Concrete Members Subjected to Pure Torsion," *Magazine of Concrete Research*, V. 24, No. 80, pp. 149-156. doi: 10.1680/macr.1973.24.80.149

Knittel, G., and Worsh, G., 1965, "Analysis of Thin-Walled Box Girder of Constant Symmetrical Cross Section," *Beton- und Stahlbetonbau*, V. 9, pp. 205-211.

Kupfer, H., 1969, *Box Beams with Elastically Stiffened Cross Section Under Line and Point Loads*, G. Knittle and H. Kupfer, eds., Ernst & Sohn, Berlin, Germany, pp. 251-263.

Kurian, B., and Menon, D., 2007, "Estimation of Collapse Load of Single-Cell Concrete Box-Girder Bridges," *Journal of Bridge Engineering*, ASCE, V. 12, No. 4, pp. 518-526. doi: 10.1061/(ASCE)1084-0702(2007)12:4(518)

Kuyt, B., 1971, "A Theoretical Investigation of Ultimate Torque as Calculated by Truss Theory and by the Russian Ultimate Equilibrium Method," *Magazine of Concrete Research*, V. 23, No. 77, pp. 155-160. doi: 10.1680/macr.1971.23.77.155

Lampert, P., and Thürlimann, B., 1968, "Torsionsversuche an Stahlbetonbalken (Reinforced Concrete Beams under Torsion)," *Bericht/Institut für Baustatik ETH Zürich*, V. 6506, No. 2.

Lampert, P., Thürlimann, B., 1971, "Ultimate Strength and Design of Reinforced Concrete Beams in Torsion and Bending," *International Association of Bridge and Structural Engineering*, V. 31, pp. 107-131.

Maisel, B. I., and Roll, F., 1974, "Methods of Analysis and Design of Concrete Box Beams with Side Cantilevers," *TRID*, 176 pp.

Megson, T. H. G., 2019, *Structural and Stress Analysis*, fourth edition, Elsevier Science, 830 pp.

Park, R., and Paulay, T., 1975, *Reinforced Concrete Structures*, John Wiley & Sons, New York.

Rasmussen, L. J., and Baker, G., 1999, "Large-Scale Experimental Investigation of Deformable RC Box Sections," *Journal of Structural Engineering*, ASCE, V. 125, No. 3, pp. 227-235. doi: 10.1061/(ASCE)0733-9445(1999)125:3(227)

Rausch, E., 1929, "Design of Reinforced Concrete in Torsion," PhD thesis, Technische Hochschule, Berlin, Germany.

Ritter, W., 1899, "Die Bauweise Hennebique (The Hennebique System)," *Schweizerische Bauzeitung*, V. 33, No. 5, pp. 41-43. (in German)

Sennah, K. M., and Kennedy, J. B., 2002, "Literature Review in Analysis of Box-Girder Bridges," *Journal of Bridge Engineering*, ASCE, V. 7, No. 2, pp. 134-143. doi: 10.1061/(ASCE)1084-0702(2002)7:2(134)

Spence, R. J. S., and Morley, C. T., 1975, "The Strength of Single-Cell Concrete Box Girders of Deformable Cross-Section," *Proceedings - Institution of Civil Engineers*, V. 59, No. 4, pp. 743-761. doi: 10.1680/iicep.1975.3637

ACI STRUCTURAL JOURNAL TECHNICAL PAPER

Title No. 121-S04

Theoretical and Experimental Study on Minimum Shear Reinforced Ratio in Concrete Beams

by S. L. Garcia, J. Ferreira, D. Dias, J. Sousa, P. Figueiredo, and J. Trindade

Failure in beams reinforced with a small amount of transverse reinforcement is brittle due to reinforcement rupture after critical shear cracking occurs. To eliminate this problem, standards recommend formulas to calculate the minimum amount of transverse reinforcement in reinforced concrete structures. Reinforcement can resist loads after the first crack's appearance, preventing beam rupture from being brittle but making it somewhat ductile. This paper presents a theoretical experimental analysis to determine the minimum transverse reinforcement ratio in beams of high-strength ordinary portland cement concrete (BHSOPCC), low-strength ordinary portland cement concrete (BLSOPCC), and low-strength geopolymeric concrete (BLSGC). The beam dimensions were 150 x 450 x 4500 mm. They were subjected to a four-point bending test to assess shear failure. The transverse reinforcement $\rho_{sw,min}f_{yk}$ *ranged from 0 to 1.16 MPa, in the ranges provided by ACI 318-19, AASHTO LRFD,* fib *Model Code, and ABNT NBR 6118:2014. This paper investigates the minimum shear reinforcement ratio for various types of concretes with different strengths and attempts to reevaluate the associated standards that have already been established. The parameter* $\tau_{wy}*/\tau_{wcr}$ *proposed in this paper to define whether or not a beam has minimum transverse reinforcement is more appropriate.*

Keywords: beam; geopolymeric concrete; minimum shear; reserve strength.

INTRODUCTION

The failure mode of reinforced portland cement concrete beams depends on the concrete and reinforcement characteristics, the dimensions, the loading type, and the transverse reinforcement's shape and distribution. From the intention and incessant search for new and better materials, high-strength concretes and geopolymeric concretes have appeared. Due to their characteristics, they can behave differently from low-strength concretes, requiring changes to structural calculation methods.

Beams subjected to load levels and/or with dimensions that, according to calculation, do not require reinforcement are normally provided with minimum reinforcement. This reinforcement aims to prevent, in the event of unforeseen overloads, sudden beam rupture as soon as cracking occurs.

The deformability of reinforced concrete elements subjected to bending depends on several factors, such as: the flexural reinforcement ratio (ρ/ρ_b), where ρ_b is the balanced longitudinal reinforcement ratio; the amount of compression reinforcement; the amount and spacing of transverse reinforcement; and the compressive strength of the concrete.[1]

Researchers[2-10] agree that the minimum transverse reinforcement ratio aims to predict a sudden rupture as soon as a critical diagonal crack occurs, and also to have control over diagonal cracking in the serviceability limit state (SLS). To prevent brittle failure, it is necessary that the amount of transverse reinforcement provides a reserve of strength after the diagonal shear crack is reached. The crack opening limitation in the SLS is also important by not only having a minimum amount of reinforcement, but also controlling its spacing.

In recent years, research on minimum transverse reinforcement has advanced greatly. The pioneer in this regard was the theoretical experimental research conducted by Krauthmmer[3] using the interface shear transfer theory, where the value of the stress resisted by the transverse reinforcement of $\rho_{sw}f_{yw} = 0.34$ MPa, prescribed by ACI 318-89,[11] was questioned, and it was concluded that the correct value should be 0.448 MPa instead of 0.34 MPa.

The focus on this topic then became shear ductility[1,2,5,7,8] (post-peak deformation characteristics), focused mainly on the advent of high-strength concretes, with the influence of variables including the concrete strength f_c, the shear span-depth ratio (a/d), and the amount of the shear (web) reinforcement ($\rho_{sw}f_{yw}$), sometimes being the minimum reinforcement recommended by the standards.

Johnson and Ramirez[4] introduced the concept of reserve strength, defined as the ratio between ultimate shear strength and diagonal cracking strength (V_u/V_{cr}), and the concept of the reserve strength index, given by the ratio between ultimate shear strength and concrete shear strength (V_u/V_c) defined by the standard's prescriptions.

It is unanimous that minimum reinforcement is a function of the compressive strength of concrete due to the decrease in beam ductility made with these concretes. Ozcebe et al.,[2] using the concept of resistance reserve, concluded that beams with $V_u/V_c \geq 1.5$ have a transverse reinforcement amount ($\rho_{sw}f_{yw}$) equal to or greater than the minimum. Also, the introduction of the ductility index concept, defined as the ratio between the final deflection and the deflection for the diagonal cracking shear, supported the conclusion that beams with $\Delta_u/\Delta_{cr} \geq 2.5$ can be considered beams with reinforcement equal to or greater than the minimum.

Lee and Kim[9] focused on the influence of longitudinal reinforcement and the a/d on the amount of minimum

---

ACI Structural Journal, V. 121, No. 1, January 2024.
MS No. S-2022-320.R1, doi: 10.14359/51739184, received April 11, 2023, and reviewed under Institute publication policies. Pertinent discussion including author's closure, if any, will be published ten months from this journal's date if the discussion is received within four months of the paper's print publication.

transverse reinforcement in beams. They concluded that, though the equations do not include these variables, with increasing longitudinal reinforcement and decreasing a/d, the reserve strength rises. Aguilar et al.[10] used test results available in the literature to indicate that the minimum amount of shear reinforcement required by ACI 318-14[12] and AASHTO LRFD[13] provides sufficient reserve strength after the formation of the first diagonal crack up to 105 MPa. An upper limit for the nominal shear strength of $0.083\sqrt{f_c}$ in concrete beams with compressive strength up to 105 MPa was shown to be adequate to prevent web-crushing failures occurring prior to the yielding of stirrups. Finally, research on minimum reinforcement was performed by Jayasinghe et al.,[14] where a minimum amount of reinforcement was considered, as recommended by different standards from a database of shear beam tests to evaluate the parameters that affect reserve strength. Through the concept of the safety margin, it was recommended to change a safety factor to the limiting shear force value to provide shear reinforcement in AS 3600:2018.[15]

With global warming and the destruction of the ozone layer, the construction industry has become the target of environmental activists because it is one of the activities that most emits carbon dioxide (CO_2) into the atmosphere. This has led researchers to search for alternatives to replace its main pollutant agent, portland cement, using geopolymeric cement, an environmentally friendly material because it uses waste by-products from different industries and presents better mechanical properties and durability compared to portland cement concrete. Research in the past years has advanced a lot in terms of materials. However, they are still limited, especially when it comes to structural elements.

Some research[16-27] has been conducted to evaluate the shear strength of geopolymeric concrete beams with and without transverse reinforcement, in addition to steel fiber-reinforced beams. There is general agreement among researchers that the beam behavior, during both bending and shear, is similar to that of portland cement concrete, but some differences were found. For instance, Madheswaran et al.[23] concluded that geopolymeric concrete has a lower modulus of elasticity—approximately 70% that of ordinary portland cement concrete—with similar strength. Also, the strain that occurs at peak stress in the stress-strain characteristics of geopolymeric concretes is larger than that of normal concrete.

With the advent and increasing application of geopolymeric concretes, several research studies are being developed, as mentioned previously, all aiming to verify whether the existing procedures prescribed by standards for portland cement concrete can be used for these types of concrete. Although its use often seems obvious, experimentation is needed to support its applicability. This paper contributes to this by evaluating the minimum shear reinforcement ratio in beams made with different types of concrete, and a parameter is proposed to experimentally evaluate which beams have the minimum transverse reinforcement ratio.

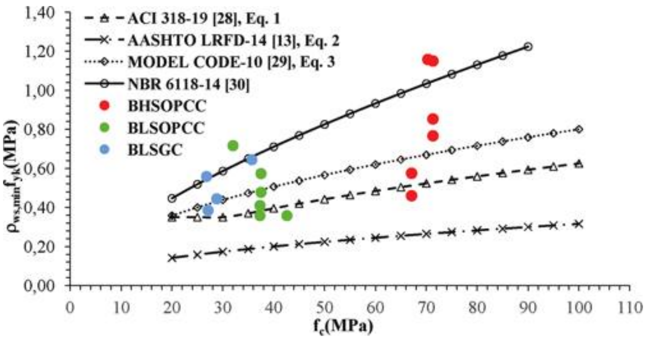

Fig. 1—Values of $\rho_{sw,min}f_{yw}$ *as function of* f_c *for some standards and groups of beams tested.*

RESEARCH SIGNIFICANCE

Little theoretical experimental research on the evaluation of the minimum transverse reinforcement ratio has been carried out in recent years, mainly due to the fact that there are no other elements that motivate such evaluation. However, the methodologies recommended to assess such facts are always controversial and depend on normative prescriptions for determining the strength capacity of concrete to shear. Another important issue is the appearance of new technologies and/or concretes with the unquestionable purpose of reducing CO_2 emissions caused by the portland cement industry. This research includes the study of five geopolymeric concrete beams to evaluate their behavior when they are manufactured with the minimum reinforcement recommended by different standards for portland cement concrete. An experimentally obtained parameter is proposed to evaluate which beams really have minimum transverse reinforcement.

EXPERIMENTAL INVESTIGATION

Minimum transverse reinforcement ratio recommended by standards

The equations for the minimum transverse reinforcement ratio recommended by the evaluated standards are presented as follows.

According to Section 9.6.3.4 in ACI 318-19,[28] the minimum area of shear reinforcement is specified as

$$\rho_{sw,min}f_{yk} = 0.0623f_c'^{0.53}\ 0.35 \tag{1}$$

According to Section 5.8.2.5 in AASHTO LRFD,[13] the minimum amount of shear reinforcement is given by

$$\rho_{sw,min}f_{yk} = 0.0316f_c'^{0.5} \tag{2}$$

According to *fib* Model Code 2010,[29] Item 7.3.3.3, the minimum shear reinforcement is given by

$$\rho_{sw,min}f_{yk} = 0.08f_c^{0.5} \tag{3}$$

According to ABNT NBR 6118:2014,[30] Section 17.4.1.1.1, the minimum transverse reinforcement ratio in elements that require transverse reinforcement is given by

$$\rho_{sw,min}f_{yk} = 0.06f_c^{0.67} \tag{4}$$

Table 1—Composition of HSOPCC and LSOPCC

Type of concrete	Material composition, kg/m^3						
	Cement	Silica fume	Sand	Coarse aggregate	Water	HRWRA	*w/c*
HSOPCC	500	50	520	1043	190	4.17	0.38
LSOPCC	329	—	520	1043	191	—	0.58

Note: HRWRA is high-range water-reducing admixture; *w/c* is water-cement ratio.

Table 2—Composition of LSGC

Type of concrete	Material composition, kg/m^3					
	Cement	Metakaolin	Sand	Coarse aggregate	KOH	Na_2SiO_3
LSGC	75.6	164.3	785.8	1178.7	67.5	180

Note: Water = 82.3 L; zinc oxide = 9.8 kg/m^3; KOH is potassium hydroxide; Na_2SiO_3 is alkaline sodium silicate.

Figure 1 shows a comparison of $\rho_{sw,min}f_{yk}$ as a function of f_c from Eq. (1) (ACI 318-19), (2) (AASHTO LRFD), (3) (*fib* Model Code), and (4) (ABNT NBR 6118:2014), as well as the beams analyzed in this research, formed by groups of beams of high-strength ordinary portland cement concrete (BHSOPCC), low-strength ordinary portland cement concrete (BLSOPCC), and low-strength geopolymeric concrete (BLSGC), considering f_{yk} = 500 MPa and f_c limits defined by the standards.

It can be observed that the evaluated codes consider the influence of concrete compressive strength. ABNT NBR 6118:2014 is the code that recommends the highest values, and the lowest is the AASHTO LRFD minimum transverse reinforcement ratio. The differences in $\rho_{sw,min}f_{yk}$ for concretes of 30, 60, and 90 MPa reach 70%, 74%, and 75%, respectively.

It is known that the minimum transverse reinforcement requirements are developed to ensure a minimum ductility after the critical diagonal cracking occurs, and also a crack width within the durability requirements of each standard.

This paper was developed from the motivation to analyze the differences between the values recommended by these codes and experimentally assess beams with the minimum transverse reinforcement ratios recommended by them to evaluate their behavior when they are made of ordinary portland cement concrete and geopolymeric concrete.

Materials

An experimental program was developed to evaluate the behavior of beams with the minimum transverse reinforcement defined in different codes. Three types of concrete were produced: a high-strength ordinary portland cement concrete (HSOPCC), a low-strength ordinary portland cement concrete (LSOPCC), and a low-strength geopolymeric concrete (LSGC). For the HSOPCC type, high-early-strength portland cement was used, classified as Type V according to ABNT NBR 5733/1991.[31] For the LSOPCC type, cement type CPII F-32 was used. Both types of concrete used natural quartz river sand and trachy-crushed rock (maximum particle diameter of 19 mm) as fine and coarse aggregates, respectively, as well as silica fume powder and high-range water-reducing admixture. LSGC was obtained from the combination of metakaolin (as the main source of aluminum and silicon), portland cement type CPII E-32 (as the source of calcium), and an alkaline solution composed of potassium hydroxide and alkaline sodium silicate (Na_2SiO_3). The coarse and fine aggregates had the same characteristics as those used in the HSOPCC and LSOPCC concretes.

Concrete proportioning

Table 1 shows the composition of the HSOPCC and LSOPCC concretes, and Table 2 shows that of the LSGC used, for 1 m^3.

All tests, including casting and curing concrete specimens, were conducted at the Civil Engineering Laboratory of the State University of North Fluminense Darcy Ribeiro, Rio de Janeiro, Brazil. To characterize each concrete type in the hardened state, six 150 x 300 mm cylindrical specimens were collected—three for compressive strength testing[32] and three for splitting tensile strength testing[33]—and both were tested on the same date, using a universal testing machine with a 2000 kN capacity.

Description of beams

Nineteen beams were tested in total, divided into three groups. The first consisted of seven BHSOPCC with a concrete compressive strength of approximately 70 MPa, $\rho_{sw}f_{yw}$ values ranging from 0 to 1.16 MPa, *a*/*d* of approximately 3.0, and a longitudinal reinforcement ratio ρ_s of 2.6%. The second group was seven BLSOPCC with an average concrete compressive strength of 36 MPa, $\rho_{sw}f_{yw}$ values varying from 0 to 0.72 MPa, *a*/*d* of approximately 3.0, and ρ_s of 1.95% and 0.97% (to show the influence of ρ_s on the diagonal cracking shear V_{cr} and ultimate capacity V_u). The third group consisted of five BLSGC with an average concrete compressive strength of 30 MPa, $\rho_{sw}f_{yw}$ values varying from 0 to 0.64 MPa, *a*/*d* of approximately 3.0, and ρ_s of 1.65%. All specimens from Group 3 had a rectangular cross section of 150 x 450 mm, with 4500 mm of total length—different from BLSOPCC.

Table 3 and Fig. 2 show the details of the tested beams, as well as the relative difference in $\rho_{sw}f_{yw}$ with respect to the adopted and calculated values according to the evaluated standards. The calculated differences were in the ranges of –13.5 to 54.9%, 42.4 to 77.1%, –45.8 to 41.7%, and –118.4 to 14.6% for ACI 318-19, AASHTO LRFD, *fib* Model Code 2010, and ABNT NBR 6118:2014, respectively.

Table 3—Characteristics of tested beams and their relative differences with analyzed standards

Beams	f_c, MPa	s, mm	ρ_{sw}, %	f_{yw}, MPa	$\rho_{sw}f_{yw}$, MPa	$(\rho_{sw}f_{yw}\text{-}\rho_{sw}f_{yw\,pred})/\rho_{sw}f_{yw}$, %			
						ACI 318-19[28]	AASHTO LRFD[13]	*fib* Model Code[29]	ABNT NBR 6118:2014[30]
BHSOPCC-01-70.2-0.00	70.2	—	—	—	0.0	—	—	—	—
BHSOPCC-02-67.1-0.46	67.1	200	0.06	760	0.46	–10.9	43.7	–45.7	–118.4
BHSOPCC-03-67.1-0.57	67.1	160	0.08	760	0.57	11.5	55.0	–14.0	–74.7
BHSOPCC-04-71.3-0.77	71.3	120	0.10	760	0.77	31.38	65.2	14.5	–36.5
BHSOPCC-05-71.3-0.85	71.3	190	0.22	390	0.85	38.34	68.7	20.8	–22.7
BHSOPCC-06-71.3-1.15	71.3	80	0.15	760	1.15	54.3	76.8	41.3	9.0
BHSOPCC-07-70.3-1.16	70.3	140	0.30	390	1.16	54.9	77.1	41.7	10.5
BLSOPCC-08-32.0-0.00	32.0	—	—	—	—	—	—	—	—
BLSOPCC-09-42.6-0.36	42.6	240	0.05	710	0.36	–13.5	42.4	–26.4	–106.9
BLSOPCC-10-37.3-0.36	37.3	240	0.05	710	0.36	–6.2	46.1	–45.8	–89.3
BLSOPCC-11-37.3-0.41	37.1	210	0.06	710	0.41	7.0	52.8	–19.4	–65.6
BLSOPCC-12-37.5-0.48	37.5	180	0.07	710	0.48	20.1	59.5	–2.3	–42.5
BLSOPCC-13-37.5-0.57	37.5	150	0.08	710	0.57	33.4	66.2	14.5	–18.7
BLSOPCC-14-32.0-0.72	32.0	120	0.10	710	0.72	50.8	75.0	31.6	14.6
BLSGC-15-27.2-0.00	27.2	—	—	—	—	—	—	—	—
BLSGC-16-22.6-0.38	27.1	300	0.06	625	0.38	15.7	57.3	–8.4	–42.2
BLSGC-17-28.8-0.44	28.8	260	0.07	625	0.44	24.7	61.8	6.2	–28.4
BLSGC-18-20.3-0.56	26.8	300	0.09	640	0.56	42.3	70.7	23.1	2.7
BLSGC-19-35.7-0.64	35.7	260	0.10	640	0.64	42.2	70.7	35.7	–2.2

Note: For Beams 01 to 07, $a/d = 3.0$ and $\rho_s = A_s/b_wd = 2.6\%$; for Beams 08 and 10 to 14, $a/d = 3.14$ and $\rho_s = A_s/b_wd = 1.95\%$; for Beam 09, $a/d = 3.06$ and $\rho_s = A_s/b_wd = 0.97\%$; and for Beams 15 to 19, $a/d = 3.60$ and $\rho_s = A_s/b_wd = 1.65\%$.

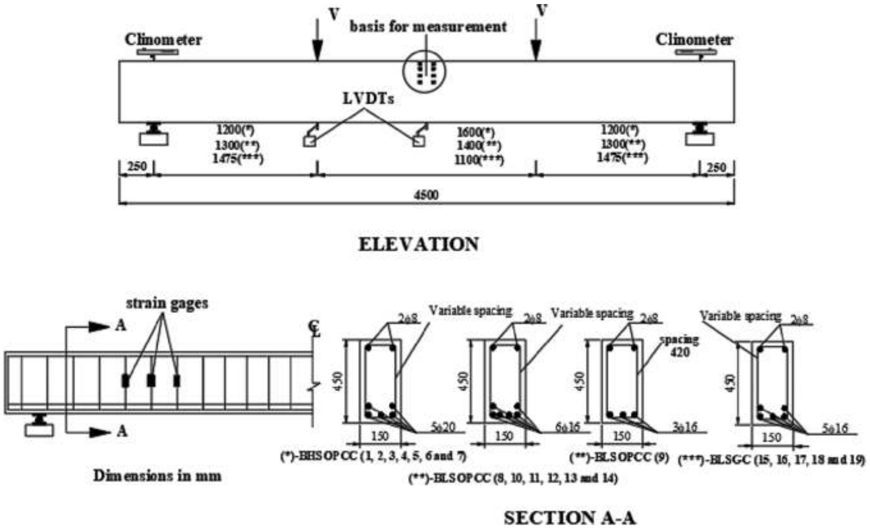

Fig. 2—Details of beams tested.

Each beam was given the following nomenclature: type of concrete, beam number, concrete compressive strength, and transverse reinforcement ($\rho_{sw}f_{yw}$); for example, BHSOPCC-01-70.2-0.00 means that it was produced with HSOPCC, Beam 01, concrete compressive strength of 70.2 MPa, and with $\rho_{sw}f_{yw} = 0.00$.

Table 4 presents the physical and mechanical characteristics of the longitudinal and transverse reinforcements used in the tested beams.

The wooden molds for BHSOPCC, BLSOPCC, and BLSGC were continuously filled with concrete and compacted with the aid of a needle-type immersion vibrator. The beams were demolded and covered with a damp blanket 24 hours after placement.

Table 5 shows the results of the compressive strength and splitting tensile strength tests for the studied concretes, as well as their age.

Table 4—Physical and mechanical characteristics of reinforcement used in beams

Beam groups	Longitudinal reinforcement				Transverse reinforcement				
	ϕ, mm	f_y, MPa	f_u, MPa	ε_y, ‰	ϕ, mm	f_y, MPa	f_u, MPa	ε_y, ‰	ε_y*, ‰
X	20	546	659	3.37	6.3	390	526	2.25	2.25
Y	20	546	659	3.37	3.4	760	840	5.75	3.80
Z	16	520	857	2.40	3.4	710	837	5.50	3.40
V	16	545	637	2.30	4.2	625	837	6.30	4.50
V	16	545	637	2.30	5.0	640	791	6.10	4.35

Note: Group X is Beams 01, 05, and 07; Y is Beams 02 to 04, and 06; Z is Beams 08 to 14; and V is Beams 15 to 19. f_y is yield strength; ε_y is yield strain; ε_y* is specific yield strain corresponding to bilinear stress versus strain diagram; and f_u is ultimate strength.

Table 5—Mechanical properties of concrete types used

Beams	Age, days	f_{cm}, MPa	$f_{ct,sp}$, MPa
BHSOPCC-01-70.2-0.00	51	70.2	3.24
BHSOPCC-02-67.1-0.46	70	67.1	4.53
BHSOPCC-03-67.1-0.57	70	67.1	4.53
BHSOPCC-04-71.3-0.77	84	71.3	4.26
BHSOPCC-05-71.3-0.85	58	71.3	4.03
BHSOPCC-06-71.3-1.15	84	71.3	4.26
BHSOPCC-07-70.3-1.16	65	70.3	4.27
BLSOPCC-08-32.0-0.00	161	32.0	2.01
BLSOPCC-09-42.6-0.36	111	42.6	2.23
BLSOPCC-10-37.3-0.36	127	37.3	2.13
BLSOPCC-11-37.3-0.41	127	37.3	2.13
BLSOPCC-12-37.5-0.48	143	37.5	2.00
BLSOPCC-13-37.5-0.57	143	37.5	2.00
BLSOPCC-14-32.0-0.72	161	32.0	2.01
BLSGC-15-27.2-0.00	279	27.2	3.70
BLSGC-16-27.1-0.38	286	27.1	3.80
BLSGC-17-28.8-0.44	279	28.8	3.90
BLSGC-18-26.8-0.56	289	26.8	3.30
BLSGC-19-35.7-0.64	286	35.7	4.30

Note: f_{cm} is concrete compressive strength; $f_{ct,sp}$ is splitting tensile strength test (Brazilian).

Test procedure

Figure 3 presents a schematic diagram of a beam test. They are all simply supported by two concentrated loads placed equidistantly from the supports. The deflection was measured at the midspan with the aid of linear variable displacement transducers (LVDTs), the deformation of the longitudinal reinforcement was measured at the midspan, and the deformation of the transverse reinforcement was measured by six stirrups (three on each side of the shear span) using strain gauges. The compressive concrete deformation was also measured at midspan using metal plates bonded to the concrete surface. The crack width was measured by a fissurometer.

Structural tests were performed using a steel frame with a hydraulic actuator controlled by a servo-hydraulic system containing two actuators of 500 kN load capacity at a speed of 1 mm/min until rupture.

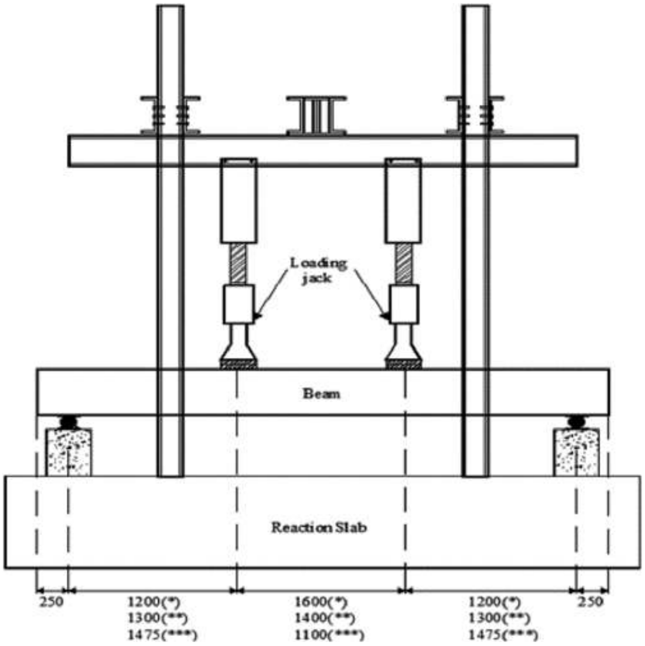

Fig. 3—Test schematic.

EXPERIMENTAL RESULTS AND DISCUSSION

Shear strength of tested beams

Table 6 shows the results obtained from the tested beams: ultimate shear (V_u), diagonal cracking shear (V_{cr}), shear at yielding of the first stirrup (V_y), shear at yielding of the longitudinal reinforcement ($V_{y,l}$), and failure modes. The V_{cr} of BHSOPCC-01-70.2-0.00, BLSOPCC-08-32.0-0.00, and BLSGC-15-27.2-0.00 was within the reference range. However, BHSOPCC-02-67.1-0.46 and BLSOPCC-09-42.6-0.36 exhibited lower values, mostly in BLSOPCC-09-42.6-0.36, where V_{cr} reduction was 25% compared to BLSOPCC-10-37.3-0.36. This was due to the decrease of the longitudinal reinforcement ratio by half. It is noteworthy that for all three groups tested, the addition of $\rho_{sw}f_{yw}$ increased the values of V_y and V_u, as expected.

Crack patterns of tested beams

The crack patterns of the tested beams where the critical diagonal crack occurred is shown in Fig. 4. During the structural tests, flexural cracking was initially seen at the midspan of the beams, which spreads vertically with increasing loads.

Table 6—Results of beams tested

Beams	V_u, kN	V_{cr}, kN	V_y, kN	$V_{y,l}$, kN	Rupture mode
BHSOPCC-01-70.2-0.00	133	110		–	Diagonal tension
BHSOPCC-02-67.1-0.46	108.5	108.5	+	–	(A)
BHSOPCC-03-67.1-0.57	185	110	116	–	(A)
BHSOPCC-04-71.3-0.77	202.5	110	150	–	(A)
BHSOPCC-05-71.3-0.85	285	110	123	250	(B)
BHSOPCC-06-71.3-1.15	240	110	220	–	(A)
BHSOPCC-07-70.3-1.16	272	110	148	247	(C)
BLSOPCC-08-32.0-0.00	90	80		–	Diagonal tension
BLSOPCC-09-42.6-0.36	60	60	+	–	(A)
BLSOPCC-10-37.3-0.36	90	80	+	–	(A)
BLSOPCC-11-37.3-0.41	80	80	+	–	(A)
BLSOPCC-12-37.5-0.48	115	80	108	–	(A)
BLSOPCC-13-37.5-0.57	168	80	138	140	(C)
BLSOPCC-14-32.0-0.72	127	80	120	125	(A)
BLSGC-15-27.2-0.00	85	65		–	Diagonal tension
BLSGC-16-27.1-0.38	135	65	118.1	–	(C)
BLSGC-17-28.8-0.44	160	65	+	–	(C)
BLSGC-18-26.8-0.56	185	65	167.5	163	(C)
BLSGC-19-35.7-0.64	210	65	199.5	175	(C)

Note: + is when yielding and rupture occur practically simultaneously; – inidicates no longitudinal reinforcement yielding; (A) is diagonal tension with rupture of the transverse reinforcement; (B) is diagonal tension with yielding of the longitudinal reinforcement and failure of the stirrups; and (C) is yielding of the transverse reinforcement with subsequent yielding of the longitudinal reinforcement and rupture of the concrete in the compression zone.

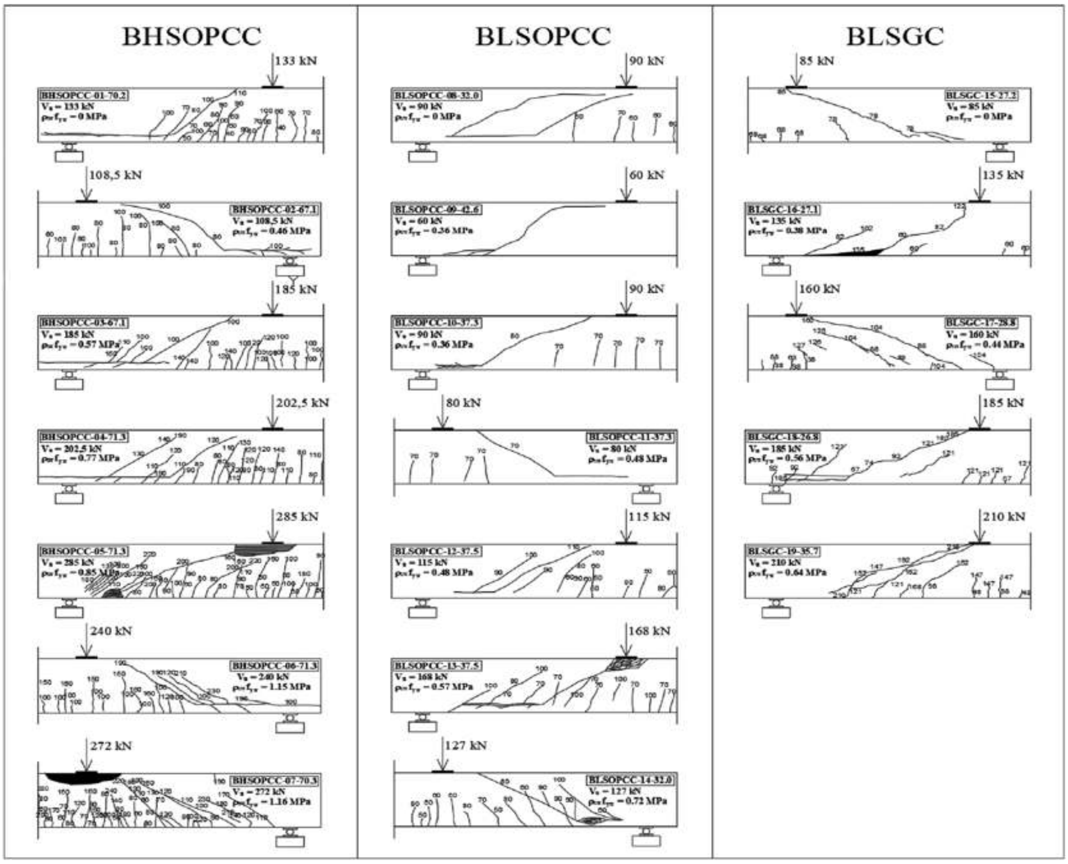

Fig. 4—Crack patterns in specimens near ultimate loads of half of beams where V_{cr} *occurred.*

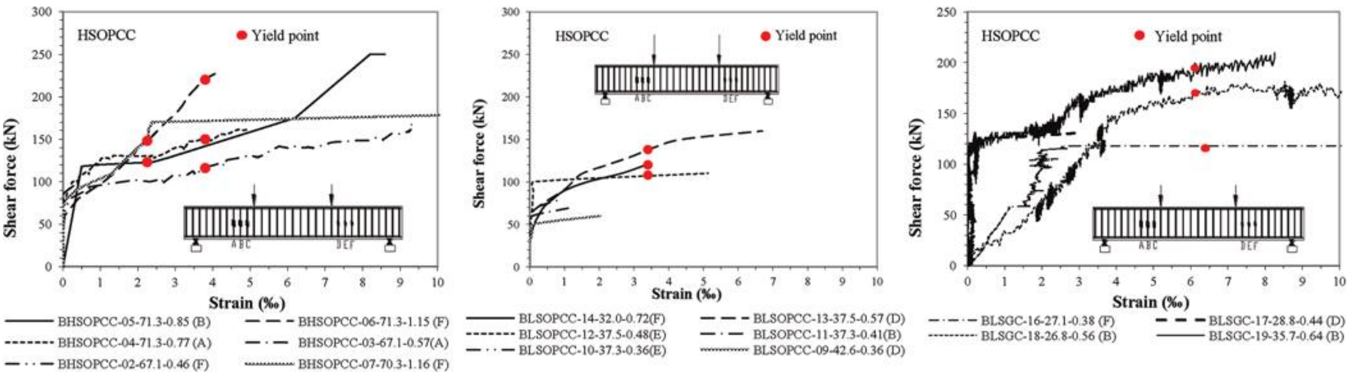

Fig. 5—Shear force versus strain of stirrups where largest strains were measured.

Table 7—Shear force values of beams that exhibited yielding in stirrups

Beams	Stirrup position						V_y, kN	V_y*, kN	V_y*,$_l$, kN	V_y*,$_r$, kN
	A	B	C	D	E	F				
BHSOPCC-03-67.1-0.57	116	157	♦	♦	148	♦	116(A)	140	137	148
BHSOPCC-04-71.3-0.77	150	♦	♦	♦	197	♦	150(A)	174	150	197
BHSOPCC-05-71.3-0.85	151	123	285	263	182	235	123(B)	206	186	227
BHSOPCC-06-71.3-1.15	♦	♦	♦	♦	♦	220	220(F)	220	♦	220
BHSOPCC-07-70.3-1.16	265	203	272	272	272	148	148(F)	238	247	231
BLSOPCC-12-37.5-0.48	♦	♦	♦	♦	108	108	108(E)	108	♦	108
BLSOPCC-13-37.5-0.57	♦	168	153	138	150	168	138(D)	155	161	152
BLSOPCC-14-32.0-0.72	120	120	♦	♦	♦	120	120(F)	120	120	120
BLSGC-16-27.1-0.38	♦	♦	♦	♦	♦	118	118(F)	118	♦	118
BLSGC-18-26.8-0.56	♦	167.5	♦	♦	♦	♦	167.5(B)	167.5	167.5	♦
BLSGC-19-35.7-0.64	♦	199.5	♦	♦	♦	♦	199.5(B)	199.5	199.5	♦

Note: ♦ indicates the shear reinforcement did not reach the yielding; A to F are positions of the stirrups where the strains were measured (refer to Table 6 and Fig. 5).

Cracks with a slight inclination were also observed in shear zones due to the interaction between normal and shear stresses.

In the final stages of loading, an inclined crack formed suddenly in one of the shear spans, rapidly spreading toward the load application point.

Strain of transverse reinforcement

Figure 5 shows the load-versus-strain diagrams of the stirrups for each tested beam where the largest strains were measured, indicated by the points (ε_{sy}*, V_y) shown in the legend, followed by the name of the beam and, in parentheses, the first stirrup that reached yielding. It can be seen that the values of (ε_{sy}*, V_y) for BHSOPCC-02-67.1-0.46, BLSOPCC-09-42.6-0.36, BLSOPCC-10-37.3-0.36, BLSOPCC-11-37.3-0.48, and BLSGC-17-28.8-0.44 are not signaled because yielding and rupture occurred practically simultaneously due to their low $\rho_{sw}f_{yw}$ values, with the exception of beam BLSGC-16-27.1-0.38, in which the first stirrup reached yielding after the beam reached V_{cr}.

The parameter V_y presented in Table 6 is not representative enough to evaluate the beam behavior; the main factor is the randomness of the crack location and the position of the strain gauge in the stirrup. The parameter V_y* was defined in this work as being the average of the shear forces at the yielding of all the stirrups of each beam that reached the strain ε_y*. This parameter considers the number of stirrups that reached yielding and the load where yielding occurred for each beam.

Table 7 shows the shear force values of the beams relative to the yielding of each stirrup where it occurred. It also shows the average values of the yielding shear forces of the stirrups of each shear span, where V_y*,$_l$ is the average yield shear of the stirrups of the left shear span and V_y*,$_r$ is the average yield shear of the stirrups of the right shear span.

ANALYSIS TO DETERMINE MINIMUM TRANSVERSE REINFORCEMENT

Reserve strength criterion proposed by Johnson and Ramirez[4] considering ratio $\tau_{u,n\ exp}/\tau_{c,n\ theo}$

Figure 6 shows the reserve strength, given by the relationship between the normalized experimental shear strength $\tau_{u,n\ exp} = V_u/b_wd\sqrt{f_{cm}}$ and the normalized concrete shear strength $\tau_{c,n\ theo} = V_c/b_wd\sqrt{f_{cm}}$, according to the requirements of the evaluated codes ($\tau_{u,n\ exp}/\tau_{c,n\ theo}$) as a function of $\rho_{sw}f_{yw}/f_{cm}$ for the tested beams, along with the minimum value of this ratio proposed by Ozcebe et al.[2] Table 8 shows the statistical parameters obtained for the types of concrete and the total values for each standard evaluated. To calculate $\tau_{c,n\ theo}$, the formulas from ACI 318-19, AASHTO LRFD, *fib* Model Code, and ABNT NBR 6118:2014 were considered.

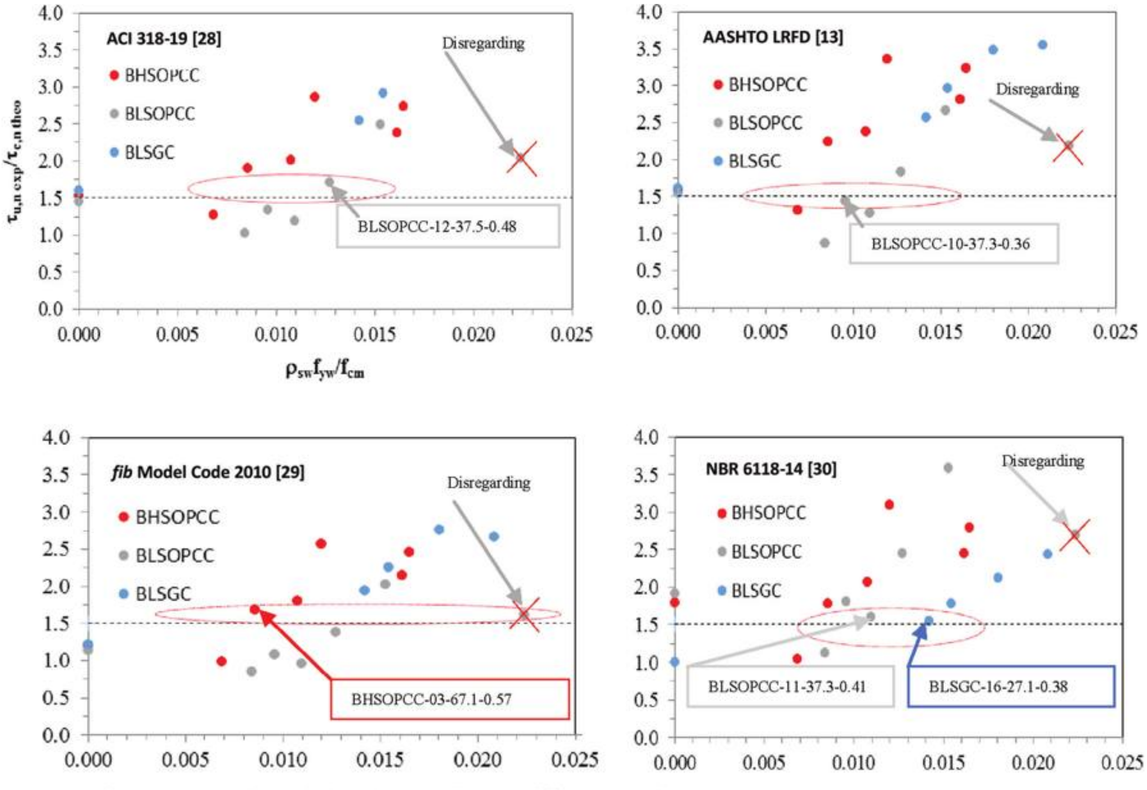

where: $\tau_{c,n\ theo}$ is calculated according to different codes.

-----------Minimum value recommended by Ozcebe et al.[2]

Fig. 6—Relationship $\tau_{u,n\ exp}/\tau_{c,n\ theo}$ *as function of* $\rho_{sw}f_{yw}/f_{cm}$.

Table 8—Statistical parameters resulting from calculation of $\tau_{u,n\ exp}/\tau_{c,n\ theo}$ for evaluated standards

Codes	Type of concrete	Average, MPa	StDev, MPa	CoV, %
ACI 318-19	HSOPCC	2.10	0.60	28.4
	LSOPCC	1.60	0.51	32.1
	LSGC	2.80	0.78	27.9
	General values	**2.10**	**0.76**	**36.0**
AASHTO LRFD	HSOPCC	2.42	0.78	32.4
	LSOPCC	2.16	0.88	40.6
	LSGC	2.83	0.79	27.9
	General values	**2.26**	**0.83**	**36.8**
fib Model Code 2010	HSOPCC	1.83	0.60	32.6
	LSOPCC	1.29	0.41	31.6
	LSGC	2.17	0.62	28.7
	General values	**1.72**	**0.63**	**36.4**
ABNT NBR 6118:2014	HSOPCC	2.14	0.69	32.3
	LSOPCC	2.17	0.82	37.6
	LSGC	1.78	0.55	31.0
	General values	**2.06**	**0.69**	**33.6**

It is worth noting that the standards had very similar statistical parameters of average, standard deviation (StDev), and coefficient of variation (CoV), where, according to the reserve strength index criterion proposed by Ozcebe et al.,[2] within a minimum value of 1.5, the beams demonstrated having a minimum reinforcement higher or lower than the minimum. ACI 318-19 provided general values of 2.10 MPa, 0.76 MPa, and 36.0% for average, StDev, and CoV, respectively. Using a reserve strength index ranging from 1.43 to 1.70, it was defined that BLSOPCC-12-37.5-0.48 ($\tau_{u,n\ exp}/\tau_{c,n\ theo}$ = 1.70) was the only beam that seemed to have the minimum transverse reinforcement. The others exhibited greater or lower reinforcement than the minimum.

AASHTO LRFD presented values of 2.26 MPa, 0.83 MPa, and 36.8% for average, StDev, and CoV, respectively. Beam BLSOPCC-10-37.3-0.36 seemed to have minimum transverse reinforcement $\tau_{u,n\ exp}/\tau_{c,n\ theo}$ = 1.43, while the others, according to the criteria, had higher or lower values than the minimum.

fib Model Code 2010 was the one that revealed the best results, with 1.72 MPa, 0.63 MPa, and 36.4% for average, StDev, and CoV, respectively. One beam appeared to have a minimum transverse reinforcement—BHSOPCC-03-67.1-0.57 ($\tau_{u,n\ exp}/\tau_{c,n\ theo}$ = 1.69); beam BLSOPCC-14-32.0-0.72 was disregarded—for an undetected reason, it had inconsistent results with the other beams. The others had higher or lower than the minimum reinforcement according to the criteria.

Lastly, ABNT NBR 6118:2014 exhibited values of 2.06 MPa, 0.69 MPa and 33.7% for average, StDev, and CoV, respectively. Two beams appeared to have a minimum transverse reinforcement—BLSOPCC-11-37.3-0.41($\tau_{u,n\ exp}/\tau_{c,n\ theo}$

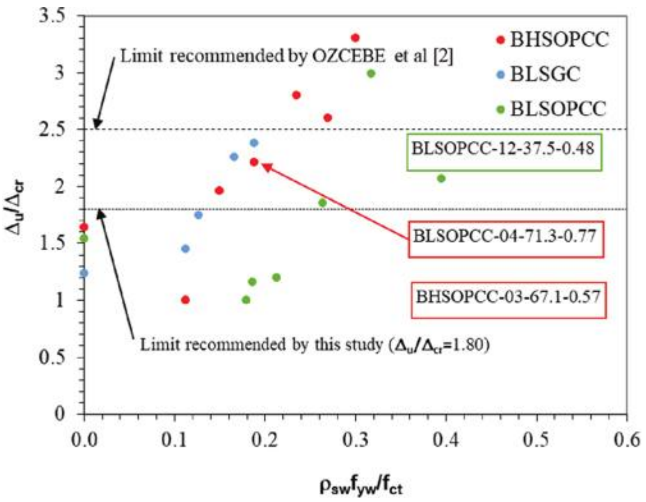

Fig. 7—Ductility index (Δ_u/Δ_{cr}) as function of $\rho_{sw}f_{yw}/f_{ct}$.

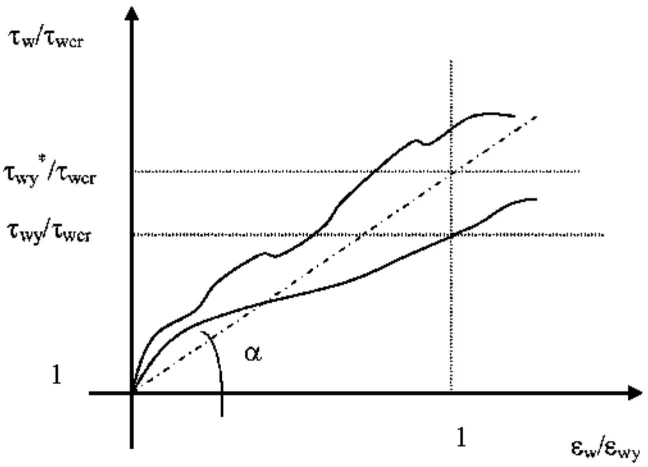

Fig. 8—Diagram of relative nominal shear stress in beam (τ_w/τ_{wcr}) as function of relative strain in stirrups ($\varepsilon_w/\varepsilon_{wy}$).

= 1.60) and BLSGC-16-27.1-0.38 ($\tau_{u,n\ exp}/\tau_{c,n\ theo}$ = 1.55)—while the others had higher or lower than the minimum reinforcement according to the criteria.

When analyzing the types of concrete, it is noted that the highest reserve strength was in beams made with LSGC, followed by beams with HSOPCC, and finally beams with LSOPCC, except for ABNT NBR 6118:2014.

Ductility index criterion proposed by Ozcebe et al.[2]

Figure 7 shows the ratios of ultimate shear deflection/diagonal cracking shear deflection Δ_u/Δ_{cr} versus $\rho_{sw}f_{yw}/f_{ct}$ for the tested beams, along with the minimum index value recommended by Ozcebe et al.[2] This figure also shows the beams that can be considered as having minimum reinforcement according to the proposed parameter. According to this criterion, only four of the 16 beams tested with transverse reinforcement satisfied the minimum ductility index: BHSOPCC-06-71.3-1.15, BHSOPCC-05-71.3-0.85, BLSOPCC-13-37.5-0.57, and BHSOPCC-07-70.3-1.16, being very conservative, with expected beams with a higher amount of transverse reinforcement $\rho_{sw}f_{yw}$. The value of Δ_u/Δ_{cr} = 1.80 is considered reasonable as a minimum index to be considered in the beams tested.

Table 9—Relative nominal tangential stresses of tested beams

Beams	$\rho_{sw}f_{yw}/f_{ct}$	τ_{wu}/τ_{wcr}	τ_{wy}/τ_{wcr}	τ_{wy}^*/τ_{wcr}
BHSOPCC-01-70.2-0.00		1.21		
BHSOPCC-02-67.1-0.46	0.11	1.00	+	+
BHSOPCC-03-67.1-0.57	0.14	1.68	1.06	1.26
BHSOPCC-04-71.3-0.77	0.13	1.84	1.36	1.57
BHSOPCC-05-71.3-0.85	0.24	2.59	1.11	1.86
BHSOPCC-06-71.3-1.15	0.27	2.18	2.00	2.00
BHSOPCC-07-70.3-1.16	0.30	2.47	1.34	2.16
BLSOPCC-08-32.0-0.00		1.13		
BLSOPCC-09-42.6-0.36	0.18	1.00	+	+
BLSOPCC-10-37.3-0.36	0.19	1.13	+	+
BLSOPCC-11-37.3-0.41	0.21	1.00	+	+
BLSOPCC-12-37.5-0.48	0.26	1.44	1.23	1.35
BLSOPCC-13-37.5-0.57	0.32	2.10	1.73	1.93
BLSOPCC-14-32.0-0.72	0.40	1.59	1.50	1.51
BLSGC-15-27.2-0.00		1.31		
BLSGC-16-27.1-0.38	0.11	2.08	1.82	1.82
BLSGC-17-28.8-0.44	0.13	2.46	+	+
BLSGC-18-26.8-0.56	0.19	2.85	2.58	2.58
BLSGC-19-35.7-0.64	0.17	3.23	3.07	3.07

Note: + indicates when yielding and rupture occur practically simultaneously.

Proposed parameter for defining minimum transverse reinforcement of tested beams

Table 9 shows the relative nominal shear stresses corresponding to the loads at which the diagonal cracks (τ_{wcr}), the yielding of the stirrups (τ_{wy} and τ_{wy}^*), and the rupture (τ_{wu}) of the beams occurred. It also shows the ratios between these stresses and the ratios between them and f_{cm} and f_{ct}, considering $f_{ct} = 0.9f_{ct,sp}$.

The criterion proposed in this work to evaluate the level of ductility of the tested beams is shown in Fig. 8. In this figure, the relationship between the relative nominal shear stress in a beam τ_w/τ_{wcr} and the relative strain of the stirrups $\varepsilon_w/\varepsilon_{wy}$ is schematically shown. In a beam with transverse reinforcement less than the minimum—$\tau_{wu}/\tau_{wcr} = \tau_{wy}/\tau_{wcr} = \tau_{wy}^*/\tau_{wcr} \approx 1$, that is—the angle α (tgα = $\tau_{wy}^*/\tau_{wcr} - 1$) shown in Fig. 8 is approximately equal to 0. Beams with reinforcement greater than the minimum lead to differences between the values of τ_{wcr}, τ_{wy}, and τ_{wu} and between τ_{wy} and τ_{wy}^*; therefore, values greater than 0 will indicate higher levels of ductility.

The parameter τ_{wy}^* is more representative of this behavior than τ_{wy} due to shear because it includes what occurs at several stirrups and not at just one.

The ratios τ_{wu}/τ_{wcr} versus $\rho_{sw}f_{yw}/f_{cm}$, τ_{wu}/τ_{wcr} versus $\rho_{sw}f_{yw}/f_{ct}$, and τ_{wy}/τ_{wcr} versus $\rho_{sw}f_{yw}/f_{ct}$ of the beams tested by the author and others[1,2,4,5,7,9,34] were not the best parameters to serve

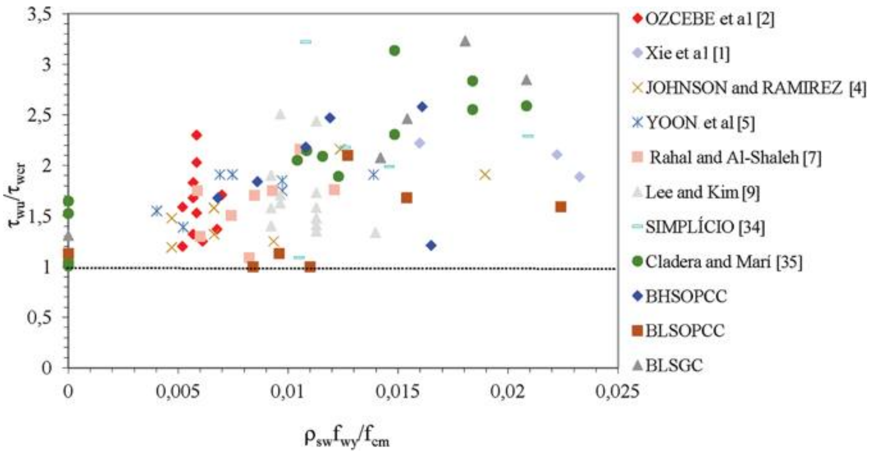

Fig. 9—Relationship τ_{wu}/τ_{wcr} as function of $\rho_{sw}f_{yw}/f_{cm}$ for beams tested by author and others.[1,2,4,5,7,9,34,35]

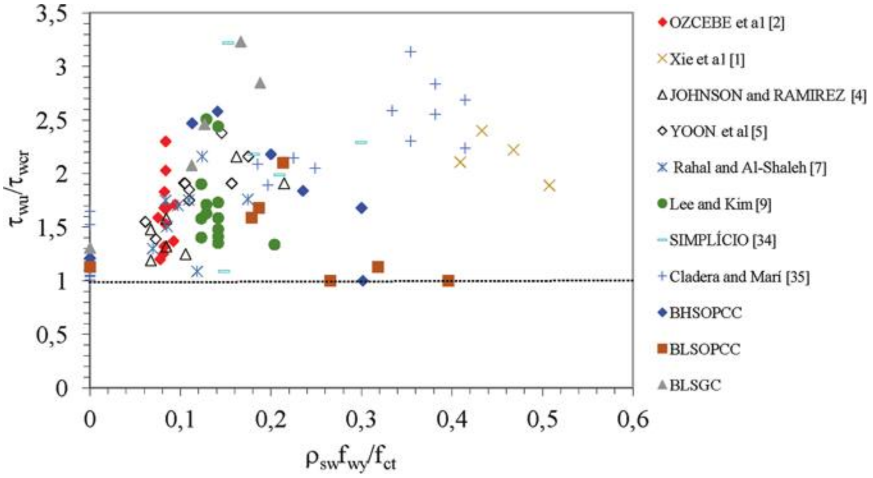

Fig. 10—Relationship τ_{wu}/τ_{wcr} as function of $\rho_{sw}f_{yw}/f_{ct}$ for beams tested by author and others.[1,2,4,5,7,9,34,35]

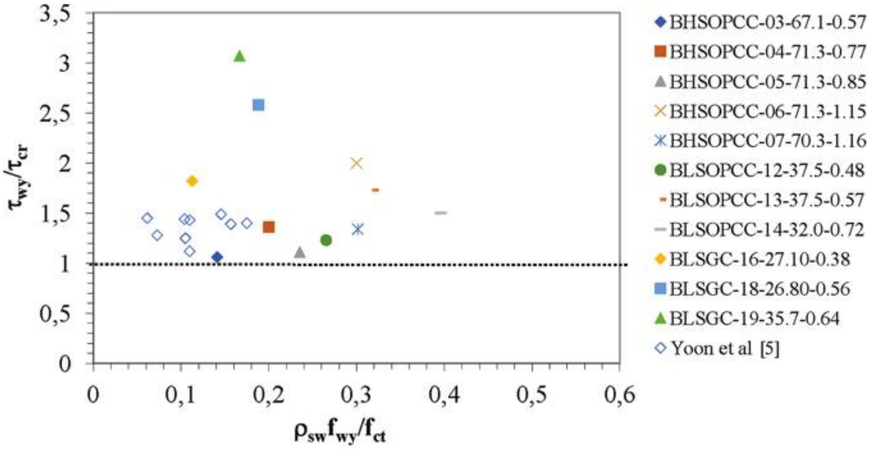

Fig. 11—Relationship τ_{wy}/τ_{wcr} as function of $\rho_{sw}f_{yw}/f_{ct}$ for beams tested by author and by Yoon et al.[5]

as a basis for defining the minimum amount of transverse reinforcement.

Figure 9 shows the relation of τ_{wu}/τ_{wcr} as a function of $\rho_{sw}f_{yw}/f_{cm}$ for the beams tested by the author and others.[1,2,4,5,7,9,34,35] Figure 10 shows the relation of τ_{wu}/τ_{wcr} as a function of $\rho_{sw}f_{yw}/f_{ct}$ for these same beams, while Fig. 11 shows the relation of τ_{wy}/τ_{wcr} of the beams tested with the one tested by Yoon et al.[5] The other authors mentioned in this section did not measure the strains in the stirrups and did not evaluate this relationship as a criterion for defining beams with the minimum transverse reinforcement.

The dispersion of data observed in these figures, and also the data in Table 9, suggests that τ_{wu}/τ_{wcr} or τ_{wy}/τ_{wcr} are not the best parameters to serve as a basis for defining the minimum transverse reinforcement.

The relationships $\tau_{wy}*/\tau_{wcr}$ versus $\rho_{sw}f_{yw}/f_{ct}$ found for the beams tested in this work can be seen in Fig. 12.

It was verified that the parameter $\tau_{wy}*/\tau_{wcr}$ can be adopted to define the minimum reinforcement ratio. A value of $\tau_{wy}*/\tau_{wcr}$ of approximately 1.4 was close to what was found for beams BHSOPCC-03-67.1-0.57, BHSOPCC-04-71.3-0.77, and BLSOPCC-12-37.5-0.48. This parameter can verify whether a beam has minimum transverse reinforcement or not. This is confirmed by the load versus deformation curves of the stirrups and the kinetics of crack openings, as well as the maximum width in the SLS, not shown in this paper. It was observed that the beams made with geopolymeric concrete experienced higher ductility, as shown by Madheswaran et al.[23]

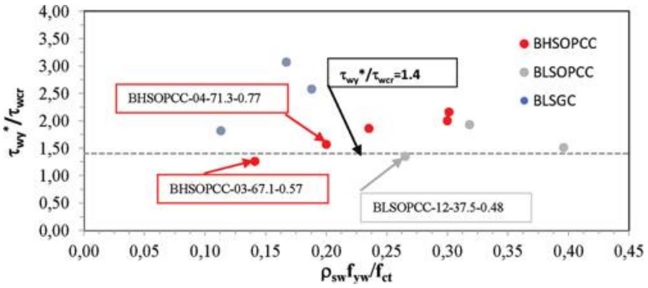

Fig. 12—Relationship $\tau_{wy}*/\tau_{wcr}$ as function of $\rho_{sw}f_{yw}/f_{ct}$.

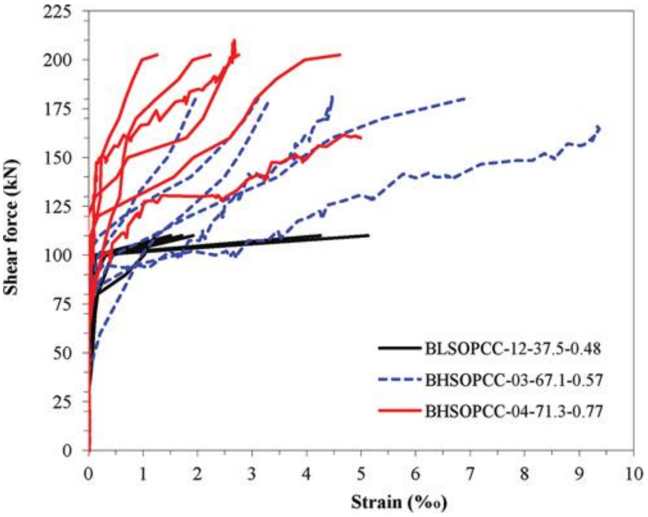

Fig. 13—Shear force versus strain of stirrups for beams having approximately minimum transverse reinforcement according to parameter proposed in this paper.

When the parameter proposed here was evaluated in relation to the reserve strength criteria defined by Johnson and Ramirez,[4] it was shown that the results provided by ACI 318-19 indicate that the BLSOPCC-12-37.5-0.48 beam provides a reasonable reserve strength, while *fib* Model Code 2010 suggests the BHSOPCC-03-67.1-0.57 beam. In the case of beam BHSOPCC-04-71.3-0.77, ACI 318-19, AASHTO LRFD, *fib* Model Code 2010, and ABNT NBR 6118:2014 provide higher reserve strength values than the one considered in this work, with 2.01, 2.37, 1.81 and 2.06, respectively.

Influence of $\rho_{sw}f_{yw}$ and f_{cm} on stirrup deformation and crack pattern

Figure 13 shows a comparison between the strains of the stirrups for BLSOPCC-12-37.3-0.48, BHSOPCC-03-67.1-0.57, and BHSOPCC-04-71.3-0.77—beams with approximately the minimum amount of transverse reinforcement—and the parameter proposed in this paper, $\tau_{wy}*/\tau_{wcr}$. Note that when increasing $\rho_{sw}f_{yw}$ and f_{cm}, the strains tend to decrease. These parameters, along with the amount of longitudinal reinforcement ρ_s, define the crack pattern of the beams.

Figure 14 shows the crack pattern of the pair BHSOPCC-03-67.1-0.57 and BLSOPCC-13-37.5-0.57 and the pair BHSOPCC-02-67.1-0.46 and BLSOPCC-12-37.5-0.48, the first two with approximately equal $\rho_{sw}f_{yw}$ and different f_{cm}, showing the influence of f_{cm} in the crack pattern. The greater the concrete compressive strength, the greater the number of cracks with a smaller opening (not shown in this paper). The beams BLSOPCC-13-37.5-0.57 and BLSOPCC-12-37.5-0.48 are also compared, with equal f_{cm} and different $\rho_{sw}f_{yw}$. This shows the influence of the transverse reinforcement $\rho_{sw}f_{yw}$ on the crack pattern. The higher the transverse reinforcement $\rho_{sw}f_{yw}$, the greater the number of cracks with a smaller opening.

CONCLUSIONS

The following conclusions are drawn from the present study:

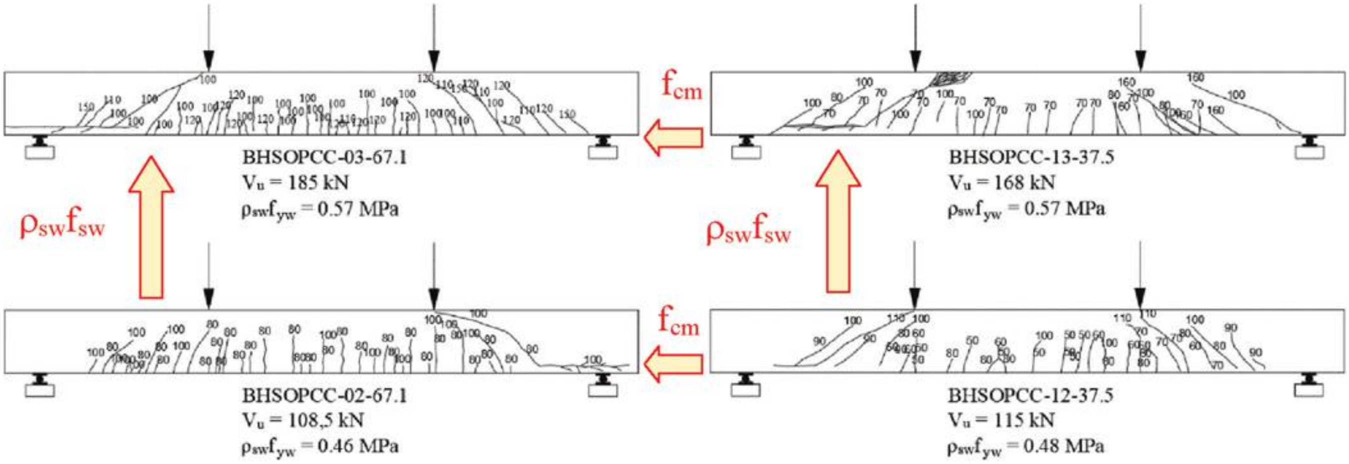

Fig. 14—Influence of $\rho_{sw}f_{yw}$ and other parameters on crack patterns.

- It was demonstrated that the design standards for concrete structures to determine the minimum amount of transverse reinforcement of beams lead to very different values. Obviously, if all the standards aim at the minimum amount of transverse reinforcement proposed only to avoid sudden breakage of the beams, in the case of diagonal cracking, there should not be much difference between the values proposed by them for this amount.
- When analyzing the results obtained using the resistance reserve criterion proposed by Johnson and Ramirez,[4] it was noted that each standard defines different models for evaluating the resistance capacity provided by the concrete (V_c). They provide differences with respect to defining which beams have approximately the minimum transverse reinforcement and beams with reinforcement lower and higher than the minimum. According to the statistical parameters evaluated, *fib* Model Code 2010 provides the best results.
- The ductility index criterion proved to be conservative for the beams tested, and an index of $\Delta_u/\Delta_{cr} = 1.80$ was proposed. This value was obtained according to the beam behavior and convergence with the proposed parameter for defining beams with the minimum transverse reinforcement ($\tau_{wy}*/\tau_{wcr}$).
- The new proposed parameter for defining whether or not a beam has the minimum transverse reinforcement is more precise and is given by the parameter $\tau_{wy}*/\tau_{wcr}$, which was more appropriate, and the tested beams suggest that a value of approximately 1.4 can be used to define beams that have the minimum transverse reinforcement.
- It was shown that of the 16 beams tested with transverse reinforcement, according to the standards analyzed, only five of them (BLSOPCC-12-37.5-0.48, BLSOPCC-10-37.3-0.36, BHSOPCC-03-67.1-0.57, BLSOPCC-11-37.3-0.41, and BLSGC-16-27.1-0.38) and three of them (HSOPCC-04-71.3-0.77, BHSOPCC-03-67.1-0.57, and BLSOPCC-12-37.5-0.48) seem to have the minimum transverse reinforcement, according to the criteria proposed in this paper ($\tau_{wy}*/\tau_{wcr}$) and their behavior in the serviceability limit state (SLS) of crack opening. The others seem to have reinforcement higher or lower than the minimum.
- The beams of low-strength ordinary portland cement concrete (LSOPCC) and those of low-strength geopolymeric concrete (LSGC) had similar behavior. The latter group exhibited higher ductility, corroborating the conclusions obtained by Madheswaran et al.[23]

AUTHOR BIOS

Sergio Luis Garcia *is a Professor and Research Engineer in the Civil Engineering Department at the State University of North Fluminense Darcy Ribeiro (UENF), Campos dos Goytacazes, RJ, Brazil. He received his BS from Universidad Central "Marta Abreu" de Las Villas, Santa Clara, Cuba, and his MS and DSc from the Federal University of Rio de Janeiro, Rio de Janeiro, RJ, Brazil. His research interests include reinforced concrete structure variations and effects.*

Juscelina Ferreira *currently teaches civil engineering at Minas Gerais State University, Belo Horizonte, MG, Brazil. She received her DSc in structural engineering from the Federal University of Minas Gerais, Belo Horizonte, MG, Brazil. Her research interests include structural reliability, probabilistic methods, and fiber-reinforced polymer strengthening of structures.*

Dylmar Dias *is a Research Engineer in the Civil Engineering Department at UENF. He received his PhD in materials science from the Military Institute of Engineering, Rio de Janeiro, RJ, Brazil. His research interests include conventional and alkali-activated binders, pathology of constructions, and repair and strengthening of reinforced concrete structures.*

Jedson Sousa *is a Research Engineer in the Civil Engineering Department at UENF. He received his BS from Universidade Veiga de Almeida, Rio de Janeiro, RJ, Brazil, and his MS from UENF. His research interests include the characterization of concrete with recycled aggregates.*

Patricia Figueiredo *is a Research Engineer in the Civil Engineering Department at UENF, where she received her BS and DSc. Her research interests include the field of concrete-concrete adherence.*

Juliana Trindade *is Research Engineer in the Civil Engineering Department at UENF, where she received her BS and DSc. Her research interests include recycled concrete.*

ACKNOWLEDGMENTS

This study was funded in part by the Coordination for the Improvement of Higher Education Personnel (CAPES) - Funding Code 001.

REFERENCES

1. Xie, Y.; Ahmad, S. H.; Yu, T.; Hino, S.; and Chung, W., "Shear Ductility of Reinforced Concrete Beams of Normal and High-Strength Concrete," *ACI Structural Journal*, V. 91, No. 2, Mar.-Apr. 1994, pp. 140-149.
2. Ozcebe, G.; Ersoy, U.; and Tankut, T., "Evaluation of Minimum Shear Reinforcement Requirements for Higher Strength Concrete," *ACI Structural Journal*, V. 96, No. 3, May-June 1999, pp. 361-369.
3. Krauthammer, T., "Minimum Shear Reinforcement Based on Interface Shear Transfer," *ACI Structural Journal*, V. 89, No. 1, Jan.-Feb. 1992, pp. 99-105.
4. Johnson, M. K., and Ramirez, J. A., "Minimum Shear Reinforcement in Beams with Higher Strength Concrete," *ACI Structural Journal*, V. 86, No. 4, July-Aug. 1989, pp. 376-382.
5. Yoon, Y.-S.; Cook, W. D.; and Mitchell, D., "Minimum Shear Reinforcement in Normal, Medium, and High-Strength Concrete Beams," *ACI Structural Journal*, V. 93, No. 5, Sept.-Oct. 1996, pp. 576-584.
6. Shehata, I. A. E. M.; Shehata, L. C. D.; and Garcia, S. L. G., "Minimum Steel Ratios in Reinforced Concrete Beams Made of Concrete with Different Strengths—Theoretical Approach," *Materials and Structures*, V. 36, No. 1, 2003, pp. 3-11.
7. Rahal, K. N., and Al-Shaleh, K. S., "Minimum Transverse Reinforcement in 65 MPa Concrete Beams," *ACI Structural Journal*, V. 101, No. 6, Nov.-Dec. 2004, pp. 872-878.
8. Angelakos, D.; Bentz, E. C.; and Collins, M. P., "Effect of Concrete Strength and Minimum Stirrups on Shear Strength of Large Members," *ACI Structural Journal*, V. 98, No. 3, May-June 2001, pp. 290-300.
9. Lee, J.-Y., and Kim, U.-Y., "Effect of Longitudinal Tensile Reinforcement Ratio and Shear Span-Depth Ratio on Minimum Shear Reinforcement in Beams," *ACI Structural Journal*, V. 105, No. 2, Mar.-Apr. 2008, pp. 134-144.
10. Aguilar, G.; Villamizar, S.; and Ramirez, J. A., "Evaluation of Shear Reinforcement Design Limits in High-Strength Concrete Beams," *ACI Structural Journal*, V. 115, No. 2, Mar. 2018, pp. 401-414. doi: 10.14359/51701132
11. ACI Committee 318, "Building Code Requirements for Reinforced Concrete (ACI 318-89) and Commentary (ACI 318R-89)," American Concrete Institute, Farmington Hills, MI, 1989, 353 pp.
12. ACI Committee 318, "Building Code Requirements for Structural Concrete (ACI 318-14) and Commentary (ACI 318R-14)," American Concrete Institute, Farmington Hills, MI, 2014, 520 pp.
13. AASHTO, "AASHTO LRFD Bridge Design Specifications," seventh edition, American Association of State Highway and Transportation Officials, Washington, DC, 2014.
14. Jayasinghe, T.; Gunawardena, T.; and Mendis, P., "A Comparative Study on Minimum Shear Reinforcement Provisions in Codes of Practice for Reinforced Concrete Beams," *Case Studies in Construction Materials*, V. 15, 2021, Article No. e00617. doi: 10.1016/j.cscm.2021.e00617
15. AS 3600:2018, "Concrete Structures," Standards Australia, Sydney, NSW, Australia, 2018.

16. Ali, A.; Thomas, J.; and Parappattu, N. B., "Geopolymer As Repair Material—A Review," *International Journal of Innovative Research in Advanced Engineering*, V. 3, No. 9, 2016, pp. 2349-2763.

17. Ambily, P. S.; Madheswaran, C. K.; Sharmila, S.; and Muthiah, S., "Experimental and Analytical Investigations on Shear Behaviour of Reinforced Geopolymer Concrete Beams," *International Journal of Civil and Structural Engineering*, V. 2, No. 2, 2011, pp. 673-688.

18. Darmawan, M. S.; Bayuaji, R.; Sugihardjo, H.; Husin, N. A.; and Anugraha Affandhie, R. B., "Shear Strength of Geopolymer Concrete Beams Using High Calcium Content Fly Ash in a Marine Environment," *Buildings*, V. 9, No. 4, 2019, Article No. 98. doi: 10.3390/buildings9040098

19. Yacob, N. S.; ElGawady, M. A.; Sneed, L. H.; and Said, A., "Shear Strength of Fly Ash-Based Geopolymer Reinforced Concrete Beams," *Engineering Structures*, V. 196, 2019, Article No. 109298. doi: 10.1016/j.engstruct.2019.109298

20. Mourougane, R.; Puttappa, C. G.; Sashidhar, C.; and Muthu, K. U., "Shear Behaviour of High Strength GPC/TVC Beams," *Proceedings of International Conference on Advances in Architecture and Civil Engineering (AARCV 2012)*, V. 1, R. Prabhakara, J. Chandra, C. R. Jetty, and A. H. Bhashyam, eds., Bangalore, Karnataka, India, 2012, pp. 142-145.

21. Ambily, P. S.; Madheswaran, C. K.; Lakhsmanan, N.; Dattatreya, J. K.; and Jaffer Sathik, S. A., "Experimental Studies on Shear Behaviour of Reinforced Geopolymer Concrete Thin Webbed T-Beams with and without Fibres," *International Journal of Civil and Structural Engineering*, V. 3, No. 1, 2012, pp. 128-140.

22. Ng, T. S.; Amin, A.; and Foster, S. J., "The Behaviour of Steel-Fibre-Reinforced Geopolymer Concrete Beams in Shear," *Magazine of Concrete Research*, V. 65, No. 5, 2013, pp. 308-318. doi: 10.1680/macr.12.00081

23. Madheswaran, C. K.; Ambily, P. S.; Lakshmanan, N.; Dattatreya, J. K.; and Jaffer Sathik, S. A., "Shear Behavior of Reinforced Geopolymer Concrete Thin-Webbed T-Beams," *ACI Materials Journal*, V. 111, No. 1, Jan.-Feb. 2014, pp. 89-98.

24. Maranan, G. B.; Manalo, A. C.; Karunasena, W. M.; Benmokrane, B.; and Mendis, P. A., "Comparison of the Shear Behaviour of Geopolymer Concrete Beams with GFRP and Steel Transverse Reinforcements," *Proceedings*, The 12th International Symposium on Fiber Reinforced Polymers for Reinforced Concrete Structures (FRPRCS-12) & The 5th Asia-Pacific Conference on Fiber Reinforced Polymers in Structures (APFIS-2015), Nanjing, Jiangsu, China, 2015, 6 pp.

25. Yacob, N. S., "Shear Behavior of Reinforced Fly Ash-Based Geopolymer Concrete," master's thesis, Missouri University of Science and Technology, Rolla, MO, 2016.

26. Visintin, P.; Mohamed Ali, M. S.; Albitar, M.; and Lucas, W., "Shear Behaviour of Geopolymer Concrete Beams without Stirrups," *Construction and Building Materials*, V. 148, 2017, pp. 10-21. doi: 10.1016/j.conbuildmat.2017.05.010

27. Maranan, G. B.; Manalo, A. C.; Benmokrane, B.; Karunasena, W.; Mendis, P.; and Nguyen, T. Q., "Shear Behaviour of Geopolymer-Concrete Beams Transversely Reinforced with Continuous Rectangular GFRP Composite Spirals," *Composite Structures*, V. 187, 2018, pp. 454-465. doi: 10.1016/j.compstruct.2017.12.080

28. ACI Committee 318, "Building Code Requirements for Structural Concrete (ACI 318-19) and Commentary (ACI 318R-19) (Reapproved 2022)," American Concrete Institute, Farmington Hills, MI, 2019, 624 pp.

29. *fib*, "*fib* Model Code for Concrete Structures 2010," International Federation for Structural Concrete, Lausanne, Switzerland, 2010.

30. ABNT NBR 6118:2014, "Projeto de Estruturas de Concreto—Procedimentos," Associação Brasileira de Normas Técnicas, São Paulo, SP, Brazil, 2014, 255 pp.

31. ABNT NBR 5733/1991, "Cimento Portland de Alta Resistência Inicial," Associação Brasileira de Normas Técnicas, São Paulo, SP, Brazil, 1991, 5 pp.

32. ABNT NBR 5739:2018, "Concreto — Ensaio de Compressão de Corpos de Prova Cilíndricos," Associação Brasileira de Normas Técnicas, São Paulo, SP, Brazil, 2018, 9 pp.

33. ABNT NBR 7222/1994, "Concreto e Argamassa - Determinação da Resistência à Tração por Compressão Diametral de Corpos de Prova Cilíndricos," Associação Brasileira de Normas Técnicas, São Paulo, SP, Brazil, 1994, 6 pp.

34. Simplício, M. A. S., "Comportamento de Vigas de Concreto de Alto Desempenho com Pequenos Percentuais de Armadura Transversal," master's dissertation, Universidade Federal de Pernambuco, Recife, PE, Brazil, 1999.

35. Cladera, A., and Marí, A. R., "Experimental Study on High-Strength Concrete Beams Failing in Shear," *Engineering Structures*, V. 27, No. 10, 2005, pp. 1519-1527. doi: 10.1016/j.engstruct.2005.04.010

CALL FOR ACTION

ACI Invites You To...

Share your expertise

Do you have EXPERTISE in any of these areas?

- BIM
- Chimneys
- Circular Concrete Structures Prestressed by Wrapping with Wire and Strand
- Circular Concrete Structures Prestressed with Circumferential Tendons
- Concrete Properties
- Demolition
- Deterioration of Concrete in Hydraulic Structures
- Electronic Data Exchange
- Insulating Concrete Forms, Design, and Construction
- Nuclear Reactors, Concrete Components
- Pedestal Water Towers
- Pipe, Cast-in-Place
- Strengthening of Concrete Members
- Sustainability

Then become a REVIEWER for the *ACI Structural Journal* or the *ACI Materials Journal*.

Become a Reviewer for the ACI Journals

How to become a Reviewer:

1. Go to: **http://mc.manuscriptcentral.com/aci**;
2. Click on "Create Account" in the upper right-hand corner; and
3. Enter your E-mail/Name, Address, User ID and Password, and Area(s) of Expertise.

Update your Manuscript Central user account information

Did you know that the database for MANUSCRIPT CENTRAL, our manuscript submission program, is separate from the ACI membership database?

How to update your user account:

1. Go to **http://mc.manuscriptcentral.com/aci**;
2. Log in with your current User ID & Password; and
3. Update your E-mail/Name, Address, User ID and Password, and Area(s) of Expertise.

QUESTIONS?

E-mail any questions to Journals.Manuscripts@concrete.org.

American Concrete Institute
Always advancing

ACI STRUCTURAL JOURNAL TECHNICAL PAPER

Title No. 121-S05

Flexural Behavior of Carbon Fiber-Reinforced Polymer Partially Bonded Reinforced Concrete Beams with Different Anchorage Methods

by Qi Cao, Xingchao Wang, Zhimin Wu, Rongxiong Gao, and Xin Jiang

Carbon fiber-reinforced polymer (CFRP) is a widely used material for reinforced concrete (RC) beam strengthening. Because of exposure to severe environments and improper construction, CFRP sheets may separate from the bottom of RC beams. To analyze the influence of this type of interfacial defect on the mechanical properties of RC beams quantitatively and provide a reference for the rehabilitation of structures, this paper investigates the flexural properties of RC beams strengthened with partially bonded CFRP by experiments and analytical studies. To measure the degree of unbonded CFRP, a new parameter called the unbonded ratio was established, which is defined as the ratio of unbonded length to the total length of strengthening CFRP in the tension zone. Twenty-six RC beams were fabricated and tested in the present study, and the experimental variables were the unbonded ratio, thickness of the CFRP sheet, and anchorage method (vertical U-jacket, inclined U-jacket, and mechanical plate). The cracking load, ultimate load, load-midspan deflection curve, ductility, crack pattern, and failure modes of these specimens are discussed. Also, the coupling effect of the unbonded CFRP and anchorage method on the flexural performance of strengthened beams was investigated. Test results indicated that the ultimate load decreased with the increase of the unbonded ratio before the unbonded ratio reached its critical value. It was also found that the mechanical-plate anchorage and inclined U-jackets were superior to traditional vertical U-jackets in terms of load-carrying capacity and flexural stiffness and postponed the debonding of CFRP. Finally, a theoretical model for the ultimate load of RC beams strengthened with inclined U-jackets was proposed, which showed a good agreement with the test results.

Keywords: anchorage; concrete beam; flexural performance; partially bonded carbon fiber-reinforced polymer (CFRP); unbonded ratio.

INTRODUCTION

Attributed to the advantages of high strength, low weight, and excellent corrosion resistance, carbon fiber-reinforced polymer (CFRP) is getting more and more attention from researchers, engineers, and project managers. Regarding the external reinforcement by CFRP, researchers have studied the influence of distinct experimental variables on CFRP-strengthened structures, such as the position of CFRP reinforcement, the thickness of the CFRP sheet, and the shape of CFRP reinforcement forms (U-shaped bonding, spaced strip bonding, or the combination of different bonding techniques).[1-5] These studies showed that the application of CFRP reinforcement could postpone the cracking[1] and enhance the structural performance of reinforced concrete (RC) beams.[4]

When the CFRP sheet is employed to enhance the bending strength of the RC beam, researchers often assume that the perfect bonding can be achieved by using adhesive resins and various anchorages.[6,7] However, due to exposure to severe environments and improper construction methods, the CFRP sheet often separates from an RC beam in its service life, leading to interfacial defects and a change in load-carrying capacity. In this case, the beam strengthened with fully bonded CFRP is converted into a beam strengthened with partially bonded CFRP. Because the delamination between CFRP sheets and the surface of RC beams is difficult to detect, it is necessary to consider the post-debonding load-carrying capacity of the member before strengthening construction to ensure safety during the service life.

Currently, there are few quantitative studies on the mechanical properties of RC beams strengthened with partially bonded CFRP, and researchers' opinions are divided. Zhou et al.[8] argued that partial debonding of CFRP at the pure bending zone will reduce the ultimate load slightly, while debonding at the shear-bending zone will reduce the ultimate load significantly. However, other researchers[9-18] treated partially bonded CFRP as a novel reinforcement system for RC beams. Burgoyne[9] proposed that it was not necessary for FRP to be fully bonded to concrete and suggested an unbonded system for FRP-strengthened beams. Lees and Burgoyne[10,11] investigated the mechanical properties of beams with partially bonded composite reinforcement and concluded that the ultimate load of the partially bonded beams was equivalent to that of fully bonded beams. Chahrour and Soudki[12] and Choi et al.[13] conducted bending tests on partially bonded CFRP-strengthened RC beams and deduced the analytical expressions for the yield load and ultimate load-carrying capacity through the moment-curvature relationship. In addition, researchers[14-18] observed in their experiments and finite element analyses that partially bonded CFRP leads to increased load-carrying capacity and ductility. Therefore, there are no widely accepted conclusions on how CFRP debonding affects the mechanical properties of RC beams. Perhaps because of the existence of controversy, current codes have a low acceptance of this new reinforcement system and most of them do not address

---

ACI Structural Journal, V. 121, No. 1, January 2024.

MS No. S-2022-402.R1, doi: 10.14359/51739185, received August 14, 2023, and reviewed under Institute publication policies. Pertinent discussion including author's closure, if any, will be published ten months from this journal's date if the discussion is received within four months of the paper's print publication.

Table 1—Mixture proportions and compressive strength of concrete

Grade	Cement, kg/m^3 (lb/yd^3)	Fine aggregate, kg/m^3 (lb/yd^3)	Coarse aggregate, kg/m^3 (lb/yd^3)	Water, kg/m^3 (lb/yd^3)	Compressive strength at 28 days, MPa (ksi)
C40	450 (759)	636 (1073)	995 (1679)	210 (354)	45.39 (6.58)

the intentionally partially bonded FRP. Instead, they always treat the delamination of FRP as a kind of defect.[19]

Also, studies on the effect of anchorage methods on the mechanical properties of RC beams in the case of partially bonded CFRP have not been reported yet. Anchorages are frequently applied to RC beams strengthened with CFRP sheets. The application of anchorages is intended to prevent CFRP from debonding from the surface of the beam or to delay the delamination and increase the load-carrying capacity. CFRP U-jackets are one of the most widespread anchorage methods that can offer resistance against plate-end debonding. Mechanical plates with bolts are also widely used to improve the load-carrying capacity.[20] In addition to the traditional anchorage methods, researchers also focused on innovative anchorage methods in recent years, such as FRP bar and FRP U-jacket composite anchorages,[21] anchored holes,[22] fiber anchor spikes,[23] mechanical end anchorages,[24] warp and woof straps,[25] and inclined FRP U-jackets,[4,26] most of which improved the load-carrying capacity or serviceability of strengthened structures. Also, by using new grooving techniques for CFRP sheets such as externally bonded reinforcement on grooves (EBROG) and externally bonded reinforcement in grooves (EBRIG), the debonding between the CFRP sheet and concrete substrate can also be delayed,[27-32] with higher load-carrying capacity than reference beams. However, inconvenient construction and high costs hinder the wide application of these anchorage or grooving methods. Furthermore, studies[4,20-26] assumed that CFRP sheets were perfectly bonded to the RC beams and did not take the debonding between CFRP and the concrete substrate into account.

To investigate the combined effects of partially bonded CFRP and anchorage methods on the mechanical properties of RC beams strengthened with CFRP, this study investigated the flexural behavior of RC beams with partially bonded CFRP and three different anchorage methods—that is, vertical U-jacket, mechanical plate, and inclined U-jacket. To measure the degree of unbonded CFRP, a new parameter called the unbonded ratio is proposed, which is defined as the ratio of unbonded length to the total length of strengthening CFRP in the tension zone and denoted as ξ. The ultimate load, cracking load, flexural stiffness, ductility, crack pattern, and failure mode were studied and analyzed. In the end, a theoretical model to evaluate the ultimate load of RC beams with U-jacket anchorages was proposed. The results of the proposed model showed good agreement with the collected test results in the literature.

RESEARCH SIGNIFICANCE

Existing research on RC beams strengthened with partially bonded CFRP does not take various anchorage methods into account. The present study aims to investigate the collaborative performance of the partially bonded CFRP sheet and different anchorage methods and proposes a theoretical model to evaluate the ultimate load of RC beams with U-jacket anchorages. The research achievements of the present study will help to select a suitable anchorage method, estimate the influence of CFRP debonding, and determine whether further repairs are needed.

EXPERIMENTAL PROCEDURE

Materials

The concrete mixture proportions were adopted from a previous study.[33] The components of the mixture were ordinary portland cement, river sand, and 5 to 10 mm (0.2 to 0.4 in.) well-graded coarse aggregate. The mixture proportions and 28-day compressive strength are shown in Table 1. The specimen size for the compressive strength test was 150 x 150 x 150 mm (5.9 x 5.9 x 5.9 in.) according to GB/T 50081-2019.[34] The one-layer CFRP sheet had a thickness of 0.167 mm (0.0065 in.), tensile strength of 3400 MPa (493 ksi), elastic modulus of 244 GPa (35,390 ksi), and ultimate strain of 0.014, in which the mechanical properties were obtained from tests according to GB/T 3354-1999.[35] The nominal yield strength of longitudinal steel bars and stirrups were 400 and 300 MPa (58 and 44 ksi), respectively, and the test yield strength of longitudinal bars was 467 MPa (68 ksi), according to GB/T 228.1-2010.[36] The elastic modulus of steel reinforcement was assumed to be 200 GPa (29,000 ksi).

Specimens

A total of 26 RC beams—including six fully bonded CFRP-strengthened beams, 18 partially bonded CFRP-strengthened beams, and two beams without external CFRP—were fabricated in this experiment. Three anchorage methods were selected for this paper, namely CFRP vertical U-jackets, mechanical plates, and CFRP inclined U-jackets as suggested by Fu et al.[4,26]

The dimensions of the specimens were 1000 x 80 x 120 mm (39.4 x 3.1 x 4.7 in.) and the length of the CFRP sheet was 800 mm (31.5 in.). The details of the specimens are shown in Table 2. The unbonded ratio, which is denoted as ξ, is defined as the ratio of unbonded length to the total length of CFRP sheet—that is, x/L_f in Fig. 1. "WB," "FB," and "PB" indicate specimens without bonded CFRP, with fully bonded CFRP, and with partially bonded CFRP, respectively. The number after "PB" indicates the percentage form of the unbonded ratio; for example, "010" stands for $\xi = 10\% = 0.1$. The number after the hyphen is the number of CFRP layers. The last letters "V," "I," and "M" indicate vertical U-jacket, inclined U-jacket, and mechanical plate, respectively.

The details of the reinforcement cages are shown in Fig. 2. Reinforcement cages were placed in wooden molds, then concrete was placed into the formwork and cured for at least 28 days before the beam bending test.

Before attaching the CFRP sheets to the bottom of the beams, the surface of the concrete beam was ground with an angle grinder, followed by a secondary cleaning with sandpaper. Polyethylene terephthalate (PET) was used to keep concrete separate from the CFRP in the unbonded area. This procedure was intended to simulate the interfacial defect of the CFRP bonding.

Table 2—Details of specimens

Specimen	Anchorage method	CFRP layers	Thickness of CFRP sheet, mm	Unbonded ratio	Unbonded length, mm
WB1	—	—	—	—	—
WB2	—	—	—	—	—
FB-1V	VU	1	0.167	0	0
FB-1I	IU	1	0.167	0	0
FB-1M	MP	1	0.167	0	0
FB-2V	VU	2	0.334	0	0
FB-2I	IU	2	0.334	0	0
FB-2M	MP	2	0.334	0	0
PB010-1V	VU	1	0.167	0.1	80
PB010-1I	IU	1	0.167	0.1	80
PB010-1M	MP	1	0.167	0.1	80
PB010-2V	VU	2	0.334	0.1	80
PB010-2I	IU	2	0.334	0.1	80
PB010-2M	MP	2	0.334	0.1	80
PB020-1V	VU	1	0.167	0.2	160
PB020-1I	IU	1	0.167	0.2	160
PB020-1M	MP	1	0.167	0.2	160
PB020-2V	VU	2	0.334	0.2	160
PB020-2I	IU	2	0.334	0.2	160
PB020-2M	MP	2	0.334	0.2	160
PB030-1V	VU	1	0.167	0.3	240
PB030-1I	IU	1	0.167	0.3	240
PB030-1M	MP	1	0.167	0.3	240
PB030-2V	VU	2	0.334	0.3	240
PB030-2I	IU	2	0.334	0.3	240
PB030-2M	MP	2	0.334	0.3	240

Note: VU is vertical U-jacket; IU is inclined U-jacket; and MP is mechanical plate. 1 mm = 0.039 in.

As previously mentioned, in the present study, three anchorage methods were considered—namely, vertical U-jackets, inclined U-jackets, and mechanical plates. The details of the three anchorage methods are shown in Fig. 3. It should be noted that the widths of each anchorage are equal, as are the distances between anchorage edges and the ends of the CFRP sheet.

Four-point bending test

After 7 days of curing of epoxy resin, the four-point bending test was conducted on a 5000 kN (1124.04 kip) hydraulic testing machine. The schematic diagram of the beam test setup is shown in Fig. 4. Figure 5 displays the experimental setup prior to loading for the typical strengthened beam specimens implemented with the three anchorage methods (vertical U-jacket, inclined U-jacket, and mechanical plate). The loading speed was 0.2 mm/min (0.008 in./min). A 200 kN (44.96 kip) load cell was used to measure the loading force. Three displacement sensors were applied to measure the deflection of the beam, one of which was used to measure the midspan deflection, and the other two were applied to measure support deflections.

During the test process, loading was sustained at every 5 kN (1.12 kip), the crack initiation and propagation were marked on one side of the beam, and the crack width was measured with a device that measures the crack width and the microcosmic defects on the concrete surface.

EXPERIMENTAL RESULTS AND ANALYSIS

Failure modes

The test results, including cracking load, ultimate load, failure mode, and damage of jacket anchorage, are summarized in Table 3 for reference. Four typical failure modes were observed during the test: concrete crushing, CFRP rupture, plate-end debonding, and intermediate crack debonding.

Concrete crushing—Concrete crushing is the typical failure mode of RC beams without externally bonded CFRP, as shown in Fig. 6(a). After yielding of the tensile reinforcement, the depth of the compression zone decreased with increasing applied load, and the concrete in the compression zone at the midspan was eventually crushed. The CFRP sheet might also separate from the bottom of the beam at the time of failure.

CFRP rupture—Figure 6(b) shows a typical CFRP rupture failure. The overall debonding of the CFRP was delayed due to the horizontal restraining force provided by the mechanical plate. As a result, the CFRP sheet could reach its ultimate strain and then ruptured with a loud sound. It is noteworthy

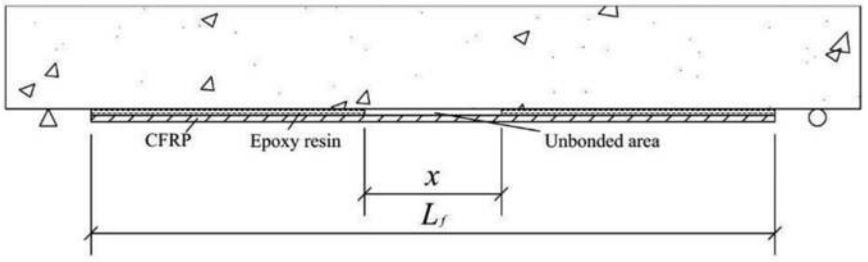

Fig. 1—Concrete beam with partially bonded CFRP.

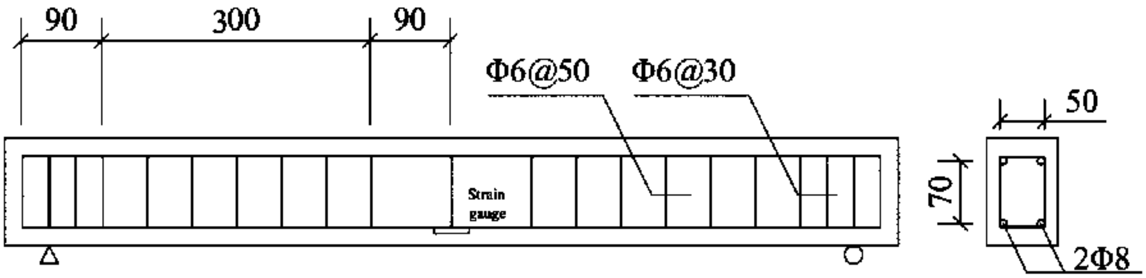

Fig. 2—Reinforcement of test beams. (Note: Units in mm; 1 mm = 0.039 in.)

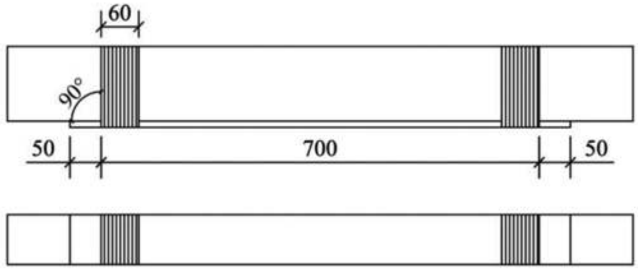

(a) Vertical U-jacket

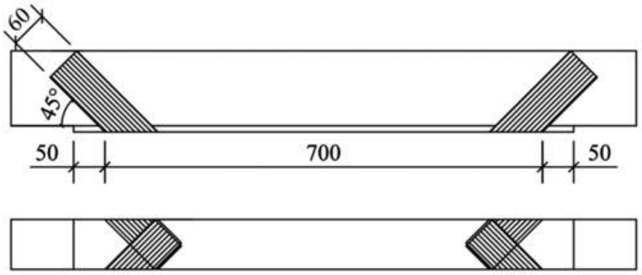

(b) Inclined U-jacket

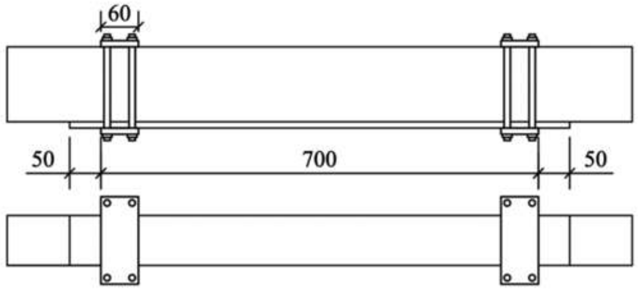

(c) Mechanical plate

Fig. 3—Schematic diagrams of anchorage methods. (Note: Units in mm; 1 mm = 0.039 in.)

that only half of the CFRP sheet broke with a smooth cross section, while the other half remained almost intact. The reason for this may be due to the uneven stress distribution inside the CFRP sheet.

Plate-end debonding—Figure 6(c) exhibits a typical plate-end debonding failure. It can be seen that local stress concentration at the end of the CFRP sheet induced wide shear cracks on the two-layer specimens with vertical U-jackets. With the increase in applied load, the cracks near the inner side of the U-jacket developed rapidly, and small and dense cracks appeared around it. At the time of failure, a bulk of concrete between two major shear cracks was torn off from the bottom of the beam at the end of the CFRP sheet.

Table 3—Experimental results

Specimen	Cracking load P_{cr}, kN	Ultimate load P_u, kN	Failure mode	Jacket anchorage damage
WB1	2.3	29.7	CC	N/A
WB2	2.5	27.7	CC	N/A
FB-1V	4.2	42.7	IC	R
FB-1I*	—	51.6	IC	N
FB-1M	5.6	49.5	CC+IC	N/A
FB-2V	6.1	44.5	PE	N
FB-2I	6.3	56.9	IC	R
FB-2M	6.2	57.8	IC	N/A
PB010-1V	4.0	44.4	IC	N
PB010-1I	3.9	47.6	IC	D
PB010-1M	4.4	49.0	IC	N/A
PB010-2V	6.1	44.2	PE	D
PB010-2I	5.7	50.5	IC	N
PB010-2M	6.3	54.3	IC	N/A
PB020-1V	3.7	44.6	IC	R
PB020-1I	4.7	49.6	CC+IC	N
PB020-1M	4.3	47.9	CR	N/A
PB020-2V	6.2	47.3	PE	N
PB020-2I	5.9	54.0	IC	R
PB020-2M	5.3	60.4	CC+IC	N/A
PB030-1V	4.5	44.8	IC	N
PB030-1I	4.0	48.8	CC+IC	N
PB030-1M	4.2	44.4	IC	N/A
PB030-2V	6.5	44.8	PE	N
PB030-2I	5.6	52.4	IC	D
PB030-2M	6.2	63.5	IC	N/A

*The cracking load of FB-1I is not accessible due to misoperation, which applied impact load on the specimen during the test.

Note: CC is concrete crushing; IC is intermediate crack debonding; PE is plate-end debonding; CR is CFRP rupture; R is U-jacket rupture; D is U-jacket debonding; N is no damage; and N/A is not applicable. 1 kN = 0.225 kip.

Intermediate crack (IC) debonding—IC debonding was the main failure mode of the test, which is shown in Fig. 6(d). After yielding of the tensile reinforcement, the CFRP sheet at the bottom of the beam made tearing sounds occasionally. Then, the tearing sound was heard continuously for a few seconds before the CFRP separated from the beam. After

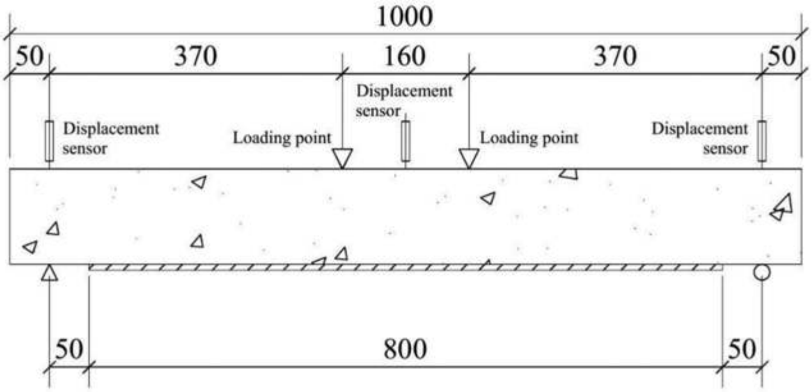

Fig. 4—Schematic diagram of beam test setup. (Note: Units in mm; 1 mm = 0.039 in.)

(a) Vertical U-jacket (FB-2V) (b) Inclined U-jacket (FB-2I)

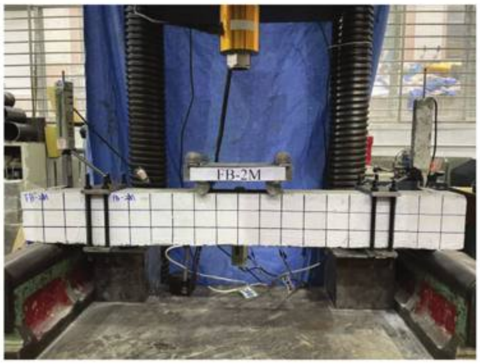

(c) Mechanical plate (FB-2M)

Fig. 5—Beam test setup prior to loading.

that, the debonding of the CFRP occurred near the midspan of the specimen with a loud noise. The CFRP sheet was observed to be split into several thin strips due to the sudden release of great energy during the debonding process. The main body of the beam was still able to carry the applied load after debonding and finally failed by crushing of the concrete. According to Teng and Chen,[37] IC debonding is induced by local interfacial stress near the cracks. Because there is a singularity and concentration in the stress distribution at the unbonded boundary, IC tends to occur from cracks near the unbonded boundary.

Depending on the pattern of the CFRP U-jacket at the time of failure, IC debonding could be subdivided into three classes: CFRP jacket rupture, CFRP jacket debonding, and debonding without additional damage to the jacket. The corresponding specimens are listed in Table 3.

Damage to the CFRP jacket was induced by the released energy caused during the debonding of the CFRP sheet at the bottom of the beam, and the specific damage form depended on the shear strength of the concrete-epoxy resin interfacial adhesive layer, the tensile strength of CFRP, and the magnitude of the energy. When the shear strength of the concrete-epoxy resin interfacial adhesive layer was sufficient to resist released energy, but the tensile strength of CFRP was not sufficient, the CFRP jacket rupture would occur, as shown in Fig. 7(a). If the aforementioned condition was reversed, then CFRP jacket debonding would occur, as demonstrated in Fig. 7(b). If each strength was sufficient to withstand the released energy, then the anchorage would remain

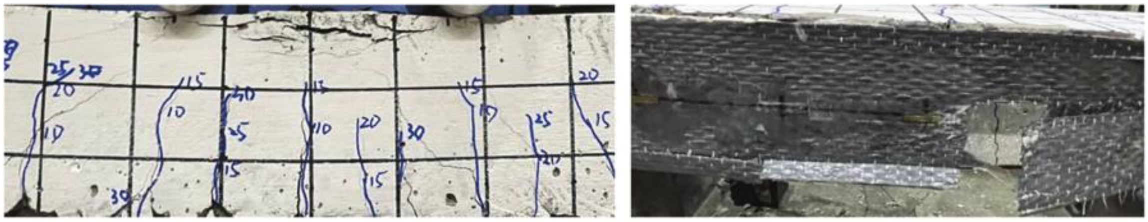

(a) Concrete crushing (FB-1M) (b) Rupture of CFRP (PB020-1M)

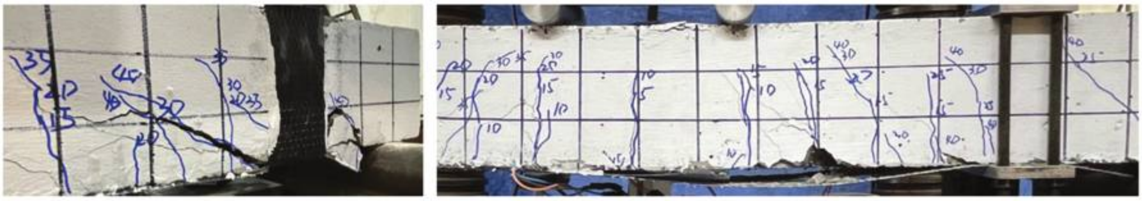

(c) Plate end debonding (FB-2V) (d) Intermediate crack debonding (PB020-2M)

Fig. 6—Failure modes.

(a) Rupture of CFRP U-jacket (PB020-2I) (b) Debonding of CFRP U-jacket (PB010-2I)

Fig. 7—Damage of CFRP U-jacket.

undamaged. This brittle damage does not occur when using mechanical plates because the concrete-epoxy resin layer was not applied. This is one advantage of the mechanical plates over the CFRP U-jacket anchorage methods.

Crack patterns and propagation

The propagation of cracks was marked and recorded during the test. It should be noted that the initial crack was formed on FB-1I, on which the impact load was applied due to mishandling. The recorded crack width of FB-1I was measured during the second loading process.

The load-maximum crack width curves (P-w_{cr} curves) of the specimens with the same unbonded ratios are shown in Fig. 8. It can be seen that when the same anchoring method is used, the cracks in the two-layer specimens are smaller than those in the one-layer specimens, regardless of the unbonded ratios. In addition, the anchorage method did not exhibit a significant effect on the crack width of the specimens.

The relationships between P and w_{cr} under the condition of the same anchorage method are shown in Fig. 9. In the case of using vertical U-jackets and mechanical plates, the FB specimens had the smallest w_{cr} regardless of the thickness of the CFRP. For specimens using inclined U-jackets, PB030-1I had the smallest w_{cr} among the one-layer specimens, while FB-1I and PB010-2I had the smallest w_{cr} in the early and late stages of the loading process, respectively. In general, fully bonded CFRP sheets were most effective in restraining crack propagation.

It should be noted that the crack width w_{cr} mentioned here refers to the width of the flexural or flexural-shear crack between two anchorages. The crack patterns of the PB010 specimens are shown in Fig. 10 as typical, and other specimens are similar to these.

Cracking load and ultimate load

Experimental results of cracking load are shown in Table 3 and Fig. 11(a).

It can be indicated that the cracking load was not significantly affected by the anchorage method and the unbonded ratio ξ. Prior to the cracking in the tensile region of the concrete beam, the deformation of the concrete surface and CFRP sheets was highly concentrated in the vicinity of the midspan, and anchorage had not worked effectively yet.

It is further exhibited in Fig. 11(a) that the number of CFRP layers was the only variable that had a significant effect on the cracking load. The average cracking loads of

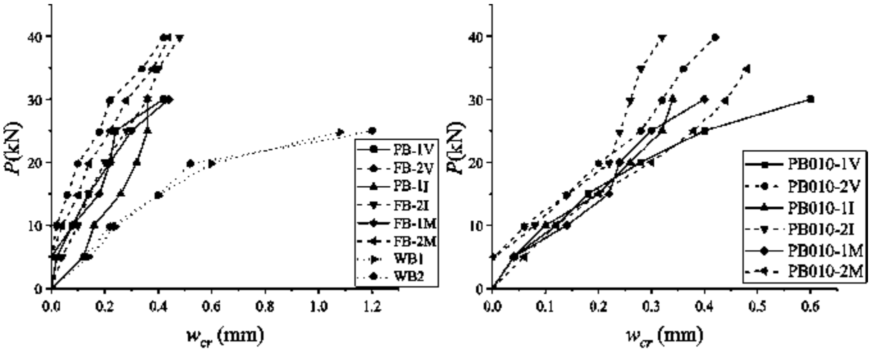

(a) FB and WB (b) PB010

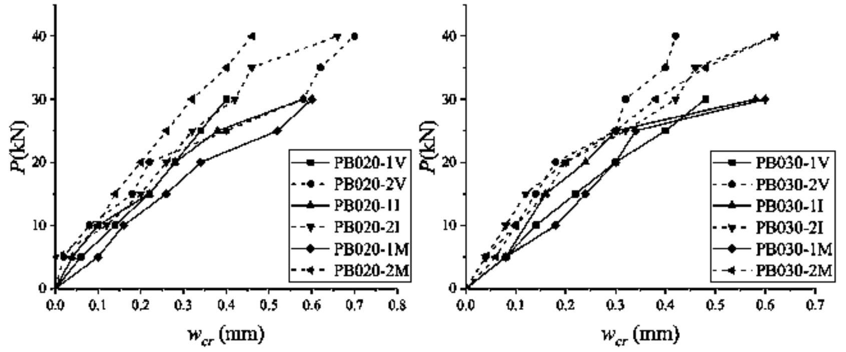

(c) PB020 (d) PB030

Fig. 8—Load-maximum crack width curves (same unbonded ratio). (Note: 1 kN = 0.225 kip; 1 mm = 0.039 in.)

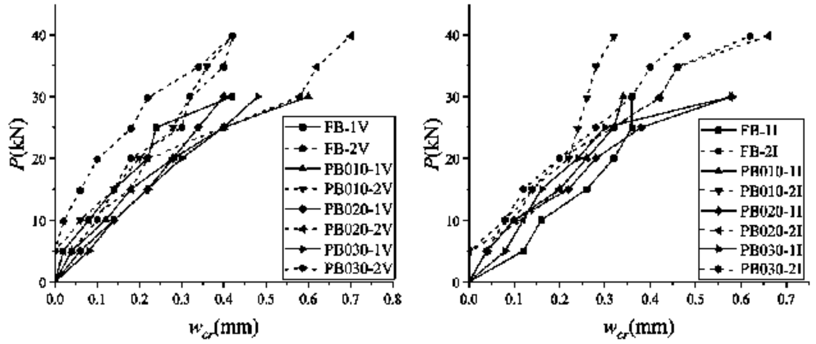

(a) Vertical U-jacket (b) Inclined U-jacket

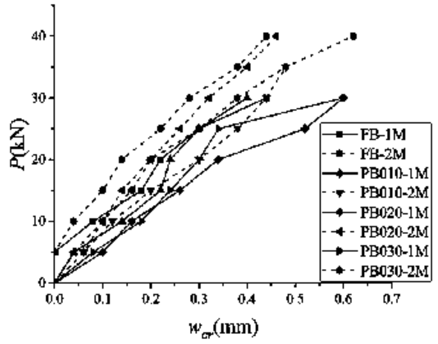

(c) Mechanical plate

Fig. 9—Load-maximum crack width curves (same anchorage method). (Note: 1 kN = 0.225 kip; 1 mm = 0.039 in.)

zero (WB specimens), one, and two CFRP layer(s) were 2.4, 4.3, and 6.0 kN (0.52, 0.97, and 1.35 kip), respectively. Hence, the cracking loads of beam specimens increased with the number of CFRP layers.

Experimental results of ultimate loads are shown in Table 3 and Fig. 11(b).

First, the effect of the unbonded ratio ξ on the ultimate load P_u was considered. In the 1I, 2I, and 1M series, the maximum P_u occurred on the FB specimen in series 1I, 2I,

Fig. 10—Crack patterns of PB010 series.

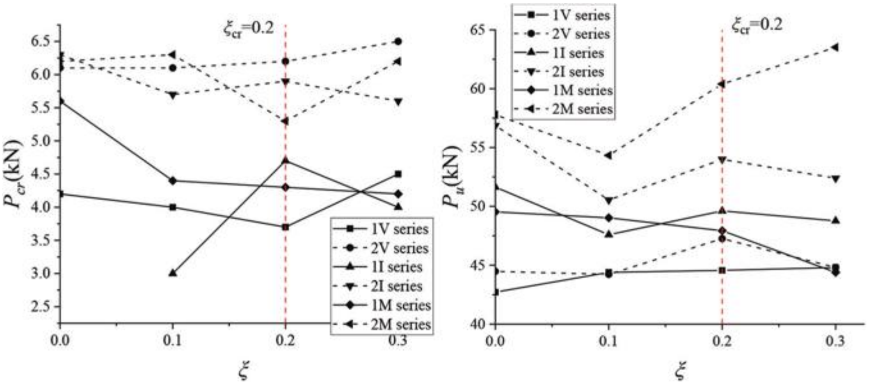

(a) Cracking load (b) Ultimate load

Fig. 11—Relationship between cracking (ultimate) load and unbonded ratio. (Note: 1 kN = 0.225 kip.)

and 1M. However, in series 1V, 2V, and 2M, the maximum P_u occurred on PB030-1V, PB020-2V, and PB030-2M, respectively, which were 15.0, 17.6, and 19.7% higher than those of the FB specimens.

It can be seen that P_u decreased as ξ increased from 0 to 0.1, except for series 1V. Figure 11(b) also shows that P_u increased when ξ increased from 0.1 to 0.2, except for series 1M. Note that the length of the pure bending zone L_{pb} and length of the CFRP sheet L_f were 160 and 800 mm (6.3 and 31.5 in.), respectively, while the abnormal improvement of P_u occurred when $\xi = L_{pb}/L_f = 0.2$. Therefore, $\xi = L_{pb}/L_f$ is defined as the critical unbonded ratio and is denoted as ξ_{cr}. It can be concluded that P_u decreases with ξ until ξ reaches ξ_{cr} and increases with ξ as ξ approaches ξ_{cr}.

When ξ increased from 0.2 to 0.3, P_u increased for the four series 1I, 1M, 2V, and 2I and decreased for the two series 1V and 2M. Therefore, no general conclusion can be determined for P_u when ξ exceeds ξ_{cr}.

Meanwhile, P_u of the two-layer CFRP specimens were higher than those of the one-layer CFRP specimens. However, P_u of the 2V series were not significantly higher than those of the 1V series. Different from vertical U-jackets, P_u of the 2I and 2M series were significantly higher than those of the corresponding one-layer series. Besides, both the inclined U-jacket and mechanical-plate specimens had higher P_u than the vertical U-jacket specimens. Because IC debonding is induced by local interfacial stress near the cracks according to Teng and Chen,[37] appropriate horizontal forces can postpone the occurrence of IC debonding by mitigating the local

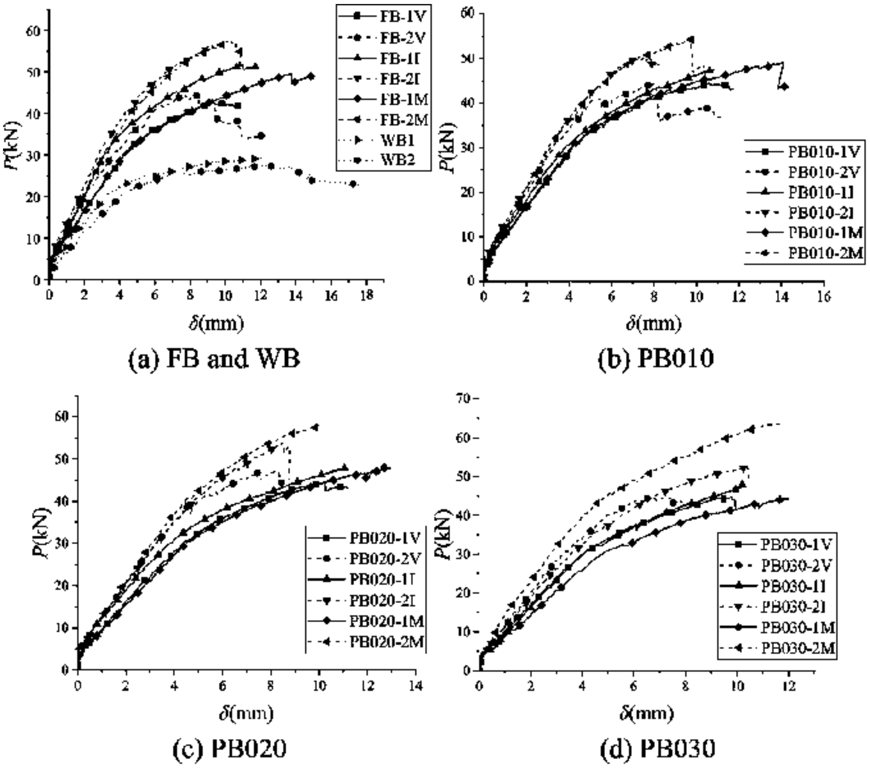

(a) FB and WB

(b) PB010

(c) PB020

(d) PB030

Fig. 12—Load-midspan deflection curves (same unbonded ratio). (Note: 1 kN = 0.225 kip; 1 mm = 0.039 in.)

interfacial stress. Inclined U-jackets and mechanical plates could provide horizontal force through decomposition of the oblique force and friction, respectively, resulting in higher ε_{fd} (debonding strain of CFRP) and thus higher P_u. Also, if the increased amount of ε_{fd} is assumed to be independent of t_f (thickness of CFRP), then P_u significantly increases with t_f because P_u is positively correlated with $\varepsilon_{fd}t_f$. In addition, P_u of the 2M series were higher than those of the 2I series, suggesting that the mechanical plates could postpone the occurrence of IC debonding more effectively than inclined U-jackets. The abnormal increase in P_u at ξ_{cr} can also be explained by the theory by Teng and Chen. The increase in individual ξ tends to decrease P_u. However, crack widths are larger at midspan in general, and the local interfacial stresses are also larger. The increase in ξ leads to the possibility that the bonded part avoids large cracks, thereby delaying the onset of IC debonding and increasing the P_u. These two effects together determine the P_u. For $\xi = 0.1$, the bonded area might not have avoided large cracks, which led to lower P_u. For $\xi = \xi_{cr} = 0.2$, the unbonded area was large enough so that the large cracks would not appear in the bonded area. Therefore, the combined effects result in higher P_u. Finally, for $\xi = 0.3$, there was no significant reduction in crack width at the bonded area, so the effect from the reduction in the unbonded ratio dominated again, leading to a lower P_u.

Load-midspan deflection curves

The load-midspan deflection curves (P-δ curves) under the condition of the same unbonded ratio are shown in Fig. 12.

For the FB series, it is indicated from Fig. 12(a) that the stiffness of the two-layer specimens was higher than that of one-layer specimens in the early stages of loading. The stiffness was similar among specimens with the same number of CFRP layers. The stiffness of all specimens decreased with increasing load, and the one-layer specimens decreased more rapidly than the two-layer specimens, which resulted in lower P_u for FB-1I than for FB-2I and FB-2M. Also, as the load increased, the longitudinal reinforcement yielded and the stiffness of FB-1I increased relative to other specimens, which was close to that of FB-2I and FB-2M, while the stiffness of FB-2V decreased relative to other specimens. Thus, the stiffness of FB-1I eventually exceeded that of FB-2V.

For the PB010 series, it is indicated from Fig. 12(b) that PB010-1I had the highest stiffness among the one-layer specimens, while PB-2V had the lowest stiffness among the two-layer specimens, which was similar to the FB series.

For the PB020 series, it is shown in Fig. 12(c) that the stiffness of PB020-1I was close to that of the two-layer specimens in the early stages of loading. As the reinforcement yielded, the stiffness of PB020-1I decreased and tended to approach the stiffness of the other two one-layer specimens. The stiffness of the two-layer specimens was almost equal because the curves of the different specimens were almost coincident.

It is shown in Fig. 12(d) that the P-δ curves of the PB030 series are significantly distinct from those of the other series. First, two specimens with mechanical plates, namely PB030-1M and PB030-2M, exhibited a significant relative decrease and increase in stiffness among the one-layer specimens and two-layer specimens, respectively. Second, the stiffness of the vertical U-jacket and inclined U-jacket specimens did not show significant differences in the PB030 series, while the stiffness of the inclined U-jacket specimens was higher than that of the vertical U-jacket specimens in the other series.

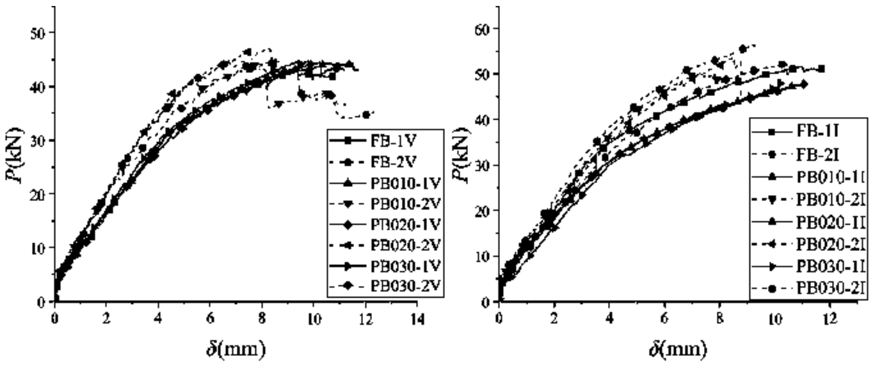

(a) Vertical U-jacket

(b) Inclined U-jacket

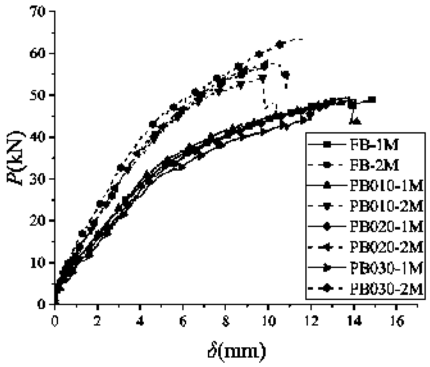

(c) Mechanical plate

Fig. 13—Load-midspan deflection curves (same anchorage method). (Note: 1 kN = 0.225 kip; 1 mm = 0.039 in.)

Based on the previous analysis, it can be inferred that the inclined U-jacket could significantly improve the stiffness of the RC beam with the best performance. The stiffness of specimens with mechanical plates was higher than that of specimens with vertical U-jackets.

Relations of *P* and δ under the condition of the same anchorage methods are shown in Fig. 13. It is indicated from Fig. 13 that ξ had little effect on the stiffness of specimens. In general, the stiffness of the two-layer specimens was higher than that of the one-layer specimens. Besides, the number of CFRP layers and the anchorage method had coupled effects in enhancing the stiffness. The difference in stiffness between the two- and one-layer specimens using mechanical plates was higher than that of the specimens using the two U-jacket anchorage methods. It showed that the mechanical plates performed much better with the thicker CFRP based on experimental results of ultimate load and stiffness.

Ductility

In general, the ductility of concrete beams can be assessed by the displacement ductility index, which is calculated by dividing the ultimate displacement δ_u by the yield displacement δ_y—namely, $\eta_D = \delta_u/\delta_y$. Because the specimens in the present study were RC beams strengthened with CFRP sheets, δ_y derived from the yielding of reinforcement could not express the ductility of the whole member. Park[38] suggested that δ_y for concrete structures could be chosen as the intersection of the straight line $y = P_u$ with the line determined by the original point and $0.75P_u$ point on the *P*-δ curve. δ_u is chosen as the midspan displacement at the time of failure of the specimen. The definitions of δ_y and δ_u are illustrated in Fig. 14(a).

The calculated η_D and all related data are listed in Table 4, and the relationship between the displacement ductility index and unbonded ratio is shown in Fig. 14(b).

As shown in Fig. 12, the *P*-δ curves of the specimens strengthened with CFRP sheets do not have significant yield platforms due to CFRP debonding, which is a type of brittle failure. Therefore, the ductility of these specimens is very low. Figure 14(b) indicates that the ductility of the one-layer specimens decreased significantly with the increase in the unbonded ratio ξ. For the two-layer specimens, the ductility of the 2V series did not change significantly with increasing ξ, while the ductility of the 2I and 2M series increased first, then decreased, and finally increased as ξ increased from 0 to 0.3. Meanwhile, it is also exhibited in Fig. 14(b) that the ductility of PB030-2I and PB030-2M were approximately equal to those of FB-2I and FB-2M, respectively.

Under the conditions of the same anchorage method and unbonded ratio, Fig. 14(b) shows that the one-layer specimens exhibited higher ductility than the two-layer specimens. This can be explained by the fact that CFRP is a linear-elastic material and does not contribute much ductility to the strengthened beam, which is mainly provided by the steel reinforcement. For this reason, the higher strengthening ratio of CFRP reduced the ductility of the beams.

With the same CFRP thickness and unbonded ratio, overall, the highest ductility was observed for the vertical U-jacket specimens, while the lowest ductility was observed for the inclined U-jacket specimens. This result is in good agreement with the study by Fu et al.[4] However, it was found

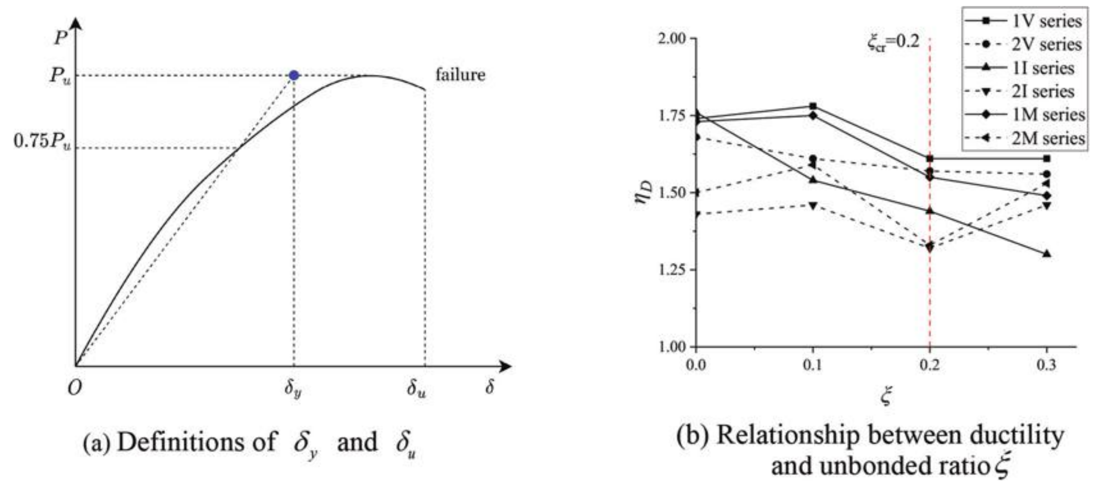

(a) Definitions of δ_y and δ_u

(b) Relationship between ductility and unbonded ratio ξ

Fig. 14—Displacement ductility index: definition and its relationship to unbonded ratio ξ.

Table 4—Displacement ductility indexes of specimens

Specimen	P_y, kN	δ_y, mm	δ_u, mm	η_D
FB-1V	36.7	6.20	10.81	1.74
FB-1I	43.8	6.70	11.77	1.76
FB-1M	41.8	8.68	15.00	1.73
FB-2V	39.6	5.73	9.61	1.68
FB-2I	49.5	6.50	9.30	1.43
FB-2M	51.0	7.21	10.84	1.50
PB010-1V	37.7	6.60	11.72	1.78
PB010-1I	40.9	7.03	10.81	1.54
PB010-1M	41.8	8.04	14.10	1.75
PB010-2V	40.6	5.08	8.18	1.61
PB010-2I	44.9	5.64	8.26	1.46
PB010-2M	47.8	6.52	10.37	1.59
PB020-1V	38.4	6.97	11.19	1.61
PB020-1I	41.5	7.67	11.08	1.44
PB020-1M	40.9	8.34	12.95	1.55
PB020-2V	40.6	5.50	8.64	1.57
PB020-2I	47.3	6.69	8.80	1.32
PB020-2M	52.6	7.51	9.96	1.33
PB030-1V	38.5	6.54	10.56	1.61
PB030-1I	42.4	7.87	10.21	1.30
PB030-1M	38.8	8.07	12.01	1.49
PB030-2V	40.3	5.08	7.91	1.56
PB030-2I	46.2	7.19	10.48	1.46
PB030-2M	54.1	7.59	11.65	1.53

Note: 1 kN = 0.225 kip; 1 mm = 0.039 in.

that the high ductility of specimens with vertical U-jackets was obtained at the expense of early yielding, and its overall deformation capacity was inferior to specimens with either mechanical plates or inclined U-jackets. It is indicated that δ_y of specimens with vertical U-jackets were smaller than those of specimens with inclined U-jackets and mechanical plates, as shown in Fig. 15(a), and δ_u of specimens with vertical U-jackets were similar to those of specimens with inclined U-jackets and smaller than those of specimens with mechanical plates, as shown in Fig. 15(b). Because δ_y serves as the denominator in the definition of η_D, it shows a greater influence on η_D than δ_u. Therefore, the specimens with vertical U-jackets had the highest calculated ductility at the cost of early yielding.

THEORETICAL EVALUATION OF ULTIMATE LOAD

Based on existing analytic research[12,39] and experimental research,[4] a new theoretical model for evaluating the ultimate load of RC beams strengthened with fully or partially bonded CFRP and U-jacket anchorage (the influence of debonding is not considered in the proposed theoretical model) that fail due to CFRP IC debonding is proposed.

Chahrour and Soudki[12] suggested that for RC beams strengthened with bonded CFRP, the applied load can be calculated by Eq. (1)

$$M = \frac{\varepsilon_c E_c b c^2}{3} + A_s f_y (h_s - c) + A_f E_f \varepsilon_f (h - c) \qquad (1)$$

where

$$c = \frac{2(A_s f_y + A_f E_f \varepsilon_f)}{\varepsilon_c E_c b} \qquad (2)$$

In fact, from Eq. (1) and (2), the ultimate load of the specimens cannot be obtained directly because of the two unknown quantities, ε_c and ε_f. For given ε_c and ε_f, Eq. (1) and (2) yield the corresponding load of the specimen. In the original research by Chahrour and Soudki,[12] ε_c and ε_f were obtained through tests. However, to assess the beams in practice, it is necessary to make reasonable assumptions about these two values. In the case of evaluating the ultimate load, it can be assumed that concrete in the compression zone reaches its compressive strength, that is, $\varepsilon_c E_c = f_c$. For ε_f, Li and Wu[39] recommended a theoretical model to calculate the debonding strain of CFRP due to IC debonding

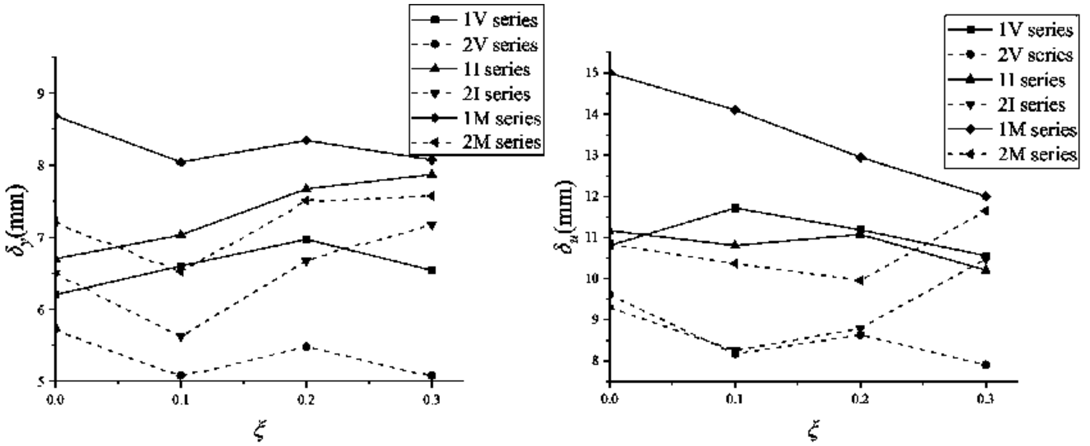

(a) Yield displacement **(b) Ultimate displacement**

Fig. 15—Relationship between yield (ultimate) displacement and unbonded ratio. (Note: 1 mm = 0.039 in.)

$$\varepsilon_{fd} = \frac{\beta_w}{\sqrt{E_f t_f}}(0.427 f_c^{0.25} + 0.588 f_c^{0.3}) \tag{3}$$

where ε_{fd} is the debonding strain of CFRP; E_f is the elastic modulus of CFRP (MPa); t_f is the thickness of the CFRP sheet (mm); f_c is the cylinder compressive strength of concrete (MPa); and $\beta_w = \sqrt{(2 - b_f/b)/(1 + b_f/b)}$, where b_f and b are the width of the attached CFRP and beam, respectively.

To consider the effect of inclined U-jackets, it is assumed in this paper that the inclined U-jackets improve the performance of the beam by exerting an action on the bottom of the beam. Therefore, in Eq. (1) and (2), additional terms need to be added to represent the influence of inclined U-jackets, as follows

$$M_i = \frac{f_c b c_i^2}{3} + A_s f_y (h_s - c) + A_f E_f \varepsilon_{fd}(h - c_i) + 2A_j E_f \varepsilon_{jd}(h - c_i)\cos\varphi \tag{4}$$

$$c_i = \frac{2(A_s f_y + A_f E_f \varepsilon_{fd} + 2A_j E_f \varepsilon_{jd}\cos\varphi)}{b f_c} \tag{5}$$

where ε_{jd} is the strain of the CFRP U-jacket at debonding; and φ is the angle between the inclined U-jacket and horizontal plane: for vertical U-jacket specimens, φ = 90 degrees.

Based on the experimental investigation by Fu et al.,[4] it is assumed that $\varepsilon_{jd} = 0.2\varepsilon_u$. The experimental results of U-jacket specimens in this study and collected from existing literature,[4,40] as well as corresponding calculated results, are listed in Table 5. It can be seen that $P_{u,c}/P_{u,e}$ has a mean of 0.99, standard deviation of 0.09, and coefficient of variation of 0.09, which indicates a good agreement between the proposed model and the experimental results.

CONCLUSIONS

This paper investigated the flexural properties of reinforced concrete (RC) beams strengthened with partially bonded carbon fiber-reinforced polymer (CFRP). A new parameter called the unbonded ratio was introduced to measure the degree of unbonded CFRP, which is defined as the ratio of unbonded length to the total length of the CFRP sheet. The combined effects of partially bonded CFRP (unbonded ratio) and anchorage methods on the mechanical properties of RC beams strengthened with CFRP are investigated. Based on the experimental investigation and analysis of experimental results, the following conclusions can be drawn:

1. The results of the analysis indicate that the mechanical-plate anchorage-strengthened RC beam specimens show the highest ultimate load, followed by the inclined U-jacket and then the vertical U-jacket. Ultimate load decreased when the unbonded ratio increased in the pure bending zone and increased when the unbonded ratio approached the critical unbonded ratio.

2. It also shows that the cracking load was not affected by the unbonded ratio and the anchorage method, but increased significantly with the increasing number of CFRP layers.

3. The flexural stiffness of CFRP-strengthened RC beams was significantly influenced by the anchorage method. Inclined U-jacket anchorages increased stiffness the most effectively among the three anchorage methods, and the stiffness of specimens with mechanical plates was higher than that with vertical U-jackets.

4. It shows that the ductility of the test beams decreased with the increase in the number of CFRP layers and was significantly influenced by the anchorage method. The ductility of the specimens with vertical U-jackets was higher than that of specimens with mechanical plates, and the latter was higher than that of specimens with inclined U-jackets. However, specimens with vertical U-jackets yielded prematurely and had less overall capacity of deformation than specimens with mechanical-plate anchorage.

5. It exhibits that the crack width was not significantly affected by the unbonded ratio and anchorage method, but the crack propagation was restrained effectively by increasing the CFRP layers. All specimens showed similar crack patterns, except the two-layer specimens with vertical U-jackets, which had major shear cracks near supports.

6. A theoretical model for the ultimate load of RC beams strengthened with inclined U-jackets was proposed. The ratio of calculated to experimental result has a mean of 0.99, standard deviation of 0.09, and coefficient of variation

Table 5—Ultimate loads of U-jacket specimens: values and comparison

Study	Specimen	$P_{u,e}$, kN	$P_{u,c}$, kN	$P_{u,c}/P_{u,e}$
Present study	FB-1V	42.7	39.5	0.93
	FB-1I	51.6	44.1	0.85
	FB-2V	44.5	46.1	1.04
	FB-2I	56.9	50.5	0.89
	PB010-1V	44.4	40.8	0.92
	PB010-1I	47.6	45.4	0.95
	PB010-2V	44.2	47.4	1.07
	PB010-2I	50.5	51.8	1.03
	PB020-1V	44.6	40.8	0.91
	PB020-1I	49.6	45.4	0.92
	PB020-2V	47.3	47.4	1.00
	PB020-2I	54.0	51.8	0.96
	PB030-1V	44.8	40.8	0.91
	PB030-1I	48.8	45.4	0.93
	PB030-2V	44.8	47.4	1.06
	PB030-2I	52.4	51.8	0.99
Fu et al.[4]	I45W100H350	122.9	134.1	1.09
	I45W150H350	140.7	143.3	1.02
	I45W200H350	150.3	152.6	1.02
	I45W400H350	159.2	188.8	1.19
	I45W150H141	133.3	143.3	1.08
	V90W150H350	95.5	115.3	1.21
	I135W150H350	92.5	86.7	0.94
Al-Saawani et al.[40]	1U45W50L1	250.1	267.2	1.07
	1U45W100L1	289.6	283.4	0.98
	1U45W150L1	316.1	299.3	0.95
	1U45W200L1	337.5	315.1	0.93
	1U45W300L1	360.0	346.0	0.96
			Mean	0.99
			S.D.	0.08
			C.V.	0.08

Note: S.D. is standard deviation; C.V. is coefficient of variation. 1 kN = 0.225 kip.

of 0.09, which indicates a good agreement between the proposed model and the tests.

AUTHOR BIOS

Qi Cao *is an Associate Professor at Dalian University of Technology, Dalian, Liaoning, China. He received his MS from Washington State University, Pullman, WA, and his PhD from the University of Tennessee, Knoxville, Knoxville, TN. His research interests include fiber-reinforced polymer (FRP)-reinforced and strengthened concrete structures.*

Xingchao Wang *is a Graduate Student at Dalian University of Technology, where he received his BS and MS. His research interests include FRP and steel-plate composite walls.*

Zhimin Wu *is a Professor at Dalian University of Technology, where he received his PhD. His research interests include fracture mechanics of concrete.*

Rongxiong Gao *is a Professor at Huazhong University of Science and Technology, Wuhan, Hubei, China. He received his PhD from Wuhan University of Technology, Wuhan, Hubei, China. His research interests include bridge engineering and FRP rehabilitation and repair in bridges.*

Xin Jiang *is a Professor at Wuhan Institute of Technology, Wuhan, Hubei, China. He received his MS from Changsha University of Science and Technology, Changsha, Hunan, China, and his PhD from the University of Tennessee, Knoxville. His research interests include bridge analysis and FRP.*

ACKNOWLEDGMENTS

This work is supported by the National Natural Science Foundation of China (Grant No. 52271264) and the Natural Science Foundation of Liaoning Province (Project No. 2021-MS-129).

NOTATION

A_f, A_j, A_s = cross-section area of CFRP sheet, CFRP U-jacket (one side), and longitudinal steel bars, respectively
b, b_f = width of beam and CFRP sheet, respectively
c, c_i = location of neutral axis without and with inclined U-jacket, respectively
E_c, E_f = elastic modulus of concrete and CFRP, respectively
f_c, f_y = compressive strength of concrete and yield strength of longitudinal steel bars, respectively
h, h_s = height of beam and location of longitudinal steel bars, respectively
L_f, L_{pb} = length of attached CFRP sheet and pure bending zone, respectively
M, M_i = bending moment without and with inclined U-jacket, respectively
P, P_{cr}, P_u = applied load, cracking load, and ultimate load, respectively
$P_{u,e}$, $P_{u,c}$ = experimental and calculated ultimate load, respectively
w_{cr} = crack width
x = unbonded length
δ, δ_y, δ_u = displacement, yield displacement, and ultimate displacement at midspan, respectively
ε_c, ε_f = strain of concrete in compression face and attached CFRP, respectively
ε_{fd}, ε_{jd} = debonding strain of attached CFRP sheet and strain of U-jacket when IC debonding failure occurs, respectively
η_D = displacement ductility index
φ = angle between inclined U-jacket and horizontal plane
ξ = x/L_f, unbonded ratio
ξ_{cr} = L_{pb}/L_f, critical unbonded ratio

REFERENCES

1. Cao, Q., and Ma, Z. J., "Behavior of Externally Fiber-Reinforced Polymer Reinforced Shrinkage-Compensating Concrete Beams," *ACI Structural Journal*, V. 108, No. 5, Sept.-Oct. 2011, pp. 592-600.

2. Dai, J.-G.; Gao, W. Y.; and Teng, J. G., "Bond-Slip Model for FRP Laminates Externally Bonded to Concrete at Elevated Temperature," *Journal of Composites for Construction*, ASCE, V. 17, No. 2, Apr. 2013, pp. 217-228. doi: 10.1061/(ASCE)CC.1943-5614.0000337

3. Zhang, S. S.; Teng, J. G.; and Yu, T., "Bond Strength Model for CFRP Strips Near-Surface Mounted to Concrete," *Journal of Composites for Construction*, ASCE, V. 18, No. 3, June 2014, p. A4014003. doi: 10.1061/(ASCE)CC.1943-5614.0000402

4. Fu, B.; Tang, X. T.; Li, L. J.; Liu, F.; and Lin, G., "Inclined FRP U-Jackets for Enhancing Structural Performance of FRP-Plated RC Beams Suffering from IC Debonding," *Composite Structures*, V. 200, Sept. 2018, pp. 36-46. doi: 10.1016/j.compstruct.2018.05.074

5. Ye, H.; Zhang, Q.; Liu, C.; Wu, C.; and Duan, Z., "Failure Mechanisms Governing Anchoring Force of Friction-Based Wedge Anchorage for Prestressed CFRP Plate," *Composite Structures*, V. 225, Oct. 2019, Article No. 111142. doi: 10.1016/j.compstruct.2019.111142

6. Lu, X. Z.; Teng, J. G.; Ye, L. P.; and Jiang, J. J., "Intermediate Crack Debonding in FRP-Strengthened RC Beams: FE Analysis and Strength Model," *Journal of Composites for Construction*, ASCE, V. 11, No. 2, Apr. 2007, pp. 161-174. doi: 10.1061/(ASCE)1090-0268(2007)11:2(161)

7. Cao, Q.; Zhou, J.; Wu, Z.; and Ma, Z. J., "Flexural Behavior of Prestressed CFRP Reinforced Concrete Beams by Two Different Tensioning Methods," *Engineering Structures*, V. 189, June 2019, pp. 411-422. doi: 10.1016/j.engstruct.2019.03.051

8. Zhou, A.; Qin, R.; Feo, L.; Penna, R.; and Lau, D., "Investigation on Interfacial Defect Criticality of FRP-Bonded Concrete Beams,"

Composites Part B: Engineering, V. 113, Mar. 2017, pp. 80-90. doi: 10.1016/j.compositesb.2016.12.055

9. Burgoyne, C. J., "Should FRP be Bonded to Concrete?" *Fiber-Reinforced-Plastic Reinforcement for Concrete Structures – International Symposium*, SP-138, A. Nanni and C. W. Dolan, eds., American Concrete Institute, Farmington Hills, MI, 1993, pp. 367-380.

10. Lees, J. M., and Burgoyne, C. J., "Experimental Study of Influence of Bond on Flexural Behavior of Concrete Beams Pretensioned with Aramid Fiber Reinforced Plastics," *ACI Structural Journal*, V. 96, No. 3, May-June 1999, pp. 377-385.

11. Lees, J. M., and Burgoyne, C. J., "Analysis of Concrete Beams with Partially Bonded Composite Reinforcement," *ACI Structural Journal*, V. 97, No. 2, Mar.-Apr. 2000, pp. 252-258.

12. Chahrour, A., and Soudki, K., "Flexural Response of Reinforced Concrete Beams Strengthened with End-Anchored Partially Bonded Carbon Fiber-Reinforced Polymer Strips," *Journal of Composites for Construction*, ASCE, V. 9, No. 2, Apr. 2005, pp. 170-177. doi: 10.1061/(ASCE)1090-0268(2005)9:2(170)

13. Choi, H. T.; West, J. S.; and Soudki, K. A., "Analysis of the Flexural Behavior of Partially Bonded FRP Strengthened Concrete Beams," *Journal of Composites for Construction*, ASCE, V. 12, No. 4, Aug. 2008, pp. 375-386. doi: 10.1061/(ASCE)1090-0268(2008)12:4(375)

14. Qi, L.; Yang, Y.; Zhang, Z.; and Zhang, Y., "Experiment and Study on RC Beams Strengthened by Bonding CFRP Partially," *Highway*, No. 10, 2007, pp. 21-26. (in Chinese)

15. Zhang, Z.; Qi, L.; and Zhang, Y., "Experiment and Study on Normal Section of RC Beams Strengthened by Bonding CFRP Partially," *Railway Engineering*, No. 11, 2007, pp. 17-19. (in Chinese)

16. Yin, J., "Study on Ductility of Reinforced Concrete Flexural Members Strengthened with Partially Bonded CFRP," master's dissertation, Anhui University of Science and Technology, Huainan, Anhui, China, 2017. (in Chinese)

17. Zhang, Z., and Yin, J., "Effect of Mid-Span Blank Bonding Length on Mechanical Properties of Beams Strengthened by CFRP," *Journal of Henan University of Engineering*, V. 33, No. 4, 2021, pp. 26-30, 47. (in Chinese)

18. Zhang, Z., and Huang, Q., "Study on Flexural Behavior of Partially Bonded FRP Strengthened RC Beams," *Journal of Railway Science and Engineering*, V. 17, No. 4, 2022, pp. 965-971. (in Chinese)

19. ACI Committee 440, "Guide for the Design and Construction of Externally Bonded FRP Systems for Strengthening Concrete Structures (ACI 440.2R-17)," American Concrete Institute, Farmington Hills, MI, 2017, 112 pp.

20. Siddika, A.; Al Mamun, M. A.; Alyousef, R.; and Amran, Y. H. M., "Strengthening of Reinforced Concrete Beams by Using Fiber-Reinforced Polymer Composites: A Review," *Journal of Building Engineering*, V. 25, Sept. 2019, Article No. 100798. doi: 10.1016/j.jobe.2019.100798

21. Zaki, M. A., and Rasheed, H. A., "Behavior of Reinforced Concrete Beams Strengthened Using CFRP Sheets with Innovative Anchorage Devices," *Engineering Structures*, V. 215, July 2020, Article No. 110689. doi: 10.1016/j.engstruct.2020.110689

22. Al-Rousan, R., and Al-Saraireh, S., "Impact of Anchored Holes Technique on Behavior of Reinforced Concrete Beams Strengthened with Different CFRP Sheet Lengths and Widths," *Case Studies in Construction Materials*, V. 13, Dec. 2020, Article No. e00405. doi: 10.1016/j.cscm.2020.e00405

23. Ekenel, M.; Rizzo, A.; Myers, J. J.; and Nanni, A., "Flexural Fatigue Behavior of Reinforced Concrete Beams Strengthened with FRP Fabric and Precured Laminate Systems," *Journal of Composites for Construction*, ASCE, V. 10, No. 5, Oct. 2006, pp. 433-442. doi: 10.1061/(ASCE)1090-0268(2006)10:5(433)

24. Dong, K.; Ji, Z.; Yang, S.; Du, D.; and Liu, Y., "Experimental Study on Bearing Capacity of FRP-Concrete Bonding Interface with Mechanical End Anchorage," *Journal of Building Structures*, V. 41, No. S1, 2020, pp. 399-405. (in Chinese)

25. Mostofinejad, D.; Hosseini, S. M.; Nader Tehrani, B.; Eftekhar, M. R.; and Dyari, M., "Innovative Warp and Woof Strap (WWS) Method to Anchor the FRP Sheets in Strengthened Concrete Beams," *Construction and Building Materials*, V. 218, Sept. 2019, pp. 351-364. doi: 10.1016/j.conbuildmat.2019.05.117

26. Fu, B.; Chen, G. M.; and Teng, J. G., "Mitigation of Intermediate Crack Debonding in FRP-Plated RC Beams Using FRP U-Jackets," *Composite Structures*, V. 176, Sept. 2017, pp. 883-897. doi: 10.1016/j.compstruct.2017.05.049

27. Mostofinejad, D., and Mahmoudabadi, E., "Grooving as Alternative Method of Surface Preparation to Postpone Debonding of FRP Laminates in Concrete Beams," *Journal of Composites for Construction*, ASCE, V. 14, No. 6, Dec. 2010, pp. 804-811. doi: 10.1061/(ASCE)CC.1943-5614.0000117

28. Mostofinejad, D., and Tabatabaei Kashani, A., "Experimental Study on Effect of EBR and EBROG Methods on Debonding of FRP Sheets Used for Shear Strengthening of RC Beams," *Composites Part B: Engineering*, V. 45, No. 1, Feb. 2013, pp. 1704-1713. doi: 10.1016/j.compositesb.2012.09.081

29. Hosseini, A., and Mostofinejad, D., "Experimental Investigation into Bond Behavior of CFRP Sheets Attached to Concrete Using EBR and EBROG Techniques," *Composites Part B: Engineering*, V. 51, Aug. 2013, pp. 130-139. doi: 10.1016/j.compositesb.2013.03.003

30. Mostofinejad, D., and Moghaddas, A., "Bond Efficiency of EBR and EBROG Methods in Different Flexural Failure Mechanisms of FRP Strengthened RC Beams," *Construction and Building Materials*, V. 54, Mar. 2014, pp. 605-614. doi: 10.1016/j.conbuildmat.2014.01.002

31. Mostofinejad, D., and Akhlaghi, A., "Experimental Investigation of the Efficacy of EBROG Method in Seismic Rehabilitation of Deficient Reinforced Concrete Beam–Column Joints Using CFRP Sheets," *Journal of Composites for Construction*, ASCE, V. 21, No. 4, Aug. 2017, p. 04016116. doi: 10.1061/(ASCE)CC.1943-5614.0000781

32. Mashrei, M. A.; Makki, J. S.; and Sultan, A. A., "Flexural Strengthening of Reinforced Concrete Beams Using Carbon Fiber Reinforced Polymer (CFRP) Sheets with Grooves," *Latin American Journal of Solids and Structures*, V. 16, No. 4, 2019, Article No. e176. doi: 10.1590/1679-78255514

33. Cao, Q.; Tao, J.; Ma, Z. J.; and Wu, Z., "Axial Compressive Behavior of CFRP-Confined Expansive Concrete Columns," *ACI Structural Journal*, V. 114, No. 2, Mar.-Apr. 2017, pp. 475-485. doi: 10.14359/51689450

34. GB/T 50081-2019, "Standard for Test Methods of Concrete Physical and Mechanical Properties," Ministry of Housing and Urban-Rural of the People's Republic of China, Beijing, China, 2019, 103 pp. (in Chinese)

35. GB/T 3354-1999, "Test Method for Tensile Properties of Oriented Fiber Reinforced Plastics," General Administration of Quality Supervision, Inspection and Quarantine of the People's Republic of China, Beijing, China, 1999, 4 pp. (in Chinese)

36. GB/T 228.1-2010, "Metallic Materials – Tensile Testing – Part 1: Method of Test at Room Temperature," General Administration of Quality Supervision, Inspection and Quarantine of the People's Republic of China, Beijing, China, 2010, 61 pp. (in Chinese)

37. Teng, J. G., and Chen, J. F., "Mechanics of Debonding in FRP-Plated RC Beams," *Proceedings of the Institution of Civil Engineers - Structures and Buildings*, V. 162, No. 5, Oct. 2009, pp. 335-345. doi: 10.1680/stbu.2009.162.5.335

38. Park, R., "State-of-the Art Report: Ductility Evaluation from Laboratory and Analytical Testing," *Proceedings of the Ninth World Conference on Earthquake Engineering (9WCEE)*, V. 8, Tokyo-Kyoto, Japan, Aug. 1988, pp. 605-616.

39. Li, X.-H., and Wu, G., "Finite-Element Analysis and Strength Model for IC Debonding in FRP-Strengthened RC Beams," *Journal of Composites for Construction*, ASCE, V. 22, No. 5, Oct. 2018, p. 04018030. doi: 10.1061/(ASCE)CC.1943-5614.0000863

40. Al-Saawani, M. A.; El-Sayed, A. K.; and Al-Negheimish, A. I., "Inclined FRP U-Wrap Anchorage for Preventing Concrete Cover Separation in FRP Strengthened RC Beams," *Arabian Journal for Science and Engineering*, V. 48, No. 4, Apr. 2023, pp. 4879-4892.

ACI STRUCTURAL JOURNAL TECHNICAL PAPER

Title No. 121-S06

A Framework to Set Performance Requirements for Structural Component Models: Application to Reinforced Concrete Wall Shear Strength

by Matías Rojas-León, Saman A. Abdullah, Kristijan Kolozvari, and John W. Wallace

Numerous models to predict the shear strength of reinforced concrete structural walls have been proposed in the literature. Evaluation of the predictive performance of new models relative to existing models is often challenging because the models were created with different levels of complexity and calibrated using different databases. More complex models are expected to have less variance than simpler models, and target performance metrics for models of different complexity do not exist. In addition, a common, comprehensive database should be used to enable direct comparisons between different models. To address these issues, the present study applies statistical and machine-learning approaches to propose a five-step framework to establish target performance metrics for models with different levels of complexity. Application of the framework is demonstrated by addressing the problem of estimating wall shear strength using a comprehensive database of 340 shear-controlled wall tests.

Keywords: machine learning; model performance; statistics; structural wall; wall shear.

INTRODUCTION

Over the last several years, researchers have assembled comprehensive component databases to enable the development of more complex capacity (for example, stiffness, strength, and deformation) models using more sophisticated statistical and machine-learning (ML) approaches. Evaluating and comparing the performance of different capacity models proposed in the literature is often challenging because: a) they were developed using different databases and a model may have substantially different performance (bias, variance) when evaluated against a different database; b) more complex models are expected to have less variance than a less-complex model—however, target performance metrics for models of different complexity do not exist; and c) optimal model performance is often not studied, so it is unknown whether a model with better performance is possible. In addition, many existing models were calibrated using relatively small databases—for example, less than 100 or so tests—such that insufficient data existed to properly train and test model performance, or training and testing were not even considered as part of the model development process.

To address these challenges, a framework is proposed to apply statistical and ML approaches to establish target performance requirements for models with different levels of complexity based on the use of a common, comprehensive database. Application of the proposed framework requires training of ML models to establish specific model performance requirements, where target errors are expressed in terms of the mean value and coefficient of variation (COV) of the true-to-predicted ratios. Once these metrics have been established, an additional study is required to develop a model that meets these requirements; this additional step is not addressed in this paper.

The methodology is demonstrated by addressing the problem of assessing wall shear strength using a comprehensive database of 340 walls reported to have failed in shear. This database was extracted from a larger database of more than 1100 tests collected from more than 250 experimental programs recently compiled by Abdullah and Wallace (2018, 2021) and Abdullah (2019). This application was picked because the wall shear strength equation in ACI 318-19 has remained essentially unchanged for the last 60 years despite a significant number of models being published in the literature. Although most of the published models (equations) are similar in complexity, significant model variance was noted when the models were assessed against a database that was different from the one used to develop and calibrate a given model (Gulec et al. 2009; Sánchez-Alejandre and Alcocer 2010; Carrillo and Alcocer 2013; Kassem 2015). These issues arise because the databases typically are of different sizes (number of tests), do not include the same wall tests, and have different ranges of parameters (for example, walls with rectangular cross sections versus walls with rectangular and flanged cross sections). Most of the studies also did not address the trade-off between underfitting versus overfitting (Höge et al. 2018) to examine the possibility that a model of equivalent complexity might have better predictive performance. The number of tests included in the wall shear database (340) and the number of variables for each test are expected to be typical of engineering problems that would benefit from the proposed methodology. Finally, none of the models met the set of performance requirements established in this paper for the given level of model complexity.

ACI Structural Journal, V. 121, No. 1, January 2024.
MS No. S-2022-407.R1, doi: 10.14359/51739186, received August 1, 2023, and reviewed under Institute publication policies. Pertinent discussion including author's closure, if any, will be published ten months from this journal's date if the discussion is received within four months of the paper's print publication.

RESEARCH SIGNIFICANCE

Evaluating and comparing the performance of models used to estimate structural component capacities is often challenging because the models were created with different levels of complexity and calibrated using databases with different numbers of tests and parameters. In addition, sufficient data may not have existed to properly train and test model performance, or training and testing were not considered. To address these challenges, a framework is proposed to apply statistical and ML approaches to establish model performance requirements for models of different complexities by training ML models to establish target errors expressed in terms of the mean value and COV of the true-to-predicted ratios. Application of the proposed framework is demonstrated by assessing the problem of estimating reinforced concrete (RC) wall shear strength.

REVIEW OF EXISTING WALL SHEAR STRENGTH MODELS

Models calibrated using statistical inference

Rojas-León (2022) presented a detailed literature review of existing models used in building codes and standards to predict the shear strength of RC walls (Appendix A,* Table A.1). The review reveals that all models use a $V_n = V_c + V_s$ format, where V_c and V_s are the concrete and reinforcement contributions, respectively; however, the parameters considered vary between the models. For example, the NZS 3101-06 (1995) and ASCE/SEI 43-05 models consider the influence of axial load on V_c (ACI 318 does not), the EC8-04 and ASCE/SEI 43-05 models include the impact of the vertical web reinforcement, and the detailed model of NZS 3101-06 (1995) uses $M/(Vl_w)$ instead of h_w/l_w, which is used by ACI 318-19, ASCE/SEI 43-05, and AIJ 1999.

The literature review by Rojas-León (2022) also includes an evaluation of wall shear strength equations reported in the literature, along with a description of the databases used in the calibration/validation of the models (Appendix A, Table A.2). For most of these studies, wall shear strength relations were developed by identifying relevant parameters based on a literature review, investigating the mechanics of the problem, and using statistical analysis of a data set or data sets. Subsequently, a calibration process was employed to fit the coefficients of the proposed model to the data; however, the performance of these equations was not typically checked against unseen data. Results presented in Table 1 enable a comparison of models analyzed in four studies (Sánchez-Alejandre and Alcocer 2010; Carrillo and Alcocer 2013; Kassem 2015; Looi and Su 2017) in terms of their mean and COV. As noted previously, the models are typically valid and perform well only when the parameters are within the ranges of the parameters used to calibrate the model. Because different databases were used and these databases used different criteria to determine which wall tests to include in the database, as well as different numbers of tests, different test parameters, and different ranges of test parameters, a model developed with a given database can be biased when it is evaluated with another database. Even if the ranges of relevant parameters are comparable, the size of the databases influences the reported means and COVs (Tanaka 1987). In addition, as databases become large, it often becomes infeasible to completely interpret the data using statistical models. In such cases, the application of ML is valuable (Dey 2016).

ML models

Although ML models can be powerful, they tend to be complex, challenging to use, and difficult to interpret (Bzdok et al. 2018). Several recent studies developed ML models to estimate wall shear strength (Chen et al. 2018; Moradi and Hariri-Ardebili 2019; Keshtegar et al. 2021; Feng et al. 2021); Appendix A, Table A.3 provides a summary of the databases, variables, and error indicators used in some of these studies. The results reported in Table A.3 demonstrate the potential and significant predictive power of ML models relative to other models (Table 1); however, these models suffer drawbacks, as described in the following paragraphs.

To train an ML model, a more extensive database is required; however, it also is critical to carefully screen the tests included in the database to ensure that they are aligned with the goals of the model being developed. For example, if the study is related to assessing wall shear strength, then the tests used in the database should include only walls that failed in shear, and outliers should be carefully reviewed to ensure that the data should be included (for example, inconsistent results are reported; an additional test variable is included that would impact results, such as corrosion; and the test variables satisfy code-minimum requirements, such as material properties). Model performance should be reported, including a well-known error indicator such as the mean and COV of the true-to-predicted ratio, to facilitate comparisons. Also, if an ML model is compared with other models (for example, Table 1), then the comparison should also include results of other (adequately trained) ML models to judge the performance of the ML model. ML models are more complex than models developed based on a (simple) equation; therefore, better performance is expected. If this is not the case, it implies that a complex model has similar (or worse) performance than a simple model; therefore, the added complexity is redundant because the simple model already captures the relevant patterns and relationships in the data.

A vast majority of structural tests reported in the literature were conducted at less than full-scale (for example, one-fifth to three-quarters); therefore, it is essential to develop models using dimensionless and/or mechanics-based normalized variables (for example, aspect ratio versus wall height and wall length, stress versus force) such that the database and model results are representative of both reduced-scale tests and full-scale components (for example, walls). The need for this step becomes clear when the relationship between the predicted variable and the error indicator selected for the optimization problem is evaluated. For example, if shear strength is the variable being estimated and an error such as the root-mean-squared error (RMSE) is used to train the

---

*The Appendix is available at **www.concrete.org/publications** in PDF format, appended to the online version of the published paper. It is also available in hard copy from ACI headquarters for a fee equal to the cost of reproduction plus handling at the time of the request.

Table 1—Wall shear strength model comparisons reported in different studies: V_{true}/V_{pred}

Model	Sánchez-Alejandre and Alcocer (2010)		Carillo and Alcocer (2013)		Kassem (2015)		Looi and Su (2017)	
	Mean	COV	Mean	COV	Mean	COV	Mean	COV
ACI 318-19, Ch. 18*	1.43	0.26	0.82	0.24	1.65	0.37	1.01	0.37
ACI 318-11, Ch. 11	—†	—	0.90	0.21	—	—	—	—
ACI 318-14, Ch. 11	—	—	—	—	—	—	0.96	0.37
AIJ (1999)	1.00	0.27	—	—	—	—	—	—
CSA A23.3-14	—	—	—	—	—	—	1.35	0.44
EC8 (2004)	—	—	—	—	2.54	0.71	—	—
Barda et al. (1977)	—	—	—	—	1.39	0.47	—	—
Wood (1990)	0.99	0.24	—	—	0.78	0.32	—	—
Hwang and Lee (2002)	1.06	0.22	—	—	1.26	0.56	—	—
Sánchez-Alejandre and Alcocer (2010)	1.00	0.13	0.79	0.12	1.91	0.29	0.84	0.35
Gulec and Whittaker (2011)	—	—	1.06	0.09	1.34	0.24	0.89	0.31
Carrillo and Alcocer (2013)	—	—	1.00	0.08	—	—	—	—
Kassem (2015)	—	—	—	—	1.00	0.21	—	—
Looi and Su (2017)	—	—	—	—	—	—	1.04	0.27

*Sánchez-Alejandre and Alcocer (2010) use ACI 318-08 Ch. 21; Carrillo and Alcocer (2013) and Kassem (2015) use ACI 318-11 Ch. 21; Looi and Su (2017) use ACI 318-14, Ch. 18. These equations are same as those in ACI 318-19 Ch.18.

†Model not included in comparison.

model, then the direct difference between the observed value (or true value, V_{true}) and the predicted shear strength value (V_{pred}) is minimized (that is, not a percentage error), which can lead to large errors for lower values of V_{true}. Another option is to use an error indicator equal to the difference in the true-to-predicted value; however, this does not address the issue of reduced scale tests. Finally, the coefficient of determination ($R^2 \in [0,1]$) is another error indicator that is commonly used; however, results can be misleading because this approach compares a given model to the null model, and larger R^2 values can be obtained for less precise models (Barret 1974).

For ML models, it is common to use two data sets: a training set and a testing set. The training set is used to train (calibrate) the model, and the testing set is used to verify that the trained model will perform similarly when predicting unseen data. Acceptable performance is achieved where the value of the error obtained for the testing set is comparable to that obtained for the training set. Although this comparison should be carefully addressed and ideally verified in terms of the error used in the optimization process and other meaningful error indicators to demonstrate model robustness, this added step is often not adequately considered.

FRAMEWORK

The proposed framework uses statistical and ML approaches to establish target performance requirements for component capacity models (for example, models for column and wall shear strength, beam flexural strength, reinforcement development length, and so on), or other models with similar characteristics, with different levels of complexity based on the use of a common, comprehensive database. The framework overcomes the limitations highlighted in the Introduction by allowing the user to define model performance requirements based on the desired level of model complexity.

The proposed framework adopts the generic steps of ML—that is, collection and preparation of data, feature selection, selection of ML algorithms, selection of model and hyper-parameters, model training, and model performance evaluation (Alzubi et al. 2018)—but also requires specific sub-steps to: a) define relevant (starting) features based on the mechanics of the problem; b) address the issue of using reduced-scale tests to predict capacities of full-scale specimens; c) develop an iterative sensitivity analysis to train the ML model; and d) train Elastic Net Models (ENMs) using engineered features defined from the starting features. Each of these steps is described in detail in the following subsections.

Step 1: Collection and preparation of data

A data set of walls with reported flexure-shear (F-S), diagonal-tension (D-T), or diagonal-compression (D-C) failure modes was obtained using the UCLA-RC Walls Database, which includes detailed and parametrized information on more than 1100 RC wall tests (Abdullah and Wallace 2018, 2021; Abdullah 2019). Tests with incomplete material test information were excluded because this information is required to define the variables used in this study. The reduced data set included a total of 412 wall tests. The dataset was further evaluated resulting in the removal of 72 tests because: a) test walls included artificial cracks to study corrosion (six tests, Zheng et al. [2015]); b) reported lateral load readings did not match the values reported in figures provided in various papers or reports (nine tests, Li and Li [2002]); c) test walls had asymmetric cross-sectional

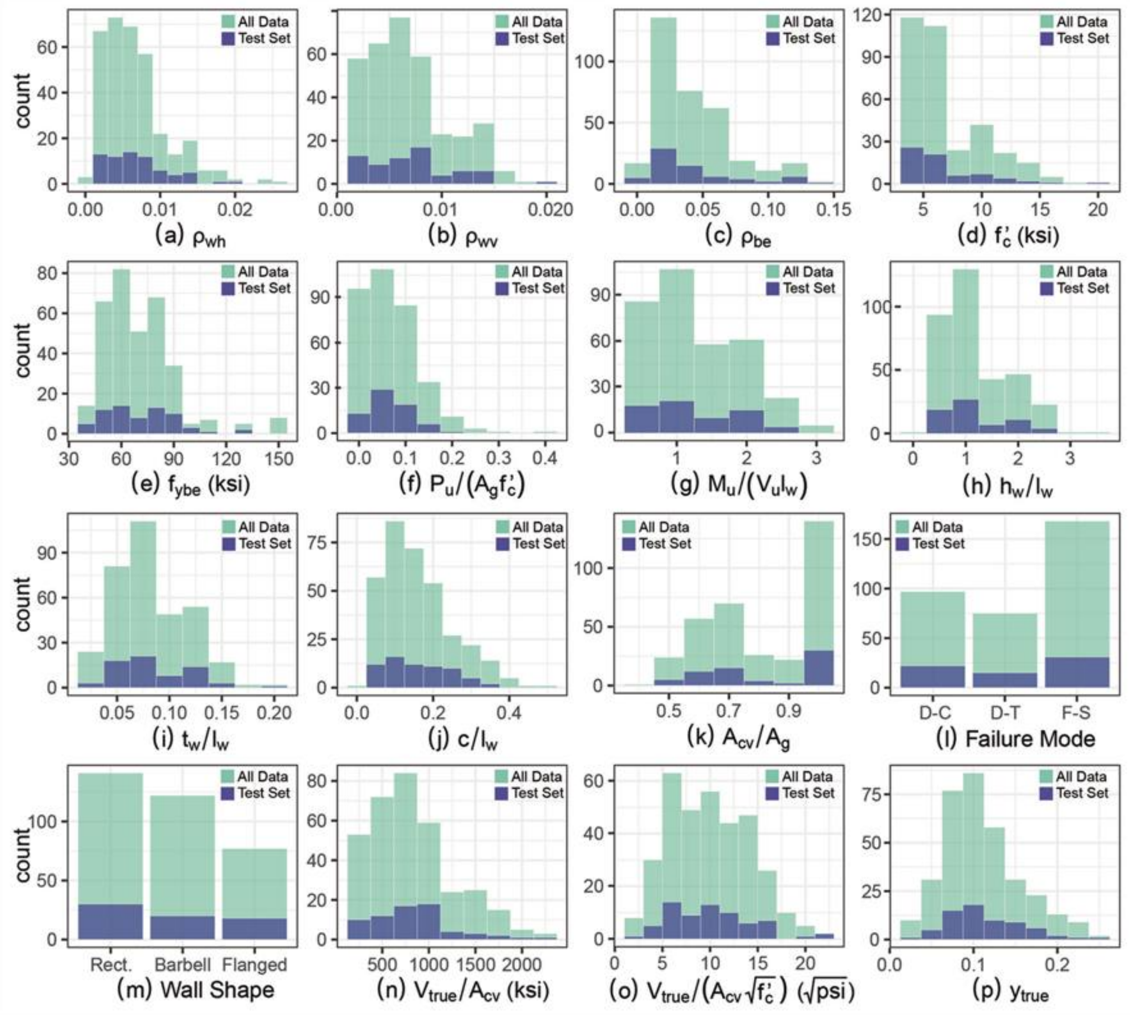

Fig. 1—Histograms of relevant parameters. (Note: 1 ksi = 6.895 MPa; 1 kip = 4.448 kN.)

shapes such as T-shape, L-shape, half barbell, and wing walls (20 tests); or d) reported values for tested compressive strength of concrete f_c' were less than the limit of 20.7 MPa (3.0 ksi) given in ACI 318-19 for special seismic systems (37 tests). Asymmetric walls were excluded because the number of walls with these cross-sectional shapes was low (20) compared to the number of rectangular, barbell, or flanged walls. Thus, if these tests are incorporated into the larger dataset of symmetric walls, the optimization process will likely overlook the inherent differences between asymmetric and symmetric walls. A more appropriate approach in this case, as implemented by Rojas-León (2022), is to develop a model excluding asymmetric wall cross sections and then evaluate whether simple changes to the model could be implemented to address shear strength estimates for the asymmetric walls.

Based on the aforementioned filters, a final (clean) dataset of 340 symmetric wall tests was obtained (refer to the Appendix) and randomly split into a training set with 80% of the tests (272) and a testing set with 20% of the tests (68) to verify the performance of the models. Figure 1 compares histograms for various database parameters of the entire data set and the testing set, where f_c' is the specified compressive strength of concrete; ρ_{be} is the boundary region longitudinal reinforcement ratio; f_{ybe} is the specified yield strength of the boundary region longitudinal reinforcement; ρ_{wh} and f_{ywh} are the ratio and specified yield strength of the horizontal web reinforcement, respectively; ρ_{wh} and f_{ywv} are the ratio and specified yield strength of the vertical web reinforcement, respectively; P_u, M_u, and V_u are the measured axial load, moment, and shear, respectively; l_w is the wall length in the direction of the applied shear force; h_w is the total wall height; A_{be} is the cross-sectional area bounding the longitudinal reinforcement at a wall boundary; A_{cv} is the cross-sectional area bounded by the wall length and the web thickness (t_w); A_g is the gross cross-sectional area; c is the neutral axis depth; and y_{true} is the normalized shear stress (introduced later).

Step 2: Defining ML models and features

This step involves identifying the potentially relevant parameters based on a literature review and studying relatively simple mechanics-based models and appropriate free-body diagrams. For this application—that is, RC wall shear strength—a free-body diagram of a wall with a diagonal crack was used. Based on these considerations, the following relationships were derived (Rojas-León 2022).

$$V_u \underset{\sim}{\propto} A_g f_c' \tag{1}$$

Table 2—ENMs definition

Model	Short reference	Long reference
ENM1	$y \sim \mathbf{X}$	$y_j \sim N(\mu_j, \sigma),\ \mu_j = \mathrm{x}_j^T\beta,\quad \forall j \in \{1, 2, \ldots, n\}$
ENM2	$y \sim \tilde{\mathbf{X}}$	$y_j \sim N(\mu_j, \sigma),\ \mu_j = \tilde{\mathrm{x}}_j^T\beta,\quad \forall j \in \{1, 2, \ldots, n\}$
ENM3	$\sqrt[3]{y} \sim \tilde{\mathbf{X}}$	$\sqrt[3]{y_j} \sim N(\mu_j, \sigma),\ \mu_j = \tilde{\mathrm{x}}_j^T\beta,\quad \forall j \in \{1, 2, \ldots, n\}$
ENM4	$\log(y) \sim \tilde{\mathbf{X}}$	$\log(y_j) \sim N(\mu_j, \sigma),\ \mu_j = \tilde{\mathrm{x}}_j^T\beta,\quad \forall j \in \{1, 2, \ldots, n\}$
ENM5	$y \sim \mathbf{X}_{poly}$	$y_j \sim N(\mu_j, \sigma),\ \mu_j = \mathrm{x}_{poly_j}^T\beta,\ \forall j \in \{1, 2, \ldots, n\}$
ENM6	$\sqrt[3]{y} \sim \mathbf{X}_{poly}$	$\sqrt[3]{y_j} \sim N(\mu_j, \sigma),\ \mu_j = \mathrm{x}_{poly_j}^T\beta,\ \forall j \in \{1, 2, \ldots, n\}$
ENM7	$\log(y) \sim \mathbf{X}_{poly}$	$\log(y_j) \sim N(\mu_j, \sigma),\ \mu_j = \mathrm{x}_{poly_j}^T\beta,\ \forall j \in \{1, 2, \ldots, n\}$
ENM8	$y \sim \tilde{\mathbf{X}}_{poly}$	$y_j \sim N(\mu_j, \sigma),\ \mu_j = \tilde{\mathrm{x}}_{poly_j}\beta,\ \forall j \in \{1, 2, \ldots, n\}$
ENM9	$\sqrt[3]{y} \sim \tilde{\mathbf{X}}_{poly}$	$\sqrt[3]{y_j} \sim N(\mu_j, \sigma),\ \mu_j = \tilde{\mathrm{x}}_{poly_j}\beta,\ \forall j \in \{1, 2, \ldots, n\}$
ENM10	$\log(y) \sim \tilde{\mathbf{X}}_{poly}$	$\log(y_j) \sim N(\mu_j, \sigma),\ \mu_j = \tilde{\mathrm{x}}_{poly_j}^T\beta,\ \forall j \in \{1, 2, \ldots, n\}$

Note: *n* is number of features model uses.

$$V_u \overset{\propto}{\sim} \rho_{wh} f_{ywh} h_w t_w \tag{2}$$

$$V_u h_{eff} \overset{\propto}{\sim} \rho_{wv} f_{ywv} (l_w - c)^2 t_w \tag{3}$$

$$V_u h_{eff} \overset{\propto}{\sim} \rho_{be} f_{ybe} A_{be} l_w \tag{4}$$

$$V_u h_{eff} \overset{\propto}{\sim} \left(f_c' + \frac{P}{A_g}\right) t_w c^2 \tag{5}$$

$$V_u h_{eff} \overset{\propto}{\sim} \left(f_c' - \frac{P}{A_g}\right) t_w (l_w - c)^2 \tag{6}$$

Based on these relationships, and to address the use of reduced-scale test specimens, the following 10 non-dimensional variables are selected and are named the "starting features." These variables can be identified by normalizing V_u by $A_g f_c'$ in Eq. (1) through (6) and by applying reasonable approximations in some cases (for example, considering *c* as a fraction of l_w, and neglecting constants because the model calibration process will address this).

$$x_1 = \rho_{wh}(f_{ywh}/f_c') \tag{7}$$

$$x_2 = \rho_{wv}(f_{ywv}/f_c') \tag{8}$$

$$x_3 = \rho_{wbe}(f_{ybe}/f_c') \tag{9}$$

$$x_4 = 1 + P_u/(A_g f_c') \tag{10}$$

$$x_5 = c/l_w \tag{11}$$

$$x_6 = M_u/(V_u l_w) \tag{12}$$

$$x_7 = t_w/l_w \tag{13}$$

$$x_8 = t_w/h_w \tag{14}$$

$$x_9 = h_w/l_w \tag{15}$$

$$x_{10} = A_{be}/A_g \tag{16}$$

The predicted variable is the normalized shear strength defined as

$$y_{true} = V_{true}/(A_g f_c') \tag{17}$$

Between $(1 + P_u/(A_g f_c'))$ and $(1 - P_u/(A_g f_c'))$, only one option is considered because they are related to the same parameters in Eq. (5) and (6), and because the presence of a constant (that is, "intercept" or equivalent) in the calibration process would suggest dropping one of the terms because it is linearly dependent on the other. The height of the wall used to define the effective flange width according to ACI 318-19 Section 18.10.5.2 was estimated as $h_w \approx$ effective height $(h_{eff})/0.7$, where h_{eff} corresponds to the shear span, defined as M_u/V_u. It is well established that flanged walls have a larger shear strength (Gulec et al. 2009; Gulec and Whittaker 2011; Kassem 2015; Kim and Park 2020); thus, cross-sectional area A_g is used instead of A_{cv} in Eq. (17).

The feature matrix **X** contains the 10 starting features defined in Eq. (8) through Eq. (17). The following feature matrixes ($\tilde{\mathbf{X}}$, $\mathbf{X}_{poly}$, and $\tilde{\mathbf{X}}_{poly}$) are obtained by using feature engineering. Feature matrix $\tilde{\mathrm{X}}$ contains 140 features because the following 14 functions were applied to the 10 original (starting) features: identity function, $(\cdot)^{-1}$, $(\cdot)^2$, $(\cdot)^{-2}$, $(\cdot)^{1/2}$, $(\cdot)^{-1/2}$, $(\cdot)^3$, $(\cdot)^{-3}$, $(\cdot)^{1/3}$, $(\cdot)^{-1/3}$, $exp(\cdot)$, $exp(-\cdot)$, $\log(\cdot)$, and $-\log(1 + \cdot)$. Feature matrix $\mathbf{X}_{poly}$ has 285 features (combining the 10 starting features with a cubic polynomial). Feature matrix $\tilde{\mathbf{X}}_{poly}$ has 679 features that are obtained by combining the 14 more significant features of the $\tilde{\mathbf{X}}$ matrix with cubic polynomial coefficients. Cubic polynomials were used because Eq. (1) through (6) can be formed by multiplying up to three starting features. Also, to reduce skewness or highlight trends, other variations of the output variable *y* (refer to Eq. (17)) are defined as $\sqrt[3]{y}$ and $\log(y)$. The subset of 14 more significant features of $\tilde{\mathbf{X}}$ is obtained after performing the sensitivity analysis (explained later) for ENM2 (introduced later in Table 2).

The starting features will be the input parameters of one or more complex ML models, which will predict the normalized shear stress defined in Eq. (17). The selected complex ML models for this study are the artificial neural network (ANN) and Random Forest (RF) regression models because they are applicable for this study (the predicted parameter is a continuous variable), and because they are well-known models that are not complicated to implement in programming languages (for example, Matlab, R, and Python, which have various built-in functions to simplify their implementation). The starting and engineered features are also used to create a suite of ENMs; a total of 10 ENMs are defined (refer to Table 2).

ENMs (Zou and Hastie 2005) are a simple and more interpretable ML model type because they are a penalized linear modeling approach with a mixture of ridge regression (Hoerl and Kennard 1970) and Least Absolute Shrinkage and Selection Operator (LASSO) regression (Tibshirani 1996). Ridge regression reduces the impact of collinearity on the features, whereas LASSO reduces the dimension of the problem by shrinking some of the coefficients to zero (less significant

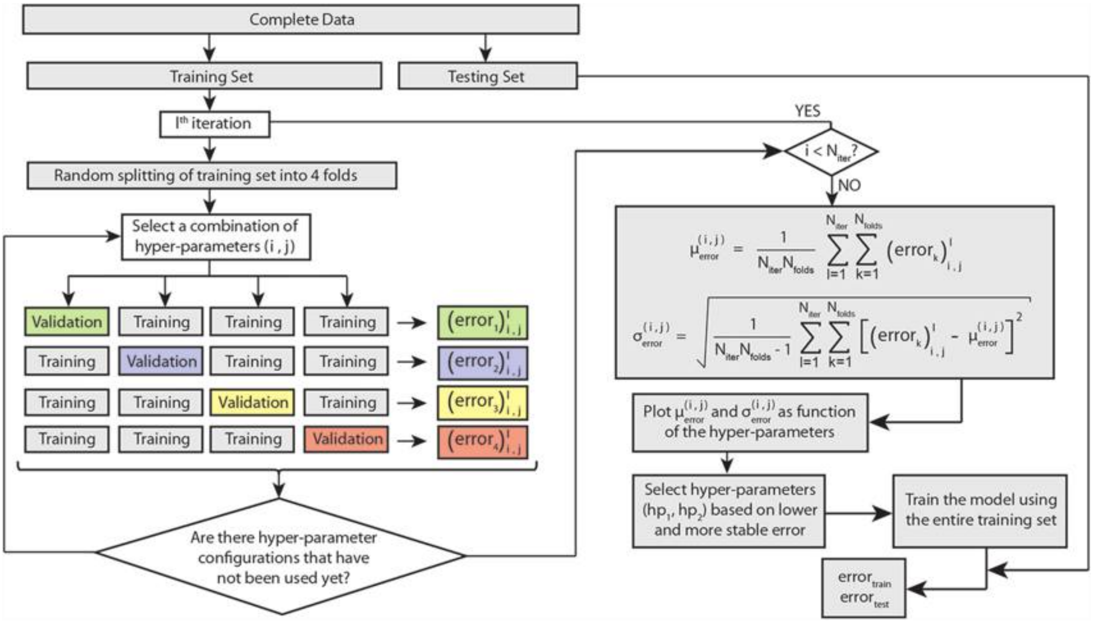

Fig. 2—Sensitivity analysis algorithm to select optimum set of hyper-parameter values.

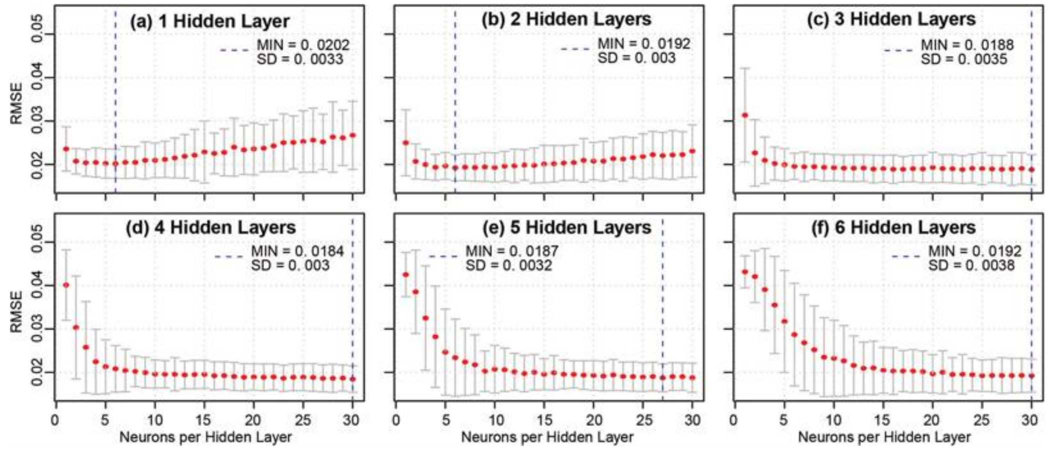

Fig. 3—Sensitivity analysis results to define optimum ANN configuration.

parameters). ENMs have two hyper-parameters: a) $\lambda > 0$ is the complexity parameter that controls the weight of the penalization factors; and b) $\alpha \in [0,1]$ is the compromise between Ridge ($\alpha = 0$) and LASSO ($\alpha = 1$). Small λ values can result in an overfitted model (too complex), whereas high λ values can result in an underfitted model (too simple).

Step 3: Sensitivity analysis and selection of hyper-parameters

The hyper-parameter sensitivity analysis described in Fig. 2 was implemented for the 12 ML models (1 ANN, 1 RF regression, and 10 ENMs) using an iterative k-fold cross-validation (CV) method with, in this case, $N_{iter} = 100$ iterations and $k = 4$ folds. K-fold CV is useful for data scientists when dealing with small databases (a few thousand data samples). Iterations are included because, in Structural Engineering, the database is typically even smaller (just a few tens or hundreds). The number of folds was set as $k = 4$ because it makes the validation set representative of the testing set (that is, the same size). Once the sensitivity analysis is completed, $k \times N_{iter} = 4 \times 100 = 400$ RMSE values are computed for each configuration of hyper-parameters. The mean and standard deviation of the calculated RMSEs are obtained for each of these configurations. The optimal hyper-parameters are selected based on the lower mean error and standard deviation.

ANN—Rules suggesting values for the number of hidden layers and neurons per layer (main hyper-parameters) can be found in the literature (Chen et al. 2018; Moradi and Hariri-Ardebili 2019), which are covered by the ranges selected for the sensitivity analysis. The sensitivity analysis results are shown in Fig. 3; a blue dashed line indicates the best ANN configuration for each number of hidden layers considered. From there, the optimum ANN is the one with four hidden layers and 30 neurons in each layer because it has the lowest mean error (MIN RMSE) and the lowest standard deviation (SD). Previous configurations (the same four hidden layers, but fewer neurons) show an extensive range of similar and stable results.

RF regression—A large number of decision trees (1000 trees) are selected to ensure that a stable error level is reached. For this study, the error became stable at approximately 300 trees. Two other hyper-parameters could have

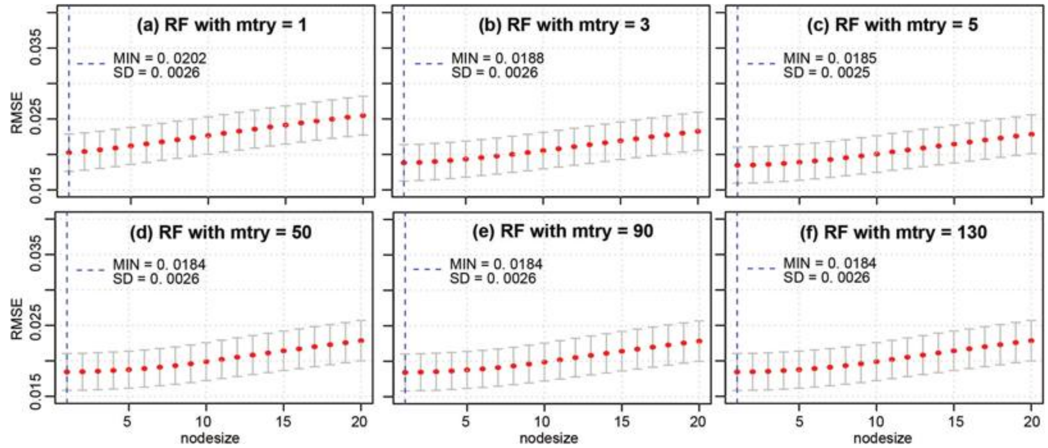

Fig. 4—Sensitivity analysis results to define optimum RF configuration.

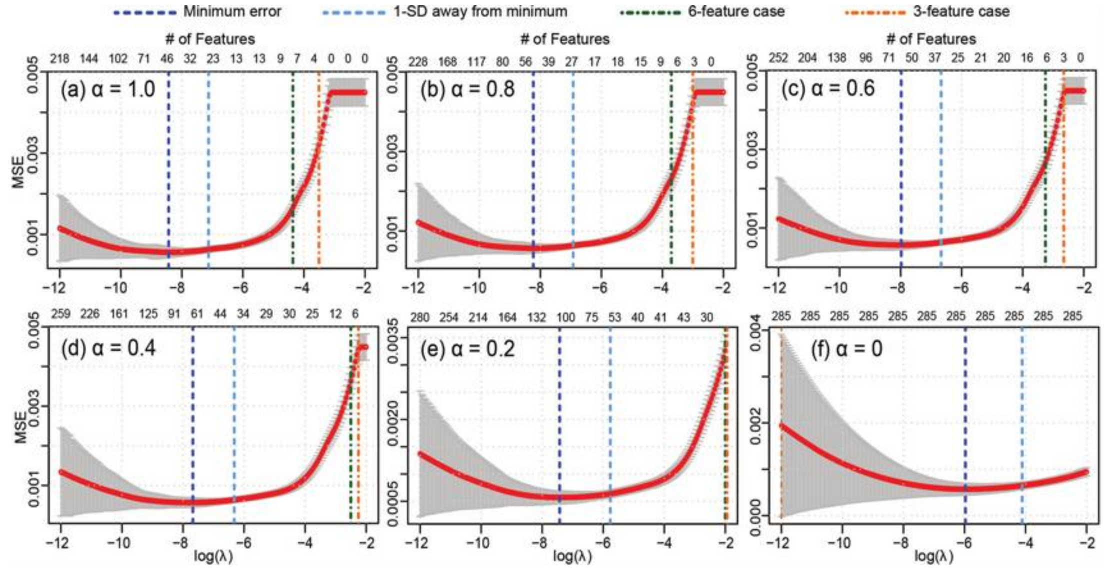

Fig. 5—Sensitivity analysis results for ENM6 model: $\sqrt[3]{\mathrm{y_j}} \sim \mathrm{N}(\mu_\mathrm{j}, \sigma), \mu_\mathrm{j} = x_{\mathrm{poly_j}}{}'\beta$.

an impact on the performance of the model (Zhang and Ma 2012): 1) the number of variables (selected among all the features) in each cell (*mtry*); and 2) the prespecified threshold of maximum observation per cell (*nodesize*). The sensitivity analysis covered ranges of values for both hyper-parameters according to observations by Zhang and Ma (2012) concerning *mtry*, and according to Breiman (2001) and Segal and Xiao (2011) concerning *nodesize*. Figure 4 shows that the RF results are only slightly sensitive to *mtry*, and that having large trees (small *nodesize*) results in low errors (RMSE). Optimal hyper-parameters are selected as *mtry* = 50 and *nodesize* = 1 (minimum mean and SD).

ENMs—The log(λ) values ranged from –12 to –2, while the α values were 1.0, 0.8, 0.6, 0.4, 0.2, and 0.0 for all 10 ENMs defined in Table 2. As an example, Fig. 5 presents the sensitivity analysis results for ENM6; the optimum version of the model is indicated with a black dashed vertical line, while the blue, green, and orange vertical dashed lines indicate the λ values associated with the selected underfitting levels. In this study, three levels of underfitting are selected: 1) one in which the error corresponds to the error that is one standard deviation away from the error of the optimum model (“1-SD away” version); 2) an underfitted model that uses six features only (“6-feature” version); and 3) an underfitted model that uses three features only (“3-feature” version). These underfitting levels were selected because they are representative of models adopted in building codes and standards, and a model with this complexity level is of particular interest in this study.

Figure 6 presents the mean errors obtained from the sensitivity analysis of the 10 ENM models and demonstrates that regardless of the value of α considered, there is a λ value where practically the same optimum error is reached. Figure 7 indicates that it is difficult for the models to exclude features to achieve the defined underfitted levels of interest for lower α values. Because of these reasons, for each ENM in this study, the selected hyper-parameter configuration for the optimum and underfitted complexity levels is α = 1, and its associated corresponding λ value—that is, all selected ENMs are LASSO models.

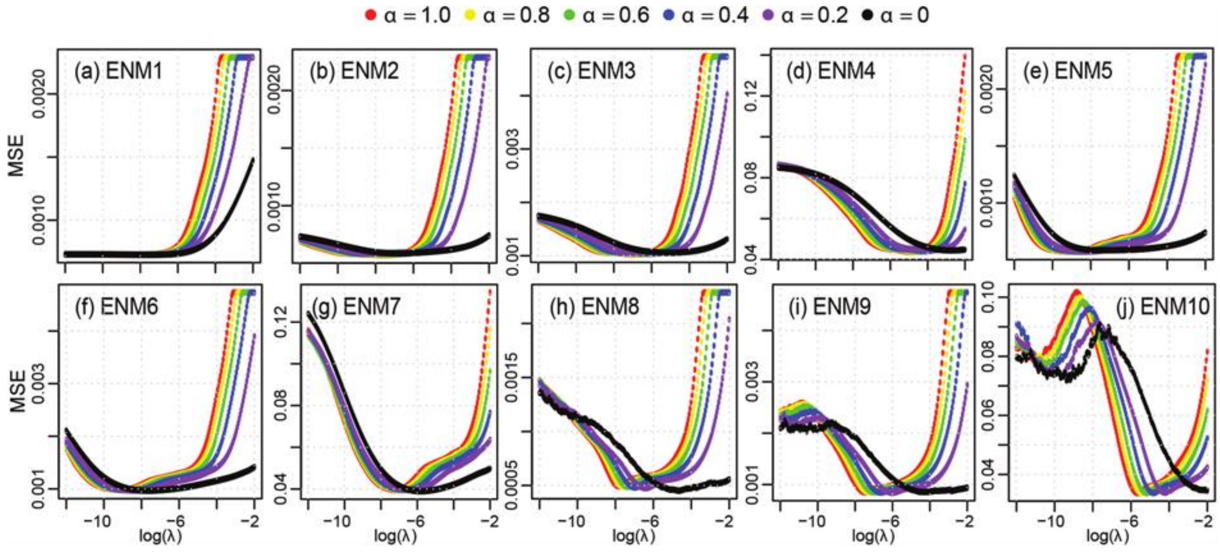

Fig. 6—Mean of MSE obtained from sensitivity analysis of all ENM models.

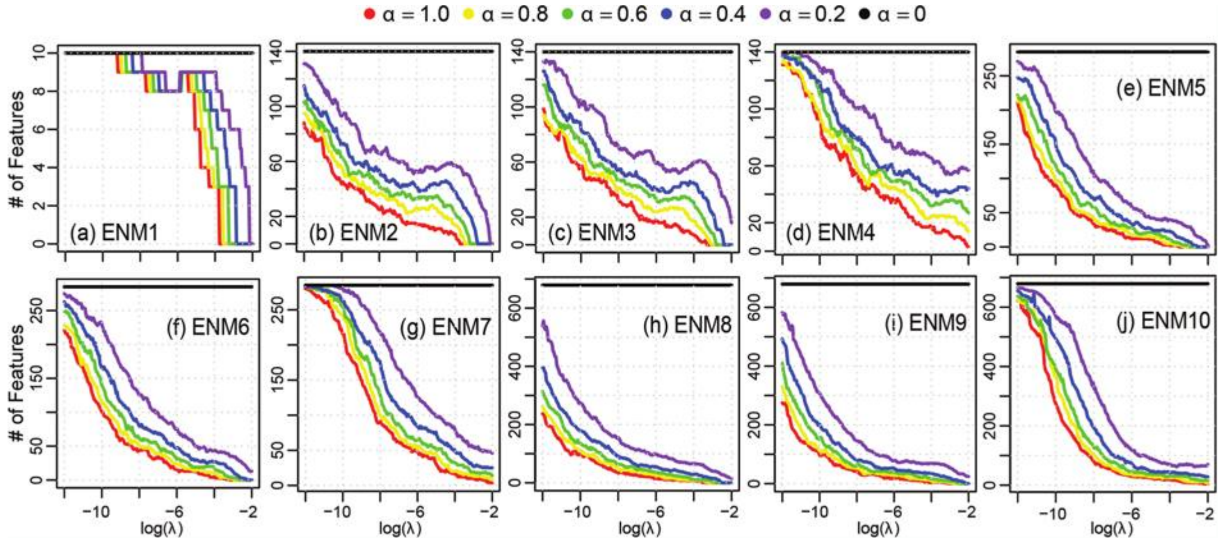

Fig. 7—Mean non-zero coefficients obtained from sensitivity analysis of all ENM models.

Step 4: Training, verification, and selection of best-performing models

All the models are trained using the training set with selected sets of hyper-parameters. This results in 42 trained ML models: the optimum ANN (1 model), the optimum RF Regression (1 model), the optimum version of each LASSO (10 models), the 1-SD away version of each LASSO (10 models), the 6-feature version of each LASSO (10 models), and the 3-feature version of each LASSO (10 models). The acceptability criterion adopted in this study defines a model as acceptable when the errors of the training and testing sets are both within a defined margin away from the converging error, which is ±20% for the optimum models and ±10% for the underfitted models. The converging error is taken as the average of the training and testing errors. Optimum models have a larger margin because they are right on the balanced point between the underfitted and overfitted models. Thus, they have the potential to "keep learning" (for example, re-adjust their coefficients a bit) if new data are provided for training. On the other hand, by definition, underfitted models are not capable of capturing enough details, and they follow more rough trends identified from the data, which is the reason for the stricter margin around the converging error. The performance of existing models and the training of several new models also informed the selection of the acceptable bandwidth around the converging error (Rojas-León 2022).

Optimum ANN and RF—Although the training process was based on the RMSE between y_{true} and y_{pred} (refer to Fig. 8(a) and 9(a)), similar model performance (that is, training and testing errors within ±20% of the converging error) is verified when using the predicted values from the training and testing sets to compute the mean and COV of V_{true}/V_{pred} for the optimum ANN (Fig. 8(b) and (c)) and optimum RF (Fig. 9(b) and (c)). Figures 8(c) and 9(c) also show that the predictions for the training and testing sets have the same distribution shapes.

Optimum and underfitted LASSO models—All 40 LASSO models selected (four from each ENM defined in Table 2) are trained using only the features associated with each chosen hyper-parameter configuration—that is, they are linear

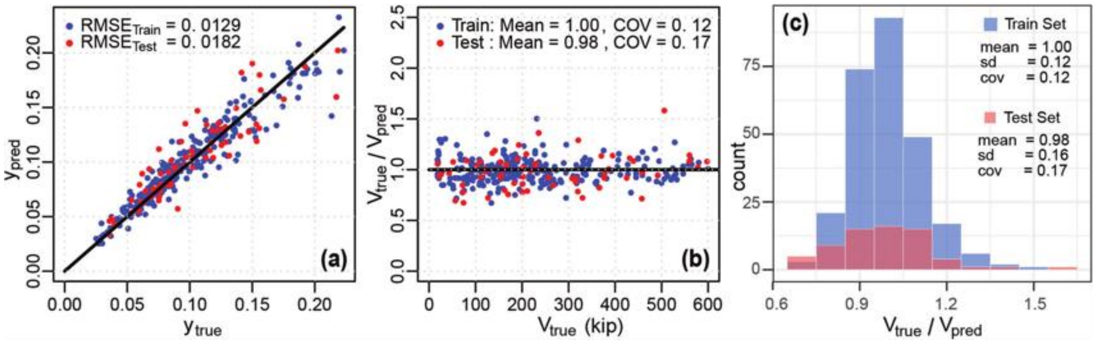

Fig. 8—Performance of selected ANN on training and testing sets in terms of: (a) normalized shear stress; (b) V_{true}/V_{pred} *versus* V_{true}*; and (c) distributions of* V_{true}/V_{pred}*. (Note: 1 kip = 4.448 kN.)*

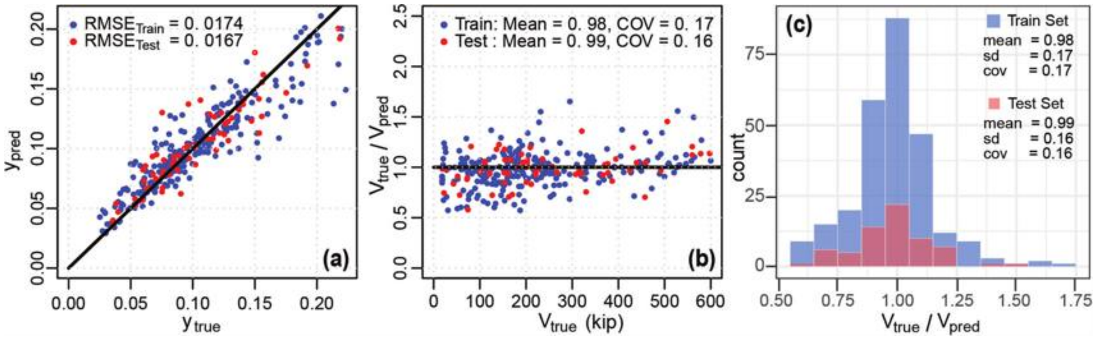

Fig. 9—Performance of selected RF on training and testing sets in terms of: (a) normalized shear stress; (b) V_{true}/V_{pred} *versus* V_{true}*; and (c) distributions of* V_{true}/V_{pred}*. (Note: 1 kip = 4.448 kN.)*

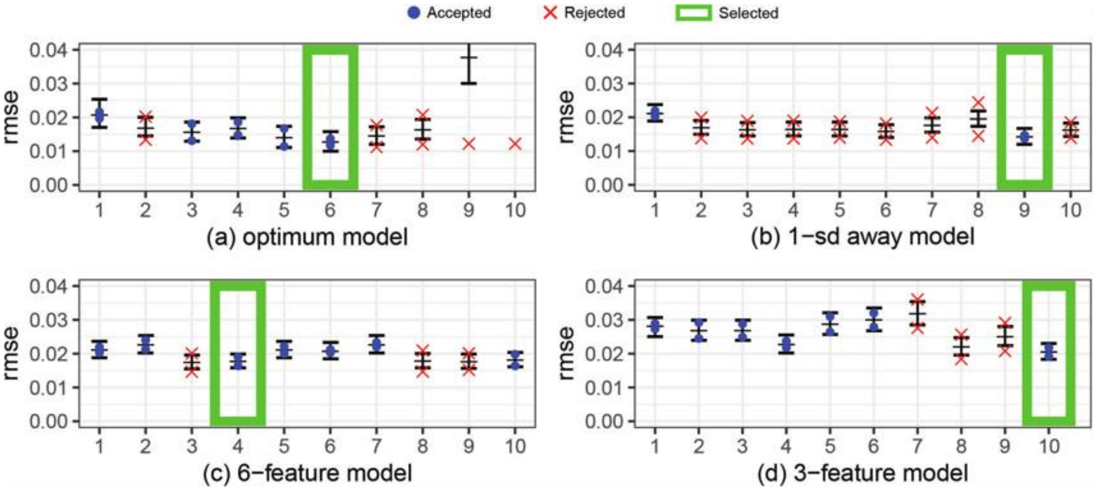

Fig. 10—Selection of best LASSO model for each complexity level based on acceptability criterion.

regressions with different engineered features. Figures 10(a) to (d) show the training and testing errors (RMSE between y_{true} and y_{pred}) with a blue dot or a red cross, depending on whether they meet or do not meet the acceptability criterion, respectively. For each complexity level, the model meeting the acceptability criterion with the smaller converging error was selected (which are highlighted with a green box in Fig. 10; full-color version can be accessed at www.concrete.org); the best optimal LASSO model, the best 1-SD away LASSO model, the best 6-feature LASSO model, and the best 3-feature version. Note that the optimum LASSO models No. 9 and 10 have significant errors, which is attributed to the implemented automated selection of hyper-parameters that are just a little past the underfitted-overfitted sweet spot, which is the reason that the 1-SD away model was included (especially for those LASSO models that are more complex). Figure 11 verifies the good and similar performance (training versus testing errors) in terms of the same error indicators used for the optimum ANN and optimum RF. The error goes up gradually, and distributions of the y_{true}/y_{pred} become wider as the complexity level of the models is relaxed. Nonetheless, the errors obtained for the 6-feature and 3-feature linear regressions are still very low compared to the results of existing equations in Table 1.

Except for the RF regression, all the learning curves shown in Fig. 12 (also obtained by iterating at each set size)

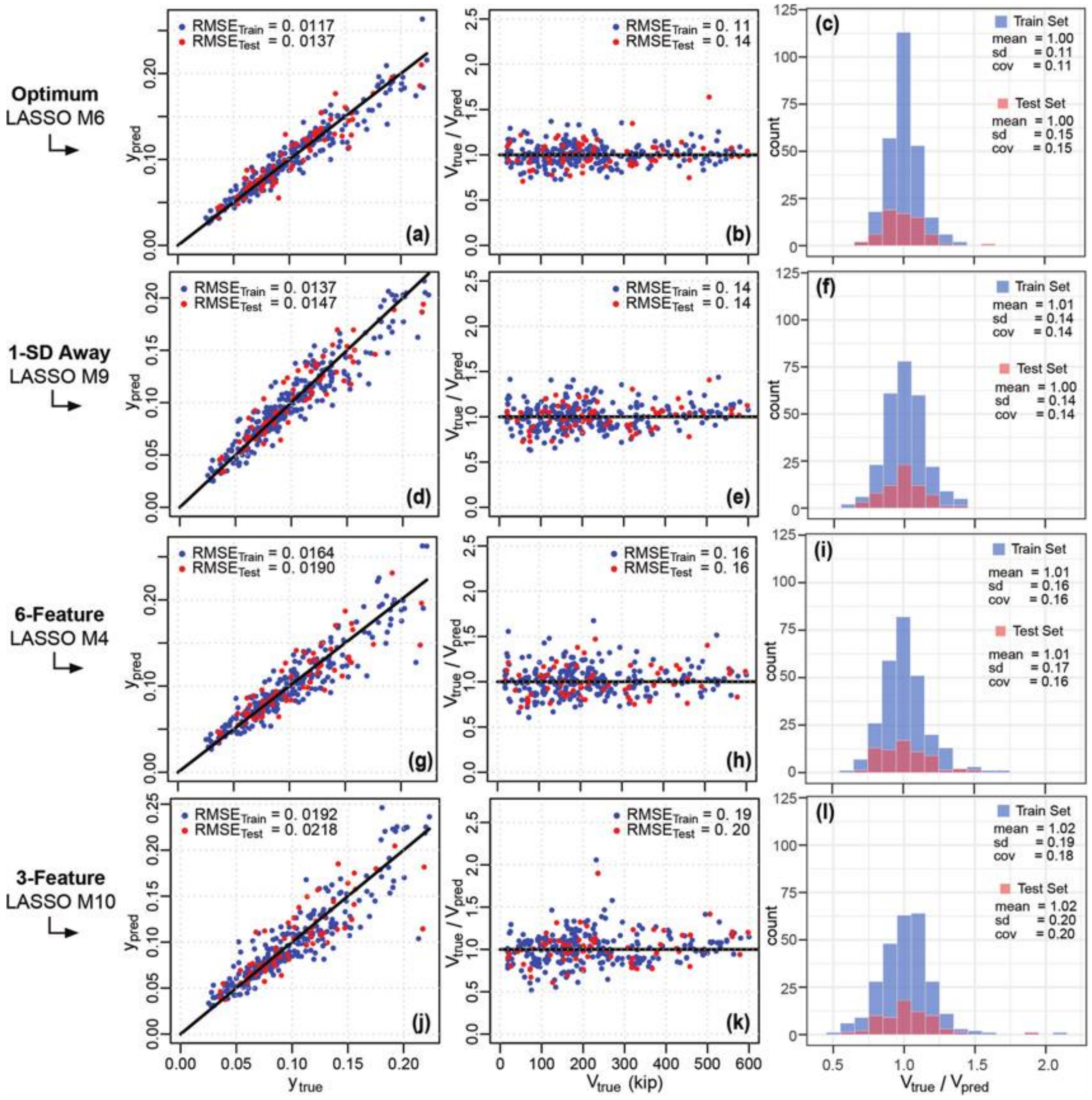

Fig. 11—Performance of selected LASSO models on training and testing sets in terms of: (a), (d), (g), and (j) normalized shear stress; (b), (e), (h), and (k) V_{true}/V_{pred} *versus* V_{true}*; and (c), (f), (i), and (l) distributions of* V_{true}/V_{pred}*. (Note: 1 kip = 4.448 kN.)*

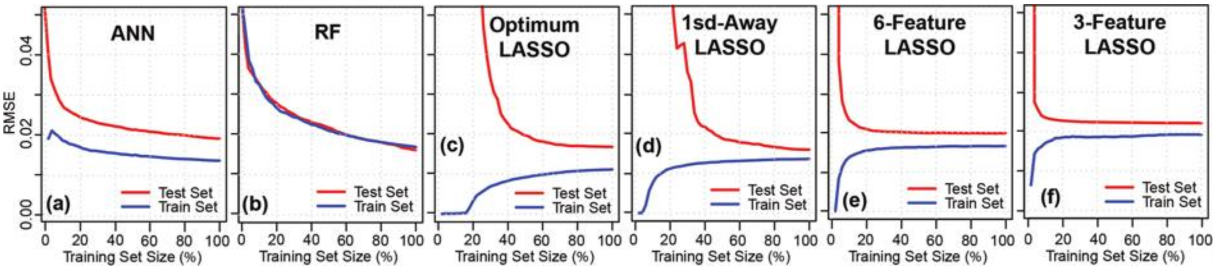

Fig. 12—Learning curves of selected and verified ML models.

have a gap between the training and testing curves and reach a plateau when approaching the use of 100% of the training set. Because of this, the error obtained when including future data into the training set to refine these same models (that is, keeping the same hyper-parameters and relevant features already identified) should fall between the training and testing errors, but closer to the training error. On the other hand, the training and testing learning curves for RF regression are very close to each other because a very large number of trees are selected. However, it is observed that the slope of the learning curves reduces (reaches a plateau) when the training size becomes larger. This behavior means that, if additional data are provided for training the same RF regression, the converging error would get closer to that plateau, resulting in a slightly lower error.

Step 5: Setting target errors for different model complexity levels

Because the six selected models demonstrate good performance that has been verified, adding data with a distribution

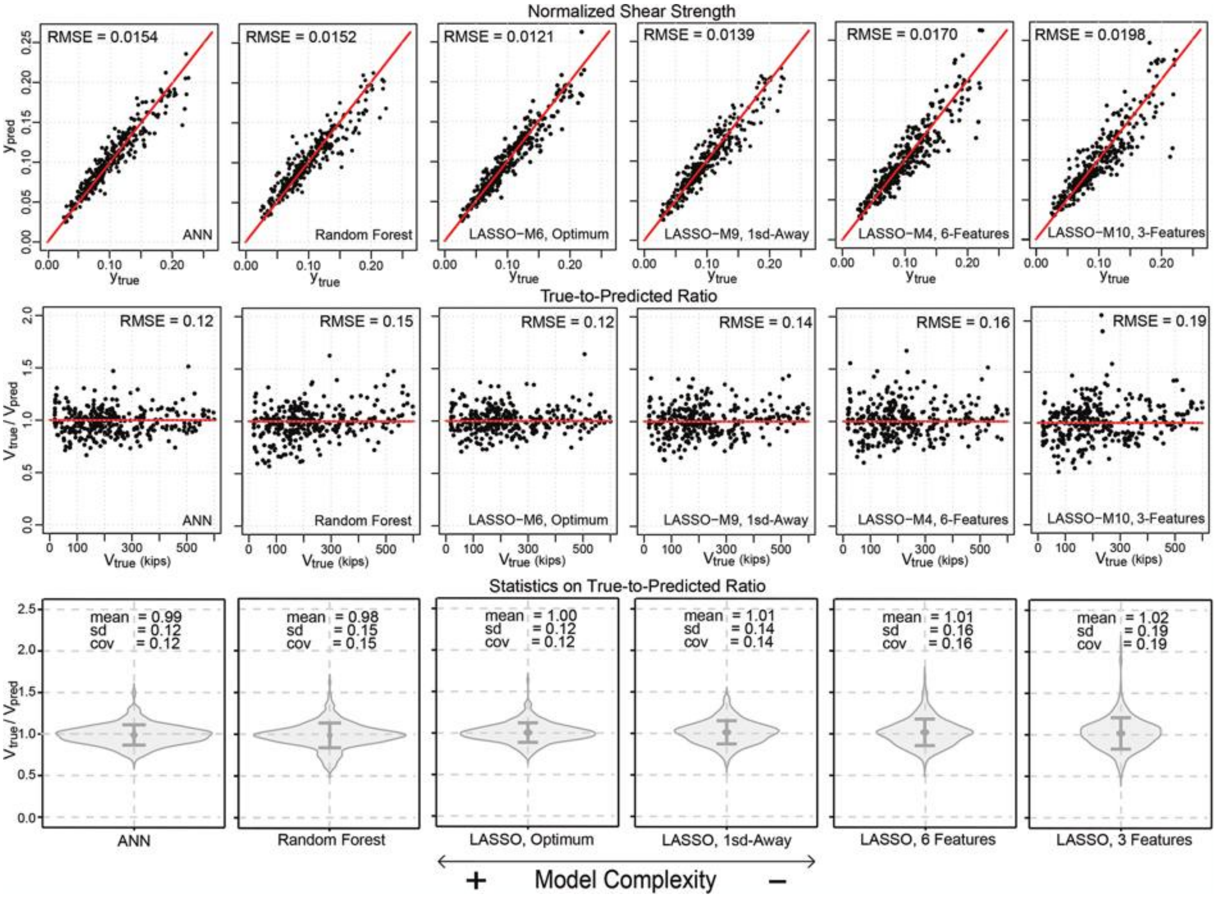

Fig. 13—Selected and trained ML models applied to entire database.

similar to that of the training data will only refine these models (Amazon Web Services 2019). Thus, the testing set is incorporated into the database used to train these models, but the same selected hyper-parameters and input features are kept. The results are presented side by side in Fig. 13, sorted from higher model complexity level (left) to lower model complexity level (right): optimum ANN, optimum RF, optimum LASSO M6, 1-SD away LASSO M9, 6-feature LASSO M4, 3-feature LASSO M10. As expected, performances are similar to those obtained previously and aligned with the observations derived from the learning curves. This good behavior is verified for all different error indicators used before.

Figure 13 shows that the ANN performs better (smaller error) than RF, but there is still room for the RF to improve if additional data are added to the database. The optimum LASSO model performs practically the same as the optimum ANN, or even slightly better if the RMSE between y_{true} and y_{pred} is considered. This is a relevant finding for two primary reasons: 1) the LASSO model is much less complex than the ANN model because, as noted before, LASSO models are linear regressions using those selected features only (which, for the optimum LASSO model, are 45 features engineered from the 10 starting features); and 2) the underfitted LASSO models can be understood as a smooth relaxation away from the optimum when looking for target model performances (errors) that fulfill user requirements for less complex models. The 1-SD away LASSO model is a linear regression of 14 features engineered from seven of the 10 starting features (x_1, x_2, x_3, x_6, x_8, x_9, and x_{10}), the 6-feature LASSO model is a linear regression of six features engineered from six of the 10 starting features (x_1, x_2, x_3, x_4, x_6, and x_8), and the 3-feature LASSO model is a linear regression that uses three features engineered from five of the 10 starting features (x_1, x_2, x_3, x_6, and x_{10}). Unlike the ANN or RF regression models, the LASSO models could be easily implemented in an Excel spreadsheet. Therefore, for the comprehensive database used in this study or for a similar one (similar parameter ranges and distributions, as is the case of the testing set with respect to the entire database accordingly with Fig. 1), models with different levels of complexity noted should comply with the requirements stipulated in Table 3.

Table 3—Target performances for different model complexity levels

Requirements	Model complexity level	
	Complex ML models	Simplified models
Number of parameters	—	~3 to 6
V_{true}/V_{pred} mean ratio	0.99 to 1.01	0.98 to 1.02
COV	≤0.12	0.16 to 0.19
Training versus testing error margin	±20% of converging error	±10% of converging error

COMMENTS ON RELEVANT PARAMETERS

Among the starting features defined from Eq. (7) to (16), the ones used in the 6- and the 3-feature LASSO models defining the performance requirement for a

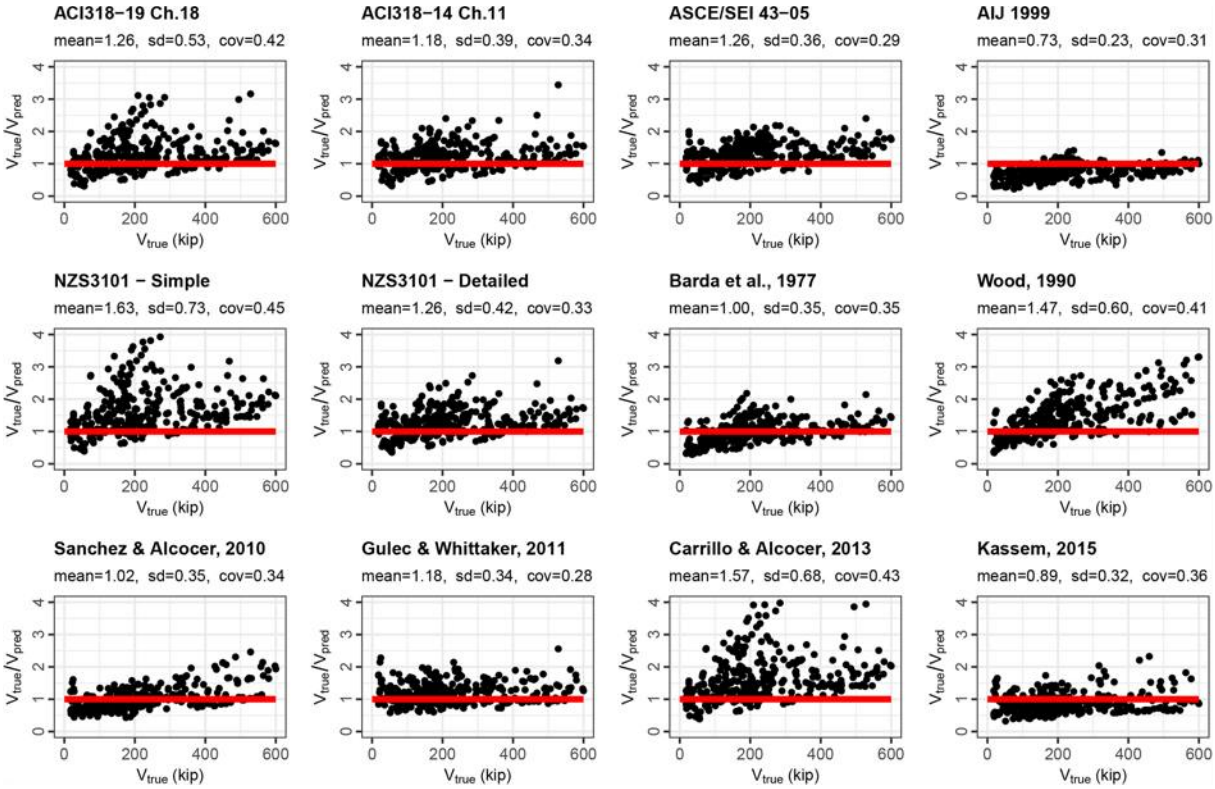

Fig. 14—Performance comparison of existing models using single, comprehensive database.

code-oriented equation are: $x_1 = \rho_{wh}(f_{ywh}/f_c')$, $x_2 = \rho_{wv}(f_{ywv}/f_c')$, $x_3 = \rho_{wbe}(f_{ybe}/f_c')$; $x_4 = 1 + P_u/(A_g f_c')$, $x_6 = M_u/(V_u l_w)$, $x_8 = t_w/h_w$, and $x_{10} = A_{be}/A_{cv}$. The only ones that are not listed herein are $x_5 = c/l_w$, $x_7 = t_w/l_w$, and $x_9 = h_w/l_w$. The absence of $x_5 = c/l_w$ can be attributed to the presence of $x_{10} = A_{be}/A_{cv}$ and $x_3 = \rho_{wbe}(f_{ybe}/f_c')$ because these two features can be used to represent the forces of compression or tension that are developed at the wall edges (and thus the neutral axis depth). The absence of $x_7 = t_w/l_w$ can be attributed to the presence of $x_8 = t_w/h_w$, which already accounts for the wall thickness and can be used together with $x_6 = M_u/(V_u l_w)$ to reproduce values that have a high correlation with $x_7 = t_w/l_w$. On the other hand, the absence of $x_9 = h_w/l_w$ might be surprising because some existing models used by codes or standards, or reported in the literature, use the wall aspect ratio (h_w/l_w) as a parameter to estimate wall shear strength (ACI 318-19 is one of those), whereas some other models use moment-to-shear span ratio ($M_u/(V_u l_w)$). In many of the tests reported in the literature (82% of the tests in the database used), these values are the same because the test involves a cantilever wall, fixed at the base, with a single point load applied near the top of the wall (that is, $M_u = V_u h_w$). For some tests reported in the literature, these values are not the same (for example, for a partial-height wall with an applied lateral load and moment at the top of the wall), and it is necessary to define an effective wall height $h_{w,eff}$ and wall aspect ratio ($h_{w,eff}/l_w$). As for the database used in this study, there are 32 specimens with a moment applied to the top of a partial height wall, three cantilever walls with two or more lateral loads, and 26 specimens tested with a double curvature configuration. For tests with multiple applied lateral loads (Cardenas and Magura 1972) or a moment applied at the top of the wall test (Segura and Wallace 2018), or both, the effective wall aspect ratio $h_{w,eff}$ was defined as M_u/V_u at the wall critical section (wall-foundation interface). If this approach is used, then identical results are produced from the wall test database using either h_w/l_w or $M_u/(V_u l_w)$. Thus, the constructed wall height was used to define $x_9 = h_w/l_w$ because that is how the aspect ratio has been defined in other studies. However, for the reasons given previously, it was expected that $x_6 = M_u/V_u l_w$ would be a better parameter to assess the shear strength of walls in buildings.

COMMENTS ON PERFORMANCES OF EXISTING MODELS

The performance of the existing models in codes and standards was evaluated using the common, comprehensive database gathered for this study (refer to Fig. 14). Upper limits (for example, $10\sqrt{f_c'}A_{cv}$ from the ACI 318-19 equation) were not considered to avoid introducing bias (conservatism) into the equations. Mean values varied from 0.73 to 1.63, and the COV values ranged from 0.28 to 0.45, and none of the existing models performed particularly well. The Gulec and Whittaker (2011) model had the least variation but with a mean value of 1.19. The Barda et al. (1977) model and the Sánchez-Alejandre and Alcocer (2010) model had mean values very close to 1.0, but COV values greater than 0.3. The ASCE 43-05 model (which is based on Barda et al. [1977]) resulted in a mean value of 1.26 and a COV of 0.29. None of these models satisfy the simplified model complexity level requirements stated in Table 3.

Also, none of the ML models analyzed in the literature review meet the target performance requirements for a complex model because the error is not small enough or because the difference between the training and testing error is too large. The proposed framework provides a means to better train ML models, particularly when the addressed problem is based on basic mechanical principles. Applying the proposed framework resulted in similar results for all ML model types studied at their respective optimum complexity level. The observation that essentially the same performance of complex ML models (ANN, RF) was achieved with a simple LASSO model in this study indicates that the size of databases used for many civil engineering problems may still be too small to benefit from the use of complex ML model types because a linear regression with the right features has similar performance, or even slightly better. This is aligned with the rule of thumb that says ML models should be trained on at least an order of magnitude more samples than input model parameters (Morgan and Bourlard 1989; Google Developers 2022; Gonfalonieri 2019).

SUMMARY AND CONCLUSIONS

This study proposes a framework to obtain different target model performance requirements for models with different complexity levels. The approach is particularly useful when addressing a mechanics-based problem with a small database. The framework leads to properly trained machine-learning (ML) models (more than one) that enable the quantification of the gap between the performance of existing models and the best performance that can be achieved with currently available data; this allows the user to make informed decisions on the value of developing improved models (with less complexity than the ML models).

The framework is demonstrated by addressing the problem of assessing wall shear strength using a comprehensive database of 340 walls reported to have failed in shear. This application highlights how the framework can be used to address issues such as: a) existing reinforced concrete (RC) wall shear strength equations (used in building codes or standards or proposed in the literature) perform very differently when evaluated with different databases and the performance is generally poor when evaluated against a common, comprehensive database (that is, high error, high variance, or both); b) existing ML models were trained without addressing the issue that most databases are comprised of tests conducted at less than full scale or do not represent the spectrum parameters for as-built walls in buildings; and c) existing models with higher complexity suggest good performance by showing that they are better than models with less complexity, which is an unfair comparison. Finally, where models of similar complexity are compared, it is insufficient to conclude that the model with best performance should be selected because a third model with equivalent complexity could perform better—that is, model performance requirements are needed to guide this assessment.

When applied to the problem of assessing RC wall shear strength, the framework shows that a systematic methodology that recognizes the mechanics of the problem, the availability of limited data (compared to those databases with thousands or millions of samples available in fields where ML shows its greats potential), and avoids training issues such as those highlighted in this paper, can produce simple models with performance as good as (or nearly as good as) complex ML models. Because all ML models considered in this study at their optimum complexity level (ANN, RF regression, and LASSO model) result in very similar predictive performance, underfitted models derived from the optimum LASSO model can be taken as a smooth relaxation away from the optimum when looking for target model performance (errors) that fulfill user requirements for less-complex models.

For the application and database used in this study, the framework establishes a V_{true}/V_{pred} mean ratio very close to 1.0 with a COV in the range of 0.16 to 0.19 as the performance requirements for a less-complex model that could be used in codes and standards to predict RC wall shear strength. In addition, the training and testing errors should be within a margin of ±10% of the converging error (at least, in terms of the error used in the optimization process and in terms of COV). For complex ML models, the mean ratio of V_{true}/V_{pred} should be very close to 1.0 with a COV of 0.12, or less, and training and testing errors should be within a margin of ±20% of the converging error. Similar findings are expected for other similar applications with similar size databases.

Finally, none of the assessed existing code-oriented models meet the target performance requirements for a simplified shear strength model, which suggests there is room for improvement in code equation predictive performance. Also, none of the ML models analyzed in the literature review meet the performance requirements for complex ML models, which reflects the impact of improper training.

AUTHOR BIOS

Matías Rojas-León *is a Practicing Engineer. He received his BS, professional engineer degree, and MS from the University of Chile, Santiago, Chile; and his PhD in structural/earthquake engineering from the University of California, Los Angeles (UCLA), Los Angeles, CA. His research interests include seismic design and behavior of reinforced concrete structures, machine learning (ML) and statistical approaches in structural engineering, laboratory testing, and structures equipped with anti-seismic devices.*

Saman A. Abdullah *is a Research Scholar in the Department of Civil and Environmental Engineering at UCLA and a Lecturer in the Department of Civil Engineering, College of Engineering, at the University of Sulaimani, Sulaymaniyah, Kurdistan, Iraq. He is a member of ACI Committee 374, Performance-Based Seismic Design of Concrete Buildings, and ACI Subcommittees ACI 318-H, Seismic Provisions; 318-1W, Wind Provisions; and 369-F, Retrofit. His research interests include seismic and wind design of concrete structures and laboratory testing.*

Kristijan Kolozvari *is an Associate Professor in the Department of Civil and Environmental Engineering at California State University, Fullerton, Fullerton, CA. He is a member of ACI Committee 374, Performance-Based Seismic Design of Concrete Buildings. His research interests include developing and applying innovative analytical tools for nonlinear analysis of reinforced concrete structures, performance-based seismic design, seismic retrofit, tall building behavior and design, and earthquake resiliency.*

John W. Wallace, *FACI, is a Professor of civil engineering at UCLA. He is Chair of ACI Subcommittee 318-H, Seismic Provisions, and a member of ACI Committees 318, Structural Concrete Building Code; 369, Seismic Repair and Rehabilitation; and 374, Performance-Based Seismic Design of Concrete Buildings. His research interests include the response and design of buildings and bridges to earthquake actions, laboratory and field testing of structural components and systems, and seismic structural health monitoring.*

ACKNOWLEDGMENTS

M. Rojas-León acknowledges the support from the National Agency for Research and Development (ANID) Scholarship Program/DOCTORADO BECAS CHILE/2019-72200499. Any opinions, findings, and conclusions

expressed in this material are those of the authors and do not necessarily reflect those of the sponsors.

REFERENCES

Abdullah, S. A., 2019, "Reinforced Concrete Structural Walls: Test Database and Modeling Parameters," PhD dissertation, University of California, Los Angeles, Los Angeles, CA, 304 pp.

Abdullah, S. A., and Wallace, J. W., 2018, "UCLA-RC Walls Database for Reinforced Concrete Structural Walls," *Proceedings of the 11th National Conference in Earthquake Engineering*, Los Angeles, CA.

Abdullah, S. A., and Wallace, J. W., 2021, "New Nonlinear Modeling Parameters and Acceptance Criteria for RC Structural Walls," The 2021 Annual Conference of Los Angeles Tall Buildings Structural Design Council, Nov. 12, Los Angeles, CA.

ACI Committee 318, 2008, "Building Code Requirements for Structural Concrete (ACI 318-08) and Commentary (ACI 318R-08)," American Concrete Institute, Farmington Hills, MI, 473 pp.

ACI Committee 318, 2011, "Building Code Requirements for Structural Concrete (ACI 318-11) and Commentary (ACI 318R-11)," American Concrete Institute, Farmington Hills, MI, 503 pp.

ACI Committee 318, 2014, "Building Code Requirements for Structural Concrete (ACI 318-14) and Commentary (ACI 318R-14)," American Concrete Institute, Farmington Hills, MI, 520 pp.

ACI Committee 318, 2019, "Building Code Requirements for Structural Concrete (ACI 318-19) and Commentary (ACI 318R-19) (Reapproved 2022)," American Concrete Institute, Farmington Hills, MI, 624 pp.

AIJ, 1999, "Structural Design Guidelines for Reinforced Concrete Buildings," Architectural Institute of Japan, Tokyo, Japan.

Alzubi, J.; Nayyar, A.; and Kumar, A., 2018, "Machine Learning from Theory to Algorithms: An Overview," *Journal of Physics: Conference Series*, 2nd National Conference on Computational Intelligence (NCCI 2018), Bangalore, India, IOP Science, V. 1142, pp. 012012

Amazon Web Services, Inc., 2016, "Amazon Machine Learning Developer Guide," AWS, Seattle, WA.

ASCE/SEI 43-05, 2005, "Seismic Design Criteria for Structures, Systems, and Components in Nuclear Facilities," American Society of Civil Engineers, Reston, VA.

Barda, F.; Hanson, J. M.; and Corley, W. G., 1977, "Shear Strength of Low-Rise Walls with Boundary Elements," *Reinforced Concrete Structures in Seismic Zones*, SP-53, American Concrete Institute, Farmington Hills, MI, pp. 149-202.

Barret, J., 1974, "The Coefficient of Determination – Some Limitations," *The American Statistician*, V. 28, No. 1, pp. 19-20.

Breiman, L., 2001, "Random Forests," *Machine Learning*, V. 45, No. 1, pp. 5-32. doi: 10.1023/A:1010933404324

Bzdok, D.; Altman, N.; and Krzywinski, M., 2018, "Points of Significance: Statistics Versus Machine Learning," *Nature Methods*, V. 15, No. 4, pp. 233-234. doi: 10.1038/nmeth.4642

CSA A23.3-14, 2014, "Design of Concrete Structures," CSA Group, Toronto, ON, Canada.

Cardenas, A. E., and Magura, D. D., 1972, "Strength of High-Rise Shear Walls-Rectangular Cross Section," *Special Publication (American Philosophical Society)*, V. 36, pp. 119-150.

Carrillo, J., and Alcocer, S., 2013, "Shear Strength of Reinforced Concrete Walls for Seismic Design of Low-Rise Housing," *ACI Structural Journal*, V. 110, No. 3, May-June, pp. 415-426.

Chen, X. L.; Fu, J. P.; Yao, J. L.; and Gan, J. F., 2018, "Prediction of Shear Strength for Squat RC Walls Using a Hybrid ANN-PSO Model," *Engineering with Computers*, V. 34, No. 2, pp. 367-383. doi: 10.1007/s00366-017-0547-5

Dey, A., 2016, "Machine Learning Algorithms: A Review," *International Journal of Science and Research*, V. 7, No. 3, pp. 1174-1179.

EN 1998-1:2004, 2004, Eurocode 8, "Design of Structures for Earthquake Resistance, Part 1: General Rules, Seismic Actions and Rules for Buildings," European Committee for Standardization, Brussels, Belgium.

Feng, D. C.; Wang, W. J.; Mangalathu, S.; and Taciroglu, E., 2021, "Interpretable XGBoost-SHAP Machine-Learning Model for Shear Strength Prediction of Squat RC Walls," *Journal of Structural Engineering*, ASCE, V. 147, No. 11, p. 04021173. doi: 10.1061/(ASCE)ST.1943-541X.0003115

Gonfalonieri, A., 2019, "5 Ways to Deal with the Lack of Data in Machine Learning," KDnuggets, https://www.kdnuggets.com/2019/06/5-ways-lack-data-machine-learning.html. (last accessed Nov. 2, 2023)

Google Developers, 2022, "The Size and Quality of a Data Set," Google, Mountain View, CA, https://developers.google.com/machine-learning/data-prep/construct/collect/data-size-quality. (last accessed Nov. 2, 2023)

Gulec, C., and Whittaker, A. S., 2011, "Empirical Equations for Peak Shear Strength of Low Aspect Ratio Reinforced Concrete Walls," *ACI Structural Journal*, V. 108, No. 1, Jan.-Feb., pp. 80-89.

Gulec, C. K.; Whittaker, A. S.; and Bozidar Stojadinovic, B., 2009, "Peak Shear Strength of Squat Reinforced Concrete Walls with Boundary Barbells or Flanges," *ACI Structural Journal*, V. 106, No. 3, May-June, pp. 368-377.

Hoerl, A. E., and Kennard, R. W., 1970, "Ridge Regression: Biased Estimation for Nonorthogonal Problems," *Technometrics*, V. 12, No. 1, pp. 55-67. doi: 10.1080/00401706.1970.10488634

Höge, M.; Wöhling, T.; and Nowak, W., 2018, "A Primer for Model Selection: The Decisive Role of Model Complexity," *Water Resources Research*, V. 54, No. 3, pp. 1688-1715. doi: 10.1002/2017WR021902

Hwang, S.-J., and Lee, H.-J., 2002, "Strength Prediction for Discontinuity Regions by Softened Strut-and-Tie Model," *Journal of Structural Engineering*, ASCE, V. 128, No. 12, pp. 1519-1526. doi: 10.1061/(ASCE)0733-9445(2002)128:12(1519)

Kassem, W., 2015, "Shear Strength of Squat Walls: A Strut-and-Tie Model and Closed-Form Design Formula," *Engineering Structures*, V. 84, pp. 430-438. doi: 10.1016/j.engstruct.2014.11.027

Keshtegar, B.; Nehdi, M. L.; Trung, N.-T.; and Kolahchi, R., 2021, "Predicting Load Capacity of Shear Walls Using SVR–RSM Model," *Applied Soft Computing*, V. 112, Nov., p. 107739. doi: 10.1016/j.asoc.2021.107739

Kim, J.-H., and Park, H.-G., 2020, "Shear and Shear-Friction Strengths of Squat Walls with Flanges," *ACI Structural Journal*, V. 117, No. 6, Nov., pp. 269-280. doi: 10.14359/51728075

Li, H., and Li, B., 2002, "Experimental Study on Seismic Restoring Performance of Reinforced Concrete Shear Walls," *Journal of Building Structures*, V. 32, No. 5, pp. 728-732.

Looi, D. T. W., and Su, R. K. L., 2017, "Predictive Seismic Shear Capacity of Rectangular Squat RC Shear Walls in Flexural and Shear Zones," 16th World Conference on Earthquake Engineering, Santiago, Chile, pp. 9-13.

Moradi, M., and Hariri-Ardebili, M., 2019, "Developing a Library of Shear Walls Database and the Neural Network Based Predictive Meta-Model," *Applied Sciences*, V. 9, No. 12, p. 2562. doi: 10.3390/app9122562

Morgan, N., and Bourlard, H., 1989, "Generalization and Parameter Estimation in Feedforward Nets: Some Experiments," *Advances in Neural Information Processing Systems*, pp. 630-637

NZS 3101-06, 1995, "New Zealand Concrete Structures Standards," Standards New Zealand, Wellington, New Zealand.

Rojas-León, M., 2022, "Framework to Set Model Performance Requirements Applied to the RC Wall Shear Strength Problem and Proposition of New Code-Oriented Equation," PhD dissertation, University of California, Los Angeles, Los Angeles, CA, 260 pp.

Sánchez-Alejandre, A., and Alcocer, S., 2010, "Shear Strength of Squat Reinforced Concrete Walls Subjected to Earthquake Loading – Trends and Models," *Engineering Structures*, V. 32, No. 8, pp. 2466-2476. doi: 10.1016/j.engstruct.2010.04.022

Segal, M., and Xiao, Y., 2011, "Multivariate Random Forests," *Wiley Interdisciplinary Reviews. Data Mining and Knowledge Discovery*, V. 1, No. 1, pp. 80-87. doi: 10.1002/widm.12

Segura, C. L., and Wallace, J. W., 2018, "Seismic Performance Limitations and Detailing of Slender Reinforced Concrete Walls," *ACI Structural Journal*, V. 115, No. 3, May, pp. 849-859. doi: 10.14359/51701918

Tanaka, J. S., 1987, "How Big Is Big Enough?: Sample Size and Goodness of Fit in Structural Equation Models with Latent Variables," *Child Development*, V. 58, No. 1, pp. 134-146. doi: 10.2307/1130296

Tibshirani, R., 1996, "Regression Shrinkage and Selection via the Lasso," *Journal of the Royal Statistical Society*, V. 58, No. 1, pp. 267-288.

Wood, S. L., 1990, "Shear Strength of Low-Rise Reinforced Concrete Walls," *ACI Structural Journal*, V. 87, No. 1, Jan.-Feb., pp. 99-107.

Zhang, C., and Ma, Y., 2012, *Ensemble Machine Learning: Methods and Applications*, Springer.

Zheng, S.; Qin, Q.; Yang, W.; Gan, C.; Zhang, Y.; and Ding, S., 2015, "Experimental Research on the Seismic Behaviors of Squat RC Shear Walls Under Offshore Atmospheric Environment," *Journal of Harbin Institute of Technology*, V. 47, No. 12, pp. 64-69. (in Chinese)

Zou, H., and Hastie, T., 2005, "Regularization and Variable Selection via Elastic Net," *Journal of the Royal Statistical Society. Series B, Statistical Methodology*, V. 67, No. 2, pp. 301-320. doi: 10.1111/j.1467-9868.2005.00503.x

ACI STRUCTURAL JOURNAL TECHNICAL PAPER

Title No. 121-S07

New Equations to Estimate Reinforced Concrete Wall Shear Strength Derived from Machine Learning and Statistical Methods

by Matías Rojas-León, John W. Wallace, Saman A. Abdullah, and Kristijan Kolozvari

Wall shear-strength equations reported in the literature and used in building codes are assessed using a comprehensive database of reinforced concrete wall tests reported to have failed in shear. Based on this assessment, it is concluded that mean values varied significantly, and coefficients of variation were relatively large (>0.28) and exceeded the target error for a code-oriented equation defined in a companion paper (Rojas-León et al. 2024). Therefore, a methodology employing statistical and machine-learning approaches was used to develop a new equation with a format similar to that currently used in ACI 318-19. The proposed equation applies to walls with rectangular, barbell, and flanged cross sections and includes additional parameters not considered in ACI 318-19, such as axial stress and quantity of boundary longitudinal reinforcement. Parameter limits—for example, on wall shear and axial stress—and an assessment of the relative contributions to shear strength are also addressed.

Keywords: code equation; machine learning (ML); shear strength; shear wall; statistics; structural wall.

INTRODUCTION

In ACI 318-19 (ACI Committee 318 2019) Eq. (18.10.4.1), wall nominal shear strength (V_n) is computed using a $V_n = V_c + V_s$ format, where V_c and V_s are the concrete and reinforcement contributions to nominal shear strength, respectively. Other U.S. standards and building codes in other countries typically use the same format; however, the parameters considered for concrete and reinforcement contributions differ. For example, the expressions used in NZS 3101:2006 (2006) and ASCE/SEI 43-05 (2005) consider the influence of axial load on V_c, whereas ACI 318 does not, and the detailed model of NZS 3101:2006 uses the shear-span ratio ($M_u/(Vl_w)$), whereas ACI 318 uses the wall aspect ratio (h_w/l_w) to estimate V_c, where h_w and l_w are the wall total height and length, respectively. The ASCE/SEI 43-05 model considers the influence of vertical web reinforcement on V_s, whereas the ACI 318 model only considers the influence of web horizontal reinforcement. These predictive equations, as well as equations proposed in the literature (Gulec et al. 2009; Sánchez-Alejandre and Alcocer 2010; Carrillo and Alcocer 2013; Kassem 2015), show significant variance when used to predict the wall shear strength of specimens from various databases reported in the literature that were not used to develop the equations, including the comprehensive database of this study.

Machine-learning (ML) models, which have become popular in recent years, typically demonstrate excellent predictive power; however, these models are often complex and challenging to interpret, rendering them unsuitable for adoption in building codes (for example, ACI 318) or standards (for example, ASCE/SEI 41). Further, Rojas-León et al. (2024) identified several drawbacks in the ML models used to predict the shear strength of reinforced concrete (RC) walls (Chen et al. 2018; Moradi and Hariri-Ardebili 2019; Keshtegar et al. 2021; Feng et al. 2021) and developed a framework to address these issues by establishing performance requirements for structural component models, as shown in Table 1 for wall shear stress.

Rojas-León et al. (2024) evaluated various models reported in the literature (Gulec et al. 2009; Sánchez-Alejandre and Alcocer 2010; Carrillo and Alcocer 2013; Kassem 2015) and observed that the mean and coefficient of variation (COV) of true-to-predicted shear strength values (V_{true}/V_{pred}) changed and increased, respectively, sometimes substantially, when different databases were used to evaluate the same model. Reasons for these observations include: a) the number of wall tests in each database; b) the type of tests included in each database (for example, a database of walls with rectangular cross sections only versus one with walls with rectangular and flanged cross sections); and c) the level of detail included in the databases. In addition, the wall aspect ratio (h_w/l_w) was typically used to determine which tests were included in each database (for example, $h_w/l_w < 1.5$ or 2.0); however, the study by Abdullah and Wallace (2021) indicates that h_w/l_w is not the best indicator of the expected wall failure mode. Therefore, databases used to develop the models reported in the literature often included walls that did not fail in shear (that is, exhibited a flexural failure mode). More detailed information about existing models and associated drawbacks is available in Rojas-León (2022) and Rojas-León et al. (2024).

Based on these observations, the same data set of 340 wall specimens with reported shear failure modes used by Rojas-León (2022) and Rojas-León et al. (2024) (obtained from the database of more than 1100 wall tests gathered by Abdullah [2019]) was used to assess the existing models. The performance of the existing models was generally poor, with mean

---

ACI Structural Journal, V. 121, No. 1, January 2024.

MS No. S-2022-408.R1, doi: 10.14359/51739187, received August 1, 2023, and reviewed under Institute publication policies. Pertinent discussion including author's closure, if any, will be published ten months from this journal's date if the discussion is received within four months of the paper's print publication.

Table 1—Requirements for code-oriented wall shear-strength model

Model characteristics	Requirement
Number of variables	~3 to 6
Range of mean V_{true}/V_{pred}*	0.98 to 1.02
Range of COV of V_{true}/V_{pred}	0.16 to 0.19
Training versus testing error margin†	±10% of converging error

*V_{true} is true shear strength measured in a test. V_{pred} is predicted shear strength obtained using an equation ($V_{pred} = V_n$).

†Inclusion of other error indicators, in addition to one used in optimization process, is strongly recommended to assess this requirement.

Table 2—Performance of existing models using single, comprehensive database

	Statistics for V_{true}/V_{pred}		
Model	Mean	Median	COV
ACI 318-19, Chapter 18	1.26	1.17	0.42
ACI 318-11, Chapter 11	1.18	1.12	0.34
ASCE/SEI 43-05	1.26	1.25	0.29
AIJ 1999	0.73	0.74	0.31
NZS 3101:2006 – Simple	1.63	1.46	0.45
NZS 3101:2006 – Detailed	1.26	1.21	0.33
Barda et al. (1977)	1.00	1.00	0.35
Wood (1990)	1.47	1.41	0.41
Sánchez-Alejandre and Alcocer (2010)	1.02	0.95	0.34
Gulec and Whittaker (2011)	1.18	1.12	0.28
Carrillo and Alcocer (2013)	1.57	1.44	0.43
Kassem (2015)	0.89	0.83	0.36

values that often varied substantially from 1.00 (ranging from 0.73 to 1.63) and large COV values (ranging from 0.28 to 0.45), as shown in Table 2. Further, none of the existing models met the target performance requirements given in Table 1, indicating that there is potential to develop better models.

This study presents code-oriented equations to estimate RC wall shear strength that addresses this need. The equations were developed by applying a methodology that implements ML and classical statistics approaches in the training process. The approach begins with a model (starting model) that is more complex than the desired model (and thus it is expected to have a smaller error than the target error), and then a reduction (or shrinking) process is applied to derive a simpler model that satisfies the target performance requirements. This approach was applied using the same database of 340 walls with symmetrical cross sections (rectangular, barbell, and H-shaped) used by Rojas-León (2022) and Rojas-León et al. (2024), and additional studies were conducted to extend the use of the proposed equation to walls with asymmetrical cross sections (L- and T-shaped). In addition, two sets of companion tests were identified from the database to enable comparisons of the relative contribution of V_c and V_s for the ACI 318-19 and proposed models. Finally, the database was used to establish an upper limit on nominal wall shear stress and upper and lower limits on wall axial stress, as well as a preliminary study to establish that the use of a strength reduction factor of 0.75 is most likely appropriate to meet the probability of failure criterion in ASCE/SEI 7-16 (2017) Table 1.3-2.

RESEARCH SIGNIFICANCE

Because the equation used in ACI 318-19 to determine wall shear strength is conservative and inaccurate, a new wall shear strength equation with a true-to-predicted mean ratio of 1.00 and a COV = 0.17 is proposed to meet the target performance objectives for an equation appropriate for adoption in building codes and standards. The proposed equation includes additional variables known to influence wall shear strength, increases the upper limit on shear stress for walls with a compression flange, enables a more uniform level of safety, and potentially allows for a more economical design of buildings with core walls.

APPROACH TO DEVELOPING CODE-APPROPRIATE EQUATION

The approach combines ML and statistical methods to shrink (simplify) an equation (starting equation) with a code-oriented format until a defined target error is achieved. Once a code-appropriate equation was developed using the database of walls with symmetrical cross sections, additional studies were conducted to determine modifications needed to apply the equation to walls with asymmetrical cross sections (for example, L- and T-shaped) because these wall shapes are commonly used; however, insufficient test data existed for these wall cross sections to justify their inclusion in the broader ML and statistical studies. The following steps describe the details of the approach.

Step 1: Collection and preparation of test data

In this study, the same database of 340 symmetrical walls reported to have failed in shear used by Rojas-León et al. (2024) is used (refer to that paper's Appendix), which has already been rigorously reviewed to filter out tests that do not meet predefined criteria or where inconsistent results were reported. The data set was split into a training set of 272 samples (80%) and a testing set of 68 samples (20%). A second testing set of walls with asymmetrical cross sections—with 13 out of the 20 samples corresponding to specimens identified with a T-shaped, L-shaped, half-barbell-shaped (walls with a column at one end), or wing-shaped (columns with a wing wall on each side) cross sections in the original (larger) data set (Rojas-León et al. 2024)—was also part of this study. This second subset was studied separately because 13 tests is a small number compared to 340 tests, and thus the inherent differences associated with these tests would be overlooked in the training process if included as part of the larger training and testing data sets. Because the use of wing walls is not common in

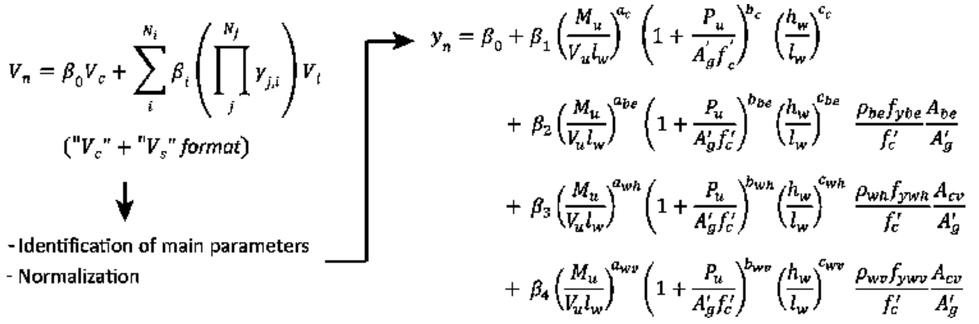

$$V_n = \beta_0 V_c + \sum_{i}^{N_i} \beta_i \left(\prod_{j}^{N_j} \gamma_{j,i} \right) V_i$$

$$\begin{aligned} y_n = \beta_0 &+ \beta_1 \left(\frac{M_u}{V_u l_w}\right)^{a_c} \left(1 + \frac{P_u}{A_g' f_c'}\right)^{b_c} \left(\frac{h_w}{l_w}\right)^{c_c} \\ &+ \beta_2 \left(\frac{M_u}{V_u l_w}\right)^{a_{be}} \left(1 + \frac{P_u}{A_g' f_c'}\right)^{b_{be}} \left(\frac{h_w}{l_w}\right)^{c_{be}} \frac{\rho_{be} f_{ybe}}{f_c'} \frac{A_{be}}{A_g'} \\ &+ \beta_3 \left(\frac{M_u}{V_u l_w}\right)^{a_{wh}} \left(1 + \frac{P_u}{A_g' f_c'}\right)^{b_{wh}} \left(\frac{h_w}{l_w}\right)^{c_{wh}} \frac{\rho_{wh} f_{ywh}}{f_c'} \frac{A_{cv}}{A_g'} \\ &+ \beta_4 \left(\frac{M_u}{V_u l_w}\right)^{a_{wv}} \left(1 + \frac{P_u}{A_g' f_c'}\right)^{b_{wv}} \left(\frac{h_w}{l_w}\right)^{c_{wv}} \frac{\rho_{wv} f_{ywv}}{f_c'} \frac{A_{cv}}{A_g'} \end{aligned}$$

Fig. 1—Definition of starting equation.

U.S. practice, and the Japanese Code (AIJ 1999) includes detailed recommendations on determining wing-wall shear strength, the seven wing-wall samples (corresponding to seven specimens) were excluded from the second testing set. The remaining subset of 13 samples is derived from 11 specimens; two of the tests reported failures in both directions of loading (specimen HW2 tested by Kabeyasawa et al. [1996] and specimen SWBT-L40 tested by Bae et al. [2010]); therefore, the two tests generate four samples.

Step 2: Identification of relevant parameters and starting equation

This step involves identifying the relevant parameters based on a literature review and then normalizing these parameters (for example, using shear stress versus shear strength because most tests were done on reduced-scale specimens). In this case, the parameters considered in the starting model are the relevant features used in the simplest ML models reported by Rojas-León et al. (2024) when applying the proposed target performance framework to the problem of assessing wall shear strength, that is, the six- and three-feature Least Absolute Shrinkage and Selection Operator (LASSO) models: $\rho_{wh}(f_{ywh}/f_c')$, $\rho_{wv}(f_{ywv}/f_c')$, $\rho_{be}(f_{ybe}/f_c')$, $1 + (P_u/(A_g'f_c'))$, $M_u/(V_u l_w)$, t_w/h_w, and A_{be}/A_{cv} (these variables are defined in the next paragraph). The selected parameters include material-related parameters (V_i) and other parameters ($\gamma_{j,i}$):

- Material-related parameters (V_i): concrete strength and correlated cross-sectional area (A_g', f_c'), quantity and yield stress of longitudinal reinforcement at the wall boundary in tension (ρ_{be}, f_{ybe}), quantity and yield stress of horizontal web reinforcement (ρ_{wh}, f_{ywh}), and quantity and yield stress of vertical web reinforcement (ρ_{wv}, f_{ywv})
- Other parameters ($\gamma_{j,i}$): axial load ratio ($P_u/(A_g'f_c')$) and shear-span ratio ($M_u/(V_u l_w)$) (or aspect ratio h_w/l_w)

where f_c' is the specified compressive strength of concrete; ρ_{be} is the boundary region longitudinal reinforcement ratio defined as A_{sb}/A_{be}; f_{ybe} is the specified yield strength of the boundary region longitudinal reinforcement; ρ_{wh} and f_{ywh} are the ratio and specified yield strength of the horizontal web reinforcement, respectively; ρ_{wv} and f_{ywv} are the ratio and specified yield strength of the vertical web reinforcement, respectively; P_u, M_u, and V_u are the factored (or test) axial load, moment, and shear, respectively; l_w is the wall length in the direction of the applied shear force; h_w is the total wall height; A_{be} is the cross-sectional area bounding the longitudinal reinforcement at a wall boundary; A_{cv} is the cross-sectional area bounded by the wall length and the web thickness (t_w); A_g' is the wall web area (A_{cv}) plus the area of the effective overhanging flange width (if present) at the edge (or boundary) of the wall subjected to compressive stresses due to overturning moment; and A_{sb} is the area of concentrated longitudinal tension reinforcement at a wall boundary within $0.20l_w$ from the wall edge, including the area of longitudinal reinforcement located within an effective tension flange width, if it exists. If wall web longitudinal reinforcement is uniformly distributed, then A_{sb} includes the area of longitudinal reinforcement within $0.20l_w$ from the wall edge, as well as longitudinal reinforcement within the effective flange.

These parameters are rearranged into an equation that follows the "$V_c + V_s$" (concrete contribution plus steel contribution) format. The other parameters ($\gamma_{j,i}$) are normalized unitless weights that multiply each of the material parameters (V_i) terms, which have units of force (for example, kN, kip, and so on). Figure 1 shows the general form of the equation, which is used as the starting equation that is then reduced in the shrinking process. The starting equation is normalized to avoid the many potential issues that could arise during the training process (Rojas-Leon et al. 2024). It is noted that this normalization process is based on the physics of the problem—that is, different than the normalization or scaling concepts used in statistics, which are still required prior to training a model. The predicted variable is $y_{true} = V_{true}/(A_g'f_c')$, which is slightly different from the one used by Rojas-León et al. (2024), where A_g was used in the normalization; the reason for this is described later.

It is necessary to define an effective wall height $h_{w,eff}$ for wall tests with multiple lateral loads applied over the wall test specimen height or for walls with a moment applied at the top of the wall (sometimes referred to as a wall panel test). A common approach is to use $h_{w,eff} = M_u/V_u$ (Segura and Wallace 2018) at the wall-foundation interface; therefore, for most of the tests in the database (82%), with a single-point load applied near the top of a fixed-based cantilever wall, $h_{w,eff} = h_w$. With this definition, the same predictive equation is achieved using either $h_{w,eff}/l_w$ or $M_u/(V_u l_w)$. In this study, $M_u/(V_u l_w)$ is used because, for a real building, use of h_w/l_w versus $M_u/(V_u l_w)$ would produce different results. This issue is addressed later.

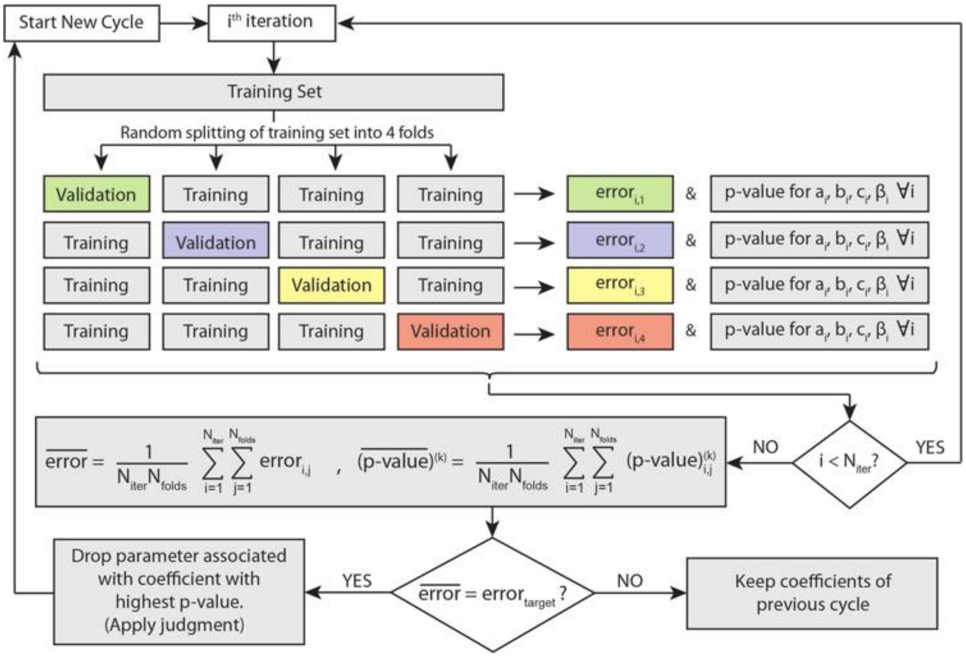

Fig. 2—Algorithm implementing four-fold CV to shrink starting equation.

Step 3: Training process, equation simplification, and performance verification

The unknown coefficients to be evaluated and fitted are a_i, b_i, c_i, and β_i of the normalized equation shown in Fig. 1. The iterative k-fold cross-validation (CV) method implemented by Rojas-León et al. (2024) is used. In this case, in addition to keeping track of the model error, p-values are also recorded because they indicate the statistical significance of each model variable; the higher the p-value, the less significant the variable is (Murtaugh 2014). The algorithm shown in Fig. 2 is implemented to shrink (simplify) the starting equation until the model error meets the target error (refer to Table 1).

The training process produces p-values for each a_i, b_i, c_i, and β_i coefficient, whereas the model error is computed from model predictions using the validation data set. Although root-mean-square error (RMSE) is used in the optimization process, the mean and COV of the true-to-predicted ratio (V_{true}/V_{pred}) are also computed. Here, k = four folds and $N_{iter} = 50$ iterations were used; therefore, once the iterative process is completed, $N_{iter} \times k = 200$ errors and $N_{iter} \times k = 200$ p-values for each a_i, b_i, c_i, and β_i coefficient are obtained. The average error and p-value for each coefficient are calculated. If the average error is lower than the target error, the variable associated with the largest average p-value is dropped. Judgment is applied so that the shrinking process is gradual; for example, if the p-values of β_4 and b_{wv} are the first and second highest, respectively, the parameter associated with b_{wv} is the one that is dropped because it results in a more gradual equation shrinking. p-values were used instead of a more automated ML method because it is simple and allows for the application of judgment before shrinking the model after each cycle.

The starting equation (with all the parameters) had an average RMSE of 0.0178 and a mean and COV of the true-to-predicted ratio of 1.00 and 0.152, respectively. The resulting equation at the end of the shrinking process, given in Eq. (1), has an average RMSE of 0.0188 and a mean and COV of the true-to-predicted ratio of 1.00 and 0.161, respectively. Because the nonlinear regressions resulted in very similar values for a_{be} and a_{wh} (after the axial load ratio parameters associated with coefficients b_{be} and b_{wh} were both dropped), these values were both set equal to a_s ($a_{be} = a_s$; $a_{wh} = a_s$).

$$y_n = \beta_0 + \beta_1\left(\frac{M_u}{V_u l_w}\right)^{a_c}\left(1 + \frac{P_u}{A_g' f_c'}\right)^{b_c} + \left(\frac{M_u}{V_u l_w}\right)^{a_s}\left[\beta_2\frac{\rho_{be} f_{ybe}}{f_c'}\frac{A_{be}}{A_g'} + \beta_3\frac{\rho_{wh} f_{ywh}}{f_c'}\frac{A_{cv}}{A_g'}\right] \quad (1)$$

Results of the nonlinear regressions also produce fitted values for the a_c, b_c, a_s, and β coefficients of Eq. (1). However, these fitted values (for example, $a_c = –0.404$, $b_c = 2.808$, $a_s = –0.339$, $\beta_0 = –0.060$, $\beta_1 = –0.097$, $\beta_2 = 0.384$, and $\beta_3 = 0.344$) are not commonly used (or typical) of a code equation; therefore, the algorithm shown in Fig. 3 with $k = 4$ and $N_{iter} = 50$ was implemented to simplify the equation.

This process involved selecting a range of values around the fitted values for a_c, b_c, and a_s, and only calibrating β_i coefficients by using linear regression for each combination of (a_c^*, b_c^*, a_s^*). The (a_c^*, b_c^*, a_s^*) values associated with the minimum average error are selected for use in the final equation. Judgment can be applied in this process—that is, the error obtained for different combinations of a_c, b_c, and a_s values might be similar (and meet the target error); therefore, the most "convenient" values can be selected. Finally, the coefficients β_0, β_1, β_2, and β_3 are defined based on the average values obtained from the $N_{iter} \times k = 200$ linear regressions associated with only the selected (a_c^*, b_c^*, a_s^*). The resulting equation is given in Eq. (2)

$$V_n = \alpha_c A_g' f_c' + \alpha_s(\rho_{sb} f_{ysb} + \rho_{wh} f_{ywh})A_{cv} \quad (2)$$

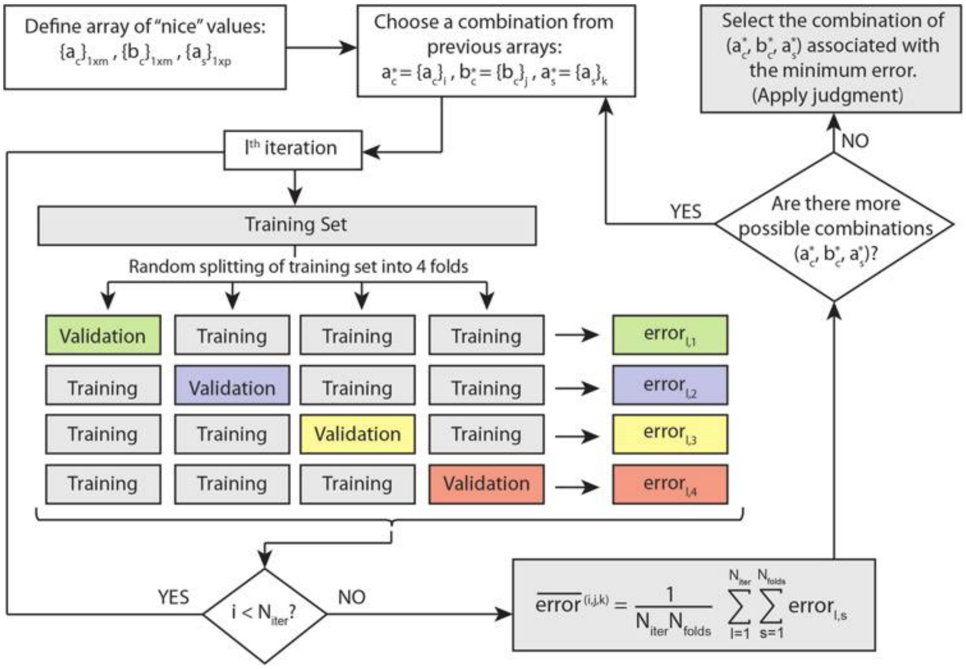

Fig. 3—Algorithm to determine optimum closed values for $\mathrm{a_c}$, $\mathrm{b_c}$, *and* $\mathrm{a_s}$ *coefficients.*

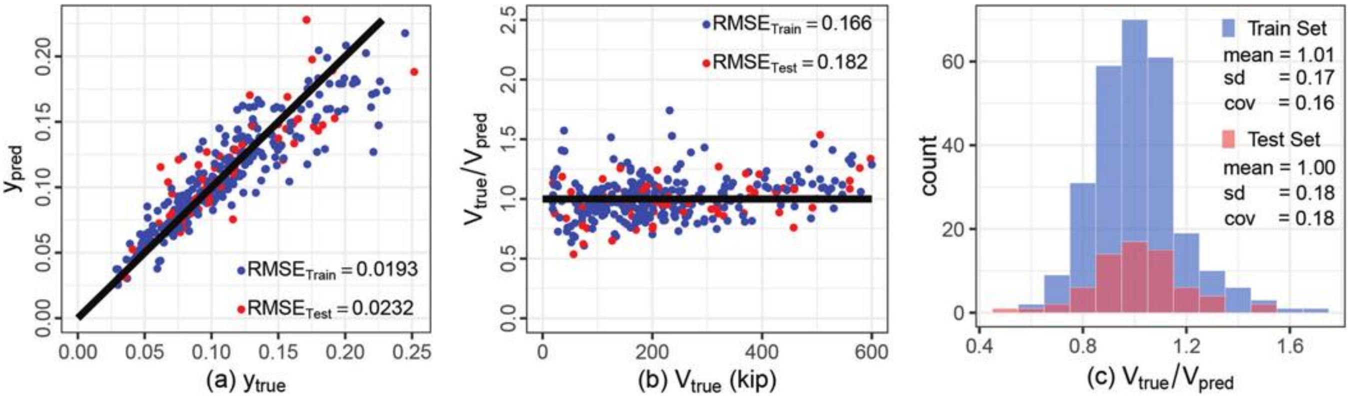

Fig. 4—Performance of Eq. (2) against wall tests with symmetrical cross sections.

where ρ_{sb} is longitudinal reinforcement at the tension edge defined as A_{sb}/A_{cv}; and the α_c and α_s coefficients are

$$\alpha_c = \frac{1}{100}\left(9\frac{\left(1+\dfrac{P_u}{A_g' f_c'}\right)^3}{\left(\dfrac{M_u}{V_u l_w}\right)^{1/3}} - 6\right), \quad \alpha_s = \frac{2}{5\left(\dfrac{M_u}{V_u l_w}\right)^{1/3}} \quad (3)$$

The performance of Eq. (2) is summarized in Fig. 4, where it is verified that similar values of RMSE, mean, and COV are obtained for both the training and testing sets and the different error indicators meet the requirements for a code-oriented model given in Table 1.

It is noted that it would be a relatively simple process to develop an even further simplified model (with a higher error) that could be used to simplify design for cases where wall shear demands are not expected to control or for preliminary design. Equation (4), along with the coefficients defined in Eq. (5), is a simplified equation whose error (refer to Fig. 5) is still smaller than all the existing equations evaluated by Rojas-León et al. (2024) (refer to Table 2). The lower complexity level of this equation comes from the exclusion of the axial load and the removal of one term.

$$V_n = \alpha_c A_g' f_c' + \alpha_s \rho_{wh} f_{ywh} A_{cv} \quad (4)$$

$$\alpha_c = \frac{\left(\dfrac{\rho_{sb} f_{ysb}}{f_c'}\right)^{1/4}}{6\left(\dfrac{M_u}{V_u l_w}\right)^{1/2}}, \quad \alpha_s = \frac{2}{3}\left(\frac{\rho_{sb} f_{ysb}}{f_c'}\right)^{1/3} \quad (5)$$

Step 4: Assessment of walls with asymmetrical cross sections

The entire methodology was first applied using A_g, and a model similar to that given in Eq. (2) and (3) was obtained. However, the use of A_g could not easily be applied to walls with asymmetrical cross-sectional shapes because the longitudinal reinforcement at the wall boundaries and the concrete area in compression differ depending on the loading direction.

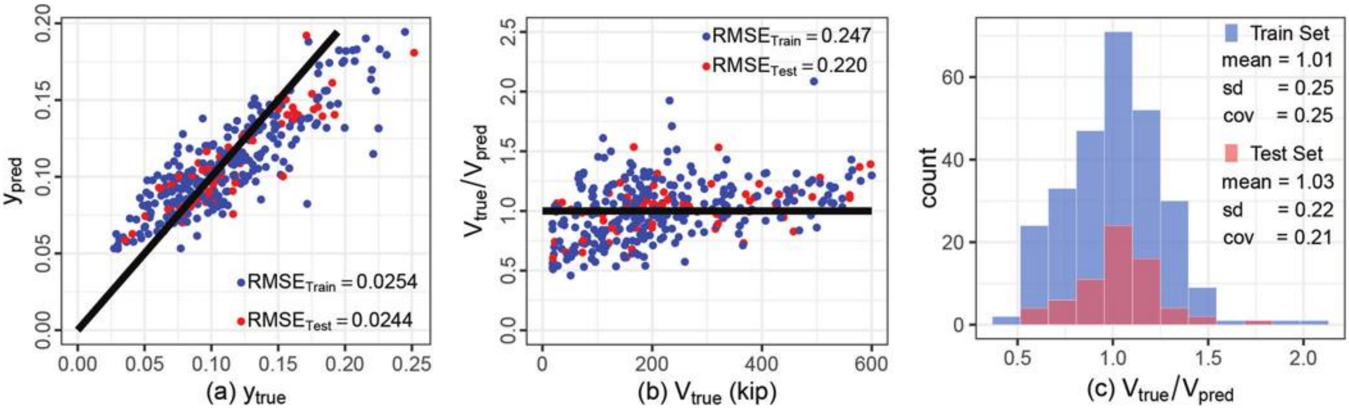

Fig. 5—Performance of Eq. (4) against wall tests with symmetrical cross sections.

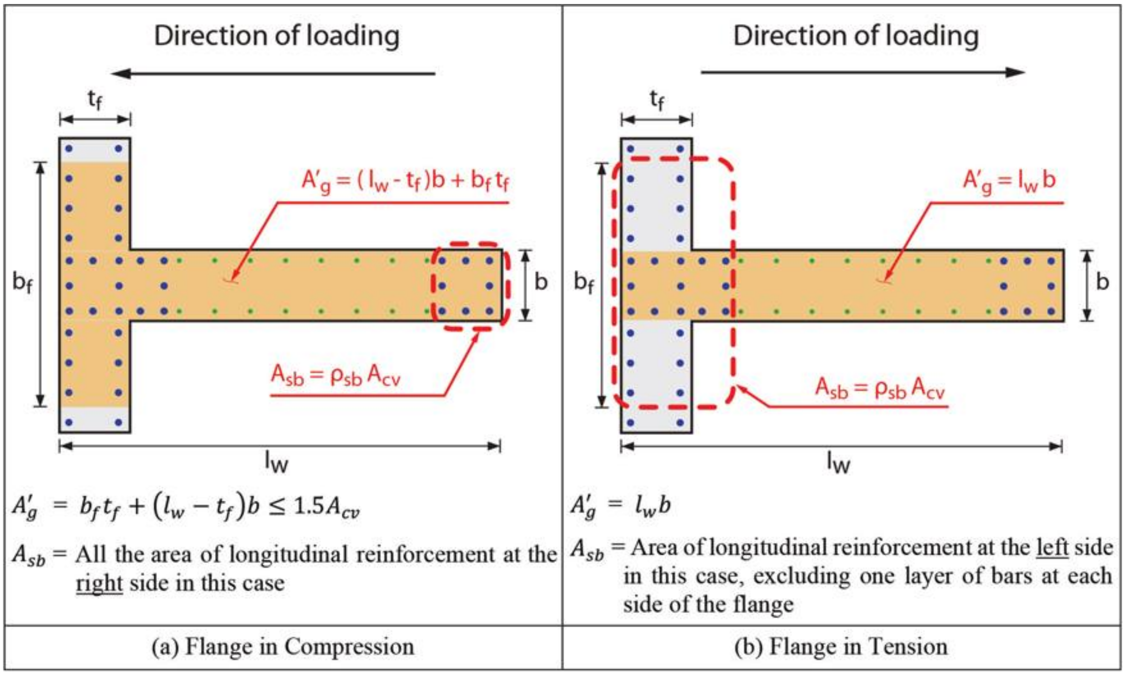

Fig. 6—Example of concrete cross-sectional area and longitudinal tension reinforcement.

Prior studies have shown that beams (Joint ASCE-ACI Task Committee 426 1973) and walls (Gulec and Whittaker 2011; Kassem 2015; Kim and Park 2020) with flanges in compression have greater shear strength than beams and walls with rectangular cross sections and the same area of longitudinal tension reinforcement. Because the initial equation (and the proposed Eq. (2)) already account for the longitudinal boundary reinforcement in tension (including any reinforcement within the effective tension flange width), A_{sb}, it was decided to use the variable A_g' (instead of A_g). Equation (2) was developed using the data set of 340 walls with symmetric cross-sectional shapes, which included walls with H- and barbell-shaped cross sections, using the variable A_g'. It is noted that the performance of the initial equation and Eq. (2) were essentially the same, which indicates that the use of A_g' works to extend the application of the model. Figure 6 demonstrates how A_g' and A_{sb} are defined for an asymmetrical wall (a T-shaped wall in this case) based on the direction of loading; therefore, different wall shear strengths are obtained for each direction of loading. Results presented for the data set of asymmetric walls are provided in Fig. 7 and demonstrate that the performance of the proposed approach is similar to that for the data set of 340 symmetric walls. It is noted that the data set of asymmetrical walls is limited; therefore, this approach should be reassessed when additional data become available.

Step 5: Performance of proposed equation over complete data set

The good performance of the equation is verified because the training and testing learning curves (in terms of the error computed as RMSE between y_{true} and y_{pred}, and as COV of the ratio V_{true}/V_{pred}) have the signature of an underfitted model (that is, rapid convergence and a long plateau of the training and testing error curves), but the converging error meets the target error range (Table 1), and the training and testing errors are within the ±10% band around the converging error (Rojas-León 2024). This behavior means the model's predictive performance is stable and will be essentially the same if data that follow a similar distribution are added to

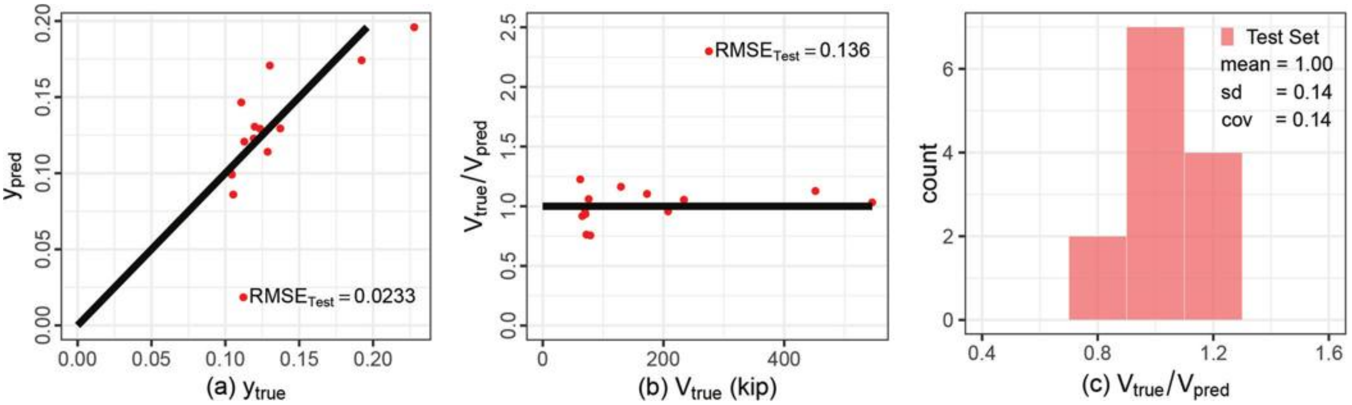

Fig. 7—Performance of Eq. (2) against wall tests with asymmetrical cross sections.

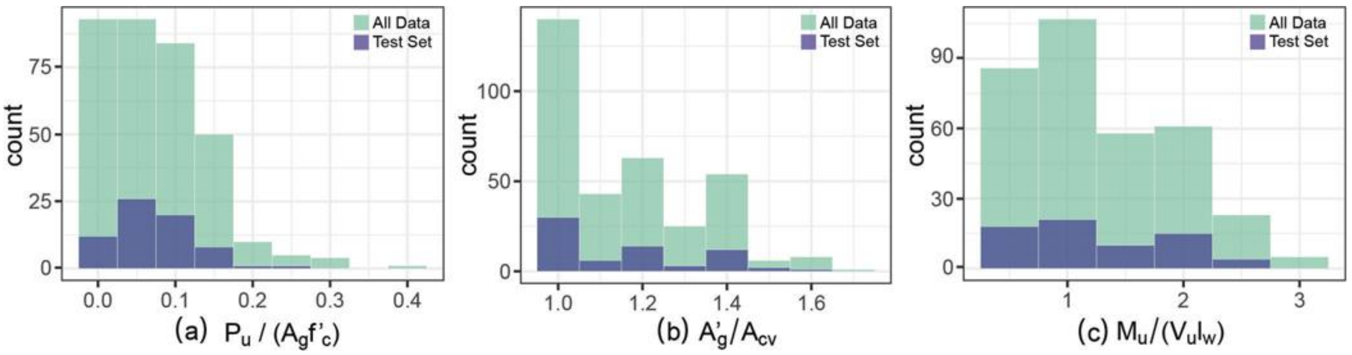

Fig. 8—Histograms of parameters used in Eq. (2) and (3).

the training data set (Amazon Web Services, Inc. 2016). Therefore, the same equation (that is, no retraining was performed) was applied to estimate the shear strength of the entire database of 340. The error indicators obtained with the entire data set are: RMSE = 0.0188 for y_{pred} versus y_{true}, RMSE = 0.170 for V_{true}/V_{pred} versus 1.0, and mean and COV values of 1.00 and 0.17 for V_{true}/V_{pred}.

PARAMETER RANGE LIMITATIONS OF DATA SET

Histograms from the data set of 340 walls for $P_u/(A_g'f_c')$, A_g'/A_{cv}, and $M_u/(V_u l_w)$ are presented in Fig. 8. Based on the histograms for $P_u/(A_g'f_c')$ and A_g'/A_{cv}, limits of $0 \leq P_u/(A_g'f_c') \leq 0.20$ and $A_g'/A_{cv} \leq 1.5$ are proposed for Eq. (2). Given that shear strength tends to increase with an increase in these variables, the proposed limits should produce conservative predictions for ratios outside of these limits, except for the case of a wall in tension, which also is not addressed in the ACI 318-19 equation for wall shear strength. Based on the information presented in Fig. 8, the following limits are established for the coefficients in Eq. (2): $0.010 \leq \alpha_c \leq 0.100$, and $0.30 \leq \alpha_s \leq 0.50$. These limits are chosen as convenient, round numbers, determined by the threshold values where the extreme tail data comprises approximately 5% of the database. Similarly, the coefficients in Eq. (4) are bounded by $0.05 \leq \alpha_c \leq 0.15$ and $0.20 \leq \alpha_s \leq 0.50$.

COMMENTS ON USE OF $M_u/(V_u l_w)$

Current engineering practice is to use total wall height above the critical section (refer to ACI 318-19, Chapter 2, h_w or $h_{w,cs}$) to determine the value of the aspect ratio (h_w/l_w) to use in ACI 318-19 Eq. (18.10.4.1) (to determine α_c). In general, h_w/l_w is significantly larger than the value of $M_u/(V_u l_w)$ because the latter uses the height from the critical section to the resultant lateral force. Ratios of $M_u/(V_u l_w)$ and h_w/l_w are compared in Fig. 9 for a single cantilever wall representing the lateral-force-resisting system for buildings ranging from one to 15 stories (15 ft [4.57 m] height for the first story and 12 ft [3.66 m] height for the stories above) using the ASCE/SEI 7-16 Equivalent Lateral Force (ELF) procedure (Section 12.8) with $T_u = C_u T_a$. The results presented in Fig. 9(a) indicate that using h_w/l_w versus $M_u/(V_u l_w)$ produces a conservative estimate of wall shear strength. Furthermore, in ACI 318-19, the ASCE/SEI 7 wall shear demand V_u is amplified—that is, $V_e = \Omega_v \omega_v V_u$—to account for overstrength and higher mode contributions, where $\Omega_v = M_{pr}/M_u$ for walls with $h_w/l_w > 1.5$ and $\Omega_v = 1.0$ for $h_w/l_w \leq 1.5$. Therefore, to account for overstrength and higher modes, a more realistic value of moment-to-shear demand would be: $M_{pr}/V_e = \Omega_v M_u/(\Omega_v \omega_v V_u l_w) = M_u/(\omega_v V_u l_w)$. Again, because $\omega_v \geq 1.0$, use of overall wall height ($h_{w,es}/l_w$) to estimate wall shear strength would produce even more conservative results, as shown in Fig. 9(b) for h_w/l_w ranging from 1.0 to 5.0 (Fig. 9(b) was created assuming l_w = 30 ft [9.14 m]). Given these observations, the proposed shear strength equation is based on using $M_u/(\omega_v V_u l_w)$ as opposed to h_w/l_w. An alternative approach would be to propose modifications to h_w/l_w to address these issues, which might simplify the implementation of the proposed equation (Eq. (2)) and the simplified equation (Eq. (4)), but possibly lead to added conservatism.

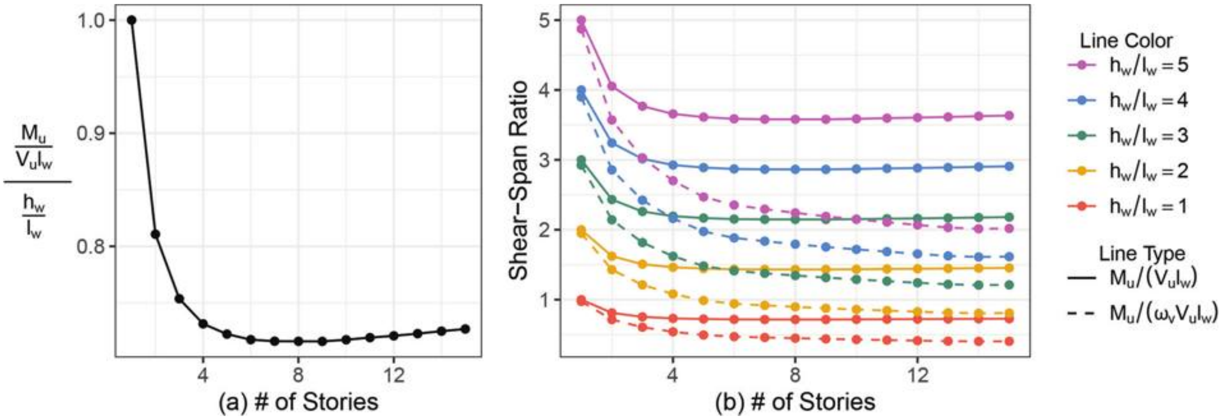

Fig. 9—Comparisons of: (a) $M_u/(\omega_v V_u l_w)$ *versus* h_w/l_w*; and (b)* $M_u/(V_u l_w)$ *versus* $M_u/(\omega_v V_u l_w)$ *for different aspect ratios. (Note: Full-color PDF is available on www.concrete.org.)*

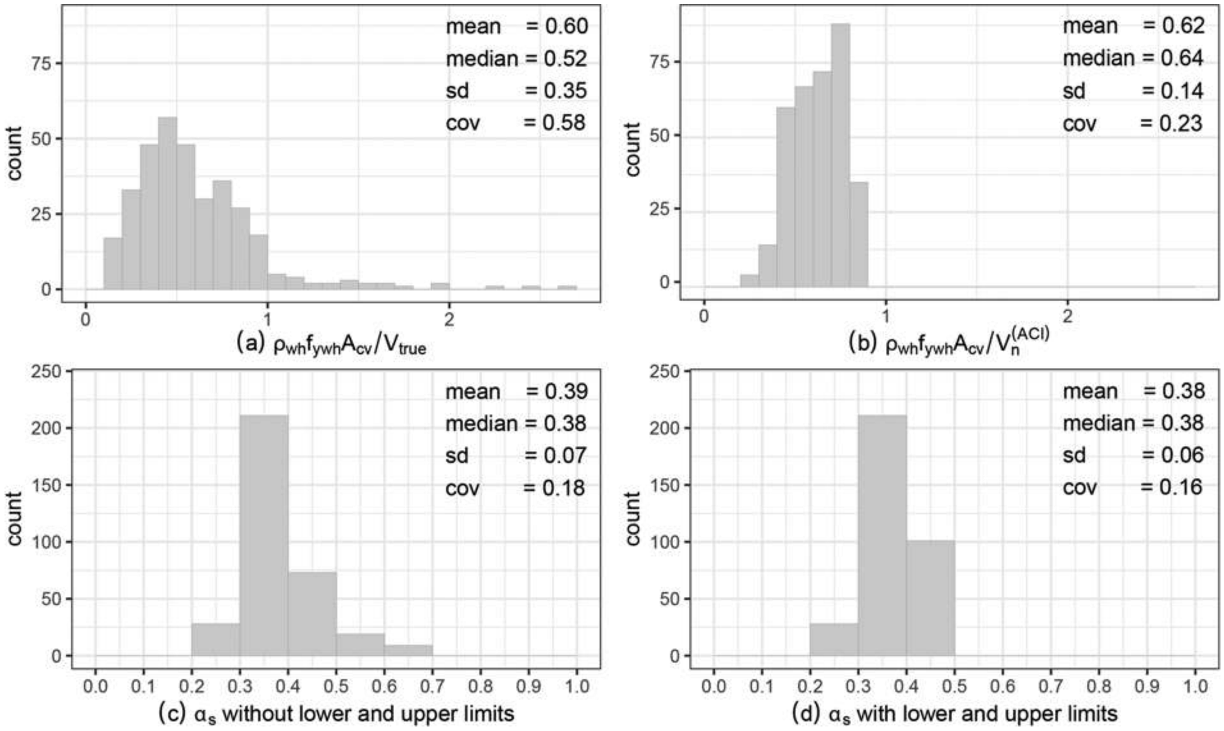

Fig. 10—Web horizontal reinforcement contribution relative to: (a) V_{true} *and (b)* V_n *according to ACI 318-19; and* α_s*: (c) without limits and (d) with limits.*

RELATIVE CONTRIBUTIONS OF CONCRETE AND HORIZONTAL REINFORCEMENT TO WALL SHEAR STRENGTH

ACI 318-19 Eq. (18.10.4.1) assumes that wall shear strength is directly proportional to the quantity of horizontal web reinforcement provided—that is, in Eq. (2), the term α_s would be equal to 1.0. This assumption is evaluated with results shown in Fig. 10, where histograms for ratios of $(\rho_{wh} f_{ywh} A_{cv})/V_{true}$ (Fig. 10(a)) and $(\rho_{wh} f_{ywh} A_{cv})/V_{\text{ACI 318-19}}$ (Fig. 10(b)) are presented. First, it is noted that the range of values for Fig. 10(a) is broad, with a mean of 0.60, median of 0.52, and standard deviation (SD) of 0.35, with 8% of the values greater than 1.0. Second, the histogram in Fig. 10(b) is slightly moved to the right with respect to the histogram in Fig. 10(a), suggesting that the ACI 318-19 approach overpredicts the contribution of horizontal web reinforcement to wall shear strength. In the proposed equation, α_s multiplies $\rho_{wh} f_{ywh} A_{cv}$ and thus represents an effectiveness factor. The histogram of α_s values for the walls in the database is presented in Fig. 10(c) (without the lower limit applied) and Fig. 10(d) (with the lower limit applied) and indicates that the mean value of the effectiveness of horizontal web reinforcement is 0.38 with low dispersion (COV of 0.16).

To further evaluate the contribution of horizontal web reinforcement to wall shear strength, 66 pairs of companion tests were identified from the 57,630 different pairs that can be formed out of the 340 samples in the database). The only variable that changed significantly for these 66 companion tests is the quantity of horizontal web reinforcement; the difference in $\rho_{wh} f_{ywh} A_{cv}$ values is at least 3%, with an average difference of 70%, whereas all other parameters did not vary by more than 10%. Therefore, because the primary change

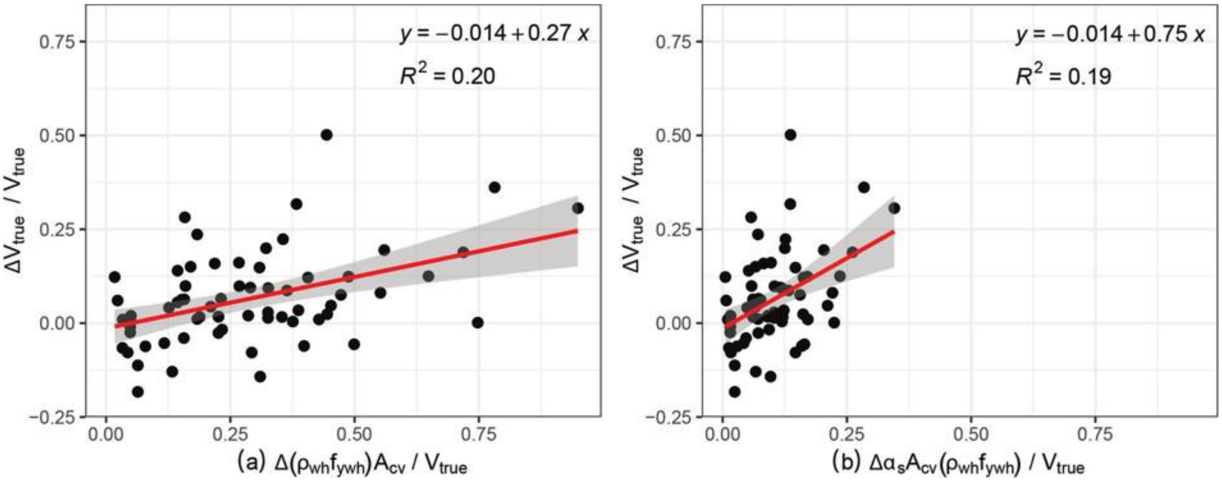

Fig. 11—Change in shear-strength companion group 1 tests predicted by: (a) V_s *in ACI 318-19; and (b)* V_s *in proposed Eq. (2).*

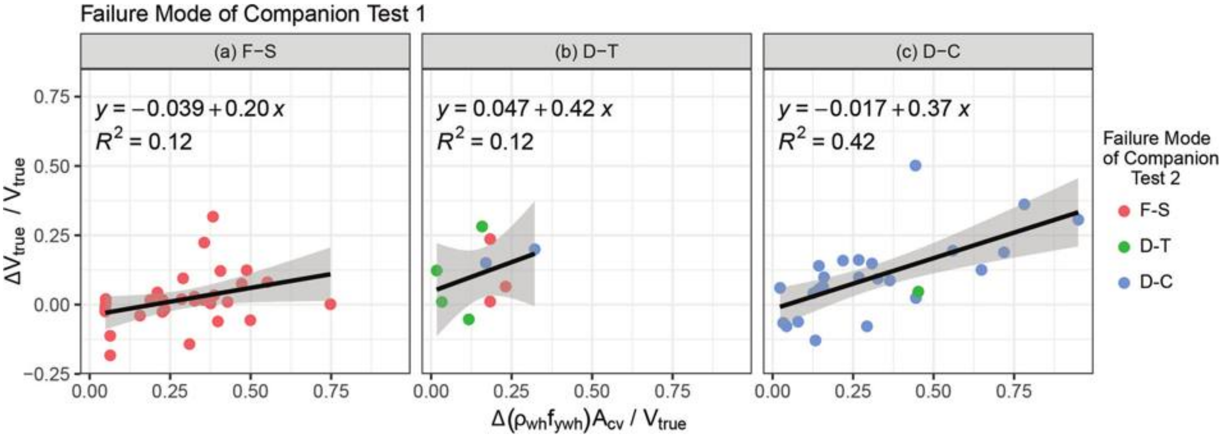

Fig. 12—Change in shear-strength companion group 1 tests assuming full contribution of horizontal web reinforcement, by failure mode.

between the wall specimen (Test 1) and its companion wall specimen (Test 2) is related to $\rho_{wh}f_{ywh}$, the change in the total shear strength should be $\Delta V_n = \Delta(\rho_{wh}f_{ywh}A_{cv})$. Figures 11 and 12 show the predicted shear strength, where the true and the predicted values have been normalized by the measured shear strength of the companion Test 1 (V_{true}).

Results presented in Fig. 11(a) indicate that assuming 100% efficiency for the horizontal web reinforcement, as is the case for the ACI 318-19 equation, overestimates the actual contribution coming from this term—that is, the slope of the linear regression in Fig. 11(a) can be interpreted as the efficiency multiplier α_s. Figure 11(b) shows that incorporating the proposed factor to predict the change in shear strength results in substantially better results, that is, a slope closer to 1.0. Slopes obtained with these companion tests in Fig. 12 are in the range of the values of the proposed α_s (refer to Fig. 10(d)) for walls that failed in diagonal-compression (D-C) and diagonal-tension (D-T), and slightly smaller for walls that failed in flexure-shear (F-S). Because this companion group is relatively small (66 tests) with considerable dispersion, the observed trends vary somewhat depending on which companion test is called Test 1 or Test 2. In this study, the companion test with a lesser $\rho_{wh}f_{ywh}$ was designated Test 1. Additional data are needed to enable further interpretation of these trends.

A second analysis of companion tests is carried out on 688 pairs of companion tests with identical cross-sectional shapes, essentially the same quantity of horizontal web reinforcement (the difference in $\rho_{wh}f_{ywh}A_{cv}$ values is zero for 238 pairs and less than 3% for the rest), and without any restrictions on other parameters. In this case, according to the current ACI 318 equation, the change in the total shear strength should be directly proportional to the change in the concrete contribution: $\Delta V_n = \Delta V_c$. Figure 13(a) shows that the ACI 318-19 equation underpredicts the change in shear strength by more than 50% of the true value (the linear regression slope is larger than 2.0). Figure 13(b) shows that the proposed equation predicts the true shear strength change much more accurately as the linear regression slope is close to 1.0. Note that the change in the total shear strength for these companion tests is obtained as $\Delta V_n = \Delta(\alpha_c A_g' f_c' + \alpha_s A_{sb} f_{ysb})$ when using the proposed equation. The true and predicted changes in shear strength have also been normalized by the measured shear strength of companion Test 1 (V_{true}).

Figures 14(a) to (c) show the change in wall shear strength for the companion tests with constant web horizontal

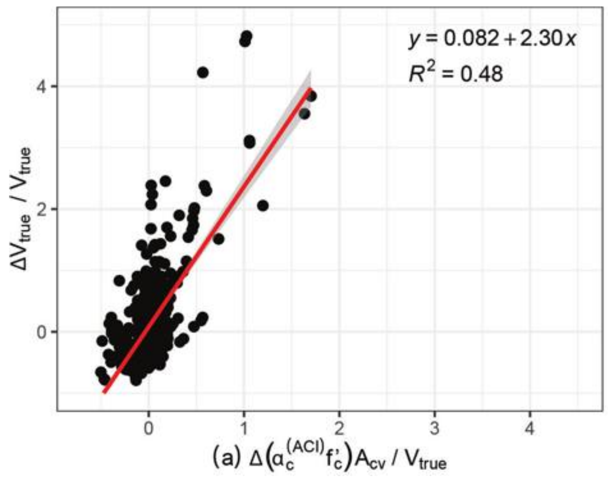

Fig. 13—Change in shear-strength companion group 2 tests predicted by: (a) V_c *in ACI 318-19; and (b)* $(\alpha_c A_g' f_c' + \alpha_s A_{sb} f_{ysb})$ *in proposed Eq. (2).*

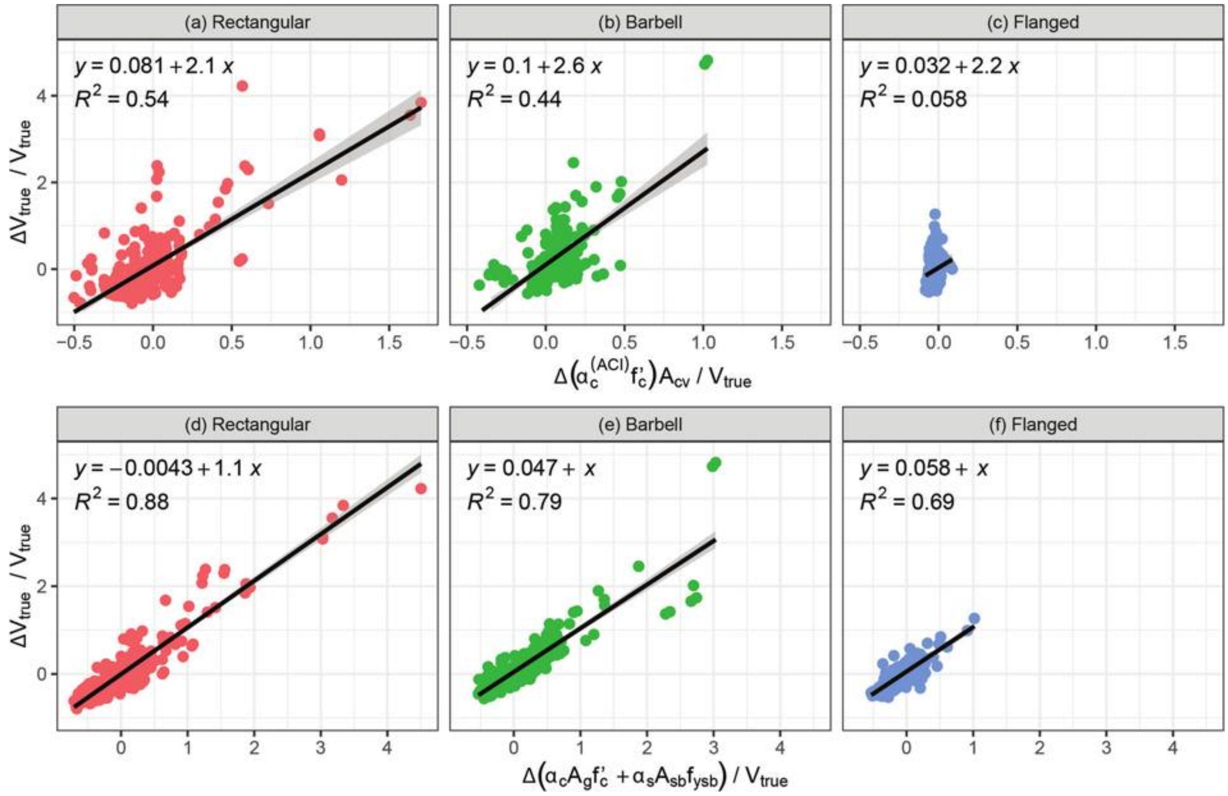

Fig. 14—(a), (b), and (c) Change in shear strength of companion group 2 tests predicted by ACI 318-19 equation; and (d), (e), and (f) proposed Eq. (2), per wall cross section.

reinforcement using the ACI 318-19 equation for walls with rectangular, barbell, and flanged cross sections, respectively. Figures 14(d) to (f) plot the same information using the proposed equation. The results indicate that the proposed equation does a significantly better job of predicting the change in wall shear strength for all three wall cross-section shapes.

The concrete contribution from the ACI 318-19 and the proposed equations are compared to better understand the proposed equation. To accomplish this, the α_c coefficient in ACI 318-19 Eq. (18.10.4.1), which has units of $\sqrt{\text{psi}}$, is normalized by pre- and post-multiplying the ACI 318-19 concrete contribution by $\sqrt{f_c'}$—that is, $V_c = (\alpha_c/\sqrt{f_c'}) \cdot \lambda A_{cv}\sqrt{f_c'} \cdot \sqrt{f_c'}$. Therefore, the ACI 318-19 normalized α_c coefficient is defined as $\alpha_{c,norm}^{(ACI)} = \alpha_c/\sqrt{f_c'}$. From the database, the mean value of $1/\sqrt{f_c'}$ is $0.013/\sqrt{\text{psi}}$.

Figure 15(a) presents values for the proposed α_c term for various values of $M_u/(V_u l_w)$ and $P_u/(A_g' f_c')$ that exist within the database (but over a more extended range than the proposed limits on these values). Figure 15(b) shows the analytical values for the proposed α_c and $\alpha_{c,norm}^{(ACI)}$ assuming $M_u/(V_u l_w)$ is equal to the aspect ratio—that is, $h_w/l_w = M_u/(V_u l_w)$—although, as noted in Fig. 9, h_w/l_w is likely to be considerably greater than $M_u/(V_u l_w)$ for design applications.

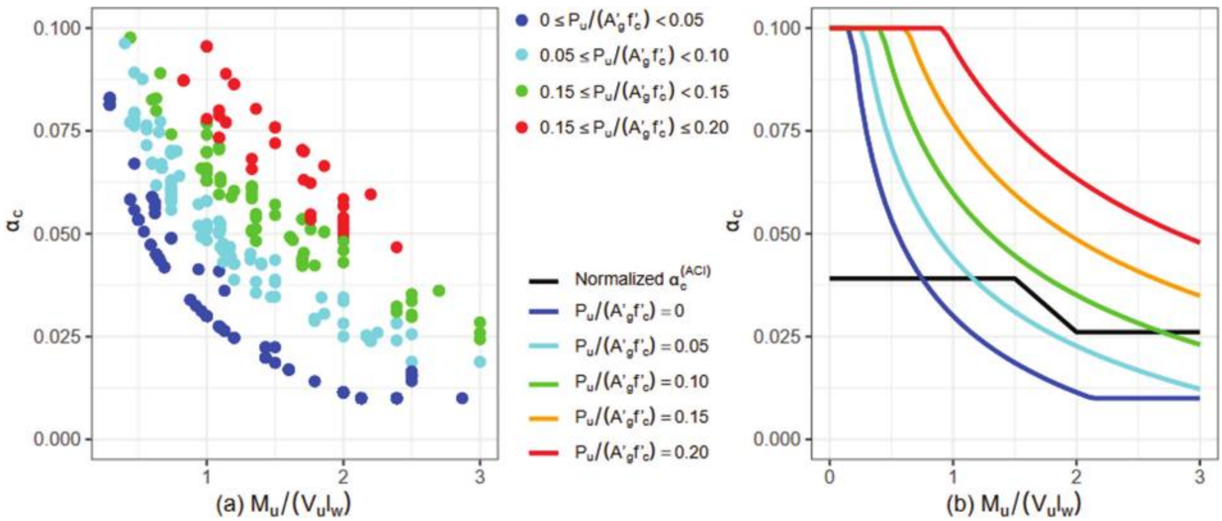

Fig. 15—Range of values covered by α_c for: (a) database; and (b) lines for different axial load ratio levels and for $\alpha_{c,norm}^{(ACI)}$.

The normalized $\alpha_{c,norm}^{(ACI)}$ corresponds to values associated with $P_u/(A_g'f_c')$ between 5 and 10% for $M_u/(V_u l_w) \ge 1.0$ and tends to significantly underestimate the concrete contribution for higher $P_u/(A_g'f_c')$ and for $M_u/(V_u l_w) < 1.0$.

It is important to note that, in this comparison (and in Eq. (2)), the influence of the longitudinal boundary reinforcement on wall shear strength was included as a "reinforcement" contribution—that is, $V_s = \alpha_s(\rho_{sb} f_{ysb} + \rho_{wh} f_{ywh})A_{cv}$. This term also could be considered as a "concrete" contribution, as one physical interpretation is that an increase in wall longitudinal reinforcement results in an increase in wall neutral axis depth, which results in a greater concrete contribution (for example, as is done in ACI 318-19 Table 22.5.5.1 for one-way shear strength). However, analysis of the data suggests that the increase in wall shear strength might also be due, in part, to an increase in reinforcement contribution (for example, dowel action). This is apparent in Eq. (4) because the coefficients defined in Eq. (5) include the longitudinal reinforcement at the wall edge as a variable for both α_c and α_s. In this study, the contribution from longitudinal reinforcement is treated as steel contribution in Eq. (2), although an alternative form, where this term is treated as a concrete contribution, could also be derived.

SHEAR STRESS UPPER LIMIT

To avoid diagonal compression failures, ACI 318-19 includes an upper limit on wall shear strength of $10\sqrt{f_c'(\text{psi})}\,A_{cv}$ for an individual wall segment (Barda et al. 1977); this limit is $8\sqrt{f_c'(\text{psi})}\,A_{cv}$ for wall segments sharing a common lateral force to also allow for some redistribution. The $10\sqrt{f_c'}A_{cv}$ limit was evaluated using the entire data set, which included walls failing due to F-S, D-T, and D-C. Results presented in Fig. 16 demonstrate that the current shear strength upper limit is too conservative when applied to the entire data set; however, the limit does provide a reasonable upper limit on wall shear strength for walls with rectangular cross sections with D-C failures (blue dot symbols). Most of the rectangular walls failing in F-S or D-T are below the current ACI 318-19 limit (which is also shown in Fig. 17(a)), whereas approximately half of the rectangular walls failing in D-C are above the limit (which is better represented by the fitted normal distribution shown in Fig. 17(d)). However, the current limit does a poor job of separating flanged walls that fail in D-C from flanged walls with other failure modes, as several walls that failed in F-S and D-T exceed the current limit (refer to the red and green crosses in Fig. 16, the histogram presented Fig. 17(b), or its fitted normal distributions in Fig. 17(e); full-color PDF can be accessed at www.concrete.org).

Therefore, a study was conducted to assess the potential to propose a new (but simple) upper limit using a logistic regression model designed to differentiate between walls that failed in F-S and D-T from those that failed in D-C (Rojas-León 2022). The proposed approach (Eq. (6)) uses a factor to modify the current shear stress upper limit where most of the walls failing in F-S or D-T fall below this limit, and roughly half of those failing in D-C fall above this limit for walls with either rectangular cross sections (Fig. 17(d)) or wall cross sections with flanges (Fig. 17(f)). More details on the approach and the results are included in Rojas-León (2022). The proposed upper limit results in the condition that wall shear stress $v_n = V_n/A_{cv}$ shall satisfy the following equation

$$v_n = \frac{V_n}{A_{cv}} \le \alpha_{shape} 10\sqrt{f_c'} \tag{6}$$

where α_{shape} is 1.0 for walls with a rectangular cross section (same as for ACI 318-19) and is computed using Eq. (7) for flanged walls

$$\alpha_{shape} = 0.7(1 + b_f t_f / A_{cv})^2 \tag{7}$$

where α_{shape} need not be taken less than 1.0 and shall not exceed 1.5; and $b_f t_f$ is the total area of the effective flange width (on both sides of the web if flanges exist on both sides). If the flange length is different on each end (boundary) of a wall, then the wall shear strength may be evaluated independently for each direction of loading or the wall shear strength may be conservatively based on the smaller flange

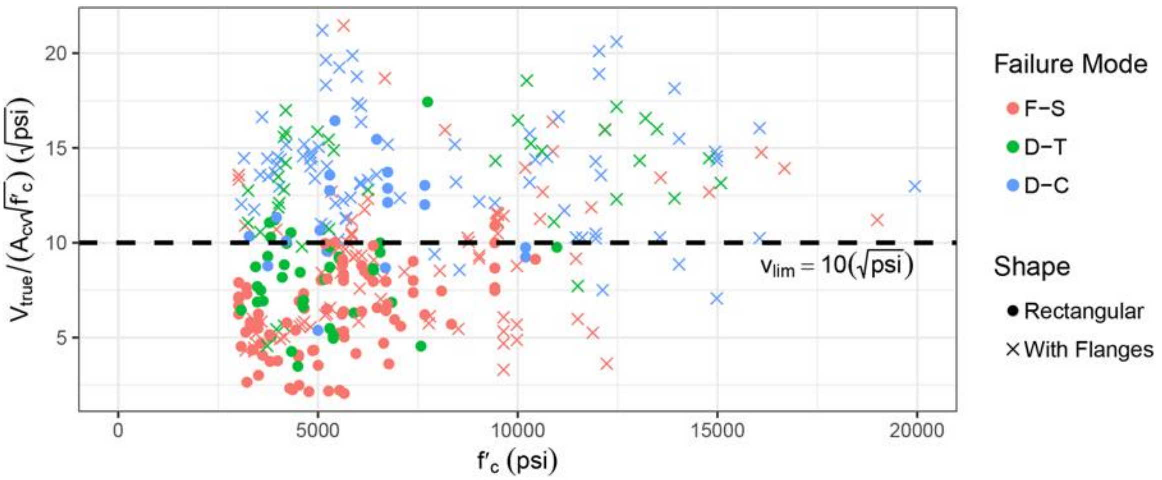

Fig. 16—Comparison of ACI 318-19 upper limit on wall shear stress with test data. (Note: 145.04 psi = 1 MPa.)

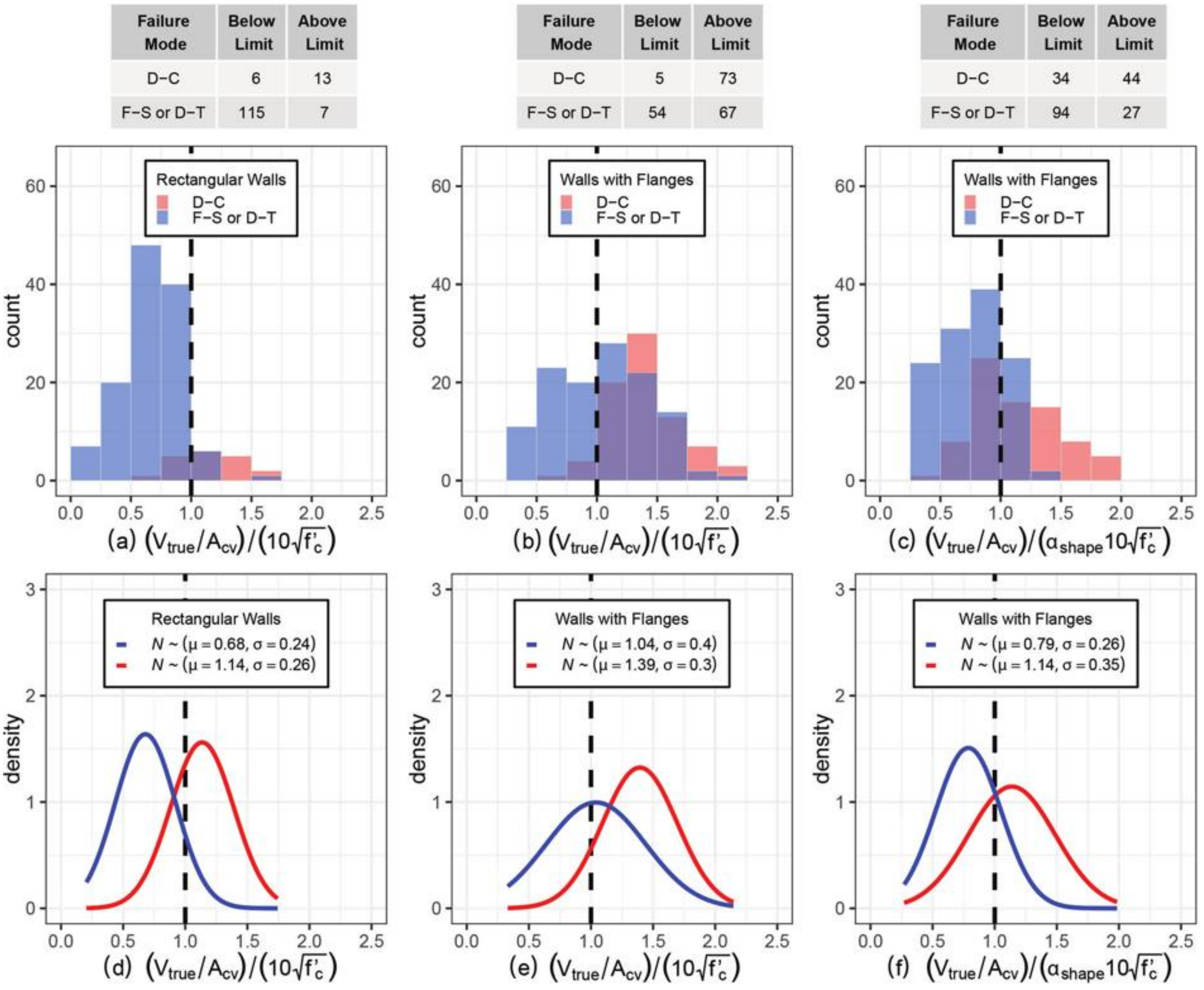

Failure Mode	Below Limit	Above Limit
D−C	6	13
F−S or D−T	115	7

Failure Mode	Below Limit	Above Limit
D−C	5	73
F−S or D−T	54	67

Failure Mode	Below Limit	Above Limit
D−C	34	44
F−S or D−T	94	27

Fig. 17—Proposed new upper limit for shear strength.

width. For walls sharing a common lateral force, to be consistent with ACI 318-19, the limiting stress should be based on the sum of $\alpha_{shape}8\sqrt{f_c'}A_{cv}$ for these walls.

STRENGTH REDUCTION FACTOR FOR DESIGN PURPOSES

A limited reliability study was performed on three building archetypes (same floor plan but different building height) by Rojas-León (2022) to assess what value or values of strength reduction factor ϕ would be appropriate to use with Eq. (2). It is noted that the strength reduction factor did not change from ACI 318-14 (ACI Committee 318 2014) to ACI 318-19, despite the introduction of wall shear amplification, which in some cases produces wall shear demands V_e in ACI 318-19 that are three times the V_u demands used in ACI 318-14. This preliminary study suggests that use of ϕ =

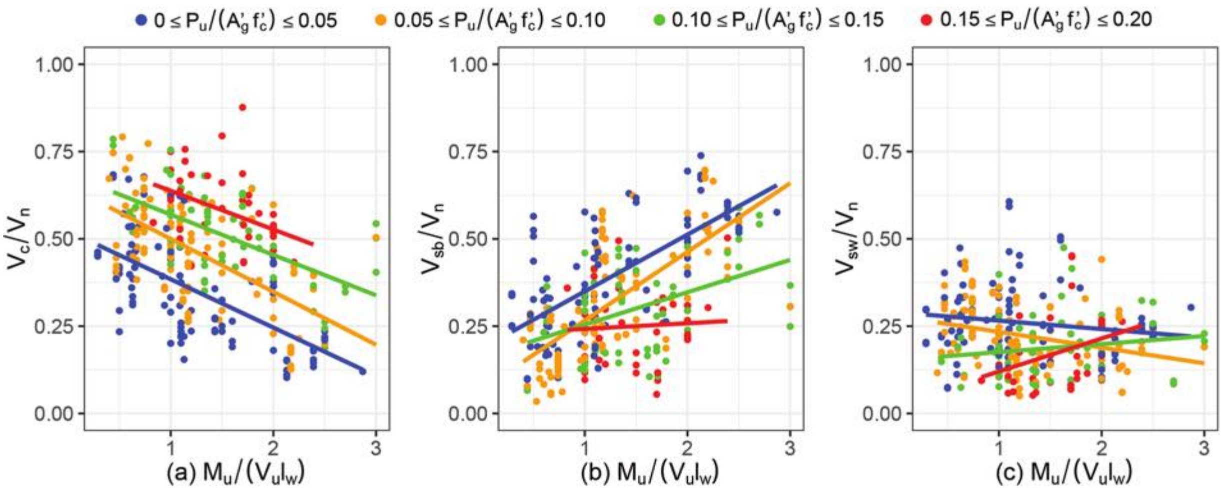

Fig. 18—Relative shear-strength contribution for proposed Eq. (2).

0.75, which is currently used in ACI 318-19, meets the criterion of having a probability of wall shear failure less than 10% for Risk Category I and II buildings for the Maximum Considered Earthquake (MCE_R) hazard level (as required in ASCE/SEI 7-16 Table 1.2-3). However, the preliminary study indicates that use of a constant value of $\phi = 0.75$ may be overly conservative because values above $\phi = 0.90$ are reached in some cases and the probability of failure is still ASCE/SEI 7-16 compliant. A more comprehensive study that includes more building archetypes is needed to obtain a clearer relationship between the strength reduction factor and the probability of failure; however, it appears likely that use of $\phi = 0.75$ is conservative.

INTERPRETATION OF PROPOSED EQUATION

The proposed equation explicitly accounts for the effects of axial load and longitudinal reinforcement at the edge of the wall in tension (neither is considered in ACI 318-19) and uses the shear-span ratio instead of the aspect ratio (used in ACI 318-19). From the mechanics of the problem, all these parameters were known to influence wall shear strength (or column shear strength).

Figure 18 shows the relative contributions of each term of the proposed equation when estimating the shear strength of the walls in the database. Figure 18(a) indicates that the contribution coming from $V_c = \alpha_c A_g' f_c'$ increases with increasing axial load ratios and with lower shear-span ratios, as expected. Figure 18(b) shows that at zero or low axial stress, wall shear strength increases substantially with increases in boundary longitudinal reinforcement ($V_{sb} = \alpha_s \rho_{sb} f_{ysb} A_{cv}$), likely because neutral axis depth and dowel action increase; V_{sb} also increases with increasing shear-span ratios, likely because overturning moment increases, requiring greater quantities of boundary longitudinal reinforcement. Figure 18(c) shows that the average relative contribution of the term related to horizontal web reinforcement ($V_{sw} = \alpha_s \rho_{wh} f_{ywh} A_{cv}$) is only 22% and it is insensitive to changes in both shear-span ratio and axial load ratio.

Figures 19 and 20 show that the ACI 318-19 equation is biased and that the proposed equation performs similarly against different variables (for example, axial load ratio, shear-span ratio, and shear stress). The ACI 318-19 approach is generally conservative, except for walls with low axial load ratios and low normalized shear stress (Fig. 19(a)) (which are likely to be correlated), and it produces significantly different mean values for walls with higher axial loads (Fig. 19(a)) or with different cross-section shapes (Fig. 20(a)). In addition, limiting the shear stress has the biggest impact on walls with axial load ratios greater than 0.05 (Fig. 19(b)) and affects walls with different cross-section shapes similarly (Fig. 20(b)). The proposed approach provides fairly uniform mean and COV values prior to the application of a limiting shear stress (Fig. 19(c) and Fig. 20(c)), except for a modest increase in the dispersion at very low normalized shear strength (Fig. 19(a)), which mainly corresponds to walls with axial load ratios lesser than 0.05. However, this increase in dispersion is less than that for the ACI 318-19 equation within the same range of normalized shear stress. Applying the limiting shear stress for the proposed approach influences primarily barbell- and H-shaped walls (Fig. 20(d)) and walls with low and high axial stress ratios (Fig. 19(d)). These wall configurations are likely to be correlated: a higher shear strength contribution from $V_c = \alpha_c A_g' f_c'$ (Fig. 18(a)) for a barbell- or H-shaped wall with a large axial load, whereas a higher shear strength contribution from $V_{sb} = \alpha_s \rho_{sb} f_{ysb} A_{cv}$ (Fig. 18(b)) for a barbell- or H-shaped wall with a very low axial load.

Figure 21(a) confirms that the ACI 318-19 equation is generally more conservative than the proposed equation for walls with axial load ratios larger than 5% or for walls with barbell- or H-shaped cross sections (Fig. 21(c)). Applying the upper limit on the equations accentuates the conservatism of the ACI 318-19 equation with respect to the proposed equation for walls with axial load ratios larger than 10% (Fig. 21(b)) and for walls with rectangular cross sections (Fig. 21(d)).

CONCLUSIONS

A new wall shear strength equation is obtained using a methodology based on statistical and machine learning (ML) approaches applied to a comprehensive data set of 340 walls with reported shear failures. The proposed equation (Eq. (2))

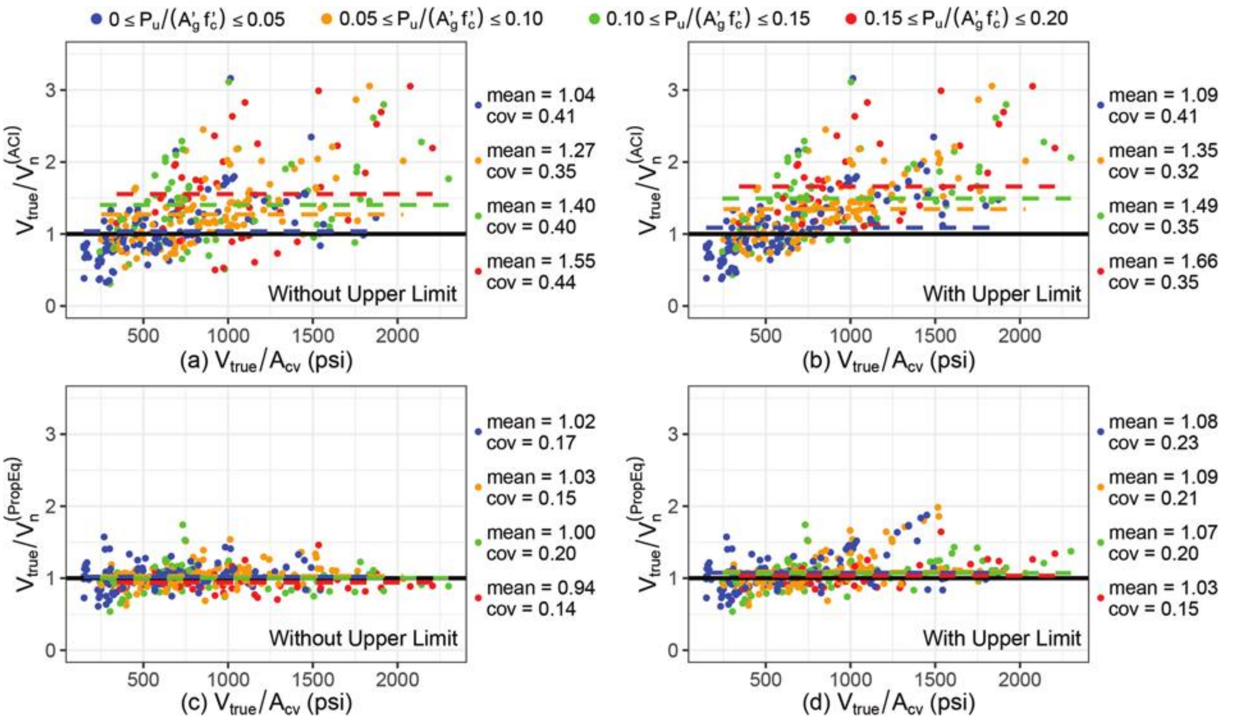

Fig. 19—True-to-predicted ratio using ACI 318-19: (a) without; and (b) with upper limit; and proposed Eq. (2): (c) without; and (d) with upper limit, versus shear stress.

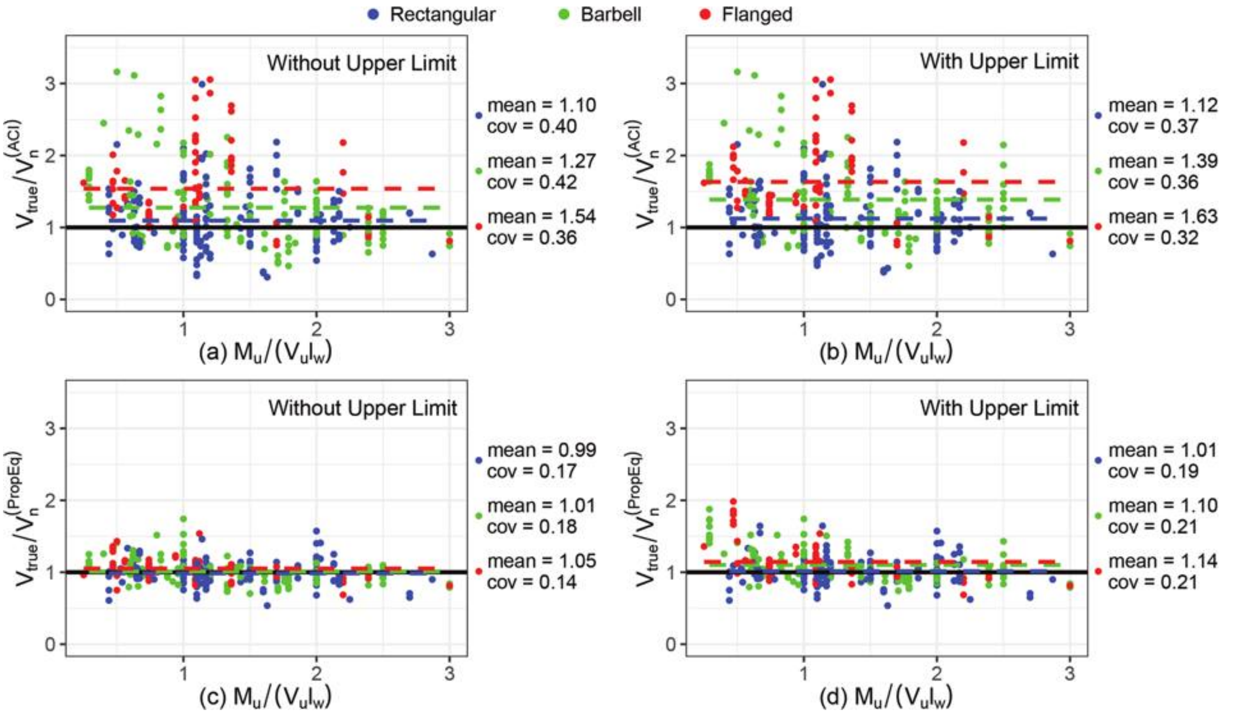

Fig. 20—True-to-predicted ratio using ACI 318-19: (a) without; and (b) with upper limit; and proposed Eq. (2): (c) without; and (d) with upper limit, versus shear-span ratio.

meets the target model performance requirements defined for a code-oriented equation. The methodology can also be used to develop simpler models, for example, a simplified version of the proposed equation (with a slight increase in the error) that does not include axial load as a design variable, such as Eq. (4), which could be used to simplify the design process for cases where wall shear demands are not expected to govern and/or for preliminary design.

The proposed equation has the same format as ACI 318-19 Eq. (18.10.4.1)—that is, $V_n = V_c + V_s$—but is based on unitless modification factors, which is not the case for ACI 318-19.

The proposed equation applies to walls with rectangular, barbell, and flanged (C-, H-, T-, and L-shaped) cross sections, although the validation was limited for asymmetric cross-section shapes due to a lack of data (13 wall tests with asymmetric cross sections). The proposed equation has

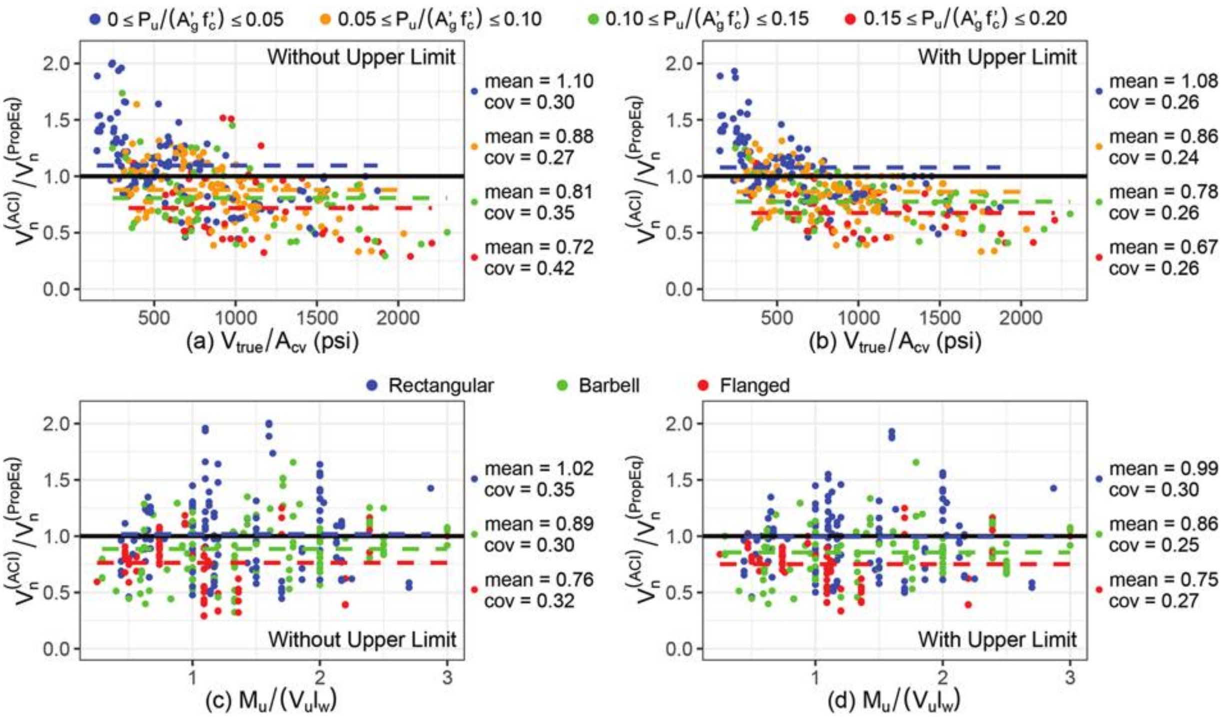

Fig. 21—Ratio of shear strength predicted by ACI 318-19 versus shear strength predicted with proposed Eq. (2).

practically the same performance (before applying limiting shear stress) for walls with different cross-section shapes, axial load ratios, shear-span ratios, or aspect ratios, which is not the case for ACI 318-19.

Analyses of two companion test groups indicate that the shear strength contributions from the terms in the proposed equation are more accurate than the contributions from the terms in the ACI 318-19 equation, which tends to significantly underestimate and overestimate the contributions associated with concrete and horizontal web reinforcement, respectively.

A new upper limit on wall shear stress is proposed primarily to address the observation that walls with compression flanges can achieve higher stresses prior to diagonal compression (D-C) failure. The proposed upper limit is simple and is the same as in ACI 318-19 for walls with rectangular cross sections but allows shear stresses as high as $15\sqrt{f_c'}$ for flanged walls (that is, 1.5 times the current ACI 318-19 limit).

A limited reliability study performed on three archetypes indicates that a strength reduction factor ϕ of 0.75 produces conservative results when applied to the proposed Eq. (2). Further research is recommended to conduct a comprehensive assessment of the capacity reduction factor and to evaluate the implications of using the proposed design equations on building design.

It is observed that the proposed equations for wall shear strength generally result in higher values of V_n, should allow for an increase in the value of f_c' used to determine V_c, and include a higher shear stress limit for flanged walls. Given these observations, it appears likely that the proposed equations will result in more economical wall designs given shear strength typically controls the size of the wall cross section for building design.

AUTHOR BIOS

Matías Rojas-León *is a Practicing Engineer. He received his BS, professional engineer degree, and MS from the University of Chile, Santiago, Chile; and his PhD in structural/earthquake engineering from the University of California, Los Angeles (UCLA), Los Angeles, CA. His research interests include seismic design and behavior of reinforced concrete structures, machine learning (ML) and statistical approaches in structural engineering, laboratory testing, and structures equipped with anti-seismic devices.*

John W. Wallace, *FACI, is a Professor of civil engineering at UCLA. He is Chair of ACI Subcommittee 318-H, Seismic Provisions, and a member of ACI Committees 318, Structural Concrete Building Code; 369, Seismic Repair and Rehabilitation; and 374, Performance-Based Seismic Design of Concrete Buildings. His research interests include the response and design of buildings and bridges to earthquake actions, laboratory and field testing of structural components and systems, and seismic structural health monitoring.*

Saman A. Abdullah *is a Research Scholar in the Department of Civil and Environmental Engineering at UCLA and a Lecturer in the Department of Civil Engineering, College of Engineering, at the University of Sulaimani, Sulaymaniyah, Kurdistan, Iraq. He is a member of ACI Committee 374, Performance-Based Seismic Design of Concrete Buildings, and ACI Subcommittees ACI 318-H, Seismic Provisions; 318-1W, Wind Provisions; and 369-F, Retrofit. His research interests include seismic and wind design of concrete structures and laboratory testing.*

Kristijan Kolozvari *is an Associate Professor in the Department of Civil and Environmental Engineering at California State University, Fullerton, Fullerton, CA. He is a member of ACI Committee 374, Performance-Based Seismic Design of Concrete Buildings. His research interests include developing and applying innovative analytical tools for nonlinear analysis of reinforced concrete structures, performance-based seismic design, seismic retrofit, tall building behavior and design, and earthquake resiliency.*

ACKNOWLEDGMENTS

M. Rojas-León acknowledges the support from the Chilean National Agency for Research and Development (ANID) Scholarship Program/ DOCTORADO BECAS CHILE/2019-72200499. Any opinions, findings, and conclusions expressed in this material are those of the authors and do not necessarily reflect those of the sponsor.

REFERENCES

Abdullah, S. A., 2019, “Reinforced Concrete Structural Walls: Test Database and Modeling Parameters,” PhD dissertation, University of California, Los Angeles, Los Angeles, CA, 304 pp.

Abdullah, S. A., and Wallace, J. W., 2021, “New Nonlinear Modeling Parameters and Acceptance Criteria for RC Structural Walls,” *Proceedings*, The 2021 Annual Conference of Los Angeles Tall Buildings Structural Design Council Conference, Nov. 12, Los Angeles, CA, pp. 72-85.

ACI Committee 318, 2011, “Building Code Requirements for Structural Concrete (ACI 318-11) and Commentary (ACI 318R-11),” American Concrete Institute, Farmington Hills, MI, 503 pp.

ACI Committee 318, 2014, “Building Code Requirements for Structural Concrete (ACI 318-14) and Commentary (ACI 318R-14),” American Concrete Institute, Farmington Hills, MI, 520 pp.

ACI Committee 318, 2019, “Building Code Requirements for Structural Concrete (ACI 318-19) and Commentary (ACI 318R-19) (Reapproved 2022),” American Concrete Institute, Farmington Hills, MI, 624 pp.

AIJ, 1999, “Structural Design Guidelines for Reinforced Concrete Buildings,” Architectural Institute of Japan, Tokyo, Japan.

Amazon Web Services, Inc., 2016, “Amazon Machine Learning Developer Guide,” AWS, Seattle, WA.

ASCE/SEI 7-16, 2017, “Minimum Design Loads and Associated Criteria for Buildings and Other Structures,” American Society of Civil Engineers, Reston, VA.

ASCE/SEI 43-05, 2005, “Seismic Design Criteria for Structures, Systems, and Components in Nuclear Facilities,” American Society of Civil Engineers, Reston, VA.

Bae, Y.; Tanizawa, K.; Yun, K.; and Kabeyasawa, S., 2010, “Experimental Study on Structural Characteristics of Columns with Sleeve Walls,” *Proceedings of the Japan Concrete Institute*, V. 32, No. 2, pp. 115-120. (in Japanese)

Barda, F.; Hanson, J. M.; and Corley, W. G., 1977, “Shear Strength of Low-Rise Walls with Boundary Elements,” *Reinforced Concrete Structures in Seismic Zones*, SP-53, American Concrete Institute, Farmington Hills, MI, pp. 149-202.

Carrillo, J., and Alcocer, S. M., 2013, “Shear Strength of Reinforced Concrete Walls for Seismic Design of Low-Rise Housing,” *ACI Structural Journal*, V. 110, No. 3, May-June, pp. 415-426.

Chen, X. L.; Fu, J. P.; Yao, J. L.; and Gan, J. F., 2018, “Prediction of Shear Strength for Squat RC Walls Using a Hybrid ANN–PSO Model,” *Engineering with Computers*, V. 34, No. 2, Apr., pp. 367-383.

Feng, D.-C.; Wang, W.-J.; Mangalathu, S.; and Taciroglu, E., 2021, “Interpretable XGBoost-SHAP Machine-Learning Model for Shear Strength Prediction of Squat RC Walls,” *Journal of Structural Engineering*, ASCE, V. 147, No. 11, Nov., p. 04021173.

Gulec, C. K., and Whittaker, A. S., 2011, “Empirical Equations for Peak Shear Strength of Low Aspect Ratio Reinforced Concrete Walls,” *ACI Structural Journal*, V. 108, No. 1, Jan.-Feb., pp. 80-89.

Gulec, C. K.; Whittaker, A. S.; and Stojadinovic, B., 2009, “Peak Shear Strength of Squat Reinforced Concrete Walls with Boundary Barbells or Flanges,” *ACI Structural Journal*, V. 106, No. 3, May-June, pp. 368-377.

Joint ASCE-ACI Task Committee 426, 1973, “The Shear Strength of Reinforced Concrete Members,” *Journal of the Structural Division*, ASCE, V. 99, No. 6, June, pp. 1091-1187.

Kabeyasawa, T.; Ohkubo, T.; and Nakamura, Y., 1996, “Tests and Analyses of Hybrid Wall Systems,” *Proceedings*, Eleventh World Conference on Earthquake Engineering (11WCEE), Acapulco, Mexico, Paper No. 470, 8 pp.

Kassem, W., 2015, “Shear Strength of Squat Walls: A Strut-and-Tie Model and Closed-Form Design Formula,” *Engineering Structures*, V. 84, Feb., pp. 430-438. doi: 10.1016/j.engstruct.2014.11.027

Keshtegar, B.; Nehdi, M. L.; Trung, N.-T.; and Kolahchi, R., 2021, “Predicting Load Capacity of Shear Walls Using SVR–RSM Model,” *Applied Soft Computing*, V. 112, Nov., Article No. 107739.

Kim, J.-H., and Park, H.-G., 2020, “Shear and Shear-Friction Strengths of Squat Walls with Flanges,” *ACI Structural Journal*, V. 117, No. 6, Nov., pp. 269-280. doi: 10.14359/51728075

Moradi, M. J., and Hariri-Ardebili, M. A., 2019, “Developing a Library of Shear Walls Database and the Neural Network Based Predictive Meta-Model,” *Applied Sciences*, V. 9, No. 12, June, Article No. 2562.

Murtaugh, P. A., 2014, “In Defense of *P* Values,” *Ecology*, V. 95, No. 3, Mar., pp. 611-617. doi: 10.1890/13-0590.1

NZS 3101.1&2:2006, 2006, “Concrete Structures Standard,” Standards New Zealand, Wellington, New Zealand.

Rojas-León, M., 2022, “Framework to Define Performance Requirements for Structural Component Models and Application to Reinforced Concrete Wall Shear Strength,” PhD dissertation, University of California, Los Angeles, Los Angeles, CA, 260 pp.

Rojas-León, M.; Abdullah, S. A.; Kolozvari, K.; and Wallace, J. W., 2024, “A Framework to Set Performance Requirements for Structural Component Models: Application to Reinforced Concrete Wall Shear Strength,” *ACI Structural Journal*, V. 121, No. 1, Jan., pp. 75-88.

Sánchez-Alejandre, A., and Alcocer, S. M., 2010, “Shear Strength of Squat Reinforced Concrete Walls Subjected to Earthquake Loading – Trends and Models,” *Engineering Structures*, V. 32, No. 8, Aug., pp. 2466-2476. doi: 10.1016/j.engstruct.2010.04.022

Segura, C. L. Jr., and Wallace, J. W., 2018, “Seismic Performance Limitations and Detailing of Slender Reinforced Concrete Walls,” *ACI Structural Journal*, V. 115, No. 3, May, pp. 849-859.

Wood, S. L., 1990, “Shear Strength of Low-Rise Reinforced Concrete Walls,” *ACI Structural Journal*, V. 87, No. 1, Jan.-Feb., pp. 99-107.

ACI STRUCTURAL JOURNAL TECHNICAL PAPER

Title No. 121-S08

Experimental Investigation of Size Effect on Shear Strength of Reinforced Concrete Pile Caps

by Lucas Laughery, Toshikatsu Ichinose, Kazuhiko Kasai, Srinivas Mogili, and Shyh-Jiann Hwang

Engineers design structures based on physics, experiments, and experience. But due to increasing demands, structures today are being built at scales that far exceed experience and experimental testing. Bažant summarized the problem well in 1984: "Most laboratory tests are carried out on a reduced scale, from which generalizations must be made for much larger real structures." Tall structures often require deep foundations with thick reinforced concrete pile caps. In the United States, pile-cap strength is calculated according to ACI 318 provisions, which now include a size effect factor for concrete shear strength. This factor reduces concrete unit shear strength in proportion to effective depth for sections built without minimum shear reinforcement. This strength reduction forces engineers seeking to eliminate vertical ties to either increase concrete strength or deepen pile caps. But there is a gap in knowledge. This strength reduction is calibrated to databases for which tests do not vary across a large scale, and for which key unitless ratios are not always controlled. The present study fills this gap by quantifying the strength reduction due to size effect while controlling other key ratios using new laboratory tests. Experimental tests of tripod pile caps with effective depths of 250, 500, and 1000 mm (9.84, 19.68, and 39.37 in.) are presented. Results showed a reduction of 13% in shear strength from 250 to 500 mm and a total reduction of 14% from 250 to 1000 mm. The findings indicate the new ACI 318-19 size effect factor may underestimate strength for deep pile caps.

Keywords: experimental investigation; pile caps; reinforced concrete; shear strength; size effect; two-way shear.

INTRODUCTION

Size effect is a general phenomenon by which the unit strength of a body scales with the size of the member. In reinforced concrete structures, size effect typically refers to a reduction in unit shear strength for large elements when compared with smaller counterparts. Size effect for concrete shear is often attributed to two sources: 1) statistical variations related to material strength and defect randomness; and 2) energetic releases related to the energy released during cracking. For the first time, in 2019, ACI 318 incorporated a size effect factor for concrete elements loaded in shear when said elements have shear reinforcement less than the Code minimum $A_{v,min}$ (ACI 318-19).[1] This size effect factor, labeled as λ_s, reduces unit shear strength of concrete elements with depths exceeding 250 mm (9.84 in.) using the following factor

$$\lambda_s = \sqrt{\frac{2}{1 + d/250\ (\text{mm})}} \leq 1.0 \qquad (1)$$

where d is the effective depth in mm (when effective depth is expressed in inches, the 250 mm denominator becomes 10 in.). This factor penalizes one-way unit shear strength by 18% as effective depth doubles from 250 to 500 mm (9.84 to 19.68 in.), and by another 19% as it doubles again to 1000 mm (39.37 in.).

For structural engineers designing tall buildings, deep foundations and pile caps are frequently needed to resolve overturning forces. For such foundations, in addition to one-way shear, two-way shear is a critical limit state that must be checked. At present, the same size effect factor applied to one-way shear following Eq. (1) is also applied to members loaded in two-way shear. However, one-way shear failures differ from two-way punching shear failures of slabs and diagonal compression shear failures of deep pile-cap elements. As a result, it is logical to evaluate size effect in two-way shear separately from one-way shear. But there are few to no tests of geometrically scaled specimens loaded in two-way shear across a large range of sizes for which key unitless ratios were held constant, prompting the present investigation. Herein, results are presented from an experimental study of geometrically scaled specimens with effective depths of 250, 500, and 1000 mm (9.84, 19.68, and 39.37 in.), for which current ACI 318-19 provisions would assign up to a 37% reduction in strength for the largest size.

RESEARCH SIGNIFICANCE

Accurate estimates of strength are critical for the safe design of reinforced concrete structures. Toward that goal, ACI 318-19 incorporated a "size effect" factor that reduces the unit shear strength of deep elements built with shear reinforcement less than the Code minimum. This factor has a theoretical basis supported by analyses of two databases of experimental results. For two-way shear, the database lacks experimental results across a significant size scale with strict geometric scaling. To address these issues, geometrically scaled pile caps with effective depths from 250 to 1000 mm (9.84 to 39.37 in.) were tested under uniaxial loading to failure. Results indicate the current size effect factor for two-way shear may underestimate the strength of deep pile caps.

ACI Structural Journal, V. 121, No. 1, January 2024.

MS No. S-2022-431.R2, doi: 10.14359/51739188, received July 6, 2023, and reviewed under Institute publication policies. Pertinent discussion including author's closure, if any, will be published ten months from this journal's date if the discussion is received within four months of the paper's print publication.

BACKGROUND

In designing reinforced concrete slabs and pile caps, structural engineers must consider a number of limit states beyond flexure, including one-way shear at a distance of *d* (effective depth) from a vertical member and two-way shear at a critical perimeter located *d*/2 away. Recent ACI 318-19 Code provisions have adopted a size effect factor for concrete unit shear strength reduction factor that penalizes sections deeper than 250 mm (10 in.). While it is uncommon to have large differences from this "baseline" depth for above-grade slabs, it is quite common for pile caps to range from a half meter deep for small structures to multiple meters deep for particularly tall and slender structures. In the latter case specifically, the unit shear strength of concrete is heavily penalized by the new size effect factor, requiring engineers to deepen foundations, increase concrete strength, or add tie reinforcement, all of which add cost. Thus, the size effect in two-way shear for pile caps in particular is relevant to structural engineers practicing across a range of scales. The focus of the present investigation is whether the newly adopted shear size effect factor is appropriate for deep pile caps loaded in two-way shear.

For reinforced concrete elements, size effect refers to the reported decrease in unit shear strength with increasing member depth. In 1984, Bažant[2] presented a critical study on size effect in concrete and other materials. In this study, he presented a theoretical basis for a size effect factor and a simple formulation for capturing it—very similar to that which was later adopted in ACI 318-19. Key in Bažant's formulation was a nondimensional factor that varied with the ratio of effective depth to aggregate size (d/d_a). Herein, a larger ratio would imply a large structure with small aggregate (for example, a dam or deep footing with small aggregate). For such a large structure, unit shear strength would be predicted to be smaller than that of a smaller structure such as a beam. One implication of this expression is if this unitless ratio of structural element depth to aggregate size could be held constant, no size effect would be expected when compared with test results upon which strength formulations are based. However, most experimental tests are conducted on reduced-scale specimens. And due to constructability and material availability, it is not always practical to scale aggregate size with member depth. For example, 20 mm aggregate for a 300 mm deep beam (0.79 in. for a 11.81 in. deep beam) is equivalent to 80 mm for a 1200 mm beam (3.15 in. for a 47.24 in. deep beam). In the latter case, such large aggregate size would be impractical and would cause issues with workability and reinforcing bar clearance. For this reason and more, size effect remains a prudent consideration for engineers, and has thus also received considerable attention in experimental investigations.

Bažant and Cao[3] went on to study size effect in two-way shear, publishing their findings in 1987. Herein, the authors considered the phenomenon from the ground up using dimensional analysis and similitude. The authors also reported findings considering a database of prior tests along with new experimental tests of circular slab-like specimens with thicknesses of 25, 51, and 102 mm (1.0, 2.0, and 4.0 in.). Bažant and Cao observed that larger specimens had a steeper post-peak decline curve; in other words, the specimens experienced a more drastic reduction in stiffness after peak loads. The authors concluded that the results supported the notion of a size effect for two-way shear and went on to suggest the need for geometrically similar tests to study size effect.

Since this study, there has been a lack of such geometrically similar experimental tests. This lack of controlled tests does not mean size effect in two-way shear has been totally neglected. Rather, the focus has been on other parameters. Past studies have typically focused on reinforcement layout or support configuration rather than purely size. For example, among the earliest experimental investigations of pile caps was that by Blévot and Frémy[4] in 1967 on 116 pile caps at half scale and full scale. The focus of these authors was on the strength of pile caps with two, three, and four pile supports with effective depths of up to 926 mm (36.46 in.).

Additional experimental investigations have been conducted much more recently and were well-summarized and studied by Adebar and Zhou in 1996.[5] Considering a subset of 48 pile-cap specimens, Adebar and Zhou evaluated ACI shear strength provisions, concluding that one-way shear provisions overestimated pile-cap strength, while traditional flexural design provisions for slabs underestimated strength. The authors concluded that ACI 318 sectional provisions at the time—with an average test-to-estimated strength ratio of 3.03 and a coefficient of variation of 56.6%—were overly conservative for deep pile caps, and that traditional flexural provisions were unconservative. Strut-and-tie model (STM) predictions were comparatively better but more so in flexure design where strength may be controlled by the yielding of ties.

More recently, Miguel-Tortola et al.[6] presented results from larger-scale experimental tests of three-pile-cap specimens aimed at understanding the influence of shear span-depth ratio and secondary reinforcement. The specimens ranged in effective depth from 200 to 400 mm (7.87 to 15.75 in.), with shear span-depth ratios ranging from 0.84 to 1.68. The researchers noted a possible redistribution of internal forces in pile caps after the yielding of primary reinforcement, and that failure load increased with shallower shear-span ratios. Nevertheless, once again size was not a primary focus: despite specimens ranging in effective depth from 200 to 400 mm (7.87 to 15.75 in.), other variations in test parameters make it challenging to use these test data to study size effect specifically. Specific parameters, including reinforcement configurations, were varied across the three series, and even for a given reinforcement configuration across sizes, the top bearing area and shear span were held constant rather than as a ratio of size.

Despite the volume of research on two-way shear, until the study presented herein, there had yet to be an experimental study of the effect of depth on two-way shear strength across a very large range of depths for which the ratio of specimen depth to aggregate size varies while holding constant the ratios of depth to key geometric properties such as bar spacing and bar size. This combination represents the reality for engineers designing large structures with reasonable limits on aggregate size. It thus represents an area of study of particular need. The ratio of depth to aggregate size has time and again been observed to be an important predictor for unit shear strength, but designers do not always have the option to scale aggregate size with depth due to issues with workability. Here, results are presented from an experimental study in which specimen effective depths were varied from 250 to 1000 mm (9.84 to 39.37 in.) while holding aggregate size constant at 10 mm (0.39 in.). Unitless ratios such as bar cover and bar size to effective depth were also kept constant while varying the reinforcement ratio and concrete strength.

EXPERIMENTAL INVESTIGATION

Twelve triangular pile-cap specimens were tested under uniaxial loading to failure at the laboratory of the National Center for Research on Earthquake Engineering (NCREE) in Tainan, Taiwan. Load was applied through a single circular bearing plate at the top of each pile cap, reacted by three circular bearing plates at the bottom, each with an area one-third that of the top plate area. All specimens used the same maximum aggregate size of 10 mm (0.39 in.). Effective depth, reinforcement ratio, and concrete compressive strength were varied. The following sections describe in detail the specimens, testing program, and results.

Test specimens

The primary focus of this investigation was the effect of size on unit two-way shear strength. For this reason, dimensions of each series of specimens were scaled linearly from the smallest-scale specimens. An illustration of this scaling is shown in Fig. 1. The largest specimens, referred to herein as "L-size" specimens, had effective depths (*d*) and shear spans (*a*) of 1000 mm (39.37 in.), the latter being measured from the centerline of the upper bearing plate to the centerline of the lower support plates (Fig. 2). Dimensions for the next-smallest specimens were halved ("M-size", $d = a = 500$ mm [19.68 in.]), and then halved again to the smallest in this test program ("S-size", $d = a = 250$ mm [9.84 in.]). Nominal concrete strength was specified as $f_c' = 40$ MPa (5800 psi), but this strength was increased for specimen L3H to $f_c' = 60$ MPa (8700 psi) to study the effect of concrete strength on two-way shear strength.

Each specimen was assigned an alphanumeric ID that described its size, number of layers of reinforcement, and concrete strength or label:

- **Letter:** L, M, or S, indicating effective depth and overall size, as described previously.

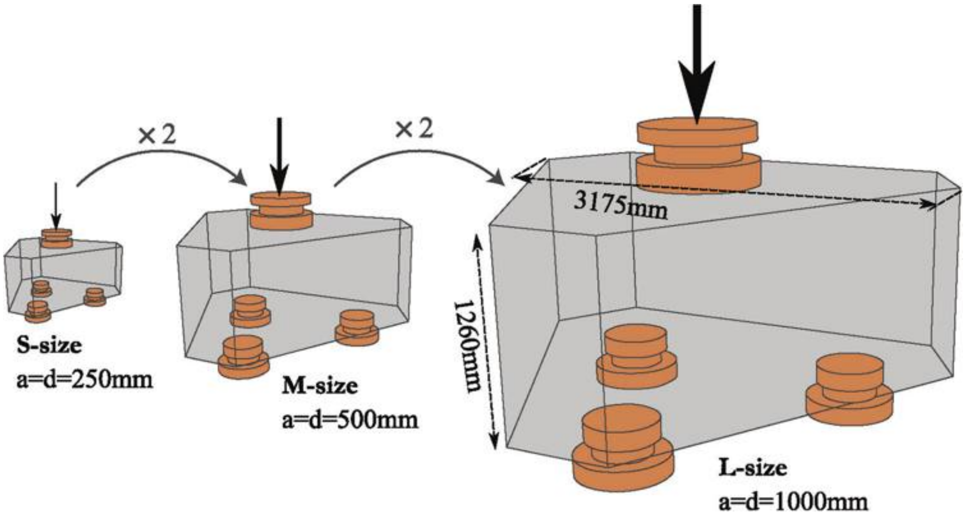

Fig. 1—Specimen scales for S-, M-, and L-sizes. (Note: 1 mm = 0.039 in.)

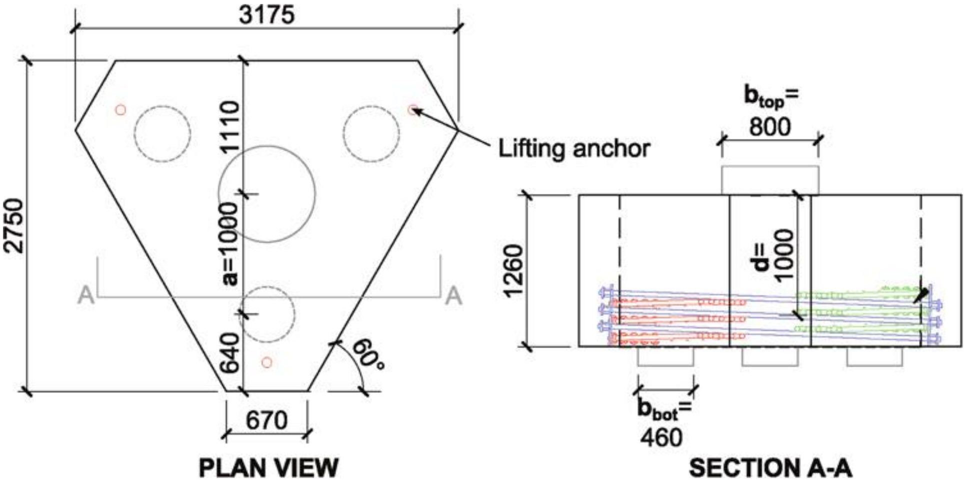

Fig. 2—Geometry and reinforcement layout for Specimen L3. (Note: Dimensions in mm; 1 mm = 0.0394 in.)

Table 1—Properties of test specimens

Size	Type	H, mm	$d = a$, mm	c, mm	d_a, mm	b_{top}, mm	b_{bot}, mm	f_c', MPa	f_y, MPa	d_b, mm	n_b	A_t, mm^2	ρ_l, %
L	L1	1260	1000	240	10	800	460	40	685	38.1 (No. 12)	5	9873	0.49%
	L3			100							15	29,620	1.48%
	L3H			100				60					
M	M1	630	500	120		400	230	40		19.1 (No. 6)	5	2468	0.49%
	M3			50							15	7405	1.48%
S	S1	315	250	60		200	115			9.5 (No. 3)	5	617	0.49%
	S3			25							15	1852	1.48%

Note: H is total thickness; d is effective depth; a is shear span; c is approximate clear cover; d_a is maximum aggregate size; b_{top} is top bearing diameter; b_{bot} is bottom bearing diameter; f_c' is target concrete compressive strength; f_y is nominal steel yield strength; d_b is steel bar diameter; n_b is number of bars spanning between lower supports; A_t is equivalent reinforcing bar area along plane along top and bottom centerlines approximated as $2\cos30° \times n_b \times 0.25\pi d_b d_b$; $\rho_l = A_t/(2a \times d)$; 1 mm = 0.0394 in.; 1 MPa = 145 psi; 1 mm^2 = 0.0016 in.^{2}.

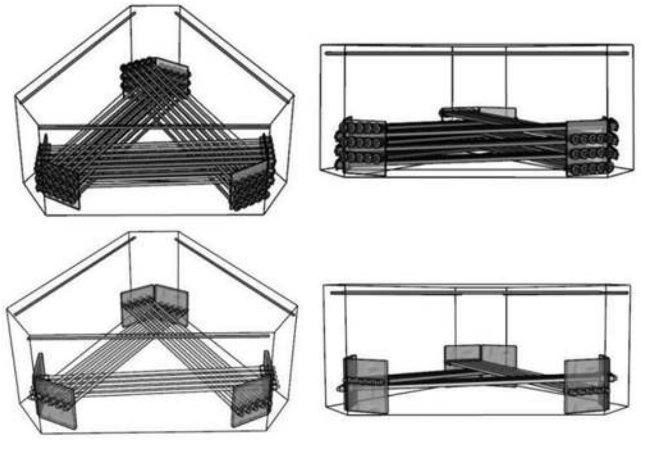

Fig. 3—(Top) representative figure showing reinforcement layouts for three-layer specimens; and (bottom) one-layer specimens (from Nakagami[10]).

- **Number:** 1 or 3, indicating the number of layers of bottom reinforcing steel.
- **Label:** a, b, or c, indicating unique specimen labels for otherwise identical specimens constructed from normal-strength concrete within a given group. H indicates a specimen constructed from high-strength concrete.

For example, L3H was a large-sized specimen with three layers of reinforcement and high-strength concrete. Specimen M3c was a medium-sized specimen with three layers of reinforcement and normal concrete and was a replicate of M3a and M3b.

Table 1 shows the test matrix, which allows for comparisons on the effect of:

- **Size:** Comparisons of S-, M-, and L-size specimens allow comparison of size effect.
- **Concrete strength:** Comparison of L-size specimens with the same reinforcement but different concrete strength.
- **Reinforcement ratio:** Comparison of over-reinforced specimens (three layers) to under-reinforced specimens (one layer) to study the impact of reinforcement ratio on strength and behavior (refer to Fig. 3 for example).

Maximum aggregate size (d_a) was fixed across all specimen sizes at 10 mm (0.39 in.). This constraint was applied because structural engineers are limited on maximum aggregate size based on factors such as structural element size, required clear cover, bar clear spacing, and material availability. This aggregate size was approximately the maximum that could clear reinforcing bars in the smallest specimens, ensuring good consolidation across the range of specimens tested. The typical maximum aggregate size in practice is approximately 20 mm (0.79 in.) for aboveground applications. There are instances in which maximum aggregate size is increased—such as the case of some bridge foundations in the United States—but the current ACI 318-19 approach does not include explicit consideration when maximum aggregate size is varied in proportion to effective depth. Nevertheless, d_a is particularly important for the size effect discussion. Had d_a been scaled along with d, the characteristic depth (d/d_a) would have remained the same and no size effect would be expected. However, scaling of d_a is not practical, as it is controlled by workability considerations. Thus, the ACI expression for size effect given by Eq. (1) is calibrated with the data of specimens with d_a in the range of 16 to 20 mm.[7]

The concrete of all S- and M-size specimens came from a single batch. The concrete of each L-size specimen came from a different batch. After casting concrete, each specimen was covered with plastic sheets to improve curing by slowing evaporation. All specimens were tested long after casting, at a minimum of 28 days.

Figure 3 shows a typical reinforcement layout. Like geometry, bottom reinforcing bar sizes were scaled linearly between specimens to the extent such bar sizes were available. L-size specimens had D38 bars (d_b = 38.1 mm [1.52 in.]), M-size had D19 (d_b = 19.1 mm [0.75 in.]), and S-size had D10 (d_b = 9.5 mm [0.37 in.]). All bars were high-strength steel, of Grade SD685 (f_y = 685 MPa [99,350 psi]). Average measured yield stresses are reported in Table 2. Because the primary objective of this study was the size effect on unit shear strength of concrete, all specimens were over-reinforced with high-strength reinforcement such that steel would remain elastic and concrete would govern strength. In other words, the specimens were designed to fail in two-way shear prior to flexural yielding.

Reinforcing bars were not anchored using straight development lengths due to the concern that slip may introduce deformation that could impact results. Using standard hooks at the ends of bars also was not possible due to congestion associated with the high reinforcement ratio

Table 2—Summary of average measured material properties

Reinforcing bar layers	Size	Specimen ID	Measured cylinder strength f_c', MPa	Average core cylinder strength $f_c'{}_{,core}$, MPa	Bar measured yield f_{ym}, MPa	Bar measured strength f_{um}, MPa
Three-layer	L	L3a	37.3	37.2	690	901
		L3b	47.7	43.9		
		L3H	71	58.6		
	M	M3a	42.9	45.1	715	865
		M3b	38.3	39.6		
		M3c	39.8	48.9		
	S	S3a	46.7	43.0	758	958
		S3b	44.5	41.9		
		S3c	45.3	41.8		
One-layer	L	L1	49.7	44.9	690	901
	M	M1	42.7	43.4	715	865
	S	S1	42.1	41.5	758	985

Note: 1 MPa = 145 psi.

meant to induce shear failure. Instead, all main bars were anchored through anchorage plate assemblies, as illustrated in Fig. 3. For L- and M- size specimens, factory "plate nuts" were available for this purpose, which were subsequently injected with epoxy.[8] For S-size specimens, no such hardware was available. To achieve similar boundary conditions, the reinforcing bars were threaded and nuts were installed.

Test setup

The specimens were tested under unidirectional loading to failure in the Bi-Axial dynamic Testing System (BATS) at NCREE. The BATS system is depicted in Fig. 4(a) and (b) (reproduced from Lin et al.[9]). Photographs of test specimens loaded onto BATS are shown in Fig. 4(c) and (d). Each specimen was loaded through a single bearing plate at the center of the top surface, which was reacted by three plates on the bottom side, each with areas one-third the area of the upper bearing plate. Bearing plate diameters are summarized in Table 1. The upper bearing plates were 800 mm, 400 mm, and 200 mm in diameter (b_{top}), respectively, for L-, M-, and S-size specimens (31.50 in., 15.75 in., and 7.87 in.). The diameters of lower bearing plates (b_{bot}) were 460 mm, 230 mm, and 115 mm (18.11 in., 9.06 in., and 4.53 in.), respectively. These dimensions are illustrated in Fig. 2. Plate diameters were selected such that bearing stresses at the top plate and bottom plates would be identical. A thin layer of gypsum cement was placed between these bearing plates and the specimens to provide uniform contact. Monotonic displacement-controlled loading was applied to the specimens until a 20% reduction in peak load was observed for small and medium specimens, followed by gradual unloading and pressure relief until the loading platen was separated from the top face. For large specimens, loading was applied until a 40% reduction in peak load.

To release rotational constraints, spherical bearings were placed between the bearing plates and the loading platens of BATS. To release horizontal translational restraints that could artificially increase strength due to friction, layers of acetal and liquid detergent were placed between the lower set of spherical bearings and the lower loading platen. This setup provides a simply supported boundary condition for test specimens. Acetal was used as an alternative to polytetrafluoroethylene (PTFE) due to its higher compressive strength while still maintaining a low friction coefficient. Had these acetal sheets and liquid detergent not been used, friction would have resisted the outward spreading of lower supports, resulting in additional vertical components of resistance that could muddy strength estimates.

The specimens were instrumented with displacement transducers, strain gauges, and optical sensors. In studies such as this in which shear is expected to govern, displacements at failure are very small. For example, specimens with *a*/*d* of 1.15 tested by Miguel-Tortola et al.[6] reached maximum load at downward displacements, on average, of approximately 3 mm for a shear span of 462 mm (0.12 in. for 18.20 in.), or 0.65%. These specimens each had a single layer of reinforcement and developed flexural cracks at midspan at peak load. For the over-reinforced specimens tested in this study, although there was flexural cracking, the relative deformations at peak load could be expected to be even smaller. For this reason, it was critical that measurements from the displacement transducers could be processed in such a way to exclude seating losses of the bearings. To do so, transducers were attached to a truss that hung beneath the specimen, as shown in Fig. 5.

In addition, transducers were installed to measure the rotations at the vertical faces behind each support, relative deformations at supports, crack width development, and vertical extension on each long face. A detailed discussion of sensor layouts is available in Nakagami.[10] Strain gauges were attached at the midspan of longitudinal reinforcement, with alphanumeric labels indicating their relative position as follows:

- **First number:** Edge (1, 2, or 3);
- **Second letter:** Bar position from the center (a, b, c, d, e) starting from inside; and
- **Third letter:** Bar layer: L is Lower, C is Center, U is Upper.

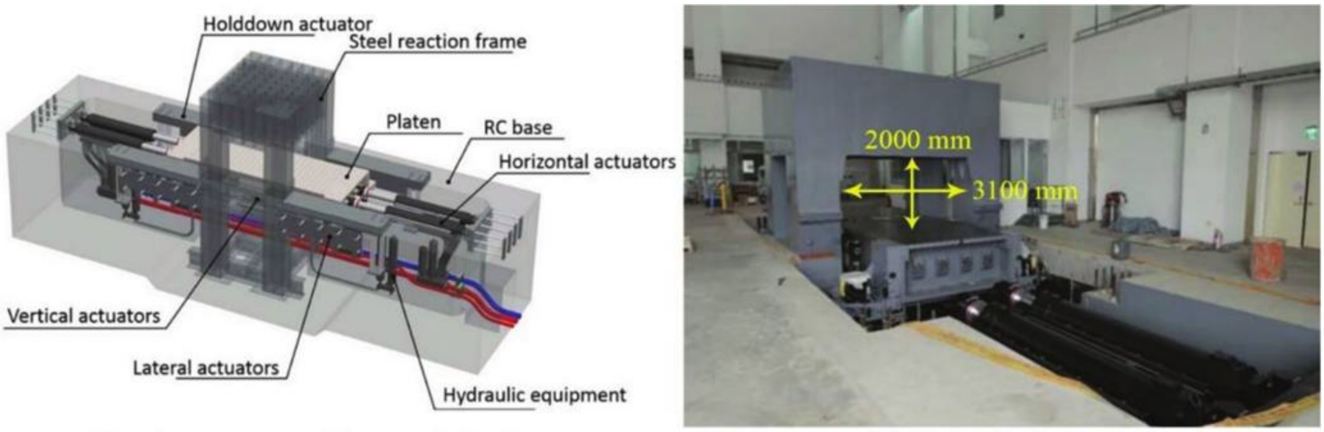

(a) Primary parts and layout of BATS

(b) Photo of BATS

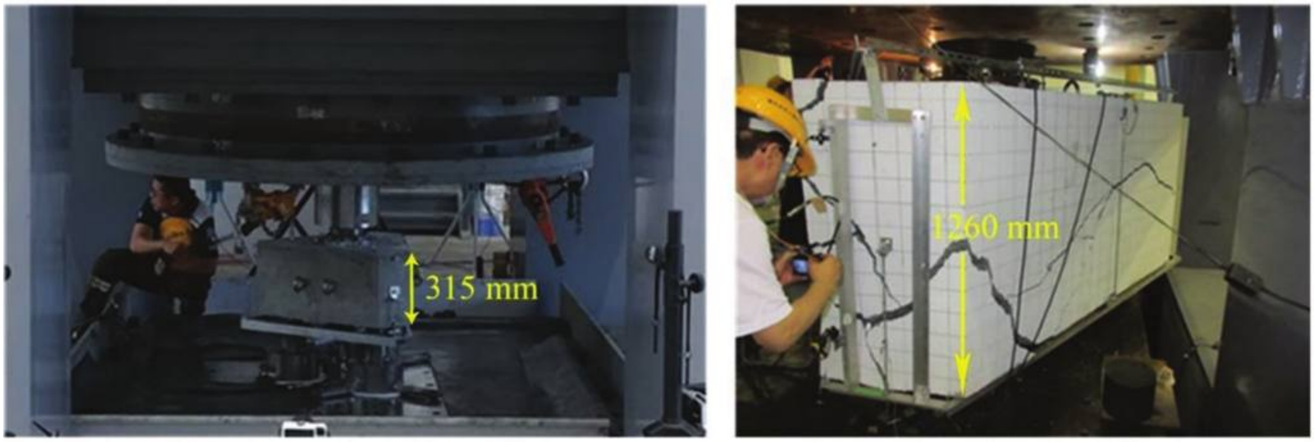

(c) Smallest specimen loaded into BATS

(d) Largest specimen loaded into BATS

Fig. 4—BATS key parts, overall view, and photos of smallest and largest specimens loaded into BATS.

Fig. 5—(Left) underhung truss for bottom transducers; and (right) photograph of Specimen L3h showing: (a) transducer to measure side crack width; and (b) mounting of underhung truss.

These alphanumeric labels were prefixed with a lowercase "s," indicating strain. Their positions on reinforcement are illustrated in Fig. 6.

EXPERIMENTAL RESULTS

In this section, load-deformation plots for the specimens are presented. As described in the "Test setup" section, an instrumentation frame was hung beneath each specimen to offset errors in displacement measurement associated with bearing seating losses. In the plots that follow, deformation is reported relative to the reference frame such that bearing seating has been removed already, leading to accurate measures of stiffness. The effect of gravity on the measured strength is also negligible, with the weight of the large specimen approximately equal to 1% of the observed capacity.

Load deformation

Figure 7 shows plots of applied downward force versus displacement for all specimens. Displacement scales with length, so to facilitate comparison, the axes are scaled between different sizes. The displacement axis (x-axis) is scaled by (500 mm/1000 mm) = 0.5 when going from L-series to M-series specimens. Two-way shear capacity scales with the area, so the force axis (y-axis) is scaled by (500 mm/1000 mm) × (500 mm/1000 mm) = 0.25 when going from L-series to M-series specimens. The same

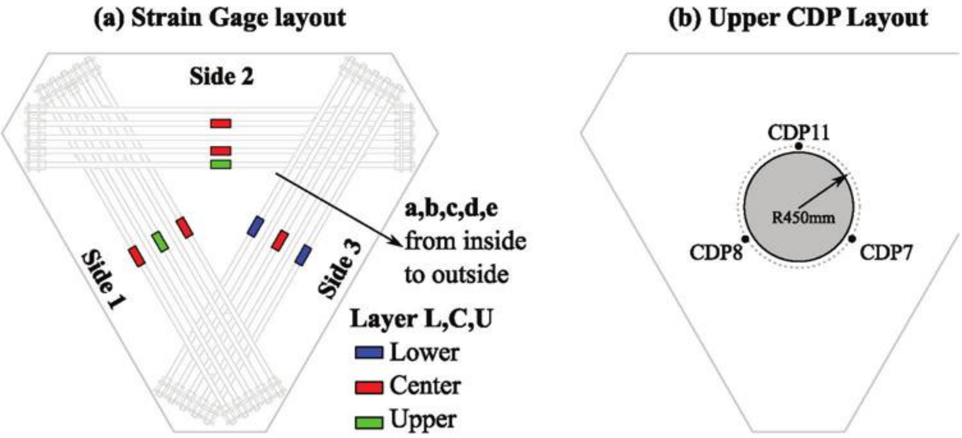

Fig. 6—Layout of: (a) strain gauges; and (b) upper displacement transducers.

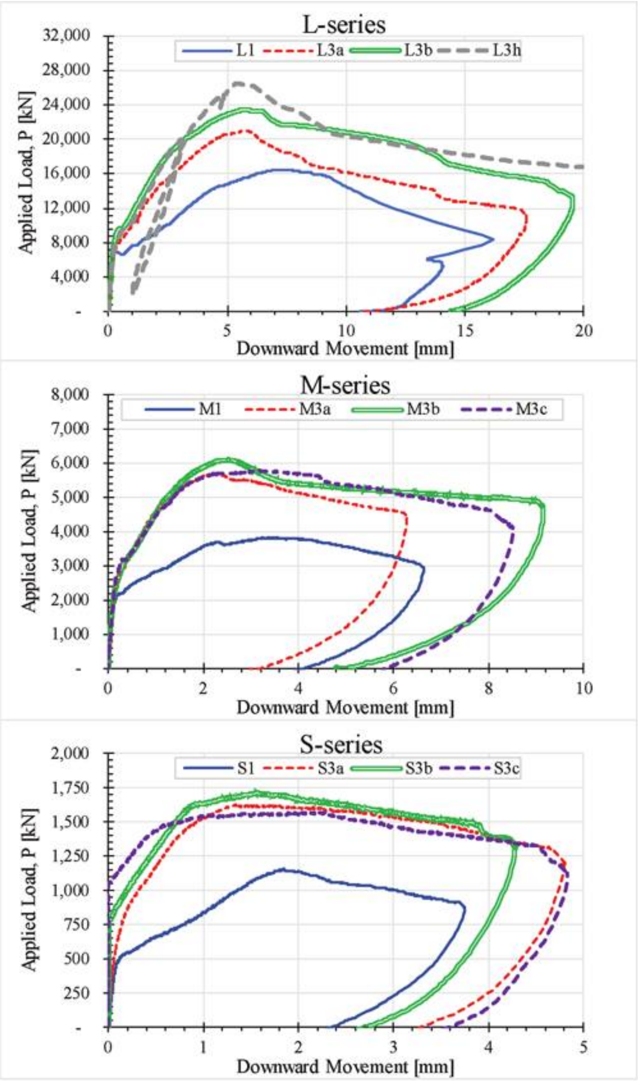

Fig. 7—Applied force versus downward displacement plots for all specimens. (Note: 1 mm = 0.0394 in.; 1 kN = 0.224 kip.)

scaling logic is applied again going from M-series to S-series specimens.

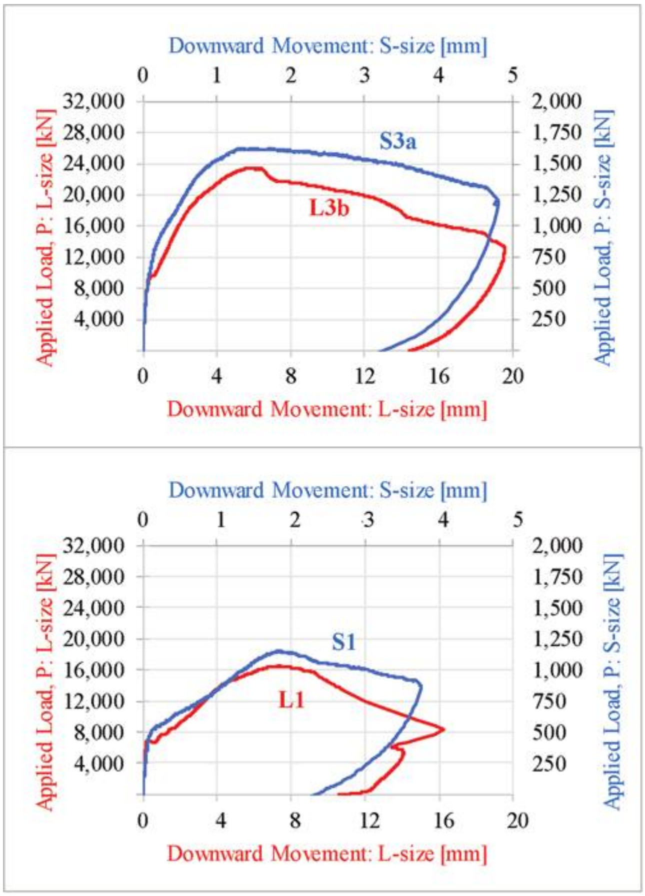

Fig. 8—Comparison of load versus downward displacement for: (top) S3a and L3b; and (bottom) S1 and L1. (Note: 1 mm = 0.0394 in.; 1 kN = 0.224 kip.)

Figure 8 shows load-versus-deformation plot comparisons for Specimens S3a and L3b, which were at each end of the size spectrum but had similar concrete compressive strengths. Dual axes are used in this plot to facilitate comparison, as described previously. Curves for these two specimens reveal similar initial stiffness but different post-cracking stiffness and strength, with the larger specimen having a smaller post-cracking stiffness and peak load. Also shown in this figure are plot comparisons for Specimens S1 and L1, which showed a similar trend.

Load strain

Figure 9 shows applied load versus longitudinal bar strain for four specimens (L1, S1, L3b, and S3a). These specimens

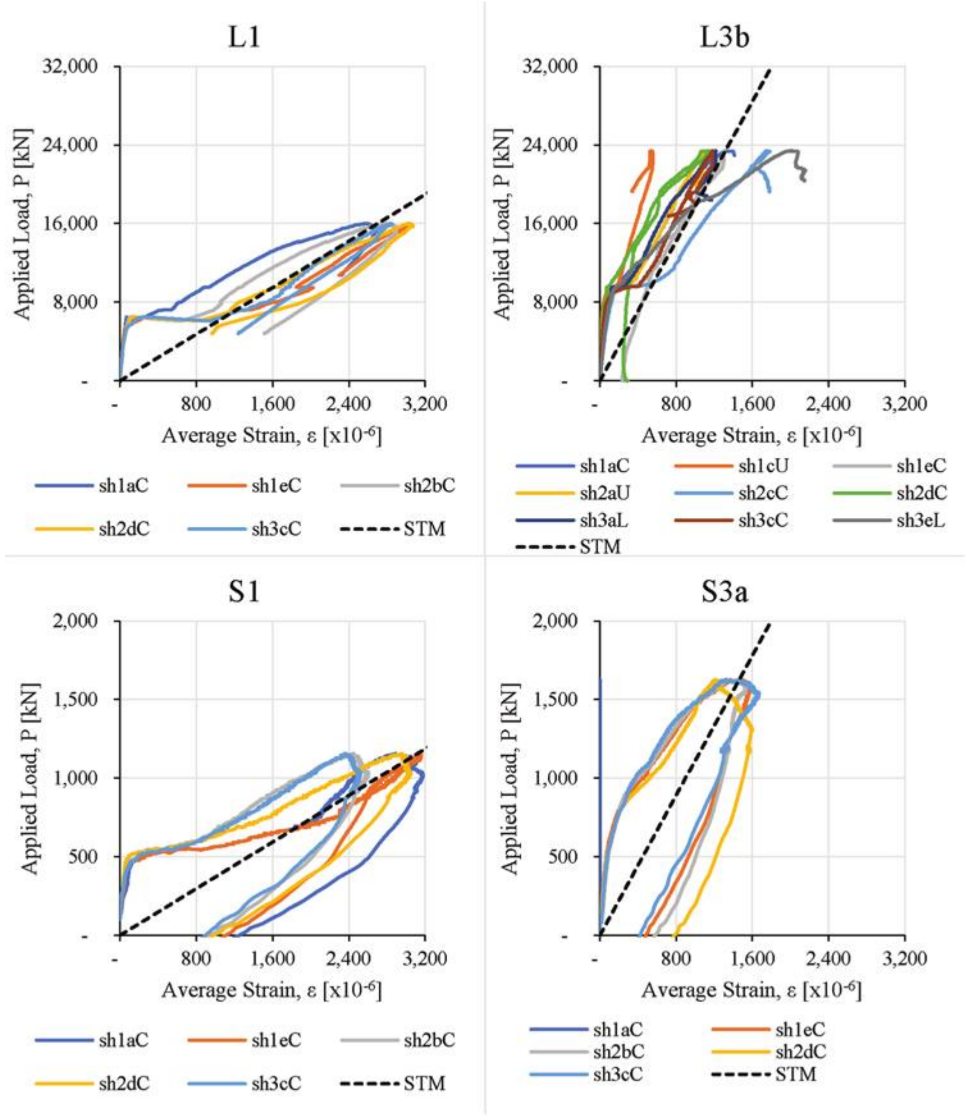

Fig. 9—Vertical load versus measured strain in longitudinal bars. Predicted strains based on idealized STM are also shown for comparison. Note that nominal yield strain would correspond approximately to 3400×10^{-6}. (Note: 1 kN = 0.224 kip.)

were selected because they lie at the extreme ends of variables tested in this study in terms of size and number of layers of reinforcement. Initially, there is virtually no strain in the steel. At cracking, steel strain starts to increase rapidly with applied load. This cracking occurs earlier in Specimen L1 at approximately 6000 kN (1350 kip), compared with 500 kN (112 kip) for Specimen S1 (equivalent to 8000 kN [1800 kip] at L-scale). This parallels the trend observed for specimens with three layers of reinforcement, although the maximum load was reached at a smaller peak strain. Furthermore, Fig. 9 also highlights that both in one-layer and three-layer specimens, the strain is well below the yield value, indicating that the reinforcement remained elastic until the failure in all specimens, thereby validating the shear failure of test specimens. This is expected, as all specimens were designed to fail in shear rather than flexure.

Failure mechanism

Figure 10 shows a failed specimen after the removal of loose concrete, with an idealized STM illustration superimposed. The superimposed simplified STM with added nomenclature is presented on the right side of Fig. 10. The observed failure was similar in shape to those observed in previous tests by Miguel-Tortola et al.[6] and to the idealized punching shear mechanism described by Jensen and Hoang[11] in their study describing an upper-bound plasticity approach for estimating pile-cap strength.

To understand resistance mechanisms better, selected specimens were cut after testing to generate three-dimensional (3-D) crack maps. These cuts were made from the top bearing plate toward the lower supports. Readers should note that these section cuts represent cracks that could have formed and propagated in the post-peak stage as well, and therefore may have more crack density and width relative to the cracking near the peak-load (strength) stage. One crack map is illustrated in Fig. 11 alongside images showing similar cuts for Specimens S3b, M3b, and M1. Here, the inclined plane at which sliding is assumed to have occurred is clearly visible, emanating from the upper bearing plate downward. The crack in M1 in this figure appears shallower than its counterparts, but subsequent cutting of the other planes revealed a steeper crack. Not all specimens were cut

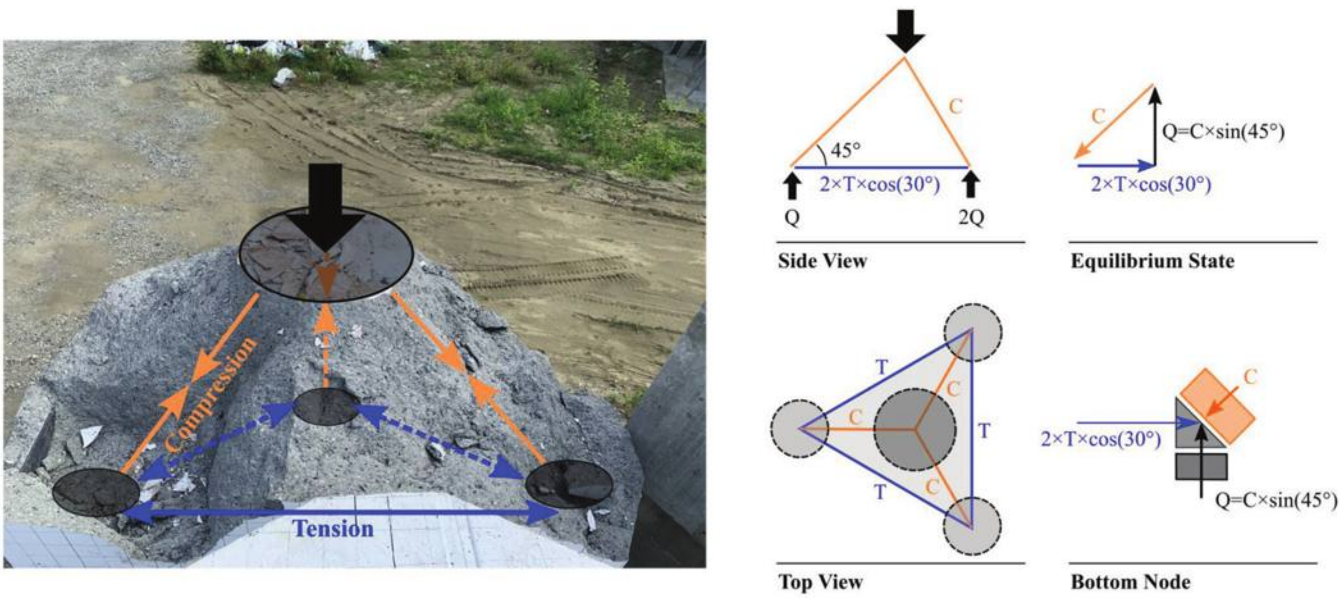

Fig. 10—(Right) failed Specimen L1 after removal of upper loose concrete, with STM superimposed; and (left) simplified STM.

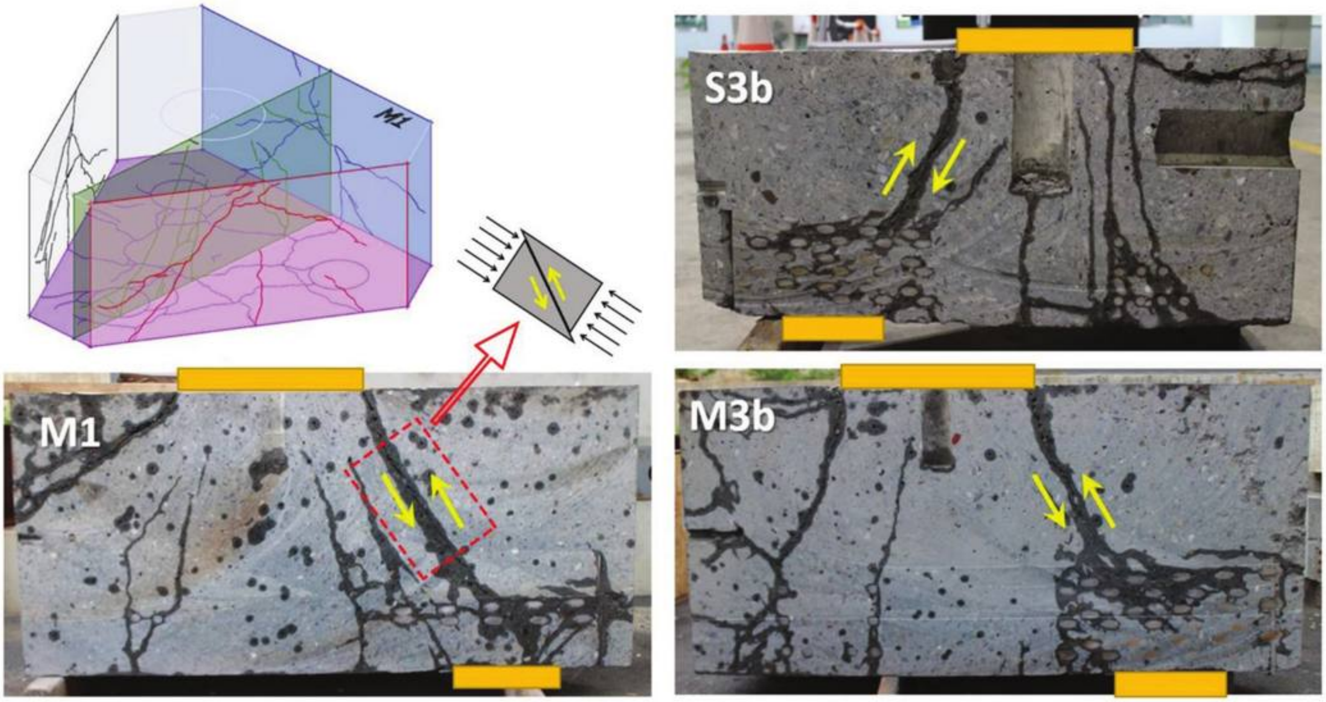

Fig. 11—Three-dimensional crack map showing plane at which specimens were cut after testing, and photographs of sliced specimens showing crack pattern and sliding plane. Positions of loading plates are indicated by orange rectangles. (Note: Full-color PDF can be accessed at www.concrete.org.)

along multiple axes following testing and, for brevity, not all specimen cuts are included in this paper. The figure shown is meant to highlight observed behavior.

Downward movement of the concrete directly beneath the upper bearing plate relative to the surrounding concrete is referred to herein as "sinking" displacement, which is shown in Fig. 12. This "sinking" displacement does not necessarily correspond to overall downward movement of the underside of the specimen. In other words, it is possible for the top platen to move downward without causing underside deflection, as sinking is most apparently caused by localized crushing of the concrete surrounding the loading plate rather than by crushing of concrete immediately beneath the loading plate. Concrete beneath the loading plate experiences a near-hydrostatic state of stress owing to the surrounding compressive stress state. This near-hydrostatic state results in larger localized capacity of the concrete. This can explain the intactness of concrete beneath the plates following testing (Fig. 11).

The specimen plate vertical "sinking" deformations relative to adjacent concrete were driven by vertical displacement of the upper loading plate (Fig. 12) caused by sliding

Fig. 12—Vertical settlement of top bearing area (Specimen L3a).

Table 3—Summary of concrete strengths and test results

Specimen	Cylinder strength f_c', MPa	Average f_c' (cores), MPa	Core average $f_{c,core}'$, MPa	Capacity P_u, kN	Deflection at peak load Δ_u, mm	Bearing stress $\sigma_b = P_u/A_{top}$ (Eq. (3)), MPa	Two-way shear stress $v_{c2} = P_u/A_{v2}$ (Eq. (2)), MPa	Normalized shear stress $v_{c2,norm} = \frac{\sqrt{40\text{ MPa}}}{\sqrt{f_{c,core}'}} v_{c2}$ (Eq. (4)), MPa
L3a	37.3	37.2	37.2	20,990	5.65	41.9	3.71	3.85
L3b	47.7	43.9	43.9	23,390	5.83	46.6	4.14	3.95
L3H	71	58.6	58.6	26,450	5.49	52.9	4.68	3.86
M3a	42.9	45.1	44.3	5690	2.31	45.4	4.02	3.82
M3b	38.3	39.6		6100	2.52	48.6	4.31	4.10
M3c	39.8	48.9		5790	3.19	46.2	4.10	3.89
S3a	46.7	43.0	42.1	1630	1.34	53.4	4.61	4.50
S3b	44.5	41.9		1710	1.55	55.4	4.84	4.72
S3c	45.3	41.8		1570	2.14	50.3	4.44	4.33
L1	49.7	44.9	44.9	16,480	7.31	32.8	2.91	2.75
M1	42.7	43.4	44.3	3820	3.45	30.4	2.70	2.57
S1	42.1	41.5	42.1	1160	1.85	38.5	3.28	3.20

Note: 1 mm = 0.0394 in.; 1 MPa = 145 psi; 1 kN = 0.224 kip.

of the concrete along an inclined plane from the edges of the upper plate to the edges of the lower support plates (Fig. 11). This vertical displacement was measured in Specimens L3b, L3H, and L1 along the periphery of the upper plate using transducers.[9] The movement began at approximately 70 to 80% of the peak load, at which it was on the order of 0.5 to 0.6 mm (0.002 in.) based on the average of the three upper transducers, as shown in Fig. 6. At the peak load, observed local downward movement surrounding the top plate was between 3 and 4 mm (0.12 and 0.16 in.), which was approximately one-half of the total deflection at that state. This corroborates that upper-plate vertical "sinking" deformation was not always accompanied by underside vertical movement. At the maximum deflection, the movement was between 17 and 24 mm (0.67 and 0.94 in.), which was close to the total deflection. The large deflection and apparent ductility beyond the peak load can be attributed to dowel action, which was engaged after primary cracking, as well as sliding along the internal critical shear crack. In the case of the specimens tested in this study, this critical crack and the corresponding struts were fully surrounded by concrete, which facilitated larger ductility. Said dowel action would have been engaged after initiation of the sinking and would have increased as sinking increased.

DISCUSSION

Load versus deformation

Due to variations in size, specimen strengths had to be normalized to facilitate comparison. The two measures of strength most pertinent here are measured two-way shear stress and bearing stress. Two-way shear stress was calculated as follows

$$v_{c2} = P_u/A_{v2} \tag{2}$$

where P_u is the ultimate load carried by each specimen; and A_{v2} is the shear area at calculated distance $d/2$ from the edge of the top bearing plate. For the L-size specimens, this diameter is 800 mm + 2(1000 mm/2) = 1800 mm (70.87 in.). Two-way shear strength thus calculated is summarized in Table 3. Also shown in Table 3 are bearing stresses, normalized relative to the top bearing area as follows

$$\sigma_b = P_u/A_{top} \tag{3}$$

where P_u is the ultimate load carried by each specimen; and A_{top} is the bearing area below the top bearing. Recall from the "Test setup" section that the bottom bearings were sized such that support bearing stress would be approximately equal.

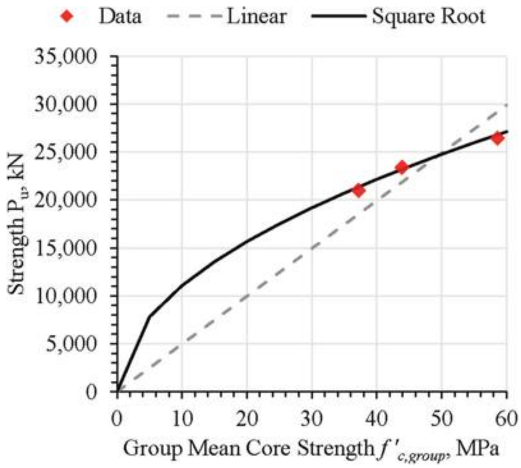

Fig. 13—Strengths of largest specimens with three layers of reinforcement versus group mean core compressive strengths. Approximate linear and square-root scaling with concrete compressive strength superimposed.

Effect of concrete strength

Nominal concrete compressive strength was varied deliberately in L3-series specimens from $f_c' = 40$ to 60 MPa (5800 to 8700 psi). Figure 13 shows the normalized strength for L3-type specimens plotted against concrete compressive strength. Additional curves in this figure represent estimates from: 1) a linear regression from the origin; and 2) a square-root regression from the origin. Although the STM assumes a linear variation of capacity with concrete strength, this figure shows that strength tracks better with the square root of concrete compressive strength.

Strength normalization

The primary objective of this test program was to study the size effect. Results shown in the previous section were meant to calibrate the study and provide additional insight into the effect of concrete compressive strength. However, concrete compressive strength can seldom be held constant in any test program. Variations in concrete compressive strength across specimens with nominally equal strengths and sizes mean that additional normalization relative to concrete strength was needed to bring test results to the same reference compressive strength before comparing the effects of other factors.

Specimen strength was observed to track well with the square root of concrete compressive strength, as shown in Fig. 13, which is consistent with the approach followed by ACI 318-19. Measurements of cylinder cores sampled after testing best represent the true strengths of specimens given actual curing conditions and sizes. For this reason, measured strengths were normalized to the square root of the ratio of the target compressive strength ($f_c' = 40$ MPa [5800 psi]) to the measured core compressive strength as follows

$$v_{c2,norm} = \frac{\sqrt{f_c' \ = \ 40\text{ MPa}}}{\sqrt{f_c'{}_{,core}}} v_{c2} \tag{4}$$

where $f_c'{}_{,core}$ is the average compressive strength obtained for a group of cores for a given specimen size. Thus, where observed concrete compressive strength was larger than nominal, the aforementioned approach would normalize observed strength to a 40 MPa (5800 psi) baseline. Concrete cores were sampled from undisturbed regions of the specimens after testing. Ordinarily, a design engineer would use cylinder compressive strength for this purpose, as cores are not always taken for new structures. But because cores were taken for the test specimens, and because these cores better reflect curing conditions and concrete compressive strength for each specimen, these cores were used instead to obtain the best estimate of concrete strength. The average strength of two cores sampled after testing from undisturbed regions of each specimen was used as the basis for this normalization. The L-size specimens were each cast using a single batch of concrete, so they were normalized relative to individual core averages. The M- and S-size specimens were cast altogether from one batch of concrete and cured under similar conditions. For these sizes, the average of all cores for a given size was used.

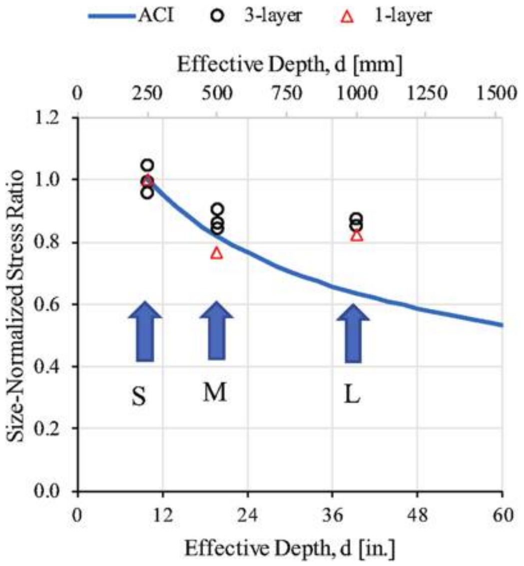

Fig. 14—Size-normalized stress ratios plotted alongside ACI 318-19 size effect factor.

Effect of size on strength

Strengths after compressive strength normalization were normalized one last time such that the group mean ratios for S3- and S1-size specimens were unity. The purpose of this normalization was to facilitate comparison with current size effect provisions, for which the size effect factor is $\lambda_s = 1.0$ for specimens with effective depth $d = 250$ mm (9.84 in.) (S-size). These results are plotted in Fig. 14. Although Fig. 14 shows a reduction in strength, it is not as severe as current ACI 318-19 two-way shear provisions would suggest. As effective depth increased from 250 to 500 mm (9.84 to 19.68 in.), as with S3- to M3-size specimens, strength reduced by 13% on average. As effective depth increased again from 500 to 1000 mm (19.68 to 39.37 in.), the reduction was even smaller at 1%. This total reduction of only 14% is much smaller than the 37% reduction required

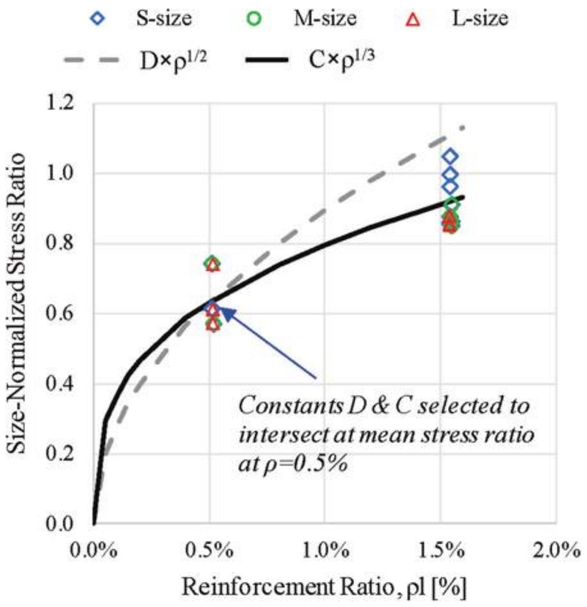

Fig. 15—Size-normalized stress ratios plotted against reinforcement ratio.

in ACI 318-19 for d = 1000 mm (39.37 in.) and the 29% estimated in JSCE[12] using a quadratic root of effective depth.

This observation highlights that the square-root term in Eq. (1) currently used by ACI 318-19 can underestimate strength for very deep foundations. It also highlights that, such as what was proposed by Kim et al.[13] for size effect in compression, there may be a saturation point beyond which further reductions are negligible (that is, a floor to the size effect reduction factor). A similar floor has been adopted in Eurocode 2 for reinforced concrete.[14]

Effect of size on stiffness

Perhaps the most notable difference observed between specimens was that of post-cracking stiffness, as observed in Fig. 7 and 8. Cracking occurs after 750 kN (169 kip) for S3a and after 9000 kN (2023 kip) for L3b. The change in stiffness after cracking is also clearly visible in Fig. 9, where steel strain in S3a approaches the STM idealization more gradually than it does in L3b. This tendency is consistent with expectations based on tension stiffening, as described previously by Bentz.[15] Bentz describes the proportionality of tension stiffening to a "bond parameter," M, as follows

$$M = A_c/\Sigma d_b\pi \tag{5}$$

where A_c is the area of concrete reinforced by the bar; and d_b is the reinforcing bar diameter. In this expression, smaller tension stiffening is expected for elements with larger M (that is, larger ratios of concrete area to bar surface area). Here, bond parameter M for L3-series specimens is four times that of M for S3-series specimens. As a result, less tension stiffening would be expected for the larger specimen and a shallower slope in the plot of load versus strain or deformation, as was observed in shallower slopes for both one- and three-layer L-size specimens compared with S-size counterparts in Fig. 8.

Effect of reinforcement ratio

Recall that all specimens were over-reinforced such that shear failures would occur prior to flexural yielding. Although reinforcement remained elastic during the test program, the reinforcement ratio does affect how much concrete is active in resisting applied load. Figure 15 shows test results normalized as per Fig. 14 plotted against longitudinal reinforcement ratio ρ_l. Also shown in this plot are curves based on the stress ratios varying with either the cube root or square root of the reinforcement ratio. Designers typically use these factors in determining shear strength, which are incorporated by both ACI and JSCE. ACI provisions use a cube root on longitudinal reinforcement for one-way shear (ACI 318-19, 22.5.5.1(b) and (c)). JSCE provisions use a cube root in general for one-way shear (JSCE 15-2017, Section 9.2.3). To facilitate comparison, these curves have been multiplied by constants such that they intersect at the same average stress at approximately ρ_l = 0.5% across all scales. It is notable that the cube root tends to provide a better estimate of peak strength when compared with the square root. This observation is also consistent with recommendations proposed by Mogili et al.[16] to add a cube-root factor of ρ to current ACI 318 two-way shear strength provisions for more accurate estimations. In the sections that follow herein, the behavior and failure mechanisms of the specimens are described in detail.

Approximate STM

Figure 10 shows an approximate STM of the pile caps herein overlaid upon a test specimen, alongside a simplified model with added nomenclature. This representation shows the struts at an idealized 45-degree inclination. Based on this inclination and an equilateral triangle-shaped bottom layer of steel, an applied load on the top plate P would be expected to result in an average steel tensile force of $P/(6 \times \cos 30°)$. This tensile force can be normalized by the total bar area to obtain the tensile stress, and then again by the modulus to obtain the strain. Restated

$$\varepsilon_{avg} = \frac{P}{6\cos 30°} \cdot \frac{1}{A_b} \cdot \frac{1}{E_s} \tag{6}$$

where P is the applied load at the top plate; A_b is the total bottom bar area; and E_s is the elastic modulus of steel. Equation (6) can be used to create a plot of expected load versus average strain, which are shown as straight lines in Fig. 9. Notably, in both figures, measured strains converge near this line at the observed peak load. The average strain calculated following this simplified method shows reasonable agreement with the load-deformation response of these specimens.

SUMMARY AND CONCLUSIONS

This paper presents results from a study of tripod pile-cap specimens loaded in two-way shear. Specimens were geometrically proportional to one another, with effective depths of 250, 500, and 1000 mm (9.84, 19.68, and 39.37 in.). Maximum aggregate size was held constant at 10 mm (0.39 in.). Specimens contained either three layers or one layer of high-strength reinforcement. All specimens were over-reinforced with high-strength steel such that strength would be driven by shear failure. Observations from this study are summarized as follows.

1. Within the ranges of variables considered, results show a diminishing decrease in unit strength with increasing effective depth. For the specimens tested, as effective depth doubled from 250 to 500 mm (9.84 to 19.68 in.), normalized unit strength decreased by 13%. As effective depth doubled again, unit strength decreased by another 1% for a total of 14%. These observations suggest the possible need for a floor for size effect in compression, as proposed by Kim et al.[13]

2. Shear strengths of specimens were proportional to the square root of the concrete strength and the cube root of the reinforcement ratio.

3. Specimen behavior was dominated by vertical movement of the top plate, followed by sliding along a crack that emanated from the edge of the top plate to the edge of the support plate.

4. Observed strains in the bottom reinforcement at peak load agreed well with the predictions of simple strut-and-tie models (STMs).

AUTHOR BIOS

Lucas Laughery *is a Senior Structural Engineer at ICON in Austin, TX. He received his PhD from Purdue University, West Lafayette, IN. He is a member of ACI Committee 133, Disaster Reconnaissance, and Joint ACI-ASCE Subcommittee 445-B, Shear & Torsion-Seismic Shear. His research interests include large-scale structural testing, additive manufacturing, and the design of structures for extreme wind and blast demands.*

Toshikatsu Ichinose *is a Professor at Meijo University, Nagoya, Japan. He received his doctoral degree from The University of Tokyo, Tokyo, Japan. His research interests include seismic behavior and retrofit of reinforced concrete structures.*

Kazuhiko Kasai *is Professor Emeritus at the Tokyo Institute of Technology, Tokyo, Japan. He received his PhD from the University of California, Berkeley, Berkeley, CA. His research interests include large-scale structural testing, seismic design and analysis, steel structures, passive control systems, and base isolation systems.*

Srinivas Mogili *is an Assistant Professor at Indian Institute of Technology Delhi, Delhi, India, and was formerly a Postdoctoral Researcher at National Taiwan University, Taipei, Taiwan. He received his PhD from The Hong Kong University of Science and Technology, Hong Kong, China. His research interests include the seismic design, analysis, and testing of reinforced concrete members such as beam-column joints, columns, pile caps, and flat slabs.*

Shyh-Jiann Hwang, *FACI, is a Professor of civil engineering at National Taiwan University. He received his PhD from the University of California, Berkeley. His research interests include seismic behavior of reinforced concrete members and seismic retrofitting of reinforced concrete structures.*

ACKNOWLEDGMENTS

This research was an international cooperation by Tokyo Institute of Technology (Tokyo Tech), the National Center for Research on Earthquake Engineering (NCREE), and the Nagoya Institute of Technology (Nagoya Tech). It was conducted using funds from NCREE, Tokyo Tech, and Kasai Laboratory supported by KYB Corporation, SWCC Corporation, the Japan Iron and Steel Federation, Bridgestone Corporation, and OILES Corporation. The reinforcing bars and anchor devices were provided by Kyoei Seiko Co., Ltd., and Tokyo Tekko Co., Ltd. Special thanks are given to S. Komatsu (Assistant Professor, Shimane University, Japan), K. Y. Liu (Professor, National Cheng Kung University [NCKU], Taiwan), K. Y. Liu (former student, NCKU), Y. Nakagami (former student, Nagoya Tech), and the laboratory technicians at NCREE Tainan Laboratory.

REFERENCES

1. ACI Committee 318, "Building Code Requirements for Structural Concrete (ACI 318-19) and Commentary (ACI 318R-19) (Reapproved 2022)," American Concrete Institute, Farmington Hills, MI, 2019, 624 pp.

2. Bažant, Z. P., "Size Effect in Blunt Fracture: Concrete, Rock, Metal," *Journal of Engineering Mechanics*, ASCE, V. 110, No. 4, 1984, pp. 518-535. doi: 10.1061/(ASCE)0733-9399(1984)110:4(518)

3. Bažant, Z. P., and Cao, Z., "Size Effect in Punching Shear Failure of Slabs," *ACI Structural Journal*, V. 84, No. 1, Jan.-Feb. 1987, pp. 44-53.

4. Blévot, J., and Frémy, R., "Semelles sur Pieux: Méthodes de Calculs, Compte Rendu d'Essais, Dispositions Constructives," Annales de l'Institut Technique du Bâtiment et des Travaux Publics, V. 230, Feb. 1967. (in French)

5. Adebar, P., and Zhou, L., "Design of Deep Pile Caps by Strut-and-Tie Models," *ACI Structural Journal*, V. 93, No. 4, July-Aug. 1996, pp. 437-448.

6. Miguel-Tortola, L.; Pallarés, L.; and Miguel, P. M., "Punching Shear Failure in Three-Pile Caps: Influence of the Shear Span-Depth Ratio and Secondary Reinforcement," *Engineering Structures*, V. 155, 2018, pp. 127-143. doi: 10.1016/j.engstruct.2017.10.077

7. Bažant, Z. P.; Yu, Q.; Gerstle, W.; Hanson, J.; and Ju, J. W., "Justification of ACI 446 Proposal for Updating ACI Code Provisions for Shear Design of Reinforced Concrete Beams," *ACI Structural Journal*, V. 104, No. 5, Sept.-Oct. 2007, pp. 601-610.

8. Tokyo Tekko Steel, "PLATE-NUT," Tokyo Tekko Co., Ltd., Oyama, Japan, http://www.tokyotekko.co.jp/en/prd/tekko/nst/nst10.html. (last accessed Nov. 28, 2022)

9. Lin, T.-H.; Chen, P.-C.; and Lin, K.-C., "The Multi-Axial Testing System For Earthquake Engineering Researches," *Earthquakes and Structures*, V. 13, No. 2, 2017, pp. 165-176.

10. Nakagami, Y., "Size Effect of Footing Under Two-Way Shear," master's thesis, Nagoya Institute of Technology, Nagoya, Japan, 2020. (in Japanese)

11. Jensen, U. G., and Hoang, L. C., "Collapse Mechanisms and Strength Prediction of Reinforced Concrete Pile Caps," *Engineering Structures*, V. 35, 2012, pp. 203-214. doi: 10.1016/j.engstruct.2011.11.006

12. JSCE-15, "Standard Specification for Concrete Structures," Japan Society of Civil Engineers, Tokyo, Japan, 2017, 469 pp.

13. Kim, J.-K.; Yi, S.-T.; Park, C.-K.; and Eo, S.-H., "Size Effect on Compressive Strength of Plain and Spirally Reinforced Concrete Cylinders," *ACI Structural Journal*, V. 96, No. 1, Jan.-Feb. 1999, pp. 88-94.

14. EN 1992-1-1:2004, "Eurocode 2: Design of Concrete Structures – Part 1-1: General Rules and Rules for Buildings," European Committee for Standardization, Brussels, Belgium, 2004, 227 pp.

15. Bentz, E. C., "Explaining the Riddle of Tension Stiffening Models for Shear Panel Experiments," *Journal of Structural Engineering*, ASCE, V. 131, No. 9, 2005, pp. 1422-1425. doi: 10.1061/(ASCE)0733-9445(2005)131:9(1422)

16. Mogili, S.; Lin, J.-Y.; and Hwang, S.-J., "Vertical Punching Capacity of Reinforced Concrete Flat Plates without Shear Reinforcement," *ACI Structural Journal*, V. 121, No. 1, Jan. 2024. doi: 10.14359/51739193

ARE YOU A RESEARCHER?

SIGN UP FOR ORCID TODAY!

1 Register

2 Use your ORCID ID

3 Share

ORCID provides a digital identifier that distinguishes you from every other researcher and, through integration in key research workflows such as manuscript and grant submission, supports automated linkages between you and your professional activities, ensuring that your work is recognized.

ORCID services are FREE and it's as easy as **1-2-3**.

WWW.ORCID.ORG

ACI STRUCTURAL JOURNAL TECHNICAL PAPER

Title No. 121-S09

Flexural Noncontact Lap Splices in Ultra-High-Performance Concrete

by Jason Hock, Kevin R. Mackie, Georgios Apostolakis, and Tiancheng Wang

*Ultra-high-performance concrete (UHPC) has the potential to create more-durable structures that can be economized based on performance criteria. An experimental program consisting of 47 small-scale, noncontact lap splice specimen tests under four-point loading was conducted to investigate the bond strength and slip mechanisms within UHPC. Parameters studied in the testing matrix included aspect ratio, clear cover, lap length, and bar size. An inverse analysis on a numerical model of the flexural tests was employed to compute the bond stress-slip parameters representative of each specimen group. Results showed an enhanced bond stress-slip behavior inducing reinforcing bar yielding for clear cover greater than 1.5*d_b *and lap splice lengths of 9*d_b*. The post-peak response of all specimens exhibited ductile behavior, including those that experienced slip. By controlling the lap parameters and using this ductile mechanism, the maximum bar stress can be limited to a target value in the design process.*

Keywords: bond strength; cover; development length; noncontact lap splice; slip; ultra-high-performance concrete (UHPC).

INTRODUCTION

Ultra-high-performance concrete (UHPC) is a type of ultra-high-performance fiber-reinforced cementitious composite material that is a relatively new innovation in concrete materials for structural engineering. This class of concrete became commercially available in the 1990s with applications in bridges and building structures. UHPC-class materials are characterized by improved mechanical and durability properties that surpass conventional and high-strength concrete. The dense pore structure improves durability to freezing and thawing and other environmental conditions, with a significant improvement in service life compared to conventional concrete.[1] The rapid expansion of material and structural research on UHPC is covered in Hung et al.[2]

UHPC is defined as having a compressive strength greater than 21.7 ksi (150 MPa) and a post-cracking tensile strength greater than 0.72 ksi (5.0 MPa).[3] These mechanical properties are affected by many factors, including curing type (thermal, steam, ambient, and so on), curing time, and steel microfiber reinforcement. Earlier studies have shown that volume fractions up to 5% of high-strength steel microfiber reinforcement facilitates tension hardening, higher tensile ductility, increased post-peak energy dissipation capacity, spalling resistance, and enhanced bond strength.[3] UHPC offers improved bond strength and confinement behavior over conventional reinforced concrete (RC), allowing for the reduction of development and lap splice length requirements and the reduction of required confining reinforcement.

In the United States, the Federal Highway Administration (FHWA) investigated and promoted the use of UHPC in highway bridges. Since then, the number of bridges using UHPC elements has grown exponentially. Among the initial applications were field-cast connections, typically used in bridge construction with precast elements. Lap-spliced deck connections using UHPC closure pours were demonstrated to achieve desired performance under static and cyclic loads.[4,5] In recent years, the Florida Department of Transportation (FDOT) conducted research for the use of UHPC in closure pours between Florida slab beams for improved interfacial bond and simplified reinforcement.[6]

The expected behavior of any RC member is dependent on the bond performance between concrete and the reinforcing steel. Without sufficient bond, the reinforcing bars will slip within the concrete, leading to splitting cracks, spalling, and failure. The bond strength depends on key parameters, including concrete strength, bar spacing, bar strength, embedment length, concrete cover, and bar size. As a RC section is first loaded, the axial force of the reinforcing bar is transferred as radial pressure to the surrounding concrete by bearing force from the outermost lugs, friction force, and chemical adhesion.[3] This transfer of forces is linear until the concrete around the reinforcing bar lugs begin to crush, which breaks the friction and adhesion bond, allowing the bar to slip. The presence of this slip allows the reinforcing bar lugs in the surrounding area to contribute to resisting the axial force until all of the lugs are evenly bearing against the concrete.

Numerous bond and development length investigations use pullout tests on reinforcing bars embedded in UHPC.[7-12] Many studies concluded that increased cover, embedment length, and bar strength are the primary parameters that control bond performance; however, there is also a dependence on the fiber volume fraction and tensile strength. With sufficient arching action and fiber bridging in the UHPC cover when properly sized (clear cover is usually 2 to $3d_b$), relatively short development lengths are needed to yield normal-strength steel (NSS) bars, usually $10d_b$, and high-strength steel (HSS) bars, usually $12d_b$.

Lap splices are typically used throughout a concrete structure and are critical elements that rely on fully bonded

---

ACI Structural Journal, V. 121, No. 1, January 2024.
MS No. S-2023-017.R1, doi: 10.14359/51739189, received May 22, 2023, and reviewed under Institute publication policies. Pertinent discussion including author's closure, if any, will be published ten months from this journal's date if the discussion is received within four months of the paper's print publication.

Table 1—Material ASTM C1856 compression tests

Test age, days	Curing type	Average strength, ksi (MPa)
4	Thermal	26.3 (181.2)
7	Thermal	25.8 (178.2)
7	Ambient	15.5 (106.7)
14	Ambient	18.5 (127.2)
21	Thermal	28.1 (193.9)
21	Ambient	21.8 (150.2)
28	Thermal	25.7 (177.3)
28	Ambient	22.2 (152.9)
70	Ambient	24.2 (166.6)

behavior. The splice length must be long enough to fully develop the bond and transfer tensile forces to the adjacent bars.[3] For conventional RC, this relationship has been extensively researched and well defined; however, the behavior of UHPC lap splices do not conform to standard models due to the improved compressive strength and enhanced tensile strength from steel fibers. The fiber bridging effect and crack localization provide the ductile post-peak behavior in UHPC, facilitating the post-cracking strain-hardening effects.[3] Fibers in tension lead to discrete regions of internal confinement—referring to the augmentation of the concrete's strength and ductility due to the inclusion of fibers—that further increase bond performance.[13] The lap splice length is frequently assumed to be shorter than the development length from direct tension setups,[8] although more appropriate states of bar-concrete stresses in flexural lap splice studies are limited.

Select flexural studies showed 8 to $14d_b$ may not be sufficient to yield even normal-strength bars without sufficient cover.[10,14] However, other flexural tests have shown that yield occurs under shorter splice lengths and outside cover,[9] particularly in the case where confinement is present.[15] Flexural studies using one side of the reinforcing bar debonded in polyvinyl chloride (PVC) tubes have suggested bonded lengths as low as 2 to $5d_b$ are sufficient to develop bar yielding prior to bond failure.[13,16,17] Studies employing noncontact lap splices have usually erred on the conservative side for lap length in both flexural members and columns—that is, $24d_b$ for a column repair.[18] Cyclic testing showed deterioration of strength but similar bond ductility to monotonic tests in unconfined specimens.[19]

To develop efficient and economical structural connections, the bond strength behavior of UHPC must be thoroughly researched and detailed. The objective of this study is to investigate the flexural behavior of lap splices in UHPC in the shorter range of lap lengths and cover dimensions where slip occurs. The results from an experimental program of 47 small-scale flexural specimens and material characterization tests are presented and interpreted. Parameters studied in the testing matrix included aspect ratio, clear cover, lap length, and NSS bar size. The flexural load-displacement and load-strain results are used to compute bond-slip parameters by employing inverse analysis on a numerical model of the flexural tests.

RESEARCH SIGNIFICANCE

Past research has demonstrated an important benefit of UHPC is a reduction in the length necessary (over normal-strength concrete) to fully develop both NSS and HSS longitudinal reinforcement. The research presented extends these findings to noncontact lap-spliced reinforcement and demonstrates that slip is a ductile mechanism that can be used to control the stress transfer between the bars for capacity-controlled design. Experimental results on 47 small-scale flexural specimens demonstrate a range of acceptable flexural behaviors between bar yielding (longer lap lengths) and slip before yielding (shorter lap lengths).

EXPERIMENTAL PROGRAM

Materials

A commercially available UHPC product was used. The target compressive strength is 25 ksi (172 MPa) under controlled curing conditions. The UHPC is composed of proprietary preblended constituents, local masonry sand, portland cement, water, high-range water-reducing admixture (HRWRA), corrosion inhibitor, and 2% smooth straight steel fiber content by volume. The fibers are 0.008 in. (0.203 mm) in diameter and 0.5 in. (12.7 mm) in length.

Various material tests were conducted on the UHPC to identify the uniaxial compressive strength, tensile strength, flexural strength, modulus of elasticity, and Poisson's ratio. The ASTM C1856 uniaxial cylinder compression test results and specimen areas are shown in Table 1 for various testing ages and curing types. The strength of the material gradually increased with time to approximately 25 ksi (172 MPa) at time of testing.

Two third-point loading flexural performance tests (ASTM C1609) were conducted after 29 days of ambient curing the specimens. The standard beam dimensions of 4 x 4 x 14 in. (101.6 x 101.6 x 355.6 mm) were used for these tests. The average peak load and deflection at peak load for both tests are 15.8 kip (70.3 kN) and 0.018 in. (0.46 mm), respectively. A single split cylinder tensile test (ASTM C496) was conducted after 28 days of ambient curing the specimen. The specimen behaved linear up to failure at a strength of 2.5 ksi (17.2 MPa). A single modulus of elasticity/Poisson's ratio test (ASTM C469) was also conducted after 28 days of ambient curing. The specimen was loaded for three cycles to 40% of the ultimate load, approximately 8.8 ksi (60.7 MPa). The average rounded modulus of elasticity and Poisson's ratio are 7225 ksi (49,815 MPa) and 0.19, respectively.

Beam specimens

The experimental program consists of 47 total small-scale beam flexural tests split into two tiers of 20 and 27 specimens, respectively. The first test tier primarily investigated the influence of variable aspect ratios with respect to variable splice lengths, while maintaining the reinforcing bar clear cover. The second test tier examined the effect of variable beam sizes, clear cover, and bar size with respect to variable splice lengths, while maintaining the aspect ratio. The test matrix variables include beam dimensions, splice length l_s (6, 9, and $12d_b$), reinforcing bar diameter d_b (0.75, 1.0, and 1.27 in. [19.1, 25.4, and 32.3 mm]), reinforcing bar clear cover C_s (1, 1.5, and 2d_b), and shear aspect ratio a/H (1.5, 1.75, 2.5, and 3.5). All parameters of the 47 beam specimens are detailed in Table 2.

Specimens 1-7 to 1-12 have a 32 in. (813 mm) clear span, while all others have a 24 in. (610 mm) clear span. Two main types of reinforcement layouts are included in the program, lap-spliced and continuous, with a third control case with no reinforcing bars. All reinforcement is ASTM A615 Grade 60 mild steel with 90-degree hooks at each beam end. The corresponding longitudinal steel reinforcement ratios (A_s/A_c) vary between 1.5% and 4.1% for all beam specimens, excluding 1-13, 1-14, and 1-15 (UHPC only). The length of bar from the end of the lap to the end of the hook was selected to be larger than the lap length for all specimens, thereby ensuring failure in the lapped region and minimizing transverse stress generated. No transverse shear reinforcement was used in any of the specimens. The beam specimens with lapped bars included a lateral bar-to-bar clear spacing of 0.5d_b.

The fabrication and layout of beam specimen 1-3 is shown in Fig. 1; all other specimens are similar. All splices are placed such that half the splice length lies on each side of the beam midspan. All specimens were cast in plywood formwork, which was initially painted with interior latex-based paint. The formwork was then coated in mineral oil before casting to facilitate removal; refer to Fig. 1(a). Each specimen was cast from the center to ensure even fiber dispersion and flow alignment at the midspan. All specimens were wetted with a proprietary solution and ambient cured for 70 days prior to testing.

Testing methods

The four-point bending test setup for beam specimen 1-3 is shown in Fig. 2; all other tests are similar. All beams are tested with a 6 in. (152.4 mm) loading span; refer to Fig. 1(b). The four-point setup was selected so that only flexural stresses impacted the lap response (the center of the lapped region in all cases was in the constant moment region). The beams were tested under displacement control at a rate of 0.1 in./min (2.5 mm/min) in a universal testing machine (UTM). The testing protocol was terminated when the load was reduced to approximately 20% of the peak load capacity, or when excessive displacement occurred. Two support and two midspan linear variable displacement transducers (LVDTs) were mounted to each specimen to capture support displacement effects and torsional movement to measure the average midspan deflection.

The specimens with reinforcing bars included two strain gauges affixed to the bottom surface of the longitudinal reinforcing bars. The strain gauges were 120 Ω foil-backed resistive gauges with a 5000 με maximum. For the specimens with continuous (single) bars, only a single strain gauge was installed at the midspan of the beam. For the specimens with lap splices, one strain gauge was installed on each bar, located at the termination point of the adjacent lapped bar (that is, strain was measured at the initiation of the transfer region), as shown in Fig. 1.

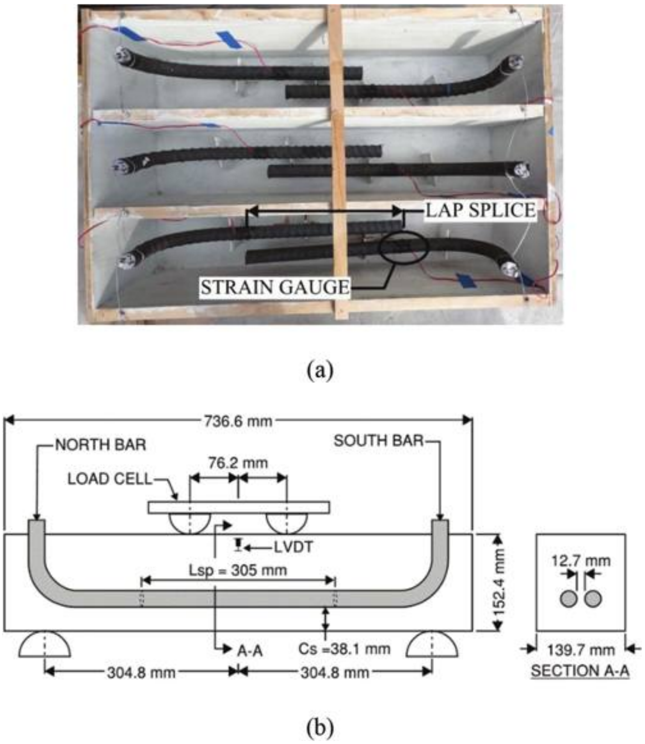

Fig. 1—Beam specimen 1-3: (a) fabrication; and (b) layout.

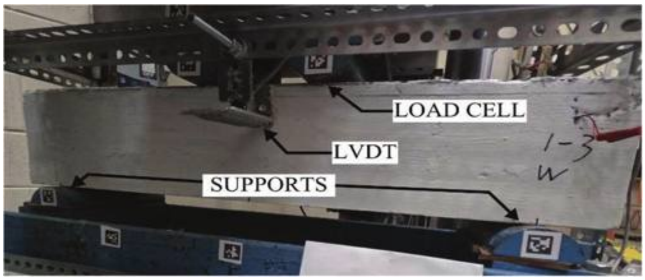

Fig. 2—Beam specimen 1-3 test setup.

EXPERIMENTAL RESULTS

The force-displacement responses of the beam specimens exhibited similar characteristics for all cases except those control cases with continuous bars. The peak force versus deflection at peak force is shown in Fig. 3. The control cases, continuous bar cases, and beams with 32 in. (813 mm) clear span are excluded from the figure. In addition, the two outliers exhibiting larger deflections at lower peak forces (Specimens 1-6 and 2-9 from groups C_s = 1.5d_b, L_{sp} = 12d_b, and C_s = 2.0d_b) were excluded from the results because they exhibited asymmetrical (one-sided) lap failure, as discussed later. The coefficient of determination R^2 in Fig. 3 is displayed for each linear trend line and color-coded to match each data set. For all beam specimens, the correlation of force to deflection decreased with the increase in concrete cover, which can be attributed to the more consistent ductile strength plateau displayed in beams with larger cover and splice length.

The normalized force versus normalized displacement curves for all lapped specimens in tier two are shown in Fig. 4. The normalized force is relative to the peak force, whereas the normalized displacement is relative to the

Table 2—Specimen description and test parameters

ID	Size W x H, in. (mm)	Clear span L_c, in. (mm)	Aspect ratio, a/H	C_s/d_b	Bar size d_b, in. (mm)	A_s/A_c	L_{sp}/d_b
1-1	5.5 x 6.0 (140 x 152)	24.0 (610)	1.5	1.5	1.0 (25.4)	2.4%	6
1-2	5.5 x 6.0 (140 x 152)	24.0 (610)	1.5	1.5	1.0 (25.4)	2.4%	9
1-3	5.5 x 6.0 (140 x 152)	24.0 (610)	1.5	1.5	1.0 (25.4)	2.4%	12
1-4	5.5 x 5.5 (140 x 140)	24.0 (610)	1.75	1.5	1.0 (25.4)	2.6%	6
1-5	5.5 x 5.5 (140 x 140)	24.0 (610)	1.75	1.5	1.0 (25.4)	2.6%	9
1-6	5.5 x 5.5 (140 x 140)	24.0 (610)	1.75	1.5	1.0 (25.4)	2.6%	12
1-7	5.5 x 5.0 (140 x 127)	32.0 (813)	2.5	1.5	1.0 (25.4)	2.9%	6
1-8	5.5 x 5.0 (140 x 127)	32.0 (813)	2.5	1.5	1.0 (25.4)	2.9%	9
1-9	5.5 x 5.0 (140 x 127)	32.0 (813)	2.5	1.5	1.0 (25.4)	2.9%	12
1-10	5.5 x 3.5 (140 x 89)	32.0 (813)	3.5	1.5	1.0 (25.4)	4.1%	6
1-11	5.5 x 3.5 (140 x 89)	32.0 (813)	3.5	1.5	1.0 (25.4)	4.1%	9
1-12	5.5 x 3.5 (140 x 89)	32.0 (813)	3.5	1.5	1.0 (25.4)	4.1%	12
1-13	5.5 x 6.0 (140 x 152)	24.0 (610)	1.5	N/A	N/A	N/A	N/A
1-14	5.5 x 6.0 (140 x 152)	24.0 (610)	1.5	N/A	N/A	N/A	N/A
1-15	5.5 x 6.0 (140 x 152)	24.0 (610)	1.5	N/A	N/A	N/A	N/A
1-16	5.5 x 6.0 (140 x 152)	24.0 (610)	1.5	1.5	1.0 (25.4)	2.4%	N/A
1-17	5.5 x 6.0 (140 x 152)	24.0 (610)	1.5	1.5	1.0 (25.4)	2.4%	N/A
1-18	5.5 x 6.0 (140 x 152)	24.0 (610)	1.5	1.5	1.0 (25.4)	2.4%	N/A
1-21	5.5 x 6.0 (140 x 152)	24.0 (610)	1.5	1.5	1.0 (25.4)	2.4%	N/A
1-22	5.5 x 6.0 (140 x 152)	24.0 (610)	1.5	1.5	1.0 (25.4)	2.4%	N/A
2-1	3.5 x 6.0 (89 x 152)	24.0 (610)	1.5	1.0	0.8 (19.1)	2.1%	6
2-2	4.5 x 6.0 (114 x 152)	24.0 (610)	1.5	1.5	0.8 (19.1)	1.6%	6
2-3	5.0 x 6.0 (127 x 152)	24.0 (610)	1.5	2.0	0.8 (19.1)	1.5%	6
2-4	3.5 x 6.0 (89 x 152)	24.0 (610)	1.5	1.0	0.8 (19.1)	2.1%	9
2-5	4.5 x 6.0 (114 x 152)	24.0 (610)	1.5	1.5	0.8 (19.1)	1.6%	9
2-6	5.0 x 6.0 (127 x 152)	24.0 (610)	1.5	2.0	0.8 (19.1)	1.5%	9
2-7	3.5 x 6.0 (89 x 152)	24.0 (610)	1.5	1.0	0.8 (19.1)	2.1%	12
2-8	4.5 x 6.0 (114 x 152)	24.0 (610)	1.5	1.5	0.8 (19.1)	1.6%	12
2-9	5.0 x 6.0 (127 x 152)	24.0 (610)	1.5	2.0	0.8 (19.1)	1.5%	12
2-10	4.5 x 6.0 (114 x 152)	24.0 (610)	1.5	1.0	1.0 (25.4)	2.9%	6
2-11	5.5 x 6.0 (140 x 152)	24.0 (610)	1.5	1.5	1.0 (25.4)	2.4%	6
2-12	6.5 x 6.0 (165 x 152)	24.0 (610)	1.5	2.0	1.0 (25.4)	2.0%	6
2-13	4.5 x 6.0 (114 x 152)	24.0 (610)	1.5	1.0	1.0 (25.4)	2.9%	9
2-14	5.5 x 6.0 (140 x 152)	24.0 (610)	1.5	1.5	1.0 (25.4)	2.4%	9
2-15	6.5 x 6.0 (165 x 152)	24.0 (610)	1.5	2.0	1.0 (25.4)	2.0%	9
2-16	4.5 x 6.0 (114 x 152)	24.0 (610)	1.5	1.0	1.0 (25.4)	2.9%	12
2-17	5.5 x 6.0 (140 x 152)	24.0 (610)	1.5	1.5	1.0 (25.4)	2.4%	12
2-18	6.5 x 6.0 (165 x 152)	24.0 (610)	1.5	2.0	1.0 (25.4)	2.0%	12
2-19	6.0 x 6.0 (152 x 152)	24.0 (610)	1.5	1.0	1.3 (32.3)	3.5%	6
2-20	7.0 x 6.0 (178 x 152)	24.0 (610)	1.5	1.5	1.3 (32.3)	3.0%	6
2-21	8.5 x 6.0 (216 x 152)	24.0 (610)	1.5	2.0	1.3 (32.3)	2.5%	6
2-22	6.0 x 6.0 (152 x 152)	24.0 (610)	1.5	1.0	1.3 (32.3)	3.5%	9
2-23	7.0 x 6.0 (178 x 152)	24.0 (610)	1.5	1.5	1.3 (32.3)	3.0%	9
2-24	8.5 x 6.0 (216 x 152)	24.0 (610)	1.5	2.0	1.3 (32.3)	2.5%	9
2-25	6.0 x 6.0 (152 x 152)	24.0 (610)	1.5	1.0	1.3 (32.3)	3.5%	12
2-26	7.0 x 6.0 (178 x 152)	24.0 (610)	1.5	1.5	1.3 (32.3)	3.0%	12
2-27	8.5 x 6.0 (216 x 152)	24.0 (610)	1.5	2.0	1.3 (32.3)	2.5%	12

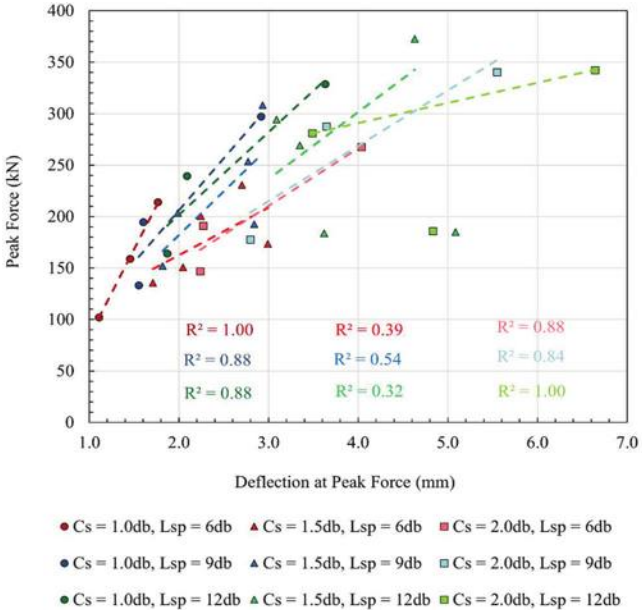

Fig. 3—Peak force versus deflection at peak force. (Note: 1 in. = 25.4 mm; 1 ksi = 6.89 MPa.)

deflection at peak force. The results showed increased post-peak strength with the increase of splice length and concrete cover. In general, beam specimens with smaller splice length and concrete cover showed reduced peak force accompanied with a rapid strain-softening phase. Beam specimens with larger splice length and cover showed increased peak force followed by an extended, gradually decreasing strain-softening phase. All beams demonstrated substantial residual capacity at large post-peak displacements.

Table 3 summarizes the key results from each of the specimen tests, including the deflection at peak force Δ_{peak} as a percentage of clear span length, maximum applied force F_{max}, maximum strains in the north and south reinforcement $\varepsilon_{s,max}$, the cracking pattern as classified in Fig. 5, the average maximum steel force $f_{s,max}$, the average bond stress of the reinforcing bars μ_{TEST}, the normalized moment M_{max}/bd^2, and the shape factor (E_{50}/E_{peak}). The shape factor is defined as the ratio of the energy (integral of force-deformation curve) up to 50% post-peak strength to the energy up to the peak strength. All specimens achieved yielding strain or larger in one or both lapped bars, except for specimens 2-1, 2-10, 2-11, and 2-19 (L_{sp} = 6d_b specimens with increasing bar sizes) and 2-23 (L_{sp} = 9d_b). Although these beam specimens successfully developed both sides of the lap splice, they ultimately experienced unloading before yielding due to slippage of both reinforcing bars.

Failure modes and cracking patterns

Each specimen was visually inspected to identify the UHPC cracking pattern and ultimate failure mode. The UHPC cracking damage was denoted flexural (F), shear (S), compression (C), tension (T), or a combination of these four. All damage patterns and combinations are shown in Fig. 5 to establish criteria for the classification used in Table 3. The flexure-only cracking pattern was observed exclusively in the control cases without reinforcement; all other specimens with reinforcement had a combination cracking pattern of flexural with shear, compression, or tension.

The flexure-compression cracking pattern was the most common, with no bias toward a specific splice length. The shear-compression pattern only occurred in splice lengths of 9 and 12d_b; all other cracking patterns did not exhibit any trends with varying splice length.

The beam specimens that experienced failure in the lapped region displayed a distinct diagonal cracking pattern on the bottom side, as shown in Fig. 6. This type of failure mode, known as splitting failure, occurs between the ends of adjacent lapped bars within the flexure region. It is often observed in lap splices with shorter lap splice lengths, insufficient cover, and lack of confinement. In general, the specimens that showed no yielding in at least one bar had a smaller splice length. This can be attributed to not fully developing the required bond strength to reach the yield strain; these beams are slip-controlled. For larger splice lengths and cover, the improved compressive strength and sustained post-cracking tensile strength of the UHPC allows for the tensile reinforcement to fully develop before the concrete crushes, resulting in most specimens reaching yielding of both reinforcing bars.

One-sided failure was characteristic of specimens with longer lap length (9 to 12d_b) and larger cover (1.5 to 2d_b). Asymmetrical beam failure was prominent in specimens 1-3, 1-6, 1-9, 1-11, 1-12, 1-21, 1-22, 2-8, 2-9, 2-15, 2-17, 2-24, and 2-27; this mechanism explains why specimens 1-6 and 2-9 produced exceptionally low peak force. With the same dimensions, specimens with larger M_{max}/bd^2 dissipated larger energy. Specimens with a larger shape factor (E_{50}/E_{peak}) have more ductile behavior. When the shape factor is larger than 2.5, concrete flexural failure happens before lap-splice slipping. If the shape factor is smaller than 2.5, the slipping of the lap splice is the main reason for the failure of the beam.

Bond strength

At the peak force of the beam specimen, the average bond strength can be calculated by dividing the maximum reinforcing bar tensile force by the overall contact area between the reinforcing bar and concrete, using the following equation

$$\mu_{TEST} = \frac{f_{s,max}A_b}{\pi d_b L_{sp}} = \frac{f_{s,max}\,d_b}{4L_{sp}} \qquad (1)$$

where A_b and d_b are the nominal bar area and diameter; $f_{s,max}$ is the maximum tensile bar stress; and μ_{TEST} is the average bond strength at maximum tensile stress assuming the force is uniformly distributed along the splice length L_{sp}. Using the average peak reinforcing bar strains measured during the beam tests, the average bond strength can be calculated for each specimen (refer to Table 3).

The maximum stress in the reinforcing bars is calculated from the measured strains shown in Table 3 using lab-measured stress-strain behavior for each size reinforcing bar with a yield strength of 60 ksi (413.7 MPa). The average bond stress (averaged between the two bars) versus the splice length L_{sp}/d_b is shown in Fig. 7(a). In general, the

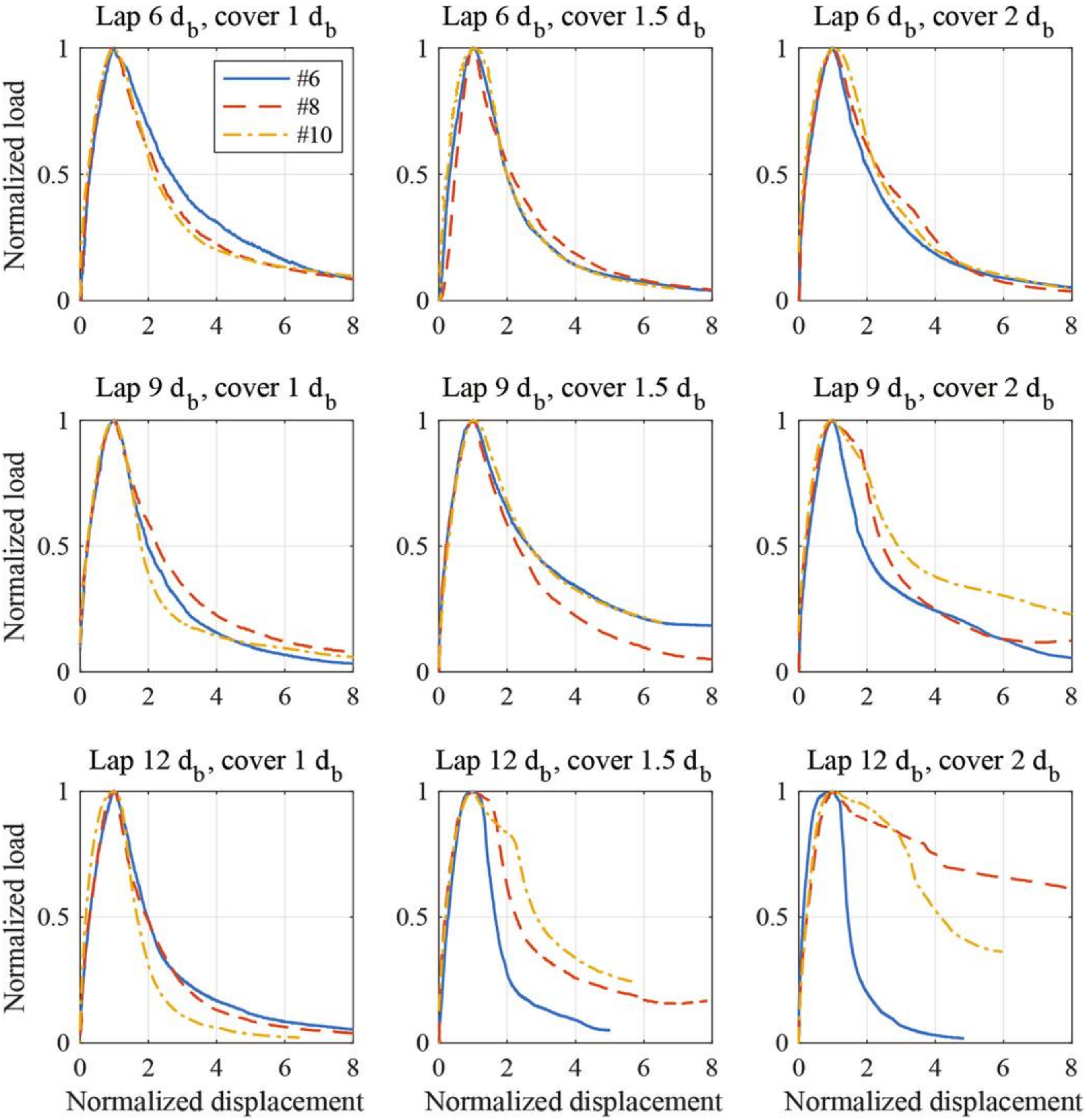

Fig. 4—Normalized load-displacement curves for tier two specimens. Vertical axis is load normalized by peak load; and horizontal axis is midspan displacement normalized by displacement at peak load.

maximum stress is indirectly proportional to the splice length, with a stronger correlation for larger C_s/d_b specimens. The average bond stress versus C_s/d_b and bar diameter d_b are shown in Fig. 7(b) and (c), respectively. As the concrete cover and splice length (L_{sp}) increases, the variation between groups becomes larger with little correlation; the correlation between the linear trends is exceptionally low, suggesting there are other variables affecting the maximum stress that should be included in the regression evaluation. The control cases, continuous bar cases, and beams with 32 in. (813 mm) clear span are excluded from Fig. 7(a) to (c). The outlier from group L_{sp}/d_b = 12 with low average bond stress was excluded from the correlation results.

Moment capacity

To better understand the dependence of the achieved strength on the parameter space studied, the results are presented in Fig. 8 in the form of normalized moments (M_{max}/bd^2). These normalized moments have units of stress and can be understood relative to the value obtained for the control specimens with continuous reinforcing bars (1-16 to 1-18) of approximately 3.0. The lapped specimens with longer splice length achieved higher capacity values than

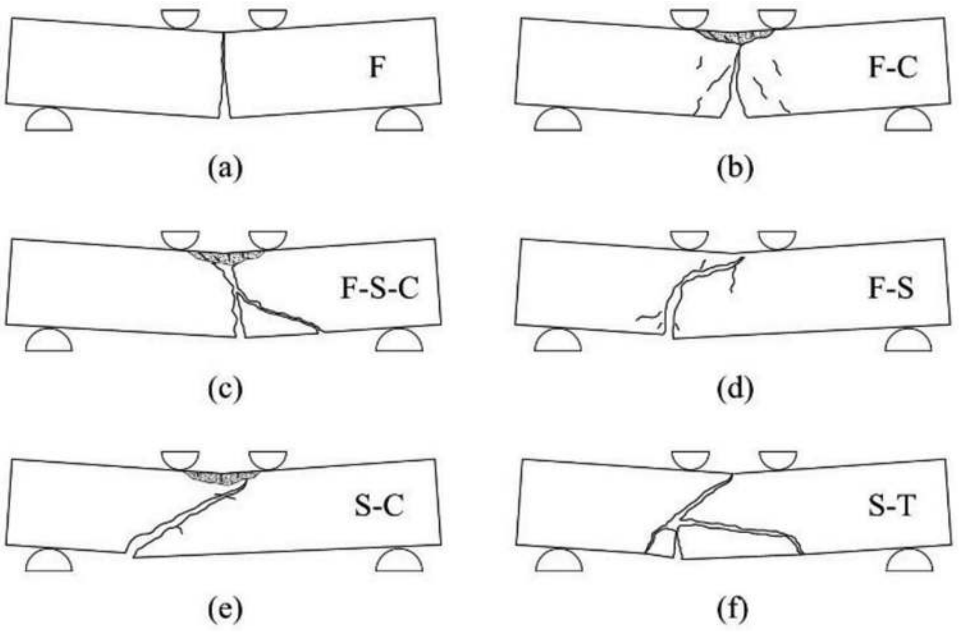

Fig. 5—UHPC cracking pattern classifications: (a) flexure; (b) flexure-compression; (c) flexure shear-compression; (d) flexure-shear; (e) shear-compression; and (f) shear-tension.

Fig. 6—Cracking pattern on bottom of beam specimen 1-2.

this due to the presence of two bars in the lapped region. Comparison with the capacity of approximately 5.0 from control specimens with two bars (1-21 and 1-22) bound these behaviors.

Results show the two-factor interaction between each pair of parameters, in addition to the trends with aspect ratio. While increased moment capacity with lap length and cover were evident in Fig. 3 and Table 3, the figure also confirms an increase in capacity with bar size (as would be expected), implying the total bond force increased with larger bar diameters. The bond strength investigation in the next section confirms this finding. In addition, there is an increase in moment capacity with aspect ratio (for a constant lap length). However, the moment capacity did not increase (or decrease for some specimens) between L_{sp} = 9d_b and 12d_b, particularly for larger aspect ratios.

BOND STRENGTH CALIBRATION

Bond strength is a critical component for lap-spliced connections. While loading the beam specimens to failure, the bond stress may vary nonlinearly along the lapped length, which affects the flexural strength and failure mode. Due to the continuously bonded lap splice in the experimental specimens (as opposed to other flexural setups where bond is average over a short distance), the material-point bond-slip behavior was obtained using inverse analysis. To capture the bond-slip backbone parameters, a nonlinear least-squares regression was performed by calls to a unique parameterized nonlinear numerical model developed in OpenSees for each flexural specimen.

The specimens' force-deformation and strain-deformation responses were used in the nonlinear fitting. For each specimen, the deformation was sampled at 200 points of equal displacement increment. The corresponding force, strain in the north reinforcing bar, and strain the south reinforcing bar at each displacement were differentiated with the predicted numerical value to obtain the residual for minimization. The force responses were weighted by a factor of 4 (over the strains) to influence the search more heavily. The parameters used for fitting included five points on the bond stress versus bond-slip material-point curve, as described in more detail in the "Constitutive Model" section. Using the least squares nonlinear curve-fitting function lsqcurvefit with the Levenberg-Marquardt algorithm, the bond-slip inputs are calibrated based on the force-deflection data gathered from the experimental program.

Numerical model geometry

The general geometry layout used to model each beam specimen within OpenSees is illustrated in Fig. 9. This layout has six main components: a beam with concrete rectangular fiber section with layers through the depth (representing the compression block and tension block), a beam with steel circular fiber section for each lapped bar (or single beam in continuous case), a bond-slip (horizontal) spring connected to reinforcing bar, a dowel action (vertical) spring connected to reinforcing bar, a rigid link connecting the concrete to the reinforcing bar springs, and a stiff elastic spring to simulate the 90-degree hook at each end of the beam. The explicit reinforcing bar beam element is located at the correct geometry relative to the geometric centroid of the concrete beam element. The rigid links ensure that the correct kinematics are recovered for the overall beam under small loads (plane

Table 3—Summary of test results

ID	Δ_{peak} (% of L_c)	F_{max}, kip (kN)	$\varepsilon_{s,max}$ (north)[*]	$\varepsilon_{s,max}$ (south)[*]	Cracking pattern[†]	$f_{s,max}$, ksi (MPa)	μ_{TEST}, ksi (MPa)	M_{max}/bd^2, ksi (MPa)	E_{50}/E_{peak}
1-1	0.36%	45.1 (201)	0.0021	0.0023	F-C	65.2 (450)	2.7 (19)	2.3 (16)	2.5998
1-2	0.46%	57.0 (253)	0.0031	0.0061	F-C	65.6 (453)	1.8 (13)	2.9 (20)	4.4189
1-3	0.51%	66.3 (295)	0.0191	0.0056	F-C	77.8 (536)	1.6 (11)	3.4 (23)	5.7407
1-4	0.34%	33.9 (151)	0.0032	0.002	F-C	65.4 (451)	2.7 (19)	2.3 (16)	2.0232
1-5	0.47%	43.3 (193)	0.0029	0.0034	F-S-C	65.4 (451)	1.8 (13)	2.9 (20)	2.8908
1-6	0.80%	41.6 (185)	0.0229	0.0016	F-S-C	81.3 (561)	1.7 (12)	2.8 (19)	6.889
1-7	0.56%	24.0 (107)	0.0033	0.0024	F-S-C	65.4 (451)	2.7 (19)	2.9 (20)	2.97
1-8	0.64%	29.8 (133)	0.0030	0.0038	F-S-C	65.5 (451)	1.8 (13)	3.6 (25)	4.1734
1-9	0.91%	30.2 (135)	0.0033	0.0197	F-C	78.5 (541)	1.6 (11)	3.7 (25)	6.3869
1-10	1.17%	10.3 (46)	0.0021	0.0045	F-C	65.5 (452)	2.7 (19)	5.0 (34)	2.8361
1-11	1.33%	13.3 (59)	0.0194	0.0078	F-C	78.1 (539)	2.2 (15)	6.4 (44)	4.0227
1-12	1.32%	11.4 (51)	0.0155	0.0034	F-C	73.8 (509)	1.5 (11)	5.5 (38)	3.3066
1-13	0.06%	13.9 (62)	N/A	N/A	F	N/A	N/A	0.3 (2)	0.16251
1-14	0.21%	19.1 (85)	N/A	N/A	F	N/A	N/A	0.4 (3)	0.78121
1-15	0.20%	20.8 (93)	N/A	N/A	F	N/A	N/A	0.5 (3)	0.84876
1-16	3.89%	60.7 (270)	>0.05[‡]	N/A	F-S-C	N/A	N/A	3.1 (21)	52.826
1-17	0.41%	58.5 (260)	>0.05[‡]	N/A	F-C	N/A	N/A	3.0 (21)	3.5422
1-18	0.51%	59.4 (264)	>0.05[‡]	N/A	F-C	N/A	N/A	3.0 (21)	4.7907
1-21	0.78%	98.4 (438)	0.004	0.028	F-S-C	75.5 (520)	N/A	5.0 (35)	4.2743
1-22	0.76%	89.5 (398)	0.02	0.009	F-S-C	72.6 (500)	N/A	4.6 (32)	6.1304
2-1	0.18%	23.0 (102)	0.0015	0.0015	F-S	39.4 (272)	1.6 (11)	1.2 (9)	13.608
2-2	0.28%	30.5 (136)	0.0018	0.0028	F-S	66.7 (460)	2.8 (19)	1.5 (10)	10.752
2-3	0.36%	33.0 (147)	0.0028	0.0027	F-S	66.7 (460)	2.8 (19)	1.7 (12)	0.64549
2-4	0.26%	30.0 (133)	0.0024	0.0024	S-C	60.9 (420)	1.7 (12)	1.6 (11)	1.2855
2-5	0.30%	34.2 (152)	0.0035	0.0019	F-C	67.5 (465)	1.9 (13)	1.7 (12)	2.0363
2-6	0.46%	40.0 (178)	0.0027	0.0028	F-C	66.7 (460)	1.9 (13)	2.1 (15)	1.2943
2-7	0.31%	37.0 (164)	0.0028	0.0029	F-S	67.1 (463)	1.4 (10)	2.0 (14)	1.739
2-8	0.40%	41.3 (184)	0.0123	0.0037	F-S	73.1 (504)	1.5 (11)	2.0 (14)	3.0145
2-9	0.78%	41.8 (186)	0.0107	0.0091	F-S	71.0 (489)	1.5 (10)	2.2 (15)	1.8061
2-10	0.23%	35.8 (159)	0.0016	0.0021	F-S	65.1 (449)	2.7 (19)	1.8 (12)	4.0896
2-11	0.22%	39.0 (174)	0.0014	0.0017	S-T	60.1 (414)	2.5 (17)	2.0 (14)	6.5291
2-12	0.37%	42.9 (191)	0.0035	0.0034	F-C	65.4 (451)	2.7 (19)	2.4 (17)	1.388
2-13	0.26%	43.8 (195)	0.0023	0.0024	S-T	65.3 (450)	1.8 (13)	2.2 (15)	2.3297
2-14	0.33%	45.8 (204)	0.0027	0.0029	F-S	65.4 (451)	1.8 (13)	2.3 (16)	2.7167
2-15	0.61%	64.7 (288)	0.0222	0.0043	F-C	80.8 (557)	2.2 (15)	3.7 (25)	2.0105
2-16	0.34%	53.8 (239)	0.0037	0.0027	S-T	65.5 (451)	1.4 (9)	2.7 (18)	2.4939
2-17	0.62%	60.7 (270)	0.0057	0.0198	F-C	78.6 (542)	1.6 (11)	3.1 (21)	6.7473
2-18	0.57%	63.2 (281)	0.0238	N/A	S-C	82.2 (567)	1.7 (12)	3.6 (25)	2.9995
2-19	0.29%	48.2 (214)	0.0018	0.0018	F-C	49.7 (343)	2.1 (14)	2.2 (15)	6.0159
2-20	0.51%	51.9 (231)	0.0032	0.0019	F-S	67.4 (464)	2.8 (19)	2.8 (19)	6.1211
2-21	0.67%	60.3 (268)	0.0036	0.0031	F-C	67.4 (465)	2.8 (19)	4.0 (28)	2.4049
2-22	0.48%	66.9 (298)	0.0035	N/A	F-S	67.4 (465)	1.9 (13)	3.0 (21)	3.8941
2-23	0.48%	69.3 (308)	0.0017	0.002	F-C	54.5 (376)	1.5 (10)	3.7 (26)	7.281

Table 3 (cont.)—Summary of test results

ID	Δ_{peak} (% of L_c)	F_{max}, kip (kN)	$\varepsilon_{s,max}$ (north)*	$\varepsilon_{s,max}$ (south)*	Cracking pattern†	$f_{s,max}$, ksi (MPa)	μ_{TEST}, ksi (MPa)	M_{max}/bd^2, ksi (MPa)	E_{50}/E_{peak}
2-24	0.86%	76.6 (341)	0.0027	0.0116	F-C	69.6 (480)	1.9 (13)	5.1 (35)	5.5786
2-25	0.59%	74.0 (329)	0.0032	0.0027	S-C	67.4 (464)	1.4 (10)	3.3 (23)	5.4522
2-26	0.76%	83.8 (373)	0.002	0.0028	F-S	67.3 (464)	1.4 (10)	4.5 (31)	12.761
2-27	1.09%	77.0 (342)	0.0016	>0.05‡	F-C	44.6 (308)	0.9 (6)	5.1 (35)	8.1583

*Highlighted values indicate yielding of reinforcing bar.

†F is flexural; S is shear; C is compression; T is tension (refer to Fig. 5).

‡Out of strain gauge limit (max 0.05).

Table 4—OpenSees UHPC material properties

Parameter	Symbol	Value
Uniaxial compressive strength, ksi (MPa)	f_c	22.0 (152)
Young's modulus, ksi (MPa)	E_c	7000.0 (48,263)
Tensile strength, ksi (MPa)	f_t	0.90 (6.2)
Ultimate tensile strength, ksi (MPa)	f_{tu}	1.10 (7.6)
Ultimate tensile strain	ε_u	0.0035
Residual tensile strength, ksi (MPa)	f_{tres}	0.13 (0.9)
Residual tensile strain	ε_{res}	0.025
Maximum strain	ε_{max}	0.035
Ultimate compression strain multiplier	c_{max}	2.0
Ultimate tension strain multiplier	t_{max}	1.0

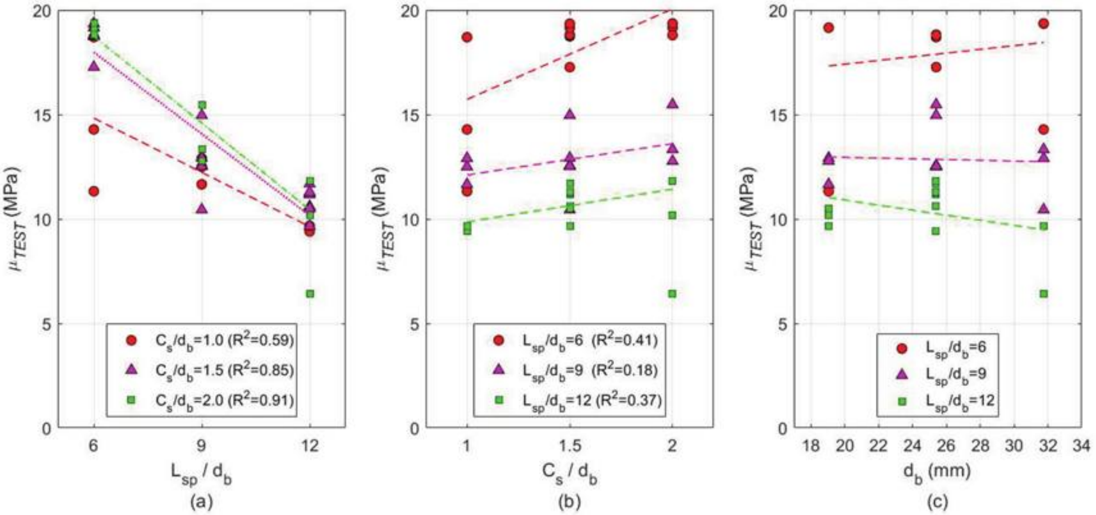

Fig. 7—Average bond stress versus: (a) L_{sp}/d_b*; (b)* C_s/d_b*; and (c)* d_b.

sections remain plane). The modeling approach is consistent with that taken by Al-Jelawy and Mackie.[20]

Horizontal discretization of the model was calibrated to ensure sufficient springs in the lapped region. The results presented used 15 displacement-based beam elements in each of the shear spans and a proportional number of elements within the loading span such that the element sizes remained constant along the length. Large displacements were enabled with the corotational coordinate transformation for the concrete beam, reinforcing bar beam, and rigid link elements.

Each component of the model has a specific constitutive model associated with it to capture all nonlinear effects of the flexural specimens. Two-point loads were applied to the concrete beam at the same locations as the experimental specimen, and the boundary conditions were pinned at the left end and roller at the right end of the concrete beam. The analysis used displacement control based on the midspan deflection and automatically adjusted the step size to ensure convergence up to the maximum displacement from the experiment.

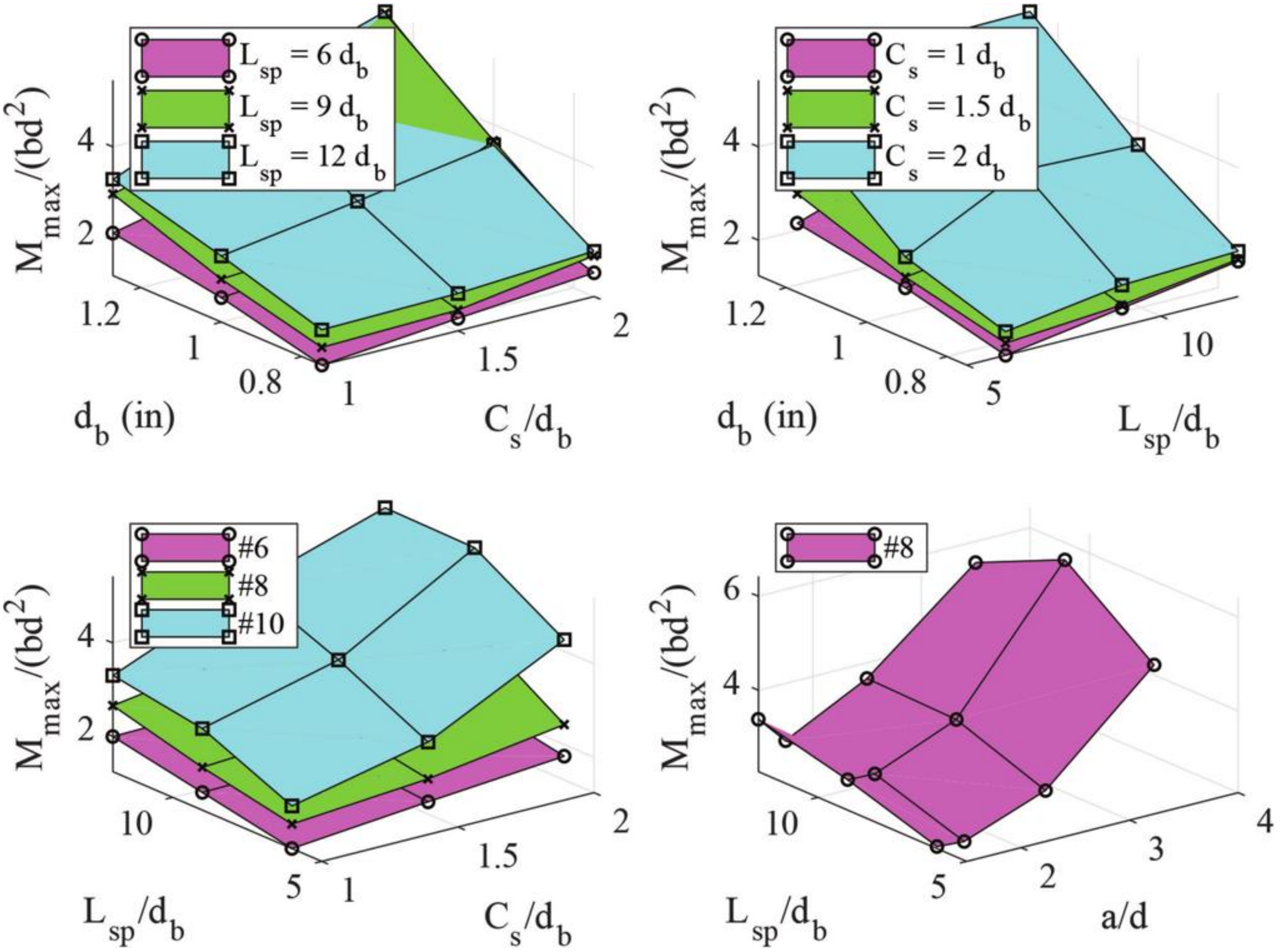

Fig. 8—Normalized moment capacity with respect to experimental parameters.

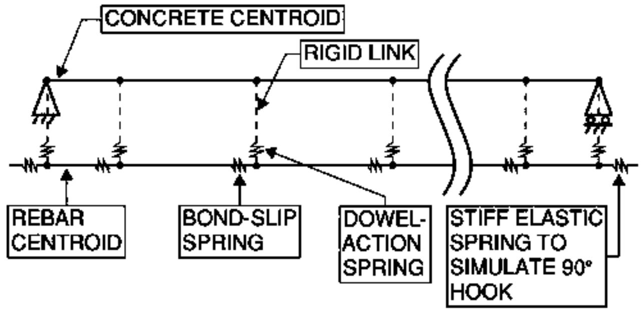

Fig. 9—OpenSees geometry layout.

Constitutive models

The OpenSees *Hysteretic* material model was selected to represent UHPC. This model constructs a uniaxial trilinear material with damage formulation due to ductility and energy; refer to Fig. 10(a). All material properties used for UHPC hysteretic material are summarized in Table 4. The *ReinforcingSteel* material model was selected to represent the embedded reinforcement. This model constructs a uniaxial nonlinear material specifically implemented for RC fiber sections. Refer to Table 5 for all reinforcing steel material properties.

The reinforcing steel interacts with the surrounding concrete through two mechanisms: bond-slip and dowel action. The bond-slip relates the transverse movement of the reinforcing bar to the stress required to slip. The bond-slip mechanism is represented by the *MultiLinear* material model, having slip and stress inputs. The shape of the bond-slip curve was adopted from Eligehausen et al.[21]; the general bond-slip material model is shown in Fig. 10(b). The slip inputs u_1 to u_3 and bond inputs f_{peak} and f_{res} are the values calibrated for each beam specimen using the nonlinear least-squares regression on the parameterized nonlinear numerical model. Unlike the infinite plateau residual stress f_{res} in most models, u_4 and f_4 were assumed to be 0.2 in. (5.1 mm) and 0.1 ksi (0.7 MPa), respectively, to improve convergence of the optimization algorithm. The variable ΔL denotes the discretized length of reinforcing bar used to calculate the contact area for each bar element. It was assumed that the bond stress between the reinforcement and cementitious matrix is uniformly distributed along the perimeter of the reinforcing bar. This assumption becomes unreliable as the ratio of d_b/H increases (that is, larger curvatures). The calibrated slip and bond values are summarized in Table 6 for each beam specimen.

Dowel action is the ability of reinforcing bars to carry shear force due to slipping of cracked surfaces normal to the reinforcing bar. This is used to define the perpendicular interaction between the reinforcing bar and the surrounding concrete. The dowel action mechanism is represented by uniaxial elastic-perfectly plastic gap (ElasticPPGap) and

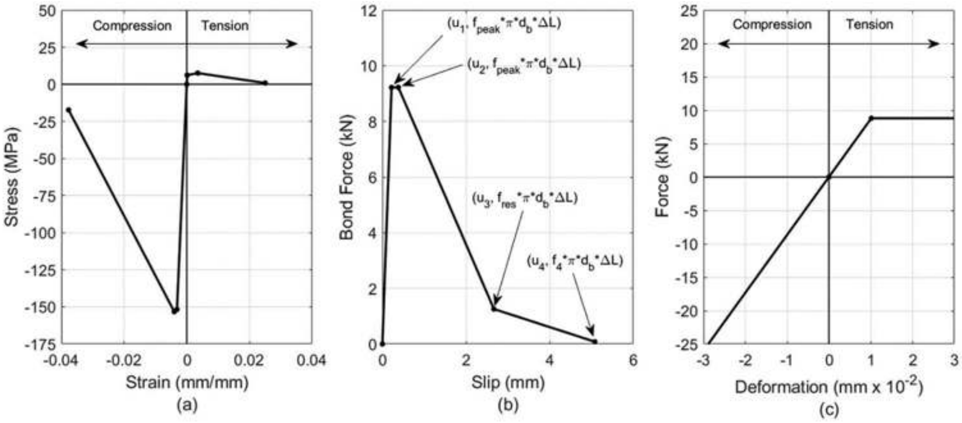

Fig. 10—OpenSees material model for: (a) UHPC; (b) general bond-slip; and (c) dowel action.

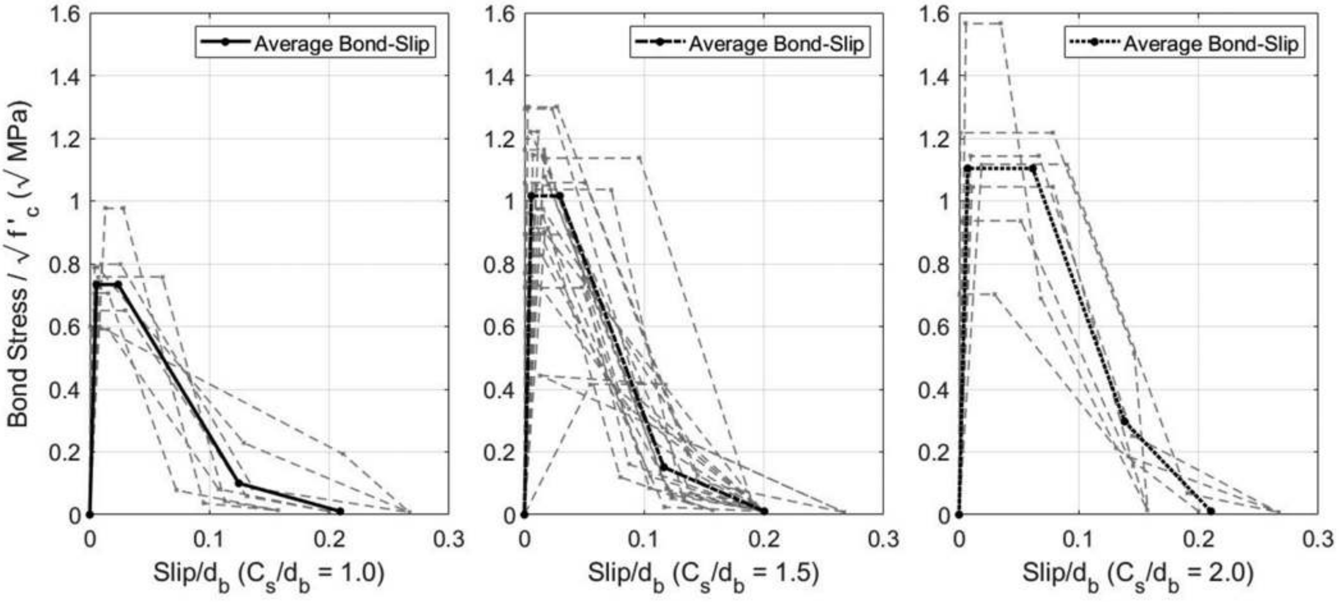

Fig. 11—Normalized bond stress versus slip/d_b.

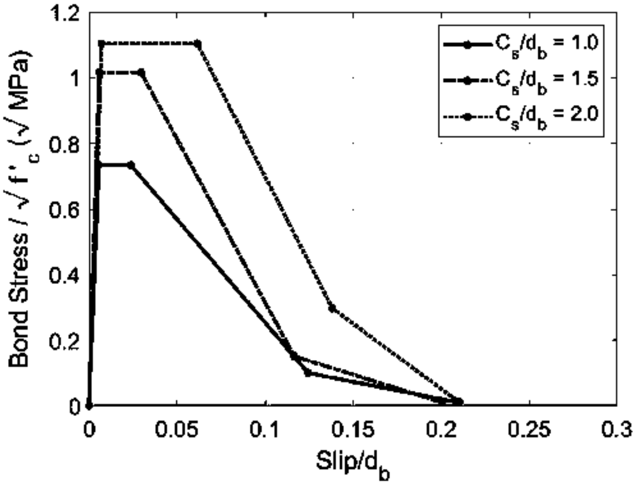

Fig. 12—Average normalized bond stress versus slip/d_b.

elastic no tension (ENT) OpenSees material models. The strength was based on shear plane area for pulling through bottom cover multiplied by the tension strength of UHPC. The stiffness was obtained from a similar calculation for the displacement d_0 = 0.0004 in. (0.01 mm) from Xia et al.,[22] which is from $(f_t/E_c)l_c$, where l_c is critical crack width equal to $2/3H$. The flexural stress to crack width was assumed to be applicable even though it was applied to failure of the bottom cover. The other two inputs to the nonlinear curve-fitting function are the UHPC yield strength and stiffness multipliers for the dowel action material model. These parameters will be changed to better fit the experimental force-deformation plot, with a minimum and maximum allowable limit of 0.1 and 25, respectively. The general dowel action material model is shown in Fig. 10(c).

Bond-slip results

All calibrated bond-slip and dowel action parameters are summarized in Table 6. Because specimens 1-13 to 1-18 are the control cases and continuous bar cases, they are excluded from the analysis. Due to issues encountered during the analysis, beam specimens 1-12, 2-10, 2-12, and 2-15 could not produce results. This is caused by either convergence problems or insufficient quality of measured force-deformation curve used to calibrate the parameters. For all other specimens, the calibrated results are plotted

Table 5—OpenSees reinforcing material properties

Parameter	Symbol	Value
Yield stress in tension, ksi (MPa)	f_y	65.0 (448)
Ultimate stress in tension, ksi (MPa)	f_u	104.0 (717)
Initial elastic tangent, ksi (MPa)	E_s	29,000 (199,948)
Tangent at initial strain hardening, ksi (MPa)	E_{sh}	1305.0 (8998)
Strain at initial strain hardening	ε_{sh}	0.0070
Strain at peak stress	ε_{ult}	0.1170

Table 6—Specimen bond-slip results

ID	u_1, mm	u_2, mm	u_3, mm	f_{peak}, MPa	f_{res}, MPa	Ω^*	Ψ^*
1-1	0.0127	1.0055	2.2187	11.00	1.98	0.1	5.2
1-2	0.1813	0.3946	3.0113	14.12	1.00	0.6	12.6
1-3	0.4142	2.4460	4.8642	14.00	0.26	0.1	1.4
1-4	0.0400	0.1270	2.9689	11.85	0.30	0.1	2.6
1-5	0.4052	0.4365	2.7089	13.27	2.88	0.1	0.2
1-6	0.4366	0.4198	5.0800	11.11	0.07	25.0	2.0
1-7	0.0739	0.6962	3.6697	16.01	1.55	25.0	17.3
1-8	0.0127	0.5886	2.4562	15.93	4.51	0.1	25.0
1-9	0.2968	0.1270	3.5231	15.04	0.86	14.9	7.7
1-10	0.2102	0.3841	2.6660	11.73	1.50	10.9	6.6
1-11	0.0127	0.4118	2.0088	14.32	4.87	1.3	0.3
2-1	0.0127	0.1575	4.0291	7.39	2.38	0.1	0.1
2-2	0.0127	0.9701	2.7526	13.04	1.31	0.1	0.1
2-3	0.0592	0.9836	2.6853	11.54	2.29	0.1	0.1
2-4	0.0767	0.1270	2.4511	9.71	2.81	25.0	2.3
2-5	0.2215	0.2936	2.6351	12.01	2.83	2.5	2.5
2-6	0.1867	1.2700	2.7594	14.08	3.11	2.5	2.5
2-7	0.1887	0.4893	2.5988	9.84	1.04	3.1	2.3
2-8	1.0510	2.2377	0.2540	5.12	5.46	3.1	1.6
2-9	0.3600	1.7227	3.6281	13.75	0.84	0.1	6.9
2-11	0.0127	1.2235	2.6569	8.91	1.03	0.1	0.1
2-13	0.0312	0.3908	2.7342	7.27	1.00	0.1	2.6
2-14	0.1538	0.3752	3.1447	10.17	0.76	2.8	25.0
2-16	0.1042	0.7585	3.3254	8.01	0.71	2.2	25.0
2-17	0.0127	0.1270	2.2327	9.46	4.18	24.8	25.0
2-18	0.0127	0.7497	3.3207	8.65	2.63	25.0	25.0
2-19	0.1309	0.4980	2.3335	8.70	0.96	7.6	1.2
2-20	0.2289	0.6448	2.5769	11.25	1.48	0.1	1.6
2-21	0.1890	1.1274	2.2107	19.28	8.51	0.1	12.9
2-22	0.4199	0.9000	3.0632	12.03	0.45	0.2	12.9
2-23	0.3187	0.6737	3.9529	12.93	0.65	25.0	25.0
2-24	0.0363	2.5400	4.7253	14.99	6.31	25.0	25.0
2-25	0.2424	1.9504	3.6410	9.34	0.52	0.1	25.0
2-26	0.3073	2.3403	4.2764	12.77	0.57	0.2	25.0
2-27	0.3529	2.5400	4.6952	12.87	1.93	25.0	25.0

$^*\Omega$ is stiffness multiplier; Ψ is yield strength multiplier.

Note: 1 in. = 25.4 mm; 1 ksi = 6.89 MPa.

versus either lap splice length or concrete cover, depending on which has a greater correlation.

The calibrated bond stress normalized by $\sqrt{f_c'}$ versus slip normalized by d_b for all beam specimens separated by C_s/d_b is shown in Fig. 11. The average bond-slip curves from each category are summarized in Fig. 12. Due to poor bond-slip parameter results, beam specimens 1-6, 1-9, and 2-8 were excluded from their respective average curves. In general, C_s/d_b is directly proportional to the yield limit (f_{peak}) and length of yield plateau, while the average initial elastic response is constant for all beam specimens. The curves, which follow the backbone introduced by Eligehausen et al.,[21] show a higher correlation to C_s/d_b than L_{sp}/d_b. Increasing d_b and C_s/d_b independently led to an increase in normalized peak bond stress (f_{peak}). However, the increase of f_{peak} and the decrease of normalized residual bond stress (f_{res}) is only slightly affected by the bar diameter. The improvement in bond and residual strengths is attributed to fiber bridging and internal confinement effects around the reinforcement.

The limitations of the model mechanics used in the inverse analysis include the use of one-dimensional elements, absence of out-of-plane behavior, and uncoupled bond-slip springs on both lapped bars. These restrict the ability to accurately predict the flexural behavior of all specimens, particularly those that fail on one side of the lap due to imperfections or small spacing differences. An alternative approach that has the potential to overcome these limitations is the incorporation of a three-dimensional nonlinear finite element analysis with a coupled damage-plasticity microplane concrete material model. However, such an approach is only practical for single-specimen investigations, not the inverse analysis performed herein.

CONCLUSIONS

The experimental program of 47 small-scale flexural specimens presented was used to investigate the mechanical properties and behavior of ultra-high-performance concrete (UHPC) noncontact lap splices. Compared to conventional reinforced concrete (RC), UHPC exhibits improved compressive, tensile, and bond behaviors that do not conform to standard concrete models. The parameters considered in the experimental program included lap splice lengths (6, 9, and $12d_b$), bar diameters (0.75, 1.0, and 1.27 in. [19.1, 25.4, and 32.3 mm]), clear cover (1, 1.5, and $2d_b$), and aspect ratios (1.5, 1.75, 2.5, and 3.5).

Results from the small-scale beam tests showed that splice lengths of 9 to $12d_b$ coupled with cover of 1.5 to $2d_b$ allows for the tensile reinforcement to fully develop prior to large concrete compressive strains being reached. To achieve yield, the lap length necessary was dependent on bar size and occurred in specimens with smaller d_b with $C_s \geq 1.5d_b$. However, regardless of whether the lap was sufficient to transfer the yield stress in the bar, all specimens exhibited a ductile post-peak response regardless of the degradation of the post-peak strength. Conclusions are limited to UHPC beams having 2% fiber volume, 0.90 ksi (6.2 MPa) tensile strength, and the aspect ratios, bar diameters, and span lengths used in the flexural tests.

A numerical model using one-dimensional elements was developed to represent the small-scale flexural tests and used with an inverse analysis to investigate the material-point bond stress versus slip relationships. Each beam was analyzed to compute the unique bond-slip and dowel action properties, which simulate the specimen test force-deformation response through parameter optimization. The bond-slip backbone curve, shown in Fig. 10(b), was adopted from Eligehausen et al.,[21] while the dowel action mechanics, considering the flexural stress-crack width relation to the stress-strain, were adopted from Xia et al.[22] The normalized concrete cover C_s/d_b is directly proportional to the normalized bond strength (0.28, 0.39, and 0.42 √ksi [0.74, 1.02, and 1.10 √MPa] corresponding to $C_s = 1d_b$, $1.5d_b$, and $2d_b$, respectively), and the correlation with bar diameter and lap length are weak, as would be expected. The inverse analysis modeling assumptions restrict the capability of capturing one-sided lap failure and cases where large curvatures lead to a large strain gradient around perimeter of the reinforcing bar. Further investigation may be necessary to evaluate different UHPC material models (such as Hognestad or FHWA[3]) and bond-slip constitutive models (such as exponential or models characterized by decreased strain-softening properties) functional forms.

In the noncontact lap splice specimens investigated experimentally and for the associate bond strength calibration, slip served as a ductile mechanism that effectively controlled the stress transfer between bars that can be adopted for a capacity-controlled design philosophy. However, further research is required to determine the design limit states for ductile mechanisms in this context, as well as a larger array of specimen sizes and parameters. Additional research is required to establish a stronger correlation between the findings of bond-slip and bond strength in direct tension pullout tests and their applicability to flexural testing, particularly the influence of bar curvature on the bottom clear cover.

AUTHOR BIOS

ACI member **Jason Hock** *is a Graduate Student at the University of Central Florida, Orlando, FL, studying structural and geotechnical engineering, and is a Structural E.I. at HighSpans Engineering, Inc. He received his BS in civil engineering from Florida Gulf Coast University, Fort Myers, FL. His research interests include bridge engineering, prestressed concrete, and finite element methods.*

ACI member **Kevin R. Mackie** *is a Professor of structural engineering at the University of Central Florida. He received his BS in civil engineering from The Cooper Union, New York, NY, and his MS and PhD in structural engineering from the University of California, Berkeley, Berkeley, CA. He is past Chair and current member of ACI Committee 341, Performance-Based Seismic Design of Concrete Bridges. His research interests include performance-based engineering, advanced materials and composites, sustainability assessment, structural reliability, and engineering under uncertainty.*

ACI member **Georgios Apostolakis** *is an Assistant Professor of structural engineering at the University of Central Florida. He received his BEng in civil engineering from the University of Patras, Patras, Greece, and his MSc and PhD in structural engineering from the University at Buffalo, Buffalo, NY. His research interests include structural mechanics, performance-based engineering, material topology optimization, theoretical and experimental mechanics, and multiscale material modeling.*

Tiancheng Wang *is a PhD Student at the University of Central Florida in the area of structural engineering. He received his bachelor's degree in civil engineering from Guangxi University, Nanning, China, and his master's degree in structural engineering from Texas Tech University, Lubbock, TX.*

ACKNOWLEDGMENTS

The authors thank M. Zeman (Dura-Stress Inc.) and Cor-Tuf UHPC for providing with the UHPC material used in the experimental study.

REFERENCES

1. ACI Committee 239, “Ultra-High-Performance Concrete: An Emerging Technology Report (ACI 239R-18),” American Concrete Institute, 2018, 21 pp.

2. Hung, C.-C.; El-Tawil, S.; and Chao, S.-H., “A Review of Developments and Challenges for UHPC in Structural Engineering: Behavior, Analysis, and Design,” *Journal of Structural Engineering*, ASCE, V. 147, No. 9, 2021, p. 03121001. doi: 10.1061/(ASCE)ST.1943-541X.0003073

3. FHWA, “Properties and Behavior of UHPC-Class Materials (FHWA-HRT-18-036),” Federal Highway Administration, Washington, DC, 2018.

4. Hwang, H., and Park, S. Y., “A Study on the Flexural Behavior of Lap-Spliced Cast-in-Place Joints Under Static Loading in Ultra-High Performance Concrete Bridge Deck Slabs,” *Canadian Journal of Civil Engineering*, V. 41, No. 7, 2014, pp. 615-623. doi: 10.1139/cjce-2013-0281

5. Haber, Z. B., and Graybeal, B. A., “Lap-Spliced Rebar Connections with UHPC Closures,” *Journal of Bridge Engineering*, ASCE, V. 23, No. 6, 2018, p. 04018028. doi: 10.1061/(ASCE)BE.1943-5592.0001239

6. Chitty, F. B.; Freeman, C. J.; and Garber, D. B., “Joint Design Optimization for Accelerated Construction of Slab Beam Bridges,” *Journal of Bridge Engineering*, ASCE, V. 25, No. 7, 2020, p. 04020029. doi: 10.1061/(ASCE)BE.1943-5592.0001561

7. Graybeal, B., “Bond Behavior of Reinforcing Steel in Ultra High-Performance Concrete (FHWA-HRT-14-090),” Federal Highway Administration, Washington, DC, 2014, 12 pp.

8. Yuan, J., and Graybeal, B., “Bond of Reinforcement in Ultra-High-Performance Concrete,” *ACI Structural Journal*, V. 112, No. 6, Nov.-Dec. 2015, pp. 851-860. doi: 10.14359/51687912

9. Lee, J.-K., “Bonding Behavior of Lap-Spliced Reinforcing Bars Embedded in Ultra-High Strength Concrete with Steel Fibers,” *KSCE Journal of Civil Engineering*, V. 20, No. 1, 2016, pp. 273-281. doi: 10.1007/s12205-015-1396-7

10. Ronanki, V. S.; Aaleti, S.; and Valentim, D. B., “Experimental Investigation of Bond Behavior of Mild Steel Reinforcement in UHPC,” *Engineering Structures*, V. 176, 2018, pp. 707-718. doi: 10.1016/j.engstruct.2018.09.031

11. Lagier, F.; Massicotte, B.; and Charron, J.-P., “Bond Strength of Tension Lap Splice Specimens in UHPFRC,” *Construction and Building Materials*, V. 93, 2015, pp. 84-94. doi: 10.1016/j.conbuildmat.2015.05.009

12. Ma, F.; Deng, M.; Fan, H.; Yang, Y.; and Sun, H., “Study on the Lap-Splice Behavior of Post-Yield Deformed Steel Bars in Ultra-High-Performance Concrete,” *Construction and Building Materials*, V. 262, 2020, p. 120611. doi: 10.1016/j.conbuildmat.2020.120611

13. Saikali, R.-A.; Pantazopoulou, S. J.; and Palermo, D., “Local Bond-Slip Behavior of Reinforcing Bars in High-Performance Steel Fiber-Reinforced Concrete Beams,” *ACI Structural Journal*, V. 119, No. 2, Mar. 2022, pp. 139-153. doi: 10.14359/51734334

14. Saleem, M. A.; Mirmiran, A.; Xia, J.; and Mackie, K. R., “Development Length of High-Strength Steel Rebar in Ultra-High-Performance Concrete,” *Journal of Materials in Civil Engineering*, ASCE, V. 25, No. 8, 2013, pp. 991-998. doi: 10.1061/(ASCE)MT.1943-5533.0000571

15. Dagenais, M-A. and Massicotte, B., “Tension Lap Splices Strengthened with Ultrahigh-Performance Fiber-Reinforced Concrete,” *Journal of Materials in Civil Engineering*, ASCE, V. 27, No. 7, 2015. doi: 10.1061/(ASCE)MT.1943-5533.0001169

16. Kim, S.; Lee, J.; Joh, C.; and Kwahk, I., “Flexural Bond Behavior of Rebar in Ultra-High Performance Concrete Beams Considering Lap-Splice Length and Cover Depth,” *Engineering*, V. 8, No. 03, 2016, pp. 116-129. doi: 10.4236/eng.2016.83013

17. Wang, Z.; Wang, J.; Liu, J.; Han, F.; and Zhang, J., “Large-Scale Quasi-Static Testing of Precast Bridge Column with Pocket Connections Using Noncontact Lap-Spliced Bars and UHPC Grout,” *Bulletin of Earthquake Engineering*, V. 17, No. 9, 2019, pp. 5021-5044. doi: 10.1007/s10518-019-00649-6

18. Dagenais, M.-A.; Massicotte, B.; and Boucher-Proulx, G., “Seismic Retrofitting of Rectangular Bridge Piers with Deficient Lap Splices Using Ultrahigh-Performance Fiber-Reinforced Concrete,” *Journal of Bridge Engineering*, ASCE, V. 23, No. 2, 2018, p. 04017129. doi: 10.1061/(ASCE)BE.1943-5592.0001173

19. Shao, Y.; Tich, K. L.; Boaro, S. B.; and Billington, S. L., “Impact of Fiber Distribution and Cyclic Loading on the Bond Behavior of Steel-Reinforced UHPC,” *Cement and Concrete Composites*, V. 126, 2022.

20. Al-Jelawy, H. M., and Mackie, K. R., “Three-Dimensional Fiber-Based Models of Precast and Cast-in-Place Reinforced Concrete Columns,” *Journal of Structural Engineering*, ASCE, V. 148, No. 3, 2022, p. 04021287. doi: 10.1061/(ASCE)ST.1943-541X.0003278

21. Eligehausen, R.; Popov, E. P.; and Bértero, V. V., “Local Bond Stress-Slip Relationships of Deformed Bars Under Generalized Excitations: Experimental Results and Analytical Model,” Earthquake Engineering Research Center, University of California, Berkeley, Berkeley, CA, 1983.

22. Xia, J.; Xiao, Y.; Mackie, K. R.; Al-Ramahee, M.; and Mirmiran, A., “Dowel Action and Shear Strength Contribution of High Strength Rebar Embedded in Ultra-High Performance Fiber Reinforced Concrete,” *Engineering Structures*, V. 83, 2015, pp. 223-232. doi: 10.1016/j.engstruct.2014.11.004

ACI STRUCTURAL JOURNAL TECHNICAL PAPER

Title No. 121-S10

Beam-Column Joint Retrofitting Using Basalt Fiber-Reinforced Polymer Grid and Cementitious Matrixes

by Chhoung Lim, Yeongseok Jeong, and Minho Kwon

This paper focuses on retrofitting reinforced concrete (RC) beam-column joints using a new method—namely, fabric-reinforced cementitious matrix (FRCM). This method is expected to be a substitute for externally bonded FRP, as it works better in a moist and flammable environment. In this study, basalt fiber-reinforced polymer (BFRP) grids were used as reinforcement and high-strength mortar and engineered cementitious composites (ECCs) were used as a cementitious matrix. ECC is ductile and good for crack distribution. High-strength mortar is good for its high compressive strength, applicability, shrinkage resistance, lack of pores, and high bonding strength. The retrofitted specimens were originally fabricated by taking out the concrete cover around the joint area, and it was filled back by the cementitious matrix to make up the original dimension using two different retrofitting types. As a result, the overall performances of the retrofitted specimens were improved regarding failure level, ductility, energy dissipation, strength, and stiffness degradation. The working mechanism of the retrofitted specimen tended to change as the stress concentration also attempted to shift from joint to beam for the ECC specimen.

Keywords: basalt fiber-reinforced polymer (BFRP) grid; engineered cementitious composite (ECC); fabric-reinforced cementitious matrix (FRCM); high-strength mortar; joint failure.

INTRODUCTION

Beam-column joints play the most important role in making a structure stable, as a progressive collapse of a whole structure can occur once they fail.[1,2] The joints are very vulnerable to failure because a great extent of stress from different directions of all members is transferred to them when a structure is subjected to repeating horizontal loads such as earthquakes.[3] Hence, modern design codes attempt to prevent joint failure by placing more transverse reinforcement inside to shift the failure to nearby members. Transverse reinforcement averts excessive inelastic deformation from going through the joint by producing concrete confinement and preventing buckling of longitudinal column reinforcement.[4] Despite that, failure still appears at joints, as observed from recent earthquakes, because based on basic hypotheses in structural analysis, the joint is assumed to be powerful enough to deliver load from one member to another without considering the shear effect produced inside the joint from nearby members[5]—not to mention pre-1970s buildings, which were designed to support only gravity load.[6,7] The construction details of structures built before the 1970s are recognized to have poor seismic design and nonseismic reinforcement detailing, which lead to nonductile structural failure.[3,5-8] After realizing this problem, numerous studies have been made by researchers around the globe to propose quality solutions in retrofitting joints to avert progressive collapse. Different strategies and materials have been brought up, such as section enlargement; retrofitting using fiber-reinforced polymer (FRP) in the shape of sheets, bars, and fans; prestressed steel angles; haunch elements; alloy bars; steel jackets; and fiber-reinforced concrete.[3,5,6,8-25] The aforementioned retrofitting methods indeed illustrate promising efficacy in strengthening joints. However, they also provide some drawbacks that need to be considered. For instance, retrofitting joints using haunch elements, steel jackets, or section enlargement increases the weight of a structure. Moreover, they also take up a large space for installation. Furthermore, using steel for retrofitting is very sensitive to corrosion over time. Then, FRP was introduced to overcome these problems. FRP can be made using many types of fiber such as basalt, glass, and carbon, and it can also be fabricated in different shapes as well such as sheets, bars, fans, and grids. FRP possesses a great extent of benefits such as easy installation, chemical and corrosion resistance, light weight, durability, high tensile strength, and formability.[26,27] Currently, FRP is often used to strengthen structural members as shear and flexural reinforcement as an external bonding method.[28] Akguzel and Pampanin[8] experimentally investigated the effectiveness of the external retrofitting method using glass fiber-reinforced polymer (GFRP) sheet on an exterior beam-column joint specimen under uni- and bi-directional lateral loading. Wang et al.[23] conducted an experimental study on the performance of a retrofitted deficient reinforced concrete (RC) beam-column joint using externally bonded carbon fiber-reinforced polymer (CFRP) sheet and near-surface-mounted CFRP strip. Similarly, Murad et al.[29] used CFRP sheet to strengthen damaged RC connections repaired by recycled concrete. The results demonstrated that the performance of the specimens improved in many aspects such as strength, ductility, and failure mode. The externally bonded FRP method is effective and easy to implement. However, what concerns this method is debonding and rapid degradation of mechanical properties when performing in flammable environments.[30-36] To overcome this weakness, a new method needs to be invented.

Mostofinejad and Akhlaghi[9] proposed a two-dimensional (2-D) beam-column joint retrofitting method by placing an

---

ACI Structural Journal, V. 121, No. 1, January 2024.
MS No. S-2023-022.R1, doi: 10.14359/51739190, received June 16, 2023, and reviewed under Institute publication policies. Pertinent discussion including author's closure, if any, will be published ten months from this journal's date if the discussion is received within four months of the paper's print publication.

FRP anchor fan slightly in the concrete using the externally bonded reinforcement on grooves (EBROG) technique with an extra reinforcement of externally bonded CFRP sheet to slow down the debonding of the FRP. The groove was filled back using epoxy. This technique was further investigated by Mostofinejad and Hajrasouliha[37] by retrofitting a three-dimensional (3-D) beam-column joint using the same material. Furthermore, Golias et al.[38] implemented a similar technique to retrofit a rehabilitated damaged RC joint using a newly developed material, CFRP ropes. The specimens were grinded to make U-shaped notches for placing the CFRP ropes using epoxy resin. In the same study, they also compared this technique with the widely applied use of externally bonded CFRP sheet. This technique was more thoroughly studied by Karayannis and Golias[39] using different retrofitting configurations. As a result, the proposed method provided a promising result in strengthening RC joints. It was also able to change from shear failure at the joint to bending failure at the beam. However, as the notches in this retrofitting method were filled by epoxy resin, it is still vulnerable in flammable environment as the epoxy resin is exposed to air directly without any covers.

A new method—namely, fabric-reinforced cementitious matrix (FRCM)—is introduced to solve this problem. FRCM is a new externally bonded method that can be used to replace externally bonded FRP.[28] The FRCM system is good for stress distribution from the interface to the concrete because engineered cementitious composite (ECC) is able to produce multiple cracks and it also possesses ductile behavior with a high tensile strain up to 7%.[40] The fire resistance of FRCM is better than that of FRP due to the noncombustible nature of ECC. The flammability resistance of ECC performs better than normal mortar due to the presence of polyvinyl alcohol (PVA), which prevents explosion in compression and makes ECC still ductile at elevated temperatures.[41,42] Moreover, PVA also helps improve the durability of ECC in the long term in regards to permeability and crack resistance.[43] The FRCM system also works better in moist environments compared to FRP.[44,45] Recently, the FRCM system has been widely used to ameliorate the flexural and shear strength of structural members. For example, Guo et al.[46] used a combination of CFRP grids with polymer cement mortar (PCM) to strengthen the shear strength of I-shaped beams. Zheng et al.[47] increased the flexural strength of beams using a combination of basalt fiber-reinforced polymer (BFRP) grid and ECC. Yang et al.[28] experimented with retrofitting the shear strength of RC beams using the combination of BFRP and CFRP grid with ECC. The aforementioned literature all used the combination of FRP grid and ECC to strengthen beams, and the results illustrate that the strength of the specimens increased from 30 to 160%. FRCM has also been slightly used to retrofit beam-column joints as well. Qian et al.[24] conducted an experiment on beam-column joints retrofitted by ECC and superelastic shape memory alloy bars by preinstalling them, but this method can only be applied to newly built structures. To strengthen existing structures, Khan et al.[17] used a cementitious matrix only—without FRP—to retrofit the beam-column joint by casting in-place and bonding over the joint area of the specimen. However, a large amount of space is taken up by this retrofitting method. It also affects the architecture of the structure as the ECC cover stands out alone. To overcome this drawback, Lim et al.[3] performed an experiment on beam-column joints using a CFRP grid with high-strength mortar and ECC. The concrete cover was taken out and replaced by ECC to make up the old dimensions as the benchmark specimen. As a result, the performance of the retrofitted specimen shows better performance in terms of energy dissipation and strength. It was also able to move the failure from the joint to the end of ECC on the beam.

Therefore, in this study, a combination of BFRP grids with two different cementitious matrixes is used to retrofit a joint specimen. BFRP grid will be used instead of the CFRP grid because BFRP grid is cost-effective, and it is considered as green and environmentally friendly material compared to CFRP. BFRP grid is solely fabricated from volcanic rock without additional materials.[48,49] ECC and high-strength mortar are chosen as the cementitious matrixes. ECC is well-known for its ductility, while high-strength mortar is used for its high strength, applicability, and shrinkage resistance. Moreover, the high-strength mortar used herein is expected to be pore-free and have a high bonding strength. The specimens used in this study are fabricated in two-thirds scale following buildings constructed prior to the 1970s in New Zealand.[8] The goal of this study is to enhance the failure mode, ductility, strength, stiffness, and energy dissipation of the specimen by keeping the dimensions of the specimen the same as those of the reference.

RESEARCH SIGNIFICANCE

External bonding using FRP has been widely used to retrofit RC beam-column joints due to the enormous advantages of FRP. However, this retrofitting method also provides some downsides, such as weak performance under moisture and flammable environments. They can also easily get damaged by external factors as they are not covered by anything. Therefore, the preliminary study of this paper presents a new retrofitting method for reinforced beam-column joints to overcome the aforementioned problem by using an environmentally friendly material, BFRP grid, with cementitious matrixes.

EXPERIMENTAL PROGRAM

Specimen detailing

One normal and four retrofitted specimens representing the exterior joints were fabricated in two-thirds scale following a building in New Zealand.[8] The length of the beam and the height of the column are considered from the inflection point of the beam and the contraflexure points of the top and bottom columns from the actual structure, respectively. The height of the column is 2000 mm with a cross section of 230 x 230 mm. Six 10 mm diameter reinforcing bars are placed in the column with a 10 mm diameter stirrup with a spacing of 100 mm. The length of the beam measured from the face of the column is 1550 mm with a cross section of 230 mm in width and 330 mm in height. The main reinforcement is made of eight 10 mm diameter reinforcing bars (four at the top and four at the bottom) with a 10 mm

Table 1—Specimen types

Specimen name	Concrete compressive strength, MPa	Type of cover	BFRP wrap around beam and column
T-B-0-0	26.13	—	—
T-B-S-E	20.86	ECC	No
T-B-S-M	20.86	Mortar	No
T-B-W-E	26.13	ECC	Yes
T-B-W-M	24.39	Mortar	Yes

Table 2—Properties of BFRP grid

Resin weight ratio, %	Fiber weight ratio, %	Ultimate strength, MPa	Cross section, mm^2	Elastic modulus, MPa	Rupture strain, %
15	85	1192	1.89	51,795	2.3

Table 3—Mixing table of ECC, kg/m^3

Cement	Water	Silica sand	Fly ash	Slag	Defoamer	HPMC	PCSP	PVA fiber
500.5	375	591.68	166.675	166.675	0.833	1.667	2.5	39 (2%)

Note: HPMC is hydroxypropyl methylcellulose; PSCP is polycarboxylic high-range water-reducing admixture.

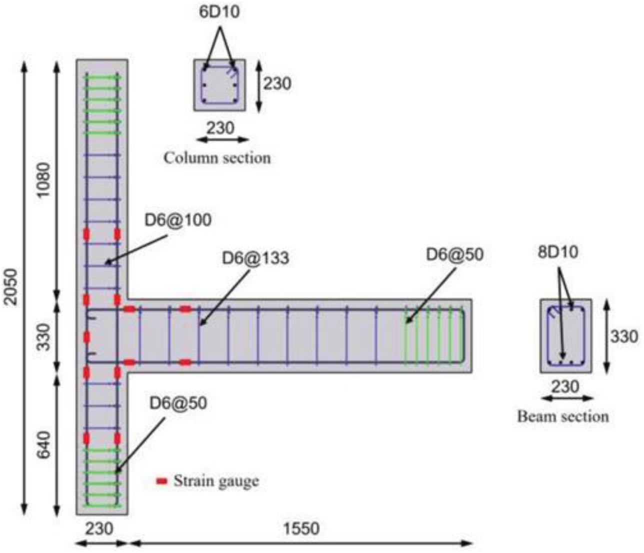

Fig. 1—Specimen detailing and strain gauge position.[3]

diameter stirrup with a spacing of 133 mm. The geometry of the specimen and the location of the steel strain gauge is demonstrated in Fig. 1.

The concrete cover of the retrofitted specimen at the joint location and at the beam and column with a distance of 250 mm, a development length for BFRP grid,[50] was initially taken out, to be replaced with a cementitious matrix. The specimens are labeled in "T-B-X-Y" style, where "T" stands for T-shaped specimen, "B" means BFRP grid, "X" represents the retrofitting style (for example, "W" for wrapping retrofitting style and "S" for side retrofitting style), and "Y" denotes the type of cementitious matrix at the joint (for example, "E" for ECC and "M" for high-strength mortar). Table 1 illustrates the name and details of each specimen.

Material properties

Ready mixed concrete with compressive strength of 24 MPa at 28 days was used to make the specimens. The yield strength of stirrups and main reinforcement are 300 and 400 MPa, respectively. BFRP grid was used to retrofit the joint with the involvement of two different types of cementitious matrix, high-strength mortar and ECC. The BFRP grid was fabricated using continuous fibers impregnated with thermoset resin with 15% weight fraction. Table 2 demonstrates the detailed properties of the BFRP grid.

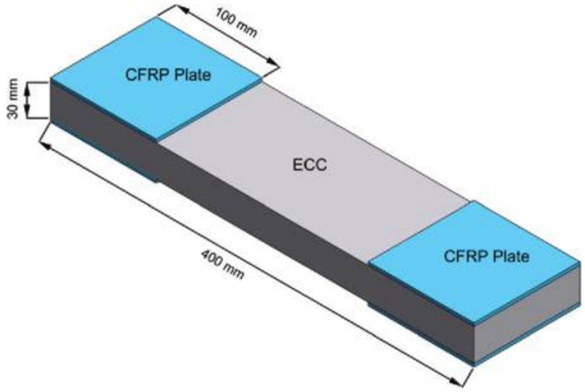

Fig. 2—Schematic detailing of ECC tensile specimen.

ECC was produced using 19.23 μm diameter PVA fibers with a length of 11 mm. The tensile strength and elastic modulus of PVA are 1393 and 26080 MPa, respectively. Table 3 exhibits the mixing table of ECC obtained from the work of Jeong et al.[51] The ECC specimen was fabricated in rectangle shape for tensile testing, as demonstrated in Fig. 2. The compressive and tensile strength of ECC are 47.5 and 2.43 MPa, respectively, with an elastic modulus of 15,451 MPa. Figure 3 demonstrates the stress-strain curve of ECC. High-strength mortar, supplied by a local Korean company, was made by mixing water and cement with a ratio of 0.15:1 (water:cement) by weight. A high-strength mortar specimen was made in cubic shape for compressive testing. The compressive strength was 58 MPa. All the properties of the materials are the results of tests in the laboratory.

Retrofitting methodology

Before applying grids to the specimen, the concrete surface where the cover was taken out was smoothened by grinding, polishing, and applying primer. Smoothening the surface of concrete ensures good bond and prevents the existence of a gap between the BFRP grid and the concrete. Then, the BFRP grid was impregnated with the specimen using epoxy. For the specimens with retrofitting style type "S," the BFRP grid was applied to only the side of the beam and column, but for the specimen with the retrofitting style type "W," one more layer of BFRP grid was applied by wrapping around the beam and column next to the joint. The wrapping is to provide stronger bond strength to the grid at the joint as well as to strengthen the structure. A schematic drawing of both retrofitting types is illustrated in Fig. 4. Lastly, cementitious matrixes were cast to make up the initial dimensions of the specimen. In this study, the specimens were laid down horizontally for casting the cementitious matrixes as the specimens cannot stand alone. However, cementitious matrixes can be cast on the existing vertical beam-column joint in a real structure by spraying. Spraying does not change the performance of ECC.[52] Detailing of the retrofitting methods for both types is illustrated in Fig. 5.

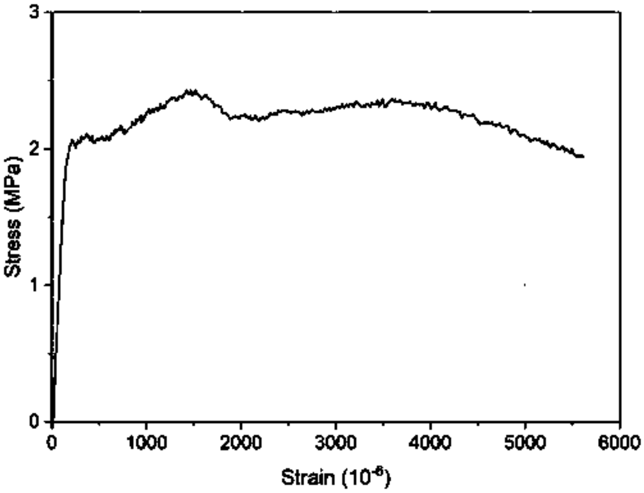

Fig. 3—Tensile stress-strain curve of ECC.

Experimental setup and test procedure

The specimens were placed on a one-directional hinge on a steel deck connected to a reaction floor, where the end of the beam was placed on an assembled support to represent a roller support made up of two hinges and one load cell. A constant 112 kN axial load was applied to the top of the column. The lateral load was applied at the top of the column by a horizontal actuator. Figure 6 demonstrates the experimental setup of the specimens. The lateral load was applied to the specimen in form of displacement ductility (μ)

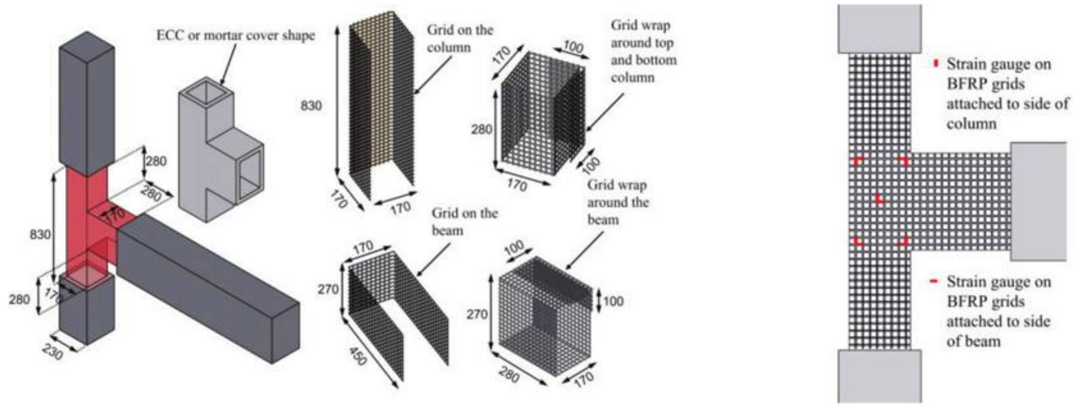

a. Schematic drawing of type "w" retrofitting specimen with BFRP grids configuration

b. Position of strain gauge on BFRP grid of type "w" retrofitting

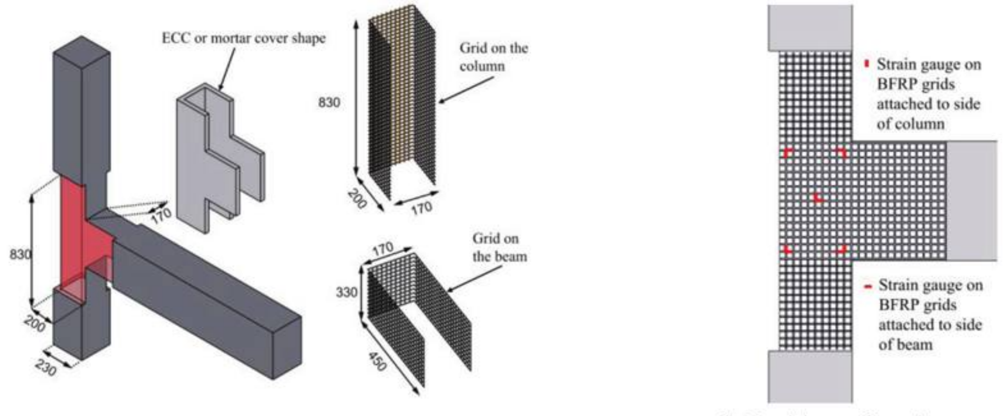

c. Schematic drawing of type "s" retrofitting specimen with BFRP grids configuration

d. Position of strain gauge on BFRP grid of type "s" retrofitting

Fig. 4—Schematic drawing of retrofitted specimens.

a. Surface treatment by grinding and polishing

b. Applying primer

c. Attaching BFRP grids

d. Casting ECC and mortar

Fig. 5—Procedure of specimen using BFRP grid and ECC.[3]

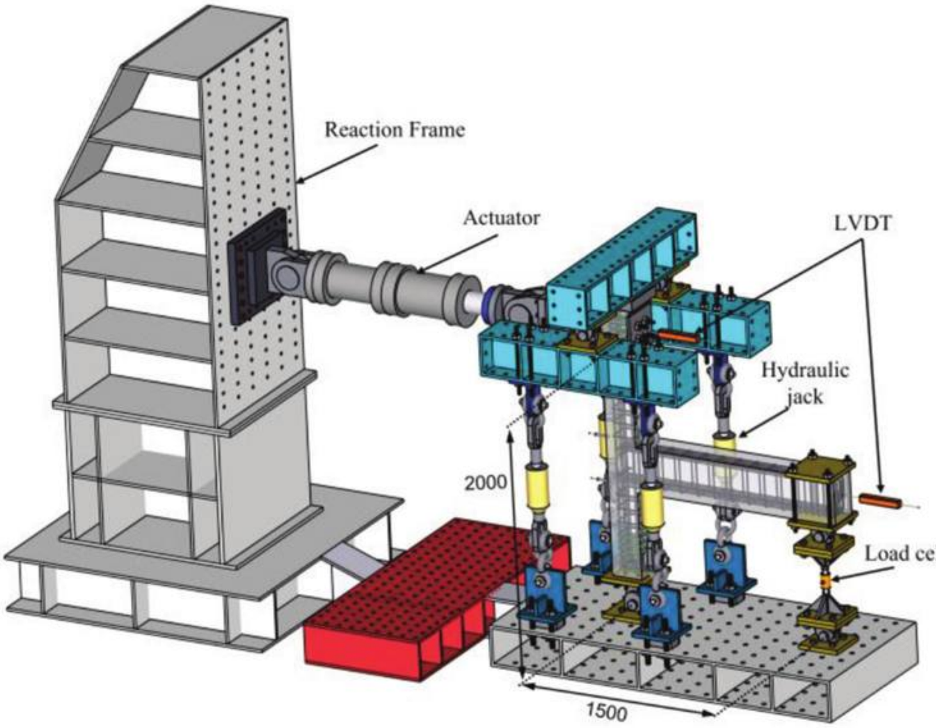

Fig. 6—Experimental setup.[3]

of the benchmark specimen under displacement rate. Each ductility level possessed only one full cycle. The first cyclic load started at 1μ, and it rose by 0.5μ every cycle until the specimens failed. Figure 7 illustrates the loading steps for the specimens. The ductility of the specimens is calculated by the proportion of the displacement when the maximum load decreases to 20% (Δu) of the displacement when the reinforcing bar exceeds elastic range (Δy).

The deformation and crack patterns of the specimens were demonstrated by the digital image correlation (DIC) technique analyzed in an open-source program named Ncorr.[53] A speckled pattern was added to the white background of

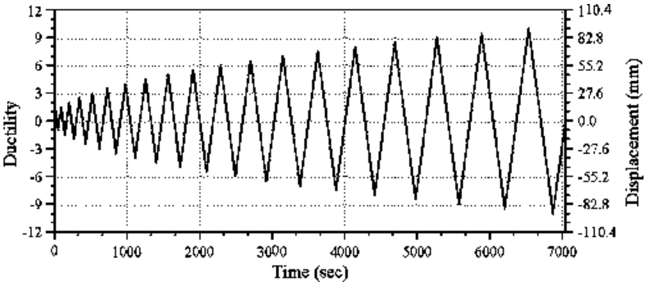

Fig. 7—Loading protocol for specimens.[3]

the joint area. A camera with a source light was employed to capture images of the specimen throughout the test. The results of the test were recorded concurrently with a frequency of 10 Hz. The captured image and testing results were matched time by time, and the images were analyzed in Ncorr, which operates in a MATLAB environment.

EXPERIMENTAL RESULTS

Failure mode and general behavior of specimens

Benchmark specimen T-B-0-0—Flexural cracks formed in vertical direction were noticed on the beam at the first ductility level, as illustrated in Fig. A1 in the Appendix.[*] Then, the cracks moved to concentrate in the joint, forming a cross shape, while an abrupt drop in the hysteretic curve of the benchmark specimens coincidentally occurred in the same ductility level, as illustrated in Fig. 8(a), ductility level 2.5. It is the effect of excessive shear force inside the joint. Subsequently, the stress concentrated on the cross-shaped crack, expanding it bigger and bigger until the specimen abruptly collapsed at ductility level 8 because of splitting of the back concrete cover resulting from the crack at the joint to the bottom and top column, plus buckling of the vertical reinforcing bars caused by immoderate compressive stress and the crushing of the concrete inside the joint, as demonstrated in Fig. 9(a).

Specimen T-B-W-E—Smear cracks were first observed on the beam at the end of ECC of the retrofitted region at ductility level 2.5, as demonstrated in Fig. A2. The cracks expanded to the whole height of the beam, making a small drop of load in the load-displacement curve of the specimen, as shown in Fig. 8(b) at ductility level 3.5. Then another crack appeared to form at the intersection of the beam and joint, and they expanded slowly and vertically along the face of the beam until ductility level 8.5. Subsequently, the crack started to propagate diagonally on the column, while the hysteretic curve of the specimen shows a faster force drop rate from the same ductility level. Finally, the specimen failed abruptly at ductility level 14.5 because of the splitting of the back face cover of the column and excessive shear force inside the joint. The BFRP grid along the crack on the ECC cover also broke according to post-test observation.

Specimen T-B-W-M—As shown in Fig. A3, cracks initially occurred at the corner of the column and beam at ductility level 1.5. Then they expanded vertically before propagating diagonally into the column at ductility level 3, when the load-displacement curve of the specimen coincidentally illustrates a drop of load, as shown in Fig. 8(c). Subsequently, the crack concentrated only at the joint, spalling the mortar cover and at the same time; it also went vertically along the rear face of the column. The strength of the specimen decreases with a greater rate from ductility level 5. Finally, the specimen collapsed abruptly at ductility level 9 because of the rupture of the mortar cover at the rear face of the column and crashing of the concrete inside the joint, as demonstrated in Fig. 10(a). It was also because of debonding of the cover. Moreover, because of extreme compressive stress, the joint began bulging, breaking the BFRP grid at the corner of the side and rear face of the joint. The BFRP grid at the intersection of the beam and joint also broke according to post-test observation.

Specimen T-B-S-E—A crack was observed as early as ductility level 1 at the outermost ECC on the beam, as demonstrated in Fig. A4. Then, the crack remained concentrated at the same place on the beam, leaving the ECC cover intact; no cracks were seen on the ECC cover. However, the whole ECC cover debonded slowly from the specimen, and it was barely noticed until ductility level 7, where the concrete cover of the rear face of the column was broken. As shown in Fig. 8(d), the load-displacement graph of the specimen illustrates a steady decrease rate after the peak load. It is assumed that the ECC cover debonded slowly until the specimen broke down at ductility level 11.5. The cause of specimen failure was not only because of cover debonding, but also because of excessive shear force inside the joint, leaving a cross-shaped crack according to post-test observation, as demonstrated in Fig. 10(b). The joint bulged and all BFRP grids along the crack were also broken.

Specimen T-B-S-M—At ductility level 1, as illustrated in Fig. A5, cracks initially took place at the corner of the beam and joint and the end of mortar on the beam. The cracks expanded and penetrated the column as the load of the specimen suddenly dropped at ductility level 2.5, as demonstrated in Fig. 8(e). Then the mortar cover at the rear face of the column split, resulting from the expansion of the cracks. The specimen withstood the lateral load until ductility level 9, before progressively collapsing. The specimen failed because of splitting of the rear cover of the column plus crushing of the concrete inside the joint. The joint swelled with the breaking of the BFRP grid at the corner of the rear and side face of the joint, as shown in Fig. 9(e).

Effect of retrofit scheme on specimen mechanism

All retrofitted specimens show an overall improvement such as ductility, strength, and energy dissipation, as demonstrated in Table 4. However, the failure still occurred at the same place as the benchmark specimen, yet the retrofitted specimens could withstand longer. The maximum load of Specimen T-B-W-E increased by approximately 23% and 15% in the pulling and pushing directions, respectively, compared to the benchmark specimen. The corresponding displacement to the maximum load in both directions also increased by approximately 128% and 143%, respectively. It shows that the retrofitting scheme using the combination of

---

[*] The Appendix is available at **www.concrete.org/publications** in PDF format, appended to the online version of the published paper. It is also available in hard copy from ACI headquarters for a fee equal to the cost of reproduction plus handling at the time of the request.

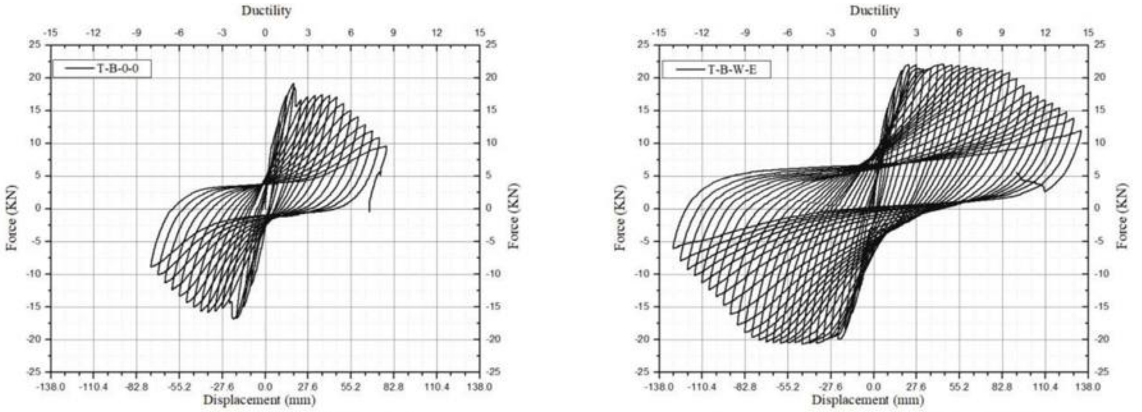

a. Specimen T-B-0-0

b. Specimen T-B-W-E

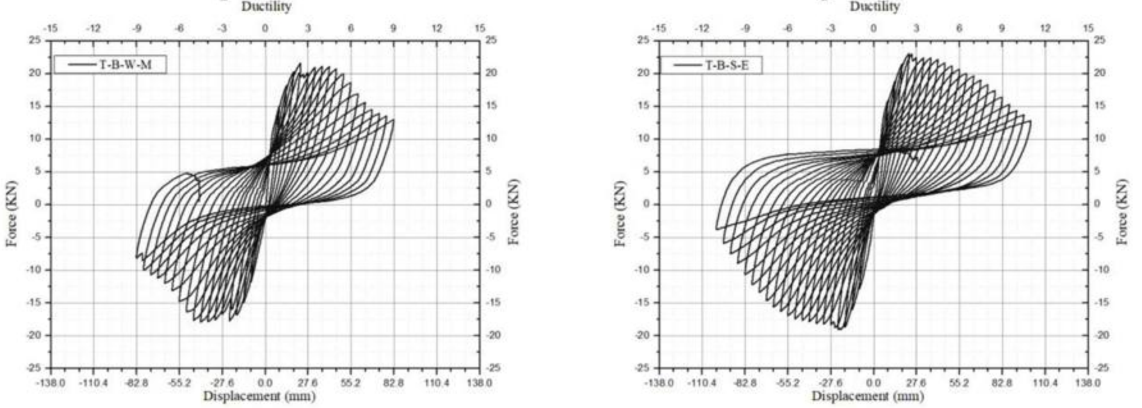

c. Specimen T-B-W-M

d. Specimen T-B-S-E

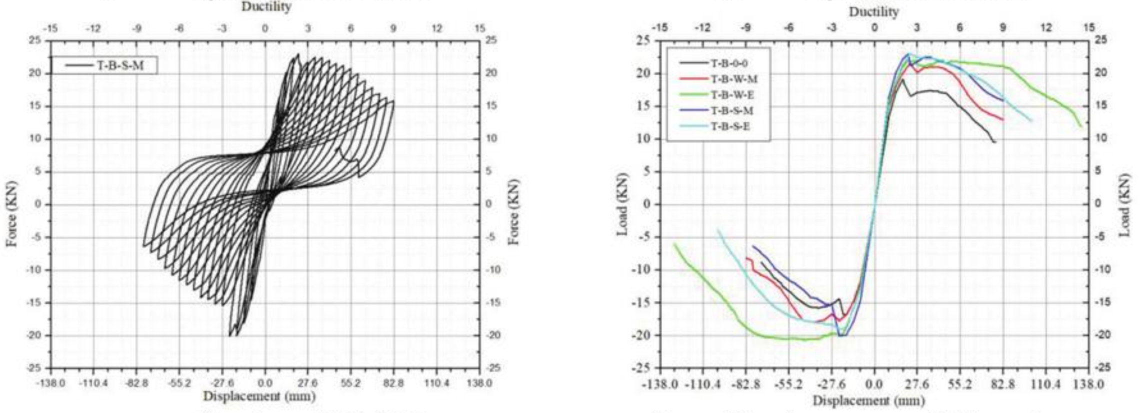

e. Specimen T-B-S-M

f. Envelope curve of all specimens

Fig. 8—Hysteretic and envelope curve of all specimens.

BFRP and ECC wrapping around the member near the joint improves the strength and makes the specimen more ductile. Specimen T-B-W-E could withstand six ductility levels longer than the benchmark specimen before it collapsed. Though the failure mode of the specimen still took place at the joint, the working mechanism of the specimen did change. Unlike the benchmark specimen, in which the stress concentrated at the joint from the start as the strain of the reinforcing bar near the joint yielded longer than that at a 250 mm distance from the joint (as shown in Fig. 11 and 12), the stress of Specimen T-B-W-E concentrated at the end of ECC on the beam at the early loading step. It clearly illustrates that the failure mode of the specimen can be shifted from joint to beam. However, due to weak bonding between the ECC and the specimen, the stress went back to concentrate at the joint area after debonding, which led to joint failure at the end of the test. As shown in Fig. 13, the BFRP grid along the beam made the joint stronger, with smaller yielding of the grid near the joint compared to the yielding of reinforcing bar at the end of the ECC on the beam at the early stage. The strain of the grid in Fig. 13 increased again at ductility level 4 because the stress concentration went back to the joint.

The maximum load of Specimen T-B-W-M rose by approximately 6% and 13% in the pulling and pushing directions, respectively, compared to the benchmark specimen. The corresponding displacement to the maximum load also increased by approximately 106% and 27% in the pulling and pushing directions, respectively. Specimen T-B-W-M failed at ductility level 9, which lasted 0.5 ductility levels longer than the reference. Although the specimen lasted

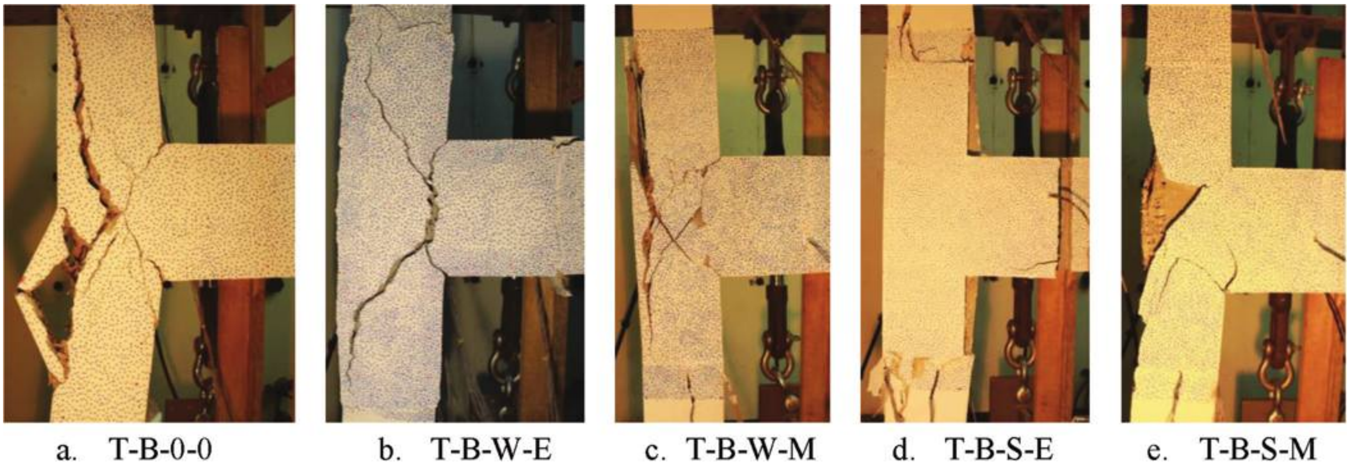
a. T-B-0-0 b. T-B-W-E c. T-B-W-M d. T-B-S-E e. T-B-S-M

Fig. 9—Final state of all specimens.

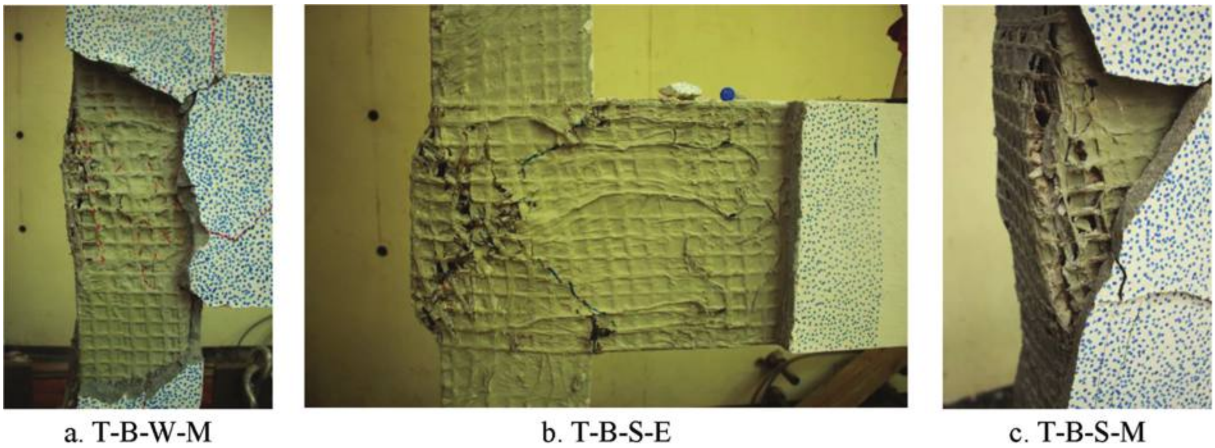
a. T-B-W-M b. T-B-S-E c. T-B-S-M

Fig. 10—Post-observation state of tested retrofitted specimens.

Table 4—Test results summary

Specimen		Ductility μ = $\Delta u/\Delta y$	Maximum load, kN	Corresponding displacement of maximum load, mm	Failure ductility level	Cumulative dissipated energy, kN·mm	Failure mode
T-B-0-0	Pushing	5.79	19.13	18.05	8.50	7703.28	Joint shear
	Pulling	7.00	–16.87	–20.07			
T-B-W-E	Pushing	11.13	22.07	43.9	14.50	36,676.01	Joint shear
	Pulling	11.96	–20.7	–45.73			
T-B-W-M	Pushing	6.38	21.6	22.93	9.00	11,038.00	Joint shear
	Pulling	7.46	–17.89	–41.373			
T-B-S-E	Pushing	7.89	23.06	22.91	11.50	18,265.00	Debonding and joint shear
	Pulling	8.76	–19.06	–21.08			
T-B-S-M	Pushing	7.21	23.04	21.56	9.00	10,486.68	Joint shear
	Pushing	3.55	–20.08	–22.9			

Note: Δu is displacement when load decreases to 20% of ultimate load of each specimen; Δy is displacement when reinforcing bars yield; positive (+) and negative (−) values of maximum load and corresponding displacement refer to pushing and pulling directions, respectively.

slightly longer, the failure still occurred at the joint same as the benchmark specimen. Even though the BFRP grid tried to strengthen the joint, the specimen could not distribute the stress to the end of the cementitious matrix on the beam like Specimen T-B-W-E due to the brittleness of the mortar cover. The crack concentrated only at the interface of the beam and column, making the strain of HB31 (the strain gauge on bottom bar at the interface of the beam and joint) bigger than that of HB41 (the strain gauge on the bottom bar at the end of mortar on the beam) throughout the test. Finally, the concrete inside the joint crushed under excessive compressive stress when the BFRP grid was broken, which

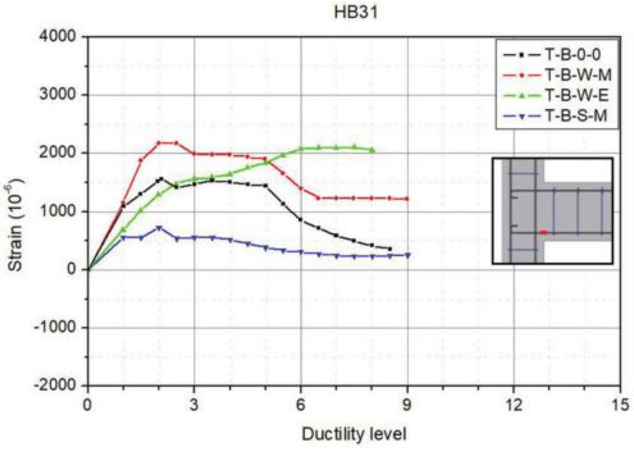

Fig. 11—Strain of HB31 strain gauge on reinforcing bar.

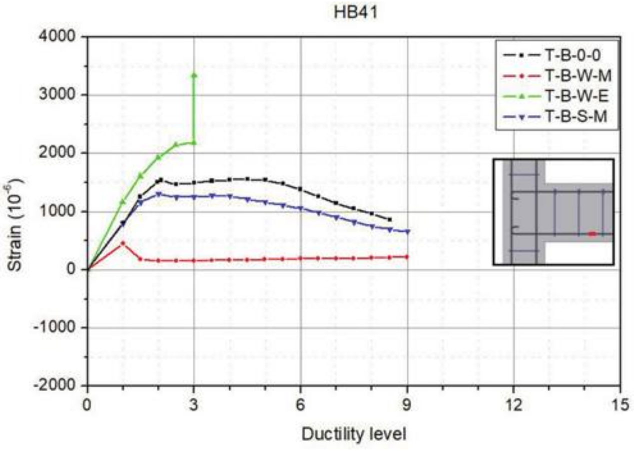

Fig. 12—Strain of HB41 strain gauge on reinforcing bar.

led to the vanishing of the confinement effect made by the BFRP grid, resulting in a bulging joint.

The maximum load of T-B-S-E increased by approximately 13% and 21% in the pulling and pushing directions, respectively. Simultaneously, the corresponding displacement also rose by approximately 5% and 27% in the pulling and pushing directions, respectively. The specimen became more ductile compared to the benchmark specimen. The specimen also lasted three ductility levels longer. Moreover, the retrofitting method also affected the working mechanism of the specimen. The stress concentrated at the end of ECC on the beam rather than at the intersection of the beam and column in the early stage as shown in Fig. A4. However, due to weak bonding strength between the ECC and the specimen, the ECC cover debonded from the specimen. The shear inside the joint was resisted by only the concrete of the specimen and the BFRP grid; the ECC cover did not contribute. As a result, the shear cracks only occur on the specimen, leaving cross-shaped cracks on the concrete joint, and the BFRP grid also broke along the cracks as demonstrated in Fig. 10(b). However, the ECC cover was intact, showing no significant cracks on it.

The maximum load of T-B-S-M increased approximately 19% and 20% in the pulling and pushing directions, respectively. The corresponding displacement also increased by approximately 14% and 19% in the respective directions as well. It shows that the specimen became stronger and more ductile; however, the specimen lasted only 0.5 ductility levels longer than the benchmark specimen. Nevertheless, the working mechanism of the specimen did change slightly as the stress first concentrated at the end of mortar on the beam rather than the interface of the joint and beam, as in the benchmark specimen, shown by comparing the strain of the reinforcing bar near the joint and at the end of mortar on the beam, as illustrated in Fig. 11 and 12. Despite that, the stress still went back to concentrate on the joint because the mortar cover is not ductile enough in distributing the stress to the end of the mortar. Once the cracks occurred on the mortar cover at the joint, the stress went back to concentrate only on that crack, making the joint fail at the end of the test. Besides the debonding of the mortar cover, the joint mainly failed due to concrete crushing after the confinement made by the BFRP grids vanished when they were broken. The joint swelled as demonstrated in Fig. 10(c).

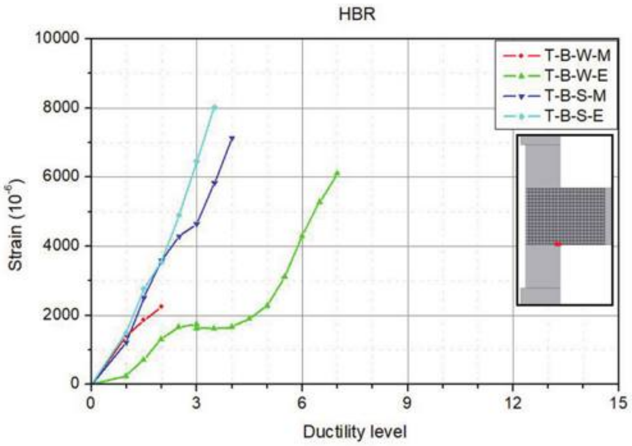

Fig. 13—Strain of HBR strain gauge on grid on beam.

Stiffness degradation

The stiffness of the specimen demonstrates how it responds to the applied loading. The stiffness will decrease after going through a larger deformation. In this paper, the secant stiffness of the specimen is computed at every loading step based on the maximum and minimum loads with their corresponding displacements as determined by

$$K_i = \frac{F_i^+ - F_i^-}{D_i^+ - D_i^-} \tag{1}$$

where K_i is the secant stiffness in cycle i; F_i^+ and F_i^- represent the maximum and minimum loads in the pushing and pulling directions in cycle i, respectively; and D_i^+ and D_i^- are the corresponding displacements to the maximum and minimum loads in cycle i, respectively. The secant stiffness degradation of all specimens in each loading step is demonstrated in Fig. 14. It shows that the stiffness of Specimen T-B-S-M is the greatest in the first ductility level, and the stiffness of Specimen T-B-0-0 is the smallest. However, at ductility level 3, the stiffness of T-B-S-M sharply decreases, making its stiffness similar to that of T-B-W-M and weaker than other retrofitted specimens, yet still stronger than the

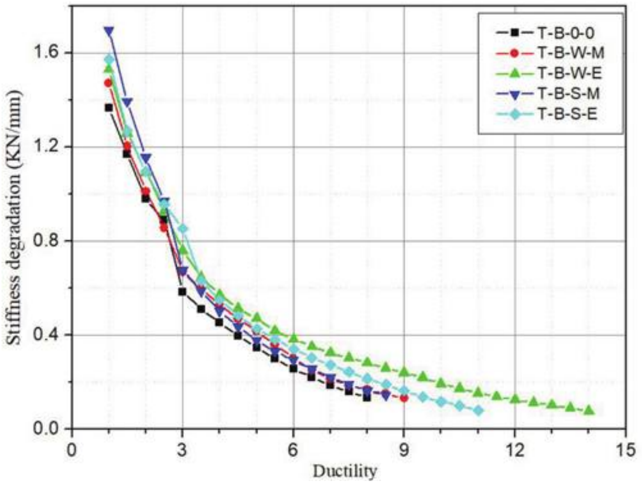

Fig. 14—Stiffness degradation of all specimens.

benchmark specimen. At ductility level 3, the stiffness of the benchmark specimen also indicates a sharp drop because at that loading step, the crack happened at the joint of both specimens. Among all specimens, the stiffness of T-B-W-E decreased at the slowest rate, and it is bigger than the rest, while the stiffness of the benchmark specimen remained the smallest in the subsequent cycle until the specimen collapsed. What makes the stiffness of T-B-W-E bigger than the rest is because of the rate of cracking. With the ductile behavior of the ECC, the stress in the specimen can be distributed, making the specimen remain strong with less-severe cracks. Moreover, the cover debonding did not occur on Specimen T-B-W-E as it did with T-B-S-E.

Cumulative energy dissipation

Energy dissipation is calculated as the closed area inside the hysteretic curve of the specimen in every cycle. It demonstrates the energy needed to produce inelastic deformation in the specimen. Figure 15 illustrates the sum of the energy released due to inelastic deformation in each loading step for the specimens. Overall, it illustrates that the retrofitting makes the specimen more ductile by producing more dissipated energy. The energy produced from all specimens does not show any significant differences at the early stage. However, Specimen T-B-W-E illustrates far more and the biggest cumulative energy dissipation compared to other counterparts, and the benchmark specimen possesses the least cumulative energy dissipation until the specimen collapsed in the consecutive loading step. What makes the cumulative energy dissipation of T-B-W-E much bigger than the rest is due to the ductile behavior of the ECC cover, which assisted the specimen in distributing the crack. Nevertheless, the cover of Specimen T-B-S-E was also made from ECC, but its dissipated energy is similar to the specimen retrofitted using mortar if the cumulative dissipated energy is compared in each loading step because debonding made the ECC cover unable to perform to its full potential to help the specimen in resisting and distributing the crack as it did in Specimen T-B-W-E. As a result, the cumulative dissipated energy produced by T-B-W-E is approximately 376% bigger than that of the benchmark specimen, followed by T-B-S-E, T-B-W-M, and T-B-S-M with approximately 137%, 43%, and 36% greater dissipated energy compared to the benchmark specimen, respectively. The dissipated energy of T-B-W-M and T-B-S-M are alike because both specimens possess similar failure mechanisms, which were cracks in the joint, splitting of the back cover, and concrete crushing inside the joint after losing the confinement effect by BFRP grids.

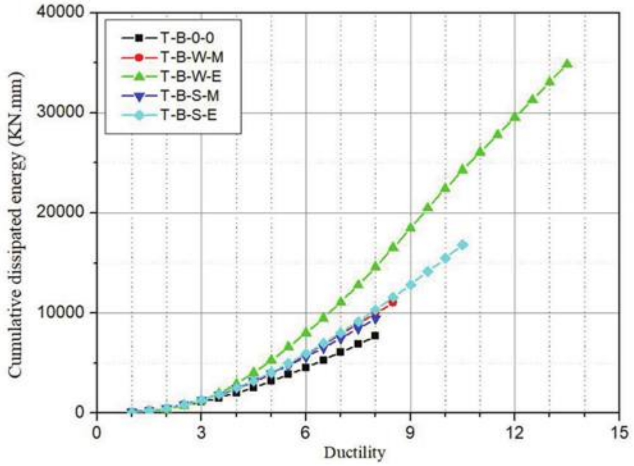

Fig. 15—Cumulative energy dissipation.

Pinching width ratio

Pinching effect happens when the specimen produces low stiffness in resisting flexural bending or shear force, which induces slippage between reinforcing bars and concrete. The pinching effect can be observed where the displacement is approximately zero in the hysteretic curve of RC specimens under cyclic loading. The pinching effect produced by the joint significantly influences the performance of the structure, such as reduction of energy absorption, change of number of hysteretic cycles, and demand for column ductility at the base.[54] The pinching width ratio (P_r), introduced by Mostofinejad and Akhlaghi,[9] is used to define the pinching effect that occurred in a particular specimen. The pinching width ratio can be used to illustrate how much damage the specimen encounters in each loading step. The index can be used to compare the effect of other specimens regardless of failure mode, reinforcement detailing, and geometry of the specimen. The formula for calculating the pinching width ratio is

$$P_r = \frac{P_a}{P_i} \tag{2}$$

where P_i is the least distance between the negative and positive loading directions near the zero displacements in a particular cycle of the ideal load-displacement graph of the specimen; and P_a is the least distance between the negative and positive loading direction near the zero displacements in a particular cycle of the real load-displacement graph of the specimen. Figure 16 explains the true definition of the pinching width ratio parameters. Figure 17 shows the pinching width ratio of all specimens. The bigger the pinching width ratio, the smaller the pinching effect. The value of the pinching width

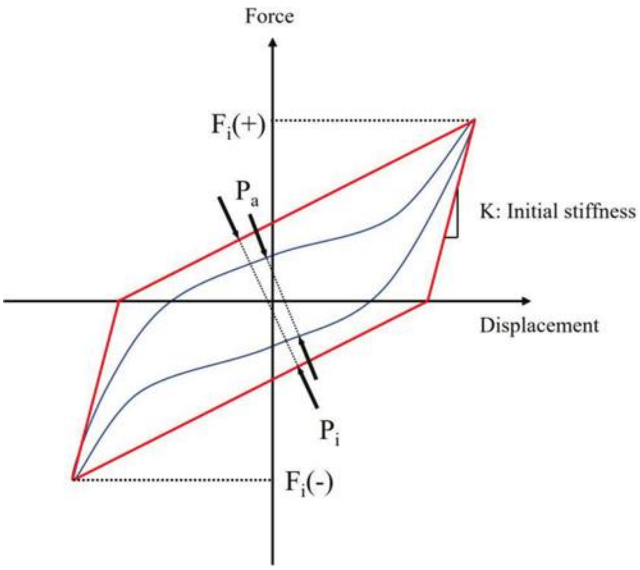

Fig. 16—Definition of pinching width ratio parameters.[3]

ratio independently demonstrates the pinching effect in the specimen from one step to another. Overall, the values of the pinching width ratio of all specimens show similar behavior at early stages. However, the value of the pinching width ratio of Specimen T-B-W-E shows better performance compared to others from ductility level 3, yet the value of the pinching width ratio of the benchmark specimen decreases and remains smaller compared to other specimens because of the propagation of the crack on the column. When the specimen is under flexural bending, the value of the pinching width ratio will increase as it did in Specimen T-B-W-E from ductility level 2 to 5, where the flexural crack is concentrated only on the beam. Once the cracks occur on the cover and penetrate the column, the value of the pinching width ratio starts to decrease.

Comparison of mortar and ECC cover

Mortar and ECC were used to replace the removed concrete cover. They both distinctly enhance the overall performance of the specimen; however, both materials are good in their own way. All specimen failures took place at the joint due to weak bonding between the specimen and cementitious matrix covers. Hence, it shows no different effect between ECC and mortar on the failure mode. Nonetheless, mortar exhibited a larger extent of cover spalling compared to ECC, especially in the column at the joint area. In terms of strength, the specimen retrofitted by ECC is approximately 8% stronger than the specimen retrofitted by mortar for retrofitting type "W," yet the specimen retrofitted by mortar is 2% stronger than the specimen retrofitted by ECC for retrofitting type "S". It shows that the strength of the retrofitted specimen does not entirely depend on the type of cementitious matrix but also retrofitting type. With the ductile behavior of ECC and brittle behavior of mortar, the specimen retrofitted by ECC produced approximately 232% and 74% bigger cumulative dissipated energy compared to its counterpart in retrofitting types "W" and "S", respectively. In terms of failure ductility level, ECC cover shows better performance than mortar cover in both types of retrofitting. The specimen retrofitted by ECC lasted 5.5 and 2.5 ductility levels longer than the specimen strengthened by mortar with types "W" and "S" retrofitting, respectively. Owing to the ductile behavior of the ECC, the ECC cover could change the stress concentration in the specimen by focusing at the outmost of the ECC on the beam if debonding did not exist. Unlike the mortar cover, the crack focused directly on the joint from the early stage after mortar cracking. Moreover, the ECC cover also makes the specimen more ductile compared to the mortar cover in all types of retrofitting types, as shown in Table 4. However, the ductility of T-B-S-M and T-B-S-E illustrates similar behavior in Fig. 8(f) and similar values of ductility in Table 4 in the pushing direction. The hysteretic curve of each specimen demonstrates similar behavior after the peak because after the peak load, the ECC in Specimen T-B-S-E did not contribute to the strength of the specimen because of debonding, and the mortar in Specimen T-B-S-M did not either because it was broken. After the peak, only the BFRP grids of both specimens were there to assist the specimen in resisting lateral force. Nevertheless, in the pulling direction, the high-strength mortar spalled as well, so it could not further assist the column in compression, yet ECC could still help the specimen in withstanding the lateral load as it was still able to take a share of compressive load from the column, preventing early concrete crushing and buckling of reinforcing bar in the column at the joint, which would have led to the failure of the specimen.

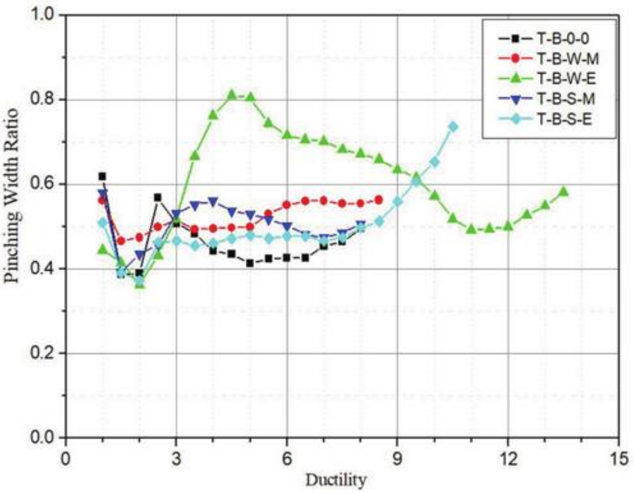

Fig. 17—Pinching width ratio.

Comparison of retrofitting type

Specimens were retrofitted using two different styles, type "W" and type "S." Both retrofitting types played different roles in supporting the specimen. The maximum loads of specimens retrofitted by ECC using both types of retrofitting are slightly different. Retrofitting using type "W" is approximately 2% stronger than that of retrofitting using type "S" with ECC cover in terms of strength. However, for mortar cover, retrofitting with type "S" is approximately 9% stronger than that of retrofitting type "W." It is because when retrofitting the specimen using type "W" with ECC cover, the ECC block still performed together, though debonding occurred due to the ductile behavior of ECC, which made the ECC block interlock with the specimen and collaborate until the deformation exceeded the ultimate strain of ECC. However, with the brittle behavior of mortar, once the cracks and debonding happened on the mortar cover, the effective section of the specimen became smaller in retrofitting type "W" as the concrete cover was taken out more than in retrofitting type "S". The mortar cover cannot continue collaborating with the specimen under large deformation to resist higher load, so only concrete was there to support the member. For this case, the effective section from type "S" retrofitting remained bigger than that of type "W" retrofitting when cracks and debonding occurred. Anyway, the specimen using retrofitting type "W" becomes more ductile as the value of ductility is bigger than that of the specimen strengthened with type "S" for both types of cementitious matrixes, as shown in Table 4. Moreover, retrofitting type "W" also made the specimen last longer compared to its counterpart. The cumulative dissipated energy of retrofitting type "W" is also bigger than that of retrofitting type "S". It is because more BFRP grids were applied to the specimen in retrofitting type "W" than in retrofitting type "S" as the grids were used to wrap around the members near the joint.

SUMMARY AND CONCLUSIONS

An experimental study had been conducted to investigate the retrofitting method using a basalt fiber-reinforced polymer (BFRP) grid combined with high-strength mortar and engineered cementitious composite (ECC) on reinforced concrete (RC) beam-column joints. Two-hundred fifty millimeters of concrete cover around the joint area, which is the development length of BFRP, was taken out of the joint. Then the BFRP grid was applied, and it was covered back by cementitious matrixes. The specimens were retrofitted using two different configurations. One style was to remove the concrete cover only from the side face of the specimen; another style was to remove the concrete cover on all nearby members at 250 mm from the face of the joint. After retrofitting, the specimen was tested under a quasi-static load test under displacement control corresponding to the ductility of the benchmark specimen. The specimen was tested until it collapsed. As the result, the following conclusions can be made:

1. All the retrofitted specimens become stronger compared to the benchmark specimen in terms of strength. The maximum load of the retrofitted specimens increased from 6 to 23%, though the size of the specimen remained the same. Furthermore, the specimens became more ductile as the displacement corresponding to the maximum load increased from 5 to 143%. Moreover, the cumulative dissipated energy of the retrofitted specimen increased from 43 to 376% compared with that of the benchmark specimen.

2. Stress concentration tended to shift from the joint to the end of ECC on the beam, as shown in the early loading stage; however, due to weak debonding between the ECC and the specimen, the stress went back to the joint, resulting in concrete crushing inside the joint. To prevent debonding, a connector between the ECC and the specimen should be introduced in a future study. However, the specimen retrofitted by ECC withstood from three to six ductility levels longer than the benchmark specimen.

3. For the specimen retrofitted by mortar, stress cannot be shifted to the end of the mortar on the beam as in the ECC specimen because of the brittle behavior of mortar. It concentrated at the face of the beam and joint as early as ductility level 1. Moreover, the specimen lasted very slightly longer than the benchmark specimen, which is only 0.5 ductility levels longer.

4. Neither the type of cementitious matrix nor retrofitting style can determine the strength of the specimen alone due to the debonding of the cover. Retrofitting type "W" with the combination of ECC provides higher strength than retrofitting type "S" with ECC; however, retrofitting type "S" with mortar provides higher strength than retrofitting type "W" with mortar. Nevertheless, using high-strength mortar as the cover exhibited a higher level of spalling than using ECC.

5. The specimen retrofitted by ECC lasted longer than the specimen retrofitted by mortar for both types of retrofitting styles. Moreover, due to the ductile behavior of ECC, the specimens retrofitted by ECC became more ductile and produced higher total dissipated energy than that of the specimens retrofitted by mortar.

6. The type "W" retrofitted specimen could withstand lateral load longer than the type "S" retrofitted specimen. Furthermore, retrofitting type "W" also makes the specimen more ductile compared with retrofitting type "S".

7. Specimen T-B-W-E showed the best performance compared to its counterparts.

AUTHOR BIOS

Chhoung Lim *is a PhD Candidate in the Department of Civil Engineering at Gyeongsang National University, Gyeongsangnam-do, South Korea. He received his BS from the Institute of Technology of Cambodia, Phnom Penh, Cambodia, in 2018, and his MS from INSA Rennes, Rennes, France, in 2019. His research interests include reinforced concrete and steel structure retrofitting.*

Yeongseok Jeong *is a Postdoctoral Associate in the Department of Civil Engineering at The University of Texas at Arlington, Arlington, TX. He received his BS, MS, and PhD in structural engineering from Gyeongsang National University in 2013, 2015, and 2021, respectively. His research interests include reinforced concrete and steel structure retrofitting.*

Minho Kwon *is a Professor in the Department of Civil Engineering at Gyeongsang National University. He received his BS and MS from Kyungpook National University, Gyeongsangbuk-do, South Korea, in 1992 and 1994, respectively, and his PhD from the University of Colorado, Boulder, Boulder, CO, in 2000. His research interests include reinforced concrete and steel structure retrofitting.*

ACKNOWLEDGMENTS

Minho Kwon is the corresponding author of this paper. This work was supported by the National Research Foundation of Korea (NRF) grant funded by the Korea government (MSIT) (No. 2019R1A2C1003007). The authors would like to thank the members of the structural engineering laboratory of Gyeongsang National University for their valuable support in performing the experiments.

REFERENCES

1. Esmaeeli, E.; Barros, J. A. O.; Sena-Cruz, J.; Fasan, L.; Li Prizzi, F. R.; Melo, J.; and Varum, H., "Retrofitting of Interior RC Beam–Column Joints Using CFRP Strengthened SHCC: Cast-in-Place Solution," *Composite Structures*, V. 122, 2015, pp. 456-467. doi: 10.1016/j.compstruct.2014.12.012

2. Esmaeeli, E.; Danesh, F.; Tee, K. F.; and Eshghi, S., "A Combination of GFRP Sheets and Steel Cage for Seismic Strengthening of Shear-

Deficient Corner RC Beam-Column Joints," *Composite Structures*, V. 159, 2017, pp. 206-219. doi: 10.1016/j.compstruct.2016.09.064

3. Lim, C.; Jeong, Y.; Kim, J.; and Kwon, M., "Experimental Study of Reinforced Concrete Beam-Column Joint Retrofitted by CFRP Grid with ECC and High Strength Mortar," *Construction and Building Materials*, V. 340, 2022, p. 127694. doi: 10.1016/j.conbuildmat.2022.127694

4. ACI Committee 318, "Building Code Requirements for Structural Concrete (ACI 318-19) and Commentary (ACI 318R-19) (Reapproved 2022)," American Concrete Institute, Farmington Hills, MI, 2019, 624 pp.

5. Bindhu, K. R.; Sukumar, P. M.; and Jaya, K. P., "Performance of Exterior Beam-Column Joints under Seismic Type Loading," *ISET Journal of Earthquake Technology*, V. 46, No. 2, 2009, pp. 47-64.

6. Gallo, P. Q.; Pampanin, S.; and Carr, A. J., "Shake-Table Testing of Non-Ductile RC Frames As-Built and Retrofitted with GFRP Laminates and Slab-Weakening," 16th World Conference on Earthquake Engineering, Santiago, Chile, 2017.

7. Esmaeeli, E.; Barros, J. A. O.; Sena-Cruz, J.; Varum, H.; and Melo, J., "Assessment of the Efficiency of Prefabricated Hybrid Composite Plates (HCPs) for Retrofitting of Damaged Interior RC Beam-Column Joints," *Composite Structures*, V. 119, 2015, pp. 24-37. doi: 10.1016/j.compstruct.2014.08.024

8. Akguzel, U., and Pampanin, S., "Effects of Variation of Axial Load and Bidirectional Loading on Seismic Performance of GFRP Retrofitted Reinforced Concrete Exterior Beam-Column Joints," *Journal of Composites for Construction*, ASCE, V. 14, No. 1, 2010, pp. 94-104. doi: 10.1061/(ASCE)1090-0268(2010)14:1(94)

9. Mostofinejad, D., and Akhlaghi, A., "Experimental Investigation of the Efficacy of EBROG Method in Seismic Rehabilitation of Deficient Reinforced Concrete Beam–Column Joints Using CFRP Sheets," *Journal of Composites for Construction*, ASCE, V. 21, No. 4, 2017, p. 04016116. doi: 10.1061/(ASCE)CC.1943-5614.0000781

10. Shafaei, J.; Hosseini, A.; Marefat, M. S.; and Ingham, J. M., "Rehabilitation of Earthquake Damaged External RC Beam-Column Joints by Joint Enlargement Using Prestressed Steel Angles," *Earthquake Engineering & Structural Dynamics*, V. 46, No. 2, 2017, pp. 291-316. doi: 10.1002/eqe.2794

11. Lu, X.; Urukap, T. H.; Li, S.; and Lin, F., "Seismic Behavior of Interior RC Beam-Column Joints with Additional Bars under Cyclic Loading," *Earthquakes and Structures*, V. 3, No. 1, 2012, pp. 37-57. doi: 10.12989/eas.2012.3.1.037

12. Dang, C.-T., and Dinh, N.-H., "Experimental Study on Structural Performance of RC Exterior Beam-Column Joints Retrofitted by Steel Jacketing and Haunch Element under Cyclic Loading Simulating Earthquake Excitation," *Advances in Civil Engineering*, V. 2017, 2017, pp. 1-11. doi: 10.1155/2017/9263460

13. Jung, W.; Kim, J.; and Kwon, M., "Performance Evaluation of RC Beam-Column Joints with Different Bonding Interfaces," *Scientia Iranica*, V. 25, No. 1, 2017, pp. 11-21. doi: 10.24200/sci.2017.4175

14. Mahini, S. S., and Ronagh, H. R., "Strength and Ductility of FRP Web-Bonded RC Beams for the Assessment of Retrofitted Beam–Column Joints," *Composite Structures*, V. 92, No. 6, 2010, pp. 1325-1332. doi: 10.1016/j.compstruct.2009.09.006

15. Yu, F.; Zhang, N.; Niu, D.; Kong, Z.; Zhu, D.; Wang, S.; and Fang, Y., "Strain Analysis of PVC-CFRP Confined Concrete Column with Ring Beam Joint under Axial Compression," *Composite Structures*, V. 224, 2019, p. 111012. doi: 10.1016/j.compstruct.2019.111012

16. Ha, G.-J.; Cho, C.-G.; Kang, H.-W.; and Feo, L., "Seismic Improvement of RC Beam-Column Joints Using Hexagonal CFRP Bars Combined with CFRP Sheets," *Composite Structures*, V. 95, 2013, pp. 464-470. doi: 10.1016/j.compstruct.2012.08.022

17. Khan, M. I.; Al-Osta, M. A.; Ahmad, S.; and Rahman, M. K., "Seismic Behavior of Beam-Column Joints Strengthened with Ultra-High Performance Fiber Reinforced Concrete," *Composite Structures*, V. 200, 2018, pp. 103-119. doi: 10.1016/j.compstruct.2018.05.080

18. Okahashi, Y., and Pantelides, C. P., "Strut-and-Tie Model for Interior RC Beam-Column Joints with Substandard Details Retrofitted with CFRP Jackets," *Composite Structures*, V. 165, 2017, pp. 1-8. doi: 10.1016/j.compstruct.2017.01.004

19. Xu, C.; Peng, S.; Wang, C.; and Ma, Z., "Influence of the Degree of Damage and Confinement Materials on the Seismic Behavior of RC Beam-SRC Column Composite Joints," *Composite Structures*, V. 231, 2020, p. 111002. doi: 10.1016/j.compstruct.2019.111002

20. Lee, W. T.; Chiou, Y. J.; and Shih, M. H., "Reinforced Concrete Beam–Column Joint Strengthened with Carbon Fiber Reinforced Polymer," *Composite Structures*, V. 92, No. 1, 2010, pp. 48-60. doi: 10.1016/j.compstruct.2009.06.011

21. Sakthimurugan, K., and Baskar, K., "Experimental Investigation on RCC External Beam-Column Joints Retrofitted with Basalt Textile Fabric under Static Loading," *Composite Structures*, V. 268, 2021, p. 114001. doi: 10.1016/j.compstruct.2021.114001

22. Pantelides, C. P.; Okahashi, Y.; and Reaveley, L. D., "Seismic Rehabilitation of Reinforced Concrete Frame Interior Beam-Column Joints with FRP Composites," *Journal of Composites for Construction*, ASCE, V. 12, No. 4, 2008, pp. 435-445. doi: 10.1061/(ASCE)1090-0268(2008)12:4(435)

23. Wang, G.-L.; Dai, J.-G.; and Bai, Y.-L., "Seismic Retrofit of Exterior RC Beam-Column Joints with Bonded CFRP Reinforcement: An Experimental Study," *Composite Structures*, V. 224, 2019, p. 111018. doi: 10.1016/j.compstruct.2019.111018

24. Qian, H.; Li, Z.; Pei, J.; Kang, L.; and Li, H., "Seismic Performance of Self-Centering Beam-Column Joints Reinforced with Superelastic Shape Memory Alloy Bars and Engineering Cementitious Composites Materials," *Composite Structures*, V. 294, 2022, p. 115782. doi: 10.1016/j.compstruct.2022.115782

25. Beydokhti, E. Z., and Shariatmadar, H., "Experimental Investigation of Damaged Exterior RC Beam-Column Joints Retrofitted by FRP Jacketing," *Asian Journal of Civil Engineering*, V. 17, 2016, pp. 899-916.

26. Li, W.; Tang, S.; Huang, Z.; Yang, X.; Shi, T.; and Xing, F., "Shear Behavior of Concrete Beam Reinforced in Shear with Carbon Fiber-Reinforced Polymer Mesh Fabric (CFRP-MF) Configuration," *Engineering Structures*, V. 218, 2020, p. 110828. doi: 10.1016/j.engstruct.2020.110828

27. Qureshi, J.; Nadir, Y.; and John, S. K., "Bolted and Bonded FRP Beam-Column Joints with Semi-Rigid End Conditions," *Composite Structures*, V. 247, 2020, p. 112500. doi: 10.1016/j.compstruct.2020.112500

28. Yang, X.; Gao, W.-Y.; Dai, J.-G.; and Lu, Z.-D., "Shear Strengthening of RC Beams with FRP grid-Reinforced ECC Matrix," *Composite Structures*, V. 241, 2020, p. 112120. doi: 10.1016/j.compstruct.2020.112120

29. Murad, Y.; Al Bodour, W.; and Ashteyat, A., "Seismic Retrofitting of Severely Damaged RC Connections Made with Recycled Concrete Using CFRP Sheets," *Frontiers of Structural and Civil Engineering*, V. 14, No. 2, 2020, pp. 554-568. doi: 10.1007/s11709-020-0613-8

30. Gao, W. Y.; Dai, J.-G.; and Teng, J. G., "Three-Level Fire Resistance Design of FRP-Strengthened RC Beams," *Journal of Composites for Construction*, ASCE, V. 22, No. 3, 2018, p. 05018001. doi: 10.1061/(ASCE)CC.1943-5614.0000840

31. Gao, W. Y.; Dai, J.-G.; and Teng, J. G., "Simple Method for Predicting Temperatures in Insulated, FRP-Strengthened RC Members Exposed to a Standard Fire," *Journal of Composites for Construction*, ASCE, V. 19, No. 6, 2015, p. 04015013. doi: 10.1061/(ASCE)CC.1943-5614.0000566

32. Palmieri, A.; Matthys, S.; and Taerwe, L., "Experimental Investigation on Fire Endurance of Insulated Concrete Beams Strengthened with Near Surface Mounted FRP Bar Reinforcement," *Composites Part B: Engineering*, V. 43, No. 3, 2012, pp. 885-895. doi: 10.1016/j.compositesb.2011.11.061

33. Ahmed, A., and Kodur, V. K. R., "Effect of Bond Degradation on Fire Resistance of FRP-Strengthened Reinforced Concrete Beams," *Composites Part B: Engineering*, V. 42, No. 2, 2011, pp. 226-237. doi: 10.1016/j.compositesb.2010.11.004

34. Zhou, H.; Torres, J. P.; Fernando, D.; Law, A.; and Emberley, R., "The Bond Behaviour of CFRP-to-Steel Bonded Joints with Varying Bond Properties at Elevated Temperatures," *Engineering Structures*, V. 183, 2019, pp. 1121-1133. doi: 10.1016/j.engstruct.2018.10.044

35. Dai, J.-G.; Gao, W.-Y.; and Teng, J. G., "Finite Element Modeling of Insulated FRP-Strengthened RC Beams Exposed to Fire," *Journal of Composites for Construction*, ASCE, V. 19, No. 2, 2015, p. 04014046. doi: 10.1061/(ASCE)CC.1943-5614.0000509

36. Gao, W.-Y.; Dai, J.-G.; and Teng, J. G., "Fire Resistance Design of Un-Protected FRP-Strengthened RC Beams," *Materials and Structures*, V. 49, No. 12, 2016, pp. 5357-5371. doi: 10.1617/s11527-016-0865-x

37. Mostofinejad, D., and Hajrasouliha, M., "Shear Retrofitting of Corner 3D-Reinforced Concrete Beam-Column Joints Using Externally Bonded CFRP Reinforcement on Grooves," *Journal of Composites for Construction*, ASCE, V. 22, No. 5, 2018, p. 04018037. doi: 10.1061/(ASCE)CC.1943-5614.0000862

38. Golias, E.; Zapris, A. G.; Kytinou, V. K.; Kalogeropoulos, G. I.; Chalioris, C. E.; and Karayannis, C. G., "Effectiveness of the Novel Rehabilitation Method of Seismically Damaged RC Joints Using C-FRP Ropes and Comparison with Widely Applied Method Using C-FRP Sheets—Experimental Investigation," *Sustainability*, V. 13, No. 11, 2021, p. 6454. doi: 10.3390/su13116454

39. Karayannis, C. G., and Golias, E., "Full-Scale Experimental Testing of RC Beam-Column Joints Strengthened Using CFRP Ropes as External Reinforcement," *Engineering Structures*, V. 250, 2022, p. 113305. doi: 10.1016/j.engstruct.2021.113305

40. Zhou, J.; Qian, S.; Ye, G.; Copuroglu, O.; van Breugel, K.; and Li, V. C., "Improved Fiber Distribution and Mechanical Properties of Engineered Cementitious Composites by Adjusting the Mixing Sequence,"

Cement and Concrete Composites, V. 34, No. 3, 2012, pp. 342-348. doi: 10.1016/j.cemconcomp.2011.11.019

41. Tan, K. H., and Liu, J.-C., "Fire Performance of Engineered Cementitious Composite," 7th Protection of Structures against Hazards Conference, Hanoi, Vietnam, 2018.

42. Mahmoudi, F.; Abdalla, J. A.; Hawileh, R. A.; and Zhang, Z., "Tensile and Compressive Strength of Polyethylene Engineered Cementitious Composite (PE-ECC) at Elevated Temperature," *Materials Today: Proceedings*, V. 65, 2022, pp. 2081-2085. doi: 10.1016/j.matpr.2022.06.451

43. Zhang, P.; Li, Q.-F.; Wang, J.; Shi, Y.; and Ling, Y.-F., "Effect of PVA Fiber on Durability of Cementitious Composite Containing Nano-SiO_2," *Nanotechnology Reviews*, V. 8, No. 1, 2019, pp. 116-127. doi: 10.1515/ntrev-2019-0011

44. Gao, W.-Y.; Hu, K.-X.; Dai, J.-G.; Dong, K.; Yu, K.-Q.; and Fang, L.-J., "Repair of Fire-Damaged RC Slabs with Basalt Fabric-Reinforced Shotcrete," *Construction and Building Materials*, V. 185, 2018, pp. 79-92. doi: 10.1016/j.conbuildmat.2018.07.043

45. Ding, Z.; Xu, M.-R.; Dai, J.-G.; Dong, B.-Q.; Zhang, M.-J.; Hong, S.-X.; and Xing, F., "Strengthening Concrete Using Phosphate Cement-Based Fiber-Reinforced Inorganic Composites for Improved Fire Resistance," *Construction and Building Materials*, V. 212, 2019, pp. 755-764. doi: 10.1016/j.conbuildmat.2019.04.038

46. Guo, R.; Cai, L.; Hino, S.; and Wang, B., "Experimental Study on Shear Strengthening of RC Beams with an FRP Grid-PCM Reinforcement Layer," *Applied Sciences*, V. 9, No. 15, 2019, p. 2984. doi: 10.3390/app9152984

47. Zheng, Y.-Z.; Wang, W.-W.; and Brigham, J. C., "Flexural Behaviour of Reinforced Concrete Beams Strengthened with a Composite Reinforcement Layer: BFRP Grid and ECC," *Construction and Building Materials*, V. 115, 2016, pp. 424-437. doi: 10.1016/j.conbuildmat.2016.04.038

48. Bastani, A.; Das, S.; and Kenno, S. Y., "Flexural Rehabilitation of Steel Beam with CFRP and BFRP Fabrics—A Comparative Study," *Archives of Civil and Mechanical Engineering*, V. 19, No. 3, 2019, pp. 871-882. doi: 10.1016/j.acme.2019.04.004

49. Chen, W.; Pham, T. M.; Sichembe, H.; Chen, L.; and Hao, H., "Experimental Study of Flexural Behaviour of RC Beams Strengthened by Longitudinal and U-Shaped Basalt FRP Sheet," *Composites Part B: Engineering*, V. 134, 2018, pp. 114-126. doi: 10.1016/j.compositesb.2017.09.053

50. Ali, N. M.; Wang, X.; Wu, Z.; and Hassanein, A. Y. A., "Basalt Fiber Reinforced Polymer Grids as an External Reinforcement for Reinforced Concrete Structures," *Journal of Reinforced Plastics and Composites*, V. 34, No. 19, 2015, pp. 1615-1627. doi: 10.1177/0731684415594487

51. Jeong, Y.-S.; Kwon, M.-H.; Seo, H.-S.; Kim, G.-Y.; and Kim, G.-Y., "Torsional Behavior of Beams Retrofitted by PVA-ECC," *Journal of the Korean Society for Advanced Composite Structures*, V. 6, No. 1, 2015, pp. 30-37. doi: 10.11004/kosacs.2015.6.1.030

52. Zhu, H.; Yu, K.; and Li, V. C., "Sprayable Engineered Cementitious Composites (ECC) Using Calcined Clay Limestone Cement (LC3) and PP Fiber," *Cement and Concrete Composites*, V. 115, 2021, p. 103868. doi: 10.1016/j.cemconcomp.2020.103868

53. Blaber, J.; Adair, B.; and Antoniou, A., "Ncorr: Open-Source 2D Digital Image Correlation Matlab Software," *Experimental Mechanics*, V. 55, No. 6, 2015, pp. 1105-1122. doi: 10.1007/s11340-015-0009-1

54. Favvata, M. J., and Karayannis, C. G., "Influence of Pinching Effect of Exterior Joints on the Seismic Behavior of RC Frames," *Earthquakes and Structures*, V. 6, No. 1, 2014, pp. 89-110. doi: 10.12989/eas.2014.6.1.089

ACI STRUCTURAL JOURNAL TECHNICAL PAPER

Title No. 121-S11

Modified Shear Design Model for Steel- and Fiber-Reinforced Polymer-Reinforced Concrete Beams

by A. N. Tarawneh, E. F. Saleh, A. M Alghossoon, G. S. Almasabha, O. S. Alajarmeh, A. Manalo, and B. Benmokrane

This study proposes a unified shear design provision for slender steel- and fiber-reinforced polymer (FRP)-reinforced concrete (RC) members. The proposed model is a modification of the ACI 318-19 model to include the axial stiffness of the longitudinal reinforcement by introducing a new modification term, n_c, *representing the elastic modular ratio of the longitudinal reinforcement to the concrete. The new relation is* $V_c = (0.4\ [n_c \rho_{fl}]^{1/3}\ \lambda_s \sqrt{f_c'} + N_u/[6A_g])b_w d$. *The unified shear model was assessed with five experimental data sets: FRP-RC beams without shear reinforcement (288 beams), steel-RC beams without shear reinforcement (759 beams), FRP-RC beams with shear reinforcement (56 beams), steel-RC beams with shear reinforcement (157 beams), and steel-RC beams with axial force (prestressed) but without shear reinforcement (209 beams). The unified shear model provided better performance than the ACI 318-19 and ACI CODE-440.11-22 provisions in terms of mean, coefficient of variation, standard deviation (SD), and absolute average error (AAE). The unified model also showed improved performance over a wider range of material properties. In addition, reliability analysis using Monte Carlo simulation indicated that the unified shear model provides a consistent satisfactory safety level with a reliability index between 3.5 and 4.0 for both steel- and FRP-RC members. The reliability index provided by the unified model is similar to the reliability index provided by the ACI 318-19 shear provision. In contrast, the ACI CODE-440.11-22 results in highly conservative estimates with a reliability index between 4.5 and 5.0.*

Keywords: ACI 440; axial stiffness; code evaluation; fiber-reinforced polymer (FRP)-reinforced concrete (RC) beams; fiber-reinforced polymer (FRP) reinforcement; reliability analysis; shear strength; steel-reinforced concrete beams; steel reinforcement.

INTRODUCTION

The shear strength of reinforced concrete (RC) beams has been extensively investigated. Researchers have also examined different mechanisms describing the shear behavior of RC members over the past 50 years.[1-4] These researchers, however, have indicated that the shear strength of RC members cannot be easily estimated, considering the nonhomogeneous nature of concrete, the effect of dowel action, and aggregate interlock. Several shear force transfer mechanisms have been proposed to estimate the shear strength of RC beams.[5-8] While the truss analogy theory[9] and other more sophisticated approaches have greatly enhanced the understanding of RC shear behavior, the complexity of these prediction models makes it challenging to incorporate them directly into design code equations. Consequently, the majority of design codes adopt semiempirical approaches that are calibrated with experimental databases.[10] Nevertheless, this approach does not allow for a straightforward extension of the design model to cover new advancements in reinforcement properties and behavior.[10] As a result, further extensive experimental testing and investigation of a wide range of design parameters are often required to establish a new shear capacity model for a new type of reinforcement, such as fiber-reinforced polymer (FRP) reinforcing bars.

Over the last decade, FRP reinforcing bars have emerged as a promising alternative to steel in harsh environments, given their corrosion resistance, high tensile strength-to-weight ratio, and high fatigue resistance properties. FRP bars encompass aligned fibers made of carbon (CFRP), glass (GFRP), basalt (BFRP), or aramid (AFRP). They are recognized for their linear-elastic behavior until failure with no yielding plateau behavior. Generally, FRP bars have higher tensile strength than steel reinforcing bars; however, they have a lower elastic modulus, ranging from 20 to 80% of the steel elastic modulus, depending on the type of fibers.[11]

Several research studies have been devoted to investigating the shear capacity of FRP-RC members. These studies indicating that FRP-RC beams exhibited a similar shear mechanism similar to that of steel-RC beams[10] but with overall lower shear capacity.[12,13] This can be attributed to the lower axial stiffness (elastic modulus) of FRP bars. Compared with steel reinforcement, the lower axial stiffness in FRP reinforcement tends to increase the width and depth of diagonal cracks due to higher deflection, reducing the shear transfer through aggregate interlock and the contribution of the uncracked concrete in the compression zone.[13,14] The shear contribution through dowel action in FRP reinforcement is also small because of its low transverse strength and stiffness.[15,16] In addition, it should be acknowledged that the bent portion of FRP stirrups exhibits significantly lower tensile strength than the straight portion, implying a lower contribution of the shear reinforcement, which decreases the load resistance contribution considering the low elastic modulus of FRP bars.[16]

Relationships in ACI 318-14 for calculating the concrete contribution to shear resistance V_c in RC members have been replaced by one general relationship in ACI 318-19. The model considers the combined effects of member depth

---

ACI Structural Journal, V. 121, No. 1, January 2024.

MS No. S-2023-031.R1, doi: 10.14359/51739191, received July 6, 2023, and reviewed under Institute publication policies. Pertinent discussion including author's closure, if any, will be published ten months from this journal's date if the discussion is received within four months of the paper's print publication.

(size effect λ_s), longitudinal reinforcement percentage ρ_w, concrete compressive strength f_c', and axial stress's effect N_u on the predicted shear-strength capacity.[17,18] Although the model accounts for several influencing factors that were not directly considered in previous versions of the Code and has been calibrated with a large database, the model does not account for the axial stiffness of reinforcing bars. This can be justified because the elastic modulus for steel is constant. As a result, the model cannot be generalized to FRP-RC members due to the lower and varying elastic modulus of FRP reinforcement compared to steel.

The ACI 440.1R-15[19] model (proposed by Tureyen and Frosh[14]) uses the same simplified ACI shear model ($0.17\sqrt{f_c'}b_wd$ [MPa]) multiplied by $2.5k$ to reduce the effective depth. The model assumes that only the uncracked flexural compression zone contributes to shear resistance. Various studies have indicated that the ACI 440.1R-15 model is less accurate and much more conservative than other design models.[16] The recent edition of ACI CODE-440.11-22[20]—released in September 2022—uses the same shear model modified to include size effect and imposing a minimum shear strength.

To fill this gap, this study presents a unified shear model applicable to both design practices of steel- and FRP-RC beams. The proposed model is based on a modification of the ACI 318-19 model to account for the axial stiffness of the reinforcing bars. As the ACI 318-19 model is familiar to structural designers, the proposed model should be easy to use and implement in the design process of steel- and FRP-RC beams. The proposed model's applicability and accuracy have been evaluated statistically using five surveyed experimental datasets with over 1400 tested specimens of steel- and FRP-RC beams, as highlighted in detail in the next section. The model reliability has been assessed using data-driven reliability analysis.

RESEARCH SIGNIFICANCE

Design codes adopt simple semiempirical approaches for shear design that are calibrated with experimental databases. Nevertheless, this approach does not allow for a straightforward extension of the design model to cover new reinforcement materials. ACI 318-19 and ACI CODE-440.11-22 have different shear models for steel- and FRP-RC despite the similar shear mechanism. This study presents a unified shear model for steel- and FRP-RC beams. The proposed model is based on a modification of the ACI 318-19 model to account for the axial stiffness of the reinforcing bars applied to a wide range of experimental data. Detailed statistical evaluation and comparison of the proposed model have been conducted with five experimental data sets: FRP-RC beams without shear reinforcement (288 beams), steel-RC beams without shear reinforcement (759 beams), FRP-RC beams with shear reinforcement (56 beams), steel-RC beams with shear reinforcement (157 beams), and steel-RC beams with axial force (prestressed) but without shear reinforcement (209 beams). In addition, the model safety has been assessed using Monte Carlo reliability analysis.

REVIEW OF ACI 318-19 AND ACI CODE-440.11-22 SHEAR DESIGN METHODS

Similarly to other design codes, the shear design philosophy adopted by ACI for RC members considers the beam nominal shear capacity V_n as the combined contributions of concrete V_c and shear reinforcement V_f or V_s. The updated shear provision in ACI 318-19 aimed to resolve-different concerns in past shear provisions, including: 1) V_c does not consider size effect in shear-stress capacity for members without shear reinforcement; 2) ACI 318-14 has eight different relationships for V_c for different conditions; 3) several influencing factors are not directly considered, including reinforcement and size effect; and 4) design relationships are calibrated with experimental test results for beams that are not representative of common practice.[17] ACI 318-19 adopts one general relationship for concrete shear resistance (shown in Eq. (1)) that considers the combined effects of member depth (Eq. (2)), percentage of longitudinal reinforcement, and the effect of axial stress on predicted shear-strength capacity. The shear resistance of stirrups—which is based on a 45-degree truss model—was not changed (Eq. (3)).

Tremendous effort and collaboration between different ACI committees went into updating the shear provision. Updating the concrete shear resistance V_c included developing an extensive database, an open call for proposals, and an assessment of proposed models. The comparative evaluation of the proposed models was based on the relative merits of the different methods and how they could be modified to balance accuracy, ease, practicality of use, and transparency.[17] Therefore, the concrete shear resistance in ACI 318-19 had better accuracy than previous models.

$$\begin{cases} A_v < A_{v,\,min},\ V_c = \left[0.66\lambda(\rho_w)^{\frac{1}{3}}\sqrt{f_c'} + \dfrac{N_u}{6A_g}\right] b_w d \\ A_v < A_{v,\,min},\ V_c = \left[0.66\lambda\lambda_s(\rho_w)^{\frac{1}{3}}\sqrt{f_c'} + \dfrac{N_u}{6A_g}\right] b_w d \end{cases} \tag{1}$$

$$\lambda_s = \sqrt{\frac{2}{1 + 0.004d}} \leq 1.0 \tag{2}$$

$$V_f = \frac{A_v f_y d}{s} \tag{3}$$

Tureyen and Frosh[14] proposed the shear model adopted in ACI CODE-440.11-22 for FRP-RC (Eq. (4) to (6)). The model assumes that only the uncracked flexural compression zone contributes to shear resistance, considering the axial stiffness of longitudinal FRP bars $E_{ft}A_f$. This assumption is justified by the lower axial stiffness of FRP bars, which results in wider cracks and a smaller concrete compression region (smaller neutral axis depth) compared to steel-RC. In addition, a lower limit for the shear capacity is included (Eq. (7)), as recommended by Nanni et al.[21] The lower limit was proposed because Eq. (4) may lead to unreasonably low estimates of shear capacity for lightly reinforced members such as slabs and foundations.[20] The contribution of shear reinforcement V_f is given in Eq. (8), which is similar to the

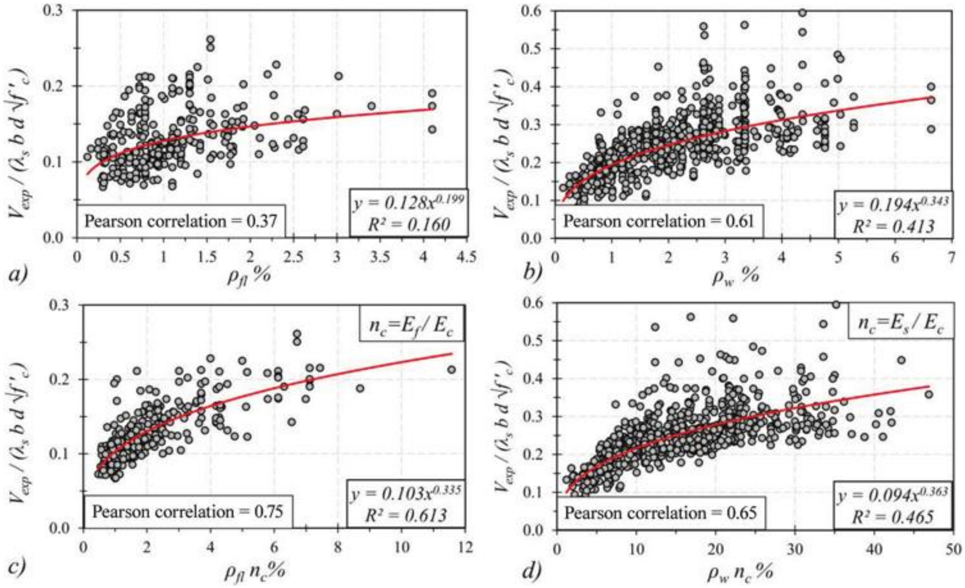

Fig. 1—Correlation between normalized experimental shear capacities and: (a) longitudinal reinforcement ratio ρ_{fl} for FRP-RC beams; (b) longitudinal reinforcement ratio ρ_w for steel-RC beams; (c) $n_c\rho_{fl}$ for FRP-RC beams; and (d) $n_c\rho_w$ for steel-RC beams.

steel shear reinforcement contribution equation. The stress in the shear reinforcement should be limited to avoid failure at the bent region, according to Eq. (9)

$$V_c = 0.4\sqrt{f_c'}\lambda_s b_w k d \tag{4}$$

$$k = \sqrt{2\rho_{fl}n + (\rho_{fl}n)^2} - \rho_{fl}n \tag{5}$$

$$n = \frac{E_{fl}}{E_C} \tag{6}$$

$$V_{c_{min}} = 0.067\sqrt{f_c'}\, b_w d \tag{7}$$

$$V_f = \frac{A_{fv} f_{fv} d}{s} \tag{8}$$

$$f_{fv} = 0.005E_{fv} \le f_{fb} \le f_{fu} \tag{9}$$

EXPERIMENTAL DATABASE

A comprehensive data base comprising five experimental data sets was used in developing and verifying the applicability of the unified one-way shear model. The first two data sets are for one-way shear tests of slender steel-RC beams, with and without shear reinforcement. Steel-RC evaluation data sets were created and examined through the combined efforts of Joint ACI-ASCE Committee 445 and the German Committee of Reinforced Concrete (DAfStb), as presented by Reineck et al.[22,23] The data sets originally consisted of 784 RC members without shear reinforcement A_v and 157 tests on RC members with $A_v \geq A_{v,min}$. Out of the 941 beams, 29 were excluded for having either a depth less than 10 mm, a depth greater than 1500 mm, or a width less than 70 mm. These 29 specimens were excluded due to their impractical dimension range or for not constituting a representative sample set.

Two other experimental data sets with a total of 344 beams for FRP-RC one-way shear (with and without FRP shear reinforcement) were compiled from experimental studies published in the literature.[10,12,14,24-64] Out of the 344 specimens, 288 beams were tested without FRP shear reinforcement A_{vf} and 56 beams with FRP shear reinforcement. Collecting the database was subject to several conditions, including: 1) only specimens exhibiting shear failure were included; 2) only slender beams with a shear span-depth ratio $a/d > 2.5$ were retained[16]; and 3) all specimens were tested in a simply supported configuration under three-point or four-point loading test and reinforced with different types of FRP bars: CFRP, GFRP, or BFRP.

Lastly, the fifth data set consisted of 209 prestressed concrete elements with a shear span-depth ratio $a/d > 2.5$. This data set has been included to test the effect of axial compression N_u induced by prestressing, as in Eq. (1). The original dataset was presented in a research report by Reineck et al.[65] Specimens that experienced flexural failure were excluded. The number of specimens in each database is controlled by available experimental studies on it.

MODIFICATION OF ACI 318-19 MODEL CONSIDERING REINFORCEMENT AXIAL STIFFNESS

The ACI 318-19 model was originally developed for steel-RC beams and did not account for the axial stiffness of longitudinal reinforcement because the elastic modulus of steel is a common value regardless of the grade. Several studies on the shear capacity of FRP-RC beams, however, have indicated that the axial stiffness of the tensile reinforcement influences the shear strength contribution of concrete.[37,38] To examine the effect of the longitudinal reinforcement on the experimental shear capacities (of FRP- and steel-RC beams without shear reinforcement) and modify the ACI 318-19 model accordingly, the experimental shear

Table 1—Proposed unified model

Reinforcement	Criteria	V_c
Steel reinforcement	$A_v < A_{v,min}$	$V_c=\left[0.4\lambda(n_c\rho_w)^{1/3}\sqrt{f_c'}+\dfrac{N_u}{6A_g}\right]b_wd$
	$A_v > A_{v,min}$	$V_c=\left[0.4\lambda\lambda_s(n_c\rho_w)^{1/3}\sqrt{f_c'}+\dfrac{N_u}{6A_g}\right]b_wd$
FRP reinforcement	$A_{vf} < A_{v,min}$	$V_c=\left[0.4\lambda(n_c\rho_w)^{1/3}\sqrt{f_c'}\right]b_wd$
	$A_{vf} > A_{v,min}$	$V_c=\left[0.4\lambda\lambda_s(n_c\rho_w)^{1/3}\sqrt{f_c'}\right]b_wd$

capacities were normalized for size effect, beam width and depth, and the square root of the concrete compressive strength. The normalized capacities were then plotted against the reinforcement ratio, as shown in Fig. 1(a) and (b) for FRP- and steel-RC beams, respectively. The figures show an increase in the shear stress with higher reinforcement axial stiffness. Statistical correlation analysis indicated a Pearson correlation coefficient of 0.37 and 0.61 for the FRP- and steel-RC beams, respectively. The Pearson correlation coefficient ranges from –1 to 1, where 0 indicates no correlation, and –1 and 1 indicate the highest negative and positive correlations, respectively. Steel-RC beams are expected to have a higher correlation because the steel has a constant elastic modulus. In addition, the power-function trend line results in an R^2 of 0.16 and 0.41 for FRP- and steel-RC beams, respectively.

To improve the correlation of normalized capacities and account for the axial stiffness of different FRP types, the reinforcement ratio was multiplied by the elastic modular ratio between the reinforcing bars and concrete $n_c = E_{rnft.}/E_c$ (Fig. 1(c)). It can be seen that including the modular ratio significantly improved the trend line's correlation and accuracy for FRP-RC members. Including elastic modular n_c also improved the accuracy for steel-RC members (Fig. 1(d)) but not as significantly as for FRP-RC. The R^2 improved to 0.61 and 0.46 for FRP- and steel-RC beams, respectively.

In addition, the power-function trend lines indicate a function of power of 0.335 and 0.363, which is consistent with the power of 1/3 used in ACI 318-19 and other design codes, such as Eurocode 2. Accordingly, the power of 1/3 in ACI 318-19 was maintained.

Various shear models[66,67] for FRP-RC beams account for the axial stiffness effect by including the modular ratio between the reinforcing bars and the steel ($E_{rnft.}/E_s$). In this study, however, the modular ratio $n_c = E_{rnft.}/E_c$ was selected for two reasons: 1) $E_{rnft.}/E_c$ provided higher correlation and accuracy for FRP- and steel-RC beams than $E_{rnft.}/E_s$; and 2) to adjust for the reduction in the conservatism of the ACI 318-19 model for shear strength at high compressive strength (which is why a limitation on compressive strength was imposed), as discussed by Kuchma et al.[17] and in the "Comparative Assessment of ACI 318-19, ACI CODE-440.11-22, and Proposed Model" section of this study. Table 1 provides the proposed model. The constant 0.4 has been shown to provide an acceptable level of reliability, as is shown in the "Reliability-Based Assessment for ACI 318-19, ACI CODE-440.11-22, and Proposed Models" section. The effect of axial compression on the shear capacity of FRP-RC beams has not been included due to the lack of a large database to prove its applicability.

COMPARATIVE ASSESSMENT OF ACI 318-19, ACI CODE-440.11-22, AND PROPOSED MODEL

This section presents a comparative assessment of the proposed unified shear-strength model for slender beams and one-way slabs (Table 1) and the ACI 318-19/ACI CODE-440.11-22 provisions (Eq. (1) to (9)). Five data sets from the literature were used for the assessment; no range limitations were imposed on the mechanical properties of materials in the assessment to evaluate the accuracy of each model and range of applicability. The comparison was based on statistical measures, including the mean, standard deviation (SD), coefficient of variation (CoV), and the average absolute error (AAE) of the strength ratio $V_{exp.}/V_{pred.}$. The percentage of specimens with a strength ratio of less than 0.75 (strength reduction factor for shear) was also included. Moreover, the comparative assessment examined the trends of the $V_{exp.}/V_{pred.}$ with key design parameters, such as effective beam depth, concrete compressive strength, reinforcement ratio, and axial stiffness.

The AAE was considered among the statistical measures as it provides a direct indication of the absolute error in the forecasted shear strength, while CoV might be a misleading measure. For instance, a very high mean model will result in a low CoV, where the SD is divided by the mean of predicted values to measure the CoV. The AAE is calculated according to Eq. (10)

$$\mathrm{AAE} = \frac{1}{N}\sum_{i=1}^{N}\left|\frac{V_{pred.,i}-V_{exp.,i}}{V_{exp.,i}}\right| \tag{10}$$

Comparative assessment of ACI CODE-440.11-22/ACI 318-19 and proposed models for FRP- and steel-RC beams without A_{vf} or N_u

Figure 2 presents the $V_{exp.}/V_{pred.}$ for FRP-RC members without shear reinforcement versus depth d, axial stiffness, and concrete compressive strength (f_c') based on ACI CODE-440.11-22 (Fig. 2(a) to (c)) and proposed unified methods (Fig. 2(d) to (f)). The figure shows significantly less scatteredness with the proposed unified model. This is also evidenced by the significantly lower SD and AAE, where the unified model resulted in 33% and 53% lower SD and AAE, respectively, than the ACI CODE-440.11-22 method. This is due to considering the stiffness of the reinforcement material n_c compared to considering only the uncracked concrete in the design equation. Despite the unified model having a

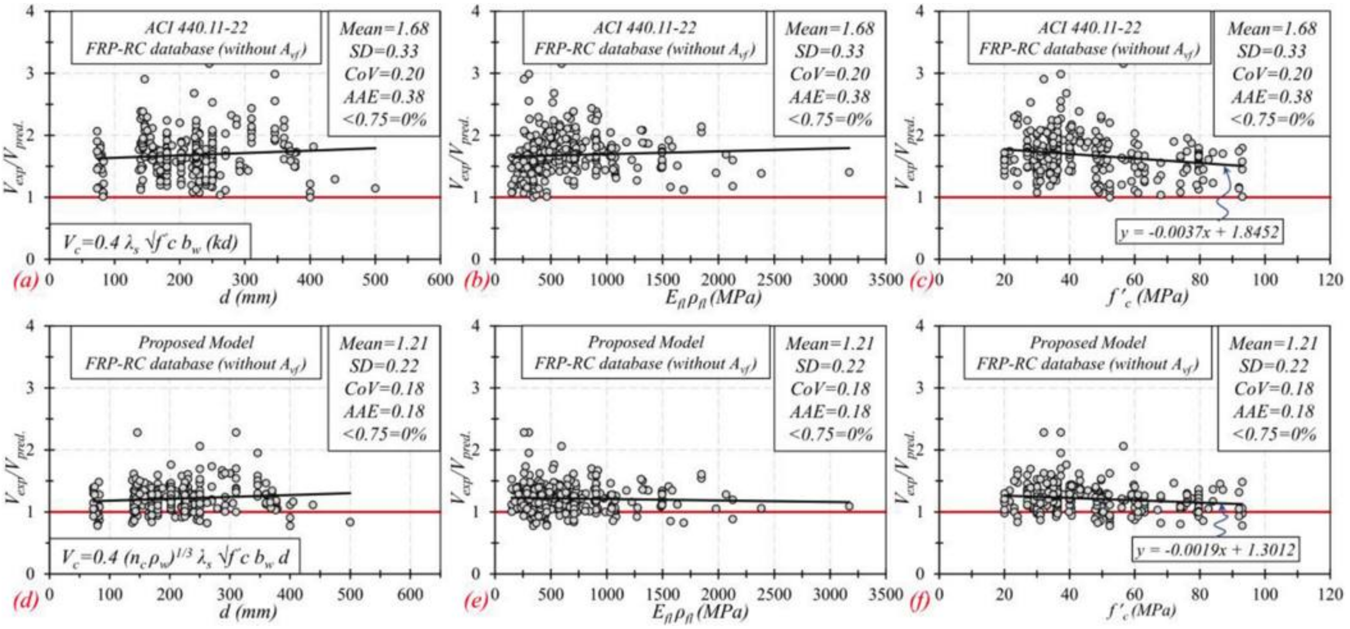

Fig. 2—Strength ratio V$_{exp.}$/V$_{pred.}$ *for FRP-RC beams without shear reinforcement using: (a) to (c) ACI CODE-440.11-22 provisions; and (d) to (f) proposed unified shear model.*

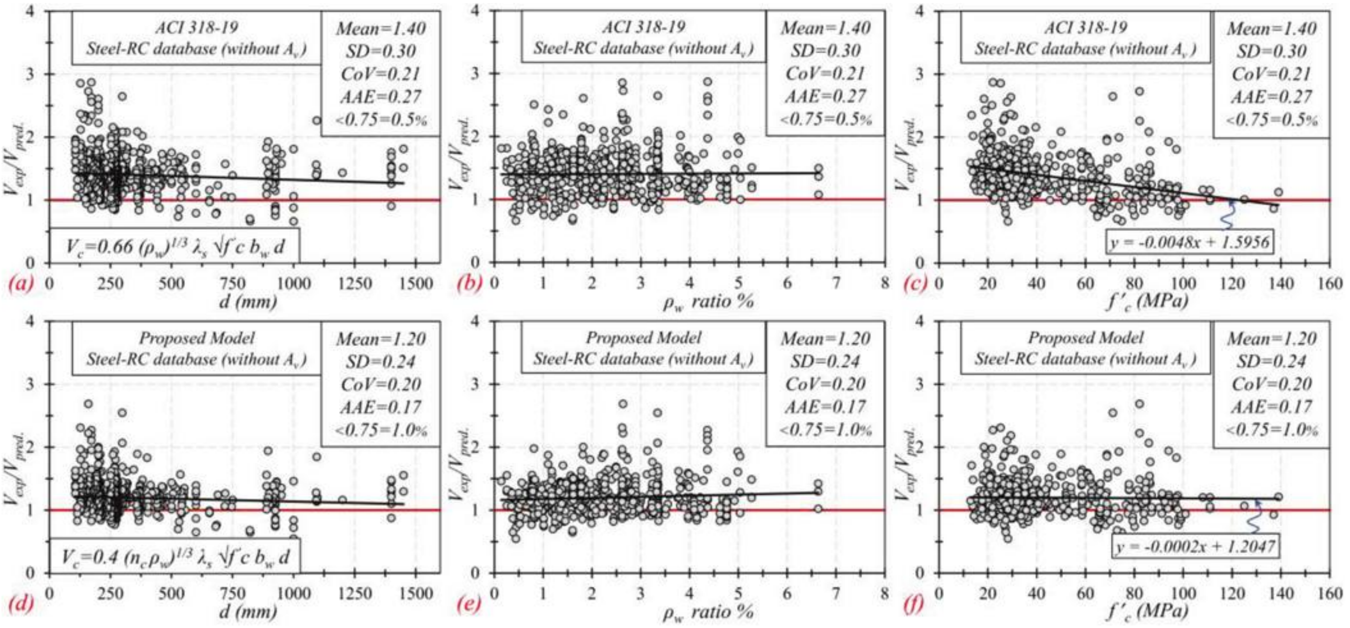

Fig. 3—Strength ratio V$_{exp.}$/V$_{pred}$ *for steel-RC beams without shear reinforcement using: (a) to (c) ACI 318-19; and (d) to (f) proposed unified shear model.*

lower mean, neither model had specimens with a strength ratio of less than 0.75. In addition, the unified model resulted in a flatter trend line with f_c' compared to ACI CODE-440.11-22. This can extend the range of applicable compressive strength in the model.

Figure 3 presents the $V_{exp.}/V_{pred.}$ for the steel-RC members without shear reinforcement versus effective beam depth d, longitudinal steel reinforcement ratio ρ_w, and f_c' based on the ACI 318-19 (Fig. 3(a) to (c)) and the proposed unified methods (Fig. 3(d) to (f)). The unified model also provides less scatteredness and lower mean, SD, CoV, and AAE than the ACI 318-19 method.

As shown in Fig. 3(c) and as discussed in Kuchma et al.,[17] the ACI 318-19 model has a steep downward trend line for the shear-strength ratio versus f_c'. This downward slope led to limiting the f_c' to 70 MPa in ACI 318-19 for beams with shear reinforcement under the minimum (Section 22.5.3.1). In contrast, the slope of the strength ratio was nearly horizontal with the proposed unified model. Based on the proposed model, the f_c' limit can be increased to 100 MPa, as the trend line shows consistency in prediction accuracy. This increase in the range of f_c' is significant as the use of high-strength and ultra-high-performance concrete is becoming more common. That notwithstanding, the number of specimens with f_c' higher than 100 MPa is limited.

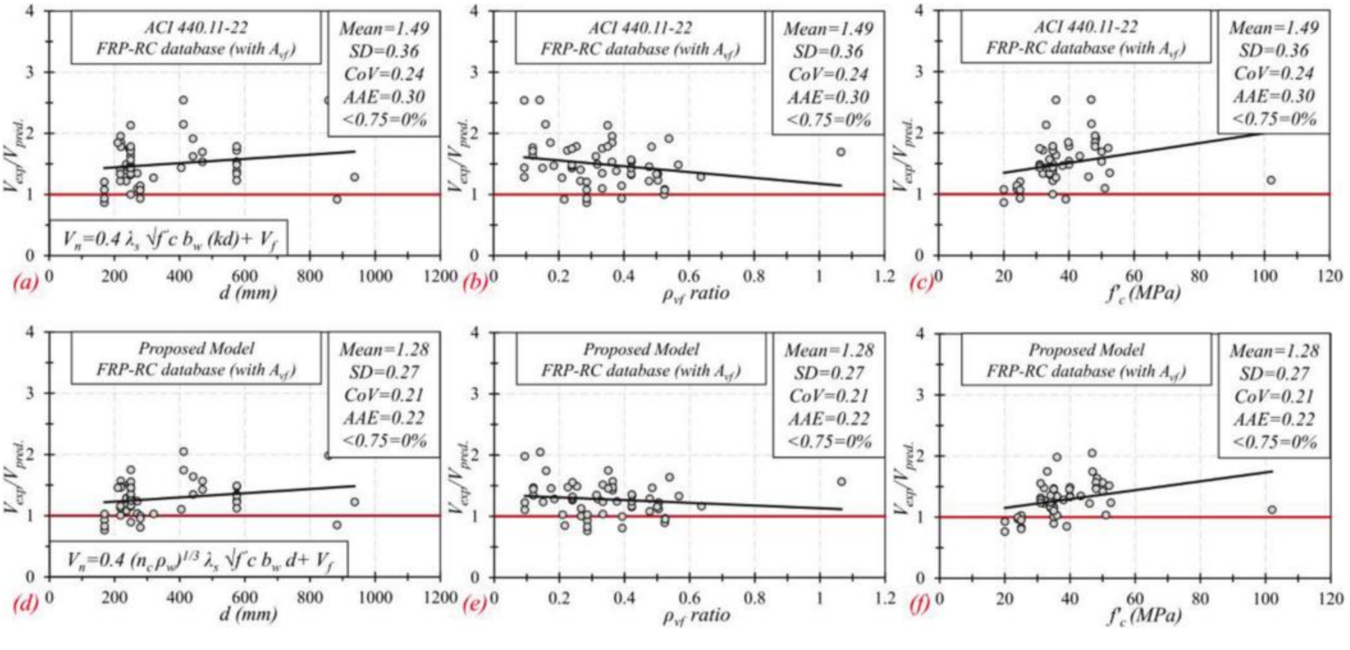

Fig. 4—Strength ratio $V_{exp.}/V_{pred.}$ *for FRP-RC beams with FRP shear reinforcement using: (a) to (c) ACI CODE-440.11-22 provisions; and (d) to (f) proposed unified shear model.*

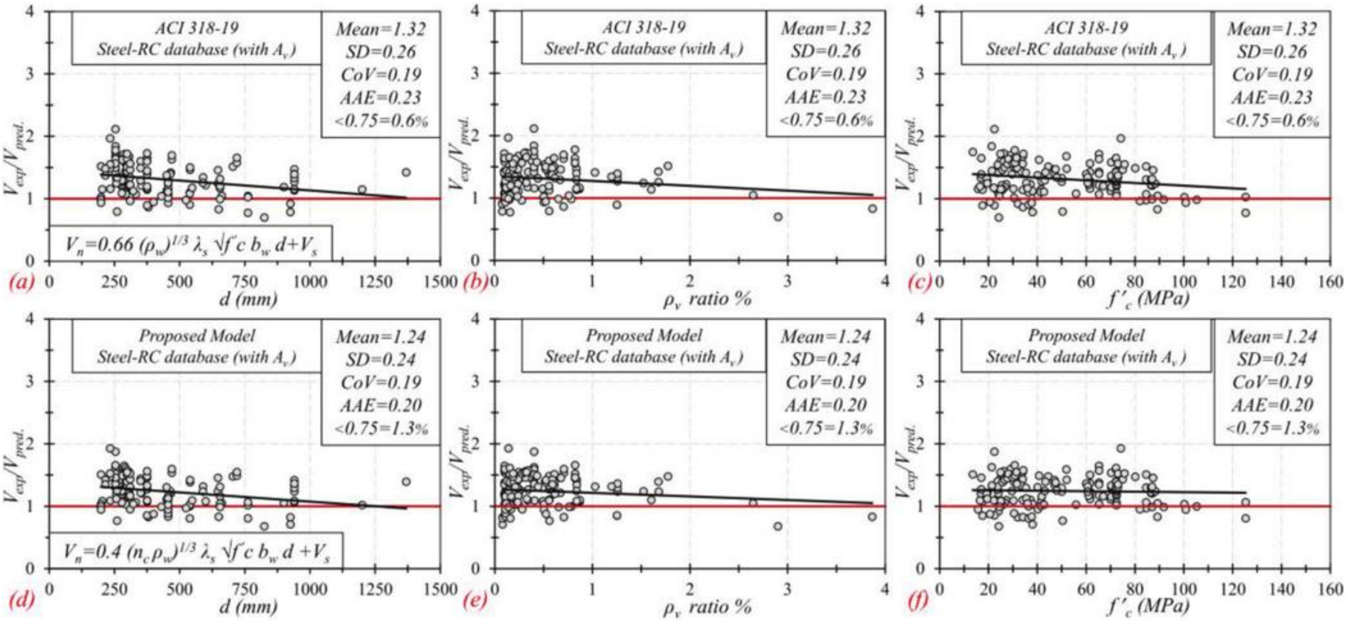

Fig. 5—Strength ratio $V_{exp.}/V_{pred.}$ *for steel-RC beams with shear reinforcement using: (a) to (c) ACI 318-19 provisions; and (d) to (f) proposed unified shear model.*

Comparative assessment of ACI CODE-440.11-22/ ACI 318-19 and proposed models for FRP- and steel-RC beams with A_{vf} and A_v but no N_u

Figures 4 and 5 present a comparative assessment of the unified shear model and the ACI CODE-440.11-22 and ACI 318-19 models, respectively, for FRP- and steel-RC beams with shear reinforcement. The stress in the FRP shear reinforcement was fixed at $0.005E_{fv}$ for comparison reasons (Eq. (9)). The results indicate a 5% and 14% improvement in the prediction accuracy when using the unified model proposed herein as compared to the ACI CODE-440.11-22 and ACI 318-19 predictions. The improvement, however, is not as evident as in specimens without shear reinforcement, because both cases have similar contributions from the shear reinforcement. Both models result in a low percentage of specimens with $V_{exp.}/V_{pred.}$ under 0.75.

When shear reinforcement is provided (in excess of minimum shear reinforcement), ACI 318-19 does not consider the size effect (that is, $\lambda_s = 1$). Figure 5(a), however, shows a downward trend for the $V_{exp.}/V_{pred.}$ of the steel-RC data set with shear reinforcement. Kuchma et al.[17] observed this downward slope. Because there are only a few tests with $V_{exp.}/V_{pred.}$ between 0.7 and 0.75, it was considered unnecessary to include the size effect for members with minimum shear reinforcement. Figure 6 shows the $V_{exp.}/V_{pred.}$ for steel-RC beams with steel shear reinforcement using the

Table 2—Statistics of one-way shear provisions versus unified shear model based on five data sets

Experimental data set	Method	Mean	SD	CoV	AAE	<0.75, %
Steel-RC without A_v (759 beams)	ACI 318-19 model	1.40	0.30	0.21	0.27	0.5
	Proposed unified model	1.20	0.24	0.20	0.17	1.0
Steel-RC with A_v (157 beams)	ACI 318-19 model	1.32	0.26	0.19	0.23	0.6
	Proposed unified model	1.24	0.24	0.19	0.20	1.3
FRP-RC without A_{vf} (288 beams)	ACI CODE-440.11-22 model	1.68	0.33	0.2	0.38	0.0
	Proposed unified model	1.21	0.22	0.18	0.18	0.0
FRP-RC with A_{vf} (56 beams)	ACI CODE-440.11-22 model	1.49	0.36	0.24	0.30	0.0
	Proposed unified model	1.28	0.27	0.21	0.22	0.0
Steel-PC without A_v (209 beams)	ACI 318-19 model	1.78	0.50	0.28	0.40	0.0
	Proposed unified model	1.59	0.44	0.28	0.34	0.0

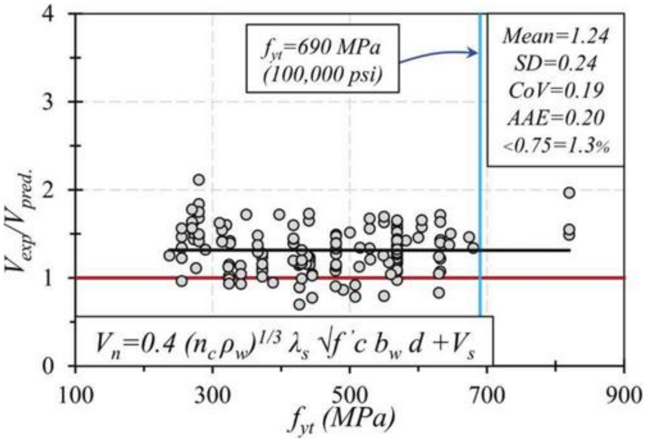

Fig. 6—Strength ratio $V_{exp.}/V_{pred.}$ *for steel-RC beam using proposed unified shear model with respect to yield stress of stirrups.*

unified model. The results suggest that the yield stress of the steel shear reinforcement up to 690 MPa could be used with no change in $V_{exp.}/V_{pred.}$.

Comparative assessment of ACI 318-19 and proposed unified models for steel-RC beams with N_u but no A_{vf}

Both the ACI 318-19 and proposed unified models behaved similarly for steel-RC members (Fig. 7), with the proposed unified model providing slightly better predictions. Figures 7(b) and (e) show a downward-sloping trend line of $V_{exp.}/V_{pred.}$; high $V_{exp.}/V_{pred.}$ at low a/d are expected due to the arch action, which is more effective for beams with a net axial compression and where the member might be uncracked in flexure.[17] It should be highlighted that a/d stands for shear-span ratio. The impact of a/d is not directly considered in the ACI 318-19 provisions. The performance of the ACI 318-19 shear provisions is considered reasonable because most members have a slenderness ratio of $a/d >$ 4. The performance of the ACI 318-19 shear provisions is considered reasonable in this range. Figures 7(c) and (f) show no discernable trend with increasing levels of axial compressive stress. Table 2 presents a summary of the statistical measures for the five data sets.

RELIABILITY-BASED ASSESSMENT FOR ACI 318-19, ACI CODE-440.11-22, AND PROPOSED MODELS

The level of reliability of a design equation and the corresponding factor of safety requires including the uncertainty of the applied load, material properties, distribution of the normalized strength $V_{exp.}/V_{pred.}$, and the probability of failure at different load ratios (that is, live-to-dead load ratio [L/D]). A data-driven reliability analysis was conducted to assess the reliability level in the proposed unified shear model in comparison to current code provisions (ACI 318-19/ACI 440.1R-15) in terms of the probability of failure and the associated reliability index β. The probability of failure and β are considered direct measurements of the level of reliability. Statistically, the reliability index represents the number of SDs between zero and the mean in the resistance-load distribution. Current design practices recommend reliability indexes based on the consequences of failure and the economic design aspects. The reliability index β is taken between 3.5 and 4 for sudden failures or failures having severe consequences.[68,69]

The procedure adopted in this study for data-driven reliability analysis using Monte Carlo simulation (MCS) is an improved version of the Farrow et al.[70] procedure. Farrow et al. conducted reliability analyses for anchors loaded in shear and tension to assess the reliability of the design model and to calibrate the appropriate strength reduction factors, which were adopted in ACI 318-19. Their procedure, however, assumes normal distributions for load and resistance, considers only live load, and conducted only 10,000 simulations, which does not guarantee convergence.[70] Their procedure was modified and improved to overcome such limitations by considering more realistic distribution types, adding combinations of live and dead loads to cover a wide range of L/D, and using up to 100 million simulations to guarantee convergence.

A failure state occurs when the applied load exceeds the capacity. This definition can be written in equation form

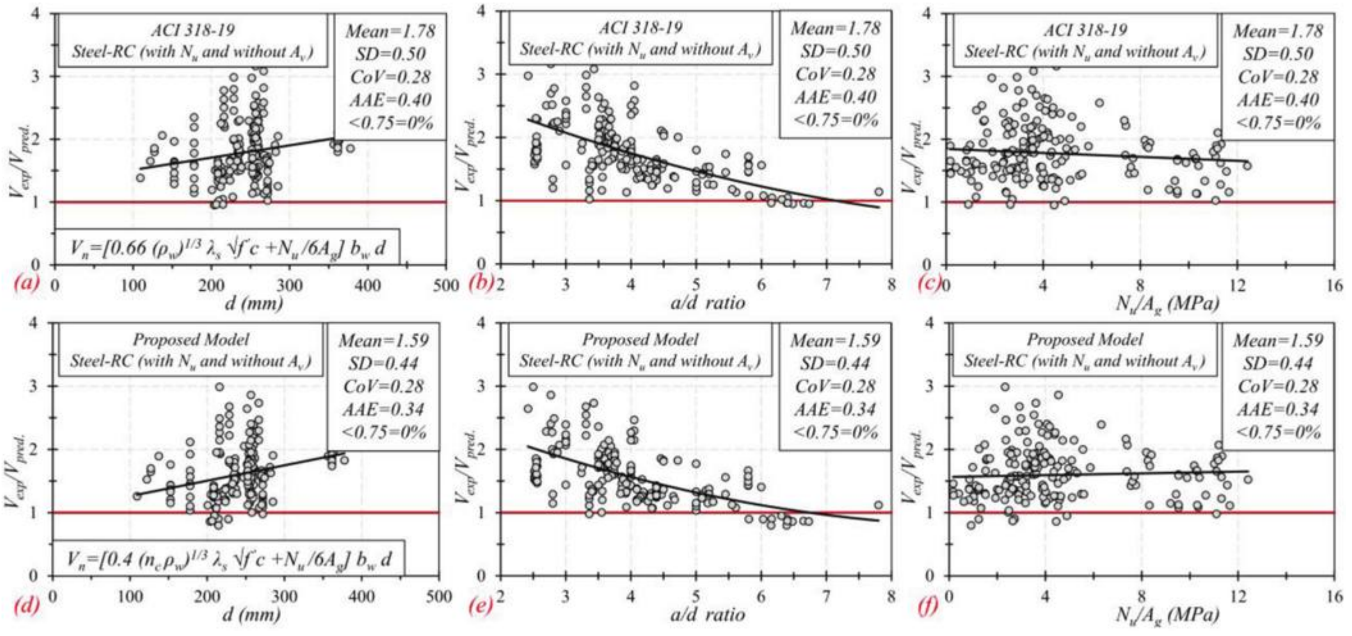

Fig. 7—Strength ratio $V_{exp.}/V_{pred.}$ *for steel-RC beams with* N_u *and no* A_{vf} *using: (a) to (c) ACI 318-19; and (d) to (f) proposed unified shear model.*

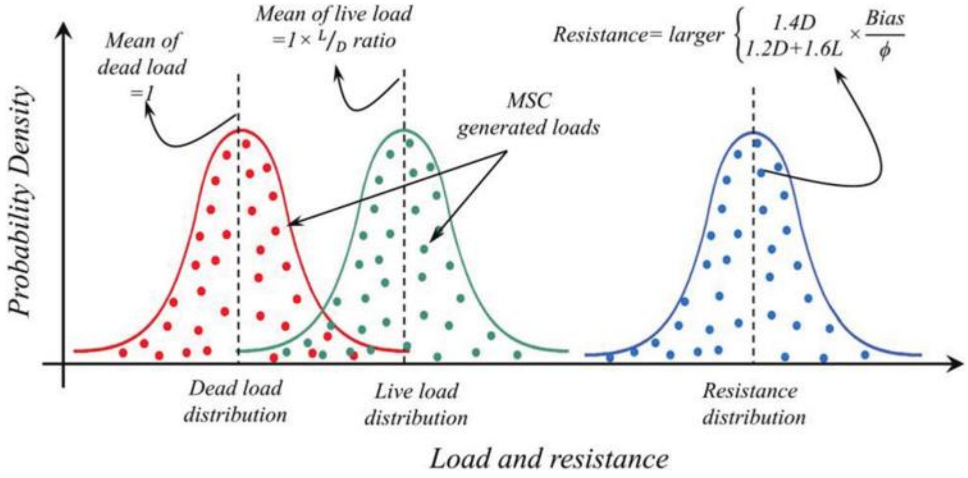

Fig. 8—Illustration of adopted MCS reliability analysis.

(Eq. (11)), where R is the resistance; P_D is the dead load; and P_L is the live load. A negative G value in Eq. (11) indicates a failure state. Accordingly, statistical distributions for P_D, P_L, and capacity must be established (Fig. 8). First, P_D distribution was assumed to have a nominal mean of 1.0. Szerszen and Nowak[71] reported that P_D exhibited a normal distribution with a bias of 1.05 and CoV of 10%. In contrast, P_L distribution exhibited an extreme Type I distribution with a bias and CoV of 1.00 and 18%, respectively. The nominal mean for live-load distribution equaled 1 (mean of P_D) multiplied by the L/D. The actual mean was equal to the nominal mean multiplied by the bias in each distribution. In this paper, the analysis was conducted on a range of L/D from 0 to 4 to cover the probable load range.

$$G = R - P_D - P_L \qquad (11)$$

The nominal mean for the capacity distribution is determined with the load and resistance factor design (LRFD) Eq. (12), where the controlling load combination is divided by the strength reduction factor. A strength reduction factor of 0.75 according to ACI 318-19 was used through the analysis. The resistance distribution type and properties were informed from the $V_{exp.}/V_{pred.}$ data.

$$\max\left\{\begin{array}{c}1.4P_D\\1.2P_D+1.6P_L\end{array}\right. \leq \varnothing R_n \qquad (12)$$

After establishing the three distributions, an MCS was performed to generate 5×10^9 simulations (points) in each distribution (Fig. 8). To calculate the probability of failure, the limit state function in Eq. (11) was calculated. A negative value for the G function represents a failure state, while a safe state is otherwise. The probability of failure was calculated by dividing the frequency for which the G function presented a failure state by the total number of simulations.

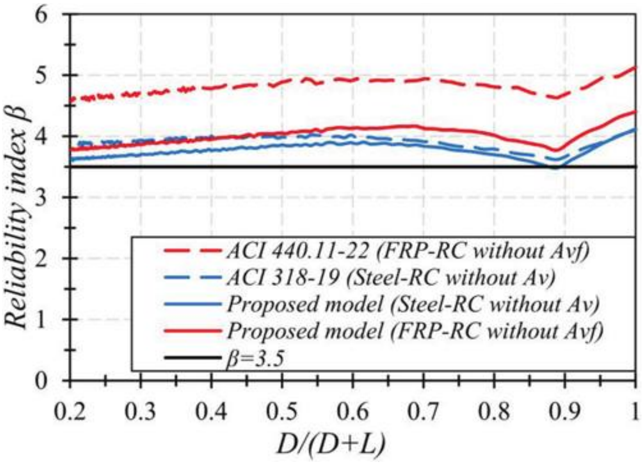

Fig. 9—Reliability analysis results for ACI 318-19, ACI CODE-440.11-22, and proposed unified shear model.

In reliability analysis, L/D is usually expressed by the term $D/(D + L)$. The adopted range of L/D corresponds to a $D/(D + L)$ of 0.2 to 1. In addition, the probability of failure is expressed by the term reliability index β.

The reliability index was evaluated for: 1) steel-RC beam without A_v using ACI 318-19 model; 2) steel-RC beam without A_v using the proposed unified shear model; 3) FRP-RC beam without A_{vf} using ACI CODE-440.11-22 model; and 4) FRP-RC beam without A_{vf} using proposed unified shear model. These four cases were selected because the proposed unified shear model is for V_c, and no changes in the shear contribution were made. The results of the reliability analysis are presented in Fig. 9. For steel-RC beams (labeled in blue [refer to the full-color PDF online at www.concrete.org]), it can be seen that both ACI 318-19 and the proposed model result in a similar reliability index between 3.5 and 4.0. Although the unified model has a lower mean, the unified shear model has a similar reliability index due to its higher accuracy. For the FRP-RC beam (labeled in red), the proposed unified model results in a reliability index between 3.5 and 4.0, similar to the steel-RC models previously discussed. However, the ACI CODE-440.11-22 model results in conservative estimates with a reliability index between 4.5 and 5.0. It can be concluded that the unified shear model results in a consistent reliability index (safety level) for both steel and FRP-RC members.

CONCLUSIONS

The majority of design codes use semiempirical models that are calibrated using experimental databases. These design models cannot, however, be simply extended to include new reinforcement properties. A unified shear model for both slender steel and fiber-reinforced polymer (FRP)-reinforced concrete (RC) beams is presented in this paper that is calibrated using a large experimental database and accounts for the contribution of the axial stiffness of the reinforcement material as one of the critical design parameters. The proposed model modifies the ACI 318-19 model by introducing a new term, n_c, that represents the modular ratio between the modulus of elasticity of reinforcement and the concrete to account for the axial stiffness of the reinforcing bars. Detailed statistical evaluation and comparison of the proposed model have been conducted over five experimental data sets comprising over 1400 test results. The five databases include: FRP-RC beams without shear reinforcement (288 beams) and with shear reinforcement (56 beams), steel-RC beams without shear reinforcement (759 beams) and with shear reinforcement (157 beams), and steel-RC beams with axial force (prestressed) and without shear reinforcement (209 beams). In addition, the model reliability was assessed using Monte Carlo reliability analysis. The following conclusions can be drawn from the study:

1. The unified shear model considers the reinforcement material's axial stiffness, resulting in significantly high accuracy and less scatteredness for FRP-RC beam without shear reinforcement. The unified model resulted in 33% and 53% lower standard deviation (SD) and average absolute error (AAE), respectively, than ACI CODE-440.11-22. In addition, the unified model resulted in a flatter trend line with f_c' compared to ACI CODE-440.11-22. This can extend the range of applicable compressive strength in the model.
2. The unified model shows promising performance in predicting the shear strength for steel-RC beams without shear reinforcement by providing less scatteredness and lower mean, SD, coefficient of variation (CoV), and AAE. This is due to considering the axial stiffness of the reinforcing bars as a critical design parameter using the factor n_c. The ACI 318-19 model showed a steep downward-sloping trend line of shear-strength ratio to f_c'. In contrast, with the proposed unified model, the slope of the strength ratio was nearly horizontal as the predictions were corrected considering the variable elastic modulus of the concrete. Based on the proposed model, the limitation of f_c' could be increased to 100 MPa as the trend line shows consistency in the prediction accuracy. Nevertheless, the model should be calibrated against more experimental data involving specimens with f_c' higher than 100 MPa when it becomes available.
3. For FRP- and steel-RC beams with shear reinforcement, the unified model showed improvement in prediction accuracy. The improvement was not as evident as in the specimens without shear reinforcement, because both cases have similar contributions from the shear reinforcement. For members with axial compression but no shear reinforcement, both the ACI 318-19 and proposed unified models behaved similarly for steel-RC members, with slightly better predictions with the proposed unified model.
4. Monte Carlo simulation (MCS) reliability analysis indicated that both ACI 318-19 and the proposed model result in a similar reliability index between 3.5 and 4.0. Although the unified model has a lower mean, the unified shear model has a similar reliability index due to its higher accuracy. For the FRP-RC beam, the proposed unified model also results in a reliability index between 3.5 and 4.0. The ACI CODE-440.11-22 model, however, yielded conservative estimates with a reliability index between 4.5 and 5.0. The unified shear model can be confidently used to predict the shear strength of both steel and FRP-RC members with consistent reliability indexes.

AUTHOR BIOS

ACI member **Ahmad N. Tarawneh** *is an Associate Professor in the Department of Civil Engineering, Faculty of Engineering, The Hashemite University, Zarqa, Jordan, and Head of the Building Environment and Structural Systems Center. He received his PhD from Clemson University, Clemson, SC. He is a member of ACI Committees 355, Anchorage to Concrete, and 440, Fiber-Reinforced Polymer Reinforcement. His research interests include anchorage to concrete and the use of fiber-reinforced polymers (FRPs) in reinforced concrete structural elements.*

Eman F. Saleh *is an Assistant Professor in the Department of Civil Engineering, Faculty of Engineering, at The Hashemite University. She received her PhD from Illinois Institute of Technology, Chicago, IL. Her research interests include reliability analysis, risk assessment, and nondestructive assessment of concrete damage.*

Abdullah M Alghossoon *is an Assistant Professor in the Department of Civil Engineering, Faculty of Engineering, at The Hashemite University. He received his PhD from Purdue University, West Lafayette, IN. His research interests include the behavior and design of composite materials.*

Ghassan S. Almasabha *is an Assistant Professor in the Department of Civil Engineering, Faculty of Engineering, at The Hashemite University. He received his PhD in structural engineering from The University of Texas at Arlington, Arlington, TX, in 2019. His research interests include disaster-resilient structures, large- to full-scale experimental testing of shear walls, and finite element analysis (FEA).*

Omar S. Alajarmeh *is a Senior Researcher and Lecturer at the Centre for Future Materials at University of Southern Queensland (UniSQ), Toowoomba, QLD, Australia, where he received his PhD. His research interests include the design and manufacturing of composite materials, the behavior of hybrid composite structures and their sustainability, finite element modeling and analysis, and optimization.*

Allan Manalo *is a Professor at the School of Civil Engineering and Surveying, acting Executive Director of the Institute for Advanced Engineering and Space Sciences, and the Theme Leader of the Civil Composites Research Group at UniSQ. His research interests include engineered composite materials and structures, polymer railway sleepers, and structural testing.*

Brahim Benmokrane, *FACI, is a Professor in the Department of Civil and Building Engineering at the University of Sherbrooke, Tier-1 Canada Research Chair in Advanced Composite Materials Used for Civil Engineering Structures, Senior Industrial Research Chair in Innovative FRP Composite Materials for Concrete Infrastructure, and Director of the University of Sherbrooke Research Center on Structural FRP Composite Materials for Concrete Structures (CRUSMAC), Sherbrooke, QC, Canada. He is a member and past Co-Chair of ACI Subcommittee 440-K, FRP-Material Characteristics, and a member of ACI Committees 435, Deflection of Concrete Building Structures, and 440, Fiber-Reinforced Polymer Reinforcement; and ACI Subcommittees 440-E, FRP-Professional Education; 440-F, FRP-Repair-Strengthening; 440-H, FRP-Reinforced Concrete; 440-I, FRP-Prestressed Concrete; and 440-L, FRP-Durability. He received the ACI Foundation Arthur J. Boase Award in 2022. His research interests include the development of FRP reinforcement for concrete structures and their durability, structural performance, and field applications.*

ACKNOWLEDGMENTS

This research was conducted with funding from the Built Environment and Structural Systems Center at The Hashemite University in Jordan, the Natural Sciences and Engineering Research Council of Canada (NSERC), and the NSERC-Alliance on Innovative FRP Reinforcement for Sustainable Concrete Structures.

NOTATION

A_f = area of longitudinal FRP bars
A_g = beam gross cross-sectional area
A_v = shear reinforcement area
A_{vf} = FRP shear reinforcement area
a/d = shear span-depth ratio
b_w = longitudinal FRP reinforcement ratio
d = beam effective depth
E_c = elastic modulus of concrete
E_{fl} = elastic modulus of FRP longitudinal bars
E_{fv} = elastic modulus of FRP shear reinforcement
$E_{reft.}$ = elastic modulus of longitudinal bars
E_s = elastic modulus of steel reinforcement
f_c' = concrete compressive strength
N_u = axial compression force
R_n = nominal resistance
s = shear reinforcement center-to-center spacing
V_c = concrete shear resistance
$V_{exp.}$ = experimental shear capacity
V_f = FRP shear reinforcement resistance
$V_{pred.}$ = predicted shear capacity
V_s = steel shear reinforcement resistance
β = reliability index
λ_s = size effect factor
ρ_{fl} = longitudinal FRP reinforcement ratio
ρ_{vf} = FRP shear reinforcement ratio
ρ_w = longitudinal reinforcement ratio

REFERENCES

1. Regan, P. E., "Shear in Reinforced Concrete: An Analytical Study," Construction Industry Research and Information Association, Department of Civil Engineering, Imperial College, London, UK, 1971.

2. Kupfer, H.; Hilsdorf, H. K.; and Rusch, H., "Behavior of Concrete Under Biaxial Stresses," *ACI Journal Proceedings*, V. 66, No. 8, Aug. 1969, pp. 656-666.

3. Taylor, H. P. J., "Investigation of the Forces Carried Across Cracks in Reinforced Concrete Beams in Shear by Interlock of Aggregate," 1970.

4. Reineck, K. H., "Ultimate Shear Force of Structural Concrete Members without Transverse Reinforcement Derived from a Mechanical Model," *ACI Structural Journal*, V. 88, No. 5, Sept.-Oct. 1991, pp. 592-602.

5. Nielsen, M. P., and Hoang, L. C., *Limit Analysis and Concrete Plasticity*, CRC Press, Boca Raton, FL, 2016.

6. Mitchell, D., and Collins, M. P., "Diagonal Compression Field Theory – A Rational Model for Structural Concrete in Pure Torsion," *ACI Journal Proceedings*, V. 71, No. 8, Aug. 1974, pp. 396-408.

7. Vecchio, F. J., and Collins, M. P., "The Modified Compression-Field Theory for Reinforced Concrete Elements Subjected to Shear," *ACI Journal Proceedings*, V. 83, No. 2, Mar.-Apr. 1986, pp. 219-231.

8. Kotsovos, M. D., "Compressive Force Path Concept: Basis for Reinforced Concrete Ultimate Limit State Design," *ACI Structural Journal*, V. 85, No. 1, Jan.-Feb. 1988, pp. 68-75.

9. Mrsch, E., *Concrete Steel Construction*, McGraw Hill, New York, NY, 1909.

10. Guadagnini, M.; Pilakoutas, K.; and Waldron, P., "Shear Resistance of FRP RC Beams: Experimental Study," *Journal of Composites for Construction*, ASCE, V. 10, No. 6, 2006, pp. 464-473. doi: 10.1061/(ASCE)1090-0268(2006)10:6(464)

11. Tarawneh, A. N.; Dwairi, H. M.; Almasabha, G. S.; and Majdalaweyh, S. A., "Effect of Fiber-Reinforced Polymer-Compression Reinforcement in Columns Subjected to Concentric and Eccentric Loading," *ACI Structural Journal*, V. 118, No. 3, May 2021, pp. 187-197

12. Bentz, E. C.; Massam, L.; and Collins, M. P., "Shear Strength of Large Concrete Members with FRP Reinforcement," *Journal of Composites for Construction*, ASCE, V. 14, No. 6, 2010, pp. 637-646. doi: 10.1061/(ASCE)CC.1943-5614.0000108

13. Farghaly, A., and Benmokrane, B., "Shear Behavior of FRP-Reinforced Concrete Deep Beams without Web Reinforcement," *Journal of Composites for Construction*, ASCE, V. 17, No. 6, 2013, p. 04013015. doi: 10.1061/(ASCE)CC.1943-5614.0000385

14. Tureyen, A. K., and Frosch, R. J., "Shear Tests of FRP-Reinforced Concrete Beams without Stirrups," *ACI Structural Journal*, V. 99, No. 4, July-Aug. 2002, pp. 427-434.

15. Kanakubo, T., and Shindo, M., "Shear Behavior of Fiber-Mesh Reinforced Plates," *Non-Metallic (FRP) Reinforcement for Concrete Structures: Proceedings of the Third International Symposium (FRPRCS-3)*, Sapporo, Japan, 1997, pp. 317-324.

16. Peng, F.; Xue, W.; and Xue, W., "Database Evaluation of Shear Strength of Slender Fiber-Reinforced Polymer-Reinforced Concrete Members," *ACI Structural Journal*, V. 117, No. 3, May 2020, pp. 273-281.

17. Kuchma, D. A.; Wei, S.; Sanders, D. H.; Belarbi, A.; and Novak, L. C., "Development of the One-Way Shear Design Provisions of ACI 318-19 for Reinforced Concrete," *ACI Structural Journal*, V. 116, No. 4, July 2019, pp. 285-296. doi: 10.14359/51716739

18. ACI Committee 318, "Building Code Requirements for Structural Concrete (ACI 318-19) and Commentary (ACI 318R-19) (Reapproved 2022)," American Concrete Institute, Farmington Hills, MI, 2019, 624 pp.

19. ACI Committee 440, "Guide for the Design and Construction of Structural Concrete Reinforced with Fiber-Reinforced Polymer Bars (ACI

440.1R-15)," American Concrete Institute, Farmington Hills, MI, 2015, 88 pp.

20. ACI Committee 440, "Building Code Requirements for Structural Concrete Reinforced with Glass Fiber-Reinforced Polymer (GFRP) Bars—Code and Commentary (ACI CODE-440.11-22)," American Concrete Institute, Farmington Hills, MI, 2022, 260 pp.

21. Nanni, A.; De Luca, A.; and Zadeh, J. H., *FRP Reinforced Concrete Structures—Theory, Design and Practice*, CRC Press, Boca Raton, FL, 2014, 400 pp.

22. Reineck, K. H.; Bentz, E. C.; Fitik, B.; Kuchma, D. A.; and Bayrak, O., "ACI-DAfStb Databases for Shear Tests on Slender Reinforced Concrete Beams without Stirrups," *ACI Structural Journal*, V. 110, No. 5, Sept.-Oct. 2013, pp. 867-876. doi: 10.14359/51685839

23. Reineck, K. H.; Bentz, E. C.; Fitik, B.; Kuchma, D. A.; and Bayrak, O., "ACI-DAfStb Databases for Shear Tests on Slender Reinforced Concrete Beams with Stirrups," *ACI Structural Journal*, V. 111, No. 5, Sept.-Oct. 2014, pp. 1147-1156. doi: 10.14359/51686819

24. Kaszubska, M.; Kotynia, R.; Barros, J. A.; and Baghi, H., "Shear Behavior of Concrete Beams Reinforced Exclusively with Longitudinal Glass Fiber Reinforced Polymer Bars: Experimental Research," *Structural Concrete*, V. 19, No. 1, 2018, pp. 152-161. doi: 10.1002/suco.201700174

25. Razaqpur, A. G.; Shedid, M.; and Isgor, B., "Shear Strength of Fiber-Reinforced Polymer Reinforced Concrete Beams Subject to Unsymmetric Loading," *Journal of Composites for Construction*, ASCE, V. 15, No. 4, 2011, pp. 500-512. doi: 10.1061/(ASCE)CC.1943-5614.0000184

26. El-Sayed, A.; El-Salakawy, E.; and Benmokrane, B., "Shear Strength of One-Way Concrete Slabs Reinforced with Fiber-Reinforced Polymer Composite Bars," *Journal of Composites for Construction*, ASCE, V. 9, No. 2, 2005, pp. 147-157. doi: 10.1061/(ASCE)1090-0268(2005)9:2(147)

27. Issa, M. A.; Ovitigala, T.; and Ibrahim, M., "Shear Behavior of Basalt Fiber Reinforced Concrete Beams with and without Basalt FRP Stirrups," *Journal of Composites for Construction*, ASCE, V. 20, No. 4, 2016, p. 04015083. doi: 10.1061/(ASCE)CC.1943-5614.0000638

28. El Refai, A., and Abed, F., "Concrete Contribution to Shear Strength of Beams Reinforced with Basalt Fiber-Reinforced Bars," *Journal of Composites for Construction*, ASCE, V. 20, No. 4, 2016, p. 04015082. doi: 10.1061/(ASCE)CC.1943-5614.0000648

29. Tomlinson, D., and Fam, A., "Performance of Concrete Beams Reinforced with Basalt FRP for Flexure and Shear," *Journal of Composites for Construction*, ASCE, V. 19, No. 2, 2015, p. 04014036. doi: 10.1061/(ASCE)CC.1943-5614.0000491

30. Khaja, M. N., and Sherwood, E. G., "Does the Shear Strength of Reinforced Concrete Beams and Slabs Depend Upon the Flexural Reinforcement Ratio or the Reinforcement Strain?" *Canadian Journal of Civil Engineering*, V. 40, No. 11, 2013, pp. 1068-1081. doi: 10.1139/cjce-2012-0459

31. Abdul-Salam, B., "Behaviour of Shear Critical FRP Reinforced Concrete One-Way Slabs," doctoral dissertation, Université de Sherbrooke, Sherbrooke, QC, Canada, 2014.

32. Chang, K., and Seo, D., "Behavior of One-Way Concrete Slabs Reinforced with GFRP Bars," *Journal of Asian Architecture and Building Engineering*, V. 11, No. 2, 2012, pp. 351-358. doi: 10.3130/jaabe.11.351

33. Ashour, A. F., and Kara, I. F., "Size Effect on Shear Strength of FRP Reinforced Concrete Beams," *Composites Part B: Engineering*, V. 60, 2014, pp. 612-620. doi: 10.1016/j.compositesb.2013.12.002

34. Ashour, A. F., "Flexural and Shear Capacities of Concrete Beams Reinforced with GFRP Bars," *Construction and Building Materials*, V. 20, No. 10, 2006, pp. 1005-1015. doi: 10.1016/j.conbuildmat.2005.06.023

35. Tariq, M., and Newhook, J. P., "Shear Testing of FRP Reinforced Concrete without Transverse Reinforcement," *Proceedings*, Annual Conference of the Canadian Society for Civil Engineering, Moncton, NB, Canada, June 2003, pp. 1330-1339.

36. Kim, C. H., and Jang, H. S., "Concrete Shear Strength of Normal and Lightweight Concrete Beams Reinforced with FRP Bars," *Journal of Composites for Construction*, ASCE, V. 18, No. 2, 2014, p. 04013038. doi: 10.1061/(ASCE)CC.1943-5614.0000440

37. El-Sayed, A. K.; Soudki, K.; and Kling, E., "Flexural Behaviour of Self-Consolidating Concrete Slabs Reinforced with GFRP Bars," *Proceedings of the 9th International Symposium on Fiber Reinforced Polymer Reinforcement for Reinforced Concrete Structures (FRPRCS-9)*, D. Oehlers, M. Griffith, and R. Seracino, eds., Sydney, NSW, Australia, July 2009, pp. 13-15.

38. Zhao, W.; Maruyama, K.; and Suzuki, H., "Shear Behavior of Concrete Beams Reinforced by FRP Rods as Longitudinal and Shear Reinforcement," *Non-metallic (FRP) Reinforcement for Concrete Structures: Proceedings of the Second International RILEM Symposium (FRPRCS-2)*, L. Taerwe, ed., Ghent, Belgium, Aug. 1995, pp. 352-359.

39. Alkhrdaji, T.; Wideman, M.; Belarbi, A.; and Nanni, A., "Shear Strength of GFRP RC Beams and Slabs," *Proceedings of the International Conference*, Oct. 2001, pp. 409-414.

40. Deitz, D. H.; Harik, I. E.; and Gesund, H., "One-Way Slabs Reinforced with Glass Fiber Reinforced Polymer Reinforcing Bars," *Fourth International Symposium—Fiber Reinforced Polymer Reinforcement for Reinforced Concrete Structures*, SP-188, C. W. Dolan, S. H. Rizkalla, and A. Nanni, eds., American Concrete Institute, Farmington Hills, MI, 1999, pp. 279-286.

41. Duranovic, N.; Pilakoutas, K.; and Waldron, P., "Tests on Concrete Beams Reinforced with Glass Fibre Reinforced Plastic Bars," *Non-Metallic (FRP) Reinforcement for Concrete Structures: Proceedings of the Third International Symposium (FRPRCS-3)*, Sapporo, Japan, Oct. 14-16, 1997, pp. 479-486.

42. Matta, F.; El-Sayed, A. K.; Nanni, A.; and Benmokrane, B., "Size Effect on Concrete Shear Strength in Beams Reinforced with Fiber-Reinforced Polymer Bars," *ACI Structural Journal*, V. 110, No. 4, July-Aug. 2013, pp. 617-628.

43. Yost, J. R.; Gross, S. P.; and Dinehart, D. W., "Shear Strength of Normal Strength Concrete Beams Reinforced with Deformed GFRP Bars," *Journal of Composites for Construction*, ASCE, V. 5, No. 4, 2001, pp. 268-275. doi: 10.1061/(ASCE)1090-0268(2001)5:4(268)

44. Alam, M. S., "Influence of Different Parameters on Shear Strength of FRP Reinforced Concrete Beams without Web Reinforcement," doctoral dissertation, Memorial University of Newfoundland, St. Johns, NL, Canada, 2010.

45. Olivito, R. S., and Zuccarello, F. A., "On the Shear Behaviour of Concrete Beams Reinforced by Carbon Fibre-Reinforced Polymer Bars: An Experimental Investigation by Means of Acoustic Emission Technique," *Strain*, V. 46, No. 5, 2010, pp. 470-481. doi: 10.1111/j.1475-1305.2009.00699.x

46. Gross, S. P.; Yost, J. R.; Dinehart, D. W.; Svensen, E.; and Liu, N., "Shear Strength of Normal and High Strength Concrete Beams Reinforced with GFRP Bars," *High Performance Materials in Bridges*, A. Azizinamini, A. Yakel, and M. Abdelrahman, eds., 2003, pp. 426-437.

47. Ali, I.; Thamrin, R.; Abdul, A. A. S.; and Noridah, M., "Diagonal Shear Cracks and Size Effect in Concrete Beams Reinforced with Glass Fiber Reinforced Polymer (GFRP) Bars," *Applied Mechanics and Materials*, V. 621, 2014, pp. 113-119. doi: 10.4028/www.scientific.net/AMM.621.113

48. Nakamura, H., and Higai, T., "Evaluation of Shear Strength of Concrete Beams Reinforced with FRP," *Proceedings of the Japan Society of Civil Engineers*, V. 508, 1995, pp. 89-100.

49. Swamy, N., and Aburawi, M., "Structural Implications of Using GFRP Bars as Concrete Reinforcement," *Non-Metallic (FRP) Reinforcement for Concrete Structures: Proceedings of the Third International Symposium (FRPRCS-3)*, Sapporo, Japan, Oct. 14-16, 1997, pp. 503-510.

50. Liu, R., "Precast Concrete Bridge Deck Panels Reinforced with Glass Fiber Reinforced Polymer Bars," doctoral dissertation, The University of Utah, Salt Lake City, UT, 2011.

51. Farahmand, F., "Shear Behaviour of Concrete Beams Reinforced with Glass Fibre Reinforced Plastic," thesis, Department of Civil & Geological Engineering, University of Manitoba, Winnipeg, MB, Canada, 1996, pp. 234-345.

52. Gross, S. P.; Dinehart, D. W.; Yost, J. R.; and Theisz, P. M., "Experimental Tests of High-Strength Concrete Beams Reinforced with CFRP Bars," *Proceedings of the 4th International Conference on Advanced Composite Materials in Bridges and Structures (ACMBS-4)*, Calgary, AB, Canada, July 2004.

53. Maruyama, K., and Zhao, W. J., "Flexural and Shear Behaviour of Concrete Beams Reinforced with FRP Rods," *Corrosion and Corrosion Protection of Steel in Concrete*, 1994, pp. 1330-1339.

54. Caporale, A., and Luciano, R., "Indagine Sperimentale e Numerica sulla Resistenza a Taglio di Travi di Calcestruzzo Armate con Barre di GFRP," *Proceedings of XXXVIII Convegno Nazionale AIAS*, Turin, Italy, 2009. (in Italian)

57. Kilpatrick, A. E., and Easden, L., "Shear Capacity of GFRP Reinforced High Strength Concrete Slabs," *Developments in Mechanics of Structures and Materials*, V. 1, 2005, pp. 119-124.

56. Kilpatrick, A. E., and Dawborn, R., "Flexural Shear Capacity of High Strength Concrete Slabs Reinforced with Longitudinal GFRP Bars," *Proceedings*, Second International *fib* Congress, Naples, Italy, 2006, pp. 1-10.

57. Johnson, D. T. C., "Investigation of Glass Fibre Reinforced Polymer (GFRP) Bars as Internal Reinforcement for Concrete Structures," PhD dissertation, University of Toronto, Toronto, ON, Canada, 2014.

58. Maranan, G. B.; Manalo, A. C.; Benmokrane, B.; Karunasena, W.; Mendis, P.; and Nguyen, T. Q., "Shear Behaviour of Geopolymer-Concrete Beams Transversely Reinforced with Continuous Rectangular GFRP

Composite Spirals," *Composite Structures*, V. 187, 2018, pp. 454-465. doi: 10.1016/j.compstruct.2017.12.080

59. Shehata, E.; Morphy, R.; and Rizkalla, S., "Fibre Reinforced Polymer Shear Reinforcement for Concrete Members: Behaviour and Design Guidelines," *Canadian Journal of Civil Engineering*, V. 27, No. 5, 2000, pp. 859-872. doi: 10.1139/l00-004

60. Niewels, J., 2008, "Zum tragverhalten von botonbauteilen mit faserverbundkunststoffbewerhung," PhD dissertation, Aachen University, Aachen, Germany, 164 pp. (in German)

61. Imjai, T., "Design and Analysis of Curved FRP Composites as Shear Reinforcement for Concrete Structures," PhD dissertation, University of Sheffield, Sheffield, UK, 264 pp.

62. Yang, F., "Deformation Behaviour of Beams Reinforced with Fibre Reinforced Polymer Bars under Bending and Shear," PhD dissertation, University of Sheffield, Sheffield, UK, 2014, 138 pp.

63. Ascione, F., "A Preliminary Numerical and Experimental Investigation on the Shear Stress Distribution on Multi-Row Bolted FRP Joints," *Mechanics Research Communications*, V. 37, No. 2, 2010, pp. 164-168. doi: 10.1016/j.mechrescom.2010.01.006

64. Alsayed, S. H., "Flexural Behavior of Concrete Beams Reinforced with GFRP Bars," *Cement and Concrete Composites*, V. 20, No. 1, 1998, pp. 1-11. doi: 10.1016/S0958-9465(97)00061-9

65. Reineck, K. H.; Kuchma, D. A.; and Fitik, B., "Extended Databases with Shear Tests on Structural Concrete Beams without and with Stirrups for the Assessment of Shear Design Procedures," Nuclear Regulatory Commission, Rockville, MD, 2010.

69. Nehdi, M.; El Chabib, H.; and Saïd, A. A., "Proposed Shear Design Equations for FRP-Reinforced Concrete Beams Based on Genetic Algorithms Approach," *Journal of Materials in Civil Engineering*, ASCE, V. 19, No. 12, 2007, pp. 1033-1042. doi: 10.1061/(ASCE)0899-1561(2007)19:12(1033)

66. Kara, I. F., "Prediction of Shear Strength of FRP-Reinforced Concrete Beams Without Stirrups Based on Genetic Programming," *Advances in Engineering Software*, V. 42, No. 6, 2011, pp. 295-304. doi: 10.1016/j.advengsoft.2011.02.002

68. MacGregor, J. G., "Safety and Limit States Design for Reinforced Concrete," *Canadian Journal of Civil Engineering*, V. 3, No. 4, 1976, pp. 484-513. doi: 10.1139/l76-055

69. Ellingwood, B.; Galambos, T.; MacGregor, J.; and Cornell, C. A., "Development of a Probability Based Load Criterion for American National Standard A58," NBS Special Publication 577, National Bureau of Standards, U.S. Department of Commerce, Washington, DC, June 1980, 222 pp.

70. Farrow, C. B.; Frigui, I.; and Klingner, R. E., "Tensile Capacity of Single Anchors in Concrete: Evaluation of Existing Formulas on an LRFD Basis," *ACI Structural Journal*, V. 93, No. 1, Jan.-Feb. 1996, pp. 128-137.

71. Szerszen, M. M., and Nowak, A. S., "Calibration of Design Code for Buildings (ACI 318): Part 2—Reliability Analysis and Resistance Factors," *ACI Structural Journal*, V. 100, No. 3, May-June 2003, pp. 383-391.

ACI STRUCTURAL JOURNAL TECHNICAL PAPER

Title No. 121-S12

Bond-Slip Relationships in High-Performance Concrete with Plain Steel Bars

by Marcin Dyba and Andrzej Seruga

This paper investigates the bond behavior between plain steel bars and high-performance concrete (HPC) to study the effect of embedment length and concrete compressive strength on bond performance. A total of 48 concrete specimens were cast and tested under uniaxial load. The main test parameters include the active bond length and concrete compressive strength. Test results show that the ratio of maximum bond stress to concrete compressive strength ranges from 0.12 to 0.17. Moreover, it can be concluded that the maximum bond stress is increased with an increase in concrete compressive strength and is decreased with a longer embedment length of plain steel bars. The adhesive bond stress is approximately 55% of the maximum bond stress. Finally, a new bond stress-slip model was proposed, and good agreement can be achieved between the test research and the theoretical prediction based on the proposed model.

Keywords: bond behavior; bond stress-slip relationship; high-performance concrete (HPC); pullout test.

INTRODUCTION

Nowadays, ribbed reinforcing bars are used to construct reinforced concrete (RC) structures. Due to that fact, most research regarding the characteristics of bond stress-slip relationships is based on elements made with ribbed reinforcing bars. Bond stress-slip relationships for plain bars are still not well recognized, and existing terms (equations) defined experimentally are still not accurate enough.

For the last 20 years, for RC structures, high-strength concrete (HSC) with ribbed reinforcing bars made of normal-strength steel has been used more and more often, as well as concrete containing bars made of higher-tensile-strength steel of 700 to 800 MPa. HSC—in particular, a high-performance one whose compressive strength equals 80 to 120 MPa—is used in prefabricated units for manufacturing pretensioned girders and other precast members. In the case of both HSC/high-performance concrete (HPC) uses, it is crucial to define the bond stress-slip relationships between HSC and ribbed reinforcing bars, as well as between HSC and steel prestressing strands.[1,2] Although, for obvious reasons, plain reinforcing bars are not used in RC elements made of HSC, it was considered fully justified, for educational reasons, to analyze the phenomenon of bond stress-slip relationships for both of these materials. It is particularly important to define adhesion and its relation to maximum and residual bond stress. It allows specifying or correcting existing calculation models used for both plain and ribbed bars, as well as for strands.

Plain bars were used to reinforce concrete structures in the United States and Canada until approximately the mid-1950s. In Europe, they were used as reinforcement until the mid-1960s, while in the United Kingdom, they were used for a few years in the mid-1970s. Although they are no longer used in new construction, a significant proportion of existing structures are reinforced with plain bars.[3] In Italy, 70% of concrete structures were reinforced with plain bars until 2002.[4]

The mechanisms by which forces transfer between reinforcement and the surrounding concrete differ for plain and ribbed bars. While ribbed bars transfer a large portion of these forces by mechanical interlock between surface deformations on the bars and the surrounding concrete, plain bars must rely on the transfer of forces by adhesion between the concrete and the reinforcement prior to bar slip, and by the wedging action of small particles that break free from the concrete surface following a slip, otherwise known as sliding friction.[5]

ACI 318-63[6] was the last to include provisions for the bond of plain bars. Research relating to plain bars essentially ceased once ribbed bars became the norm in construction, and so provisions for the bond of plain bars as included in historical editions of U.S. concrete codes were based on a limited number of investigations.[3] The 1970 edition of the Canadian standard CSA A23.3-1970[7] was the last to include provisions for plain reinforcement.

For RC structures built before the 1970s, designed according to old codes, and built with plain reinforcing bars, the influence of the bond-slip relationship is particularly important. In these types of structures, the bond stress developed at the interface between the concrete and steel is insufficient to avoid the slippage of the bar, and consequently, the deformations of the structures are largely increased. This phenomenon was discussed in recent studies carried out on RC elements built with plain bars.[8,9]

This paper aims to study the bond stress-slip relationship for RC elements built with plain bars and proposes a new bond stress-slip model based on experimental results. HPC is used for the production of test samples with varied embedment lengths.

ACI Structural Journal, V. 121, No. 1, January 2024.
MS No. S-2023-056.R2, doi: 10.14359/51739192, received August 19, 2023, and reviewed under Institute publication policies. Pertinent discussion including author's closure, if any, will be published ten months from this journal's date if the discussion is received within four months of the paper's print publication.

BACKGROUND

A limited number of studies are available in the literature on bond-slip mechanisms in structural elements with plain bars. Few expressions are also available for the parameters used in the definition of the constitutive bond-slip relationship. For ribbed reinforcing bars, several theoretical models may be found for the interaction mechanisms between steel bars and the surrounding concrete.[10-12]

One of the first studies on bond-slip behavior in RC was conducted by Abrams,[5] who describes the results of more than 1000 tests carried out on beams and pullout specimens with plain and ribbed bars. Different variables were studied, such as bar diameter, embedment length, concrete block dimensions, bar surface, age and concrete mixture, anchoring ends, and storage conditions. Abrams concluded that the bond between concrete and plain reinforcing bars is influenced in terms of resistance by two main components: adhesive and sliding resistance.[8] Adhesive resistance takes place before the slippage starts and is responsible for approximately 60% of the maximum bond stress ($f_{b,a} = 0.60f_{b,max}$). This ratio does not vary much for a wide range of mixtures, ages, bar sizes, and conditions of storage. Sliding resistance starts when the relative movement between both materials begins. Another conclusion was that the maximum bond stress $f_{b,max} = 0.19f_c$ is reached at the slip value (s_{max}) of approximately 0.25 mm. The frictional bond stress $f_{b,f} = 0.50f_{b,max}$.

In the twenty-first century, Feldman and Bartlett[13,14] performed bond tests on pullout specimens made of concrete with a compressive strength equivalent to that used by Abrams (12 to 14 MPa). Additional specimens were cast with a target compressive strength of 40 to 45 MPa. Embedment lengths of 12, 24, and 48 times the bar diameter were selected. Both round and square (to represent historical uses) steel bars with diameters of 16 and 32 mm were investigated. For all specimens, failure occurred at the interface between the reinforcing bar and the surrounding concrete. The maximum load P_{max} occurred at negligible end slip and is (principally) a function of the adhesion bond mechanism. The load then dropped asymptotically to a limiting residual load P_{res}. The load-slip curve exhibited the same shape as reported for polished bars by Abrams.[13] No maximum load plateau was observed. The maximum tensile load occurred at a very small slip $s = 0.01$ mm. Separate regression analyses of each specimen group confirmed that bond μ_{max} and μ_{res} are proportional to the square root of concrete compressive strength.

Stocker and Sozen[15] stated that the bond-slip on plain reinforcing bars is provided by two mechanisms: a physical interlocking between the microscopic, rough steel surface and the surrounding concrete before the slip starts; and a frictional mechanism between two sliding contact surfaces after the original interlocks have sheared off. Stocker and Sozen[15] also stated that the bond-slip relationship may be represented by a curve idealized by three linear branches: one vertical to represent the initial interlocking mechanism between steel and concrete, followed by a descending transition linear branch, and one horizontal branch to represent the mechanism of sliding friction. The bond strength increases by approximately 10% per 6.9 MPa of concrete compressive strength. $f_{b,max}$ increases approximately linearly with the bar diameter.

The CEB-FIP Model Code[16] and *fib* Bulletin No. 10[17] provide design guidelines for plain reinforcement. For plain hot-rolled bars, the bond-slip relationship is given by Eq. (1)

$$\tau_b = \tau_{b,max} \cdot \left(\frac{s}{s_{max}}\right)^{\alpha} \tag{1}$$

The model includes a nonlinear branch until s_{max}, followed by a second constant branch. In this case, s_{max} is defined as the slip value corresponding to the maximum bond stress. Reports[16,17] suggest $s_{max} = 0.10$ mm and the empirical factor $\alpha = 0.5$. A maximum bond stress ($\tau_{b,max}$) equal to $0.30(f_{ck})^{1/2}$ is proposed for good bond conditions and $0.15(f_{ck})^{1/2}$ for poor bond conditions, where f_{ck} is the characteristic cylindrical concrete compressive strength (in MPa).

Verderame et al.[18,19] realized a series of monotonic and cyclic pullout tests with plain bars. Based on the experimental results, they proposed a modification of the bond-slip model presented by Eligehausen et al.[20] for ribbed bars. The proposed model is very similar to the model suggested by Eligehausen et al.[20] but without the plateau. The experimental pullout tests were carried out on samples with a 12 mm reinforcing bar diameter, an embedment length equal to 120 mm, and an average concrete cylindrical strength equal to 15.8 MPa. Based on the results obtained from experimental investigation, Verderame et al.[18,19] proposed the following parameters for the model: $\tau_{b,max} = 0.31(f_c)^{1/2}$, $s_{max} = 0.23$ mm, $\alpha = 0.26$, $\tau_{b,f} = 0.43\tau_{b,max}$, and $p = 0.06$, where $\tau_{b,max}$, s_{max}, and α have the same meaning as in the CEB-FIP Model Code.[16] f_c is the cylindrical concrete compressive strength, $f_{b,f}$ is the frictional bond stress, and p represents the slope of the softening branch expressed as a function of the secant stiffness ($\tau_{b,max}/s_{max}$).

Melo et al.[9] proposed a new empirical bond-slip model that is derived based on the results of 27 experiments. This model adopts the Verderame et al.[19] shape up to the peak but better characterizes the descending branch of the bond-slip model. A series of monotonic and cyclic pullout tests were carried out on specimens built with plain bars to characterize the bond-slip relationship in old RC structures. Plain steel bars of 10, 12, and 16 mm diameter were used to build concrete samples ($f_{cm} = 15.8$ MPa). For each bar diameter and specimen type studied, a set of three specimens was built. One set was built with deformed bars of 12 mm diameter for comparison with the results for the specimens with plain bars. In total, 33 specimens were tested: 30 under monotonic pullout and three under cyclic pullout.

In the Verderame et al.[19] and Melo et al.[9] models, the ascending branch is defined by Eq. (1), where α is computed so that the area underneath ($A_{1,mod}$) the bond-slip curve until s_{max} equals the corresponding area from experimental results. The Verderame et al. model for slip values larger than s_{max} is defined by two linear branches: a softening branch (from s_{max} to s_f), followed by a plateau until the ultimate slip (s_u). In the Melo et al. model, after s_{max}, the bond-slip relationship is defined by a third-degree polynomial function until the ultimate slip (s_u) and is followed by a plateau. A value of 10 mm is assumed for s_u, which is based on experimental observation.

To investigate bond-slip behaviors of reinforcement in high-volume fly ash concrete (HVFAC), Zhao et al.[11] studied 189 pullout specimens under monotonic static load. The main research variables involved the volume of fly ash (FA), the type and diameter of the steel bars, and the water-cement ratio (*w*/*c*). The tensile loading in their study was applied to the steel bar, which increased stably by controlling the gradual increase of the steel bar's slip until the end of the tests. The obtained results indicate that the bond strengths of the steel bars increased along with the decrease in the *w*/*c* and decreased when the diameter of the steel bar increased. Moreover, other results also show that the type of steel bar has a significant influence on bond and slip behavior, and similar bond-slip relationship curves are presented in HVFAC, compared to conventional concrete (CC).

In the experimental program, Zhao et al.[11] used natural crushed granite stone with a maximum diameter of 20 mm and natural river sand. To obtain better workability in the concrete, lime admixture was also added to the concrete in quantities of 0.8 to 1.5% of cementitious material mass. Ordinary portland cement (OPC) and FA (Type II) were used. Two types of steel bars were used in the investigations: plain steel bars (HPB 235) and deformed steel bars (HRB 335). All the pullout specimens were designed as cubic concrete with dimensions of 150 mm, and the reinforcing bars were embedded at the center of the cross section of the concrete. All tested specimens were divided into three major groups, with a *w*/*c* of 0.30 (f_c' = 64.6 MPa), 0.34 (f_c' = 61.5 MPa), and 0.41 (f_c' = 54.9 MPa), respectively. Each of these major groups included seven small groups with different replacement ratios of FA in the concrete, where FA replaced 0, 20, 30, 40, 50, 60, and 70% of cement in the concrete, respectively.[11] The embedment length of the plain steel bar of 12 mm diameter was equal to 138 mm.

The complete bond-slip relationship curve can describe the bond-slip behavior of the reinforcing bar in fly ash concrete (FAC)/HVFAC. For the specimens with plain steel bars, the bond strength ratio-slip curves of the steel bars specimens with different *w*/*c* are similar to each other when using the same volume of FA. Before reaching the peak bond stress, the curves exhibit a linear increase stage, which has a slope that mainly depends on the *w*/*c* of the concrete. The slopes increase with an increasing *w*/*c*, while the slips s_{max} corresponding to the ultimate bond stress ratio become lower when the *w*/*c* are decreased. At the post-peak stage, the bond stress ratio begins to decline slowly until a relatively stable slip stage starts from 3 or 4 mm for all the specimens using *w*/*c* with 30 or 70% of the FA replacement ratio. The cementitious action of cement paste around the surface of the reinforcing bar was small. It indicates that the friction between the concrete and the steel bar, and the interlocking action caused by the slight surficial erosions or the manufacturing technology of the steel bar, was a crucial influence factor of the bond-slip behavior of plain steel bar.

Compared with CC specimens, the bond strengths of plain steel bars in the FAC specimens reduced with the increasing volume of FA, especially when FA was used to replace 70% of the cement. This reduction could be attributed mainly to the fact that the addition of FA resulted in a change in microstructure, such as porosity,[21] which in turn decreased the compressive strength, which will affect the gripping capacity of concrete. While the start points of the residual bond stresses are from the slip of approximately 3 mm, the residual levels of the specimens are dependent on the replacement ratio of FA in the concretes. With an increasing FA replacement ratio, the residual bond stresses decreased from 50 to 23%, corresponding to the ultimate bond strength when concrete contained 0 to 70% FA, respectively. In the specimens with the deformed steel bars, the residual bond stresses stayed at a relatively constant level of 25% of the ultimate bond strength in the specimens from a slip of 6 mm.

In 1997, Magnusson[22] conducted experimental research aimed at comparing the behavior of bond stress-slip relationships in HSC and normal-strength concrete. He used cylindrical samples with diameters of 300 and 350 mm, reinforced with ribbed bars with diameters of 16 and 20 mm. The length of the specimens in both cases was 260 mm. The active length of bar adhesion to concrete equaled 2.5 times the bar diameter, that is, 40 and 50 mm, respectively. The assumed concrete compressive strength equaled 25 and 100 MPa. The pullout test method used in the experimental research showed that the maximum bond stress increases in proportion to the average compressive strength both for normal- and high-strength concrete. Based on the results obtained, Huang et al.[23] proposed the following Eq. (2)

$$\tau_{b,max} = 0.45f_{cm} \tag{2}$$

In their opinion, in the case of HSC, maximum bond stress is reached with bar slip $s_1 = s_{max} = 0.5$ mm. In the model proposed by them, the same relation was kept as in CEB-FIP Model Code 1990[16] for the ascending branch ($\alpha = 0.3$), introducing at the same time certain modifications to the descending branch due to the different behavior of HSC. They also proposed adopting residual bond stress in Eq. (3)

$$\tau_{b,f} = 0.40\tau_{b,max} \tag{3}$$

There is no experimental research on specimens made from HSC with plain steel bars.

RESEARCH SIGNIFICANCE

The use of HPC technology in constructing structures is becoming common, even when there are no current standard provisions for describing concrete-steel bond behavior. The lack of research on the bond performance led to executing necessary bond experimental tests. A thorough study of the bond is important to provide guidelines for design. In this research, two sets of series of pullout tests with different bar embedment lengths for HPC specimens with different compressive strengths were conducted to study bond behavior. Furthermore, these results may also be used to predict development and lap length for reinforcement.

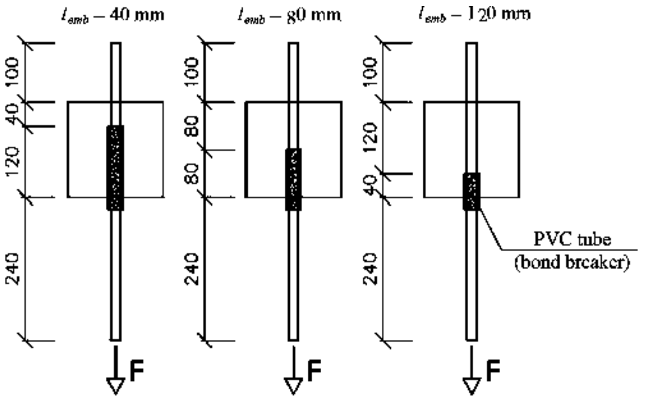

Fig. 1—Dimensions of tested specimens with different bond embedment lengths. (Note: Dimensions in mm; 1 mm = 0.0394 in.)

EXPERIMENTAL INVESTIGATION

To define bond stress-slip relationships of HPC and plain steel bars, the experimental research was carried out on pullout specimens measuring 160 x 160 x 160 mm, reinforced with an axially embedded plain bar with a diameter of 16 mm. The program of this experimental research took into account the following factors having a substantial impact on describing those relations: bond embedment length (l_{emb} = 40, 80, and 120 mm), and concrete compressive strength (f_c = 40, 60, 72, and 88 MPa).

In this paper, a detailed analysis was performed for mechanically compacted concrete design Class C80/95.

Test program

Research pertaining to HSC bond stress to a plain steel bar with a diameter of 16 mm was performed on concrete cube specimens whose sides equaled 160 mm, which is 10 times the diameter of a reinforcing bar, after 1, 3, 7, and 28 days of concrete curing.

Based on performed pilot studies, as well as taking into account research results obtained in various scientific centers[22,23] on HPC specimens, it was decided to complete the adopted test program with active bond lengths equaling 2.5 and 7.5 bar diameter. Thus, three active bond lengths were under investigation: 40, 80, and 120 mm. All these lengths can be realized in a module form equipping bars with rigid protective polyvinyl chloride (PVC) tubes 120, 80, and 40 mm long accordingly (Fig. 1). Free space between a bar and its PVC tube and between the PVC tube and the front side of the mold was filled with silicon to prevent the leakage of cement paste.

Concrete

The specimens were made from cement concrete composition Class C80/95, whose ingredients per 1 m^3 of concrete are given in Table 1.

The specimens were made in two series (labeled I and II). In each series, there were 24 specimens prepared (eight specimens for each embedment length). Standard samples ϕ150 x 300 mm and 150 x 150 x 150 mm were also collected to determine concrete compressive strength, together with the modulus of the concrete elasticity under compression.

Table 1—High-performance concrete mixture composition (per 1 m^3)

Composition	kg
Cement CEM I 42.5R	475
River sand 0 to 2 mm	665
Basalt aggregate 2 to 8 mm	650
Basalt aggregate 8 to 16 mm	580
Water	156
Silica fume	24
Polycarboxylate-based high-range water-reducing admixture	5.2

Note: 1 m^3 = 1.31 yd^3; 1 kg = 2.20 lb.

All the specimens and standard samples, once cast, were covered with several layers of polyethylene sheet, ensuring stable concrete curing conditions for 22 hours. After this period, the specimens were taken out of their mold, and some of them were prepared for experimental research.[24]

Experimental research was conducted after 1, 3, 7, and 28 days of concrete curing. At a given stage, four specimens (two from Series I and two from Series II) with the same active bond length were tested and analyzed. After demolding, all specimens and samples for standard testing were stored under three layers of polyethylene sheet. At each testing stage, the mechanical properties of concrete were defined, and the obtained results can be found in Table 2. Mechanical properties were tested for up to 90 days. During strength tests, particular samples were measured and weighed, which made it possible to define volumetric concrete density.

Plain steel bars

Plain reinforcing bars with a diameter of 16 mm, made of St3Sx-b steel, were used. Steel strength tests were performed with a materials testing machine. Tensile strength was measured automatically by an in-built force gauge. Displacement and strains were registered by an incremental extensometer synchronized with the machine software.

The extensometer's measuring base was 180 mm. Load steering was performed at the speed of 20 MPa/s up to the yield point, and then it was automatically switched into displacement control at the speed of 0.003 1/s in the range of flow. Experimental research was conducted on nine bars. Figure 2 shows load-strain relationships for particular samples. The average values and coefficients of variation of the tested mechanical properties of reinforcing steel are in Table 3.

The tensile force corresponding to high and low yield points are 63.93 kN and 61.20 kN, respectively.

Test procedure

The specimens for testing the bond stress-slip relationship with an axially embedded steel reinforcing bar were placed in a specially designed and constructed three-dimensional steel frame (Fig. 3). The structure consists of two rigid steel plates, upper and lower, joined to each other by four steel hangers made of steel bars with a hexagonal cross section.

Table 2—Mechanical properties of high-performance concrete

Concrete age	$f_{c,cyl}$, MPa (ϕ150 x 300 mm)	$f_{c,cube}$, MPa (150 x 150 x 150 mm)	$f_{ct,dir}$, MPa (ϕ150 x 300 mm)	E_c, MPa (ϕ150 x 300 mm)
24 hours	39.50	47.54	—	35,300
2 days	53.47	64.08	3.10	39,360
3 days	59.83	72.29	3.39	42,270
7 days	71.53	80.82	4.05	46,000
28 days	88.39	93.13	4.83	49,660
90 days	93.19	100.19	6.14	53,100

Note: 1 mm = 0.0394 in.; 1 MPa = 0.145 ksi.

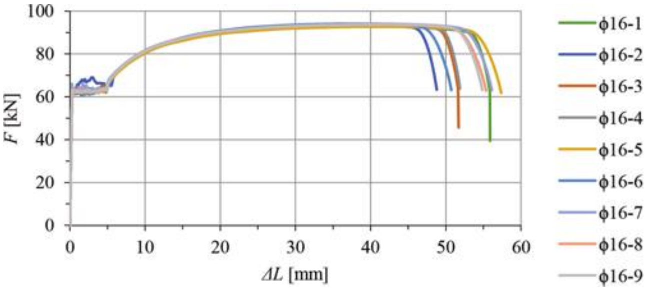

Fig. 2—Tensile force-elongation relationships for plain steel bars of ϕ16 mm. (Note: 1 mm = 0.0394 in.; 1 kN = 0.225 kip.)

The frame structure is hung through a hinge to the strength measuring machine with a steel joint (a bar made of steel, strength of 700 MPa) screwed to the upper steel plate of the frame. The bottom steel plate has a centrally drilled hole through which it is possible to pass the bar coming from the concrete specimen. A hard fiberboard is placed between the concrete specimen and the steel bottom plate, ensuring better fitting of this specimen and the steel plate. A longer, lower bar section is chucked in the gripping jaws of a new-generation testing machine. The jaw pressure on the plain bar was 250 bar. The force from the steering mechanism lifts the frame structure, which transfers the load onto the concrete specimen through pressure on the bottom surface. Chucking the reinforcement in the gripping jaws of the testing machine made it impossible to move it together with the concrete specimen, which resulted in the slip of the plain bar toward the concrete. The load was controlled by displacement with a loading rate of 0.01 mm/s. The force value was continuously recorded digitally. The initial force value was 1 kN. Relative displacement for the given force was measured by a measured system of two arms of the incremental extensometer. The upper arms recorded displacement of the free-end plain steel bar, and the lower arms registered displacement of the aluminum angles glued to the concrete surface with regard to their original location (Fig. 4). The margin of error of the extensometer reading is 0.12 μm. The research was carried out until the displacement value set in the program, that is, 10 mm, was reached. The machine was switched off automatically when a displacement of 10 mm was reached, or the force was below 50% of its maximum value in a given measurement session.

Table 3—Mechanical properties of reinforcing steel

Tensile strength	f_u = 465.09 MPa	v = 0.54%
High yield point	R_{eH} = 317.96 MPa	v = 2.03%
Low yield point	R_{eL} = 304.37 MPa	v = 0.69%
Modulus of elasticity	E_s = 207, 260 MPa	v = 1.83%
Maximum tensile force	F_m = 93.51 kN	v = 0.54%
Cross-section area	A_s = 201.06 mm^2	156
Elongation of measuring base	A_{180} = 29.65%	v = 5.49%

Note: 1 MPa = 0.145 ksi; 1 kN = 0.225 kip; 1 mm^2 = 0.00155 in.^{2}.

EXPERIMENTAL RESULTS AND DISCUSSION

Figures 5 to 8, respectively, present the results of the experimental research regarding the pullout force-slip relationships for specimens with active bond lengths of 40, 80, and 120 mm, made of HPC whose compressive strength was 40, 60, 72, and 88 MPa.

$$f_b = \frac{F}{\phi \pi l_{emb}} \tag{4}$$

where F is the pullout force measured during the test; ϕ is the bar diameter; and l_{emb} is the embedment bar length.

For all tested pullout elements, the failure mode was the same. It was observed that a slip of the bar at the free end increased gently with the pullout force. Splitting cracks did not occur along the centerline of the bar in any specimen.

To analyze the results obtained, taking into account dependency, bond stress for the slip value of 10 for each specimen was calculated; these results for concrete compressive strength of 40, 60, 72, and 88 MPa are displayed in Tables 4 to 7, respectively. Additionally, these tables contain maximum values of bond stress and slip corresponding to them, as well as bond stress values where adhesion loss was registered. What is more, the tables contain calculated average bond stress values, standard deviations, and coefficients of variation.

On the basis of the results presented, the average bond stress-slip relationship was calculated for each analyzed active bond length of a plain bar 16 mm in diameter, depending on concrete compressive strength. Figures 9 to 11 present the bond stress-slip relationships obtained. It can be seen that the bond stress of HPC increases together with

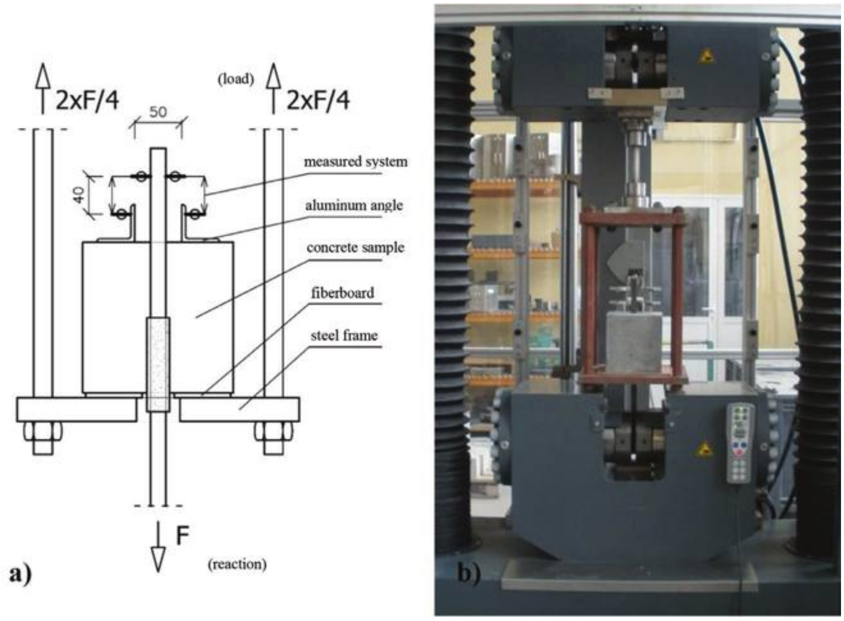

Fig. 3—General view of testing setup: (a) scheme (dimensions in mm); and (b) real setup. (Note: 1 mm = 0.0394 in.)

Fig. 4—Extensometer mounted at free end of plain steel bar during testing.

concrete compressive strength for each analyzed active bond length of the plain bar.

Additionally, Fig. 12 to 15 present the distribution of average bond stress-slip relationships for three analyzed active bond lengths, calculated for concrete compressive strengths of 40, 60, 72, and 88 MPa, respectively. It can be noticed that maximum bond stress was obtained for the active bond length of 40 mm in the case of concrete compressive strength of 60, 72, and 88 MPa.

The distribution of average bond stress in the slip function, defined for a given concrete compressive strength taking into account the analyzed active bond bar lengths, is shown in Fig. 16. The falling branch is noticed to be descending very regularly after reaching the maximum value of bond stress for each analyzed concrete compressive strength value.

Analysis of results obtained and assessment of proposed calculation models

To verify the calculation model in the 2010 and 1990 Model Codes[10,16] and the models proposed by the other researchers, the average values of the adhesive bond, the maximum values of bond stress, and the average values of bar slip corresponding to the last one are summarized in Table 8. Moreover, one can also find the average values of residual bond stress corresponding to the slip value of s = 10 mm, obtained for four analyzed concrete compressive strength values and three active bond lengths. Additionally, there is the comparison of calculated values of adhesive bond, maximum bond stress, and residual bond stress to average concrete compressive strength. The ratios of adhesive bond and residual bond stress to the maximum bond stress, as well as the ratio of residual bond stress to adhesive bond, are also presented.

Based on the experimental study and analysis of the distribution shape of bond stress-slip relationships (Fig. 16) and analysis of compared numerical values and calculated coefficients (Table 8), one can notice a clear difference between these relations for HPC and the models proposed for normal-strength concrete.

First, the slip value s_1 changes substantially. It is the value needed to reach the maximum value of bond stress. One can adopt an average value for four analyzed concrete compressive strength values equaling 0.46 mm. This value is very close to the value of 0.50 mm proposed by Huang et al.[23] in their simplified model for HSC.

Other important parameters, calculated as average values for four analyzed concrete compressive strength values, are close to the values proposed by Abrams[5,9]:

- Average adhesive stress $f_{b,a} = 0.56f_{b,max}$ in comparison to proposed value of $0.60f_{b,max}$
- Average maximum bond stress $f_{b,max} = 0.13f_{cm}$ in comparison to proposed value of $0.19f_{cm}$

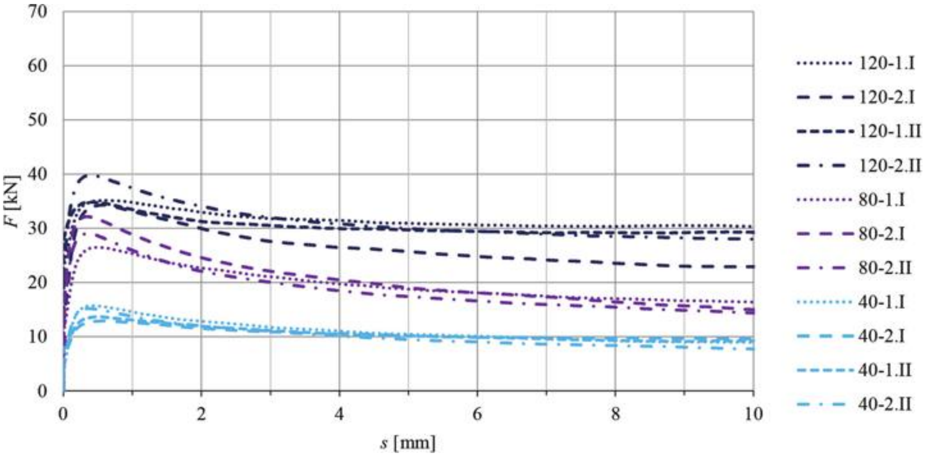

Fig. 5—Tensile force-slip relationship of plain steel bar of 16 mm diameter with effective bond length of 40, 80, and 120 mm, in specimens of HPC, f_c *= 40 MPa.*

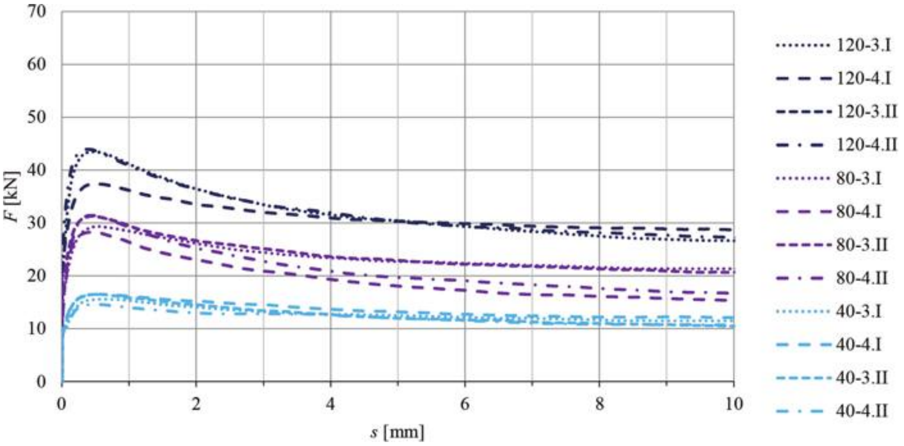

Fig. 6—Tensile force-slip relationship of plain steel bar of 16 mm diameter with effective bond length of 40, 80, and 120 mm, in specimens of HPC, f_c *= 60 MPa.*

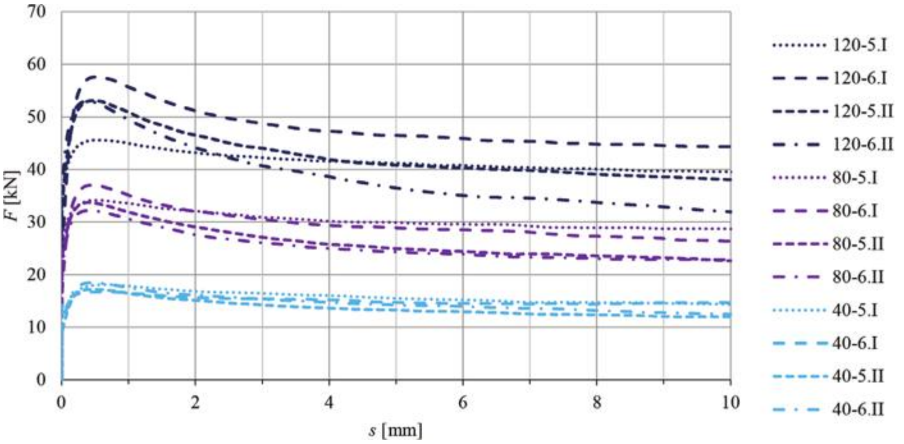

Fig. 7—Tensile force-slip relationship of plain steel bar of 16 mm diameter with effective bond length of 40, 80, and 120 mm, in specimens of HPC, f_c *= 72 MPa.*

- Average residual bond stress $f_{b,res} = 0.68f_{b,max}$ in comparison to proposed value of $0.50f_{b,max}$
- Average adhesive stress $f_{b,a} = 0.073f_{cm}$

The experimentally proved substantial increase in the slip value s_1 is doubtless caused by high adhesion equaling between 3.2 and 6.3 MPa and sufficiently high maximum bond stress between 6.8 and 10.7 MPa. It is also important to mention that after reaching $f_{b,max}$, the post-critical curve of bond stress-slip relationships falls very gently, which is proven by the reached value of $f_{b,res} = 0.68f_{b,max}$ for s = 10 mm. This value substantially exceeds the adhesive bond ($1.23f_{b,a}$).

In the case of HPC, especially concrete containing silica fume, there is a considerable adhesive bond, higher than the

Table 4—Bond strength of HPC to plain steel bars of 16 mm diameter tested on specimens of concrete compressive strength of 40 MPa

	f_b (l_{emb} = 40 mm), MPa				f_b (l_{emb} = 80 mm), MPa				f_b (l_{emb} = 120 mm), MPa				Distribution parameters	
s, mm	1.I	1.II	2.I	2.II	1.I	1.II	2.I	2.II	1.I	1.II	2.I	2.II	$f_{b,ave}$, MPa	CoV, MPa
Adhesion	2.16	3.22	3.15	2.97	2.89	—	3.53	3.35	3.58	4.04	2.6	3.8	3.21	16.9
0.01	2.37	3.35	3.31	3.09	2.9	—	3.96	3.57	3.85	4.07	2.78	3.85	3.37	16.2
0.025	2.78	3.91	3.49	3.57	3.17	—	4.66	4.15	4.01	4.35	2.99	4.25	3.76	16.08
0.1	5.34	5.03	4.65	5.68	4.68	—	6.85	6.04	4.76	5.33	3.97	5.62	5.27	14.86
0.254	7.54	6.45	6.04	7.44	6.25	—	7.93	7.14	5.61	5.72	5.33	6.49	6.54	13.17
1	7.26	6.5	6.28	6.85	6.3	—	7.18	6.45	5.77	5.55	5.49	6.2	6.35	9.34
2.54	6.12	5.73	5.55	5.7	5.42	—	5.93	5.2	5.34	5.12	4.73	5.43	5.48	7.11
4	5.5	5.22	5.27	5.06	4.91	—	5.1	4.6	5.22	4.97	4.39	5.12	5.03	6.2
6	5.03	4.94	4.92	4.51	4.5	—	4.51	4.13	5.08	4.89	4.11	4.89	4.68	7.41
8	4.62	4.63	4.86	4.17	4.24	—	4.08	3.85	5.03	4.85	3.91	4.73	4.45	9.32
10	4.46	4.59	4.78	3.85	4.07	—	3.73	3.58	5.03	4.86	3.8	4.65	4.31	11.94
$f_{b,max}$, MPa	7.83	6.81	6.42	7.57	6.59	—	8	7.22	5.83	5.78	5.69	6.61	6.76	12.1
$s(f_{b,max})$, mm	0.41	0.5	0.56	0.36	0.52	—	0.34	0.36	0.58	0.4	0.57	0.4	0.45	20.25

Note: Specimen 1.II was damaged by a worker during the demolding process; CoV is coefficient of variation. 1 mm = 0.0394 in.; 1 MPa = 0.145 ksi.

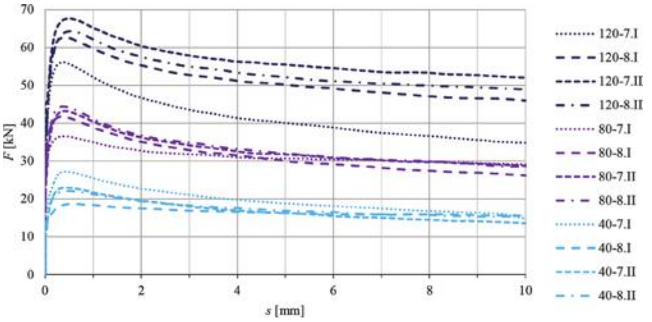

Fig. 8—Tensile force-slip relationship of plain steel bar of 16 mm diameter with effective bond length of 40, 80, and 120 mm, in specimens of HPC, f_c *= 88 MPa.*

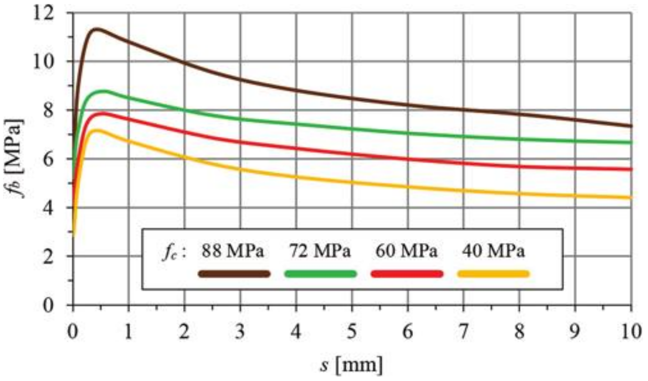

Fig. 9—Average values of bond stress-slip relationship in HPC specimen with plain steel bar (l_{emb} *= 40 mm).*

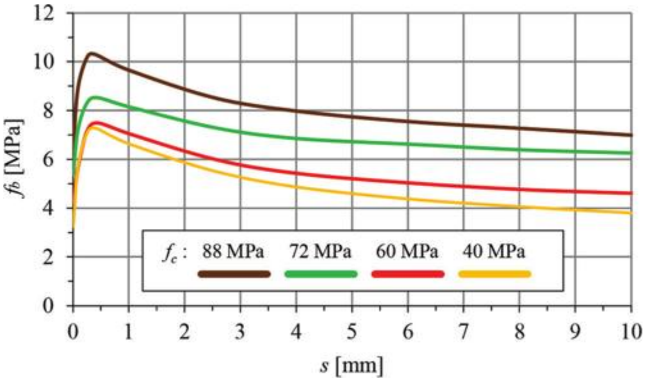

Fig. 10—Average values of bond stress-slip relationship in HPC specimen with plain steel bar (l_{emb} *= 80 mm).*

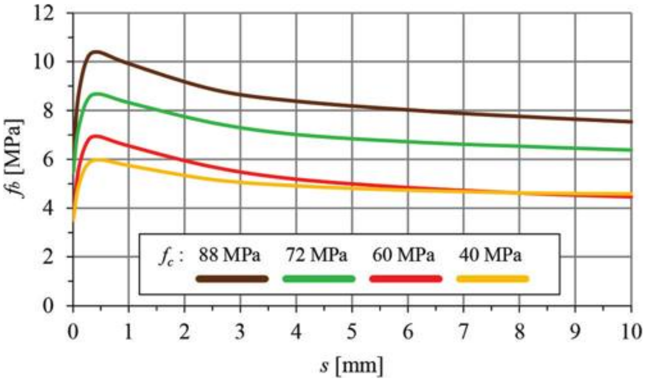

Fig. 11—Average values of bond stress-slip relationship in HPC specimen with plain steel bar (l_{emb} *= 120 mm).*

maximum bond stress reached in normal-strength concrete elements reinforced with plain steel bars. Therefore, it can be concluded that the proposed Eq. (1) for the ascending branch (based on the results obtained from the pullout test method) cannot be reliable for HPC. It should be underlined that slip values were measured at the free end of the plain steel bar. The adopted test method enables the evaluation of the real adhesive bond.

The initial bond strength $f_{b,a}$ (adhesive bond) depends on reinforcing bar diameter, concrete compressive strength, and embedment length. It can be observed from Tables 4

Table 5—Bond strength of HPC to plain steel bars of 16 mm diameter tested on specimens of concrete compressive strength of 60 MPa

	f_b (l_{emb} = 40 mm), MPa				f_b (l_{emb} = 80 mm), MPa				f_b (l_{emb} = 120 mm), MPa				Distribution parameters	
s, mm	3.I	3.II	4.I	4.II	3.I	3.II	4.I	4.II	3.I	3.II	4.I	4.II	$f_{b,ave}$, MPa	CoV, MPa
Adhesion	4.24	3.97	4.62	3.88	3.59	5.06	4.23	4.13	3.05	3.78	3.76	4.14	4.04	12.59
0.01	4.52	4.28	5.04	4.12	3.70	5.14	4.35	4.21	3.15	3.81	3.82	4.25	4.20	13.17
0.025	4.71	4.75	5.45	4.37	4.02	5.19	4.68	4.25	3.74	3.98	3.98	4.72	4.49	11.6
0.1	5.71	6.39	6.57	5.58	5.46	6.24	5.80	5.76	5.71	5.57	5.02	6.23	5.84	7.56
0.254	7.25	7.88	7.84	6.99	6.86	7.54	6.87	7.49	6.98	6.82	5.96	7.18	7.14	7.36
1	7.63	7.88	8.03	6.97	7.08	7.33	6.56	7.26	6.82	6.60	6.00	6.78	7.08	8.29
2.54	6.74	6.92	7.35	6.39	6.23	6.43	5.41	5.94	5.91	5.59	5.43	5.74	6.17	9.98
4	6.35	6.32	6.81	6.26	5.83	5.88	4.81	5.20	5.23	5.10	5.13	5.30	5.69	11.25
6	6.05	5.81	6.34	5.74	5.57	5.53	4.30	4.75	4.87	4.69	4.95	4.87	5.29	11.95
8	5.80	5.49	6.08	5.40	5.37	5.31	4.01	4.38	4.57	4.43	4.82	4.67	5.03	12.66
10	5.72	5.22	6.04	5.31	5.31	5.15	3.80	4.16	4.42	4.16	4.76	4.52	4.88	14.05
$f_{b,max}$, MPa	7.76	8.22	8.21	7.26	7.31	7.78	7.04	7.83	7.21	7.04	6.20	7.29	7.43	7.66
$s(f_{b,max})$, mm	0.59	0.54	0.54	0.43	0.53	0.44	0.43	0.42	0.47	0.43	0.53	0.38	0.48	13.92

Note: 1 mm = 0.0394 in.; 1 MPa = 0.145 ksi.

Table 6—Bond strength of HPC to plain steel bars of 16 mm diameter tested on specimens of concrete compressive strength of 72 MPa

	f_b (l_{emb} = 40 mm), MPa				f_b (l_{emb} = 80 mm), MPa				f_b (l_{emb} = 120 mm), MPa				Distribution parameters	
s, mm	5.I	5.II	6.I	6.II	5.I	5.II	6.I	6.II	5.II	5.II	6.I	6.II	$f_{b,ave}$, MPa	CoV, MPa
Adhesion	5.76	4.51	5.65	4.97	6.28	5.77	4.11	5.34	5.67	5.62	4.8	5.82	5.36	11.79
0.01	6.06	4.69	6.49	5.12	6.5	5.85	4.38	5.37	5.69	5.64	4.87	6.08	5.56	12.38
0.025	6.32	5.11	7.18	5.51	6.85	6.22	5.11	5.78	6.14	5.98	5.32	6.58	6.01	11.16
0.1	7.35	6.8	7.71	7.33	7.66	7.37	7.38	7.07	6.87	7.39	7.09	7.88	7.32	4.47
0.254	8.5	8.33	8.16	8.88	8.29	8.25	8.91	7.89	7.4	8.55	9.08	8.68	8.41	5.58
1	8.89	8.19	8.23	8.72	8.36	7.94	8.73	7.61	7.46	8.44	9.23	8.2	8.33	6.19
2.54	8.29	7.26	7.7	7.83	7.84	6.96	7.77	6.64	7.07	7.45	8.23	7.16	7.52	6.8
4	7.99	6.8	7.57	7.35	7.51	6.41	7.3	6.21	6.9	6.95	7.84	6.41	7.1	8.19
6	7.58	6.46	7.26	6.96	7.36	6.08	7.1	5.96	6.77	6.69	7.61	5.81	6.8	9.12
8	7.33	6.16	7.19	6.57	7.19	5.87	6.8	5.74	6.65	6.48	7.43	5.6	6.59	9.64
10	7.17	5.99	7.31	6.22	7.14	5.64	6.57	5.69	6.56	6.31	7.36	5.3	6.44	10.89
$f_{b,max}$, MPa	9.01	8.57	8.34	9.21	8.5	8.4	9.21	8.02	7.56	8.81	9.55	8.79	8.66	6.4
$s(f_{b,max})$, mm	0.65	0.45	0.66	0.48	0.5	0.4	0.47	0.41	0.52	0.47	0.52	0.37	0.49	18.13

Note: $f_{cm} = f_{c,cyl}$; 1 mm = 0.0394 in.; 1 MPa = 0.145 ksi.

to 7 for the specimens with longer embedment lengths that the chemical adhesion is increased with the bond area, and a larger bond area can be provided by the specimens with longer embedment lengths.

The decrease in maximum bond stress with larger embedment length is also observed in the aforementioned tables as well as in Fig. 12, 13, and 15. In each case, the maximum value of the bond stress-slip relationship is attained for the embedment length equal to 40 mm. The decrease in ultimate bond strength with larger embedment length has also been reported by other researchers.[12] The main reason is the nonlinear distribution of bond stress carried by friction and mechanical locking action along the embedment length, which becomes more nonuniform with the increasing embedment length.

Taking into consideration the results of the bond stress-slip relationship obtained for specimens with embedment lengths of 40, 80, and 120 mm for analyzed concrete compressive strength, the dependency of the relative bond stress f_b/f_{cm} and $f_b/(f_{cm})^{1/2}$ was examined. The influence of HPC compressive strength and the square root of the strength on the relative bond stress-slip relationship for 16 mm diameter plain steel bars is shown in Table 9. It can be concluded that the bond strength increases proportionally to the square root of the compressive strength of concrete.

Table 7—Bond strength of HPC to plain steel bars of 16 mm diameter tested on specimens of concrete compressive strength of 88 MPa

	f_b (l_{emb} = 40 mm), MPa				f_b (l_{emb} = 80 mm), MPa				f_b (l_{emb} = 120 mm), MPa				Distribution parameters	
s, mm	7.I	7.II	8.I	8.II	7.I	7.II	8.I	8.II	7.I	7.II	8.I	8.II	$f_{b,ave}$, MPa	CoV, MPa
Adhesion	7.18	5.15	6.25	6.51	6.65	5.71	7.09	5.95	4.89	7.05	6.68	6.13	6.27	11.85
0.01	7.54	5.21	6.32	6.74	7.16	5.95	7.92	6.24	5.05	7.23	6.84	6.17	6.53	13.48
0.025	7.76	5.91	6.58	7.15	7.48	6.61	8.34	6.97	5.93	7.53	7.33	6.46	7	10.53
0.1	10.7	9.09	7.67	9.21	8.4	9.07	9.58	9.41	8.14	9.13	8.88	8.66	8.99	8.54
0.254	13.07	11.14	8.83	10.71	9.01	10.54	10.32	10.95	9.19	10.87	10.24	10.25	10.43	10.89
1	12.69	10.81	9.14	10.56	8.7	10.05	9.67	10.23	8.65	10.81	9.9	10.31	10.13	10.8
2.54	10.85	9.34	8.64	9.28	7.99	8.85	8.4	8.84	7.45	9.77	8.9	9.29	8.97	9.66
4	9.82	8.43	8.24	8.75	7.71	8.1	7.83	8.26	6.86	9.34	8.49	8.86	8.39	9.19
6	9.01	7.7	7.93	8.22	7.57	7.67	7.26	7.71	6.45	9.05	8.16	8.48	7.93	9.14
8	8.37	7.2	7.92	7.85	7.41	7.4	6.83	7.47	6.08	8.84	7.82	8.28	7.62	9.68
10	7.31	6.75	7.74	7.6	7.24	7.15	6.52	7.06	5.78	8.63	7.63	8.14	7.3	10.27
$f_{b,max}$, MPa	13.55	11.43	9.3	11.02	9.09	10.76	10.39	11.05	9.31	11.22	10.39	10.67	10.68	11.23
$s(f_{b,max})$, mm	0.39	0.42	0.56	0.42	0.39	0.43	0.36	0.36	0.38	0.5	0.41	0.55	0.43	16.25

Note: 1 mm = 0.0394 in.; 1 MPa = 0.145 ksi.

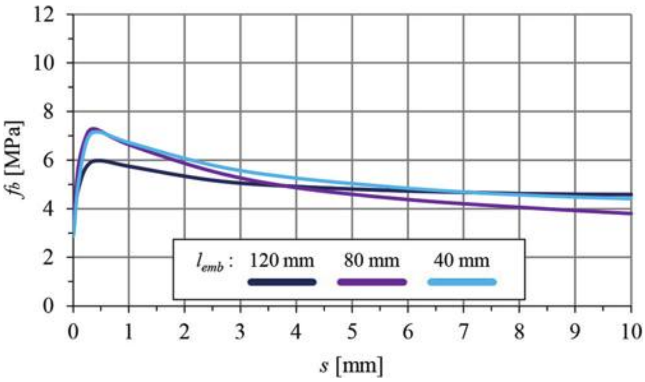

Fig. 12—Average values of bond stress-slip relationship for HPC of f$_c$ *= 40 MPa to plain steel bar with varied effective bond length.*

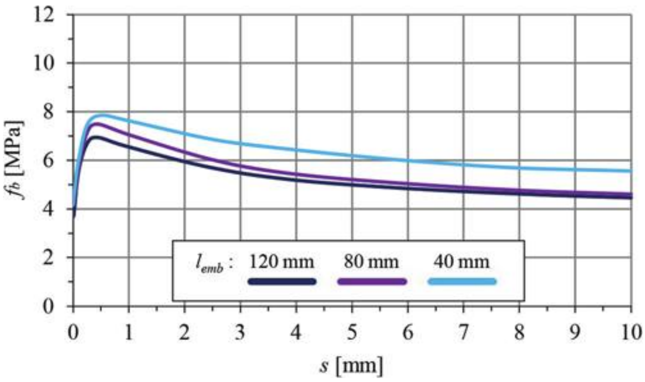

Fig. 13—Average values of bond stress-slip relationship for HPC of f$_c$ *= 60 MPa to plain steel bar with varied effective bond length.*

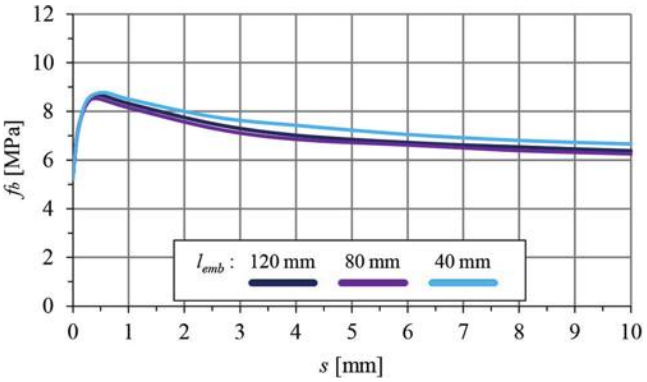

Fig. 14—Average values of bond stress-slip relationship for HPC of f$_c$ *= 72 MPa to plain steel bar with varied effective bond length.*

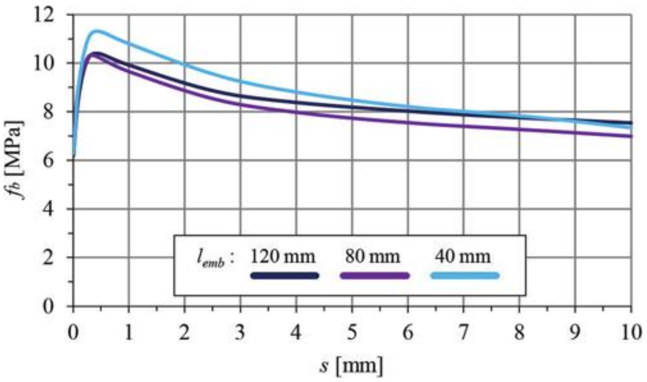

Fig. 15—Average values of bond stress-slip relationship for HPC of f$_c$ *= 88 MPa to plain steel bar with varied effective bond length.*

Table 9—Influence of HPC compressive strength and square root of strength on relative bond stress-slip relationship for plain steel bar of 16 mm diameter

	f_b/f_c						$f_b/(f_c)^{1/2}$					
s, mm	40	60	72	88	Average	CoV, %	40	60	72	88	Average	CoV, %
Adhesion	0.080	0.067	0.074	0.071	0.073	7.45	0.508	0.522	0.632	0.668	0.582	13.71
0.01	0.084	0.070	0.077	0.074	0.076	7.85	0.533	0.542	0.655	0.696	0.607	13.45
0.025	0.094	0.075	0.083	0.080	0.083	9.84	0.595	0.580	0.708	0.746	0.657	12.57
0.1	0.132	0.097	0.102	0.102	0.108	14.63	0.833	0.754	0.863	0.958	0.852	9.91
0.254	0.164	0.119	0.117	0.119	0.129	17.55	1.034	0.922	0.991	1.112	1.015	7.84
1	0.159	0.118	0.116	0.115	0.127	16.77	1.004	0.914	0.982	1.080	0.995	6.87
2.54	0.137	0.103	0.104	0.102	0.112	15.24	0.866	0.797	0.886	0.956	0.876	7.49
4	0.126	0.095	0.099	0.095	0.104	14.32	0.795	0.735	0.837	0.894	0.815	8.27
6	0.117	0.088	0.094	0.090	0.097	13.66	0.740	0.683	0.801	0.845	0.767	9.25
8	0.111	0.084	0.092	0.087	0.093	13.27	0.704	0.649	0.777	0.812	0.735	9.94
10	0.108	0.081	0.089	0.083	0.090	13.39	0.681	0.630	0.759	0.778	0.712	9.67

Note: 1 mm = 0.0394 in.

Table 8—Average values of HPC bond strength to plain steel bar of 16 mm diameter

f_c, MPa	f_{ba}, MPa	$f_{b,max}$, MPa	$f_{b,res}$, MPa	s_{max}, mm	$f_{b,a}/f_{cm}$	$f_{b,max}/f_{cm}$	$f_{b,res}/f_{cm}$	$f_{b,a}/f_{b,max}$	$f_{b,res}/f_{b,max}$	$f_{b,res}/f_{b,a}$
40	3.21	6.76	4.31	0.45	0.080	0.169	0.108	0.475	0.637	1.343
60	4.04	7.43	4.88	0.48	0.067	0.124	0.081	0.544	0.657	1.208
72	5.36	8.66	6.44	0.49	0.074	0.120	0.089	0.619	0.744	1.201
88	6.27	10.68	7.30	0.43	0.071	0.121	0.083	0.587	0.683	1.164
Average	—	—	—	0.46	0.073	0.133	0.090	0.556	0.680	1.229

Notes: 1 mm = 0.0394 in.; 1 MPa = 0.145 ksi.

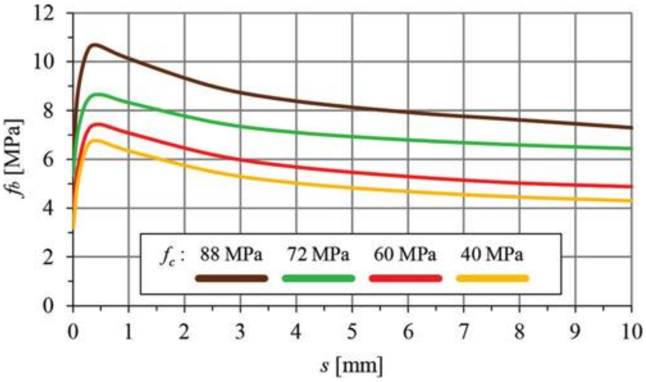

Fig. 16—Average values of bond stress-slip relationship for HPC to plain steel bar taking into consideration all tested specimens.

The most critical factor for bond strength under a certain bar diameter is concrete compressive strength. Based on the obtained results, a new bond stress-slip model was proposed as follows

$$f_b = \begin{cases} f_{b,a} + (f_{b,max} - f_{b,a}) \cdot \left(\frac{s}{s_{max}}\right)^{\alpha} & 0 \leq s \leq s_{max} \\ f_{b,max} - a \cdot \ln\left(\frac{s}{s_{max}}\right) & s_{max} < s \leq 10\,\text{mm} \end{cases} \tag{5}$$

where $f_{b,a} = 0.58(f_c)^{1/2}$; $f_{b,max} = 1.04(f_c)^{1/2}$; concrete compressive strength $f_c = f_{c,cyl}$; s is slip; slip at maximum bond $s_{max} = 0.46$ mm; and the coefficients $a = 0.85$ and $\alpha = 0.35$.

The starting point for the consideration of the bond model was the model developed by Melo et al.[9] However, the assumptions made by Melo et al.[9] involved a complex calculation of the function coefficients, making their model impractical.

The basic aims for the construction of the new model were: 1) a reflection of the real phenomenon in HPC; 2) simplification of functions for practical applications; and 3) consideration of adhesive bond.

The ascending branch starts from the adhesive bond and represents the contribution of mechanical micro-interlocking and friction on the bond strength. The descending branch represents progressive friction degradation and second-order micro-interlocking. The proposed model formulation is limited to HPC with a compressive strength range of 40 to 90 MPa.

CONCLUSIONS

Based on the experimental study and analysis conducted on the bond behavior of plain steel bars with high-performance concrete (HPC), the main conclusions can be drawn as follows:

1. The bond stress-slip relationships are stable for a concrete compressive strength range of 40 to 90 MPa. The maximum bond stress value $f_{b,max} = 0.13f_{cm}$ can be predicted

at the bar slip of 0.46 mm. The residual bond stress at the level of $0.09f_{cm}$ is predicted for the bar slip of 10 mm.

2. The initial bond strength (adhesive bond) is increased with longer embedment length and compressive concrete strength. The adhesive bond stress is approximately 55% of the maximum bond stress. In practical engineering applications, the relationship $f_{b,a} = 0.07f_{cm}$ may be adopted in the case of HPC members in which the concrete is mechanically compacted.

3. The maximum bond stress is decreased with a longer embedment length of the plain steel bar. Moreover, the difference between the maximum bond stress values resulting from these experimental investigations (l_{emb} = 40, 80, and 120 mm) with HPC strength varied from 40 to 90 MPa is at a level of 10%.

4. The experimental investigations demonstrated that the bond strength increases proportionally to the square root of the compressive strength independently of the concrete compressive strength. Suitable calculation coefficients are listed in Table 9.

5. A new bond stress-slip model with the initial bond strength (adhesive bond) and the lower convex property in predicting the post-peak branch is proposed, and good agreement can be achieved by comparing the test results with the theoretical predictions. The bond stress against free-end slip was adopted in the experimental study.

AUTHOR BIOS

Marcin Dyba *is an Associate Professor at Cracow University of Technology, Cracow, Poland, where he received his BS, MS, and PhD in civil engineering in 2008, 2010, and 2014, respectively. He also received an MS in applied computer science from AGH University of Science and Technology, Cracow, Poland, in 2011. His research interests include technology and design of precast, prestressed concrete structures; and applications of high-performance concrete to prestressed elements.*

Andrzej Seruga *is a Professor at Cracow University of Technology, where he received his MS, PhD, and DSc in civil engineering in 1969, 1978, and 2003, respectively. His research interests include the watertightness of reinforced and prestressed concrete tanks, applications of high-performance concrete to prestressed elements, strengthening of existing structures, rigid concrete pavements, shotcrete technology, and sulfur concrete.*

ACKNOWLEDGMENTS

This research was sponsored by the Faculty of Civil Engineering of Cracow University of Technology, Cracow, Poland.

REFERENCES

1. Dyba, M., and Derkowski, W., "Bond Stresses between Concrete and Prestressing in Pre-tensioned Elements: State of the Art," *Cement, Lime, Concrete*, V. 83, No. 5, 2018, pp. 358-368.

2. Derkowski, W., and Dyba, M., "Behaviour of End Zone of Pre-tensioned Concrete Elements," *Procedia Engineering*, V. 193, 2017, pp. 19-26. doi: 10.1016/j.proeng.2017.06.181

3. Feldman, L. R., and Cairns, J., "Assessing Historical Provisions for Bond of Plain Bars," *ACI Structural Journal*, V. 114, No. 2, Mar.-Apr. 2017, pp. 463-473. doi: 10.14359/51689163

4. Fabbrocino, G.; Verderame, G. M.; Manfredi, G.; and Cosenza, E., "Experimental Response and Behavioral Modelling of Anchored Smooth Bars in Existing RC Frames," *Proceedings of the International Conference on Bond in Concrete*, Budapest, Hungary, 2002, pp. 111-118.

5. Abrams, D. A., "Tests of Bond between Concrete and Steel," Bulletin No. 71, Engineering Experiment Station, University of Illinois Urbana-Champaign, Urbana, IL, Dec. 1913, 240 pp.

6. ACI Committee 318, "Building Code Requirements for Reinforced Concrete (ACI 318-63)," American Concrete Institute, Farmington Hills, MI, 1963, 144 pp.

7. CSA A23.3-1970, "Code for the Design of Plain or Reinforced Concrete Structures," CSA Group, Toronto, ON, Canada, 1970, 108 pp.

8. Fabbrocino, G.; Verderame, G. M.; and Manfredi, G., "Experimental Behaviour of Anchored Smooth Rebars in Old Type Reinforced Concrete Buildings," *Engineering Structures*, V. 27, No. 10, Aug. 2005, pp. 1575-1585. doi: 10.1016/j.engstruct.2005.05.002

9. Melo, J.; Rossetto, T.; and Varum, H., "Experimental Study of Bond–Slip in RC Structural Elements with Plain Bars," *Materials and Structures*, V. 48, No. 8, Aug. 2015, pp. 2367-2381. doi: 10.1617/s11527-014-0320-9

10. *fib*, "Model Code 2010: Final draft – Volume 1," *fib* Bulletin No. 65, International Federation for Structural Concrete, Lausanne, Switzerland, Mar. 2012, pp. 247-256.

11. Zhao, J.; Cai, G.; and Yang, J., "Bond-Slip Behavior and Embedment Length of Reinforcement in High Volume Fly Ash Concrete," *Materials and Structures*, V. 49, No. 6, June 2016, pp. 2065-2082. doi: 10.1617/s11527-015-0634-2

12. Wang, J.; Yang, L.; and Yang, J., "Bond Behavior of Epoxy-Coated Reinforcing Bars with Seawater Sea-Sand Concrete," *ACI Structural Journal*, V. 117, No. 4, July 2020, pp. 193-208.

13. Feldman, L. R., and Bartlett, F. M., "Bond Strength Variability in Pullout Specimens with Plain Reinforcement," *ACI Structural Journal*, V. 102, No. 6, Nov.-Dec. 2005, pp. 860-867.

14. Feldman, L. R., and Bartlett, F. M., "Bond Stresses Along Plain Steel Reinforcing Bars in Pullout Specimens," *ACI Structural Journal*, V. 104, No. 6, Nov.-Dec. 2007, pp. 685-692.

15. Stocker, M. F., and Sozen, M. A., "Investigation of Prestressed Reinforced Concrete for Highway Bridges – Part V: Bond Characteristics of Prestressing Strand," Bulletin No. 503, Engineering Experiment Station, University Illinois Urbana-Champaign, Urbana, IL, 1970, 119 pp.

16. *fib*, "CEB-FIP Model Code 1990," CEB Bulletin No. 213/214, International Federation for Structural Concrete, Lausanne, Switzerland, 1993, 460 pp.

17. *fib*, "Bond of Reinforcement in Concrete," *fib* Bulletin No. 10, International Federation for Structural Concrete, Lausanne, Switzerland, 2000, 434 pp.

18. Verderame, G. M.; Ricci, P.; De Carlo, G.; and Manfredi, G., "Cyclic Bond Behaviour of Plain Bars. Part I: Experimental Investigation," *Construction and Building Materials*, V. 23, No. 12, Dec. 2009, pp. 3499-3511. doi: 10.1016/j.conbuildmat.2009.07.002

19. Verderame, G. M.; De Carlo, G.; Ricci, P.; and Fabbrocino, G., "Cyclic Bond Behaviour of Plain Bars. Part II: Analytical Investigation," *Construction and Building Materials*, V. 23, No. 12, Dec. 2009, pp. 3512-3522. doi: 10.1016/j.conbuildmat.2009.07.001

20. Eligehausen, R.; Popov, E. P.; and Bertero, V. V., "Local Bond Stress-Slip Relationships of Deformed Bars under Generalized Excitations," *Proceedings of the Seventh European Conference on Earthquake Engineering*, V. 4, Athens, Greece, Sept. 1982, pp. 69-80.

21. Poon, C. S.; Lam, L.; and Wong, Y. L., "Effects of Fly Ash and Silica Fume on Interfacial Porosity of Concrete," *Journal of Materials in Civil Engineering*, ASCE, V. 11, No. 3, Aug. 1999, pp. 197-205. doi: 10.1061/(ASCE)0899-1561(1999)11:3(197)

22. Magnusson, J., "Bond and Anchorage of Deformed Bars in High-Strength Concrete," licentiate thesis, Publication 97:1, Chalmers University of Technology, Division of Concrete Structures, Gothenburg, Sweden, 1997, 234 pp.

23. Huang, Z.; Engström, B.; and Magnusson, J., "Experimental Investigation of the Bond and Anchorage Behaviour of Deformed Bars in High-Strength Concrete," *Proceedings*, Fourth International Symposium on the Utilization of High Strength/High Performance Concrete, V. 3, Paris, France, May 1996, pp. 1115-1124.

24. Dyba, M., "Influence of Technological Parameters on Concrete-Steel Bond between High Performance Concrete and Prestressing Strands," PhD thesis, Cracow University of Technology, Cracow, Poland, 2014, 340 pp.

ACI STRUCTURAL JOURNAL TECHNICAL PAPER

Title No. 121-S13

Vertical Punching Capacity of Reinforced Concrete Flat Plates without Shear Reinforcement

by Srinivas Mogili, Hsiang-Yun Lin, and Shyh-Jiann Hwang

Reinforced concrete flat-plate systems are widely adopted in buildings owing to ease of construction and facilitating larger clear story heights. Flat plates are routinely designed for two-way shear to preclude brittle punching failures. Accurate assessment of concrete contribution to shear strength is particularly important for flat plates in carrying out a reliable and economical design. To address this, an efficient analytical method based on the softened strut-and-tie model to estimate punching capacity of flat plates without shear reinforcement under gravity loading is presented. The proposed method can account for the influence of various key parameters such as concrete strength, plate thickness, column geometry, longitudinal reinforcement area, and arrangement of tension reinforcement. The proposed method, when verified against data from 224 specimens reported in the literature, showed reasonably good accuracy with a mean test-to-estimated capacity ratio of 1.20 and a coefficient of variation (CoV) of 0.19. In comparison, average capacity ratios using ACI 318-19 and Eurocode 2 provisions were 1.60 and 1.27 (CoV of 0.34 and 0.29), respectively. A comprehensive discussion on the effects of key parameters on punching behavior of flat plates without shear reinforcement is presented, and suggestions to improve existing design provisions are provided.

Keywords: ACI 318; analytical model; design codes; Eurocode 2; flat plates; punching; reinforced concrete; shear strength; softened strut-and-tie (SST).

INTRODUCTION

Reinforced concrete (RC) flat-plate systems consist of slabs and columns without beams or capitals, offering considerable benefits in clear floor height, fast constructability, and overall economy. Flat plates are routinely adopted in high-rise buildings as the improved floor height per story, architectural ease, and construction speed can result in notable time and cost savings. Nevertheless, the use of these systems comes with a drawback as they are particularly susceptible to brittle punching failure near column-slab connections owing to severe stress demands. This vulnerability can potentially lead to progressive cascading collapse.[1,2]

Punching in flat plates is typically viewed as a case of two-way shear with additive contributions from concrete and shear reinforcement. Although the addition of shear reinforcement in flat plates benefits punching capacity, there are practical difficulties in placing shear reinforcement due to restrictive thickness requirements for flat plates. As a result, researchers have focused on investigating the concrete contribution more extensively by conducting experimental studies on flat plates without shear reinforcement. Additionally, several experimental efforts were undertaken to quantify the benefits of shear reinforcement addition in the form of stirrups, as well as in special forms such as stud rails and steel plates on punching.[3-7] However, these are not within the scope of this paper. Instead, this study aims to understand and accurately estimate the contribution of concrete toward two-way shear strength in RC flat plates. It should also be noted that designers sometimes choose to add drop panels or column capitals (commonly known as flat slabs) for improving shear strength, albeit at the expense of increased material and construction costs. However, these specific elements are not the focus of this work. Nonetheless, the recommendations provided herein are also relevant for flat slabs. Hereon, the discussion is limited to interior flat plates without any shear reinforcement under monotonic gravity loading.

Current design codes such as ACI 318-19[8] and Eurocode 2[9] adopt empirical equations for estimating concrete contribution to punching resistance. These are summarized as follows:

For interior slab-column connections with normal-strength concrete, ACI 318-19, Section 22.6.5.2 recommends the least of Eq. (1), (2), and (3) for two-way shear strength estimation. Equation (2) is based on data[10] showing less efficient two-way shear action in members with higher column aspect ratios (β), whereas Eq. (3) accounts for reduction in shear strength with increase in b_o/d based on Vanderbilt.[11] In general, Eq. (2) governs the design when β is greater than 2, and Eq. (3) is applicable when b_o/d is over 20; otherwise Eq. (1) controls. In addition, shear strength not increasing in direct proportion with member depth, defined as size effect, is accounted for using Eq. (4). Detailed discussion of these geometric effects is continued in later sections. Notably, ACI 318-19 does not consider the influence of tension reinforcement on two-way shear strength for flat-plate members.

$$v_{ACI} = P/b_o d = 0.33\lambda_s\sqrt{f_c'}\ \text{(MPa) or } 4\lambda_s\sqrt{f_c'}\ \text{(psi)} \tag{1}$$

$$v_{ACI} = 0.17(1 + 2/\beta)\lambda_s\sqrt{f_c'}\ \text{(MPa) or}$$

$$2(1 + 2/\beta)\lambda_s\sqrt{f_c'}\ \text{(psi)} \tag{2}$$

ACI Structural Journal, V. 121, No. 1, January 2024.

MS No. S-2023-074.R1, doi: 10.14359/51739193, received August 2, 2023, and reviewed under Institute publication policies. Copyright © 2024, American Concrete Institute. All rights reserved, including the making of copies unless permission is obtained from the copyright proprietors. Pertinent discussion including author's closure, if any, will be published ten months from this journal's date if the discussion is received within four months of the paper's print publication.

$$v_{ACI} = 0.17(1+20d/b_o)\lambda_s\sqrt{f_c'}\ \text{(MPa) or}$$
$$2(1+20d/b_o)\lambda_s\sqrt{f_c'}\ \text{(psi)} \tag{3}$$

$$\lambda_s = \sqrt{2/(1+d/250)}\ (d \text{ in mm) or } \sqrt{2/(1+d/10)}\ (d \text{ in in.}) \leq 1.0 \tag{4}$$

Another design code, Eurocode 2 through Section 6.4.4 prescribes Eq. (5) for the estimation of punching strength of flat plates without stirrups.

$$\upsilon_{EC2} = P/b'_od = 0.18/\gamma_c \times k[100\rho f_c']^{1/3}\ \text{(MPa) or}$$
$$0.95/\gamma_c \times k[100\rho f_c']^{1/3}\ \text{(psi)} \tag{5}$$

$$k = 1+\sqrt{200/d}\ (d \textit{ in } \text{mm) or } 1+\sqrt{8/d}\ (d \textit{ in } \text{in.}) \leq 2.0 \tag{6}$$

The size effect factor in Eurocode 2 is represented by k, determined using Eq. (6). Eurocode 2 sets a lower limit of one for size effect factor ($k = 1$), while no such limit is enforced in ACI 318-19.

In contrast to ACI 318-19, which does not account for the contribution of tension reinforcement on two-way shear strength, Eurocode 2 guidelines suggest that the concrete contribution to shear strength is proportional to the cube root of tension reinforcement ratio. Another difference is that Eurocode 2 suggests that shear strength is proportional to the cube root of concrete strength, as opposed to a square root of concrete strength in ACI 318-19. Furthermore, ACI 318-19 and Eurocode 2 adopt different ways of defining the critical or control sections for punching shear. ACI 318-19 places the critical section at a distance $d/2$ away from column face, whereas Eurocode 2 positions it at four times that distance. This results in different shear stress values per each code for the same punching load. It should also be noted that design understrength is enforced in ACI 318-19 through capacity reduction factors, whereas in Eurocode 2, material safety factors address this aspect. However, for this study, both factors are disregarded and assumed to be 1.0, with any design implications overlooked. This is a common practice to provide analysts with confidence in mean predictions before introducing safety factors.

There is a lack of consensus in design provisions on what parameters are important and how much they contribute to two-way shear strength. Bridging this gap and enhancing existing code guidelines necessitates a thorough analysis of experimental data, where the goal is to verify and incorporate essential parameters into empirical code equations. This is achieved through a robust analytical model with consistent load-transfer mechanisms, which clarifies physical significance of key parameters. Estimations from such an analytical method should align reasonably well with results from available parametric test studies in the literature, thereby providing broadly accurate estimations for punching capacity. Based on experimental and analytical results, inclusions or modifications of key parameters in code equations for design are suggested in this study.

RESEARCH SIGNIFICANCE

This paper proposes a simple yet accurate analytical method to estimate the punching strength of RC flat plates without shear reinforcement under gravity loading. The proposed analytical approach can aid engineers in understanding the importance of key parameters such as tension reinforcement and other geometric variables by clarifying their role in load resistance. Punching estimations of 224 isolated flat plates without shear reinforcement using the proposed analytical model are compared with test results, as well as with estimations through code equations. Based on these comparisons, a need for improvement in code equations for better accuracy is highlighted, and suitable recommendations are made. The results and suggestions presented in this paper can help engineers advance knowledge of concrete contribution toward the two-way shear strength and punching behavior in flat plates.

PREVIOUS STUDIES

Several tests on RC flat plates have been reported by researchers in the past, studying the influence of key material, geometric, and reinforcement parameters on punching behavior of flat plates without shear reinforcement under vertical loading. A brief review of observed capacity variations associated with changes in tension reinforcement, concrete strength, column geometry, and slab geometry is provided as follows. Due to length limitations, only selected studies are discussed herein.

Tension reinforcement

The influence of tension reinforcement on punching capacity observed using two parametric studies[12,13] is compiled in Fig. 1(a). In this figure, punching strength is expressed as peak two-way shear stresses calculated on the ACI critical section (υ) and further normalized for concrete strength using $\sqrt{f_c'}$. A general trend of improvement in $v/\sqrt{f_c'}$ could be seen with increase in ρ. For instance, tests by Marzouk and Hussein[12] showed that an increase in ρ from 0.5 to 2.4% in 120 mm (4.7 in.) thick plates resulted in an improvement of $v/\sqrt{f_c'}$ by 155%. A similar improvement was also reported in both 150 and 90 mm (5.9 and 3.5 in.) thick plates. Likewise, Rankin and Long[13] also reported a substantial benefit in $v/\sqrt{f_c'}$ (by 121%) when ρ was increased from 0.4 to 2.0% for 51 mm (2.0 in.) thick plates, with similar trends observed in 46 and 64 mm (1.8 and 2.5 in.) thick slabs as shown in Fig. 1(a). Several other studies[14-17] also reported notable improvements in punching strength with higher ρ values, which led to a broad research agreement on this matter.

Tension reinforcement arranged in nonuniform distribution with more concentration near the column region was also reported to benefit flat-plate performance in terms of higher loads at initial yielding, smaller maximum crack widths, and higher punching capacities when compared with

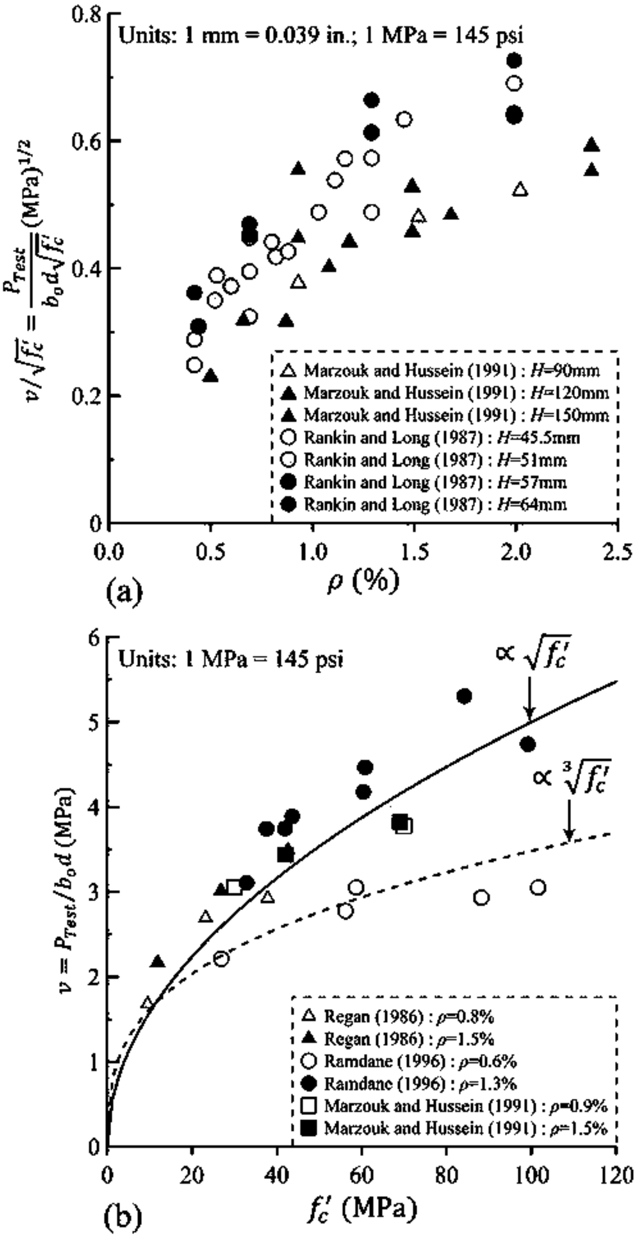

Fig. 1—Variation of observed normalized shear strengths with: (a) tension reinforcement ratio; and (b) concrete strength.

specimens with similar reinforcement areas but distributed uniformly.[14,18-20] An important caveat while dealing with specimens with concentrated reinforcement near columns (sometimes referred to as banded reinforcement) is the increased risk of anchorage failure, which is detrimental to punching capacity. When failure is initiated by anchorage failure, benefits from the concentration of tension reinforcement may not be realized.[21] Concentration of tension reinforcement was also reported to be beneficial in the post-punching performance of flat plates resisting vertical movement of the punched slab through catenary action and providing valuable post-punching resistance.[22,23]

Concrete compressive strength

The influence of concrete compressive strength on punching strength is depicted in Fig. 1(b) by plotting υ versus f_c' through data from three studies.[12,14,24] As expected, higher concrete strength is shown to benefit punching strength in flat plates. The rate of increase in υ is largely proportional to $\sqrt{f_c'}$. However, this appears to be somewhat unconservative for flat plates with low ρ (~0.6%) tested by Ramdane,[24] where failure was reportedly due to the yielding of tension reinforcement. In such cases, variation of υ appears to be proportional to $\sqrt[3]{f_c'}$. Current ACI 318-19 provisions advocate $v \propto \sqrt{f_c'}$, whereas the current Eurocode 2 suggests $v \propto \sqrt[3]{f_c'}$, as shown by Eq. (1) and (5), respectively.

Furthermore, lightweight aggregate concrete was reported to reduce punching capacity in flat plates. Based on several tests, Ramdane[24] proposed additional strength reduction proportional to the ratio of aggregate densities when using lightweight aggregates. In another study,[25] performance of flat plates with high-strength concrete with lightweight aggregates was observed to be only as good as those with normal-strength concrete with normal aggregates. A detailed discussion on the performance of flat plates with lightweight aggregates is beyond the scope of this paper.

Geometry

ACI 318-19, through Eq. (2), advocates a reduction in two-way shear strength for flat plates with rectangular columns with β (equal to c_{max}/c_{min}) greater than 2, noting that peak shear stress on the critical section reduces along the long side of column due to inefficient two-way action as compared with flat plates consisting of square columns.[10] To further examine this, $v/\sqrt{f_c'}$ reported in tests[26-29] studying column rectangularity are plotted against c_{max}/c_{min} (equal to β) in Fig. 2(a). In several specimens plotted in Fig. 2(a), critical perimeter b_o was not controlled while varying c_{max}/c_{min}. As a result, $v/\sqrt{f_c'}$ is also plotted in Fig. 2(b) against the ratio of ACI control perimeter to effective depth (b_o/d), defined as geometric ratio. Although Fig. 2 demonstrates a weak trend, indicating a reduction in $v/\sqrt{f_c'}$ with increase in c_{max}/c_{min}, a closer look in conjunction with the effect of b_o/d suggests that this reduction may be due to an increase in column perimeter and associated critical perimeter at larger values of c_{max}/c_{min}. In other words, when column perimeter (and consequently b_o/d) is controlled, the influence of c_{max}/c_{min} on $v/\sqrt{f_c'}$ may not be appreciable. Results from two studies[26,28] with controlled b_o/d corroborate this. Furthermore, ACI 318-19 recommends a reduction in two-way shear strength of flat plates with higher b_o/d through Eq. (3). When b_o/d is less than 20, this reduction is not enforced as shear strength estimated using Eq. (1) is lower than Eq. (3). However, as b_o/d exceeds 20, Eq. (3) controls the shear strength of interior flat plates. While the rationale behind Eq. (3) cannot be directly verified through Fig. 2(b), as b_o/d values for these specimens are lower than 18, there appears to be a reduction in $v/\sqrt{f_c'}$ even when b_o/d is below 20.

Another aspect of flat-plate geometry is plate thickness. Selected tests[14,16,27,30,31] capturing the influence of plate thickness (and effective depth) on normalized shear strength ($v/\sqrt{f_c'}$) are represented in Fig. 3, where a notable reduction

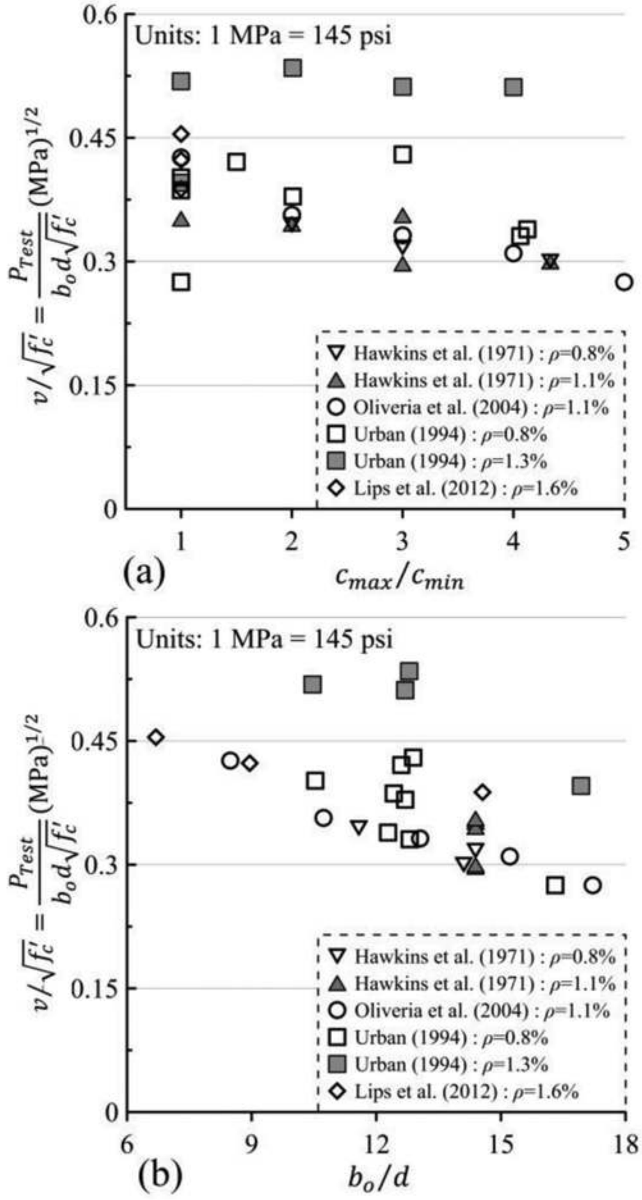

Fig. 2—Variation of observed normalized shear strengths with: (a) column aspect ratio; and (b) geometric ratio.

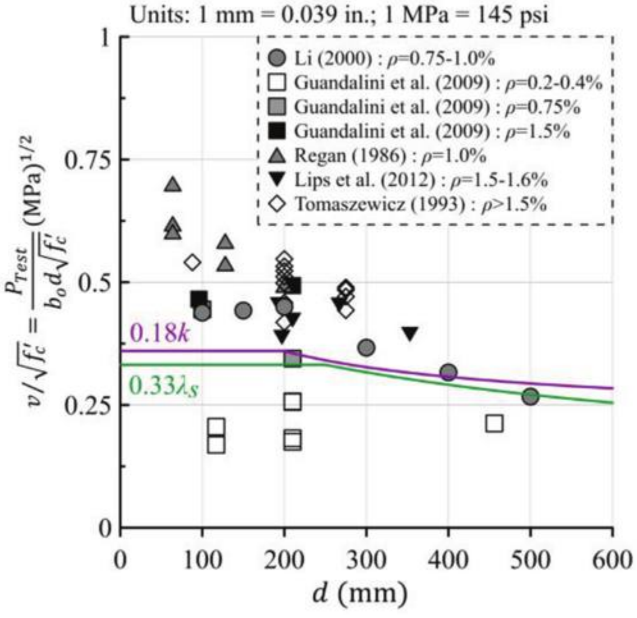

Fig. 3—Variation of normalized shear strengths with size.

in unit shear strength could be observed. This phenomenon, known as size effect, is an important consideration for shear-dominant RC members without shear reinforcement.[32] The data from Fig. 3 affirm that size effect is apparent for flat plates likely failing in shear. For flat slabs with low ρ values (≤0.4%) reported by Guandalini et al.,[31] no reduction in strength with size was observed. Ignoring these data points from lightly reinforced specimens associated with probable flexural failure, Fig. 3 illustrates a general decline in $v/\sqrt{f_c}$ with size, which is safely captured by ACI 318-19 size effect provisions, with all data points located above the trend line plotted using Eq. (4).

Comparing the size effect provisions in design codes, ACI 318-19 suggests that size effect is expected in members with d over 250 mm (10 in.), whereas Eurocode 2 proposed size effect begins at d over 200 mm (8 in.). However, both Eq. (4) and (6) indicate that the rate of strength reduction due to size is proportional to $1/\sqrt{d}$; and both equations would result in similar rate of strength reduction, as highlighted in Fig. 3. Readers are encouraged to refer to relevant literature[33,34] for a comprehensive discussion and design implications of size effect in two-way shear members.

The foregoing discussion highlights that punching performance and strength of flat slabs are significantly influenced by several key parameters. However, as underscored previously in the introduction of this paper, current design codes adopting an empirical approach do not (or only partially) consider influence of some key parameters on shear strength estimation. In this study, an effort to fill this gap is carried out by proposing a reliable analytical method based on consistent force transfer mechanisms and capturing major parameters. This analytical method is based on the softened strut-and-tie model (SST).[35] Performance of this analytical method is evaluated with estimations from existing design codes using a large database of 224 isolated interior flat-plate specimens collated by the authors. The database covers a wide range of material and geometric parametric variations. Details of all these specimens are tabulated in the Appendix[*] of this paper.

ANALYTICAL PROCEDURE FOR PUNCHING CAPACITY ESTIMATION

The proposed analytical approach for punching capacity estimation of RC flat-plate members without shear reinforcement is based on the SST model. This model has been proven to be accurate and reliable in predicting the strength of D-regions (D stands for deformed or discontinuous regions) such as beam-column joints, deep beams, and squat walls.[35,36] The SST model is also efficient in predicting punching capacities of two-way members such as pile caps by evaluating multiple single D-regions formed between

---

[*] The Appendix is available at **www.concrete.org/publications** in PDF format, appended to the online version of the published paper. It is also available in hard copy from ACI headquarters for a fee equal to the cost of reproduction plus handling at the time of the request.

columns and piles.[37,38] The analytical procedure proposed for estimating the punching capacity of flat plates under vertical loading is extended from the previously cited authors' work on pile caps. Unlike pile caps, flat plates are slender members typically characterized by D-B-D regions within a single span. Herein, the term B-region refers to a region where the Bernoulli compatibility condition is satisfied. In the proposed approach, shear and flexural performances of flat plates are separately assessed, and the smaller value of the two is chosen as the member capacity. This section outlines in detail the force transfer mechanisms and capacity estimation procedures used in the proposed approach.

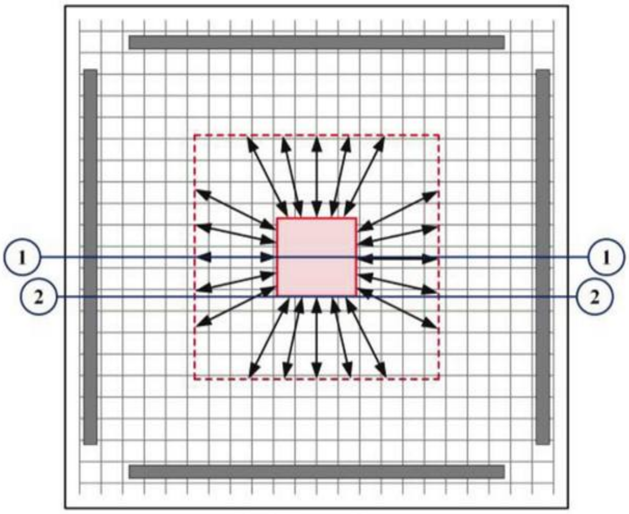

(a) Plan view

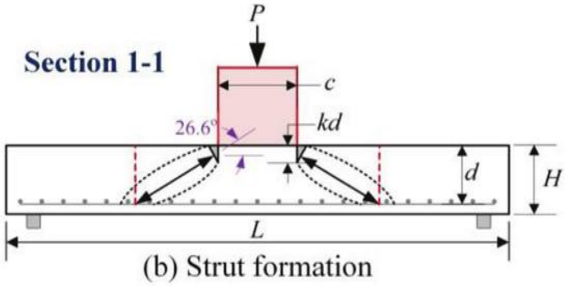

(b) Strut formation

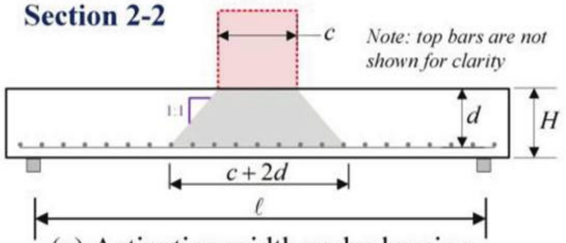

(c) Activation width under bearing

Fig. 4—Strut formation in typical flat-plate member.

Shear capacity

Shear resistance under vertical loading in flat plates is facilitated by the formation of concrete struts emerging from the column. Typical strut formation in a square flat-plate system vertically loaded through a square column is shown in Fig. 4. Shear failure in flat plates is characterized by the development of severe stresses near the column and crushing of concrete struts toward the column. Consequently, the strength of each concrete strut originating from the column region contributes to the overall shear capacity of flat plates. Thus, shear capacity corresponds to the cumulative capacity of all concrete struts originating from the column. The capacity of each strut is dependent on both inclination and area of the concrete strut providing punching resistance.

The inclination of diagonal struts in members with a single D-region within each shear span, such as pile caps and deep beams, depends on the shear span-depth ratio of these members—that is, struts extend from column or loading area to support. However, flat plates typically have high shear span-depth ratios, resulting in the formation of D-B-D regions between column and support. In flat plates, considering concrete struts to extend directly from column to support would lead to very small angles of strut inclinations that are not practical. Thus, a constant inclination angle of 26.6 degrees is assumed for concrete struts in flat plates, which is the lower limit allowed in the conventional strut-and-tie method based on strut stability.[39] Similar inclinations of struts (26.6 degrees relative to the longitudinal axis) were also observed in nonductile columns with insufficient shear reinforcement.[40,41] This limit is commonly accepted, with ACI 318-19 also advocating a similar angle (rounded off to 25 degrees) as a lower limit through Section 23.2.7, particularly for members with insufficient or no shear reinforcement.

Concrete strut area is influenced by both bearing stresses from the column and horizontal compressive stresses generated through flexural actions in flat plates. For the strut formation, which occurs at an early stage of loading, it is not reasonable to consider reinforcement over the entire width. Instead, only the tension reinforcement bars located within a 45-degree influence of truncated pyramid as highlighted in Fig. 4(c) are considered effective for struts. This follows an assumption that bearing pressure is transmitted at a 45-degree angle relative to the direction of loading. Thus, for a typical flat plate depicted in Fig. 4 with a uniformly distributed tension reinforcement of average ratio ρ, equal to A_t/Ld, the reinforcement effective for struts (A_{te}), which contributes to flexural compression, is given by Eq. (7). If tension reinforcement is nonuniformly distributed, ρ is calculated using bar spacing near the column region rather than using an average value.

$$A_{te} = \rho \times d \times (c + 2d) \qquad (7)$$

The width of concrete strut is established through the concept of effective loading width (b_e) that represents the width of stressed region surrounding the column. Both bearing and flexural actions developed within flat plate are considered simultaneously for deriving b_e. This follows an iterative procedure that aims to capture consistent interactions of flexural and bearing actions illustrated in Fig. 5. This iterative procedure aims to derive mutually consistent flexural width (b_f) and shear width (b_s). The procedure can be initialized with any practical value of b_f. However, it is suggested to use $c + d/2$ as a reasonable initial estimate for fast convergence. The corresponding reinforcement ratio is

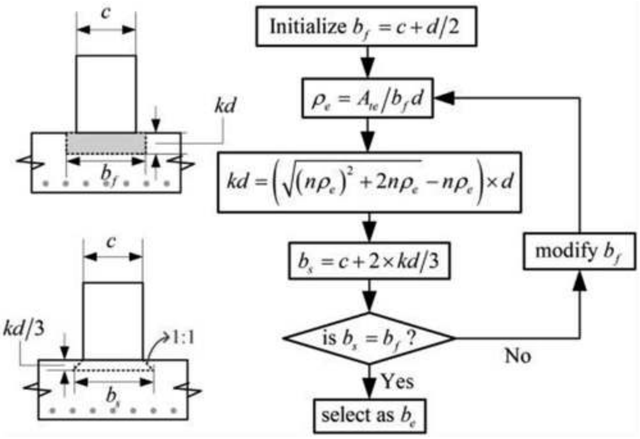

Fig. 5—Flowchart for effective loading width.

calculated using Eq. (8). Assuming a singly reinforced beam with a width b_f and a corresponding reinforcement ratio ρ_e, flexural compression depth is calculated using Eq. (9)

$$\rho_e = A_{te}/b_f d \tag{8}$$

$$kd = \left(\sqrt{(n\rho_e)^2 + 2n\rho_e} - n\rho_e\right) \times d \tag{9}$$

In the next step, b_s is calculated at the centroid of linearly varying flexural compression zone of depth kd considering the bearing stress dispersion into the plate at a 45-degree angle. Thus, b_s in the current iteration is calculated through Eq. (10) and compared with the assumed b_f in the same cycle. If they are not equal, b_f is modified and the next iteration is carried out by selecting a larger value for b_f when b_s is larger than the current b_f, and vice versa.

$$b_s = c + 2 \times kd/3 \tag{10}$$

This iterative procedure is repeated until b_f and the resultant b_s are equal. The width from the final iteration where b_f equals b_s is chosen as the width of the concrete strut (b_e). The area of concrete strut is then estimated as follows

$$A_{str} = b_e \times kd \tag{11}$$

The compression capacity of concrete strut takes into account softening behavior of concrete caused by the presence of transverse tensile strains within the strut. The compression capacity is calculated through Eq. (12). For the calculation of ζ, a simplified expression proposed by Hwang and Lee,[42] as shown in Eq. (13), is adopted.

$$C_d = \zeta f_c' \times A_{str} \tag{12}$$

$$\zeta = 3.35/\sqrt{f_c'}\,(f_c' \text{ in MPa}) \text{ or}$$

$$40/\sqrt{f_c'}\,(f_c' \text{ in psi}) \leq 0.52 \tag{13}$$

Thus, for a typical square flat plate and column arrangement as shown in Fig. 4, vertical punching load required to develop capacities in all four concrete struts (inclined at 26.6 degrees) is calculated using Eq. (14). Subsequently, the ACI-proposed Eq. (4) is adopted to account for size effect. Recall that ACI size effect factor is effective in flat plates when d exceeds 250 mm (10 in.). In case of circular columns, it is recommended to transform them into an equal-area square column for punching capacity estimations. For more complex conditions such as rectangular columns, rectangular plates, or nonequal orthogonal reinforcement arrangements, compression capacities of struts in orthogonal directions may not be equal but considered to contribute fully to the shear capacity.

$$P_{sh} = \lambda_s \Sigma C_d \sin\theta = 4\lambda_s \times C_d \times \sin 26.6° \tag{14}$$

Flexural capacity

Flat plates with low reinforcement ratios are characterized by ductile response initiated by the yielding of tension reinforcement. Large ductility enables flat plates to undergo more significant deformations, engaging more reinforcement and eventually developing a folded plate action. Such flat plates experience flexural punching failure as a result of concrete crushing in flexural compression at flexural critical sections. In such scenarios, adopting the yield-line theory for flat-plate capacity estimations is deemed reasonable.[13] Thus, the flexural punching capacity in flat plates is determined using Bernoulli sectional analysis. Flexural critical sections are positioned at column edges and span the entire length of flat plates between opposite supports. Both compression and tension reinforcement orthogonal to each critical section and located between respective supports are taken into account for calculating the corresponding nominal bending moment capacity. The vertical column load required to generate these nominal bending capacities at critical sections is calculated using the clear spans from the column face to respective supports. Flexural actions on a typical isolated flat-plate specimen with a square column are illustrated in Fig. 6. Line supports in the isolated specimen shown in Fig. 6 represent the inflection line in a prototype structure of a flat plate supported by grids of columns. The total vertical load required to develop nominal bending moments at all critical sections—assumed to occur simultaneously—is given by Eq. (15) for a square flat plate and square column setup. In cases where either the flat plate or column is rectangular, unequal spans in orthogonal directions must be considered to derive the flexural capacity.

$$P_f = \Sigma M_n/a = 4 \times M_n/a \tag{15}$$

The lesser of shear and flexural capacities, obtained by Eq. (14) and (15), respectively, govern the failure mode and overall punching capacity of flat plates using the proposed method.

$$P_{SST} = \min(P_{sh}, P_f) \tag{16}$$

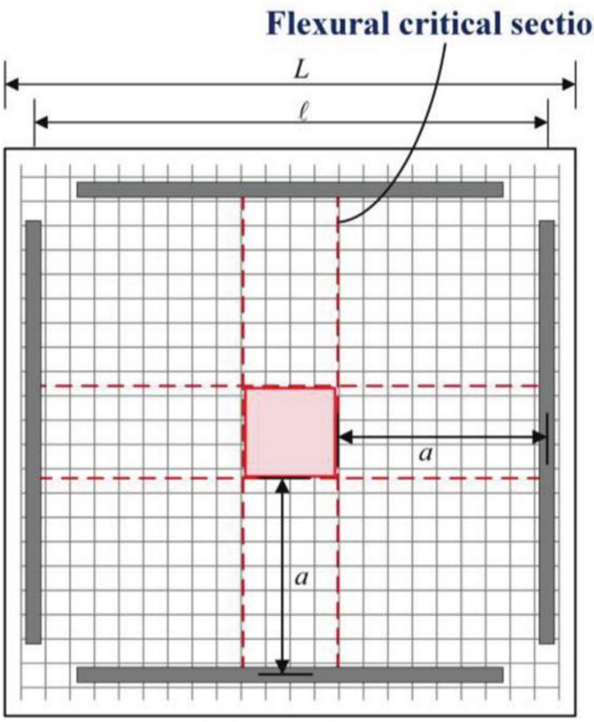

(a) Plan view

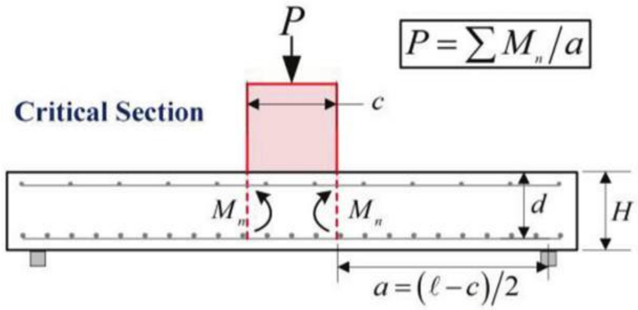

(b) Flexural actions and clear span

Fig. 6—Flexural capacity of typical flat-plate member.

VERIFICATION OF PROPOSED ANALYTICAL METHOD

To verify the robustness and efficacy of the proposed analytical approach, it is important to validate it using a diverse range of test data covering various material, reinforcement, and geometric parameters. To achieve this, the authors gathered a total of 224 isolated flat-plate specimens from 21 different test studies. These studies and the specific parameters varied in each study are listed in Table 1. Detailed information on all specimens can be found in the Appendix.

Capacity estimations for all 224 specimens were determined using three methods: proposed analytical (SST) method, ACI 318-19 method, and Eurocode 2 method. This section presents a comparison of results obtained from these three methods and conducts a relevant discussion. These three methods share a common approach when estimating flexural capacity, but they differ in their assessments of shear capacity. Hence, analyzing the variations in their performances can provide valuable insights into evaluating two-way shear strength provisions in ACI 318-19 and Eurocode 2.

Accuracy of capacity estimations

The punching capacity of flat plates as a function of various key parameters discussed in "Previous Studies" demonstrates the significance of geometry, reinforcement, and material properties. The proposed approach is employed to estimate punching capacities of all 224 specimens in the database, and these estimations are then compared with observed capacities. To gauge the accuracy of the estimates, test-to-estimated capacity ratios (or simply, capacity ratios) are presented. Mean capacity ratios and coefficients of variation (CoV) for each study are reported in Table 1. A mean ratio close to 1.0 and a low CoV indicate accurate predictions. Capacity ratios using ACI 318-19 and Eurocode 2 provisions, which are summarized in the introduction of this manuscript, are also added to Table 1 for comparison. Results in Table 1 show that the proposed SST approach performed reasonably well in estimating the punching capacity of flat plates with a wide range of parametric variations, showing an overall average capacity ratio of 1.20 and a low CoV of 0.19. Eurocode 2 specifications also proved to be reasonably accurate with an overall mean capacity ratio of 1.27, though with a slightly higher CoV of 0.29. On the other hand, ACI 318-19 estimations were more conservative, exhibiting an average capacity ratio of 1.60 and a relatively high CoV of 0.34. Further analysis is conducted to assess the efficiency of these three methods in capturing the influence of key parameters on punching capacities.

Influence of concrete strength and tension reinforcement

Capacity ratios obtained through three methods are compared visually in Fig. 7, along with respective failure modes, to illustrate their efficiency in capturing the influence of concrete strength f_c' (refer to Fig. 7(a) to (c)) and tension reinforcement ratio ρ (refer to Fig. 7(d) to (f)). For readability, x-axes in Fig. 7(d) to (f) are capped at 5% and data from eight specimens with higher ρ values are projected onto this limit line.

As discussed earlier in this manuscript, a higher f_c' is expected to improve punching capacity. The proposed approach suggests that punching capacity is directly proportional to softened concrete strength ($\zeta f_c'$) based on Eq. (12). Further, as per Eq. (13), ζ assumes an upper limit of 0.52 when f_c' is less than 42 MPa (6092 psi) and decreases as $\propto 1/\sqrt{f_c'}$ for above 42 MPa (6092 psi). As a result, capacity predictions using the proposed approach are proportional to f_c' for normal-strength concrete and proportional to $\sqrt{f_c'}$ for high-strength concrete due to the softening phenomenon. For convenience, the term "high strength" is used in this discussion to refer to concrete with a strength greater than 42 MPa (6092 psi). Results of specimens that failed in shear from Fig. 7(a) indicate that the proposed method effectively captured the influence of f_c' for both normal- and high-strength concretes, resulting in consistent capacity ratios close to 1.0. In comparison, ACI 318-19 suggests $v \propto \sqrt{f_c}$,

Table 1—Previous experimental studies and prediction accuracies

				Test-to-estimated capacity ratio					
				SST		ACI 318-19		Eurocode 2	
S. No.	Reference	No.	Parameters varied	AVG	CoV	AVG	CoV	AVG	CoV
1	Alexander and Simmonds[19]	8	f_c', d, ρ, ρ*	1.11	0.12	1.14	0.10	1.12	0.11
2	Banthia et al.[43]	1	—	1.32	—	1.32	—	1.32	—
3	Chen[44]	7	f_c',ρ	1.40	0.12	1.47	0.16	1.18	0.05
4	Chen et al.[45]	2	c, c/d	0.90	0.07	0.99	0.05	0.79	0.04
5	Corley and Hawkins[5]	2	c, ρ, c/d	1.22	0.01	1.35	0.06	0.96	0.02
6	Guandalini et al.[31]	11	d_a, f_c', L, d, c, ρ, c/d, λ_s	1.02	0.14	0.99	0.28	0.84	0.10
7	Hassan et al.[46]	1	—	1.04	—	1.29	—	0.90	—
8	Li[30]	6	L, d, c, ρ, c/d, a/d, λ_s	1.09	0.07	1.21	0.12	0.89	0.19
9	Liao[47]	6	f_c', L, ρ, a/d	1.10	0.15	1.40	0.22	1.26	0.15
10	Lin et al.[15]	64	f_c', f_y, d, c, ρ, c_{max}/c_{min}, c/d, a/d	1.31	0.22	2.15	0.27	1.68	0.23
11	Marzouk and Hussein[12]	17	f_c', d, c, ρ, c/d, a/d	1.07	0.13	1.37	0.19	1.09	0.12
12	Matthys and Taerwe[48]	4	c, ρ, c/d	1.45	0.08	2.03	0.19	1.65	0.02
13	McHarg et al.[18]	2	ρ*	0.98	0.01	1.24	0.07	0.98	0.07
14	Ospina et al.[49]	1	—	1.01	—	1.02	—	1.02	—
15	Rankin and Long[13]	27	f_c', d, c/d	1.20	0.11	1.47	0.25	1.27	0.10
16	Regan[14]	18	d_a, f_c', f_y, L, d, c, ρ, ρ^*, c/d, a/d	1.18	0.13	1.47	0.18	1.13	0.13
17	Roll et al.[50]	8	f_c', f_y, ρ	1.04	0.04	1.47	0.15	1.10	0.06
18	Sistonen et al.[51]	10	f_c', L, c, ρ, c/d	1.32	0.20	1.41	0.08	1.27	0.05
19	Swamy and Ali[20]	3	ρ, ρ^*	1.06	0.07	1.07	0.08	1.04	0.10
20	Tomaszewicz[16]	13	f_c', L, d, c, ρ, c/d, a/d	1.12	0.07	1.50	0.07	0.91	0.08
21	Urban[28]	13	f_c', f_y, c, ρ, c_{max}/c_{min}, c/d	1.14	0.16	1.40	0.22	0.99	0.07
	TOTAL	224	—	1.20	0.19	1.60	0.34	1.27	0.29

which may be reasonable for high-strength concrete but moderately overconservative for normal-strength concrete, which is reflected in Fig. 7(b). On the other hand, Eurocode 2 proposes $v \propto \sqrt[3]{f_c}$, which could result in underestimating the influence of f_c' on shear strength, especially for normal-strength concrete. However, this over-conservativeness is not reflected in Fig. 7(c), as observed in Fig. 7(b) for ACI 318-19, on account of ρ factor in Eurocode 2.

Furthermore, the effect of tension reinforcement ratio (ρ) on punching capacity is particularly noteworthy from Fig. 7(e), revealing that ACI capacity ratios were increasingly over-conservative with addition of tension reinforcement. Recall that ACI 318-19 does not account for the effect of ρ on two-way shear strength. On the other hand, Eurocode 2 estimations performed relatively better (refer to Fig. 7(f)) because these provisions consider shear strength proportional to $\sqrt[3]{\rho}$ (refer to Eq. (5)). However, even with Eurocode 2, underestimation in specimens with high ρ values (>3%) remained. The underestimation in heavily reinforced flat plates is the primary reason for a large scatter of ACI 318-19 and Eurocode 2 results shown in Fig. 7(b) and (c), respectively. The proposed approach considers the effect of ρ through the calculation of kd: high ρ values result in larger kd, which enhances strut capacity, and vice versa. As a result, the proposed analytical approach produced consistent capacity ratios over a wide range of ρ values, as depicted in Fig. 7(d). Additionally, the benefit to punching capacity with concentration of tension reinforcement near the column region is also well captured through the proposed SST method. The concentrated tension reinforcement is considered in A_{te} (Eq. (7)), which enhances strut depths and their corresponding capacities. Overall, the SST estimated punching capacities closely match test capacities in flat plates despite wide variation in ρ. This lends support to the function of tension reinforcement suggested by the proposed approach in punching resistance in flat-plate members.

It is also worth noting that previous research[52,53] on one-way shear members recognizes the softened concrete strength ($\zeta f_c'$) and tension reinforcement ratio (ρ) as two critical factors influencing failure due to shear compression. This aligns with the view of the proposed analytical model that shear punching in flat plates is a form of shear compression failure. Only 23 out of 224 specimens were predicted to experience flexural failure by the proposed approach, and all of them with ρ under 0.6%. Therefore, it is reasonable to conclude that punching in flat plates (except those with very low ρ) is generally controlled by shear.

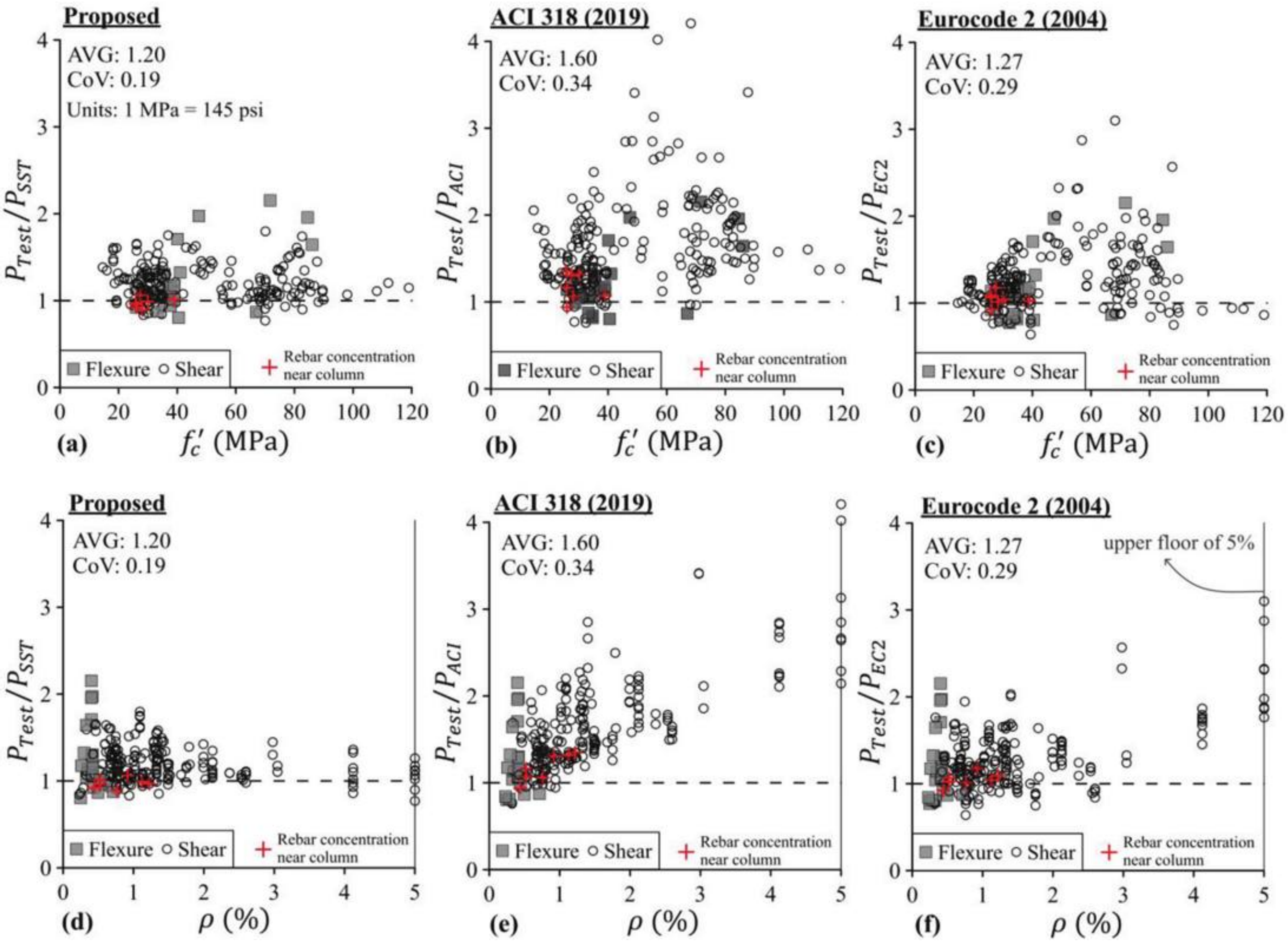

Fig. 7—Comparison of test-to-estimated capacity ratios.

Influence of geometric variations

The variation of ACI normalized peak shear stresses with geometric ratios such as c/d, c_{max}/c_{min}, and b_o/d are shown in Fig. 8. For failure classification, SST predicted failure modes were adopted. The influence of geometric parameters on punching strength, as well as relevant provisions from ACI 318-19, are assessed through subplots Fig. 8(a) to (c). These plots show that much scatter is observed in normalized shear strengths with all three geometric parameters considered; and importantly, no clear trend in strength is observed with these parameters. ACI 318-19 penalizes two-way shear strength when $c_{max}/c_{min} \geq 2$ and $b_o/d \geq 20$ through Section 22.6.5.2(b) (Eq. (2)) and Section 22.6.5.2(c) (Eq. (3)) respectively, whereas no specific provisions are applicable to capture the effect of c/d. While Fig. 8(b) showing no obvious trend in reduction of shear strength in flat plates with $c_{max}/c_{min} \geq 2$ suggests that penalizing shear strength for higher aspect ratio through Eq. (2) may not be necessary, more data on flat plates with $b_o/d \geq 20$ are necessary to comment on Eq. (3).

The proposed SST approach efficiently captured the influence of geometric parameters, resulting in more consistent stress ratios (test-to-estimated) close to 1.0 with all geometric variations, as shown in Fig. 8(d) to (f). These plots demonstrate that the proposed model efficiently captured geometric effects on shear strength, thereby reducing the scatter substantially. According to the proposed model, impact of c/d is accounted for through strut area calculations: a larger c value increases the strut area and corresponding capacity, and vice versa. Column rectangularity is taken into account by considering different strut areas (and capacities) in orthogonal directions. By reasonably capturing the influence of these two parameters, the proposed model produced consistent capacity ratios, even with variation in b_o/d, which can be seen as a derivative of c/d and c_{max}/c_{min}.

RECOMMENDATIONS FOR CODE PROVISIONS

Normalized test shear strengths of all 224 flat plates are plotted in Fig. 9 against f_c' and ρ to analyze current design provisions of ACI 318-19 and Eurocode 2, specifically Eq. (1) and (5), respectively. Recall that shear strength varies in proportion to $\sqrt{f_c'}$ in ACI 318-19 versus $\sqrt[3]{f_c'}$ in Eurocode 2. Additionally, ACI 318-19 does not consider the effect of ρ on two-way shear strength, whereas Eurocode 2 provisions consider that shear strength varies in proportion to $\sqrt[3]{\rho}$. Due to these differences, normalization is carried out separately for ACI 318-19 and Eurocode 2, considering respective parameters. Strictly speaking, Eq. (1) and (5) are applicable only in case of specimens with shear failure. Thus, a classification of data with failure modes (flexure versus shear) becomes necessary. Ideally, experimental failure modes

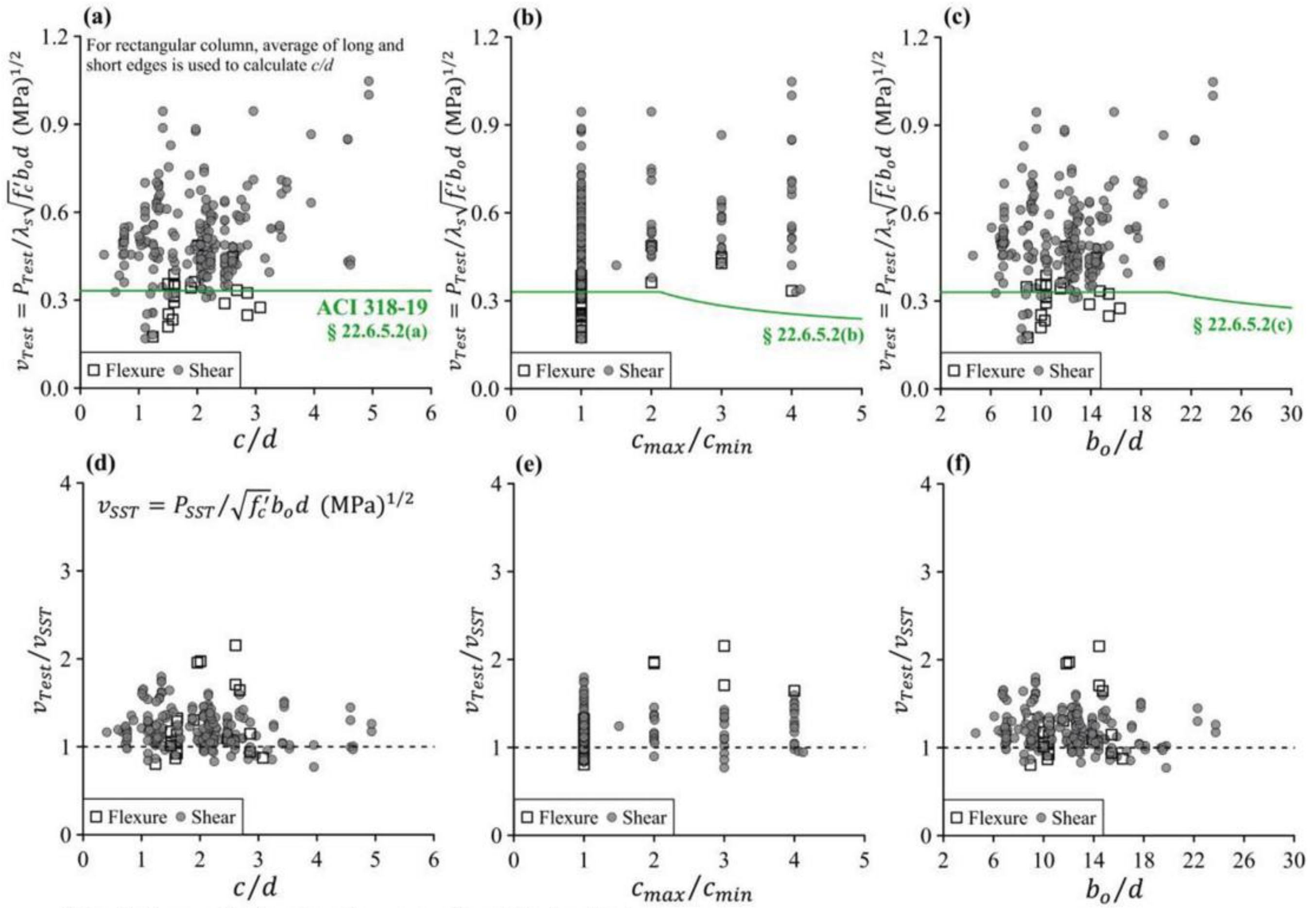

Note: Failure modes based on the proposed analytical method

Fig. 8—Model efficiency with geometric parameters.

should be used to segregate shear-controlled specimens. However, such information is not available in many studies. Therefore, failure modes predicted using the proposed SST approach are chosen for classification in Fig. 9.

Variation of test strengths calculated upon ACI critical sections with f_c' is shown in Fig. 9(a). Although a handful of specimens lie below the green-colored ACI prediction line (indicating unsafe estimation), many of them failed in flexure and therefore can be ignored for assessing Eq. (1) (Note: Full-color PDF of this paper can be accessed at www.concrete.org.). Despite a considerable scatter, observed trends support ACI's consideration that shear strength conservatively varies in proportion with $\sqrt{f_c}$ for concrete strength up to 100 MPa (14.5 ksi). From Fig. 9(c), it is evident that higher normalized strengths are observed in heavily reinforced flat plates, which is the main cause of a large scatter in Fig. 9(a). It is also evident that Eq. (1) produced unsafe predictions in flat plates with ρ less than 1%. The function of tension reinforcement as highlighted and validated by the proposed analytical approach underscores the need for incorporating a reinforcement factor into ACI 318-19 provisions for two-way shear strength. Such an inclusion could significantly enhance estimation accuracy and help designers address practical engineering challenges more efficiently. This is illustrated in Fig. 9(c) where the inclusion of $\sqrt[3]{100\rho}$ to Eq. (1) (indicated by the dashed line) is shown to capture the increasing trend in shear strengths reasonably well. Because ACI 318-19 already adopts a cube root expression for one-way shear, it is reasonable and convenient to extend the same to two-way shear. This modification not only mitigates severe underestimation in heavily reinforced plates but also addresses some unsafe shear estimations in flat plates with ρ less than 1%. Overall, this modification would improve the accuracy of ACI 318-19 for two-way shear strength while maintaining a reasonable level of conservatism. The cube root expression for reinforcement factor is also supported by Cladera et al.,[54] who suggested that neutral axis depth is proportional to $\sqrt[3]{\rho}$.

Variation of test strengths calculated upon the Eurocode 2 suggested critical section with f_c' is shown in Fig. 9(b). As Eurocode 2 includes reinforcement factor, predictions (magenta lines) using different ρ values at 0.5% (typical) and 2% (maximum permitted in Eq. (5)) are plotted separately. Several data points are considerably farther from the upper magenta line, indicating severe underestimation in many specimens. Further analysis using Fig. 9(d) reveals that even after eliminating the upper limit of 2% for ρ in estimation of two-way shear strength, predictions remained reasonably conservative. Hence, it is recommended that the upper cap for ρ (currently set at 2%) for shear strength estimation in Eurocode 2 may not be necessary. This recommendation is also consistent with the suggested ACI 318-19 modification, as well as with the proposed analytical approach.

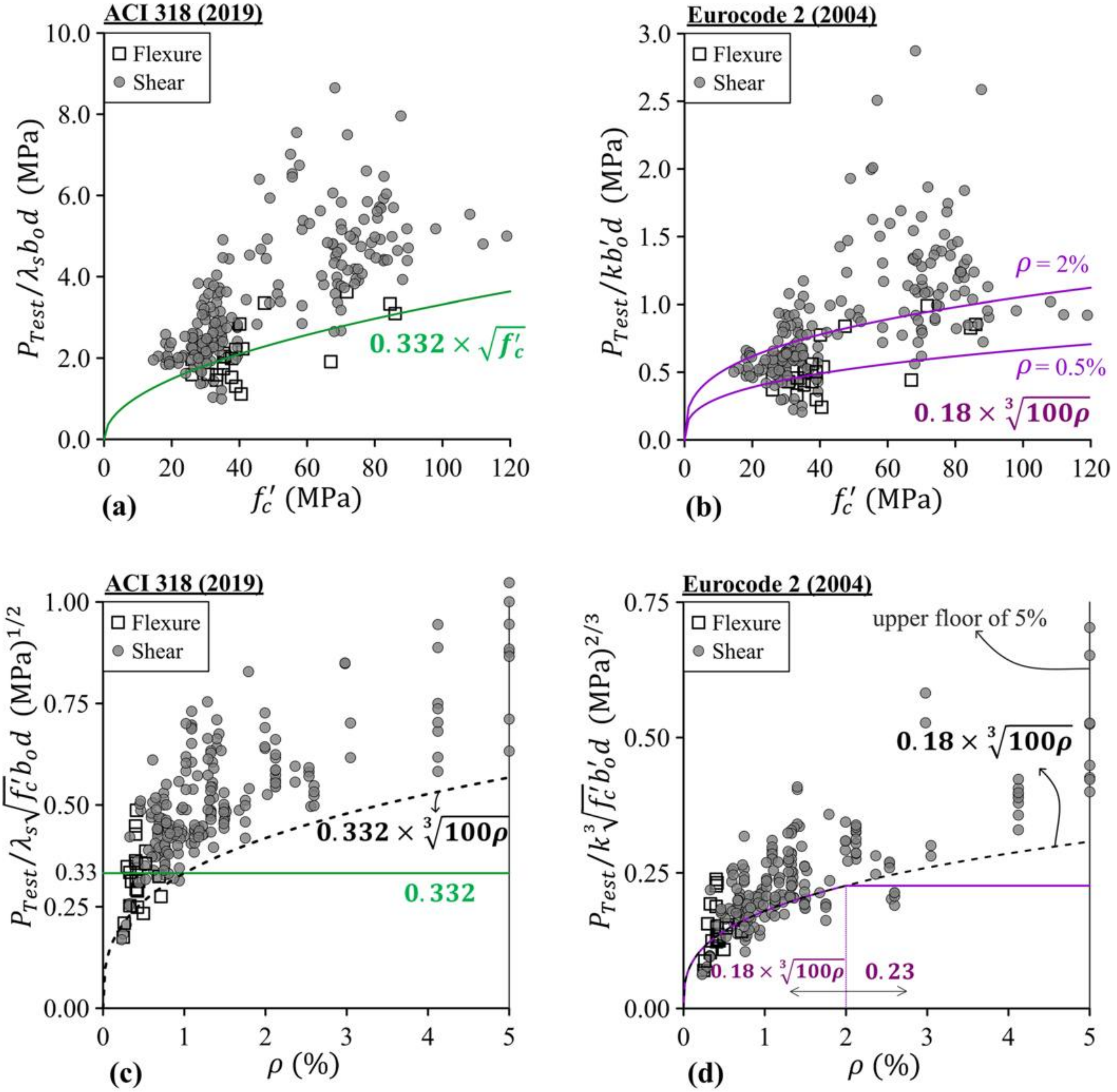

Units: 1 MPa = 145 psi; 100 mm = 3.94 in.
Note: Failure modes based on the proposed SST approach

Fig. 9—Performance of code equations and proposed suggestions.

Furthermore, concerning size effect in two-way shear, Fig. 10 compares the provisions of ACI 318-19 and Eurocode 2 with observed normalized shear strengths varying with d. Normalization was carried out with all ACI parameters in Eq. (1) other than λ_s in Fig. 10(a). Comparisons with the ACI size effect (green-colored line) show some unsafe shear estimations—that is, data points lying below the prediction line. However, as previously discussed in this paper, this could be attributed to the absence of ρ factor. Therefore, shear strengths in Fig. 10(a) are further normalized with $100\rho^{1/3}$ to plot modified ACI normalized shear strengths in Fig. 10(b). The results demonstrate satisfactory performance of modified ACI provisions, including the size effect recommendation by conservatively capturing the unit shear strength reduction in thick plates (d over 250 mm [10 in.]). Therefore, it is recommended that quantification of strength drop due to size effect should be evaluated with normalization of shear strength incorporating the ρ factor. It is also worth noting that the authors' suggestion to improve the ACI size effect based on pile cap tests to use cube root (denoted by λ_p) instead of square root also provided safe size effect estimations. However, it must be noted that differences in λ_s versus λ_p may be significant for pile caps but not as much for flat plates, where d rarely exceeds 600 mm (24 in.).

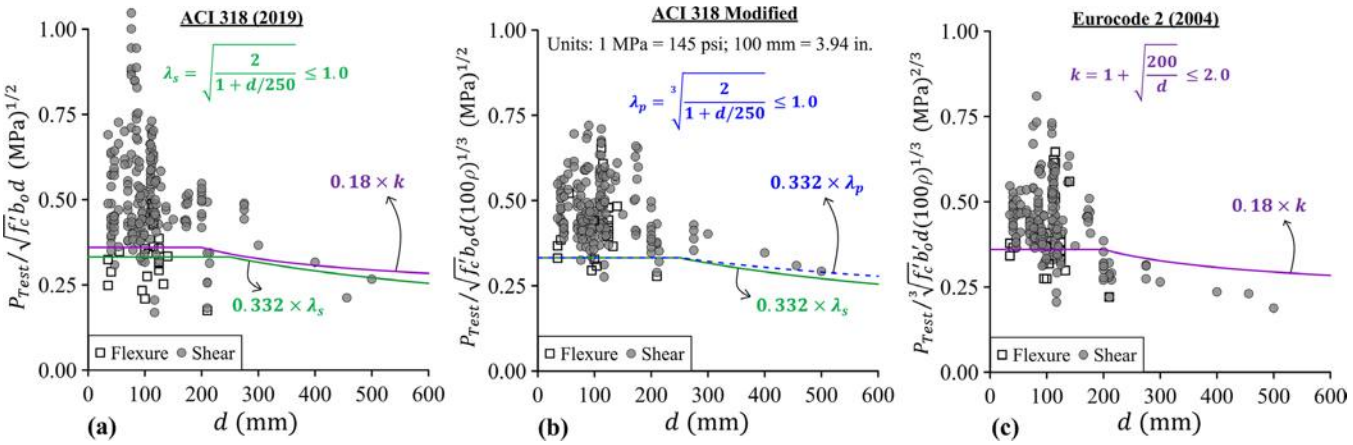

Fig. 10—Size effect in flat plates.

A similar plot is generated for Eurocode 2, wherein observed shear strengths are normalized with all Eurocode 2 parameters other than k and plotted against d, as shown in Fig. 10(c). The findings indicate that estimations provided by Eurocode 2 may be slightly inadequate for thicker slabs. This is despite both λ_s and $k/2$ exhibiting proportionality to $1/\sqrt{d}$, which results in similar size effect penalties. Thus, Eurocode 2 overestimation in thick slabs is not attributed to k. Instead, the reason for this overestimation lies in normalization, particularly in the control perimeter of Eurocode 2. For instance, the control perimeter b_o' in Eurocode 2 is located at a distance $2d$ away from the column, as opposed to b_o in ACI 318-19, which is located at one-fourth that distance. As d increases, b_o' increases at a faster rate than b_o, thereby more severely suppressing normalized shear strength in thicker plates. One way to address this is to shift the control section inwards, closer to b_o for the calculation of Eurocode 2 punching shear capacity, especially in thick flat plates. Furthermore, a comparison with the proposed approach reveals that punching is more accurately depicted through concrete crushing around the column. In other words, b_e is a more realistic measure to assess the punching phenomenon. Based on the collated database, the average b_e is found to be close to $c + 0.3d$. The ACI control section width is closer to this value and therefore resulted in better estimates in thick slabs, as shown in Fig. 10(b). On the contrary, the control section width in Eurocode 2 is positioned much farther away, especially for thick plates, resulting in unsafe Eurocode 2 predictions for such cases. Therefore, it is suggested that the location of control section for punching in two-way shear should be consistent with the concrete crushing phenomenon, and therefore, a control section width closer to b_e is more reasonable for punching. However, to comprehensively tackle this problem, a more extensive investigation of deep two-way shear members is necessary.

CONCLUSIONS

A novel analytical approach is proposed for assessing punching capacity in flat plates. In this approach, the load resistance is determined by considering multiple concrete struts in shear, with the strength of each strut independently evaluated using the softened strut-and-tie (SST) model. For estimating flexural capacity, nominal flexural bending moments in the flat plate are used. The proposed approach can not only account for primary parameters such as concrete strength and tension reinforcement ratio but also capture effects of geometric ratios such as c/d, c_{max}/c_{min}, and b_o/d. The analytical model also highlighted the functions of these parameters in punching resistance. The proposed model is verified using a database of 224 monotonically loaded isolated interior flat-plate specimens gathered from various studies and also compared with estimations using ACI 318-19 and Eurocode 2 two-way shear provisions. Test-to-estimated capacity ratios show that the proposed model is reasonably accurate in punching capacity predictions with an overall mean of 1.20 and a low coefficient of variation of 0.19, compared to 1.60 (0.34) for ACI 318-19 and 1.27 (0.29) for Eurocode 2. The proposed approach is simple yet accurate and it can be adopted for design purposes by engineers.

The underestimation of ACI 318-19 in punching capacity is primarily attributed to the omission of the tension reinforcement factor for two-way shear strength. Based on an analysis of normalized test shear strengths, it is proposed to enhance the existing ACI 318-19 provisions by incorporating $\sqrt[3]{100\rho}$ as a reinforcement factor. Furthermore, it is also suggested to reconsider the upper limit of 2.0% for ρ in Eurocode 2 provisions. Omission of this limit is shown to result in better (yet conservative) shear strength estimations, particularly in heavily reinforced flat plates with ρ exceeding 2.0%. Underestimation of punching strength using Eurocode 2 in thick flat plates is highlighted and attributed to the definition of control perimeter. It is also recommended to assess the size effect in two-way shear after incorporating the reinforcement factor for the calculation of unit shear strength.

AUTHOR BIOS

Srinivas Mogili *is a Postdoctoral Researcher at National Taiwan University, Taipei, Taiwan. He received his PhD from The Hong Kong University of Science and Technology, Hong Kong, China. His research interests include seismic design, analysis, and testing of reinforced concrete members such as beam-column joints, columns, pile caps, and flat slabs.*

Hsiang-Yun Lin *received her master's degree in civil engineering from National Taiwan University. Her research interests include reinforced concrete design and analysis of flat plates.*

Shyh-Jiann Hwang, *FACI, is a Professor of civil engineering at National Taiwan University. He received his PhD from the University of California, Berkeley, Berkeley, CA. His research interests include seismic behavior of reinforced concrete members and seismic retrofitting of reinforced concrete structures.*

ACKNOWLEDGMENTS

Funding support from the National Science and Technology Council, Taiwan under Grant No. 109-2221-E-002-007-MY3 and 110-2811-E-002-549-MY2 is acknowledged by the authors.

NOTATION

A_c = total area of compression reinforcement in each orthogonal direction
A_{str} = area of concrete strut
A_t = total area of tension reinforcement in each orthogonal direction
A_{te} = tension reinforcement area located within $c + 2d$ in each orthogonal direction
A_t^* = extra tension reinforcement provided near column within $c + 2d$ in each orthogonal direction (beyond standard uniformly distributed reinforcement), representing concentration of reinforcement
a = perpendicular distance from column face to support
b_e = effective loading width (also, width of concrete strut)
b_f = equivalent concrete width resisting flexural actions
b_o = perimeter of critical section located $d/2$ away from column in all directions
b_o' = perimeter of critical section located $2d$ away from column in all directions
b_s = shear width activated by bearing actions
C_d = compression capacity of strut
c_{max} = long dimension of rectangular column
c_{min} = short dimension of rectangular column
d = effective depth, measured from compression face to centroid of tension reinforcement
f_c' = cylinder concrete compressive strength
k = size effect factor in Eurocode 2
kd = depth of flexural compression zone
L = geometric plan dimension of flat-plate specimens
ℓ = perpendicular distance between opposite supports in flat-plate specimens
M_n = nominal bending capacity of section located at column face of width ℓ
n = ratio of elastic moduli of reinforcing steel and concrete
P = vertical punching load acting on flat plates
P_{ACI} = punching load capacity estimated using ACI 318-19
P_{EC2} = punching load capacity estimated using Eurocode 2
P_f = flexural capacity estimated using proposed method
P_{sh} = shear capacity estimated using proposed method
P_{SST} = overall punching capacity estimated using proposed method
P_{Test} = experimental vertical punching load capacity
β = ratio of long to short sides of column or reaction area—that is, c_{max}/c_{min}
γ_c = partial safety factor for concrete in Eurocode 2
λ_p = size effect factor suggested by authors
λ_s = size effect factor in ACI 318-19
θ = strut inclination in flat plates (assumed to be 26.6 degrees)
ρ = average longitudinal tension reinforcement ratio in each orthogonal direction
ρ' = average longitudinal compression reinforcement ratio in each orthogonal direction
ρ^* = concentrated tension reinforcement ratio, estimated as $A_t^*/(c + 2d)d$
ρ_e = effective tension reinforcement ratio for strut width
υ = experimental two-way shear strength calculated on ACI-defined critical section
υ_{ACI} = two-way shear strength estimated using ACI 318-19 provisions
υ_{EC2} = two-way shear strength estimated using Eurocode 2 provisions
ζ = softening coefficient adopted in SST model

REFERENCES

1. Hawkins, N. M., and Mitchell, D., "Progressive Collapse of Flat Plate Structures," *ACI Journal Proceedings*, V. 76, No. 7, July 1979, pp. 775-808.

2. Ma, F.; Gilbert, B. P.; Guan, H.; Lu, X.; and Li, Y., "Experimental Study on the Progressive Collapse Behaviour of RC Flat Plate Substructures Subjected to Edge-Column and Edge-Interior-Column Removal Scenarios," *Engineering Structures*, V. 209, 2020, p. 110299. doi: 10.1016/j.engstruct.2020.110299

3. Sherif, A. G., and Dilger, W. H., "Tests of Full-Scale Continuous Reinforced Concrete Flat Slabs," *ACI Structural Journal*, V. 97, No. 3, May 2000, pp. 455-467.

4. Cho, Y. S.; Noh, S. Y.; and Kim, H. W., "Punching Shear Reinforcing Using Studs with Steel Plates in Reinforced Concrete Flat Plates," *Magazine of Concrete Research*, V. 61, No. 9, 2009, pp. 721-729. doi: 10.1680/macr.2008.61.9.721

5. Corley, W. G., and Hawkins, N. M., "Shearhead Reinforcement for Slabs," *ACI Journal Proceedings*, V. 65, No. 10, Oct. 1968, pp. 811-824.

6. Yamada, T.; Nanni, A.; and Endo, K., "Punching Shear Resistance of Flat Slabs: Influence of Reinforcement Type and Ratio," *ACI Structural Journal*, V. 88, No. 4, July-Aug. 1992, pp. 555-563.

7. Schmidt, P.; Kueres, D.; and Hegger, J., "Punching Shear Behavior of Reinforced Concrete Flat Slabs with a Varying Amount of Shear Reinforcement," *Structural Concrete*, V. 21, No. 1, 2020, pp. 235-246. doi: 10.1002/suco.201900017

8. ACI Committee 318, "Building Code Requirements for Structural Concrete (ACI 318-19) and Commentary (ACI 318R-19) (Reapproved 2022)," American Concrete Institute, Farmington Hills, MI, 2019, 624 pp.

9. EN 1992-1-1:2004, "Eurocode 2: Design of Concrete Structures − Part 1-1 General Rules and Rules for Buildings," European Committee for Standardization, Brussels, Belgium, 2004, 230 pp.

10. Joint ASCE-ACI Committee 426, "The Shear Strength of Reinforced Concrete Members—Slabs," *Journal of the Structural Division*, ASCE, V. 100, No. 8, 1974, pp. 1543-1591. doi: 10.1061/JSDEAG.0003838

11. Vanderbilt, M. D., "Shear Strength of Continuous Plates," *Journal of the Structural Division*, ASCE,V. 98, No. 5, 1972, pp. 961-973. doi: 10.1061/JSDEAG.0003248

12. Marzouk, H., and Hussein, A., "Experimental Investigation on the Behavior of High-Strength Concrete Slabs," *ACI Structural Journal*, V. 88, No. 6, Nov.-Dec. 1991, pp. 701-713.

13. Rankin, G. I. B., and Long, A. E., "Predicting the Punching Strength of Conventional Slab-Column Specimens," *Proceedings - Institution of Civil Engineers*, V. 82, No. 2, 1987, pp. 327-346. doi: 10.1680/iicep.1987.382

14. Regan, P. E., "Symmetric Punching of Reinforced Concrete Slabs," *Magazine of Concrete Research*, V. 38, No. 136, 1986, pp. 115-128. doi: 10.1680/macr.1986.38.136.115

15. Lin, I. J.; Lin, C. J.; and Lin, S. L., "Punching Shear of Reinforced Concrete Slabs," *Journal of Chinese Institute of Civil and Hydraulic Engineering*, V. 8, No. 1, 1996, pp. 75-82. (in Chinese)

16. Tomaszewicz, A., "High Strength Concrete: SP2 - Plates and Shells Report 2.3. Punching Shear Capacity of Reinforced Concrete Slabs," Report No. STF70A93082, SINTEF, Trondheim, Norway, 1993.

17. Hallgren, M., "Punching Shear Capacity of Reinforced High Strength Concrete Slabs," doctoral thesis, KTH Royal Institute of Technology, Stockholm, Sweden, 1996.

18. McHarg, P. J.; Cook, W. D.; and Mitchell, D., "Benefits of Concentrated Slab Reinforcement and Steel Fibers on Performance of Slab-Column Connections," *ACI Structural Journal*, V. 97, No. 2, Mar.-Apr. 2000, pp. 225-234.

19. Alexander, S. D. B., and Simmonds, S. H., "Tests of Column-Flat Plate Connections," *ACI Structural Journal*, V. 89, No. 5, Sept.-Oct. 1992, pp. 495-502.

20. Swamy, R. N., and Ali, S. A. R., "Punching Shear Behavior of Reinforced Slab-Column Connections Made with Steel Fiber Concrete," *ACI Journal Proceedings*, V. 79, No. 5, Sept.-Oct. 1982, pp. 392-406.

21. Dilger, W.; Birkle, G.; and Mitchell, D., "Effect of Flexural Reinforcement on Punching Shear Resistance," *Punching Shear in Reinforced Concrete Slabs*, SP-232, M. A. Polak, ed., American Concrete Institute, Farmington Hills, MI, 2005, pp. 57-74.

22. Moehle, J., *Seismic Design of Reinforced Concrete Buildings*, McGraw-Hill Education, New York, NY, 2015.

23. Habibi, F.; Cook, W. D.; and Mitchell, D., "Predicting Post-Punching Shear Response of Slab-Column Connections," *ACI Structural Journal*, V. 111, No. 1, Jan.-Feb. 2014, pp. 123-134.

24. Ramdane, K. E., "Punching Shear of High Performance Concrete Slabs," 4th International Symposium on Utilization of High Strength High Performance Concrete, Paris, France, 1996, pp. 1015–26.

25. Osman, M.; Marzouk, H.; and Helmy, S., "Behavior of High-Strength Lightweight Concrete Slabs under Punching Loads," *ACI Structural Journal*, V. 97, No. 3, May-June 2000, pp. 492-498.

26. Hawkins, N. M.; Fallsen, H. B.; and Hinojosa, R. C., "Influence of Column Rectangularity on the Behavior of Flat Plate Structures," *Cracking, Deflection and Ultimate Load of Concrete Slab Systems*, SP-30, American Concrete Institute, Farmington Hills, MI, 1971, pp. 127-146.

27. Lips, S.; Ruiz, M. F.; and Muttoni, A., "Experimental Investigation on Punching Strength and Deformation Capacity of Shear-Reinforced Slabs," *ACI Structural Journal*, V. 109, No. 6, Nov.-Dec. 2012, pp. 889-900.

28. Urban, T., "Nośność na Przebicie w Aspekcie Proporcji Boków Słupa [Punching Resistance in Terms of Column Side Proportions]," Report 3, Łódź, Poland, Katedra Budownictwa Betonowego, Politechnika Łódzka, 1994, 76 pp. (in Polish)

29. Oliveira, D. R. C.; Regan, P. E.; and Melo, G. S. S. A., "Punching Resistance of RC Slabs with Rectangular Columns," *Magazine of Concrete Research*, V. 56, No. 3, 2004, pp. 123-138. doi: 10.1680/macr.2004.56.3.123

30. Li, K. K. L., "Influence of Size on Punching Shear Strength of Concrete Slabs," MS thesis, McGill University, Montreal, QC, Canada, 2000.

31. Guandalini, S.; Burdet, O. L.; and Muttoni, A., "Punching Tests of Slabs with Low Reinforcement Ratios," *ACI Structural Journal*, V. 106, No. 1, Jan.-Feb. 2009, pp. 87-95.

32. Bažant, Z. P., and Sun, H.-H., "Size Effect in Diagonal Shear Failure: Influence of Aggregate Size and Stirrups," *ACI Materials Journal*, V. 84, No. 4, July-Aug. 1987, pp. 259-272.

33. Bažant, Z. P., and Cao, Z., "Size Effect in Punching Shear Failure of Slabs," *ACI Structural Journal*, V. 84, No. 1, Jan.-Feb. 1987, pp. 44-53.

34. Dönmez, A., and Bažant, Z. P., "Size Effect on Punching Strength of Reinforced Concrete Slabs with and without Shear Reinforcement," *ACI Structural Journal*, V. 114, No. 4, July-Aug. 2017, pp. 875-886. doi: 10.14359/51689719

35. Hwang, S. J.; Tsai, R. J.; Lam, W. K.; and Moehle, J. P., "Simplification of Softened Strut-and-Tie Model for Strength Prediction of Discontinuity Regions," *ACI Structural Journal*, V. 114, No. 5, Sept.-Oct. 2017, pp. 1239-1248. doi: 10.14359/51689787

36. Mogili, S.; Kuang, J. S.; and Hwang, S. J., "Predicting Shear Strength of Reinforced Concrete Knee Joints in Closing and Opening Actions," *Journal of Structural Engineering*, ASCE, V. 146, No. 6, 2020, pp. 1-11. doi: 10.1061/(ASCE)ST.1943-541X.0002633

37. Mogili, S., and Hwang, S. J., "Softened Strut-and-Tie Model for Shear and Flexural Strengths of Reinforced Concrete Pile Caps," *Journal of Structural Engineering*, ASCE, V. 147, No. 11, 2021, p. 04021169. doi: 10.1061/(ASCE)ST.1943-541X.0003141

38. Mogili, S.; Hwang, S. J.; and Wu, P. W., "Estimating the Punching Shear Capacity of Reinforced Concrete Pile Caps," 17th World Conference on Earthquake Engineering, 17WCEE, Sendai, Japan, 2020, p. C002938.

39. Thurlimann, B., "Shear Strength of Reinforced and Prestressed Concrete-CEB Approach," *Concrete Design: U.S. and European Practices − ACI-CEB-PCI-FIP Symposium*, SP-59, American Concrete Institute, Farmington Hills, MI, 1979, pp. 93-116.

40. Shen, W. C.; Hwang, S. J.; and Li, Y. A., "Force-Displacement Model for Shear-Critical Reinforced Concrete Columns," *ACI Structural Journal*, V. 118, No. 1, Jan. 2021, pp. 241-249.

41. Li, Y. A.; Weng, P. W.; and Hwang, S. J., "Seismic Performance of Reinforced Concrete Intermediate Short Columns Failed in Shear," *ACI Structural Journal*, V. 116, No. 3, May 2019, pp. 195-206. doi: 10.14359/51713309

42. Hwang, S. J., and Lee, H. J., "Strength Prediction for Discontinuity Regions by Softened Strut-and-Tie Model," *Journal of Structural Engineering*, ASCE, V. 128, No. 12, 2002, pp. 1519-1526. doi: 10.1061/(ASCE)0733-9445(2002)128:12(1519)

43. Banthia, N.; Al-Asaly, M.; and Ma, S., "Behavior of Concrete Slabs Reinforced with Fiber-Reinforced Plastic Grid," *Journal of Materials in Civil Engineering*, ASCE, V. 7, No. 4, 1995, pp. 252-257. doi: 10.1061/(ASCE)0899-1561(1995)7:4(252)

44. Chen, S. L., "Punching Shear Behavior of Slab-Column Connections Strengthen with Carbon-Reinforced-Plastic Laminates," MS thesis, National Chiao Tung University, Hsinchu, Taiwan, 2000. (in Chinese)

45. Chen, C. C.; Giduquio, M. B.; Chang, S.-C. L.; and Cheng, M.-Y., "Punching Shear Capacity of RC Slab-CFT Column Connections," *Engineering Structures*, V. 218, 2020, p. 110785.

46. Hassan, M.; Rahman, A. M. A.; and Sherif, A., "Pilot Experimental Tests on Punching Shear Strength of Flat Plates Reinforced with Stirrups Punching Shear Reinforcement," *Journal of Materials and Engineering Structures*, V. 4, No. 1, 2017, pp. 3-10.

47. Liao, J. S., "Fire Resistance and Punching Shear Capacity after Fire of Reinforced Concrete Slabs," MS thesis, National Chiao Tung University, Hsinchu, Taiwan, 2013. (in Chinese)

48. Matthys, S., and Taerwe, L., "Concrete Slabs Reinforced with FRP Grids. II: Punching Resistance," *Journal of Composites for Construction*, ASCE, V. 4, No. 3, 2000, pp. 154-161. doi: 10.1061/(ASCE)1090-0268(2000)4:3(154)

49. Ospina, C. E.; Alexander, S. D. B.; and Roger Cheng, J. J., "Punching of Two-Way Concrete Slabs with Fiber-Reinforced Polymer Reinforcing Bars or Grids," *ACI Structural Journal*, V. 100, No. 5, Sept.-Oct. 2003, pp. 589-598.

50. Roll, F.; Zaidi, S. T. H.; Sabnis, G.; and Chuang, K., "Shear Resistance of Perforated Reinforced Concrete Slabs," *Cracking, Deflection and Ultimate Load of Concrete Slab Systems*, SP-30, American Concrete Institute, Farmington Hills, MI, 1971, pp. 77-102.

51. Sistonen, E.; Mika, L.; and Seppo, H., "Teräsbetonilaatan Lävistyskapasiteetinlaskentakaavan Geometrinen Malli [The Geometrical Model of the Calculation Formula of the Punching Shear Capacity of the Reinforced Concrete Slab]," Report No. 69, Helsinki University of Technology, Espoo, Finland, 1997, 95 pp. (in Finnish)

52. Hwang, S. J.; Yang, Y. H.; and Li, Y. A., "Maximum Shear Strength of Reinforced Concrete Beams," *ACI Structural Journal*, V. 119, No. 2, Mar. 2022, pp. 19-30.

53. Hwang, S. J.; Yang, Y. H.; and Li, Y. A., "Maximum Shear Strength of Reinforced Concrete Deep Beams," *ACI Structural Journal*, V. 118, No. 6, Nov. 2021, pp. 155-164.

54. Cladera, A.; Marí, A.; Bairán, J.-M.; Oller, E.; and Ribas, C., "One-Way Shear Design Method Based on a Multi-Action Model," *Concrete International*, V. 39, No. 9, Sept. 2017, pp. 40-46.

ACI STRUCTURAL JOURNAL

The American Concrete Institute (ACI) is a leading authority and resource worldwide for the development and distribution of consensus-based standards and technical resources, educational programs, and certifications for individuals and organizations involved in concrete design, construction, and materials, who share a commitment to pursuing the best use of concrete.

Individuals interested in the activities of ACI are encouraged to explore the ACI website for membership opportunities, committee activities, and a wide variety of concrete resources. As a volunteer member-driven organization, ACI invites partnerships and welcomes all concrete professionals who wish to be part of a respected, connected, social group that provides an opportunity for professional growth, networking, and enjoyment.

aci®
American Concrete Institute